MATERIALS RESEARCH SOCIETY
SYMPOSIUM PROCEEDINGS VOLUME 407

Disordered Materials and Interfaces

Symposium held November 27-30, 1995, Boston, Massachusetts, U.S.A.

EDITORS:

Herman Z. Cummins
City College of New York
New York, New York, U.S.A.

Douglas J. Durian
University of California, Los Angeles
Los Angeles, California, U.S.A.

David L. Johnson
Schlumberger-Doll Research Center
Ridgefield, Connecticut, U.S.A.

H. Eugene Stanley
Boston University
Boston, Massachusetts, U.S.A.

DISTRIBUTION STATEMENT A
Approved for public release;
Distribution Unlimited

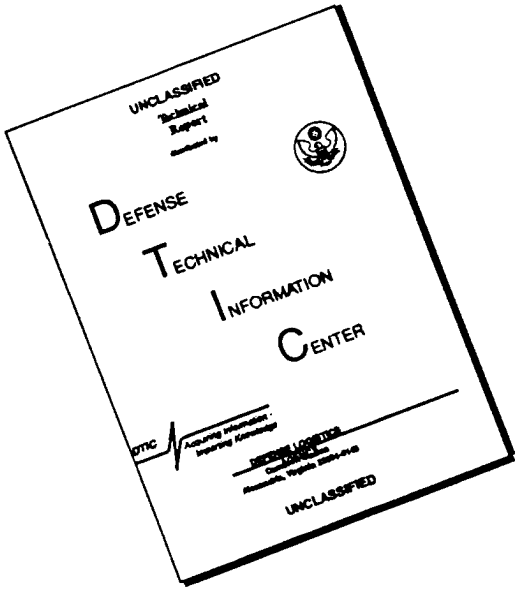
DTIC QUALITY INSPECTED 4

MRS
MATERIALS RESEARCH SOCIETY

PITTSBURGH, PENNSYLVANIA

19960813 138

DISCLAIMER NOTICE



THIS DOCUMENT IS BEST QUALITY AVAILABLE. THE COPY FURNISHED TO DTIC CONTAINED A SIGNIFICANT NUMBER OF PAGES WHICH DO NOT REPRODUCE LEGIBLY.

This work was supported in part by the Office of Naval Research under Grant Number N00014-96-1-0157. The United States Government has a royalty-free license throughout the world in all copyrightable material contained herein.

Single article reprints from this publication are available through University Microfilms Inc., 300 North Zeeb Road, Ann Arbor, Michigan 48106

CODEN: MRSPDH

Copyright 1996 by Materials Research Society.
All rights reserved.

This book has been registered with Copyright Clearance Center, Inc. For further information, please contact the Copyright Clearance Center, Salem, Massachusetts.

Published by:

Materials Research Society
9800 McKnight Road
Pittsburgh, Pennsylvania 15237
Telephone (412) 367-3003
Fax (412) 367-4373
Homepage http://www.mrs.org/

Library of Congress Cataloging in Publication Data

Disordered materials and interfaces : symposium held November 27-30, 1995, Boston, Massachusetts, U.S.A. / editors, Herman Z. Cummins, Douglas J. Durian, David L. Johnson, and H. Eugene Stanley.
p. cm.—(Materials Research Society Symposium Proceedings ; v. 407)
Includes bibliographic references and index.
ISBN 1-55899-310-X
1. Order-Disorder models—Congresses. 2. Materials—Congresses. 3. Interfaces (Physical sciences)—Congresses. I. Cummins, Herman Z. II. Durian, Douglas J. III. Johnson, David L. IV. Stanley, H. Eugene V. Series: Materials Research Society symposium proceedings ; v. 407.
QC173.4.O73D53 1996
530.4'13—dc20 96-6932
CIP

Manufactured in the United States of America

CONTENTS

Preface xi

Materials Research Society Symposium Proceedings xii

PART I: POROUS MEDIA

***Electrokinetic Phenomena in Porous Media** 3
David B. Pengra and Po-zen Wong

A Model for the Two-Phase Behavior of Fluids in Dilute Porous Media 15
James P. Donley, Rebecca M. Nyquist, and Andrea J. Liu

An Experimental Study of the Dynamics of Contact Lines 21
S. Kumar, M.O. Robbins, and D.H. Reich

Pinning of Water Imbibition Front in Porous Media 27
Po-zen Wong, Thomas Delker, Morgan Hott, and David B. Pengra

Image Analysis and SAXS Characterization of Mixed Aerogels 33
S. Blacher, Ph. Tihon, R. Pirard, J.P. Pirard, F. Brouers, B. Sahouli, B. Diez, R. Sobry, and G. van den Bosshe

SAXS Characterization of Pyrolytic Carbon Blacks 39
B. Sahouli, S. Blacher, F. Brouers, R. Sobry, G. van den Bossche, H. Darmstadt, and C. Roy

Modelling of the Structural and Dynamical Properties of Porous Silicon 45
J.L. Gavartin and C.C. Matthai

Evaluation of Inaccessible Pore Structures in Random Porous Solids 51
N. Yoshizawa, Y. Yamada, M. Shiraishi, K. Kaneko, and N. Setoyama

Influence of Spatial Correlations on Permeability and Connectivity of Sandstone 57
Hernan A. Makse, Shlomo Havlin, Peter R. King, and H. Eugene Stanley

A Simple Model for Anomalous Relaxation in Porous Media 63
Mariela Araujo and Orlando Gonzalez

*Invited Paper

PART II: COLLOIDS

*Interaction of Dilute Colloidal Particles in a Mixed Solvent 71
James V. Maher and M. Levent Kurnaz

*Microhydrodynamics With Dissipative Particle Dynamics 81
Pep Español and Ignacio Zúñiga

Evolution of the Structure Factor in Gelling Dense Colloidal Silica 87
C.D. Muzny, B.D. Butler, and H.J.M. Hanley

Formation of Colloidal Copper Hydroxides and Oxides Biopolymeric Interfaces 93
U. Hinze, M. Thies, and H.H. Paradies

Critical Behavior in the Ultrasonic Properties of Suspensions 99
R. Esquivel-Sirvent and D.H. Green

PART III: CHEMICAL REACTIONS

*Non-Classical Reaction Kinetics: Experiments 107
Raoul Kopelman and Anna L. Lin

*Study of A+B→C and A+2B→C Reaction-Diffusion System With Initially Separated Components 119
Andrew Yen and Raoul Kopelman

Dynamic Light Scattering in 5CB Confined in Disordered Porous Media 125
Fouad M. Aliev and Vladimir V. Nadtotchi

Brillouin Light Scattering Determination of the Glass Transition in Thin, Freely-Standing Poly(styrene) Films 131
J.A. Forrest, K. Dalnoki-Veress, J.R. Dutcher, A.C. Rowat, and J.R. Stevens

Anomalous Kinetics of the Trapping Reaction in One Dimension Under Steady State Conditions 137
Anna L. Lin and Raoul Kopelman

PART IV: DYNAMICAL ASPECTS OF THE LIQUID-GLASS TRANSITION

*Relaxational Dynamics and Strength in Supercooled Liquids From Impulsive Stimulated Thermal Scattering 145
Yongwu Yang, Laura J. Muller, and Keith A. Nelson

*Invited Paper

Experimental Study of the Liquid-Glass Transition in an Inorganic Polymer $Li_{0.5}Na_{0.5}PO_3$ 155
B. Ruffle, S. Beaufils, Y. Delugeard, G. Coddens, J. Etrillard, B. Toudic, M. Bertault, J. Even, J. Gallier, and C. Ecolivet

Quasi-Elastic Neutron Scattering Study of the Fragile Glass-Former SALOL 161
J. Toulouse, R. Pick, and C. Dreyfus

Structural Relaxations in a Simple Model Molten Salt 167
Matthias Fuchs

Relaxation Behavior in Polystyrene Near and Above the Glass Transition Studied by Ultrasonic Technique 173
A. Sahnoune and L. Piché

Structural Relaxation of Densified Silica Glass by Thermal Annealing 179
Naoyuki Kitamura, Kohei Fukumi, Masaki Makihara, and Hiroshi Yamashita

Simulation of Dynamics of Liquid-Glass Transition 185
Y. Kogure, K. Kunitomi, Y. Nakamura, and M. Doyama

Enthalpy Relaxation Near the Glass Transition of a Supercooled Liquid $(Ca(NO_3)_2)_{0.4}(KNO_3)_{0.6}$ 191
I.K. Moon and Yoon-Hee Jeong

Variation of the Structural Unit in Tellurite Glasses 197
Shigeru Suehara, Kazuo Yamamoto, Shunichi Hishita, Takashi Aizawa, Satoru Inoue, and Akihiko Nukui

The Role of Stochastic Noise on the Glass Transition 203
Fernando C. Perez-Cardenas and Hao Gan

Structural Developments in Fragile Glass Forming Oxides 209
J.E. Masnik, O. Nickolayev, J. Kieffer, and J.D. Bass

A Low Frequency Study of the Vibrational Modes in Alkali-Silicate Glasses by Raman Spectroscopy 215
R. Sommer, J. Toulouse, and H. Jain

Diffusional Dynamics Near the Glass Transition in Amorphous Polymer Thin Films 221
Denise D. Deppe and John M. Torkelson

Dynamics of Structural Recovery and Mechanical Response of Polymeric Liquids Near to the Glass Transition 227
D.M. Colucci, C.R. Schultheisz, and G.B. McKenna

Fractional Debye-Stokes-Einstein Law in Polymeric Liquid Crystals 233
L. Andreozzi, C. Donati, M. Giordano, and D. Leporini

Kinetic Roughening of Quenched Xenon Films 239
Ralf K. Heilmann and Robert M. Suter

Simulation of Dynamics of Solid-Liquid Transition 245
Y. Kogure, H. Masuyama, and M. Doyama

PART V: DISORDERED MATERIALS AND SURFACES

*Localization of Electrons and Acoustical Phonons in Irregular or Fractal Crystallites 253
B. Sapoval and S. Russ

*Fractal and Non-Fractal Surfaces in Ion Sputtering 259
A-L. Barabási and R. Cuerno

Topological Disorder and Conductance Fluctuations in Granular Thin Films 271
Kristin M. Abkemeier and David G. Grier

Nonequilibrium Statistical Mechanics of an Ensemble of Vesicles 275
Leonardo Golubović

Pitting Corrosion in Two-Dimensional Aluminium Thin Layers 281
L. Balázs and J-F. Gouyet

Fractal Growth of Clusters and Pores During Annealing of Aluminum Thin Films Deposited on Silica 287
Vincent Fleury, Lazlo Balázs, and Franck Duclos

Growth Equation With a Conservation Law 295
Kent Bækgaard Lauritsen

Morphology of the Fungus *Aspergillus Oryzae* and *Nidulans* 301
Sasuke Miyazima and Shu Matsuura

A Model for Ion-Sputtering: From Pattern Formation to Rough Surfaces 307
R. Cuerno, H.A. Makse, S. Tomassone, S.T. Harrington, and H.E. Stanley

Interaction of Organic Additives With Alumina Surfaces in a Ceramic Slurry 313
W.M. Sigmund, G. Wegner, and F. Aldinger

Atomic Kinetics and Dynamical Phason Disorder in a Quasicrystal 319
M. Dzugutov

*Invited Paper

Structure of Silane Films and Their Adhesion Properties 325
Y. Carolina Araujo and Pedro G. Toledo

Morphological Changes of Branched Ge Clusters Caused by Diffusion Fields and Surface Roughness of Au Underlayer 331
A. Sugawara, T. Kikukawa, Y. Haga, and O. Nittono

ATR-FTIR Spectral Investigation of SO_2-Treated Soda-Lime-Silicate Float Glass 337
U. Senturk, D.H. Lee, R.A. Condrate, Sr., and J.R. Varner

Stereological Estimation of Fractal Number of Fracture Planes in Concrete 343
P. Stroeven

Verification and Application of a New Adsorption Model for Fractal Surfaces 349
Ronald Segars and Louis Piscitelle

A Growth Model for Ramified Electrochemical Deposition 355
Guillermo Marshall, Pablo Mocskos, and Martin Olivella

Electrochemical Oscillations, Surface Morphology and Corrosion of Selected Thermal Sprayed Alloys 365
Elia V. Eschenazi, Yamlak Tsega, Ninja Ballard, and Gary Glass

PART VI: SCALING AND NANOSTRUCTURES

*Fractal and Dendritic Growth of Surface Aggregates 379
H. Brune, K. Bromann, K. Kern, J. Jacobsen, P. Stoltze, K. Jacobsen, and J. Nørskov

*Why Are Computer Simulations of Growth Useful? 391
Pablo Jensen, Laurent Bardotti, Albert-László Barabási, Hernán Larralde, Shlomo Havlin, and H. Eugene Stanley

Investigation of Aggregate Structures on Length Scales from About 5 to 10,000 Å# 399
Paul W. Schmidt, Françoise Ehrburger-Dolle, Peter Pfeifer, Thomas Rieker, Yogendra M. Kapoor, and Daniel J. Voss

Dehydration of Fractal Particles of Iron (III) and Aluminum Hydroxides 405
A.A. Vertegel, S.V. Kalinin, N.N. Oleynikov, and Yu.D. Tretyakov

*Invited Paper

Fractal Analysis of the Microstructure of AISI 304 Steel 411
M. Hinojosa, V. Trejo, and U. Oritz

Author Index 417

Subject Index 419

PREFACE

This Symposium continues the ongoing MRS series devoted to the structure and dynamics of disordered materials. It includes sections dedicated to specific classes of disordered materials of particular current interest, including porous media, foams, colloids, and glasses. Also, the structures of chemically inhomogeneous systems in which chemical reactions are taking place, and pattern formation in solidifying alloys are each the subject of a section. Finally, a variety of disordered materials of interest to materials science are included.

This symposium could not have taken place without the financial support through a grant from the Office of Naval Research. We thank Michael F. Shlesinger for his continued support of materials research; his vision and encouragement have meant a great deal to the entire community. We also thank Brookhaven Instruments Corporation, NEC Research Institute, Schlumberger-Doll Research Center, the Ford Motor Corporation, and the Exxon Corporation for their financial support.

Finally, we wish to thank J.D. Morrow and the MRS staff for their generous assistance with preparing these proceedings

Herman Z. Cummins
Douglas J. Durian
David L. Johnson
H. Eugene Stanley

January 1996

MATERIALS RESEARCH SOCIETY SYMPOSIUM PROCEEDINGS

Volume 377— Amorphous Silicon Technology—1995, M. Hack, E.A. Schiff, M. Powell, A. Matsuda, A. Madan, 1995, ISBN: 1-55899-280-4

Volume 378— Defect- and Impurity-Engineered Semiconductors and Devices, S. Ashok, J. Chevallier, I. Akasaki, N.M. Johnson, B.L. Sopori, 1995, ISBN: 1-55899-281-2

Volume 379— Strained Layer Epitaxy—Materials, Processing, and Device Applications, J. Bean, E. Fitzgerald, J. Hoyt, K-Y. Cheng, 1995, ISBN: 1-55899-282-0

Volume 380— Materials—Fabrication and Patterning at the Nanoscale, C.R.K. Marrian, K. Kash, F. Cerrina, M.G. Lagally, 1995, ISBN: 1-55899-283-9

Volume 381— Low-Dielectric Constant Materials—Synthesis and Applications in Microelectronics, T-M. Lu, S.P. Murarka, T.S. Kuan, C.H. Ting, 1995, ISBN: 1-55899-284-7

Volume 382— Structure and Properties of Multilayered Thin Films, T.D. Nguyen, B.M. Lairson, B.M. Clemens, K. Sato, S-C. Shin, 1995, ISBN: 1-55899-285-5

Volume 383— Mechanical Behavior of Diamond and Other Forms of Carbon, M.D. Drory, M.S. Donley, D. Bogy, J.E. Field, 1995, ISBN: 1-55899-286-3

Volume 384— Magnetic Ultrathin Films, Multilayers and Surfaces, A. Fert, H. Fujimori, G. Guntherodt, B. Heinrich, W.F. Egelhoff, Jr., E.E. Marinero, R.L. White, 1995, ISBN: 1-55899-287-1

Volume 385— Polymer/Inorganic Interfaces II, L. Drzal, N.A. Peppas, R.L. Opila, C. Schutte, 1995, ISBN: 1-55899-288-X

Volume 386— Ultraclean Semiconductor Processing Technology and Surface Chemical Cleaning and Passivation, M. Liehr, M. Hirose, M. Heyns, H. Parks, 1995, ISBN: 1-55899-289-8

Volume 387— Rapid Thermal and Integrated Processing IV, J.C. Sturm, J.C. Gelpey, S.R.J. Brueck, A. Kermani, J.L. Regolini, 1995, ISBN: 1-55899-290-1

Volume 388— Film Synthesis and Growth Using Energetic Beams, H.A. Atwater, J.T. Dickinson, D.H. Lowndes, A. Polman, 1995, ISBN: 1-55899-291-X

Volume 389— Modeling and Simulation of Thin-Film Processing, C.A. Volkert, R.J. Kee, D.J. Srolovitz, M.J. Fluss, 1995, ISBN: 1-55899-292-8

Volume 390— Electronic Packaging Materials Science VIII, R.C. Sundahl, K.A. Jackson, K-N. Tu, P. Børgesen, 1995, ISBN: 1-55899-293-6

Volume 391— Materials Reliability in Microelectronics V, A.S. Oates, K. Gadepally, R. Rosenberg, W.F. Filter, L. Greer, 1995, ISBN: 1-55899-294-4

Volume 392— Thin Films for Integrated Optics Applications, B.W. Wessels, S.R. Marder D.M. Walba, 1995, ISBN: 1-55899-295-2

Volume 393— Materials for Electrochemical Energy Storage and Conversion— Batteries, Capacitors and Fuel Cells, D.H. Doughty, B. Vyas, J.R. Huff, T. Takamura, 1995, ISBN: 1-55899-296-0

Volume 394— Polymers in Medicine and Pharmacy, A.G. Mikos, K.W. Leong, M.L. Radomsky, J.A. Tamada, M.J. Yaszemski, 1995, ISBN: 1-55899-297-9

Volume 395— Gallium Nitride and Related Materials—The First International Symposium on Gallium Nitride and Related Materials, R.D. Dupuis, J.A. Edmond, F.A. Ponce, S.J. Nakamura, 1996, ISBN: 1-55899-298-7

Volume 396— Ion-Solid Interactions for Materials Modification and Processing, D.B. Poker, D. Ila, Y-T. Cheng, L.R. Harriott, T.W. Sigmon, 1996, ISBN: 1-55899-299-5

Volume 397— Advanced Laser Processing of Materials—Fundamentals and Applications, D. Norton, R. Singh, J. Narayan, J. Cheung, L.D. Laude, 1996, ISBN: 1-55899-300-2

Volume 398— Thermodynamics and Kinetics of Phase Transformations, J.S. Im, B. Park, A.L. Greer, G.B. Stephenson,1996, ISBN: 1-55899-301-0

MATERIALS RESEARCH SOCIETY SYMPOSIUM PROCEEDINGS

Volume 399— Evolution of Epitaxial Structure and Morphology, R. Clarke, A. Zangwill, D. Jesson, D. Chambliss, 1996, ISBN: 1-55899-302-9

Volume 400— Metastable Metal-Based Phases and Microstructures, R.D. Shull, G. Mazzone, R.S. Averback, R. Bormann, R.F. Ziolo, 1996 ISBN: 1-55899-303-7

Volume 401— Epitaxial Oxide Thin Films II, J.S. Speck, D.K. Fork, R.M. Wolf, T. Shiosaki, 1996, ISBN: 1-55899-304-5

Volume 402— Silicide Thin Films—Fabrication, Properties, and Applications, R. Tung, K. Maex, P.W. Pellegrini, L.H. Allen, 1996 ISBN: 1-55899-305-3

Volume 403— Polycrystalline Thin Films II—Structure, Texture, Properties, and Applications, H.J. Frost, C.A. Ross, M.A. Parker, E.A. Holm, 1996 ISBN: 1-55899-306-1

Volume 404— *In Situ* Electron and Tunneling Microscopy of Dynamic Processes, R. Sharma, P.L. Gai, M. Gajdardziska-Josifovska, R. Sinclair, L.J. Whitman, 1996, ISBN: 1-55899-307-X

Volume 405— Surface/Interface and Stress Effects in Electronic Material Nanostructures, R.C. Cammarata, S.M. Prokes, K.L. Wang, A. Christou, 1996, ISBN: 1-55899-308-8

Volume 406— Diagnostic Techniques for Semiconductor Materials Processing, S.W. Pang, O.J. Glembocki, F.H. Pollack, F. Celii, C.M. Sotomayor Torres, 1996, ISBN 1-55899-309-6

Volume 407— Disordered Materials and Interfaces—Fractals, Structure, and Dynamics, H.E. Stanley, H.Z. Cummins, D.J. Durian, D.L. Johnson, 1996, ISBN: 1-55899-310-X

Volume 408— Materials Theory, Simulations, and Parallel Algorithms, E. Kaxiras, P. Vashishta, J. Joannopoulos, R.K. Kalia, 1996, ISBN: 1-55899-311-8

Volume 409— Fracture—Instability Dynamics, Scaling, and Ductile/Brittle Behavior, R. Blumberg Selinger, J. Mecholsky, A. Carlsson, E.R. Fuller, Jr., 1996, ISBN: 1-55899-312-6

Volume 410— Covalent Ceramics III—Science and Technology of Non-Oxides, A.F. Hepp, A.E. Kaloyeros, G.S. Fischman, P.N. Kumta, J.J. Sullivan, 1996, ISBN: 1-55899-313-4

Volume 411— Electrically Based Microstructural Characterization, R.A. Gerhardt, S.R. Taylor, E.J. Garboczi, 1996, ISBN: 155899-314-2

Volume 412— Scientific Basis for Nuclear Waste Management XIX, W.M. Murphy, D.A. Knecht, 1996, ISBN: 1-55899-315-0

Volume 413— Electrical, Optical, and Magnetic Properties of Organic Solid State Materials II, L.R. Dalton, A.K-Y. Jen, M.F. Rubner, C.C-Y. Lee, G.E. Wnek, L.Y. Chiang, 1996, ISBN: 1-55899-316-9

Volume 414— Thin Films and Surfaces for Bioactivity and Biomedical Applications C. Cotell, S.M. Gorbatkin, G. Grobe, A.E. Meyer, 1996, ISBN: 1-55899-317-7

Volume 415— Metal-Organic Chemical Vapor Deposition of Electronic Ceramics II, D.B. Beach, S.B. Desu, P.C. Van Buskirk, 1996, ISBN: 1-55899-318-5

Volume 416— Diamond for Electronic Applications, D. Dreifus, A. Collins, K. Das, T. Humphreys, P. Pehrsson, 1996, ISBN: 1-55899-319-3

Volume 417— Optoelectronic Materials - Ordering, Composition Modulation, and Self-Assembled Structures, E.D. Jones, A. Mascarenhas, P. Petroff, R. Bhat, 1996, ISBN: 1-55899-320-7

Volume 418— Decomposition, Combustion, and Detonation Chemistry of Energetic Materials, T.B. Brill, W.C. Tao, T.P. Russell, R.B. Wardle, 1996 ISBN: 1-55899-321-5

Volume 419— Spectroscopy of Heterojunctions, N. Tolk, G. Margaritondo, E. Viturro, 1996, ISBN: 1-55899-322-3

Prior Materials Research Society Symposium Proceedings available by contacting Materials Research Society

Part I

Porous Media

ELECTROKINETIC PHENOMENA IN POROUS MEDIA

DAVID B. PENGRA AND PO-ZEN WONG
Department of Physics and Astronomy, University of Massachusetts,
Amherst, MA 01003, U.S.A.

ABSTRACT

Electrokinetic phenomena, such as electroosmosis (fluid-flow induced by applied electric fields) and streaming potential (the complementary process) are known to exist in brine-saturated porous media, but are very difficult to measure. With modern instrumentation and an ac method, we can now determine these transport coefficients accurately, and use them to characterize the permeability k, the effective throat radius R_e, and the electric potential at the slip-plane, or ζ-potential. Our study shows that permeability can be determined by two different means: by combining the dc values of the streaming potential, electroosmotic pressure and conductivity; or from the frequency response of ac electroosmosis alone. The high sensitivity of the method allows us to measure k over the 0.1–10,000 millidarcy range with less than 10kPa applied pressure. This article reviews some of the basics of electrokinetics and describes our methods. We also discuss effects of brine salinity and possible effects due to the fractal nature of the pore surface.

INTRODUCTION

In brine-saturated porous material, such as porous rock, there are two major types of current flow: flow of the brine through the pores, and flow of electrical current by means of ionic conduction. The electric current can be carried by ions lining the surface of the pores and by the ions dissolved in the brine, with rather different characteristics. The ability of fluid to flow is characterized by the rock permeability k_r, and the ability of electricity to flow is characterized by the conductivity σ_r of the combined brine and rock. Since both types of flow depend on the microgeometry of the pores, it is reasonable to suppose that k_r and σ_r would be related. Empirically, this has been found to be true, but the theoretical justifications are model-dependent. We refer readers to Ref. [1] for a summary. Typically, the correlation is expressed as a relation between a geometric constant called the formation factor F and k_r. The formation factor is defined by

$$F \equiv \sigma_w/\sigma_r \ , \tag{1}$$

where σ_w is the conductivity of the bulk fluid. An important result is that if some microgeometric length scale, such as the pore size, throat size or grain size can be determined by other means, then k_r may be estimated from F [2, 3]. The main difficulty has been to obtain these lengths reliably. For example, in two different experiments using nuclear magnetic resonance (NMR) to determine pore sizes, the results suggested either $k_r \propto F^{-1}$or $k_r \propto F^{-2}$ [4, 5]. Most recently, we have demonstrated that this difficulty can be overcome by studying electrokinetic phenomena that results from the interaction between the fluid and electrical currents [6]. This coupling is due to the presence of a thin space charge layer at the pore surface. Although the effect is weak, it is measurable, and, leads to a *rigorous* determination of the effective pore radius R_e and the permeability k_r. We may also define an effective zeta-potential ζ_e for the pore surface in terms of the measured electrokinetic coefficients.

Mat. Res. Soc. Symp. Proc. Vol. 407 © 1996 Materials Research Society

Electrokinetic measurements date from the experiments of Saxén in the previous century [7], and the general theory was codified by Onsager in 1931 [8]. But until recently electrokinetics has not been used as a way to explore other properties, mainly because the effects are very weak and difficult to measure accurately. Advances in instrumentation, however, have made it possible to make reliable measurements, and thereby has it become practical to revisit this old territory. In this article, we briefly review electrokinetic theory, describe our measurement techniques in some detail, and show that they can be used to determine k_r. In addition, because the electrokinetic coefficients depend on the properties of the solid-liquid interface, we show that brine salinity affects the data from a collection of porous rock samples in a way not predicted by a simple model. The disparity suggests that the flow behavior is influenced by the interfacial roughness and chemistry.

THEORETICAL BACKGROUND

Electrokinetic phenomena arise from the presence of mobile space charge in an electrolyte at its interface with a solid. In shaly sandstone, exchangeable cations from the clay become solvated; for other solids without such exchangeable ions, free ions in the brine are attracted to the surface by electrostatic image forces. Typically, one species (e.g., the Cl^- anion) becomes chemically adsorbed in a tightly-bound layer called the Stern layer. The other species (e.g., the Na^+ cation), forms the diffuse layer known as the Guoy-Chapman layer. The combination is known as the electrochemical double layer. The simplest model that describes the diffuse layer for a planar surface is the Debye-Hückel theory [9]. It assumes that the ions in the electrolyte are point charges of $\pm q$ and the surface charge density qN_s is small enough to not cause too large a potential change at the interface. For a simple 1-1 electrolyte (e.g., NaCl) of concentration N_0, this theory gives the diffuse-layer thickness λ:

$$\lambda = \left(\frac{\varepsilon k_B T}{2q^2 N_0} \right)^{1/2} , \tag{2}$$

where ε is the dielectric permittivity of the electrolyte and T is the absolute temperature. The Debye-Hückel equations may also be solved for the electrostatic potential ζ at the hydraulic slip-plane. In the limit that $q\zeta \ll 2k_BT$,

$$\zeta = qN_s\lambda/\varepsilon . \tag{3}$$

In a 0.2 M NaCl solution at room temperature, $\lambda \approx 7$Å. For Eq. (3) to be valid, N_s must be much less than one ion in an area of 300Å^2, but in many cases, the surface charge density is higher and λ is not much larger than the ionic size, so the approximations are probably poor. Nevertheless, the existence of a diffuse charge layer and the dimensional relationships in Eqs. (2) and (3) are conceptually important. Because the ions in the diffuse layer are mobile and predominately of one species, a fluid flow which carries them along produces an electric current, called the *streaming current.* Conversely, under the influence of an applied electric field, those ions in the diffuse layer will migrate and drag with them the nearby fluid—a process called *electroosmosis.*

Experimentally, electrokinetic phenomena can be conveniently studied by measuring two related quantities: the *streaming potential* (STP) and the *electroosmotic pressure* (ELO). These can be understood by examining the case of a simple cylindrical capillary, as shown in Fig. 1. Assume that it is placed in an experimental cell, such as that shown in Fig. 2; the cell end-volumes are closed, the voltage and pressure across the capillary may be monitored, and electric and fluid currents may be injected. In the case of STP (Fig. 1a), a pressure ΔP_a is applied across the tube, causing fluid to flow; for low flow rates, the velocity field takes on the classic Poiseuille parabolic form (shown by the straight arrows). Because of the Gouy-Chapman layer, the streaming current is created near the capillary surface (wavy arrows). If no net current is allowed, the streaming current is counterbalanced by an opposing ohmic current in the bulk electrolyte, which is driven

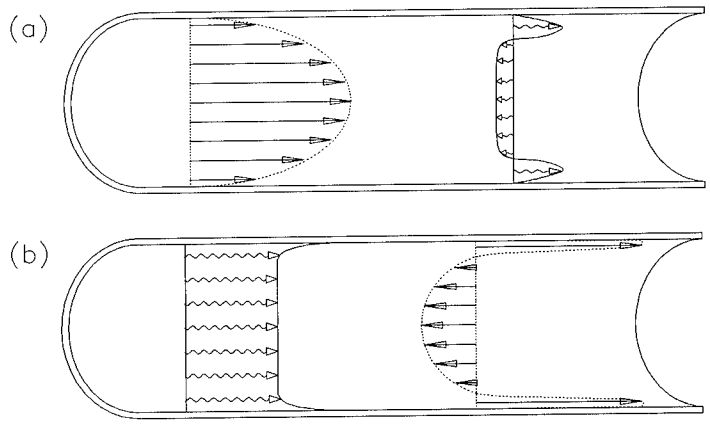


Figure 1: Schematic of the flow patterns in a capillary for electric current (wavy arrows) and fluid current (straight arrows) for the cases of streaming potential (a) and electroosmosis (b).

by the potential difference $\Delta\Phi_s$ created by the displacement of the surface charge. The streaming potential coefficient K_S, defined by

$$K_S \equiv -\Delta\Phi_s/\Delta P_a \,, \tag{4}$$

is constant over a range of applied pressure. In the reciprocal case of ELO (Fig. 1b), an applied voltage $\Delta\Phi_a$ causes an electric current distributed over the cross-section to flow; the current at the capillary wall consists of mostly one ionic species, and by viscous coupling sets up an electroosmotic fluid current. If the cell end-cavities are kept sealed, the mass transfer results in a pressure differential ΔP_e which drives a Poiseuille flow back in the interior of the capillary tube. The electroosmosis coefficient K_E is defined as

$$K_E \equiv -\Delta P_e/\Delta\Phi_a \,. \tag{5}$$

Measurements of K_S and K_E are thus very simple in principle: apply a known pressure (or voltage), and monitor the induced voltage (or pressure).

In the case of the capillary tube, assuming the validity of the Debye-Hückel model, K_S and K_E may be calculated [9]:

$$K_S = \varepsilon\zeta/\eta\sigma_w \,, \tag{6}$$

$$K_E = 8\varepsilon\zeta/R^2 \,, \tag{7}$$

where η is the viscosity, σ_w the conductivity, and ε the dielectric susceptibility of the brine. From these equations, we can see that if ζ and R are unknown, they can be determined by measuring K_S and K_E. Since fluid flow in porous media is often thought to be equivalent to flow in a capillary tube with an effective radius R_e comparable to the throat size, one might expect that the measurement of K_S and K_E would help determine R_e, and hence the permeability. In particular, we note that Johnson, Koplik and Schwartz have suggested that $k_r = R_e^2/8F$ is a good approximation for most porous media [10]. If we identify R_e with R in Eq. (7), we would have

$$k_r = \frac{R_e^2}{8F} = \frac{\varepsilon\zeta}{K_E F} = \frac{K_S\eta\sigma_w}{K_E F} = \eta\sigma_r\frac{K_S}{K_E} \,. \tag{8}$$

This result suggests that we can obtain permeability by measuring K_E, K_S and σ_r. Although Eq. (8) is obtained by assuming a simple cylindrical geometry with radius $R \gg \lambda$ and the Debye-Hückel model, it turns out to be generally valid for any random porous medium. It can be proved rigorously through nonequilibrium thermodynamics without any knowledge of the pore geometry or surface chemistry, as we now show.

For the case of an isotropic porous material, the flow equations have the form

$$\mathbf{J}_e = -L_{11}\nabla\Phi - L_{12}\nabla P \tag{9}$$

$$\mathbf{J}_f = -L_{21}\nabla\Phi - L_{22}\nabla P \tag{10}$$

where $\mathbf{J}_e$ and $\mathbf{J}_f$ are the electric and fluid-volume current densities, Φ and P are the electrostatic potential and the pressure fields. The diagonal coefficients L_{11} and L_{22} may interpreted as σ and k/η, respectively, in the respective cases of $\nabla P = 0$, and $\nabla\Phi = 0$; that is, they are not strictly equal to σ_r and k_r/η. The L_{12} term represents the streaming current and the L_{21} term represents the electroosmotic current. The coefficients K_S and K_E are found when the relevant current is equal to zero. Under steady state, K_S is obtained when there is only fluid flow and no net electric current:

$$K_S = -\left.\frac{\nabla\Phi}{\nabla P}\right|_{\mathbf{J}_e=0} = \frac{L_{12}}{L_{11}}\,, \tag{11}$$

from Eq. (9). Similarly, K_E is obtained when there is only electric current and no net fluid current:

$$K_E = -\left.\frac{\nabla P}{\nabla\Phi}\right|_{\mathbf{J}_f=0} = \frac{L_{21}}{L_{22}}\,, \tag{12}$$

from Eq. (10). Within the framework of linear nonequilibrium thermodynamics, equations such as (9) and (10) give the response of the *thermodynamic fluxes*—the electric and fluid currents—to the *thermodynamic forces*—the electric and pressure fields. Thus Onsager's theorem applies, and we have $L_{12} = L_{21}$ [11]. Consequently,

$$L_{22} = L_{11}(K_S/K_E)\,. \tag{13}$$

Experimentally, one measures k_r or σ_r in the absence of the complementary flow, but without regard to the presence of the complementary field $\nabla\Phi$ or ∇P, by use of Darcy's law, $\mathbf{J}_f = -k_r/\eta\nabla P$, or Ohm's law, $\mathbf{J}_e = -\sigma_r\nabla\Phi$. For example, to measure σ_r we apply an electric field $-\nabla\Phi$ to the system and measure $\mathbf{J}_e$ while holding $\mathbf{J}_f = 0$. From Eqs. (9)–(12), we find that $\sigma_r = L_{11}\,(1 - K_S K_E)$; similarly, $k_r/\eta = L_{22}(1 - K_S K_E)$. By Onsager's relation through Eq. (13), we obtain the final result of Eq. (8) in a way that involves no assumption of the pore geometry or double-layer structure. Indeed the generality of the argument allows us to *define*, as suggested by Eqs. (6) and (7), the effective pore radius R_e and the effective ζ-potential ζ_e through the electrokinetic coefficients [6]:

$$R_e^2 \equiv 8\eta\sigma_w(K_S/K_E)\,, \tag{14}$$

$$\zeta_e \equiv K_S\eta\sigma_w/\varepsilon_w\,. \tag{15}$$

EXPERIMENTAL METHOD

Typically K_S and K_E are small relative to the noise in the experimental environment. In an early investigation of STP [12], fluid pressure up to a few hundred PSI was used to produce a signal of about 10 mV. The coefficient K_S was not found to be constant over the range of applied pressure; this was probably because the pore structure changed with increasing pressure. Also, measurement electrodes may have polarization voltages larger than 10 mV, which vary according

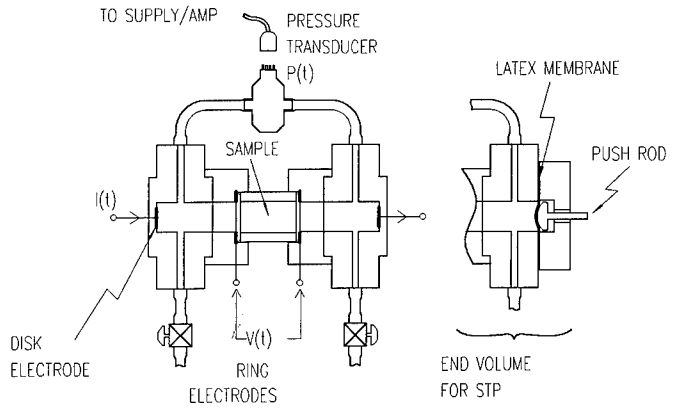


Figure 2: Experimental Cell used for electrokinetics experiments. See text for explanation.

to unknown surface conditions. To make good measurements, we have to keep the fluid pressure low and detect a signal much weaker than typical background noise.

To overcome these problems, we employ an ac technique based on lock-in amplification. This method has proven to be useful in detecting signals that are several orders of magnitude lower than the total background noise [13]. For example, in our experimental cell, we apply ac fluid pressures below 10 kPa (<1.5 psi) and ac voltages below the threshold for electrolysis (< 1 volt), both at fixed frequencies. Room vibrations give roughly 10 Pa pressure noise in the frequency window of our transducer (0–10 Hz), and electrode polarization produces broad band voltage noise at low frequencies (< 1 Hz) that varies over tens of millivolts. Yet we are able to detect ELO pressure oscillations below 1 Pa and STP voltage oscillations below 1 μV, at the driving frequencies. This level of resolution is important because typical values of K_S and K_E are at the level of 10^{-8} V/Pa and 1 Pa/V. Another advantage of the lock-in technique is that, in addition to using the low frequency data to extrapolate to the dc limit where Eq. (8) is exact, we can measure K_S and K_E over a range of driving frequencies. The frequency response of K_E gives another method to determine permeability, as we show below. We now turn to the specific implementation of the technique.

Figure 2 depicts the sample cell we used in the measurements. The samples of rock or fused-glass-beads are cut into cylinders of 4 cm length by 2 cm diameter. They are glued into a Lucite sleeve, and then vacuum-impregnated with brine and allowed to equilibrate for many days. The brine saturated sample is held by two collars fitted with Ag/AgCl *ring electrodes* that are used to sense the voltage across the sample, which are in turn held by two rigid end-cavities that connect to either end of a differential pressure transducer. Each cavity also contains an Ag/AgCl *disk electrode* for sending electric current through the cell. The overall dimensions of the cell, made of Lucite, are approximately $25 \times 10 \times 10$ cm^3.

To measure σ_r, we monitor the ac voltage between the ring electrodes and the ac current through the disk electrodes. For K_E measurements, we pass an ac current through the disk electrodes and record both the ac pressure and ac voltage across the sample. During both of these measurements, it is important that the cell be closed and free of trapped air. Only a tiny amount of fluid is moved back and forth between the two end-cavities; trapped air is highly compressible, and would

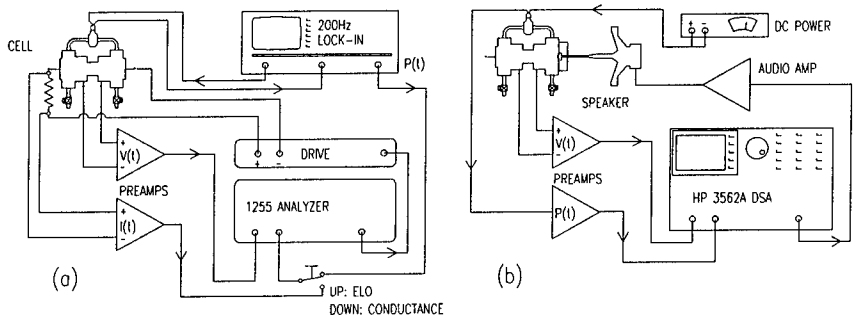


Figure 3: Schematic of experimental setup. (a) Electroosmosis and conductivity. (b) Streaming potential

substantially reduce the pressure signal.

For K_S measurements, we modify the cell slightly. One end-cavity is opened to atmospheric pressure and the other is replaced by an end-piece that is sealed with a flexible latex membrane. A linear bearing supports a push rod that is placed against membrane and attached to a loudspeaker driven by an audio amplifier. This allows us to apply an oscillating pressure to one side of the sample. K_S is obtained by comparing the applied pressure to the induced voltage oscillations across the sample.

The pressure transducer is piezo-resistive and incorporates a Wheatstone bridge—its output is proportional to the supply voltage and the pressure differential. In STP measurements, where the pressure is mechanically applied by the loudspeaker, the signal is well above the pressure noise when the bridge is powered by a 10 V dc supply. However, the differential pressure resulting from electroosmosis requires better signal-to-noise ratio. The bridge is placed in a separate lock-in amplifier loop. At 200 Hz drive frequency (much higher than the ELO response), this secondary lock-in improves the S/N ratio by 10^3–10^6 and we can detect ELO pressure down to 100 mPa RMS.

Two experimental stations measure the ac quantities. The first, shown in Fig. 3a, measures K_E and σ_r. It comprises a Solartron model 1286 Electrochemical Interface as a current source, a Solartron model 1255 Frequency Response Analyzer (FRA) as the frequency generator and dual lock-in amplifier, a Stanford Research SR850 lock-in amplifier for the pressure transducer, and two custom-built phase-matched high-impedance preamplifiers. A computer with IEEE-GPIB interface (not shown) controls the instruments and saves the data. The second station (Figure 3b), measures K_S, and consists of a Hewlett-Packard HP3562A Dynamic Signal Analyzer (DSA) in the same role as the Solartron 1255, a dc audio power amplifier and a modified loudspeaker to provide the oscillating pressure, two high-impedance preamplifiers, and a dc supply for the pressure transducer.

A third experimental station measures the Darcy permeability in the conventional way (not shown) by means of a computer-controlled syringe pump. From the pressure-drop at different flow rates, we deduce the Darcy permeability. We refer to this as the *direct* permeability and denote it by k_d, and call the permeability derived from Eq. (8) the *electrokinetic* permeability k_e.

Table 1: Measurements of the electrokinetic coefficients extrapolated to the dc limit, and the calculated permeability based on arguments given in the text. The abbreviation "FB" stands for "Fontainebleau". The brine concentration is 0.2M NaCl. The Darcy permeability k_d is measured directly. The plot in Fig. 5 is derived from this table.

Sample	Porosity ϕ (%)	K_S (nV/Pa)	K_E (Pa/V)	k_e (mD)	k_d (mD)	ζ_e (mV)	R_e (μm)
Sandstones							
FB-A	22.3	5.48(0.63)	0.334(0.069)	2562(747)	2239(385)	13.9(2.5)	15.4(4.7)
FB-B	16.8	7.42(0.38)	0.620(0.021)	1120(207)	988.7(187)	18.8(2.8)	13.1(2.8)
FB-C	6.7	7.36(0.60)	21.9(0.33)	3.710(0.711)	5.958(1.62)	18.7(3.0)	2.20(0.48)
Berea-A	22.9	9.47(0.058)	2.25(0.099)	678.5(119)	684.0(116)	24.1(3.3)	7.78(1.6)
Berea-B	20.5	8.44(0.27)	23.8(0.20)	32.08(5.69)	39.16(7.46)	21.4(3.1)	2.26(0.47)
Bandera	21.9	7.54(0.26)	684(45)	1.275(0.243)	1.431(0.247)	19.2(2.7)	0.40(0.09)
Limestones							
Whitestone	29	2.67(0.28)	28.2(0.53)	9.017(1.93)	6.403(1.72)	6.77(1.2)	1.17(0.29)
Indiana	15	4.82(0.16)	48.3(3.7)	4.897(0.935)	5.134(0.892)	12.3(1.7)	1.20(0.26)
Fused Glass Beads							
50μm-A	10.1	7.54(0.41)	27.2(0.82)	8.900(1.64)	8.091(1.41)	19.1(2.9)	2.00(0.42)
50μm-B	17.1	8.49(0.63)	14.3(0.47)	66.48(12.7)	69.28(12.2)	21.6(3.4)	2.92(0.63)
100μm	19.3	7.90(0.75)	1.87(0.33)	620.2(164)	602.3(105)	20.1(3.4)	7.79(2.2)
200μm	29.8	4.88(0.39)	0.159(0.03)	6118(2230)	4439(1410)	12.4(2.0)	21.0(9.7)

RESULTS

We chose a suite of 12 samples to carry out our investigation: six sandstones, two carbonates and four fused-glass-beads. Their basic properties are summarized in Table 1. Their permeabilities span a range over 3 decades: $\approx$ 1–4000 mD. The samples were saturated with a succession of brine concentrations: 0.05–0.8 M NaCl in deionized H_2O.

The measured frequency response of σ_r, K_E and K_S for all cases are similar [6]. The magnitude of the electrical conductivity σ_r is nearly constant over the range $10^{-2} - 10^5$ Hz, with a very slight increase of about 0.1%/decade with increasing frequency. At the same time, the phase angle does not tend asymptotically to zero at low frequency, but to a small constant value, typically about 0.1°. This is an example of the constant-phase-angle (CPA) impedance often seen in electrochemical systems [14], and is most likely due to slow adsorption-desorption of ions at the surface when the potential is varied [15, 16]. Here, because the variation with frequency is weak, we regard the response below 1 kHz as flat. The magnitude of K_S is fairly constant below 10 Hz. At 65 Hz and higher, mechanical resonances dominate the signal. Theoretically, the establishment of the streaming potential requires the fluid velocity in the diffuse layer to be in steady state and the charge density in the brine to reach equilibrium. The viscous relaxation time τ_v of the diffuse layer ($\tau_v \approx \rho\lambda^2/\eta$, where ρ is the brine density) [17], and the RC-relaxation time τ_e of the brine ($\tau_e = \varepsilon_w/\sigma_w$) must be attained. As both of these times are typically about 1 ns, the STP data can be regarded as frequency independent in our measurement window.

The data for K_E differ qualitatively from the σ_r and K_S data. Figure 4 shows that K_E has a strong relaxation below 1 Hz. This behavior follows from the combined characteristics of our cell design and the particular sample, to be discussed shortly. For testing Eq. (8), we use the data well below the relaxation frequency to estimate the dc value of K_E.

In Table 1, we list the estimated dc values of σ_r, K_E and K_S for all 12 samples saturated with 0.2M NaCl solution and the estimated error for each case. The values of k_e, R_e and ζ_e calculated from Eqs. (8), (14) and (15) are also listed. The comparison of the electrokinetic permeability k_e to

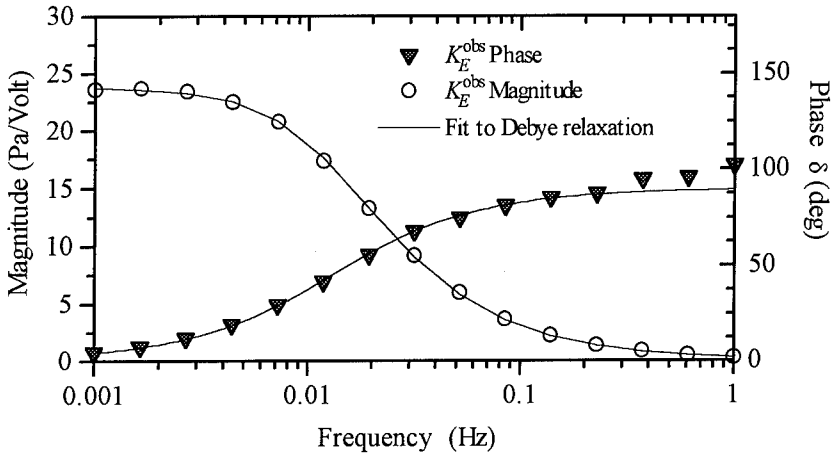


Figure 4: The magnitude (○) and phase (▼) of the electroosmosis coefficient K_E for the Berea-B sandstone saturated with 0.2M NaCl brine.The solid lines are fits to Eq. (20).

the directly measured Darcy permeability k_d for the collection of 12 samples is shown in Fig. 5 where the straight line is the prediction of Eq. (8). We can see clearly that the prediction is borne out for all the samples independent of their detailed characteristics. The reason is that Onsager's relation is a general thermodynamic relationship. The agreement between k_e and k_d is always within our measurement error. An important source of error comes from measuring dc permeability according to Darcy's law. In such measurements, a significant pressure gradient has to be applied across the sample to produce the flow. This inevitably stresses the sample in a nonuniform way which can change the pore geometry [6]. The advantage of the electrokinetic measurement is that it can be made under whatever confining pressure and fluid pressure with very small pressure gradient so that the pore geometry is not altered appreciably. Hence k_e gives the true permeability under the correct pressure condition of the sample or the rock formation.

As we have noted, the frequency response of K_E depends on the sample characteristics and the design of our cell. It is easy to show that the *relaxation frequency* ω_r is in fact directly proportional to k_r; this gives another way to determine k_r. We note that in the electroosmosis measurement, electric current driven through the sample moves fluid from one end-cavity of the cell to the other. Even though the cavities are closed, the tubing connected to the pressure transducer and the O-rings that seal the cell compartments are relatively compliant compared to the brine, sample and other parts of the cell. Thus, when a small volume of water δV is moved into an end-cavity, the cavity volume V expands slightly in response to the pressure change δP. This elastic behavior of the cavity is characterized by an effective bulk modulus $\kappa \equiv V(\delta P/\delta V)$. Assuming that the sample has length L_S, and cross-sectional area A, and the cell has end-cavity volumes V_1 and V_2 which differ in pressure and voltage by p and v, we can rewrite Eq. (10) as

$$\frac{1}{A}\frac{\mathrm{d}V}{\mathrm{d}t} = -L_{21}\frac{v}{L_S} + L_{22}\frac{p}{L_S}\,, \tag{16}$$

where $\mathrm{d}V$ is the amount of fluid moved in time $\mathrm{d}t$. The volume change in the end-cavities are

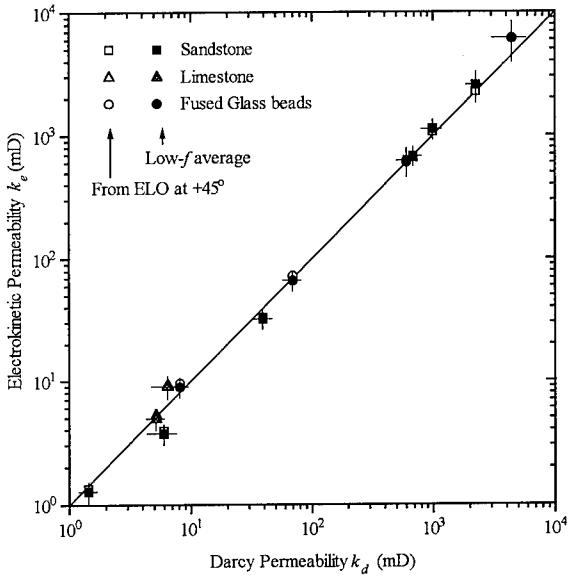


Figure 5: The Darcy permeability k_d compared to the electrokinetic permeability k_e as derived from Eq. (8) for a collection of 8 natural rock samples and 4 fused-glass-bead samples. The solid line is $k_e = k_d$. The filled symbols give the results from the true equilibrium K_E; the open symbols are from K_E calculated from its ac value at a phase angle of 45°.

$\delta V_1 = -\delta V_2 = -\mathrm{d}V$, so the resulting pressure changes in are $\mathrm{d}P_1 = -\kappa \mathrm{d}V/V_1$ and $\mathrm{d}P_2 = \kappa \mathrm{d}V/V_2$, respectively. Hence the total change in differential pressure is $\mathrm{d}p = \mathrm{d}P_2 - \mathrm{d}P_1 = \kappa \mathrm{d}V(V_1+V_2)/V_1V_2$. With this, we eliminate $\mathrm{d}V$ in Eq. (16) to obtain

$$\left(\frac{V_1V_2L_S}{\kappa(V_1+V_2)A}\right)\frac{\mathrm{d}p}{\mathrm{d}t} - L_{22}p = -L_{21}v \tag{17}$$

With Eq. (12) and the definition $\omega_r \equiv [\kappa L_{22}A(V_1+V_2)] \,/\, (L_S V_1 V_2)$, this equation is simplified to

$$\frac{1}{\omega_r}\frac{\mathrm{d}p(t)}{\mathrm{d}t} + p(t) = -K_E v(t)\,. \tag{18}$$

Equation (18) has the form of the differential equation that describes a series RC-circuit driven by an applied voltage $v(t)$, with $1/\omega_r$ playing the role of the RC time constant. Analogously, the sample plays the role of a hydraulic resistance and the end-cavities act as hydraulic capacitors. For a sinusoidal drive voltage $v(t) = v_0 e^{i\omega t}$, the solution is

$$p(t) = p_o e^{i\omega t} = \frac{-K_E v_o e^{i\omega t}}{1 + i\omega/\omega_r}\,. \tag{19}$$

Hence, even though K_E for the rock is a constant over our experimental frequency range, the observed ELO coefficient has a frequency response in the form of a Debye relaxation:

$$K_E^{\mathrm{obs}} = -\frac{p_o e^{i\omega t}}{v_o e^{i\omega t}} = \frac{K_E}{1 + i\omega/\omega_r} = \frac{K_E}{\sqrt{1+(\omega/\omega_r)^2}}e^{-i\delta} \tag{20}$$

Table 2: The formation factor and power-law exponents for the 12 samples taken from fits to the data obtained with 0.05, 0.1, 0.2, 0.4, and 0.8M NaCl brine saturation. The exponents are defined by the relations $K_S = \sigma_w^{-\nu_S}$, $K_E = \sigma_w^{-\nu_E}$, and $\zeta_e = \sigma_w^{-\nu_\zeta}$. The capillary-tube model predicts $\nu_S = 1.50$, $\nu_E = 0.50$, and $\nu_\zeta = 0.50$. The abbreviation "FB" stands for "Fontainebleau".

Sample	Form. factor $F = \sigma_w/\sigma_r$	ν_S	ν_E	ν_ζ
Sandstones				
FB-A	11.4	1.41	0.40	0.38
FB-B	19.8	1.41	0.54	0.39
FB-C	137	1.40	0.37	0.38
Berea-A	11.6	1.21	0.29	0.19
Berea-B	21.2	1.03	0.38	0.01
Bandera	19.8	0.77	0.22	-0.26
Limestones				
Whitestone	17.1	1.40	0.70	0.38
Indiana	37.0	1.30	0.32	0.28
Fused Glass Beads				
50μm-A	58.8	1.07	0.49	0.04
50μm-B	17.1	1.20	0.02	0.18
100μm	13.3	1.17	0.23	0.15
200μm	9.04	1.39	0.47	0.37

where the phase angle δ is defined by $\tan\delta = \omega/\omega_r$. Figure 4 illustrates how well the data for $K_E^{\rm obs}$ and δ fit the Debye relaxation. The same holds for all our samples.

With the above understanding of the measured $K_E^{\rm obs}$, we can use its magnitude and phase at a particular frequency to obtain K_E from Eq. (20). To illustrate, we arbitrarily choose the frequency ω where $\delta = 45°$, and record the magnitude of $K_E^{\rm obs}$ which should correspond to $K_E/\sqrt{2}$. This is used to calculate k_e according to Eq. (8). The result is depicted by the open symbols in Fig. 5, and as is evident, is essentially the same as that obtained from the low-frequency limit of $K_E^{\rm obs}$.

The ELO frequency response itself may also be used to determine k_r. Since $\omega_r \propto L_{22}$, and $L_{22} \propto k_r/\eta$, the frequency response of a known sample can be used to calibrate the cell and the permeability of an unknown sample can be obtained by comparing its relaxation frequency ω_r with the known sample. An example of this approach is shown in Fig. 6, where we plot the permeability (both k_e and k_d) versus the relaxation frequency. The proportionality between k and ω_r is represented by the straight line. Clearly, knowing the permeability of one sample will fix the position of this line so that a measurement of ω_r alone is sufficient to give k, and according to the discussion above, ω_r can be obtained by measuring the phase angle δ at a single frequency ω.

OPEN QUESTIONS

So far, we have shown how the electrokinetic coefficients K_E and K_S are related to other *macroscopic* transport coefficients such as σ_r and k_r. Much less is known about how K_E and K_S are related to the microscopic properties of the porous media, e.g., how K_E and K_S depend on the double-layer structure, which in turn depends on the brine concentration N_0, the interfacial chemistry and geometry. Of these, the first is easiest to control; what might one see by varying N_0? One prediction comes from the simple capillary tube model. For low salinity, the brine conductivity σ_w is proportional to N_0. Applying Eqs. (2) and (3) in Eqs. (6) and (7), we find [18]

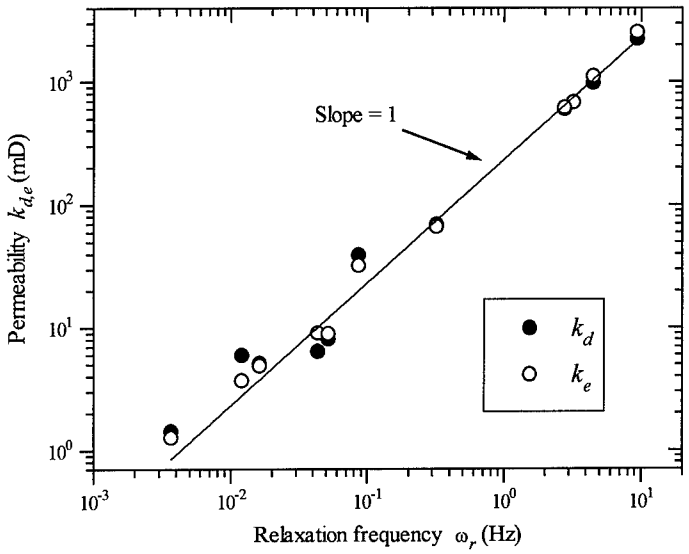


Figure 6: The relationship between the relaxation frequency ω_r and the permeability $k_{e,d}$ for the 12 samples. On the log-log plot, the slope of the line is 1, indicating a direct proportionality.

$$K_S^{\rm cap} \propto \sigma_w^{-3/2}, \tag{21}$$

$$K_E^{\rm cap} \propto \sigma_w^{-1/2}. \tag{22}$$

To test these predictions,we carried out measurements for brine concentrations of 0.05, 0.1, 0.2, 0.4, and 0.8M NaCl. Our results show that K_S and K_E follow a power-law, but the exponents *do not* agree with Eqs. (21) and (22). These are summarized in Table 2.

This discrepancy is not understood, but they suggest that the fractal nature of the pore surface and interfacial chemistry may be important. We note that, unlike a capillary tube, sandstone is known to have fractally rough pore surfaces for length scales above a few ångstroms [19, 20, 21]. The screening length λ provides a natural length scale to measure any property of the surface. Since a fractal surface is expected to exhibit scaling behavior, one expects K_S and K_E to have a power-law dependence on λ, and hence in σ_w. This qualitative argument applies to R_e and ζ_e as well but there is no quantitative theory to relate all the exponents to the fractal dimension at this time. On the other hand, the sample could be physically changed when the brine concentration was changed, but our remeasurements maintain the original trends.

Another open question is the role of interfacial chemistry, e.g., adsorption and desorption of ions in the Stern layer can occur in response to the charge movement in the diffuse layer. Eqs. (2)–(3) and (6)–(7) do not account for such effects which may be the cause for the constant-phase-angle impedance seen in our samples. These effects may depend on brine concentration, local geometry, ion type and temperature. We are currently pursuing some of these studies.

A peculiar effect, not seen in all of the samples, is that k_e and R_e can vary with σ_w. Assuming that the fractal roughness is responsible for the power-law dependence on σ_w, we have previously

suggested that flow circulations, caused by the electrokinetic dynamics may produce eddy currents that reach much farther into the pore spaces than the typical size of λ [18]. It is also possible that the presence of the double layer lead to the breakdown of the usual no-slip boundary condition of viscous flow. When the structure of the double layer is changed at the nanometer scale, it could affect the effective flow radius R_e on the micrometer scale.

CONCLUSION

We have shown that ac technique allows us to determine K_E and K_S with a high level of accuracy. The coefficients can be used to deduce k_r, as well as a unique radius that controls the flow of charge and fluid (R_e) and an effective the zeta potential (ζ_e). These two microscopic parameters of the porous media cannot be easily obtained otherwise. There is much potential for using the methods to improve our understanding of other properties of the porous media, e.g., the roles of surface roughness and chemistry in the flow dynamics.

ACKNOWLEDGMENTS

We have benefited from experimental assistance and discussions with X. Li, L. Shi and P. Johnson. This work is supported by the Gas Research Institute under Contract 5090-260-1953, and the National Science Foundation under Grant DMR-9404672.

REFERENCES

1. P.-z. Wong, MRS Bull. **19** (5) p.32 (1994).
2. P.-z. Wong, J. Koplik, and J. P. Tomanic, Phys. Rev. B **30**, 6606 (1984).
3. A. J. Katz and A. H. Thompson, Phys. Rev. B **34**, 8179 (1986).
4. W. E. Kenyon, P. I. Day, C. Straley, and J. F. Willemsen, SPE Paper No. 15643 (1986).
5. A. H. Thompson, S. W. Sinton, S. L. Huff, A. J. Katz, R. A. Rashke, and G. A. Gist, J. Appl. Phys. **65**, 3259 (1989).
6. S. X. Li, D. B. Pengra, and P.-z. Wong, Phys. Rev. E **51**, 5748 (1995).
7. U. Saxén, Ann. Physik und Chemie **47**, 46 (1892).
8. L. Onsager, Phys. Rev. **37**, 405 (1931); **38**, 2265 (1931).
9. G. Kortüm, Treatise on Electrochemistry, 2nd revised English edition (Elsevier, Amsterdam, 1965).
10. D. L. Johnson, J. Koplik and L. M. Schwartz, Phys. Rev. Lett. 57, 2564 (1986).
11. See, for example, S. R. deGroot and P. Mazur, Non-Equilibrium Thermodynamics (North-Holland, Amsterdam, 1962).
12. M. R. J. Wyllie, Petro. Trans. AIME **192**, T.P. 2940 (1951).
13. See, for example, P. Horowitz and W. Hill, *The Art of Electronics,* 2nd ed. (Cambridge University, New York, 1983), pp. 628–631.
14. A. LeMehaute and G. Crepy, Solid State Ionics **9–10**, 17 (1983).
15. T. Pajkossy, J. Electroanal. Chem. **364**, 111 (1994).
16. Q.-z. Cao, P.-z. Wong and L. M. Schwartz, Phys. Rev. B **50**, 5771 (1994).
17. T. J. Plona and D. L. Johnson, in *1980 Ultrasonics Symposium,* 868 (IEEE, 1980).
18. D. B. Pengra, S. X. Li, L. Shi, and P.-z. Wong, in *Dynamics in Small Confining Systems II,* Mat. Res. Soc. Symp. Proc. **366,** J. M. Drake, J. Klafter, R. Kopelman, S. M. Troian, eds., pp. 201–206 (MRS, Pittsburg, 1995).
19. P.-z. Wong, Physics Today **41**, No. 12, 24 (1988).
20. P.-z. Wong, J. Howard, and J.-S. Lin, Phys. Rev. Lett. **57**, 637 (1986).
21. A. H. Thompson, A. J. Katz and C. E. Krohn, Adv. in Phys. **36**, 625 (1987).

A MODEL FOR THE TWO-PHASE BEHAVIOR OF FLUIDS IN DILUTE POROUS MEDIA

JAMES P. DONLEY, REBECCA M. NYQUIST and ANDREA J. LIU
Department of Chemistry and Biochemistry, University of California, Los Angeles, CA 90095

ABSTRACT

Experiments show that the coexistence region of a vapor-liquid system or binary liquid mixture is dramatically narrowed when the fluid is confined in a dilute porous medium such as a silica aerogel. We propose a simple model of the gel as a periodic array of cylindrical strands, and study the phase behavior of an Ising system confined in this geometry. Our results suggest that the coexistence region should widen out at lower temperatures, and that the narrowness observed near the critical point may be a fluctuation-induced effect.

INTRODUCTION

Simple liquids and many binary liquid mixtures exhibit phase separation below a critical temperature. When they are confined in dilute porous media such as silica gels, however, their phase behavior is dramatically altered. For example, Wong and Chan showed that the vapor-liquid coexistence curves of ^{4}He and nitrogen are shifted to lower temperatures and higher densities, and are narrowed by factors of order 15 or more[1]. In addition, Zhuang and Cannell recently found that the coexistence curve of the binary isobutyric acid/water mixture is greatly narrowed when a silica gel is present[2]. The fact that two vapor-liquid systems and a binary liquid mixture show the same behavior when confined in dilute gels suggests some degree of universality in the phenomenon. However, it is highly surprising that a small amount of impurity in the form of a dilute gel can have such a pronounced effect on the phase diagram.

In this work, we propose a simple model that permits analytical treatment and appears to capture the observed behavior. Previous theoretical approaches have concentrated on the effects of disorder in the gel structure by modeling the system as a random field Ising model[3], and have failed to reproduce the observed narrow coexistence curve. In contrast to the random field approach, we neglect disorder and instead focus on the effects of strong surface-fluid interactions, which preferentially attract one phase over the other to the surface of the gel strands. To capture aspects of the gel structure without including disorder, we model the porous medium as a periodic array of cylindrical strands. A dilute silica gel, with volume fraction between 1-5%, is a fractal network of thin strands up to some crossover length, ξ_x, typically between 20-100 nm, and is random at larger length scales[4]. By modeling this structure as a periodic system, we neglect disorder as well as the fractal character of the structure[5], but we preserve the characteristic mesh size ξ_x as the lattice spacing of the periodic network, and we retain the fact that the internal surface is correlated into strands of nonzero radius a. The model reproduces a narrow coexistence region near the critical point, in qualitative agreement with the experimental results. At

Mat. Res. Soc. Symp. Proc. Vol. 407 © 1996 Materials Research Society

lower temperatures, however, we find that the coexistence region widens abruptly. This prediction provides a challenge to experiments.

THEORY AND ANALYSIS

The specific model porous medium that we have studied is an hexagonal array of infinitely long thin cylinders of radius a, which represent gel strands, spaced at a distance ξ_x apart. We take advantage of the proximity to a critical point to make use of universality and to couch the problem in terms of the Ising model. Thus, we picture the space in between strands as filled with a lattice of spins that can point either up or down, and that are coupled by nearest-neighbor ferromagnetic interactions. We follow previous work in the wetting literature by assuming that each cylindrical surface exerts a local surface field, H_1, that prefers spins at the surface to point up[6]. In addition, there is a uniform magnetic field, H, applied to all spins. The interesting regime is where H favors spins to point down, in opposition to H_1; if both H and H_1 favor up-spins, then the system will lie in the single-phase region with most spins pointing up[7]. We make the further approximation of coarse-graining the system and using Landau-Ginzburg theory to solve for the magnetization as a function of position, $m(\vec{r})$. The main advantage of our periodic model is that the magnetization profile is also spatially periodic. In addition, the magnetization is independent of z, the coordinate along the axial direction of the strands. It is therefore sufficient to solve for $m(\vec{r})$ in the two-dimensional hexagonal unit cell. Finally, we adopt the Wigner-Seitz approximation, replacing the hexagonal unit cell by a circular one of the same area. Thus, the final geometry that we solve is a circular annulus, where the inner radius is the strand radius a and the outer radius b is related to the distance between strands ξ_x by $b(\xi_x) = \xi_x 3^{1/4}/\sqrt{2\pi}$. In order to ensure continuity of the derivative of $m(\vec{r})$, the radial derivative of the magnetization at the boundary of the unit cell must be zero. The free energy functional to be minimized is

$$\Omega[m] = \Omega_s(m_s) + \int_a^b dr(r/a)\left[f_B(m(r)) - Hm(r) + \frac{1}{2}\kappa^2(\frac{dm}{dr})^2\right], \qquad (1)$$

where H is the uniform magnetic field and κ is a molecular length related to the interaction range. The surface free energy Ω_s is a function of the magnetization at the surface of the strand at $r = a$:

$$\Omega_s(m_s) = -H_1 m_s - \frac{1}{2}gm_s^2, \qquad (2)$$

where H_1 is the surface field and g, the surface enhancement parameter, is typically negative to reflect the fact that spins at the surface have fewer neighbors than those in the bulk[6]. Finally, the bulk free energy is

$$f_B(m) = \frac{1}{2}tm^2 + \frac{1}{4}um^4, \qquad (3)$$

where $u > 0$ sets the width of the coexistence curve of the pure system. The parameter t is proportional to the reduced temperature $(T-T_c)/T_c$. When H is negative, the minimum of

the bulk free energy lies at a negative value of m. Thus, Eq. 1 represents the competition of three effects: the surface term favors a high positive magnetization near the strand because H_1 is positive, the bulk free energy favors a negative magnetization away from the strand because H is negative, and the square gradient term favors gradual spatial changes in the magnetization. Minimization of Eq. 1 yields a second-order, nonlinear differential equation for $m(r)$ that we solve numerically, using a relaxation method[8]. We then compute the average magnetization $\bar{m} = 2\int_a^b drrm(r)/(b^2 - a^2)$. The resulting $\bar{m}$ vs. H isotherms are used to construct the coexistence curve.

The results of the analysis are shown in Fig. 1, where we have plotted the phase diagram in the magnetization-temperature plane. The solid line represents the coexistence curve of the pure system, while the dashed line is the coexistence curve of the system confined in a 4%-volume-fraction periodic gel. Note that the presence of the gel causes the critical point to shift to higher magnetization, $\bar{m}_c > 0$, and lower temperature, $t_c < 0$. The shift towards higher magnetization results from the preference of the surface for up-spins, while the shift towards lower temperature results from the competition between the surface field, $H_1 > 0$, and the bulk magnetic field, $H < 0$, which discourages long-range order. This qualitative shift of the critical point to higher $\bar{m}$ and lower t is consistent with experimental results, but there are significant differences. For example, the dashed coexistence curve in Fig. 1 is much wider than the experimentally observed coexistence curve. The second and more significant difference lies in the position of the new coexistence curve. The right edge of the dashed curve in Fig. 1 falls outside the bulk coexistence curve, while the right edge of the experimental curve falls well inside the bulk coexistence curve[1].

The fact that a mean field treatment of the periodic model fails to yield a narrow coexistence curve may indicate that fluctuations are important. Experimental evidence also points in this direction. The narrow coexistence curves observed experimentally in the confined vapor-liquid [1] and binary liquid [2] systems lie well inside the critical region of the corresponding pure systems. Thus, mean field theory provides a poor approximation to the equation of state of the pure system in the temperature regime of the experiments.

Widom scaling represents the simplest way to include fluctuation effects; it is a phenomenological generalization of mean field theory that incorporates the effects of fluctuations on the equation of state by using renormalized exponent values[9]. The approach has been useful to several other problems involving inhomogeneous composition profiles, such as the vapor-liquid interface near the critical point[10] and the critical adsorption profile near a planar surface[11]. According to Widom scaling, one simply replaces the bulk free energy in Eq. 3 with the more general form

$$f_B(m) = \frac{1}{x}t|m|^x + \frac{1}{y}u|m|^y, \qquad (4)$$

where $y > x$ and $x \geq 2$. The resulting critical exponents can be expressed in terms of x and y: for example, the coexistence curve exponent is $\beta = 1/(y - x)$, and the correlation length exponent is $\nu = \frac{1}{2}(y - 2)/(y - x)$ [12]. The choice $x = 3$, $y = 6$ yields the exponent values $\beta = 1/3$, $\nu = 2/3$, which are are close to the three-dimensional Ising estimates: $\beta \approx 0.33$, $\nu \approx 0.63$.

The results of using Eq. 4 with $x = 3$ and $y = 6$ on our periodic model are strikingly different from the mean-field results. The phase diagrams in the temperature-

magnetization plane and field-temperature plane are shown in Fig. 2. There are now two critical points crowning two narrower coexistence curves (a "double hump"). Below a triple point, marked t_t in Fig. 2, we recover the usual wide two-phase coexistence region. The triple point in the $t-\bar{m}$ diagram corresponds to the point at which two arms branch off in the $H-t$ diagram, the left-hand hump in the $t-\bar{m}$ plane corresponds to the lower arm and the right-hand hump corresponds to the upper arm in the $H-t$ diagram. We note that, although each phase may be represented in terms of a single average magnetization $\bar{m}$ as in Fig. 2, the phases are actually inhomogeneous, with high positive magnetization near the strands and lower magnetization between strands. Last, if the field H_1 is decreased below a critical value H_{1c}, the double hump disappears, leaving a single narrow hump with a shoulder. When H_1 is decreased further the shoulder disappears, and the single coexistence curve widens and moves upwards to approach the bulk coexistence curve. Since the double-hump only exists if H_1 is sufficiently strong, it can be viewed as a result of the strong surface interaction and the high surface-area/volume ratio in the periodic porous medium.

The physical origin of the double-hump behavior lies in the balance of effects that determine the shapes of the profiles. As stated above, an equilibrium profile is produced by a competition between the surface field H_1, bulk field H, and terms contributing to the interfacial energy. Increasing the exponent ν decreases the cost to form interfaces and thus alters the balance between these three effects.

Our prediction in Fig. 2 may be consistent with experimental results, which are limited to a small region near the critical point. The experimental data may represent the top of the left hump, and the right hump may exist only at temperatures below the range of the existing data. This possibility remains to be tested by experiments. Note that the width of the left-hand coexistence region is still only roughly a factor of 3 times smaller than the bulk coexistence curve, as compared to the experimentally observed factor of 15. Part of the remaining discrepancy may be due to the fractal nature of the gel, or the form of the surface interaction, which here we have crudely modeled as a contact interaction.

SUMMARY

In summary, we have shown that an Ising system confined in a dilute array of cylindrical strands shows unexpectedly rich phase behavior that may be consistent with puzzling experimental results. In particular, we find a phase diagram with two narrow coexistence curves, with two critical points, or a narrow coexistence region with a shoulder. Although experiments have observed that the coexistence region is extremely narrow near the critical point, our results imply that the coexistence region should widen at lower temperatures, below the range of existing data. The unusual behavior that we have predicted is markedly different from the phase behavior of the pure, unconfined system, and results from the strong surface interaction and the high surface-area/volume ratio of the porous medium. Both surface and bulk effects contribute to the phase behavior. The importance of both surface and bulk effects is characteristic of true mesoscopic systems such as near-critical fluids confined between two plates or in cylindrical pores. In such systems, however, the correlation length for composition fluctuations in the fluid is limited by the plate spacing

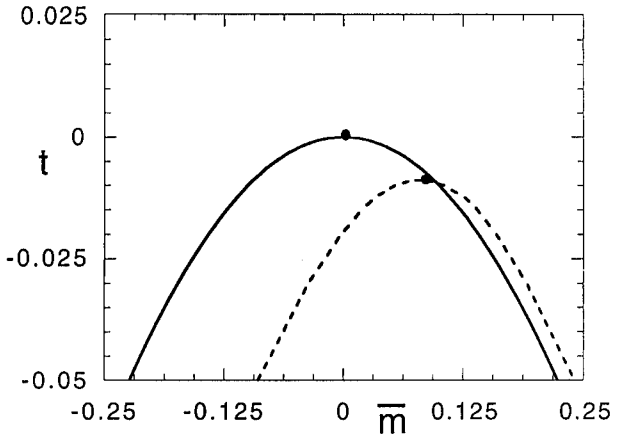


Fig. 1 The mean-field coexistence curve of the periodic model (dashed) for a 4%-volume-fraction gel with $H_1/k_BT = 2$, $g/k_BT = -1$ and $u = 1$. The coexistence curve of the pure system (solid) is shown for comparison.

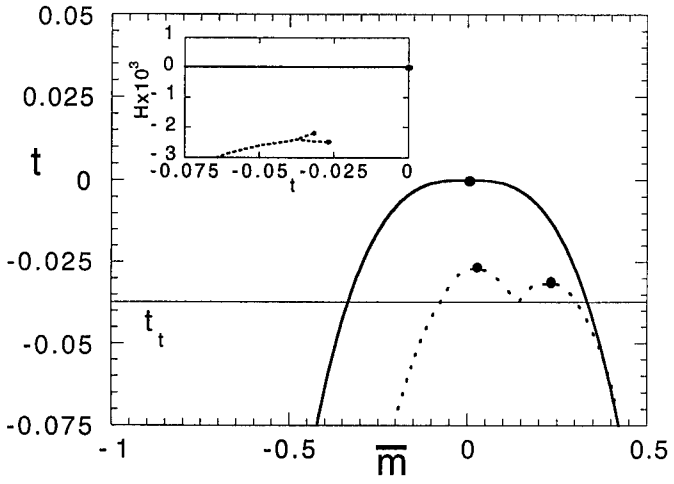


Fig. 2 The coexistence curve (dashed) of the periodic model calculated using Widom scaling under the same conditions as in Fig. 1. There are two critical points and a triple point at a reduced temperature t_t. The coexistence curve of the pure system (solid), also calculated using Widom scaling, is shown for comparison. Inset: The corresponding phase diagram in the $H - t$ plane showing the forked coexistence line (dashed); the coexistence line of the pure system at $H = 0$, $t > 0$ (solid) is shown for comparison.

or pore size. In the case of a dilute porous medium, the fluid occupies nearly all of the sample volume, so there are no complicating finite-size effects. Thus, a near-critical fluid in a dilute porous gel is an illuminating example of a *macroscopic*, fully three-dimensional system that displays *mesoscopic* behavior. Support of the Petroleum Research Fund and Exxon Education Fund is gratefully acknowledged.

REFERENCES

1. A. P. Y. Wong and M. H. W. Chan, Phys. Rev. Lett. **65**, 2567 (1990).

2. Z. M. Zhuang and D. S. Cannell, preprint (1995).

3. A. Maritan, M. R. Swift, M. Cieplak, M. H. W. Chan, M. W. Cole and J. R. Banavar, Phys. Rev. Lett. **67**, 1821 (1991).

4. F. Ferri, B. J. Frisken and D. S. Cannell, Phys. Rev. Lett. **67**, 3626 (1991).

5. Recently, Falicov and Berker used numerical simulations to study ^{3}He-^{4}He mixtures in both fractal and periodic networks. In both cases, they found that the superfluid transition becomes detached from the phase-separation transition, in accord with experiments. Although their system is different from ours, their work supports our use of a periodic model of the gel network to study near-critical fluids in dilute porous media. See A. Falicov and A. N. Berker, Phys. Rev. Lett. **74**, 426 (1995); and S. B. Kim, J. Ma and M. H. W. Chan, Phys. Rev. Lett. **71**, 2268 (1993).

6. H. Nakanishi and M. E. Fisher, J. Chem. Phys. **78**, 3279 (1983).

7. This is a manifestation of capillary condensation, where the phase transition is shifted to a value of the bulk field (or chemical potential in the fluid case) that favors the nonwetting phase.

8. W. H. Press, B. P. Flannery, S. A. Teukolsky and W. T. Vetterling, *Numerical Recipes* (Cambridge University Press, New York, 1986).

9. J. S. Rowlinson and B. Widom, *Molecular Theory of Capillarity* (Oxford University Press, New York, 1989).

10. S. Fisk and B. Widom, J. Chem. Phys. **50**, 3219 (1969).

11. M. E. Fisher and P.-G. de Gennes, C. R. Acad. Sci. Ser. B **287**, 107 (1978).

12. S. Dietrich, in *Phase Transitions and Critical Phenomena*, ed. C. Domb and J. L. Lebowitz (Academic Press, London, 1988), vol. 12, p. 1.

AN EXPERIMENTAL STUDY OF THE DYNAMICS OF CONTACT LINES

S. KUMAR, M.O. ROBBINS AND D.H. REICH
Department of Physics and Astronomy, The Johns Hopkins University, Baltimore, MD 21218

ABSTRACT

We have studied the dynamics of contact lines formed by water-alkane interfaces in capillaries with random surface disorder. We find that the contact-line velocity V scales with the applied capillary pressure P as $V \sim (P - P_t)^{\zeta}$ over two decades in V. This is consistent with a critical depinning transition. We obtain this result by using a sensitive ac differential-pressure measurement technique to measure dP/dV. We find that $dP/dV \propto V^{-0.80(5)}$ implying that $1/\zeta = 0.20(5)$.

INTRODUCTION

The scaling properties of interfaces driven through disordered media have received considerable attention in recent years [1]. In the presence of quenched disorder, the depinning of an interface is described as a non-equilibrium critical transition similar to that seen at the onset of charge density wave conduction [2]. The dynamics of an interface between two immiscible fluids in a porous medium is regarded as belonging to this class of random-field problems [3]. However, interface motion in this system is complicated by the existence of disorder on two length scales: variation in pore size as well as smaller scale defects on the pore walls. To mimic a liquid-liquid interface in an individual pore, we have studied the dynamics in a single capillary, and hence have separated the effects of the two types of disorder mentioned above.

Chemical heterogeneities or roughness on the capillary walls affect the motion of the contact line where the fluid-fluid interface meets the wall. For weak applied pressures P, disorder pins the interface into one of many metastable positions by pinning the contact line. The depinning of this line, at a threshold applied pressure P_t, is believed to be a critical transition and the subsequent nonlinear transport is expected to scale as a power law $V \propto (P - P_t)^{\zeta}$ [4,5]. There have been several predictions for the velocity exponent ζ [5–7] but few experiments have attempted to measure it. We have measured ζ by using a sensitive ac pressure measurement technique to study the low-frequency behavior of water-alkane interfaces in capillaries with random surface disorder.

EXPERIMENT

At low velocities, the capillary pressure P across the interface is related to the dynamic contact angle θ between the fluid-fluid interface and the surface by $P = (2\gamma \cos\theta)/R$ where R is the tube radius and γ the interfacial tension. We have measured the velocity dependence of θ for water-hexadecane and water-decane interfaces in Pyrex capillaries. These fluid interfaces showed substantial contact angle hysteresis (i.e. remain pinned over a range of contact angles or pressures) due to disorder on the tube walls [8]. We use an ac technique to measure the derivative $d\cos\theta/dV$ by superimposing an oscillatory velocity $V(\omega)$ upon the mean interface velocity V [8,9].

A constant mean velocity V is set by the adjustable height difference between water

Mat. Res. Soc. Symp. Proc. Vol. 407 © 1996 Materials Research Society

and alkane reservoirs, and by the high hydrodynamic impedance of a narrower capillary (R = 0.1 mm) in series with the sample capillary(R = 0.5 mm). An ac velocity $V(\omega)$ is imposed upon the flow by a speaker coupled to the fluids by a membrane. Two pressure sensors placed at the ends of the sample tube are used to measure the pressure across the interface. $V(\omega)$ is obtained from the viscous pressure drop across a third tube in series with the others. $V(\omega)$ and the ac interface response $P(\omega)$ are extracted by digital lock-in methods [10]. At low frequencies and for small $V(\omega)$, $P(\omega)/V(\omega) = dP/dV$. The large dielectric contrast between water and the alkanes ($\epsilon_{water}/\epsilon_{alkane} \sim 16$) is employed to monitor the dc interface velocity V by measurement of the capacitance of a pair of semicylindrical copper plates placed along the length of the sample capillary. The capacitance measurement is also used to monitor the interface position to ensure that $d\cos\theta/dV$ is measured over the same section of the tube at each V to minimize possible systematic effects due to variations in heterogeneity, viscosity, and tube diameter.

The interface responds to the ac velocity by bowing as well as sliding. When the measurement frequency ω is less than a characteristic frequency ω_c, the sliding mode dominates. In this limit $P(\omega)$ is primarily in phase with $V(\omega)$ and accurately reflects dP/dV [9]. The value of ω_c is found to decrease with decreasing velocity and hence, to remain in the regime of interest, ω must be lowered as V is decreased. With the use of digital lock-in techniques, we have extended the frequency range down to 0.025 Hz, consequently extending the range of V two orders of magnitude deeper into the critical regime than was previously possible with this technique [9].

RESULTS

We have measured the response of water-hexadecane (γ = 32.6 dyn/cm) and water-decane (γ = 41 dyn/cm) interfaces. The mean velocity V spanned the range 2×10^{-3} cm/s $< V < 2.3 \times 10^{-1}$ cm/s. The dimensionless capillary number $Ca \equiv \bar{\mu}V/\gamma$ where $\bar{\mu}$ is the mean viscosity of the two fluids, ranged from $5 \times 10^{-7} < Ca < 1.5 \times 10^{-4}$. The in-phase response contains a contribution from the viscous pressure $P_{visc}(\omega) = 8\bar{\mu}V(\omega)L/R^2$. The mean $P_{visc}(\omega)$ is determined by averaging the response with the interface moved outside either end of the sample tube. This has been subtracted from the data shown in the figures. This background is 2.4×10^3 and 4.8×10^3 for water-decane and water-hexadecane, respectively, in units of $d\cos\theta/dCa$.

Figure 1 shows the in-phase pressure response, expressed as the dimensionless derivative $d\cos\theta/dCa$, measured at fixed $V(\omega)$ and at frequencies ranging from 1 Hz to 0.05 Hz. Note the rollover in the in-phase response at low velocities. A corresponding increase is observed in the out-of-phase response (shown for 0.05 Hz). As ω decreases, this rollover moves to lower velocities. The characteristic frequency ω_c for the rollover was previously predicted to be given by

$$\omega_c = \frac{\gamma}{\mu R} \frac{\sin\theta(1+\sin\theta)^2}{(d\cos\theta/dCa)_{\omega\to 0}} \tag{1}$$

which is related to the time required for the curvature of the interface to adapt to changes in the contact angle [9,11,12]. This would imply that the data at, for example, $Ca = 1 \times 10^{-6}$ in Fig. 1 should be in phase with $V(\omega)$ for frequencies less than 1 Hz. However, our data at this Ca show that $d\cos\theta/dCa$ is depressed considerably at 0.5 Hz and hence, are consistent with a much lower ω_c. One possibility is that that the relevant characteristic frequency

is $\omega_c/2\pi = Ca\ \gamma/\mu R$ which is associated with the time required for the interface to move a distance R. Previous experiments have observed that this is the time required for the interface to attain the appropriate dynamic contact angle θ for the instantaneous velocity [13]. The latter frequency is 0.08 Hz at $Ca = 1 \times 10^{-6}$ for the data shown in Fig. 1.

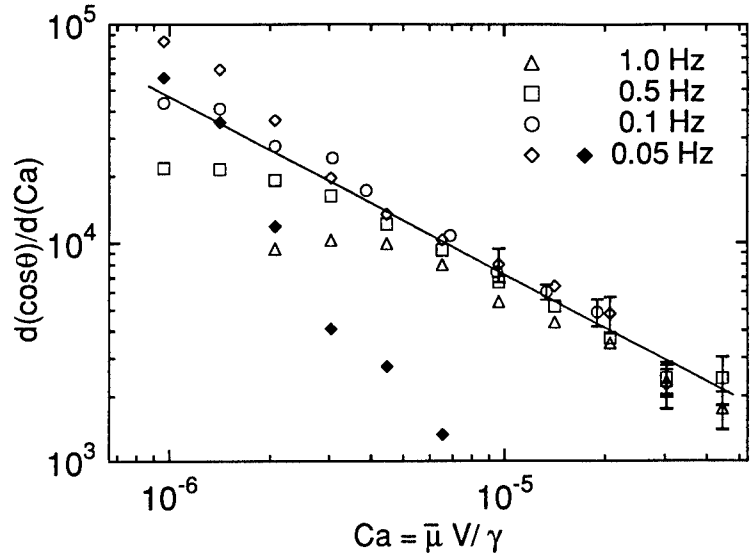


FIG. 1. Frequency dependence of the in-phase response (open symbols) of a water-decane interface with $\mu V_{ac}/\gamma = 2.5 \times 10^{-6}$. The out-of-phase response at 0.05 Hz is also indicated (closed symbols). The straight line shows the power law fit for water-decane from Fig. 2.

The derivative $d\cos\theta/dV$ is directly proportional to $P(\omega)/V(\omega)$ only in the limit of small $V(\omega)/V$. This is because higher order terms in $V(\omega)$ in the expansion for $P(\omega)$ begin to become significant and the response becomes non-linear. This rise affects the data at low Ca in Fig. 1 and is most apparent at the lowest frequencies. We found $d\cos\theta/dCa$ became independent of $V(\omega)$ as $V(\omega)$ decreased below $V/2$.

In the limit of sufficiently low ω and for $V(\omega) \leq V/3$, the in-phase response was found to obey a power law $d\cos\theta/dCa = B\ (Ca)^x$. Fig. 2 shows $d\cos\theta/dCa$ for water-decane and water-hexadecane interfaces. Fits for water advancing (solid lines) give B = 0.7(2) and x = -0.81(5) for water-decane, and B = 1.1(3) and x = -0.77(5) for water-hexadecane. Consistent data were obtained with several Pyrex tubes of similar diameter, with the reversal of flow direction(diamonds), and also for a chemically etched tube with increased surface roughness (circles). The etched tube exhibits greater contact angle hysteresis than the unetched tube [8], but fits to the data in Fig. 2 resulted in a nearly identical value of x for water-hexadecane : x = -0.81(5) and B = 1.6(3).

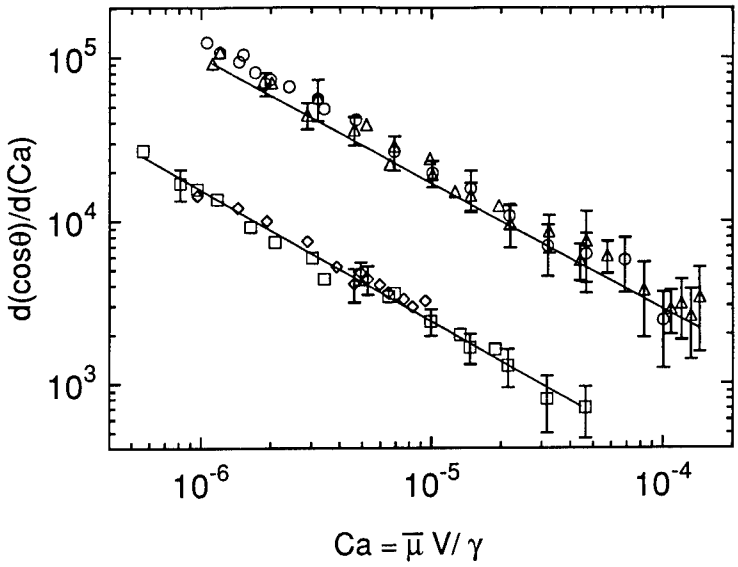


FIG. 2. Values of $d\cos\theta/dCa$ obtained from the averaged in-phase response in the low V_{ac} and low frequency limits. Data for water-decane in unetched tubes with water advancing (squares) and receding (diamonds) are divided by 3 to prevent overlap with data for water displacing hexadecane in unetched (triangles) and etched (circles) tubes. The straight lines are fits to the data shown by squares and triangles and have slope -0.81 and -0.77, respectively. Error bars are shown when uncertainties are larger than the symbol size.

CONCLUSIONS

Our value of x implies $1/\zeta = 1 + x = 0.20(5)$. This is smaller than the values of $1/\zeta$ found in experiments using liquid mixtures [9,14], and is consistent with experiments on other pure-fluid systems [15]. One possibility is that concentration gradients at the contact line in mixtures may affect the critical dynamics.

Our result clearly disagrees with the prediction $1/\zeta = 9/7$ from the functional RG calculations of Ertaş and Kardar [5]. Our exponent does, however, fall in the broad range i.e. $0 < 1/\zeta \leq 0.5$ predicted by the capillary-wave dissipation mechanism of Zhou and Sheng [11]. Our velocity exponent is also much smaller than the predictions of $1/\zeta = 2/3$ (for smooth defects) by Joanny and Robbins [6] and also by Raphael and DeGennes [7]. However both predictions are for the case of somewhat idealized defects: periodic heterogeneities in the former case and single non-interacting defects in the latter analysis. These limiting cases can be experimentally tested with artificially structured defects.

ACKNOWLEDGEMENTS

This work was supported by the NSF under grants DMR-9357518 and DMR-9110004, and by the Exxon Education Foundation. D.H.R. acknowledges support from the David and Lucille Packard Foundation.

REFERENCES

1. O. Narayan and D. S. Fisher, Phys. Rev B **48**, 7030 (1993); T. Natterman, S. Stepanow, L. H. Tang, and H. Leschhorn, J. Phys. II **2**, 1483 (1992); L. A. N. Amaral, A. L. Barabasi, H. A. Makse, and H. E. Stanley, Phys. Rev E **52**, 4087 (1995).
2. D. S. Fisher, Phys. Rev B **31**, 1396 (1985).
3. N. Martys, M. Cieplak, and M. O. Robbins, Phys. Rev. Lett. **66**, 1058 (1991); Phys. Rev. B **44**, 12294 (1991).
4. M. O. Robbins and J.F. Joanny, Europhys. Lett. **3**, 729 (1987).
5. D. Ertaş and M. Kardar, Phys. Rev. E **49**, R2532 (1994).
6. J. F. Joanny and M. O. Robbins, J. Chem. Phys. **92**, 3206 (1990).
7. E. Raphael and P. G. DeGennes, J. Chem. Phys. **90**, 7577 (1989).
8. S. Kumar, D. H. Reich, and M. O. Robbins, Phys. Rev. E (Rap. Comm.) **52** (1995).
9. J. P. Stokes, M. J. Higgins, A. P. Kushnick, S. Bhattacharya, and M.O. Robbins, Phys. Rev. Lett. **65**, 1885 (1990).
10. P. K. Dixon and L. Wu, Rev. Sci. Instrum. **60**, 3329 (1989).
11. P. Sheng and M. Zhou, Phys. Rev. A **45**, 5694 (1992).
12. E. Charlaix and H. Gayvallet, J. Phys. II **2**, 2025 (1992).
13. M. Fermigier and P. Jennfer, J. Coll. Int. Sci. **146**, 226 (1991).
14. T. A. Mumley, C. J. Radke, and M. C. Williams, J. Coll. Int. Sci. **109**, 413 (1986).
15. A. Calvo, I. Paterson, R. Chertkoff, M. Rosen, and J. P. Hulin, J. Coll. Int .Sci. **141**, 384 (1991).

PINNING OF WATER IMBIBITION FRONT IN POROUS MEDIA

PO-ZEN WONG*, THOMAS DELKER†, MORGAN HOTT AND DAVID B. PENGRA
Department of Physics and Astronomy, University of Massachusetts, Amherst, MA 01003

ABSTRACT

We report a study of the dynamics of capillary rise of water in a column of glass beads. The water column height h is measured as a function of time t. Analyzing the late-time data in terms of critical pinning, $dh/dt \propto (P - P_c)^\beta$, we find an anomalously large exponent β. A similar measurement for contact line pinning in capillary tubes indicates $\beta < 1$. We discuss these findings in light of recent theories for domain wall pinning in the random-field Ising model and suggest a new equation of motion which corresponds to the Wolf-Villain model with quenched noise.

INTRODUCTION

Pinning phenomena occur in a variety of physical systems. Koplik and Levine [1] suggested in 1985 that the dynamics of fluid interfaces [2] in random porous media is analogous to that of domain walls in random-field magnets [3]. Assuming that the fluid interface is described by a single-valued function $z = f(\mathbf{x}, t)$, where $\mathbf{x}$ is a $(d-1)$-component transverse vector, they argued that the appropriate equation of motion is

$$\frac{\partial f}{\partial t} = P + \nabla^2 f + Y(\mathbf{x}, f) \ , \tag{1}$$

where P is a uniform driving force, $\nabla^2 f$ is an effective surface tension that minimizes the surface area, and Y represents quenched random capillary forces acting on the interface. They noted that the same equation was used by Bruinsma and Aeppli [4] to study domain wall dynamics in the random-field Ising model (RFIM). The underlying connection is that Eq. (1) is the time-dependent Ginzburg-Landau equation

$$\frac{\partial f}{\partial t} = P - \frac{\delta F}{\delta f} \tag{2}$$

for the RFIM interface free energy derived by Grinstein and Ma [5]

$$F(f) = \int d^{d-1}x \left[\frac{1}{2} |\nabla f|^2 - \int_\infty^f dz Y(\mathbf{x}, z) \right] \ . \tag{3}$$

For small values of Y, Koplik and Levine find that the interface translates smoothly in response to the applied force, but for large values of Y, it can be pinned in rough configurations.

The critical behavior of the depinning transition in RFIM has recently been analyzed by Nattermann *et al.* [6], and independently by Narayan and Fisher [7]. The same results were

Mat. Res. Soc. Symp. Proc. Vol. 407 © 1996 Materials Research Society

obtained. The physical picture is that the interface fluctuation is correlated over a distance ξ along the interface which diverges as

$$\xi \propto (P - P_c)^{-\nu} \tag{4}$$

at a critical force P_c. The interface width w obeys self-affine scaling

$$w \propto \xi^{\alpha} \propto (P - P_c)^{-\nu\alpha} \tag{5}$$

with $\alpha = 2 - 1/\nu = \epsilon/3$, where $\epsilon = (5 - d)$. The advance of the interface occurs via avalanches of different sizes. The waiting time τ for an avalanche of size ξ exhibits dynamic scaling

$$\tau \propto \xi^{z} \propto (P - P_c)^{-\nu z}. \tag{6}$$

Consequently, the interface velocity is given by

$$v \propto w/\tau \propto \xi^{\alpha - z} \propto (P - P_c)^{-\nu(\alpha - z)} \equiv (P - P_c)^{\beta} \tag{7}$$

where $\beta = (z - \alpha)\nu \approx 1 - \epsilon/9 + ...$ Thus there are only two independent scaling exponents, ν and z, or equivalently α and β. For two dimensions, the theoretical predictions are $\alpha = 1$ and $\beta \approx 2/3$, and for three dimensions, $\alpha = 2/3$ and $\beta \approx 7/9$.

Experimentally, the exponent α can be determined by analyzing the interface roughness according to Eq. (5) and β may be determined by measuring the velocity v of the interface in response to the applied force P. In a previous 2D experiment [8, 9], He, Kahanda and Wong (HKW) studied the roughness of water invasion fronts in air-filled porous media. They find that the effective value of α increases towards unity as the flow rate is decreased and, at the lowest flow rates, overhangs begins to develop. This result suggests that $\alpha \to 1$ in the limit of $v \to 0$, in agreement with the prediction of the RFIM. Unfortunately, the mechanical syringe pump used in that experiment exhibits stick-slip behavior of its own as the velocity was further decreased and β could not be determined. An earlier experiment by Stokes *et al.* [10] also suggested that the critical behavior is observable for $v < 100$ μm/s, but the data were too noisy for determining β. Here we report a capillary rise experiment in 3D which does not employ any mechanical driving device. The interface is allowed to slow down on its own to approach the critical point, i.e., in a *self-organized* manner. We were able to observe the interface movement over a speed range of 0.1−1000 μm/s and estimate the value of β.

EXPERIMENTAL DESIGN

We used an 8 mm inner diameter glass tube filled with glass beads as our sample. It stands vertically in a base container filled with water. A length H_o ($\approx$ 4 cm) of the tube is immersed in the water. A Nylon filter membrane is glued to the bottom of the tube to hold the beads while letting the water through. The natural capillary pressure due to the air-water surface tension draws the water up the tube, a process known as capillary rise. A video camera records the water column height h versus time t, where h is measured from the water level of the base reservoir. The video images are digitized at set time intervals to locate the interface position. The rms width w of the interface can also be computed. Four different bead sizes are used. The average diameter D_b ranges from 180 to 510 μm ($\pm$15%). Each capillary rise experiment runs for about 24 hours. To prevent water loss due to evaporation, a small water-containing cap is placed at the top of the tube to provide 100% humidity. This cap has a 1/16-inch escape hole so that the total pressure is the same as the ambient. Additional details of the experiment are described elsewhere [11].

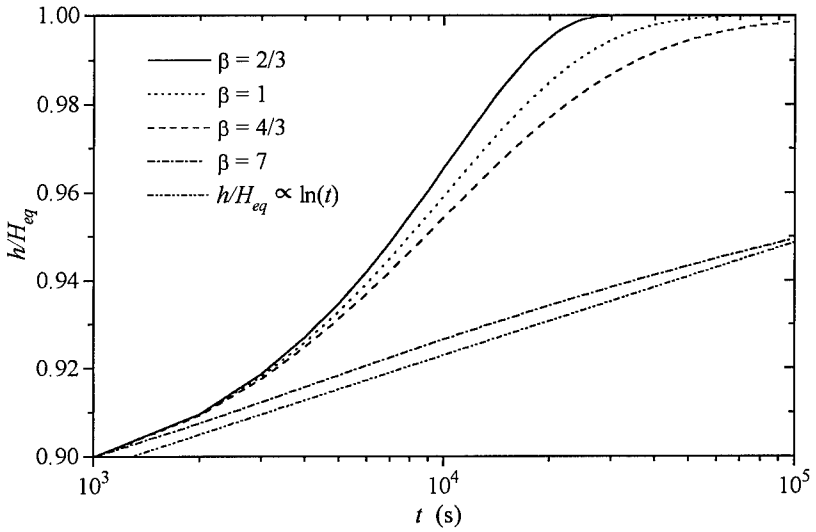


Figure 1: Effect of different values of β on the approach of h to H_{eq} through Eq. (9).

For bead diameter D_b, we expect the water column to rise to an equilibrium height $H_{eq} \propto \gamma/D_b\rho g$ where γ is the air-water surface tension, ρ is the water density and g is the gravitational acceleration. With pinning, the interface should stop at a height $H_c < H_{eq}$. Thus the *average* upward driving pressure on the interface at any height h is $P = \rho g(H_{eq} - h)$ and the threshold pinning pressure is $P_c = \rho g(H_{eq} - H_c)$. Eq. (7) leads us to write

$$\frac{dh}{dt} = v_o \left(\frac{H_c - h}{H_{eq} - H_c} \right)^{\beta} . \tag{8}$$

Integrating from initial time t_1 and height h_1 yields different results depending on the value of β. For $\beta \neq 1$, the result is

$$h(t) = H_c - (H_c - h_1)[1 + A(t - t_1)]^{1/(1-\beta)} \quad , \tag{9}$$

where $A = (\beta - 1)v_o(H_c - h_1)^{\beta-1}/(H_{eq} - H_c)^{\beta}$. If $\beta < 1$, we have $A < 0$, and h reaches H_c after a finite time given by $\tau_o = t - t_1 = -1/A$. If $\beta > 1$, h approaches H_c algebraically as $t \to \infty$. For $\beta = 1$, the integral of Eq. (8) gives,

$$h(t) = H_c - (H_c - h_1)e^{-(t-t_1)/\tau_1} \quad , \tag{10}$$

with $\tau_1 = (H_{eq} - H_c)/v_o$. Fig. 1 illustrates how the value of β affects the manner in which h approaches H_c. We note that for $\beta < 1$, h stops at H_c abruptly. For $\beta \gg 1$, the interface is slowed down severely far below H_c and cannot reach it after a long time. As we shall see, the latter behavior is qualitatively consistent with what we observed.

For the early stage of the capillary rise, the resistance to flow comes from the fluid viscosity and the behavior is expected to obey the classical Washburn equation [12]. We refer the readers to Ref. [11] for a detailed discussion.

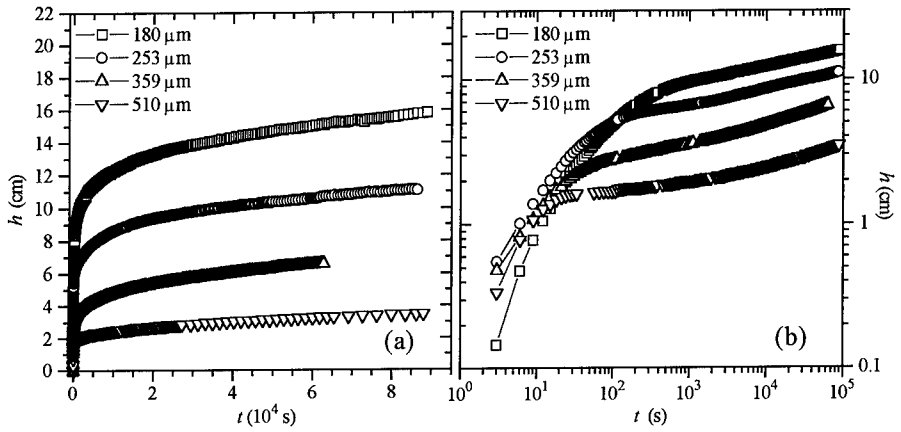


Figure 2: Height vs. time for capillary rise in glass bead columns. (a) Smaller bead diameters have higher rises and longer rise-times. (b) Log-log plot shows that rise continues, even after 24hrs.

RESULTS

Figure 2a shows the height h versus time t data for different bead sizes on a linear scale. As expected, the water column is higher for smaller beads. What is surprising is that when the data are plotted on a log-log scale in Fig. 2b, we observe that the interface is creeping upward even after 24 hours which, according to Fig. 1, strongly suggests $\beta \gg 1$. Each of the four data sets in Fig. 2b exhibits a shoulder which occurs at later times for smaller beads. This is the expected behavior based on the Washburn equation: there is a characteristic rise time τ_w given by $\tau_w \equiv Z_w \eta/\rho g k$, where $Z_w \equiv H_o + H_{eq}$, η is the water viscosity and k is the permeability of the porous medium. For bead packs, we have $k \approx D_b^2/700$ [9]. Hence we have $\tau_w \propto 1/D_b^3$ nominally. Pinning behavior should be analyzed at late times when $t \gg \tau_w$.

Figure 3a illustrates a fit of the late-time data to Eq. (8). It covers a time scale from 15 minutes to 24 hours (about 10^3 to 10^5 s). The value of β obtained from the fit is 3.4 ± 0.2. Fitting the data from different runs, with different bead sizes, and over different time scales results in an overall estimate $\beta = 6.5 \pm 3.5$, which is much larger than the prediction of $\beta = 7/9$ based on the analyses of Eq. (1). It is also interesting to note that the values of H_c obtained from the fits are always well above the experimental range of h. For example, h in Fig. 3a reaches only 7 cm and H_c is 8.4 cm. This is the consequence of the large β value, as illustrated in Fig. 1.

To contrast with the results we obtained for the bead pack, we carried out the same measurement for water rise and fall in glass capillary tubes [11, 13]. This, presumably, is an example of contact line pinning in 2D [14]. Fig. 3b shows a typical example of the result. Both the rise and fall data show abrupt pinning at finite time, indicative of the $\beta < 1$ behavior. The data before the pinning were found to fit the classical Washburn behavior extremely well. It appears that when the velocity is low enough, pinning sets in quickly and the critical region is extremely narrow. As a result, it was not possible to carry out a

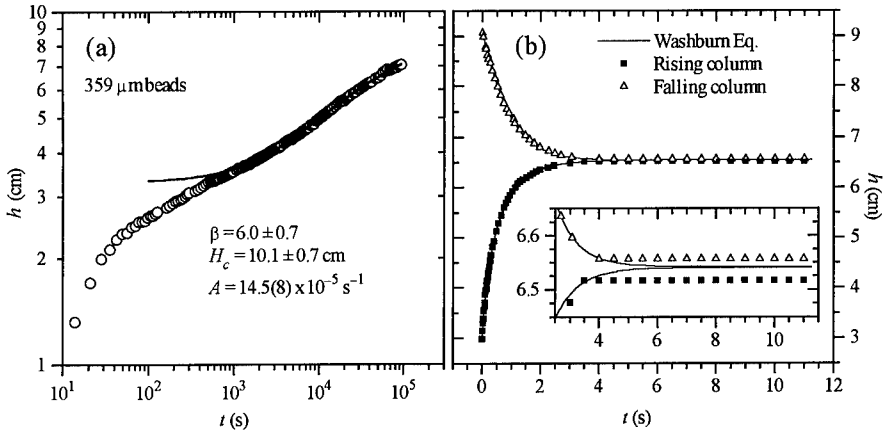


Figure 3: Comparison of pinning dynamics of (a) glass beads and (b) straight capillaries. See text for discussion.

least-squares fit to estimate the actual value of β. Nevertheless, the qualitative difference between Figs. 3a and 3b provides a striking contrast of pinning behavior in two and three dimensions.

DISCUSSION

That the value of β observed in our 3D experiment is much larger than the RFIM prediction of $\beta \approx 7/9$ may be surprising at first glance, but it is quite understandable. We note that the volume of fluid is a conserved quantity and the magnetization in the RFIM is not. As a result, while a large cluster of spins can flip all at once to cause an avalanche of the domain wall, this cannot happen to the fluid interface: a volume of fluid must flow from elsewhere to cause the interface to advance and this will naturally slow down the dynamics. The flow of fluid away from the interface is governed by a Laplacian pressure field and the importance of which was emphasized in HKW's study of 2D flow [8]. To include the effect of fluid conservation explicitly, one might consider an equation of motion of the form

$$\frac{\partial f}{\partial t} = P_a - \nabla \cdot \mathbf{J} \tag{11}$$

where the P_a-term represents a uniform applied pressure that feeds fluid into the system the $\nabla \cdot \mathbf{J}$-term represents the conserved current fluctuations about the average flow. In general, we expect $\mathbf{J} \propto -\nabla P$ where P is the pressure field in the fluid. At small enough velocity, the viscous pressure drop in fluid is negligible, only the effects of gravity and surface tension need to be considered. The gravitational pressure is $\rho g f$. The capillary pressure due to the surface tension has the form $-\gamma \nabla^2 f + Y(\mathbf{x}, f)$, where the first term represents curvature effect at the macroscopic scale and the noise term represents the effect at the single pore

level. Combining these mechanisms, the full equation of motion becomes

$$\frac{\partial f}{\partial t} = P_a - \gamma\nabla^4 f + \nabla^2 Y(\mathbf{x}, f) \ + \rho g \nabla^2 f \ . \tag{12}$$

The noise statitistics should satisfy $\langle Y \rangle = 0$ and $\langle Y(\mathbf{x}, z) Y(\mathbf{x}', z') \rangle = \Delta\delta(\mathbf{x} - \mathbf{x}')\delta(z - z')$. At short length scales, we expect the $\nabla^4 f$ term to dominate over the $\nabla^2 f$ term, and the reverse at long length scales. The crossover should occur at a length scale $L \approx \sqrt{\gamma/\rho g} \approx 0.27\ cm$, which is about the radius of our sample tube. Thus the dynamics in our system may be controlled by the $\nabla^4 f$ term and the conserved quenched noise $\nabla^2 Y$. We note that Wolf and Villain[15] have studied an equation with the $\nabla^4 f$ term and thermal noise. They found a larger value of z, i.e., slower dynamics. An interesting question is how a quenched noise of the form $Y(\mathbf{x}, f)$ or $\nabla^2 Y(\mathbf{x}, f)$ would affect that result. An intuitive guess is that the conserved noise would further slow down the dynamics because, in other studies of critical dynamics, systems with conserved order-parameters always exhibit slower fluctuations and have larger values of z [16]. We hope that the results reported here will stimulate studies of similar effects in interface growth models.

ACKNOWLEDGMENTS

We thank J. Machta for helpful discussion. This work is supported by NSF Grant No. DMR-9404672 and a supplemental grant from the Research Experience for Undergraduates program.

REFERENCES

∗. Electronic address: pzwong@phast.umass.edu.

†. Present address: Department of Physics, University of Florida, Gainesville, FL 32611.

1. J. Koplik and H. Levine, Phys. Rev. B **32**, 280 (1985).

2. J. P. Stokes *et al.*, Phys. Rev. Lett. **65**, 1885 (1990).

3. P.-z. Wong and J. W. Cable, Phys. Rev. B **28**, 5361 (1983).

4. R. Bruinsma and G. Aeppli, Phys. Rev. Lett. **52**, 1547 (1984)

5. G. Grinstein and S.-k. Ma, Phys. Rev. B **28**, 2588 (1983).

6. T. Nattermann et al., J. Physique II **2**, 1483 (1992).

7. O. Narayan and D. S. Fisher, Phys. Rev. B **48**, 7030 (1993).

8. S. He, G. L. M. K. S. Kahanda, and P.-z. Wong, Phys. Rev. Lett. **69**, 3731 (1992).

9. See, e.g., P.-z. Wong, MRS Bull. **19**, No. 5, 32 (1994), and references therein.

10. J. P. Stokes, A. P. Kushnick, and M. O. Robbins, Phys. Rev. Lett. **60**, 1386 (1988).

11. T. Delker, Senior Honors Thesis, University of Massachusetts at Amherst (1995).

12. E. W. Washburn, Phys. Rev. **17**, 273 (1921).

13. T. Delker, D. B. Pengra, and P.-z. Wong, *MRS Fall Meeting, N3.44* (Boston, 1995).

14. See, e.g., D. Ertaş and M. Kardar, Phys. Rev. E **49**, R2532 (1994).

15. D. E. Wolf and J. Villain, Europhys. Lett. **13**, 389 (1990).

16. P. C. Hohenberg and B. I. Halperin, Rev. Mod. Phys. **49**, 435 (1977).

IMAGE ANALYSIS AND SAXS CHARACTERISATION OF MIXED AEROGELS

S. Blacher*, Ph. Tihon*, R. Pirard*, J.P. Pirard* F. Brouers**, B. Sahouli**
B. Diez***, R. Sobry***, G. Van den Bosshe***

*Chemical Engineering, Liege University, B6, B-4000 Liege, Belgium
**Materials Science, Liege University, B5, B-4000 Liege, Belgium
***Experimental Physics, Liege University, B5, B-4000 Liege, Belgium

ABSTRACT

The fractal structure of $SiO_2 - ZrO_2$ mixed aerogel prepared for catalytic purpose is investigated using morphological statistical methods, small angle X-ray scattering and N_2 adsorption-desorption measurements. These three methods provide a description of the aerogel structure over several decades.

INTRODUCTION

Aerogels are highly porous materials produced using the sol-gel route followed by hypercritical drying. They exhibit a hierarchic network structure of atoms, particles, cluster of particles and clusters of clusters. Small-angle X-ray scattering (SAXS) has been widely used to characterise the structure of this kind of systems [1]. This non-destructive technique is the most reliable method to probe the structure from the particle scale (0.5nm) to the cluster scale (200nm). In that way it is possible to determine the size of primary particles which form the aggregates as well as the size and fractal dimension of the particle clusters . Using these method, silica aerogels have been described as "polymeric mass fractals" formed by lightly cross-linked chains of particles ($1 < D < 2$) or "colloidal surface fractals" formed by compact branched cluster aggregates ($2 < D < 3$). The first class has been associated with silica aerogels synthesised under acidic conditions and the second class with silica aerogels synthesized under neutral and basic conditions. From considerations based on the dynamic of the hydrolysis-condensation equilibria between monomers and cluster aggregates which is strongly pH-dependent, polymeric type aerogels are modelled by cluster-cluster growth type models (DLCA) and colloidal type aerogels by monomer-cluster growth type models (RDLA). High resolution transmission electron microscopy (TEM) provides a visual support which confirms the aerogels complex picture which has emerged from the analysis of data obtained by the two other techniques. Image analysis can be performed on 2D TEM micrograph in the range 10nm-1000nm using the traditional tools provided by the mathematical morphology [2] and the multiscaling analysis [3].

Nitrogen adsorption-desorption measurements are usually used to characterize the porous texture in the size range 0.2-5 nm. As it was shown elsewhere [4] , the traditional BET methods are unable to analyse the adsorption-desorption curves of aerogels the pore of which exhibit a complex self-similar distribution. Nevertheless, as this has been shown, the surface fractal dimension can be obtained from the fractal Frenkel-Halsey-Hill (FHH) equation [5-6]. The aim of this paper is to obtain a more comprehensive picture of the aerogel structure. We want to confront and compare the information provided for the same samples by these three different independent characterization methods which correspond to three different albeit overlapping scales. To achieve this goal, we have applied SAXS, nitrogen adsorption and image analysis methods to study the morphology of $SiO_2 - ZrO_2$ aerogels which have been synthesised in our laboratory to develop new catalytic materials.

Mat. Res. Soc. Symp. Proc. Vol. 407 © 1996 Materials Research Society

CHARACTERISATION METHODS

The gel and aerogel preparation is described in Ref.[4]. Here we will consider only aerogels prepared in acidic conditions. The SAXS spectra were obtained at the Laboratory of Experimental Physics, Lige (Belgium) with a Kratky compact camera. The Kratky X-ray tube is supplied with a power of 1.5 kW and Cu-Ka radiation is used. All the measurements were made by a step scanning procedure. The domain explored is thus in the wave-vector range $0.003 \leq q \leq 0.6\text{Å}^1$. A "blank" scattering (the scattering of the device without sample) has been systematically measured and subtracted from the intensities recorded with the sample. The collimated effects have been mathematically eliminated. This operation is called "desmearing". In our case, the corrections were made using an original method [7]. The nitrogen adsorption-desorption isotherms were determined at liquid-nitrogen boiling temperature (77K) by the classical volumetric method with Sorptomatic Carlo Erba Series 1800 apparatus controlled by an IBM Personal Computer. Nitrogen of high purity (99.98%) was used. To perform the image analysis, sections (20nm) were prepared by cryo-ultramicrotomy. These sections were observed by TEM with an Philips CM100 electron microscope with a resolution of 100kv. The micrograph were acquired by a video camera and digitized on a matrix of 512x512 pixels with 256 gray levels using the Noesis software on a SunSparc10.

SAXS RESULTS

The fractal picture of a real system formed from a particle-cluster or a cluster-cluster aggregation mechanism is characterised by the size of the primary particles which form the aggregates (r), the characteristic size of the aggregates χ and the fractal dimension of these aggregates (D). The characteristic length is related to the radius of gyration of the isolated clusters, if the fractal objects are in solution, or with the correlation length if the fractal system is a continuous structure like a gel or an aerogel. The value of the fractal dimension depends of the growth mechanism. In the small-angle-scattering theory , r, χ and D can be determined from the cross-over separating three well-defined linear ranges of the log I versus log q curve, where I is the scattered intensity, $q = 4\pi\lambda^{-1}\sin(\theta/2)$ is the modulus of the scattering vector, λ is the wavelength of the radiation and θ is the scattering angle [8]. For small q , a cross-over appears around $\chi = 1/q_1$ which defines the end of the curve where I=cte. For high q, the cross-over at , $r = 1/q_2$ corresponds to the beginning of the region where the intensity follows the Porod's law, $I \propto q^4$. This domain describes the smooth non-fractal primary particles which form the fractal aggregates. Between these two cross-over the intensity follows the simple power law $I \propto q^{-D}$, where D is the fractal dimension, which may have values from 1 to 3 according to the clustering mechanism responsible for the aerogel structure [9]. Figure 1a shows the log-log plot of the SAXS intensity curve corresponding to the studied aerogels. The SAXS plot exhibits two linear domains: a) for $q < 0.09\text{Å}^{-1}$ the intensity curve obeys the Porod's law. Then, the size of the primary particles which build up the fractal structure is $r \approx 7$nm. The form factor of the particles can be determined from the plot $\log(I \times q^4)$ versus log q. Oscillations on this curve are characteristic of a spherical particles form factor . In our case , the very small amplitude of the oscillations indicates a great particle polydispersity [10]. As the location of the cross-over is very sensitive to the particle polydispersity, the value obtained for r could be underestimated. b) for $0.008\text{Å}^{-1} < q < 0.09\text{Å}^{-1}$, the intensity curve obeys a power law $I \propto q^{-D}$ with $D = 1.70 \pm 0.10$. The correlation length of the fractal aggregates is estimated to be $\chi \approx 80$nm. Nevertheless, for $q < 0.008\text{Å}^{-1}$ the region I=cte is not yet reached. This could mean that due to the hierarchical growth process, an other level of fractal network is still present at that scale. USAXS additional measurements are necessary to confirm this assumption.

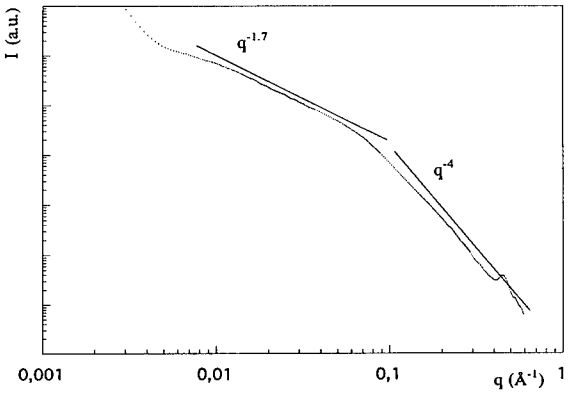


Figure 1

Figure 2

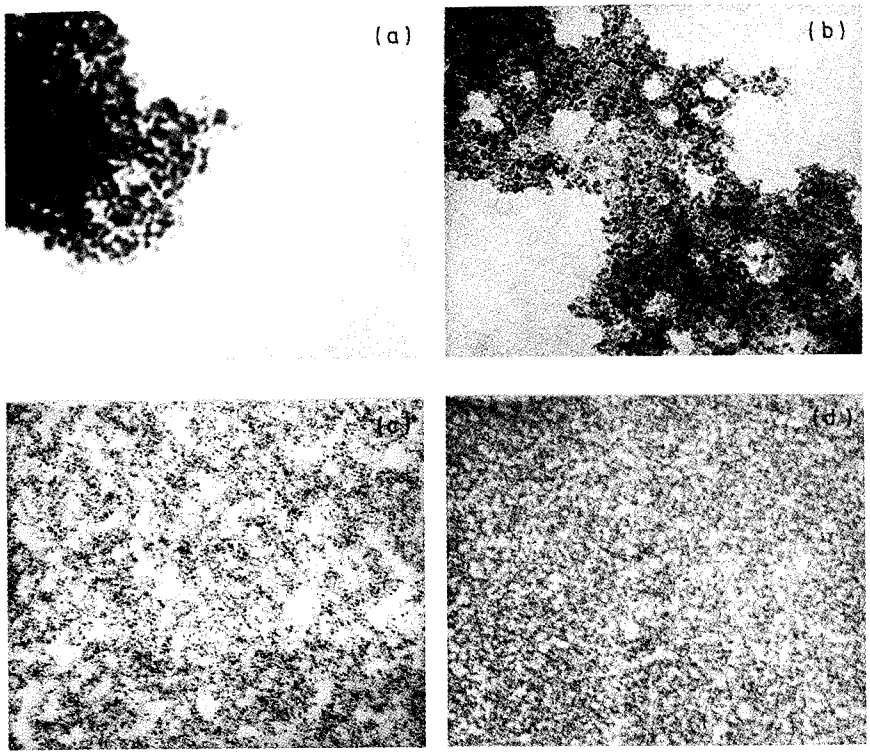


IMAGE ANALYSIS RESULTS

TEM micrographs at different resolutions are shown in figure 2a-d. At very high resolution (x1.2x106) the aerogel appears as an aggregate of sphere-like-particle. Unfortunately, the image structure is so tenuous that the primary particles cannot be clearly identified to determine its size distribution using the traditional granulometric image analysis methods. Nevertheless, from the micrograph of the Fig 1a, we can estimate the average particle radius which is in the range $5\text{nm} < r < 10\text{nm}$. At lower resolutions, the structure of the fractal aggregates appears clearly. To obtain an evaluation of the images spatial correlation, we have used two methods: the covariance function [2]. and the multifractal analysis [3]. After image digitization, morphological and linear filtering were performed to enhance the contrast of the structure. Then, a careful thresholding transformation was applied to obtain binary images (white pixels for the aerogel, black pixels for the background). To account for the statistical fluctuations between different locations within each micrograph, various positions where chosen at random. A total of five images at each resolution were digitized, filtered and binarized with the same method. To calculate the covariance function we use the method described in Ref. [2] .

The Covariance Function

Fig. 3a-d show the covariance function obtained from figures 2b,c and d. At high resolution (x2.6x105) after magnifying a small part of micrographs (see figure 2b), it is possible to distinguish the particles. The covariance function of these images present a quasi-periodicity with a period of $[r \approx 9\text{nm}$ between a maximum and a minimum. This represent the mean size of the particles. If we take now the full images, the particles have faded but the structure of the aggregate appears clearly. In this case, the decreasing covariance function presents two cross-over or characteristic lengths: $r \approx 9\text{nm}$ which corresponds to the average particle size and $\xi \approx 60\text{nm}$ which corresponds to the correlation length of the aggregate. At a smaller resolution (x1.3x10^5), the particles have disappeared (Figure 2d) and the decreasing covariance function yields a correlation length of $\xi \approx 60\text{nm}$. It is of interest to note that the value of $\xi \approx 60\text{nm}$ and r calculated from the covariance function are in agreement with those obtained from the SAXS observations.

The Fractal Analysis

As we have shown previously [3], the box counting method provides a scaling characterisation of the morphology of complex systems. We have calculated the generalized dimensions D_q $0 \leq q \leq 5$ using the method described in [3] on images at different resolutions and reported the results on the same graph. Figure 4 gives the variation of the correlation dimension D_2 with the observation scale. At large distances ($l > 200\text{nm}$) the image is seen as an average medium of dimension $D_2 = 2$. At short distances ($l < 10\text{nm}$) we are at the "grain" scale. As this "grain" scale, which coincides with the elementary pixel scale, dimension calculations are performed at the resolution limit and hence are not realistic. Finally the intermediate domain $10\text{nm} < l < 200\text{nm}$ represents the transition between the elementary pixel scale at the smaller resolution and the average image at the higher resolution. In this cross-over region, the "fractal dimension" is scale dependent (multiscaling) and varies in the interval $1.8 < D_2 < 2$. At the scale ($10\text{nm} < l < 60\text{nm}$), $D_2 \approx 1.85$ is almost constant. This value corresponds to the dimension of the projected image of a tridimensional 20nm thin objet on a plane. It is therefore not surprising that "fractal dimension" obtained in that way is slightly different from the one determined with SAXS at the same scale ($D_2 \approx 1.7$).

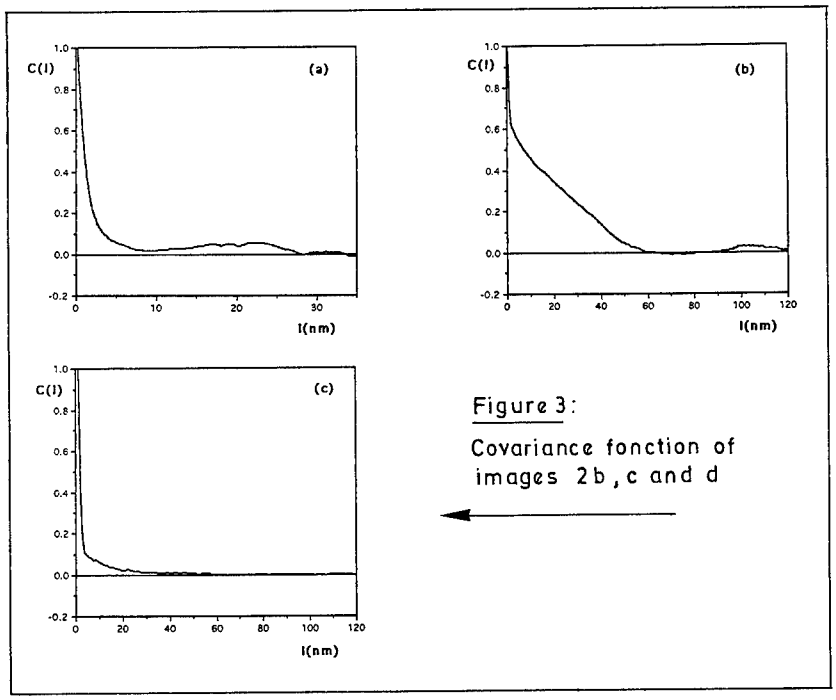


Figure 3:

Covariance fonction of images 2b, c and d

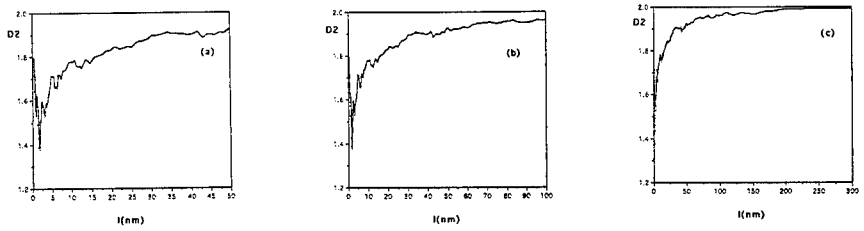


Figure 4: Correlation dimension at different scales

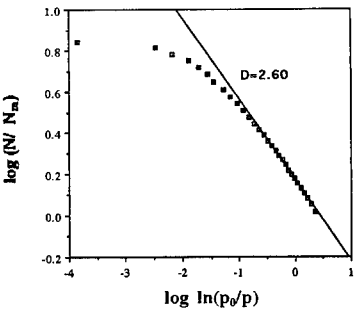


Figure 5:

The fractal FHH dimension

THE FRACTAL FHH ADSORPTION CURVE ANALYSIS

In a previous publication [4], we have shown how the fractal FHH theory [5-6] can yield the surface fractal dimension provided the dominant adsorption regime (governed by van der Waals forces or by the superficial tension) is unambiguously known. Figure 5 shows a plot of the experimental data as $\log N/N_m$ versus $\log p/p_0$. To avoid problems related to a possible modification of the aerogel structure at high relative pressure, we have only consider the adsorption data for $p/p_0 < 0.8$. In the range $0.4 < p/p_0 < 0.8$ we found $2 < m < 3$ that indicates that the CC regime is dominant. In this case , we find D=2.60. This surface fractal dimension characterizes the porous texture in the scale range 0.2-2 nm, i.e, at the molecular scale which is not accessible to SAXS measurements and image analysis.

CONCLUSIONS

We have shown for the first time that mixed aerogels if they are correctly synthetized may present a hierarchical structure that is not very different from that of pure silica aerogels. Since some physical parameters are composition dependent (for instance the addition of a few% of zirconia has been reported to substantially increase the resistance of alkaline attack [11] , this technology is able to produce a variety of new materials which keep the essential aerogel properties. The combination of three independent characterization techniques probing different scales of observation on the same samples provides an improved picture of the hierarchical structure of these complex materials.

REFERENCES

1 C.J. Brinker and G.W Scherer , Sol-Gel Science:The Physics and Chemistry of Sol-Gel Processing, ed. (Academic Press Inc.1990) Chap. 9 and references herein.

2 M.Coster and J.L Chermant, Précis d'analyse d'images, ed.(CNRS,Paris 1985).

3 S. Blacher, F. Brouers and R. Van Dyck R., Physica A,**197**,p.51,1993.

4 S.Blacher S., R.Pirard, J.P. Pirard, F. Brouers and M. Germain, Mat.Res.Soc.Symp. Proc.(1995) Vol.371

5 D.Avnir and M.Jaroniec, Langmuir, **431**, p.1, 1989

6 P.Pfeifer and M.W.Cole, New J. Chem. **14**, 221, 1990

7 R. Sobry .,Y. Rassel , F. Fontaine ., J.Ledent and J-M. Ligeois , J. Appl. Cryst., **24**, pp 692-701, 1991

8 A.Craievich , J. Phys.I (France) **2**,801,1992

9 M.Foret , J. Pelous ,R. Vacher , J. Phys. I (France), **2**,791, 1992

10 A.Hasmy , R. Vacher, R.Jullien , Physical Review **B50**,1305,199

11 A.Paul, Chemistry of glasses, ed.(Chapman et al.,London 1982)

SAXS CHARACTERIZATION OF PYROLYTIC CARBON BLACKS

B. SAHOULI*, S. BLACHER*, F. BROUERS*, R. SOBRY*, G. VAN DEN BOSSCHE*, H. DARMSTADT, C. ROY****

*Physique des Matériaux, B 5, Université de Liège , 4000 Liège (Belgium)

**Département de génie chimique, Université Laval Québec, Canada, G1K 7P4 (Canada)

ABSTRACT

The surface fractal dimension (D_S) of pyrolytic carbon blacks (CB_p) was determined using small angle X-ray scattering (SAXS). The CB_P were produced by vacuum pyrolysis of used tires at different temperatures and pressures. For the CB_P a dependence of the pyrolysis conditions on the fractal dimension was observed. The fractal dimension decreases, suggesting a smother surface, with increasing pyrolysis pressure and to a lesser intent with increasing pyrolysis temperature. Earlier SIMS and ESCA investigations have indicated that an evident correlation exists between the surface morphology and the surface chemistry of the CB_P. According to these investigations, the smoothing of the CB_P surface is due to the formation of carbonaceous deposits from adsorbed hydrocarbons on the CB_P.

INTRODUCTION

Vacuum pyrolysis of used tires is an ecological and potentially economic attractive way to recover useful products from this waste material. The two most important products obtained by this tire conversion process are oil and CB_P. The process feasibility depends on the quality of the CB_P , i.e., its ability to be used in high value commercial application. Recycling of used tires by pyrolysis has been investigated by different researchers [1-3]. At Laval University the pyrolysis is performed under vacuum. Different aspects of the tire pyrolysis such as the pyrolysis process [4,5], the characteristics of the pyrolytic oil [6-8] and CB_p [9-13] were investigated. Due to its reinforcing characteristics, carbon black is one of the key materials used in rubber compounding. For this application the surface chemistry and the surface morphology are important. It is known from scanning tunneling microscopy [14-16] and atomic force microscopy experiment [17] that commercial carbon blacks have a rough surface. The surface morphology of carbon blacks is believed to be a very important factor in rubber reinforcement. A recent model describes steps on the rough carbon black surface having sizes similar to the macromolecular chains and therefore optimizing the interaction between carbon black and elastomer [18]. For the substitution of commercial carbon black by CB_p , it is important that this latter reinforces rubber as well as commercial carbon black. Therefore their surface morphology should be similar to those of commercial rubber grade carbon blacks. The fractal geometry provides a description for irregularities on the surface and is used in this work to investigate the morphology of CB_p in comparison with the one of commercial carbon blacks. Small-angle x-ray scattering (SAXS) has been widely used to study the structure of disordered systems. Briefly, in the theory of small-angle-scattering, it is well known [19-22] that the intensity of radiation scattered on a fractal surfaces is often proportional to a negative power of the wave vector q:

$$I \propto q^{-\alpha} \qquad (1)$$

Mat. Res. Soc. Symp. Proc. Vol. 407 © 1996 Materials Research Society

where $q = 4 \pi \lambda^{-1} \sin(\theta/2)$, λ is the wavelength of the radiation and θ is the scattering angle. Usually this dependence is observed only when q satisfies the inequality $q \xi >> 1$, where ξ is the characteristic length of the structure producing the scattering. From the value of α one can determine the fractal nature of the system under investigation. For systems with fractal surfaces, the exponent α varies between 3 and 4. In such a case, this gives access to the shape of the particles, which build up the aggregate, and their surface roughness where the relationship between α and surface fractal dimension is given by:

$$\alpha = 6\text{-}D_s \qquad (2)$$

for $q \xi >> 1$. When $D_s = 2$, the intensity of the scattered radiation is proportional to q^{-4} which is the well known Porod law.

EXPERIMENT

Samples

The CB_p samples were obtained by vacuum pyrolysis of the sidewall of used tires in a laboratory scale batch reactor at temperatures and total pressures ranging from 420 to 700 ^{o}C and from 0.3 to 20.0 kPa, respectively. At these conditions the tire pyrolysis yield approximately 24 % CB_p, 72 % oil and 4 % gas. A detailed description of pyrolysis and product composition is given elsewhere [23]. As reference material for the CB_p, five commercial rubber grade carbon black (N115,N375,N539,N660 and N774) were characterized. The two most important properties of carbon blacks are the surface area and the structure, which is measured as void volume [24]. The commercial carbon black samples were provided by Cabot, Sarnia, Canada (N115, N660, N774) and Colombian Chemicals, Hamilton, Canada (N375 and N539).

SAXS Measurements

The spectra were run at Laboratoire pour l'Utilisation du Rayonnement Electromagnetique (LURE), Orsay (France) on DCI (D22 station). The fixed-exit, double-crystal monochromator is turned to provide a beam of 10 -keV X-rays (λ= 1, 24 Å). Since the size of the beam at the sample is smaller than 1 mm^2, no desmearing of the data is necessary. Two beam deflectors and NaI scintillator detectors are positioned before and after the sample chamber to constantly monitor the relative input X-ray intensity and sample absorption. The scattered X-rays are detected with a Xe-CO_2 gas-filled, one dimensional position-sensitive detector (with a resolution of 197 μm). The sample-to-detector distance is 526 mm allows SAXS data to be obtained in the q range from 0.15 to 4. 4 nm^{-1}. The data are plotted as the relative intensity versus q after correction for parasitic scattering and sample absorption. The background scattering is corrected in the standard manner. All samples are normalized to a thickness of 1 mm.

RESULTS

In Fig. 1 the determination of D_s from the experimental SAXS data is shown for a commercial carbon black and two CB_p samples. For all carbon black samples, the SAXS intensity curves show a power law variation according to the equation (1) where the exponent α is always greater than 3 indicating the fractal nature of the carbon black surfaces. The ranges of the linear parts (log-log plot),

on which the fractal dimension was calculated , extend on a length scales ($\equiv 2\pi / q$) from 5 to 38 nm. This range of fractal regime is more limited for the commercial carbon blacks than the pyrolytic samples CB_P. For the commercial carbon blacks, the fractal dimensions are presented in table 1. However, in contrast to the results obtained from nitrogen adsorption [12], the SAXS data show for the two high surface area grades (N115 and N375) slightly higher D_s values than for the low surface area grades (N539, N660, N774). More precise information on the first one or two carbon black layers can be obtained by SIMS. In the SIMS spectra of carbon black the C_2^- peak was assigned to aromatic, graphite-like carbon and the C_2H^- peak to aromatic carbon bound to hydrogen [25] Since carbonaceous deposits on carbon blacks consist of small aromatic compounds, the C_2H^-/C_2^- peak ratio can be regarded as a measure for carbonaceous deposits on carbon blacks. For commercial samples, the corresponding SIMS results showed indeed that on the high surface area slightly less carbonaceous deposits were present than on the other commercial carbon blacks. A slightly rougher surface for the two high surface area grades is, therefore, reasonable. For the CB_P samples a similar dependence of the fractal dimension on the pyrolysis conditions was found by SAXS as by the FHH method [26]. The fractal dimension measured by the two methods decreased with increasing pyrolysis pressure (table 1). A decrease of D_s with increasing pyrolysis pressure indicates a smoothing of the surface. This smoothing is due to the deposition of pyrolytic carbon or carbonaceous deposits on the surface of CB_P

The concentration of these carbonaceous deposits, measured by ESCA spectra, depends on the pyrolysis conditions. It decreases with decreasing pyrolysis pressure and increasing pyrolysis temperature as shown in the figure 2.

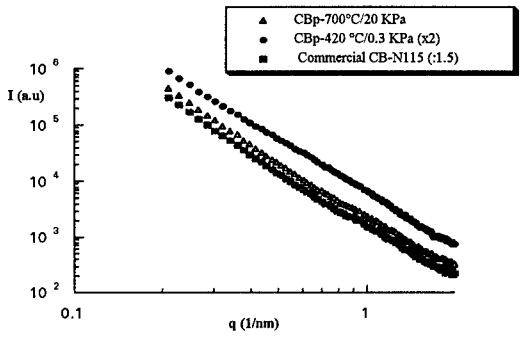


Figure 1: Determination of the fractal dimension of the carbon black surface using small angle X-ray scattering (SAXS)

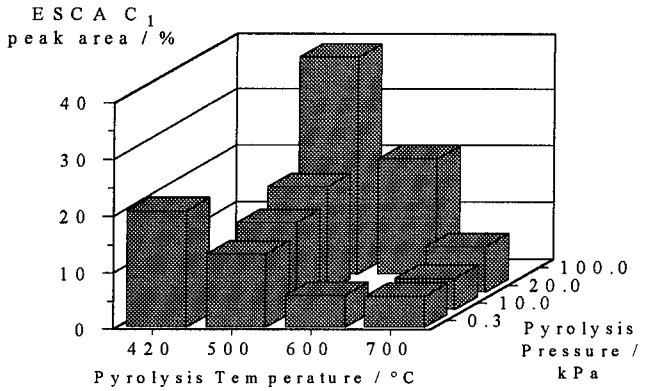


Figure 2: Area of the ESCA C_1 peak [%] of CB_P as a function of pyrolysis conditions

However, the absolute values of D_s determined for the CB_P by SAXS and the FHH method differed considerably. These differences can be attributed to the different physical background of the two methods. Most of the inorganic tire components are left in the CB_P after the pyrolysis. Prominent inorganic components are ZnO and ZnS. The surface area of these inorganic compounds is small compared with the surface area of the organic portion. Therefore, by nitrogen adsorption only the organic portion of the CB_P is probed and the fractal dimension obtained by the fractal Frenkel-Halsey-Hill (FHH) theory describes only the surface morphology of the organic portion of the CB_P. In contrast to the nitrogen adsorption experiment, the SAXS is also sensitive to the electronic atmosphere of the inorganic molecules. Therefore, we can explain the difference in values of D_S between commercial carbon blacks and CB_P by the large sensitivity of SAXS to the inorganic portion.

Table 1: Fractal Dimension (D_s) measured by SAXS of commercial and pyrolytic Carbon Blacks in comparison with the fractal dimension obtained by the FHH theory.

Commercial - Samples	D_s(FHH)	D_s(SAXS)	CBp-Samples			D_s(FHH)	D_s(SAXS)
N115	2.55	2.51	CBp	420°C	0.3 KPa	2.55	2.91
N375	2.57	2.60	CBp	500°C	0.3 KPa	2.57	2.90
N539	2.54	2.30	CBp	500°C	10 KPa	2.46	2.76
N774	2.46	2.34	CBp	700°C	20 KPa	2.52	2.69

CONCLUSIONS

By vacuum pyrolysis of used tires, the carbon black filler can be recovered. However, the obtained CB_p differ from the commercial carbon black initially present in the tire.

Fractal analysis of commercial carbon blacks and CB_P using SAXS confirms the surface roughness of these samples. For the CB_p samples, the fractal dimension depends on the pyrolysis pressure and to a lesser extent on the pyrolysis temperature. The CB_P surface is smoothened with

increasing pyrolysis pressure due to the formation of the carbonaceous deposits. For commercial carbon black, the SAXS experiments indicate that high surface area grades have a slightly rougher surface than low surface area grades. This observation is also supported by SIMS results which show that more carbonaceous deposits are present on the low surface area grades than on the high surface area grades and by the recent investigations [27] using Atomic Force Microscopy (AFM) .

REFERENCES

1. P. T. Williams, S. Besler and D. T. Taylor, *Fuel* **69**, p.1474 (1990).
2. P. T. Williams and D. T. Taylor, Pyrolysis and Gasification , G. L. Ferrero, K. Maniatis, A. Buekens and A. V. Bridgwater, Elsevier Applied Science, London, UK, 1989, pp. 486-491.
3. R. Cypres and B. Bettens, Pyrolysis and Gasification , G. L. Ferrero, K. Maniatis, A. Buekens and A. V. Bridgwater, Elsevier Applied Science, London, UK,1989, pp. 209-229.
4. C. Roy, B. Labrecque and de B. Caumia, B., Resources, Conversion and Recycling **4**, p.203, (1990).
5. C. Roy and J. Unsworth , Pyrolysis and Gasification , G. L. Ferrero, K. Maniatis, A. Buekens and A. V. Bridgwater, Elsevier Applied Science, London, UK ,1989, pp. 180-189.
6 . H. Pakdel, C. Roy, H. Aubin, G. Jean and S. Coulombe, Environ. Sci. Technol. **25**, p. 1646, (1991).
7. S. Mirmiran, H. Pakdel and C. Roy, J. Analy. Appl. Pyrolysis **22**, p.205, (1992).
8. J. L. Leblanc, C. Roy, S. Mirmiran, B. Benallal and A.E. Schwerdtfeger, Kautsch. Gummi Kunstst., in press.
9. C. Roy, A. Rastegar, S. Kaliaguine, H. Darmstadt and V. Tochev, Plastics, Rubber and Composites Processing and Applications **23**, p.21, (1995).
10. H. Darmstadt, C. Roy and S. Kaliaguine, Carbon **32**, p.1399, (1994).
11. H. Darmstadt, C. Roy and S. Kaliaguine, Kautsch. Gummi Kunstst. **47**, p.891, (1994).
12. H. Darmstadt, C. Roy, S. Kaliaguine, B. Sahouli, S. Blacher, R. Pirard and F. Brouers, Rubber. Chem. Technol., **68**, p.330, (1995).
13. J.B. Dufeu, C. Roy, A. Ajji, L. Choplin, J. Appl. Polym. Sci. **46**, p.2159, (1992).
14. J.B. Donnet, E. Custodéro, C. R. Acad. Sci. Ser. II **314**, p.579, (1992).
15. S.J. Kim, D. H. Reneker, Rubber Chem. Techn. **66**, p.559, (1993).
16. M.J. Wang, S. Wolff, B. Freund, Rubber. Chem. Techn. **67**, p.27, (1994).
17. W. Niedermeier, J. Stierstorfer, S. Kreitmeier, O. Metz, D, G`ritz, Rubb. Chem. Techn. **67**, p.148, (1994).
18. J. B. Donnet, in The second International Conference on Carbon Black, (Mulhouse, France, 27-30 Sept. 1993), pp. 1-9.
19. J.E. Martin, A. J. Hurd, J. Appl. Cryst., **20**, pp.61, (1987).
20. P-Z. Wong, Q-Z. Cao, Phys. Rev B, **45** , p.7627, (1992).
21. H.D. Bale, P.W. Schmidt, Phys. Rev. Lett., **53** , p.596, (1984)
22. P.Z. Wong, A.J. Bray, Phys. Rev. Lett. **60** , p. 1344, 13 (1988)
23. A. Rastegar, M. Sc. Thesis, Université Laval, Québec (1989).
24. D. Y. Normann, The Vanderbilt Rubber Handbook 13th. Edition , R. F. Ohn, Vanderbilt Company Inc., Norwalt, Connecticut, USA, 1990, pp. 397-426.
25. P. Albers, B. Freund, K. Seibold, S. Wolff, Kautsch. Gummi. Kunstst., **45**, p.449, (1992).
26. P. Pfeifer, M. W. Cole, New J. Chem. **14**, p. 221, (1990).
27. D. Göritz, W. Niedermeier and H. Raab, in Extended Abstracts, (Eurofillers 95, Mulhouse , France, Sept.11-14, 1995), pp.183.

MODELLING OF THE STRUCTURAL AND DYNAMICAL PROPERTIES OF POROUS SILICON

†‡ J.L. Gavartin and †C.C. Matthai
†Department of Physics and Astronomy, University of Wales Cardiff, PO Box 913, Cardiff CF2 3YB, U.K., j.gavartin@astro.cf.ac.uk
‡Institute of Chemical Physics, University of Latvia, LV1586 Riga, Latvia

Abstract

The changes in the radial distribution function (RDF) and vibrational density of states (DOS) of porous silicon (p-Si) with change of porosity are studied within a modified diffusion limited aggregation model and molecular dynamics simulations. By decomposing the first peak of the radial distribution function of p-Si on to partial RDFs, for atoms having different coordinations, and partial RDFs, for bonds connecting atoms with different coordinations, we show that appearance of the structure in the first peak of the RDF in p-Si is stipulated by bonds between undercoordinated surface atoms. The vibrational DOS projected on surface atoms are also shown to be different from that corresponding to crystalline phonons. It is characterised by the relative increase of the intensity of vibrations in the acoustic region and by appearance of surface-like vibrations split from the optical band.

Key words: Porous Silicon, Radial Distribution Function, Diffusion Limited Aggregate, Vibrational Density of States

Introduction

Porous silicon is a semiconducting material known for its ability to luminesce effectively in visible spectral region with both wavelength and integral intensity tunable by porosity level. Since it is the mesoscopic and/or microscopic structural changes that make silicon optically active, the study of these changes is crucial for an understanding of electronic processes.

Recent X-ray diffraction experiments [1] suggest that the crystalline phase in p-Si coexists with other phase(s) characterised by the appearance of a peak close to the crystalline first peak in the RDF. The position of this peak is found to change almost linearly with porosity, reaching a shift $\sim$ 1% of the crystalline bond length at 35% porosity. Further, this peak may be shifted to either longer or shorter distances depending on the sample preparation history. Another remarkable feature of porous silicon related to the microscopic structure is that the photoluminescence (PL) there is found to strongly couple to the atomic vibrations [2,3]. In order to understand whether the nature of the electron-vibrational interaction in porous media is different to that in crystalline silicon [4], one should understand first how the vibrational spectrum of p-Si changes with porosity.

In the present paper we show that some of the important structural characteristics of porous media can be qualitatively explained by a local rearrangement of the crystalline lattice near the internal surfaces. Using a simple approach for the simulation of electrochemical etching we produce the porous structures on the diamond type lattice. We then show that a relative fraction of atoms having different number of nearest neighbours is a well reproducible function of porosity. Analysing the radial distribution functions resulting from our model, we evaluate partial distribution functions corresponding to averaging over sets of atoms distinguished by their coordination numbers. We argue that the characteristic porous silicon peak in the RDF arises from the atoms at internal surfaces.

Mat. Res. Soc. Symp. Proc. Vol. 407 © 1996 Materials Research Society

Modelling procedure

The most widely used procedure of porous formation in silicon is electrochemical etching of silicon wafers in a weak solution of HF acid. We simulate this process by means of modified Diffusion Limited Aggregation (DLA) model [5]. According to this model the silicon wafer is represented by 3-dimensional slab of a diamond type lattice with all lattice sites being initially occupied by silicon atoms. The chemical dissolution was modelled as a process whereby silicon atoms are removed from the path of the advancing acid particles. The process is initiated by allowing acid particles to be deposited on the top of the surface at a constant rate, ν. The acid particles undergo a random walk through the silicon lattice with probabilities, p_{emp}, to jump to an empty site, and, p_{occ}, to a silicon atom site. The probabilities are parameters of the model and together with deposition rate, ν, they mimic acid concentration and the magnitude of the anodic current. The instantaneous porosity, p, was defined as the ratio of number of empty sites to the total number of sites in the model. For a given porosity, we have performed atomic coordination statistics, that is, the calculation of relative fractions of silicon atoms $\{f_i\}_{i=1}^4$ having one, two, three or four nearest neighbours respectively.

In order to understand the nature of the various types of bonds in p-Si we study the first pick in its radial distribution function, $R(x)$, the partial distribution functions, $G_i(x)$, corresponding to bonds of atoms having i nearest neighbours (i=1,2,3,4) and the partial distribution functions, $g_{ij}(x)$, corresponding to the bonds connecting i- and j-coordinated atoms. The distribution functions $R(x)$, $G_i(x)$, and $g_{ij}(x)$ are related by the equations:

$$R(x) = \sum_{i=1}^{4} G_i(x) \tag{1}$$

$$G_i(x) = \sum_{i=1}^{4} w_{ij} g_{ij}(x) \quad ; \quad w_{ij} = \frac{2n_{ij}}{\sum_{i,j=1}^{4} n_{ij}}, \tag{2}$$

where n_{ij} is the number of bonds of type (ij) in the system. We assumed that the distributions, $g_{ij}(x)$, are central for all types of bonds (ij) and they can be accurately represented by normal frequency functions having the same first and second central momenta, a_{ij}^0, and σ_{ij} respectively

$$g_{ij}(x) \approx \frac{1}{\sigma_{ij}\sqrt{2\pi}} \exp \frac{(x - a_{ij}^0)^2}{2\sigma_{ij}^2}. \tag{3}$$

Then, the approximate partial RDFs $\tilde{G}_i$ can be expressed as

$$\tilde{G}_i(x) = \frac{1}{\sqrt{2\pi}} \sum_{i=1}^{4} \frac{w_{ij}}{\sigma_{ij}} \exp \frac{(x - a_{ij}^0)^2}{2\sigma_{ij}^2} \tag{4}$$

One should note, that the functions $g_{ij}(x)$ represent the average distributions of bonds of different types, and *do not depend on the porosity.* So, they need to be evaluated only once in a model of arbitrary porosity. At the same time, all the dependence on porosity in the total RDF, $R(x)$, and $G_i(x)$ (Eq. (2)) is contained in the weight functions, $w_{ij}(p)$, reflecting

the relative fraction of bonds of type (ij). These weights can be directly calculated from the DLA model discussed above, or approximated by the relation:

$$w_{ij}(p) = \frac{f_i(p) f_j(p)}{2}, \tag{5}$$

where f_i is the fraction of i-coordinated atoms and can be recovered from the DLA modelling as discussed above. Finally, combining Eq. (1 - 5) one can calculate the approximate radial distribution function of p-Si as a function of porosity:

$$\tilde{R}(x,p) = \sum_{i=1}^{4} \tilde{G}_i(x,p) = \frac{1}{2\sqrt{2\pi}} \sum_{i,j=1}^{4} \frac{f_i(p) f_j(p)}{\sigma_{ij}} \exp \frac{(x - a_{ij}^0)^2}{2\sigma_{ij}^2} \tag{6}$$

To obtain the parameters a_{ij}^0 and σ_{ij} the structure of 75% porosity constructed within the DLA model was chosen and atomic positions optimised by means of simulated annealing procedure within molecular dynamics (MD) approach. For this purpose the Tersoff many-body potential model was employed [6], whose strengths and limitations are well-known. Then, we calculated the average bond lengths a_{ij}^0 and standard deviations σ_{ij} for bonds connecting i-coordinated and j-coordinated atoms for all combinations $\{ij\}_{i,j=1}^4$. Using these values we have calculated the radial distribution functions, $\tilde{R}(x,p)$, according to Eq. (6).

While studying the vibrational properties we have also assumed that atoms having different coordinations would have different influence on the vibrational density of states. To study the DOS the same system of 75% porosity was used, for which a $12ps$ molecular dynamic run at temperature $50K$ was undertaken. A statistically representative set of 20 atoms with different coordination were chosen, and their instantaneous coordinates and velocities stored every $10fs$. The vibrational DOS was determined from the power spectral density of the velocity auto-correlation function averaged over the groups of equally coordinated atoms.

Results and discussion

We evaluated the atom coordination statistics in the DLA model containing 64000, 216000, and 10^6 sites, which correspond to a cubic simulation boxes with linear sizes 108.4 $\AA$, 162.6 $\AA$, and 271 $\AA$ respectively. The fraction of atoms having different numbers of nearest neighbours as a function of porosity is depicted in Figure 1. We see that the general trend of the curves is similar for all three sizes, with the largest discrepancy (less then 8%) arising at $20 - 30\%$ porosity. The results of the numerical modelling of porous formation can be thought to be bounded between two extreme cases: i) a very slow etching process, when layer-by-layer etching is achieved and no pores formed; and ii) a fast, explosion-like fracture, characterised by a random atomic distribution for all given porosity values. In the former case a surface area remains roughly constant, so, for large systems with linear size L the fraction of surface atoms will depend on 'porosity' as

$$\sum_{i=1}^{3} f_i \sim \frac{1}{L(1-p)}. \tag{7}$$

This would be negligible compared to the bulk unless the 'porosity' is very high. It can be shown that for (ii), the relative fractions are defined by terms of the binomial expansion:

$$f_i = \binom{i}{z} (1-p)^i p^{z-i} \tag{8}$$

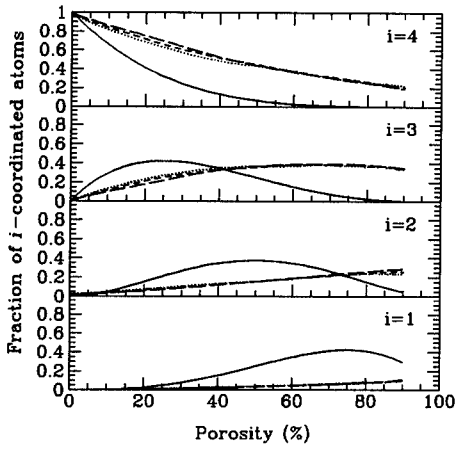


Figure 1: Fractions of atoms in the DLA having 1, 2, 3 and 4 nearest neighbours as a function of porosity: 64000 sites model (dot lines), 216000 sites (short dash lines), and 10^6 sites model (long dash lines). Solid lines represent the case of random sites occupation (Eq. (8)).

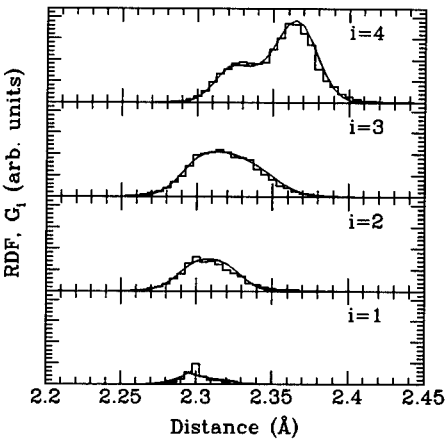


Figure 2: Histograms for the partial radial distribution functions G_i calculated at 75% porosity, and approximate partial RDF's $\tilde{G}_i$ (solid lines) calculated according to Eq. (4).

where z - is the number of nearest lattice sites ($z = 4$ in case of diamond type lattice), and $\binom{i}{z}$ - is a binomial coefficient: $\binom{i}{z} = \frac{z!}{i!(z-i)!}$. The porous formation mechanism is characterised by the development of internal surfaces and a corresponding increase in the surface/volume ratio. The dependence f_i on porosity (Figure 1) suggests that our DLA model represents porous growth. At low porosities the porous surface area (i.e. the fraction of undercoordinated atoms) grows significantly slower then in (ii) case, which indicates a great deal of correlation in atomic positions. At the same time, when the porosity increases to $70 - 90\%$, the aggregates still remain compact in the sense that more then 20% of atoms remain being in a bulk-like state (i.e. are fully coordinated).

The local relaxation effects in p-Si, were studied in the model at 75% porosity containing 12000 atoms (simulation box - 48000 sites). After the atomic positions were optimised, all the atoms in the system were sorted by their coordination. The natural cut off criteria $a_{cut} = 2.9\mathring{A}$ was chosen for this purpose. Only 5 atoms (out of 12000) where found to be 5-coordinated within the chosen cut off, so, the influence of overcoordinated atoms in RDF is negligible. There were also found a small number of isolated atoms and Si_2 clusters which where not considered in the averaging.

Histograms for the partial radial distribution functions, $G_i(x)$, calculated for differently coordinated atoms are shown in Figure 2. It is seen in the diagram that all the distributions, $G_i(x)$, display a complex structure reflecting the fact that the bonds around the undercoordinated atoms and between the 3- and 4-coordinated atoms are generally shorter then those in the bulk. One can assume that different peaks in the partial RDFs correspond to the bonds connecting atoms with different coordination. For instance, bonds connecting 4-coordinated

Table 1: Average values a_{ij}^0 and the standard deviations σ_{ij} calculated for different types of bonds.

Bonds type (ij)	2-1	2-2	3-1	3-2	3-3	4-1	4-2	4-3	4-4
a_{ij}^0 (Å)	2.298	2.300	2.298	2.302	2.312	2.320	2.320	2.338	2.366
$\sigma_{ij}/2$ (Å)	0.013	0.011	0.009	0.016	0.016	0.006	0.011	0.016	0.013

atoms have different average lengths and distribution widths compared to bonds connecting 3- and 4-coordinated atoms and so on. In order to show that, we have calculated the average bond lengths a_{ij}^0 and standard deviations σ_{ij} for different types of bonds (Table I). The results show, that bonds connecting undercoordinated atoms and 4- and 3- coordinated atoms are indeed shorter then bonds between 4-coordinated (bulk) atoms. Given the a_{ij}^0 and σ_{ij} we have also evaluated the approximate distribution functions, $\tilde{G}_i(x)$, using equation (4) (solid lines in Figure 2). The agreement between $G_i(x)$ and $\tilde{G}_i(x)$ for all types of coordination justifies the approximations (3) and (5), and allows for the description of the first peak of the RDF in porous media by the set of easily calculable parameters, such as fractions of i-coordinated atoms, f_i, average bond lengths, a_{ij}^0, and standard deviations σ_{ij}. The radial distribution function $\tilde{R}_i(x,p)$, calculated according to Eq (6) for different porosity values, is depicted in Figure 3. As may be seen in the figure, the characteristic peak of p-Si appears at shorter distances compared to crystalline peak. The amplitude of this peak grows with porosity with its maximum position shifting to shorter distances. Analysing the partial distribution functions we conclude that the p-Si structure in the RDF's first peak is entirely due to the local environment of the undercoordinated atoms. In other words, the relaxation

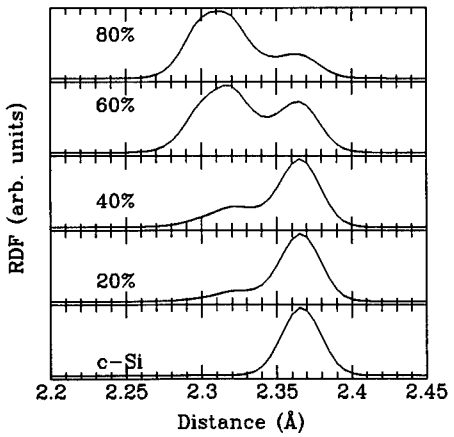


Figure 3: Total radial distribution function for c-Si and p-Si at 20%, 40%, 60% and 80% porosity, calculated according to Eq. (6)

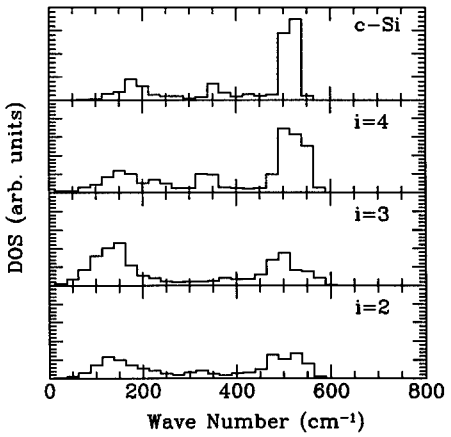


Figure 4: Histograms for the vibrational density of states for sets of atoms having different number of nearest neighbours, and for c-Si

at and near the internal surfaces in p-Si is responsible for the appearance of this structure. One should note, that in real p-Si the surface may be oxydised or passivated by hydrogen or other chemical species. This in turn could change the shape and position of the p-Si peak in the RDF depending on the bond length distribution at the surface.

Figure 4 demonstrates the influence of surface atoms on the vibrational density of states. One can see, that the ratio of the acoustic to optical vibration intensities is larger for the undercoordinated atoms then in the bulk crystal. Another remarkable feature of the DOS projected on surface atoms is the appearance of high frequency vibrations resembling the crystalline surface mode. Consequently, with the increase of porosity in p-Si, one would expect the increase of the DOS amplitudes in the acoustic region and in high frequency region beyond the optic mode. In general, vibrations of higher frequency couple more strongly to electronic transitions, and so one would expect an enhancement of the electron-phonon interaction in p-Si with increase of porosity. However, theoretical modelling suggests that some small silicon clusters containing few tens of atoms also display high frequency vibrations [6], and these are likely to be present in p-Si samples. So, the question whether the enhancement of the electron-vibrational interaction in p-Si originates from internal surfaces or from small clusters needs to be further investigated. It should also be mentioned, that the classical potential model employed in our study might not be sufficiently accurate for representing dynamical properties, especially where charge redistribution effects are important. However, the method of partial distribution functions proposed in the paper, requires the study of only one representative system of moderate size and arbitrary porosity allowing for more sophisticated schemes in total energy calculations to be employed.

In summary, we have developed a procedure for investigating the influence of porosity on the structural and dynamical properties of porous media. Applying this procedure to the porous silicon we have shown that the appearance of the structure in the first peak of the radial distribution function is stipulated by the local rearrangements of atoms on internal surface. The vibrational density of states of p-Si is also shown to be affected by surface atoms displaying the relative increase of the amplitude of acoustic band compared to the optical band and the appearance of vibrations in a frequency region higher than the optical band.

Acknowledgements

This work was funded by the Engineering and Physical Sciences Research Council (UK) (grant No GR/H98788). JLG also acknowledges the grant No 93.270 by Latvian Science Council.

References

1. D. Bellet, G. Dolino, presented at the 1995 EMRS Meeting, Starsbourg, France, 1995 (to be published); D.Bellet, private communication.
2. K.J. Nash, P.D.J. Calcott, T.L. Canham and R.J. Needs, *Phys. Rev.* **B51**(24), 17698 (1995).
3. L. Brus, *J. Chem. Phys.*, **98**, 3575 (1994).
4. C.C. Matthai, J.L. Gavartin, A.A. Cafolla, *Thin Solid Films,* **255**, 174 (1995).
5. J. Tersoff, *Phys. Rev.* **B38**, 992 (1988).
6. J.L. Feldman, E. Kaxiras, and X.-P. Li, *Phys. Rev.* **B44**(15), 8334 (1991).

EVALUATION OF INACCESSIBLE PORE STRUCTURES IN RANDOM POROUS SOLIDS

N.Yoshizawa*, Y.Yamada*, M.Shiraishi*, K.Kaneko** and N.Sctoyama**
*Carbon Materials laboratory, National Institute for Resources and Environment, Tsukuba, 305 Japan
**Department of Chemistry, Chiba University, Chiba 263, Japan

ABSTRACT

A fine pore characterization method is investigated for a disordered solid including inaccessible pores. Here inaccessible pores denote ones into which N_2 molecule cannot access at 77 K. Activated carbons prepared differently are examined. The basic idea of the method is as follows: (1) Pores are classified into effective micropores (further devided into smaller and larger micropores distinguished from DR (Dubinin-Radushkevich) analysis and inaccessible pores. (2) Volume fraction is determined for each type of pore considering densities. (3) Debye-Bueche plot derived from SAXS analysis is used to estimate the average transversal length of solid part and pore, respectively, convined with their volume fractions obtained from (1) and (2). (4) In case of a porous system with a symmetrical shape of pores, relative number and size of inaccessible pore to effective micropore are calculated.

INTRODUCTION

A precise characterization of microporous solids is requisite for further development of related sciences and technologies. In particular, the research on an "inaccessible pore" characterization[1] is stimulated by recent physical studies. Here inaccessible pore includes closed pores and small micropores in which a N_2 molecule cannot enter. The physical properties like unusual photoconductivity[2], atmosphere-sensitive ESR relaxation[3] and ferromagnetism[4] of activated carbons are presumed to be associated with disordered structures including inaccessible pores.

We have no established characterization method of inaccessible pores in a disordered solid. Small-angle X-ray scattering (SAXS) have been used to characterize the pore structures of activated carbon. Ruike *et al.*[1] extended the Debye's analysis[5] of SAXS intensity to get important information on the average size and number of inaccessible pores. Furthermore, they proposed a fine pore characterization method combining SAXS, N_2 adsorption and density data and showed almost perfect description on the average porosity of activated carbon. They used activated carbon fibers which have more ordered micropore structures than ordinary granulated activated carbons. It is necessary to apply their fine pore characterization method to activated carbon system having a more random structure. The aim of this work is on further establishment of the fine pore characterization method applicable to the inaccessible pore characterization.

EXPERIMANT

Fine Pore Characterization Method

In a fine pore characterization method, the micropores are classified into effective micropores and inaccessible pores (Fig.1) owing to the accessibility to N_2 molecule at 77 K. The effective micropores, determined with N_2 adsorption, are further divided into smaller and larger micropores which are distinguished by the DR (Dubinin-Radushkevich) analysis. The inaccessible pores consist of closed pores and the micropores for which a N_2 molecule is not accessible.

Mat. Res. Soc. Symp. Proc. Vol. 407 © 1996 Materials Research Society

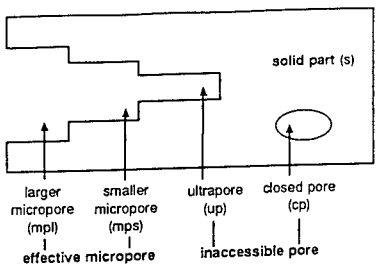


Fig.1 Schematic illustration of the effective micropore and the inaccessible pore in microporous solid.

Microporosity Determination with N2 Adsorption and Density Measurements

N_2 adsorption at 77 K provides a definite micropore volume of a microporous solid. Total micropore volume ($W_{\alpha s}$) and specific surface area ($S_{\alpha s}$) are determined by the α_s plot of N_2 adsorption isotherm.[6] The structure of the smaller micropore volume (V_{mps}) is determined from the analysis of the adsorption isotherm with the DR equation.[7] Here the larger micropore volume (V_{mpl}) equals to the subtraction of V_{mps} from $W_{\alpha s}$.

In addition, we can describe each pore shown in Fig.1 in terms of the volume fraction. These volume fractions can be experimentally obtained by using different densities, that is, X-ray density, d_X, and apparent particle density, d_{ap}. The former means the mass of the solid part divided by the solid volume. As the true density of graphite is known (2.267 g$\cdot$ cm^{-1}) and activated carbon has a structure mainly consisting of small graphitic stackings, the X-ray density of activated carbon can be approximately derived from eq.(1). This equation is obtained by the ratio of the d_{002} values for graphite (3.354 Å) and activated carbon.

$$d_x = 2.267 \times \frac{3.354}{d_{002}} \qquad (1)$$

The latter is described as the mass divided by the total particle volume. It is decided by the replacement method using deionized-distilled water. In this case the density (d_{water}) is interpreted as the value when both larger and smaller micropores are completely filled with water. Thus the apparent particle density is expressed by eq.(2) in terms of the additive value $W_{\alpha s}$ of the volumes of larger and smaller micropores.

$$d_{ap} = \frac{d_{water}}{1 + d_{water} W_{\alpha s}} \qquad (2)$$

Hence these volume fractions are given by measurable quantities, as follows.

$$\Phi_s = d_{ap} / d_x, \quad \Phi_p = 1 - d_{ap} / d_x, \quad \Phi_{mps} = d_{ap} V_{mps},$$
$$\Phi_{mpl} = d_{ap}(W_{\alpha s} - V_{mps}), \quad \Phi_{inp} = 1 - d_{ap}(W_{\alpha_s} + 1/d_x) \qquad (3)$$

Small-angle X-ray Scattering and Pore Structure

The X-ray scattering intensity in a classical theory is represented with the local fluctuations of electron density from the average, ρ. Self-correlation of ρ is often

expressed by the correlation function, γ (r). Debye *et al.*[5] introduced an exponential correlation function for the porous system with a distribution of pores of random shape and size in solids as $\gamma(r)=\exp(-r/a)$. In this equation, r is the distance between any two points in the system, and a is the correlation length which depends on the heterogeneity of the system. Substituting $\gamma(r)$ (defined above) in the classical scattering theory yields the relationship between the scattering intensity, I, and a. The "smeared" scattering intensity, $\tilde{I}$, is associated with a through eq.(4) in a line focus system.

$$\tilde{I} = \frac{A}{(1+a^2s^2)^{3/2}} \qquad (4)$$

In eq.(4) s equals to $(4\pi\sin\theta)/\lambda$, where 2θ is the scattering angle and λ is the wavelength of X-ray, and A is a constant. The linear plot of $\tilde{I}^{-2/3}$ vs. s^2, which is called "Debye-Bueche plot"[8], provides the value of a as (slope/intercept)$^{1/2}$.
In addition Φ_s and Φ_p lead to the mean transversal dimensions of the carbon pore-wall (a_s) and the pore (a_p) as $a_s = a/\Phi_p$ and $a_p = a/\Phi_s$, respectively.

An evident difference of electron density arises at the boundary of the solid and pore in a porous solid. The surface area, S_x, is therefore associated with the SAXS intensity. This relationship is expressed as eq.(5).

$$S_x = \frac{4\times10^4\Phi_s\Phi_p}{a d_{ap}} \qquad (5)$$

Experimental Conditions

Four kinds of activated carbons were examined. The precursor material and activation method of these samples are shown in Table 1. Adsorption isotherm of N_2 at 77 K was measured with a gravimetric method. The apparent particle density was determined by replacement method at 303 K using deionized-distilled water with the aid of a Gey-Lussac type pycnometer after pretreatment at 383 K for 3 h. The XRD pattern was measured with CuKa radiation at 40 kV and 35 mA.

For SAXS analysis, each sample was packed in the slit-shaped holder with thickness of 1 mm and positioned in the transmission geometry. The SAXS spectrum was measured by use of a two-axial three-slit system (Mac Science Model No.3310), with CuKa radiation at 20 kV and 15 mA. The scattered beam was detected by a linear-type position-sensitive counter (PSPC) with a step of s=0.0081 Å^{-1}. The data were corrected for the parasitic scattering and absorption.

Table 1 Preparation conditions of samples.

sample	precursor	activation type
PIT-C	pitch(coal)	chemical activation
PIT-W1	pitch(coal)	H_2O
PIT-W2	pitch(coal)	H_2O
NUT-W	coconut-shell	H_2O

RESULTS AND DISCUSSION

Determination of Pore and Solid Volume Fractions

All adsorption isotherms of N_2 at 77 K were of type I, indicating their microporosity. Table 2 summarizes the obtained parameters with the analysis of N_2 adsorption isotherms, also with densities of d_{ap} and d_x. The volume fraction calculated with eq.(4) facilitates the comparative analysis of microporosity of the samples (Fig.2). The microporosities of PIT-W1 and PIT-W2 are fairly different, that is, inaccessible pores occupy 1/4 of total pore volume in PIT-W1, while the effective micropore is predominant in PIT-W2. This predominance of the effective micropore is also observed in PIT-C with the largest Φ_p of all samples studied here. Most of effective micropores in NUT-W are smaller type and the contribution of inaccessible pores to the total porosity is great (0.23).

Table 2 Adsorption data of samples obtained from α_s and DR plots, and densities measured by XRD and replacement method.

sample	$S_{\alpha s}$ /$m^2 \cdot g^{-1}$	$W_{\alpha s}$ /$ml \cdot g^{-1}$	V_{mps} /$ml \cdot g^{-1}$	V_{mpl} /$ml \cdot g^{-1}$	d_x /$g \cdot cm^{-3}$	d_{ap} /$g \cdot cm^{-3}$
PIT-C	2270	1.30	0.98	0.32	2.11	0.55
PIT-W1	1150	0.52	0.42	0.10	2.11	0.85
PIT-W2	1370	0.71	0.54	0.17	2.11	0.81
NUT-W	650	0.23	0.22	0.01	1.84	1.19

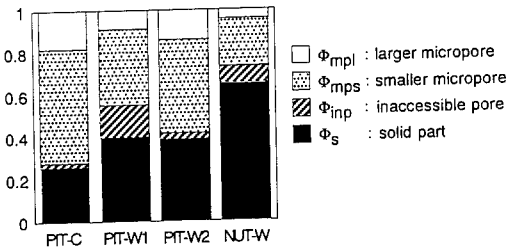


Fig.2 Volume fractions of various pores and solid part.

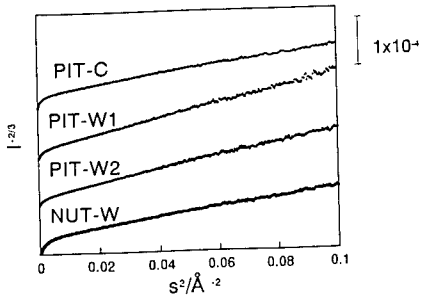


Fig.3 The Debye-Bueche plots derived from SAXS profiles.

Table 3 Correlation length (a) and average transversal length of solid (a_s) and pore (a_p) parts, compared with pore width (w) obtained from N_2 adsorption isotherm.

sample	a/Å	a_s/Å	a_p/Å	w/Å
PIT-C	5	7	22	11
PIT-W1	9	15	23	9
PIT-W2	9	14	23	11
NUT-W	6	17	9	7

Pore and Pore-Wall Structures with SAXS

The Debye-Bueche plots in Fig.3 exhibit the clear linear region in a wide range of s. It implies that the samples studied here satisfy the condition of the random porous system originally postulated by Debye *et al*.[5] The correlation length, a, for each plot was thus obtained followed by estimation of the average dimensions of pore and solid, a_p and a_s, respectively. The effectiveness of these values are assured by the fact that the obtained correlation length is converted to s value included in the linear region for every Debye-Bueche plot. Table3 shows the values of a, a_p and a_s. The average pore width (from N_2 adsorption, slit-pore assumption) w is also shown in Table 3 for comparison. Three coal-based samples have almost the same a_p, being greater than w. As a_p is the mean transversal length and w is the shortest length of the three-dimensional slit-pore, the fact of $a_p > w$ is plausible. However, the great difference of a_p and w is indicative of presence of micropores of narrow entrance. In case of NUT-W, a_p is quite close to w, indicating a symmetrical pore.

In case of a porous system with a symmetrical shape of pores, the pore volumes (V_{em}, V_i) and specific surface areas (S_{em}, S_i) of effective micropores and inaccessible pores can be geometrically expressed with the number of concentrations (n_{em}, n_i) and pore sizes (r_{em}, r_i)[1]. Here the suffixes of (em) and (i) denote the effective micropores and inaccessible pores, respectively.

$$\frac{V_i}{V_{em}+V_i} = \frac{\Phi_{up}+\Phi_{cp}}{\Phi_p} = \frac{n_i r_i^3}{n_{em} r_{em}^3 + n_i r_i^3} \equiv \frac{1}{\xi} \qquad (6)$$

$$\frac{S_i}{S_{em}+S_i} = \frac{S_x - S_{cs}}{S_x} = \frac{n_i r_i^2}{n_{em} r_{em}^2 + n_i r_i^2} \equiv \frac{1}{\eta} \qquad (7)$$

The relative number and dimension of inaccessible pores can be accordingly derived by eqs.(8) and (9).

$$\frac{n_i}{n_{em}+n_i} = \frac{(\xi-1)^2}{(\xi-1)^2+(\eta-1)^3} \qquad (8)$$

$$\frac{r_i}{r_{em}} = \frac{\eta-1}{\xi-1} \qquad (9)$$

As sample NUT-W probably has symmetrical pores as mentioned above, this method can be applied to. The result was obtained as $n_i/(n_{cm}+n_i)=0.55$ and $r_i/r_{cm}=0.33$. The precursor of NUT-W comprises inherent microporosity with inaccessible pores. Some effective micropores are produced from inaccessible pores by gasfication during activation process, following by developing the size. Consequently the fact that the size of the effective pore is three times larger than that of the inaccessible pore is quite reasonable. The absolute size of the inaccessible pore should be about 3 Å, being smaller than the size of a N_2 molecule. As such narrow micropores should work as inaccessible pores for N_2 molecules, the above inaccessible pore evaluation is helpful to characterize a disordered microporous solid.

The analysis with the Debye-Bueche plot for the SAXS profile is applicable to the characterization of microporous carbons. The integrated information from SAXS, molecular adsorption and density measurements lead to an exact characterization of pores including inaccessible pores. In particular, this combined approach is effective for characterization of a random microporous system.

REFERENCES

1. M.Ruike, T.Kasu, N.Setoyama, T.Suzuki and K.Kaneko, J.Phys.Chem. **98**, p.9594 (1994).
2. K.Kuriyama and M.S.Dresselhaus, Phys.Rev. B. **44**, p.8256 (1991).
3. A.Nakayama, K.Suzuki, T.Enoki, C.Ishii, K.Kaneko, M.Endo and N.Shindo, Solid State Commun. in press.
4. C.Ishii, Y.Matsumura and K.Kaneko, J.Phys.Chem. **99**, p.5743 (1995).
5. P.Debye, H.R.Anderson, Jr., and H.Brumberger, J.Appl.Phys. **28**, p.679 (1957).
6. K.Kaneko and C.Ishii, Colloids Surf. **67**, p.203 (1992).
7. M.M.Dubinin, Chem.Rev. **60**, p.235 (1960).
8. P.Debye and A.M.Bueche, J.Appl.Phys **20**, p.518 (1949).

INFLUENCE OF SPATIAL CORRELATIONS ON PERMEABILITY AND CONNECTIVITY OF SANDSTONE

HERNAN A. MAKSE,[1] SHLOMO HAVLIN[1,2], PETER R. KING,[3] AND H. EUGENE STANLEY[1]
[1]Center for Polymer Studies and Physics Dept., Boston University, Boston, MA 02215 USA
[2]Department of Physics, Bar-Ilan University, Ramat Gan, ISRAEL
[3]BP Exploration Operating Company Ltd., Sunbury-on-Thames, Middx., TW16 7LN, UK

ABSTRACT

Sedimentary rocks have complicated permeability patterns arising from the geological processes that formed them. Here we address the longstanding question of how such patterns are generated. We also analize data on two sandstone samples from different geological environments, and find that the permeability fluctuations display long-range power-law correlations characterized by an exponent H. For both samples, we find $H \approx 0.82 - 0.90$. These permeability fluctuations significantly affect the flow of fluids through the rocks.

INTRODUCTION

Sedimentary rocks have complex correlated patterns that influence the flow and recovery of hydrocarbons. These patterns arise from the complicated geological processes that formed the rocks. It is a major experimental and theoretical challenge to understand how the process forms the patterns. For oil companies it is also extremely important to understand how the patterns influence recovery and to make quantitative predictions of the influence.

In this paper we address the following points:

(*i*) We develop a "table top" experiment to understand the origin of the geological formation of aeolian sands. Although the formation of periodic laminae of fine and coarse grains in sedimentary structures is a widespread phenomenon [2, 3, 4, 5, 6], its origin remains an open question. Figure 1 shows a section of a Triassic, planar cross bedded Aeolian sandstone from Lochabriggs near Dumfries, Scotland where a typical example of stratification pattern is observed. We address the longstanding question of how such periodic patterns are generated by proposing a "table top" experiment. The experiment reproduces the successive layers of fine and coarse particles observed in sedimentary structures.

(*ii*) We confirm the spatial patterns predicted with the experiment by comparing with real rock samples. Figure 2a shows the result of the experiment. The size segregation into alternating layers is quite similar to that found in the geological sample and in stratigraphic records. We note two features: (*a*) **Alternation.** We clearly see the formation of alternating layers consisting of small and large particles. (*b*) **Segregation.** We observe that the layers are built up in such a way that small particles are segregated in layers near the top of the slip-face, while larger particles form layers near the substrate at the bottom.

(*iii*) We propose a physical explanation of the process involved. A numerical computer model of sand dune dynamics is developed that confirms the plausibility of the physical mechanism (Fig. 2b).

(*iv*) We quantify the spatial correlations in rocks. Permeability in sandstone can change by many orders of magnitude over very short distances. Not only are there large fluctuations in permeability but the permeability can exhibit strong anisotropy. Deriving methods to describe these spatial patterns is a major challenge. Both the efficient recovery of hydrocarbon and contaminant dispersal and control in ground water is affected by the understanding of such spatial patterns. Traditionally these patterns have been modeled with a finite range correlation scale. We analyze a detailed permeability map and show that the data are consistent with a long-range correlation model.

Mat. Res. Soc. Symp. Proc. Vol. 407 © 1996 Materials Research Society

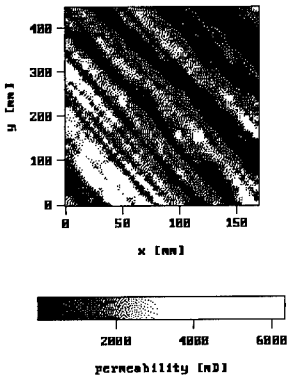


Figure 1: *Permeability map of the Lochabriggs sample.*

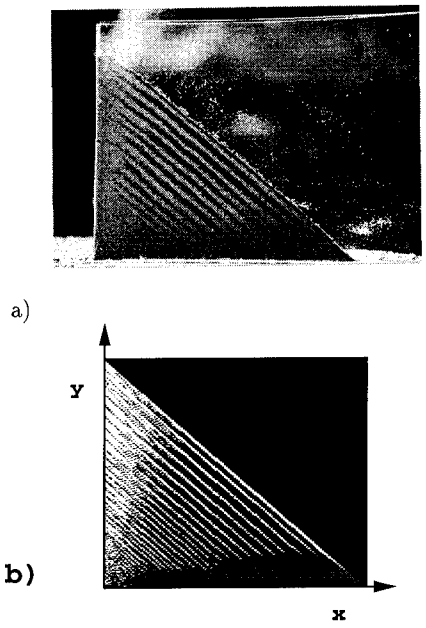


Figure 2: *a) Photograph of the experimental sandpile showing the periodic layers. b) Image obtained with the proposed sandpile model*

ROCK SLAB DATA

The Aeolian sandstone shown in Fig. 1 was formed by windblown sand [1]. A small sand accumulation (sand bar or dune) is formed as the unidirectional wind moves material along the bed. As the wind continues, sand is moved from the upstream side of the dune to the crest of the dune, and the slope of the sand bar become steeper. When the initial dune reaches a critical angle or slope, a downstream slip-face is developed where avalanches of sand begins. After this, new material is brought to the top of the dune until another avalanche occurs. The evidence of such sedimentary process can be traced in the layered structure of the Lochabriggs sample of Fig. 1.

EXPERIMENT

To understand the origin of the layering segregation we begin by developing the following "table-top" experiment [7]. The experimental setup consists of a vertical Hele-Shaw [8] cell with a gap of 5mm separating two transparent plates of 300mm by 200mm (see Fig. 2a). We close the left edge of the cell leaving the right edge free, and we pour, next to the left edge, an equal-volume mixture of white fine silica sand (typical size 0.4mm) and dark coarse sugar crystals (typical size 0.9mm). We choose this quasi-two-dimensional geometry since the actual geological system is translationally invariant along the transverse direction (due to the unidirectional flow of sand).

Figure 2a shows the result of the experiment. We note the two main features: (***a***) **Alternation**, and (***b***) **Segregation.**

PROCESS MODEL AND NUMERICAL COMPUTER MODEL

The main physical mechanism responsible for the formation of the layers appears to be related to the segregation effect and also to the existence of two critical angles controlling the avalanche process [7]. Indeed, real sandpiles are known [9, 10, 11] to be stable until the angle of the sandpile θ reaches a critical maximum angle of stability θ_m. When $\theta > \theta_m$, the sandpile produces a spontaneous avalanche. The avalanche stops when θ decreases below a second critical angle of repose θ_r. The oscillation of θ between θ_m and θ_r as sand is continually added produces the periodic layers observed in the experiment, and presumably in geological data as well.

In order to test the plausibility of this physical mechanism, we next develop a numerical sandpile model [7], defined in a semi-infinite $(1 + 1)$-dimensional lattice corresponding to the experimental setup. Particles of two different sizes are initially landed near the left edge of the semi-infinite lattice. The dynamics for the arriving particles proceed according to the critical angle θ_m until a particle reachs the substrate for first time. Then, the sandpile becomes unstable, and it relaxes toward the repose angle θ_r producing an avalanche that stops when all the particles reach stable positions respect to θ_r. Now the deposition starts again, and the above process is iterated until a large sandpile of typically 10^5 particles has been formed.

Figure 2b shows the resulting morphology of the model. Different colors represent different particle size, being white for the smaller particles and dark for the larger particles. The size segregation into alternating layers is quite similar to that found experimentally (Fig. 2a), which in turn is reminiscent of the stratification structure of the geological Lochabriggs sample (Fig. 1). Thus this model is consistent with the physical mechanism above that the relevant ingredients for the formation of the layers are the two critical angles and the segregation effect.

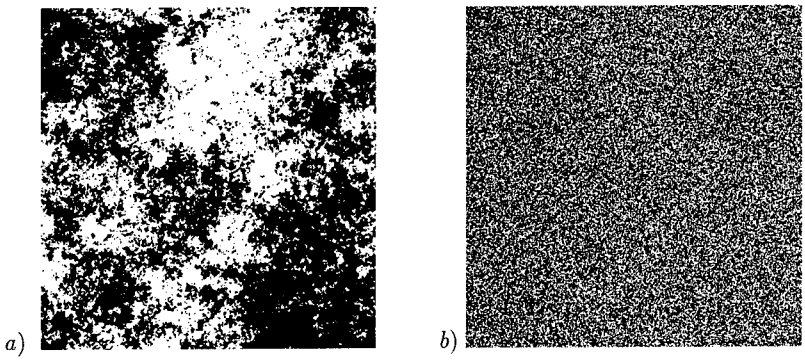


Figure 3: *Percolation at the critical concentration. a) Correlated case, and b) Uncorrelated case.*

SPATIAL CORRELATIONS AND CONNECTIVITY

In order to investigate spatial patterns in permeable rocks two samples were used. One was the *aeolian* Lochabriggs sample shown in Fig. 1, and the second sample was a Triassic, *fluvial* trough cross bedded sandstone from Hollington near Stafford in the East Midlands of England. It is clear from Fig. 1 that permeability varies significantly within a very short scale, but also that there is a strong spatial correlation. The permeability is not an independent random process. To measure the spatial correlations in the permeability we study the mean square fluctuations as a function of the lag separation between points. We find that for both set of data the correlations are well described by a power-law, indicating the existence of long-range correlations in the permeability values [12].

We incorporate these properties of real systems into the framework of the percolation problem [13], to investigate the effects that this has on the various quantities of interest, and to consider the consequent implications.

Imagine an oil reservoir made from a river system. The old river channels represent good sand with high permeability. The other rock (shale) has poor permeability. Hence, for many purposes it can be modeled by a conductor/insulator or percolation system. The sand bodies may be thought of as some shapes distributed in space. They may tend to avoid each other or stack next to each other. Fortunately for the petroleum industry, they may also overlap, so it is possible for large "clusters" of sand bodies to exist.

In order to quantify these ideas, we consider the *correlated* percolation model [14, 15, 16, 17]. In the limit where correlations are so small as to be negligible a site in the square lattice is occupied *at random* with a probability p. However, the fact that we find *spatial correlations* in the rock suggest that the process can be better modeled using the correlated percolation model where each site is not independently occupied, but is occupied with a probability that depends on the occupancy of the neighborhood. We analyse the structural and dynamic properties of the resulting connected structure. It is worth noting that the percolation model applies not only to the scale of the pore structure but also to larger scales such as the lamination scale. For both the discrete (sand/shale) and continuous systems (permeability), it is important to know how long-range correlations influence the macroscopic connectivity and flow.

The impact of correlations is apparent from Fig. 3. Figure 3a is for conventional

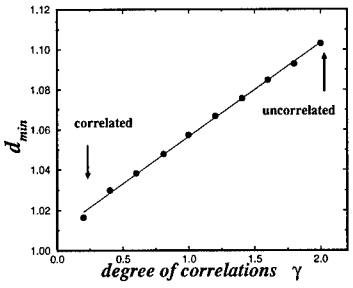


Figure 4: *Fractal dimension d_{min} as a function of the degree of correlations.*

uncorrelated percolation, and Fig. 3b is for percolation with long-range scale-invariant correlations. Both figures are plotted at the critical concentration p_c, above which fluid can flow since there exists an "incipient infinite cluster" that forms just when a connected path breaks through. The occupancy probability p_c corresponds to the net to gross or volume fraction of good sand in actual sand systems. It is apparent by visual inspection that the clustering properties for the two cases differ dramatically. For example, by comparing Figs. 3a and 3b, we see that the clusters are much larger and more compact in the case of long-range correlations. This implies that there are fewer dead-ends and hence less unswept oil. Therefore, the recovery percentage increases for such strongly correlated systems. Our preliminary results indicate an increase of about 10% in the recovery percentage of correlated systems in comparison with uncorrelated systems.

Figure 4 shows the changes with the correlation exponent γ of the fractal dimension of the minimum path, d_{min} (the shortest path that one can get through the cluster from one to the other). The correlation exponent γ measures the degree of correlation in the system, being uncorrelated for $\gamma = 2$ and strongly correlated for $\gamma = 0$. Again we see a striking dependence of this property upon the degree of correlations. The fractal dimension of the minimum path approaches one (the minimum path becomes equal to the Euclidian distance between the points) as $\gamma \to 0$ (strong correlations), meaning that the cluster becomes more compact in agreement with the above behavior. The fact that the shortest streamlines are "straighter" leads to shorter breakthrough times. As the tortuosity of the streamlines is being reduced, we expect spreading of the front to be reduced and hence better recovery efficiency.

Similar analyses have been performed with other quantities characterizing the connectivity properties of the percolation clusters. For example we find that the critical concentration p_c increases as a function of γ. Therefore one would expect better overall connectivity at lower net to gross in the correlated case than in the uncorrelated case. The quantitative changes with the degree of correlations indicate the errors that are being made with currently-used uncorrelated models.

CONCLUSIONS

Spatial patterns in permeable rocks exist and require quantitative methods to describe them. In the particular case of Aeolian systems (such as the Lochabriggs sample), we show that the observed periodic stratified pattern can be understood with a "table top" experiment. We propose a physical explanation for the formation of layers, which is related to a size segregation effect and also to the existence of *two* critical angles controlling the avalanche

process. Finally, we develop a stochastic model of sand dune dynamics that confirms the plausibility of this physical mechanism. While these results apply only to aeolian systems, the finding of long-range correlations in sandstone appears to be true independent of the geological process involved. For the two samples studied so far it has been shown that the correlations can be well modeled using a power law.

These spatial patterns have very great consequences for prediction of, for example, hydrocarbon recovery or contaminant transport in ground water. The fact that there exist long range correlations implies that the spread in contaminant transport might be much faster than would be predicted from a short range correlation model.

ACKNOWLEDGEMENTS

We thank R. Cuerno, D. Langtry, and S. Tomassone for discussions and BP for financial support.

References

[1] Bagnold, R. A. *The physics of blown sand and desert dunes* (Chapman and Hall, London 1941).

[2] McKee, E. D., Crosby, E. J. & Berryhill, H. L. JR. *Journal of Sedimentary Petrology* **37**, 829-851 (1967).

[3] Jopling, A. V. & Walker, R. G. *Journal of Sedimentary Petrology* **38**, 971-984 (1968).

[4] Borges, J. L. *The book of sand* (Emecé, Buenos Aires 1975).

[5] Fryberger, S. G. & Schenk, C. *Sedimentology* **28**, 805-821 (1981).

[6] Cheel, R. J. & Middleton, G. V. *Journal of Geology* **94**, 489-504 (1986).

[7] H. A. Makse, S. Havlin, P. R. King, and H. E. Stanley (submitted).

[8] Hele-Shaw, H. S. *Nature* **58**, 34-36 (1898).

[9] Bagnold, R. A. *Proc. Roy. Soc. London* **A 295**, 219-232 (1966).

[10] Allen, J. R. L. *Journal of Geology* **78**, 326-351 (1970).

[11] Jaeger, H. M. & Nagel, S. R. *Science* **255**, 1523-1531 (1992).

[12] H. A. Makse, G. Davies, S. Havlin, P. Ch. Ivanov, P. R. King, and H. E. Stanley (submitted).

[13] A. Bunde, S. Havlin, eds., *Fractals in Science* (Springer-Verlag, Berlin 1994).

[14] A. Coniglio, C. Nappi, L. Russo, and F. Peruggi, J. Phys. A **10**, 205-209 (1977).

[15] A. Weinrib, *Phys. Rev. B* **29**, 387-395 (1984).

[16] S. Prakash, S. Havlin, M. Schwartz, H. E. Stanley, Phys. Rev E **46**, R1724 (1992).

[17] H. A. Makse, S. Havlin, H. E. Stanley, and M. Schwartz, 1993 Int. Conf. Complex Systems in Computational Physics, Buenos Aires, Chaos, Solitons and Fractals **6**, 295 (1995).

A SIMPLE MODEL FOR ANOMALOUS RELAXATION IN POROUS MEDIA

MARIELA ARAUJO †, ORLANDO GONZALEZ ‡
† INTEVEP S.A, Apartado 76343. Caracas 1070–A Venezuela.
‡ Departamento de Física, Universidad Central de Venezuela. Caracas, Venezuela.

ABSTRACT

We present a simple model to explain anomalous relaxation in random porous media. The model, based on the properties of random walks on a disordered structure, is able to describe essential features of the relaxation process in terms of a one body picture, in which the many body effects are approximated by geometrical restrictions on the particles diffusion. Disorder is considered as a random variable (quenched and annealed) taken from a power-law distribution $|\mu|\xi^{\mu-1}$. Quantities relevant to relaxation phenomena, such as the characteristic function and the particle density are calculated. Different regimes are observed as a function of the disorder parameter μ. For $\mu > 1$ the relaxation is of exponential or Debye type, and turns into a stretched exponential as μ decreases. We compare numerical predictions (based on Monte Carlo simulations) with experimental data from porous rocks obtained by Nuclear Magnetic Resonance, and numerical data from other disordered systems.

INTRODUCTION

Anomalous relaxation has been observed in a wide variety of physical systems. Examples are found in supercooled liquids, the magnetization relaxation in spin glasses and porous materials, the viscoelastic response of solids, dielectric relaxation among others [1–3]. For these systems, the relaxation function does not follow the normal exponential form, and is usually expressed in terms of a more complicated form such as a power-law, a stretched exponential, etc,. Even though these systems are relatively well known the microscopic mechanism for the occurrence of anomalous relaxation is not well established.

In general, relaxation phenomena are consequence of many body effects within a single system. However, some of their features can be described in terms of a one-body picture by applying geometrical constraints to the movement of the particles, i.e., the motion of a particle under the influence of many body effects is approximated by its motion in a restricted geometry. In the one-body picture, the relaxation function corresponds to the characteristic function of the position vector.

Here, we present results from a study of random walks on a regular disordered lattice in one and two dimensions. The motion of the walkers is restricted by the lattice's disorder. Disorder is considered as a random variable taken from a power-law distribution $|\mu|\xi^{\mu-1}$. Its strength is measured by the exponent that characterizes the tail of the distribution i.e., μ. Two cases are treated, one with quenched variables (frozen on the lattice sites) and the other with annealed variables which are allowed to change with time. We also consider the relaxation on a structurally disordered lattice, a percolation cluster at the percolation threshold. Our numerical results demonstrate that the restrictions on the particles motion cause anomalous relaxation. This claim is supported by the measurement of several quantities related to the relaxation process. Our expectation is that the model studied here, will shed some light towards the understanding of anomalous relaxation. The model may be used as a simplified approximation to describe magnetic relaxation phenomena in natural porous media. The conclusions drawn from the simulations of

Mat. Res. Soc. Symp. Proc. Vol. 407 © 1996 Materials Research Society

low dimensional systems are qualitatively observed in Nuclear Magnetic Resonance (NMR) experiments done in sedimentary consolidated porous rocks.

MODEL AND SIMULATIONS

Inside a porous medium a particle can not move as it pleases since there are geometrical restrictions associated with the porous structure. Normally, the particle gets temporarily trapped in poorly connected regions, causing a slow down of its spreading in it, an effect known as subdiffusion. Here, we consider the relaxation of a localized signal on a disordered structure. This signal, which in the NMR experiment is the initial magnetization of the nuclear spins aligned with the magnetic field, is described by a random particle (walker) released at a given point on a lattice and then allowed to spread on the structure. The geometrical constraints that affect the motion of the random walker are expressed in terms of a "disorder" variable ξ, which is taken from a power-law distribution $|\mu|\xi^{\mu-1}$. We consider $0 \leq \mu \leq 1$. In this case, the disorder variables are in the range $0 \leq \xi \leq 1$, and as μ decreases, the distribution becomes more singular towards zero. It has been shown [4] that in this range, a random walker on such a structure displays anomalous diffusion.

Starting at a given site on the lattice, a walker is released and allowed to move if a random number (drawn from a uniform distribution) is smaller than the value of the disorder variable attached to its site. It moves to one of its nearest neighbors with equal probability. Two cases are considered for the disorder random variables, a quenched situation and the annealed. In the quenched case, the variables are frozen on the lattice while the walker moves around, whereas for the annealed case, each disorder variable is updated at each unit of time when the walker attempts to move. A sampling over many disorder configurations is done, typically for 10^4 realizations. We consider lattices in one and two dimensions, for particles motion up to 2^{20} time steps, and system sizes big enough to avoid situations where the random walker reaches the boundaries.

The transport on a fractal structure in d = 2 is also considered. Here, the relaxation process occurs on a spanning percolation cluster, near the percolation threshold. A site is randomly chosen on each percolating system, and the walker is released from it. At each unit of time, we allow the walker to move on the structure with equal probability to a nearest neighbor site, and measure its relaxation properties. Percolation spanning clusters generated on a 400 x 400 lattice were used. In the simulations, averages over 20 different cluster realizations and 10^4 samples were taken.

For all the cases, we measure the position of the particles as a function of time. From this information we calculate the relaxation function, $\mathrm{F(k,t)}$, which is the characteristic function of the random variable $\vec{r}(t) - \vec{r}(0)$, i.e.,

$$\mathrm{F(k,t)} = < e^{i\vec{k}.(\vec{r}(t)-\vec{r}(0))} >,$$

where $\vec{k}$ is the wave vector (for the 2D lattice it is chosen as $\vec{k} = (1,1)$ i.e., along the main diagonal of the lattice), $\vec{r}$ is the particle's position vector, and the angular brackets denote the sample average. Other quantities which are calculated are: the mean squared displacement, a factor that measures the deviation of the distribution from a gaussian, here called the non-gaussian parameter NGP, defined as:

$$\mathrm{NGP} \equiv \frac{< (\vec{r}(t) - \vec{r}(0))^4 >}{2\left[< (\vec{r}(t) - \vec{r}(0))^2 >\right]} - 1,$$

and the Probability density function $P(\vec{r}, t)$. These quantities are compared with their corresponding counterparts calculated for transport on a regular non-disordered structure.

RESULTS

In Figure 1 it is shown the time dependence of the relaxation function, $F(k, t)$, for a disordered lattice in one and two dimensions. The curves are for the case of quenched and annealed disorder as indicated. The corresponding curve for the relaxation on a non-disordered lattice is shown for comparison. For the three curves, k (the magnitude of the wave vector) is fixed to $k = 11\pi/250$. It is clear from the figure that for a fixed value of the wave number k, the faster decay corresponds to Debye relaxation i.e., for a non-disordered lattice. For the disordered case, the decay is faster when the variables are annealed for the same value of the exponent μ. We find the following tendencies for the case of quenched and annealed disorder:

a. Faster decay of $F(k, t)$ for μ fixed and increasing wave number value.
b. Faster decay of $F(k, t)$ for k fixed and increasing μ value (less strong disorder).

Figure 2 shows the effect of the strength of quenched disorder on a lattice in one and two dimensions. It is seen that as μ increases (disorder gets weaker) F(k,t) decays faster. The same tendency is observed for the annealed case. For the same μ values, the effect is stronger for quenched disorder on 1D ans 2D lattices.

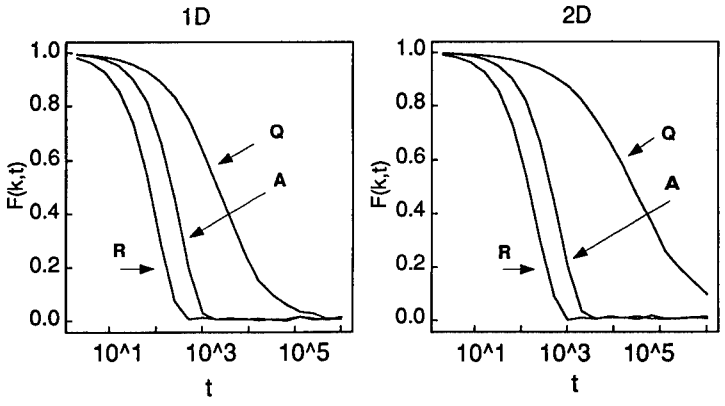


Figure 1. Decay of relaxation function F(k,t) for 1D and 2D lattices with quenched (Q) and annealed (A) disorder for μ = 0.5. Also shown F(k,t) for a lattice without disorder (R).

In terms of the relaxation time τ (calculated as the value of time at which $F(k, t)$ decays to a factor $1/e$) we find a power law dependence with the wave number value, i.e., $\tau \sim k^{-\gamma}$. The exponent γ being a function of μ for quenched disorder. γ increases as μ decreases. For

the annealed case $\gamma = 2$, as for regular transport (normal relaxation). In Table 1, we show the values of exponent γ as a function of the disorder exponent μ, for the case of quenched and annealed disorder on 2D lattice.

With relation to the probability density, we found an interesting parameter (called NGP) that allows to measure the deviations of the distribution function from a gaussian form. For the non-disordered lattice the probability density is a gaussian, therefore the NGP parameter is zero (See Fig.3). On the other hand, as we increase the strength of disorder (by effectively reducing the value of μ), the NGP increases monotonically while being almost constant with time, moving away from zero.

Our results for the relaxation process on the 2D percolation cluster are similar to those of Ref. 2. The relaxation function F(k, t), is well fitted to a stretched exponential function for small k values, and as k increases it changes to a Cole-Cole form [1]

$$\chi(\omega) = \frac{1}{1 + (-i\omega\tau)^{\alpha}} \qquad \alpha > 0 .$$

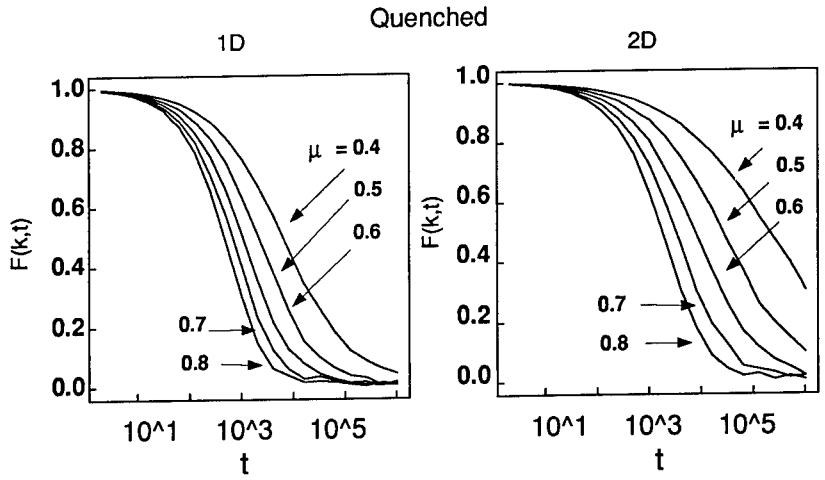


Figure 2. Decay of relaxation function F(k,t) for quenched disorder on a 1D and 2D lattice. μ measures the strength of disorder. All curves are for $k = 11\pi/250$.

Using the pulsed NMR technique [5], the magnetic relaxation of water was measured on a set of sedimentary consolidated porous rocks of various permeability values. The data can not be fitted to an exponential form but to a stretched exponential $F(t) = \exp\left[-(t/\tau)^{\beta}\right]$. The exponent β is found to monotonically increase with the width of the distribution of pore sizes, which can be considered as a disorder indicator. β values are in the range $0.51 \leq \beta \leq 0.89$.

CONCLUSIONS

In summary, we have found that anomalous relaxation could be modeled by diffusive effects in a restricted geometry. A simple model based on the motion of random walkers on a disordered structure is able to describe anomalous relaxation, which has been observed in experiments. Thus, a one-body picture is able to reproduce the essential features of the relaxation process.

The relaxation time τ, obtained from the relaxation function $\mathrm{F(k,t)}$ has a power law dependence on the magnitude of the wave number k. For the quenched case, the exponent of this power-law form depends on the strength of disorder (here measured by the value of μ), whereas for the annealed case it is rather insensitive. Its value is the same as for transport on a lattice without disorder. For $\mu \geq 1$ the relaxation becomes of Debye form; namely $\mathrm{F(k,t)}$ is well fitted by an exponential function and the complex susceptibility have the typical $1/(1 - \mathrm{i}\omega\tau)$ form. Scaling laws for these quantities are also found to exist. Our results for the relaxation process on a spanning percolation cluster are similar to those reported in Ref. 2.

The simple model presented here describes qualitatively the magnetic relaxation process observed in fully saturated consolidated porous rocks for small wave numbers.

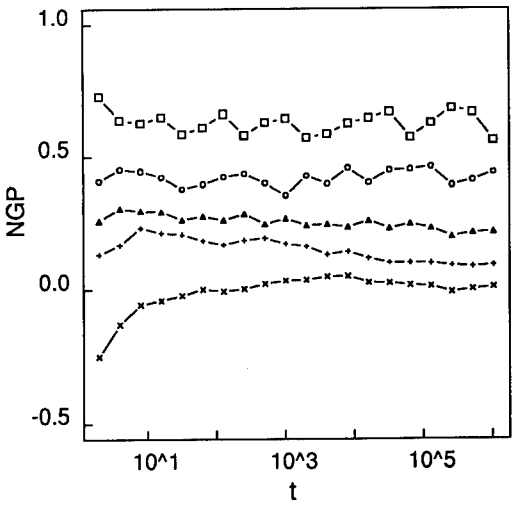


Figure 3. Time dependence of non-gaussian parameter (NGP) for quenched disorder on a 2D lattice. Different curves are for $\mu = 0.4\,(\square); 0.6\,(\mathrm{o}); 0.8\,(\triangle); 1.0\,(+)$. Bottom curve (x) corresponds to a lattice without disorder.

ACKNOWLEDGMENTS

The authors would like to thank Intevep S.A. for permission to publish this paper.

Table 1. Exponent of relaxation time τ vs k, $\tau \sim k^{-\gamma}$.

Disorder Strength μ	Quenched γ	Annealed γ
0.4	3.40±0.02	2.00±0.02
0.5	2.96±0.02	2.00±0.02
0.6	2.73±0.02	2.00±0.02
0.7	2.50±0.02	2.00±0.02
0.8	2.38±0.02	2.00±0.02

REFERENCES

1. K. Binder and A.P. Young, Rev. Mod. Phys. **58**, 801 (1986); K.H. Fisher and J.A. Hertz, Spin Glasses (Cambridge Univ. Press, Cambridge, 1991); R. Kohlraush, Ann. Phys. (Leipzig) **12**, 393 (1847) ; K.S. Cole and R.H. Cole, J. Chem Phys. **9**, 639 (1941).
2. S Fujiwara and F. Yonezawa, Phys. Rev. E **51**, 2277 (1995); Phys. Rev. Lett. **74**, 4229 (1995).
3. S. Gomi and F. Yonezawa, Phys. Rev. Lett. **74**, 4125 (1995).
4. S. Havlin and D. Ben-Avraham, Adv. Phys. **36**, 695 (1987).
5. NMR measurements were done at the Center of Magnetic Resonance of Universidad Central de Venezuela.

Part II

Colloids

INTERACTION OF DILUTE COLLOIDAL PARTICLES IN A MIXED SOLVENT

JAMES V. MAHER and M. LEVENT KURNAZ
Department of Physics and Astronomy, University of Pittsburgh, Pittsburgh, Pennsylvania 15260

INTRODUCTION

Colloidal particles in mixed solvents can show reversible aggregation in the one-phase regime of the mixture near the mixture's phase separation temperature [1-5]. This aggregation condition has been shown to be related to the affinity of the colloidal surfaces for one of the solvent components. In particular, for a 2,6 lutidine plus water (LW) mixture with colloidally dispersed polystyrene latex spheres (PLS) in a temperature range near the critical temperature, T_c, in the mixture's two-phase region, the particles will partition into one of the solvent phases, with the meniscus between the liquid phases clear to the eye and showing no sign of population by colloidal particles. Which phase of the solvent attracts the particles depends on the surface charge density of the particles, with high surface charge density particles preferring the water-rich phase and low charge density particles preferring the lutidine rich phase. As temperature is advanced deeper into the two-phase region (all effects discussed here are equilibrium effects), there is a temperature, T_W, at which particles appear on the meniscus (most particles remain in the preferred phase, whose population depletion is too small to measure). T_W changes with the surface charge density of the particles [4], but not with radius or with number density of the particles in the sample. The aggregation observed in the one-phase region [5] is then restricted to the side of the solvent's coexistence curve poor in the component which is rich in the partitioning-favored phase.

In this paper we present a measurement of the second virial coefficient for the interaction of very dilute colloidal particles deep in the one-phase region of the solvent, at temperatures ranging from very far from the point of onset of aggregation where the particle-particle interaction is clearly repulsive to near the temperature at which aggregation first appears.

EXPERIMENT AND RESULTS

Dilute suspensions of well-characterized, monodisperse PLS [6] in near-critical mixtures of LW were studied. PLS was prepared using a surfactant-free emulsion-polymerization technique, where stabilization against aggregation is provided by a net surface charge density of several $\mu C/cm^2$ sulfonated end groups preferentially located on the surface of the sphere.(We use surface charge density as measured by titration as a measure of sulfonic groups available on the surface for solvation. The actual surface charge density should depend on the local solvent composition near the particle surface and has not been measured in this experiment).

In our earlier work [4,5] we measured the onset of the aggregation zone, T_a. Figure 1 shows the results of those measurements for PLS particles of several surface charge densities, as well as the measured phase separation temperature, T_{ps}, at each of the solvent compositions used (at each

Mat. Res. Soc. Symp. Proc. Vol. 407 © 1996 Materials Research Society

point in Figure 1 when the T_a and T_{ps} symbols overlap, no aggregation was observed). In this work we used two different dilute suspensions of PLS; one of the diameter d = 0.345 μm with surface charge density σ = 0.33 μC/cm^2 and the other d = 0.555 μm with surface charge density σ = 5.70 μC/cm^2 .

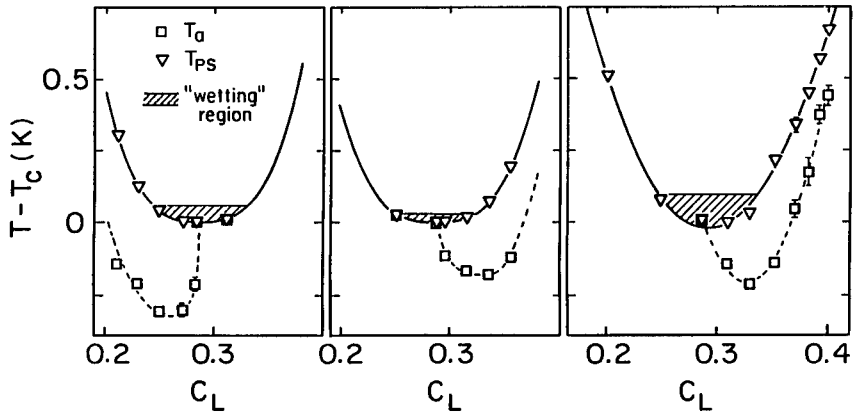


Figure 1: Measured difference of phase separation temperature, T_{ps}, and aggregation temperature, T_a , from the critical temperature, T_C, vs solvent composition, c_L. Also shown are the coexistence curve (solid line), the aggregation curve, (dashed line, drawn to guide the eye) and expected complete wetting region. Particle types are: left, d = 0.371 μm, σ = 0.38 μC/cm^2 middle, d = 0.378 μm, σ = 3.85 μC/cm^2; right, d = 0.555 μm, σ = 5.70 μC/cm^2.

Static light scattering was measured as a function of wavenumber and number density of colloidal particles at each of a variety of temperatures for each of the two solvent compositions. While identical aggregation behavior was observed over the full range of colloidal particle number density, the most reliable light scattering results were obtained for colloid particle volume fractions reported for each sample. Below these concentrations the colloidal-particle light scattering signal becomes too weak for accurate separation from the solvent-fluctuation signal, and far above this concentration multiple scattering poses a problem. Accordingly the quantitative results presented below were all obtained in the range favorable to light scattering. In addition, measurements were made at one temperature for a series of samples of varying colloidal particle density in pure water for purposes of calibration.

The colloidal particle radius was chosen large enough that it was much larger than the correlation length for solvent fluctuations throughout the range of our measurements. It was then possible to subtract the essentially flat Lorentzian background scattering from solvent fluctuations and treat the remaining scattering as pure colloidal particle scattering,

$$I_{ex}(\theta) = I_s \text{ (solution)} - I_s \text{ (solvent)} \qquad (1)$$

This colloidal scattering, $I_{ex}(\theta)$ could then be written as

$$I_{ex}(\theta) = N\, S(\theta)\, P(\theta) \tag{2}$$

where $P(\theta)$ is the form factor for scattering of a beam of intensity I_0 from an isolated colloidal particle, $S(\theta)$ is the structure factor which carries all the information about correlations among colloidal particles, and N is the number density of colloidal particles.

For spherical particles of radius R [7]

$$P(\theta) = \frac{32\pi^2 R^6 \left|m^2 - 1\right|^2}{9\lambda^4 r^2} I_0 \frac{9(\sin x - x\cos x)^2}{x^6} \tag{3}$$

with

$$x = \frac{4\pi R n}{\lambda} \sin(\theta/2) \tag{4}$$

where n is the refractive index of the solvent, m is the relative refractive index of the particles, λ is the wavelength of the light used in vacuo and I_0 is the incoming light intensity. In the present case, $m \leq 1.14$, $4\pi R/\lambda = 5.5$, and this places the present results in the range [8] where the Rayleigh-Gans-Debye approximation of Equation 3 should be correct to better than 10 %.

Figure 2 shows a Zimm plot for a typical case. In the Zimm analysis using a Guinier approximation the form factor is approximated as a straight line, but as our particles are large we have to use the full expression for the form factor given in Equation 3 which results in the fit shown in Figure 2. This fit allows us to extract the structure factor S(q) from the measured intensities $I(\theta)$ where $q = (4\pi n/\lambda)\sin(\theta/2)$ is the wavenumber of the scattering. The problem remains to extrapolate S(q) to determine S(0). In this experiment we have the advantage that we are performing our measurements at extraordinarily small values of the colloidal particle number density, such small values that reasonable estimates of the q dependence of the structure factor in the region of the first form factor maximum have their first q-dependent terms of order 10^{-5} times the constant term which represents the value of the structure factor at zero wavenumber. This approximately flat expected structure factor is quite consistent with our observations. We do not understand the origin of the simultaneous appearance of the very small q-dependence exhibited by the data and the very large N-dependence presented below. The effect is, however, very reproducible.

The scattered light intensity at $\theta = 0^0$ is only a function of the number density of the particles and the structure factor S(0), i.e.,

$$I_{ex}(0) = N\, S(0)\, K \tag{5}$$

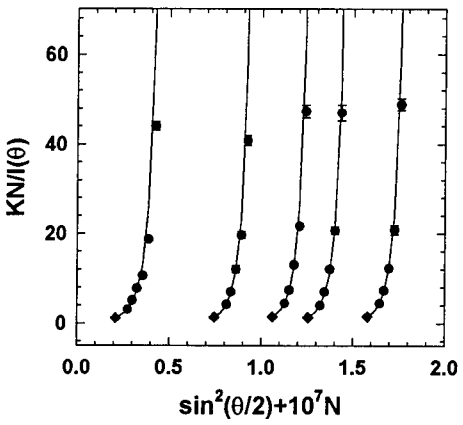


Figure 2: Measured variation K N / I(θ) of as a function of colloidal number density plus the scattering angle (Zimm plot) at $|T-T_{coex}| = 2.80$ K and $c_L = 0.35$, where K = P(0). The lines drawn through the data are fits to the full form of the form factor. The extrapolations of these fits to $\theta = 0^0$ are shown by the solid diamonds.

where K = P(0). We can also rewrite this equation in a more useful form as

$$\frac{1}{S(0)} = \frac{KN}{I_{ex}(0)} \tag{6}$$

In the dilute colloid limit where the colloidal particles might be expected to approach ideal gas behavior, the density expansion of the zero-wavenumber-limit of the structure factor can meaningfully be truncated to retain only the first term correcting the ideal gas approximation, the term containing B_2, the second virial coefficient

$$\frac{1}{S(0)} = 1 + \frac{2NB_2}{N_A} \tag{7}$$

where N_A is Avogadro's number and

$$B_2(T) = 2\pi N_A \int_0^\infty \left(1 - e^{-U(r)/kT}\right) r^2 \, dr \qquad (8)$$

where r is the distance between the particles and U(r) is the interaction potential.

Figure 3 shows measured virial coefficients for the high surface charge density PLS (σ = 5.70 $\mu C/cm^2$) on the aggregating side of the aggregation curve as a function of absolute temperature difference from the coexistence temperature for that solvent composition. In addition, a horizontal line shows the value of the measured virial coefficient for the pure water sample.

The magnitude of the virial coefficient deep in the repulsive regime is very large. If one naively modeled the particles as hard spheres, this magnitude would correspond to a hard sphere radius of R = 4.2 μm, roughly ten times the radius of the particles and comparable to the average interparticle spacing. A hard sphere model with a repulsive-core radius of two particle radii (0.6 μm) should be plausible in this case, since no reasonable estimate of the Debye screening length allows that length to be comparable to the colloidal particle size. Using the published electrolytic dissociation constant for 2,6-lutidine [9], in our earlier paper we estimated the Debye screening length to be 7-10 nm [5]. This large-apparent-radius effect has been measured by Philipse and Vrij in a different system and treated with a speculation that the spheres interact significantly over distances of several radii [10]. Similarly, Thirumalai [11] found a need to set the effective hard sphere radius of colloidal particles to the mean interparticle distance in his calculations in order to explain colloidal crystallization at observed volume fractions.

The measured virial coefficients for the same PLS on the critical trajectory (c_L = 0.287) are shown on Figure 4. We have never observed aggregation on the critical trajectory in any of our earlier measurements. However, the virial coefficients show somewhat similar behavior to that seen for the aggregating sample in Figure 3, with smaller magnitudes in the apparently attractive region (and somewhat larger uncertainties near T_C, as critical opalescence forces a larger subtraction for solvent composition fluctuations in the data analysis).

The behavior of the virial coefficient on the non-aggregating side of the coexistence curve can be seen in Figure 5. The virial coefficient shows no decrease as the temperature approaches the coexistence curve until the temperature is brought within 1K of T_C, and even near T_C the observed negative values of the virial coefficient are compatible with zero (no interaction) or even a slightly repulsive interaction, and in any case are much smaller in magnitude than in the previous two cases.

As was noted above, in our earlier measurements we observed that the low surface charge density PLS (σ = 0.33 $\mu C/cm^2$) aggregate on the lutidine-rich-side of the coexistence curve. Figure 6 shows the result of the virial coefficient measurements on the aggregating side for these low surface charge density spheres. The behavior is quite similar to the high surface charge density spheres on their aggregating side of the coexistence curve, with the attractive region confined to a narrower temperature zone but with a large magnitude virial coefficient in this zone.

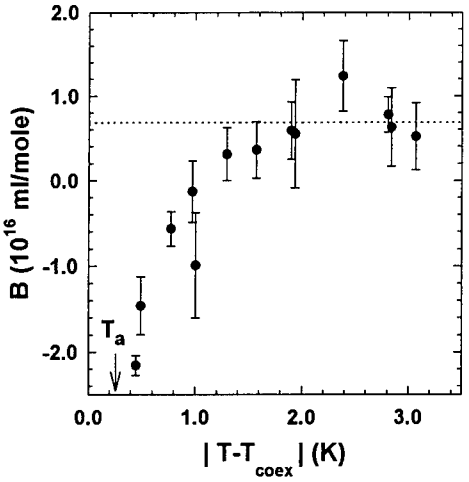


Figure 3: Temperature dependence of the measured second virial coefficient for $\sigma = 5.70\ \mu C/cm^2$ at $c_L = 0.35$. The horizontal dotted line shows the value of the measured virial coefficient for the pure-water calibration samples. The arrow indicates the temperature, T_a, at which aggregation sets in.

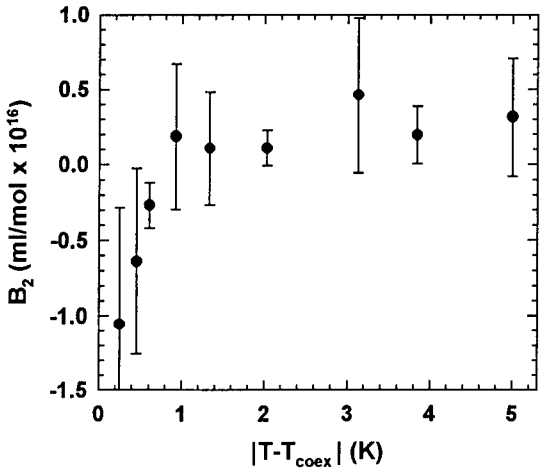


Figure 4: Temperature dependence of the measured second virial coefficient for $\sigma = 5.70\ \mu C/cm^2$ at $c_L = 0.287$ (critical).

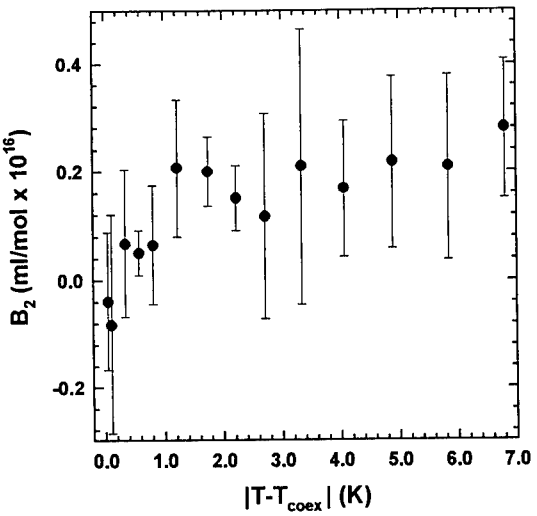


Figure 5: Temperature dependence of the measured second virial coefficient for σ = 5.70 $\mu C/cm^2$ at c_L = 0.224 .

CONCLUSIONS

We have measured second virial coefficients for very dilute colloidal dispersions of charge-stabilized polystyrene latex spheres in the one-phase region of the mixed solvent 2,6-lutidine plus water. These measurements were made as a function of temperature for PLS of two different surface charge density and various solvent compositions. The temperature ranges started deep in the one-phase region and approached the coexistence curve. Far from the coexistence curve, all of the systems showed similar behavior, the virial coefficients are large and positive, indicating significant repulsion at much longer range than would be expected from the known particle diameter and any reasonable estimate of the Debye screening length. As the temperature is brought nearer, but definitely not into, the aggregation zone, on the aggregating side of the coexistence curve and on the critical trajectory, the virial coefficient plunges through zero to large negative (attractive interaction) values, whereas on the nonaggregating side the virial coefficient remains positive until the coexistence curve is nearly reached. It is difficult to model the interactions in terms of known particle properties because the long range of the repulsive interactions is difficult to explain. Crude modeling suggests that the observed changes in the

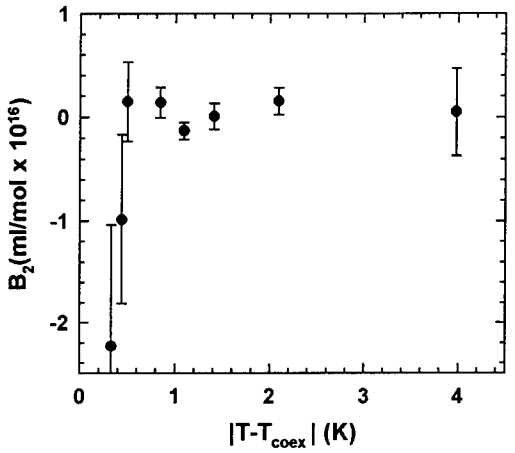


Figure 6: Temperature dependence of the measured second virial coefficient for $\sigma = 0.33$ $\mu C/cm^2$ at $c_L = 0.250$.

interactions are not inconsistent with a temperature dependent attraction arising from adsorption layer energetics operating at distances of a few solvent-fluctuation-correlation-lengths from the particle surfaces. Since all samples show at least a weakening of repulsion near the solvent coexistence curve, the confinement of the observed reversible aggregation should be understandable as arising from the magnitude of the solvent attraction effects and not from any abrupt change in kind. It is plausible that long-standing work on attractions of walls across mixed solvent [12,13] and recent work on interactions of polymer brushes with mixed solvents [14] could be adapted to shed light on these colloidal-particle interactions if the unexpected repulsive effects can be separated out of the problem.

REFERENCES

1. D. Beysens and D. Esteve, Phys. Rev. Lett. **54**, 2123 (1985).

2. V. Gurfein, F. Perrot, and D. Beysens, Phys. Rev. A **40**, 2543 (1989).

3. J. S. van Duijneveldt and D. Beysens, J. Chem. Phys. **94**, 5222 (1991).

4. P. D. Gallagher, Ph.D. thesis, University of Pittsburgh, 1991, (unpublished); P. D. Gallagher and J. V. Maher, Phys. Rev. A 46, 2012 (1992).

5. P. D. Gallagher, M. L. Kurnaz, and J. V. Maher, Phys. Rev. A **46**, 7750 (1992).

6. Interfacial Dynamics Corp., P.O. Box 279, Portland, OR 97207.

7. H. C. van de Hulst, Light Scattering by Small Particles (Dover Publications, New York, 1981).

8. M. Kerker, The scattering of light and other electromagnetic radiation (Academic Press, Inc., New York, 1969).

9. K. H. Hellwege, A. M. Hellwege, K. Schafer, and E. Lax, Eigenschaften der Materie in ihren Aggregatzustanden (Springer-Verlag, Berlin, 1960).

10. A. P. Philipse and A. Vrij, J. Chem. Phys. **88**, 6459 (1988).

11. D. Thirumalai, J. Phys. Chem **93**, 5637 (1989).

12. M. E. Fisher and P. G. de Gennes, C.R. Acad. Sci. (Paris) **B287**, 207 (1978).

13. H. Nakanishi and M. E. Fisher, Phys. Rev. Lett. **49**, 1565 (1982).

14. T. C. Tran, A. J. Liu, and P. Pincus, J. Phys. II **4**, 1417 (1994).

MICROHYDRODYNAMICS WITH DISSIPATIVE PARTICLE DYNAMICS

PEP ESPAÑOL, AND IGNACIO ZÚÑIGA
Departamento de Física Fundamental, Universidad Nacional de Educación a Distancia, Madrid, Spain

ABSTRACT

Dissipative particle dynamics is essentially a coarse-grained molecular dynamic simulation technique that captures the essential physics with considerably less computer effort. We have given a sound theoretical foundation to the technique with respect to the equilibrium and hydrodynamic properties. In this paper we further explore the connection of the model parameters of DPD with the underlying microscopic dynamics for the case of a simple model of a solid. This provides some insight into the difficulties of interpretation of DPD simulations.

INTRODUCTION

The simulation of colloidal suspensions with molecular dynamics techniques requires a large number of particles in order to capture the hydrodynamic behaviour that is essential in the dynamic of these systems. There have been several attemps to simulate hydrodynamic flows with purelly MD algorithms [3]-[6], and the results are deceptive from the computational burden point of view. For this reason, faster, more efficient algorithms have been proposed that capture the hydrodynamic collective behaviour at lower computational cost. In particular, lattice gas (LG) cellular automata [7] and lattice Boltzmann (LB) dynamics [8] have proven to be useful tools in studying complex flows.

Another technique that has been recently proposed by Hoogerbrugge and Koelman is Dissipative Particle Dynamics (DPD)[1],[2]. This technique is essentially a molecular dynamics of point particles that interact through pair-wise conservative forces *and* pair-wise Brownian dashpots. The point particles are interpreted not as molecules of a fluid but rather as clusters or "droplets" of fluid. DPD thus represents a coarse-graining of MD. One expects that this coarse graining implies that the droplets move more hydrodynamically than the molecules in an MD simulation, this is, the collective motion is better represented with the dissipative particles. A small number of particles already exhibit hydrodynamic behaviour, thus reducing the computational efford.

The main advantadge of DPD over LG or LB simulations is that it is an off-lattice technique. The lattice in LG/LB may induce spurious dynamics (due to the absence of perfect isotropy and, in LG, Galilean invariance). Although some of the problems can be eliminated with convenient lattices and rescaling of velocities, the problems show up in more severe forms when dealing with complex flows in complex boundaries as in immiscible mixtures or colloidal suspension. Also the lattice makes it difficult to deal with the forcing boundary conditions required for sheared or extensional flows.

Recently, we have provided a theoretical foundation for DPD, clarifying the role of temperature [9] and the connection between the model parameters and the speed of sound and viscosity characterizing the hydrodynamic behaviour of the system [10]. However, there is

Mat. Res. Soc. Symp. Proc. Vol. 407 © 1996 Materials Research Society

still a link missing in the relationship between the different levels of description involved. The missing link is how the DPD model parameters relate to the underlying microscopic system (MD) for which supposedly DPD is a coarse graining.

Here we present a derivation from first principles of DPD starting from the microscopic dynamics for the case of a simple model system, the 1D harmonic chain (the simplest model for a solid).

EQUILIBRIUM AND HYDRODYNAMIC PROPERTIES

The appropriate stochastic differential equations (SDE) describing DPD are [9]

$$\begin{aligned} d\mathbf{r}_i &= \frac{\mathbf{p}_i}{m_i} dt \\ d\mathbf{p}_i &= \left[\sum_{j \neq i} \mathbf{F}_{ij}^C(\mathbf{r}_{ij}) + \sum_{j \neq i} -\gamma \omega(r_{ij})(\mathbf{e}_{ij} \cdot \mathbf{v}_{ij}) \mathbf{e}_{ij} \right] dt + \sum_{j \neq i} \sigma \omega^{1/2}(r_{ij}) \mathbf{e}_{ij} dW_{ij} \end{aligned} \tag{1}$$

where $\mathbf{r}_i, \mathbf{p}_i$ are the position and momentum of particle i, m_i is its mass, $\mathbf{F}_{ij}^C$ is the conservative force between particles i, j, $\omega(r)$ is a weight function defining the range of dissipative interaction, γ is the friction coefficient, σ is the amplitude of the noise and $dW_{ij} = dW_{ji}$ are independent increments of the Wiener process.

We have shown [9] that the above equations have a well-defined equilibrium distribution given by the Gibbs ensemble $\rho(r,p) = \exp\{-\beta H(r,p)\}/Z$ where Z is the partition function, $H(r,p)$ is the Hamiltonian of the conservative part of the system (i.e. (1) with $\gamma = \sigma = 0$) and β is the inverse of the kinetic temperature defined by $3k_BT/2 \equiv \langle p^2/2m \rangle$. We have further shown that the temperature is given in terms of the model parameters by

$$k_BT = \frac{\sigma^2}{2\gamma} \tag{2}$$

which is a fluctuation-dissipation theorem. These results show that the thermodynamics of a system of dissipative particles is given by the equilibrium properties of the conservative part of the system, and that dissipation does not alter this thermodynamics.

We have also shown that in the hydrodynamic limit $\mathbf{k}, \omega \to 0$ the density and momentum fields obey the usual continuity and Navier-Stokes equations (energy is not conserved in DPD and no energy transport equation can be derived). The only parameters entering into the hydrodynamic equations are the speed of sound and the shear and bulk viscosities. The sound speed does not depend on the friction coefficient, a result that is expected because it is a thermodynamic, not a transport, quantity. On the other hand, the viscosity coefficients have two contributions that are given in terms of Green-Kubo formulas. The first contribution comes from the conservative part of the dynamics whereas the second contribution comes from the dissipative part. In the limit $\gamma = 0$ the viscosity reduces to the usual expressions for a simple liquid.

FROM MICROSCOPIC TO MESOSCOPIC DESCRIPTIONS: THE HARMONIC CHAIN

Our aim is to derive the algorithm of DPD for the simplest model of an elastic solid, the 1D harmonic chain. The simplicity of the model allows for an explicit analysis and furnishes

valuable insight into the general problem of relating the model parameters of DPD and the microscopic dynamics of the underlying system that is being modeled.

The essential idea consists on coarse-graining the original model and deducing the equations of motion for the coarse-grained variables. Within this spirit, the particles of the chain are grouped in bunches of a given size. The "mesoscopic" state of the system is now described by the position and the momentum of the center of mass of these clusters of particles.

Let us consider a set of N particles moving in one dimension and connected through Hookean springs. The equations of motion are

$$\begin{aligned} \dot{x_i} &= \frac{p_i}{m} \\ \dot{p_i} &= \kappa(x_{i+1} - 2x_i + x_{i-1}) \end{aligned} \tag{3}$$

where x_i is the deviation from the equilibrium position $\overline{x}_i = ia$ of particle i (a is the lattice spacing), p_i is its momentum, κ is the elastic constant and m the mass of the particles. We assume fixed ends.

Now we group the particles in bunches of size n so that the position and the momentum of the center of mass of each bunch are taken as the set of mesoscopic variables that describe the chain in a coarse grained way, i.e.

$$\begin{aligned} X_\mu &= \frac{1}{n} \sum_{i_\mu \in \mathcal{R}_\mu}^{n} x_{i_\mu} \\ P_\mu &= \sum_{i_\mu \in \mathcal{R}_\mu}^{n} p_{i_\mu} \end{aligned} \tag{4}$$

where $\mathcal{R}_\mu$ is the list of indices of particles that constitute the μ-th group. By using a standard technique of projection operators we deduce the equations of motion for the mesoscopic variables which are

$$\begin{aligned} dX_\mu(t) &= \frac{P_\mu(t)}{m} dt \\ dP_\mu(t) &= -\left[\frac{\kappa}{n} A_{\mu\nu} X_\nu(t) + \frac{\gamma}{nm} A_{\mu\nu} P_\nu(t)\right] dt \\ &+ (k_B T \gamma)^{1/2} [dW_{\mu+1\mu}(t) - dW_{\mu\mu-1}(t)] \end{aligned} \tag{5}$$

where $dW_{\mu\nu} = dW_{\nu\mu}$ are independent increments of the Wiener process which satisfy

$$dW_{\mu\nu}(t) dW_{\mu'\nu'}(t) = (\delta_{\mu\mu'}\delta_{\nu\nu'} + \delta_{\mu\nu'}\delta_{\nu\mu'}) dt \tag{6}$$

The friction coefficient γ is defined in terms of a Green-Kubo formula, i.e.

$$\gamma = \frac{1}{k_B T} \int_0^\infty du \gamma(u) = \frac{1}{k_B T} \int_0^\infty du \langle \delta r_\mu \delta r_\mu(u) \rangle \tag{7}$$

where the projected microscopic spring length has been introduced

$$\delta r_\mu = r_\mu - (r_\mu, X_\sigma) A_{\sigma\nu} X_\nu. \tag{8}$$

Sumarizing, starting from a microscopic description of an harmonic chain in terms of the positions and momenta of the atoms of the chain we have deduced the equations of motion for a coarse-grained chain constructed from the original one by grouping the atoms in clusters of definite size n. The chain is assumed to be in a statistical state near equilibrium. In the limit of very long chains and for large groupings of particles, the clusters interact elastically and dissipatively, with a friction force that depends on the relative velocity of neighbouring particles. Moreover, the clusters are subject to thermal random delta-correlated forces that take into account the eliminated degrees of freedom and which depend on the temperature of the equilibrium state. The structure of the equations of the renormalized chain is thus identical to that of Dissipative Particle Dynamics as applied to fluid systems. More precisely, the particularization of the equations of DPD as given in Ref. [9] to the harmonic chain produce exactly the equations (5). Therefore, we have derived for this particular system the equations of DPD from first principles.

The elastic constant and the friction coefficient of the coarse-grained chain are defined in terms of microscopic variables. Worthnoting is the fact that they are inversely proportional to the size of the clusters. This corresponds to the intuitive idea that the time scales of the coarse grained variables grow as the size of the cluster and it is consistent with the Markovian approximation taken in the deduction of the equations.

CONCLUSIONS

DPD is a promising technique for simulating complex collective hydrodynamic behaviour as that appearing in colloidal suspensions. It is a well-sounded technique as far as its equilibrium and hydrodynamic transport properties is concerned. In order to better understand the physical meaning of the model parameters appearing in DPD, we have derived from first principles the algorithm of DPD for a simple model of an elastic solid. A coarse-graining length is introduced and explicit expressions for the conservative and dissipative parameters of DPD are derived, which depend strongly on this length.

A similar analysis for fluid systems appears to be more elusive. For example, one would like to know the expressions for the conservative force $\mathbf{F}^c$, the weighting function $\omega(r)$ and the value of γ in terms of the microscopic conservative potentials, i.e. a Lennard-Jones potential. Nevertheless, one can propose intuitive expressions for the conservative and dissipative forces. But then one does not have a clear idea about the time and length scales DPD is addressing.

A related point worth investigation is how much better is DPD versus MD regarding the simulation of hydrodynamics. There have been so far no systematic investigations of the effect of the different model parameters and its improvement on the production of a collective hydrodynamic behaviour.

ACKNOWLEDGEMENTS

Partial financial support from project DGICYT No PB94-382 is acknowledged.

References

[1] P.J. Hoogerbrugge and J.M.V.A. Koelman *Europhys. Lett.*, **19** 155 (1992).

[2] J.M.V.A. Koelman and P.J. Hoogerbrugge, *Europhys. Lett.*, **21** 363 (1993).

[3] D.C. Rapaport and E. Clementi, *Phys. Rev. Lett.*, **57** 695 (1986).

[4] M. Mareschal, M.M. Mansour, A. Puhl and E. Kestemont, *Phys. Rev. Lett.* **61** 2550 (1988).

[5] D.C. Rapaport, *Phys. Rev. Lett.*, **60** 2480 (1988).

[6] I. Zúñiga and P. Español, *Phys. Rev. Lett.*, **71** 3665 (1993).

[7] U. Frisch, B. Hasslacher, and Y. Pomeau, *Phys. Rev. Lett.*, **56** 1505 (1986).

[8] A.J.C. Ladd, J. Fluid Mech., **271** 285, 311 (1994).

[9] P. Español and P. Warren Europhysics Letters, **30**, 191 (1995).

[10] P. Español Physical Review E, **52**, 1734 (1995).

EVOLUTION OF THE STRUCTURE FACTOR IN GELLING DENSE COLLOIDAL SILICA[1]

C.D. MUZNY, B.D. BUTLER, and H.J.M. HANLEY
Thermophysics Division, National Institute of Standards and Technology, Boulder, CO 80303

ABSTRACT

A solution of 30 % by mass, 7 nm diameter, colloidal silica spheres has been studied during gelation using small angle neutron scattering (SANS). A peak in the static structure factor appears early at a wavevector $q \approx 0.1\,\mathrm{nm}^{-1}$, and then grows in height and shifts to lower wavevectors as gelation proceeds. This is consistent with a cluster growth model in which this low-q peak in the structure factor indicates the presence of correlations between growing clusters. The peak continues to grow after the solution has visibly gelled indicating that the gel coarsens even after a stiff solid-like network has formed. The clear presence of cluster correlations at length scales only one order of magnitude larger than the particle size means that the usual fractal slope analyses are invalid in this system. We interpret the results by comparing the measured time evolution of the structure factor with computer simulations of Lennard-Jones particles quenched far below the critical line.

INTRODUCTION

In a series of recent papers [1-3] we have pointed out that the fractal analysis normally applied to understand the scattering from dilute gels is unlikely to be appropriate when one examines the behavior of a dense gel. It is well known from small angle x-ray [4], neutron [5], and light scattering[6] studies that low density gels can show a power law increase in intensity with decreasing wave vector q. Here, $q = (4\pi/\lambda)\sin(\theta/2)$, λ is the incident wavelength, and θ is the scattering angle. For such low density gels formed of fractal aggregates, it is easily shown that the structure factor $S(q)$ varies as

$$S(q) \sim q^{-d_f} \quad , \tag{1}$$

where d_f is a fractal dimension. Equation (1), however, is valid, and the fractal dimension has meaning, only when the length scales probed are much larger than the size σ of the individual particles but smaller than the characteristic size ξ of the fractal aggregate. Thus,

$$\frac{2\pi}{\xi} << q << \frac{2\pi}{\sigma} \, . \tag{2}$$

Although the simple dilute gel fractal aggregate approach may be invalid for dense gels, we have suggested [2] that a fractal dimension of a dense system can still be obtained by studying the time evolution of the gelation process. In this short paper we present the first experimental data to test our hypothesis.

EXPERIMENTAL

Small angle neutron scattering measurements were made on the NIST 30 m SANS instrument designated NG3 at the NIST Cold Neutron Research Facility. The incident neutron

[1] Work of NIST, not subject to copyright in the USA.

Mat. Res. Soc. Symp. Proc. Vol. 407 © 1996 Materials Research Society

wavelength was set to 0.5 nm with a bandwidth measured at FWHM of 15%. The sample-to-detector distance was set at 13.15 m and the source location relative to the sample, adjustable by the placement of neutron guide tubes, was set at 14.77 m. Scattered neutrons were detected using a 2D position sensitive detector. Because all measured scattering patterns were isotropic, the measured counts were azimuthally averaged to place the data on simple wavevector vs. intensity plots. These data were converted to absolute scattering units by comparing, under identical experimental conditions, the measured intensities with that from H_2O, which has a total neutron scattering cross section of 0.85 ± 0.03 cm^{-1}.

The sample contained 7 nm colloidal silica spheres in H_2O at a mass fraction of 30%, initially as a suspension at a pH of 9.8. Gelation was initiated by adding a sufficient amount of concentrated HCl to the stock solution to reduce its pH to approximately 6.3. This solution was quickly loaded into a quartz cell (1 mm path length) and placed in the neutron beam. Measurements were taken as soon after initiation as possible — approximately 5 min. The scattering intensity was then followed as a function of time by making, in succession, measurements for periods of 1, 2, 4, 8, 16, and 32 min. Further 30 min duration measurements were made at 2 h, 24 h, and 40 h after the reaction had begun. The behavior of a sample of the solution used for the scattering experiments showed that a gel network, strong enough to support its own weight, had formed after approximately 20 min.

RESULTS

Figure 1 shows a plot of the scattered intensity of the suspension (t = 00:00) and plots of the gel as a function of time after initiation. The low scattering power of the suspension indicates that it is relatively homogeneous over length scales of approximately 30–160 nm. The rise in intensity near $q = 0.4$ nm^{-1} reflects an average (charged) colloidal particle separation distance of about 16 nm. At very early times after gel initiation, this particle-particle separation peak disappears, and there is a sudden marked increase in scattering at low q. The disappearance of the particle-particle separation peak is expected because the addition of HCl increases the screening of the charged colloidal spheres, which decreases their effective interaction diameter and thus the effective volume fraction of the particles. Hence, the particle-particle interaction peak will shift to higher q and decrease substantially in intensity.

The sudden rise in scattering power after gel initiation at low q indicates the onset of clustering. This creates inhomogeneities at length scales of several particle diameters and thus a sharp rise in intensity at wavevectors corresponding to these length scales. As time progresses the low-q scattering continues to increase indicating coarsening of the clusters. At later times a peak in this low angle scattering (at approximately $q = 0.08$ nm^{-1}) can be easily identified. This peak clearly indicates the presence of the cluster-cluster correlations and its location can be used as a rough measure of the cluster-cluster correlation distance; ~ 80 nm. It is interesting to note that this peak continues to grow long after the 20 min it takes to visibly gel.

Figure 2 displays the measured scattering intensity for the suspension (pre-initiation) and the gel measured 40 h after initiation at three separate detector positions giving a wider range of wavevector coverage. For the gelled sample we sees a peak at low q. Two "linear" regimes on this log scale at intermediate q indicate power-law-like behavior. The intensity falls off very rapidly at the highest wavevectors, but there is an indication of a small peak at $q \approx 1.0$ nm^{-1}, which corresponds to direct contact between the 7 nm colloidal particles. For reference, the theoretical form factor for 7 nm spheres is also plotted in Fig. 2. Since the measured scattering will be a product of this form factor and the structure function (appropriately convolved with the instrument function), the origin of the sudden change in slope of the measured intensity at

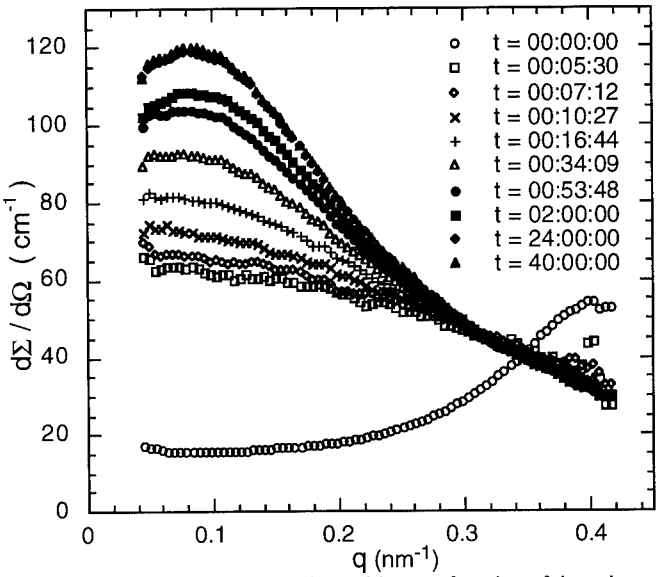


Figure 1: Measured neutron scattering intensities as a function of time since gel initiation for a 30 wt. %, 7 nm solution of colloidal silica. Note that a peak forms at intermediate times.

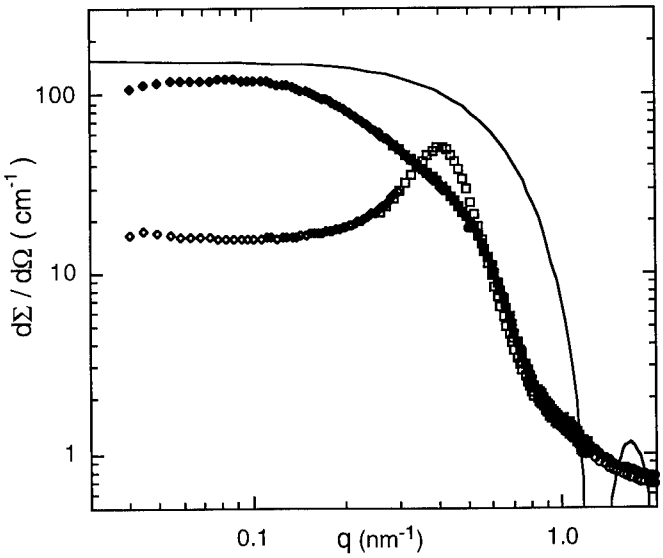


Figure 2: Measured neutron scattering intensities from 30 wt. %, 7 nm colloidal silica spheres both in suspension and several hours after gel formation. The peak in the suspension data corresponds to an average particle separation distance of approximately 16 nm. The large wavevector range was obtained by combining data from 3 detector positions. The 7 nm form factor is included for reference.

$q = 0.5$ nm^{-1} is clear. It results from the behavior of the form factor but otherwise has no special structural significance. Figure 2 also shows the charged colloidal suspension particle-particle separation peak, which is now more completely defined by using three separate detector positions.

DISCUSSION

Power-law growth in $S(q)$, such as that seen in the intermediate q range of Fig. 2, is normally interpreted as a signature of fractal aggregation. It would thus be natural to apply Eq. (1) to these data and derive a fractal dimension from the slope of the measured structure factors. This interpretation, however, is incorrect in the present situation because the inequality (2) is clearly not satisfied in this experimental system: the length scale associated with the cluster size (about 80 nm using the cluster-cluster correlation peak as a measure) is only a factor of 10 larger than the particle diameter. To define a fractal aggregate over a range in size from only 2 particle diameters to 5 diameters (where the logarithmic plot is linear) would stretch the definition of a fractal object. Furthermore, derivation of the scattering equation (1) neglects the effect of cluster-cluster correlations. Therefore, (1) may be used only under the condition that the cluster-cluster correlation distance is much larger than the fractal length scale – a condition that is obviously not satisfied in these experiments, which show a distinct correlation peak near this linear regime.

COMPUTER SIMULATION

We believe that, in contrast to the simulation methods that model gelation as a process in which a single large aggregate is grown, the gelation of dense colloidal systems is more appropriately understood in terms of nucleation and growth and/or spinodal decomposition. In such models, a system of particles at the appropriate density is quenched from a high temperature state into a metastable or unstable region of the phase diagram. The particles will immediately begin to form clusters; as time progresses, these clusters will coarsen.

In Fig. 3 we show the results from such a simulation using molecular dynamics methods. The simulation studies the evolution of a 14 336 particle, 2D Lennard-Jones system, when quenched from a liquid state at reduced temperature $T = 1.0$ to $T = 0.2$. The triple point for this system is approximately $T_{tp} \approx 0.41$. The system was allowed to evolve at a reduced density $\rho = 0.325$ for a total reduced time of $t = 1000$, with an integration time step $\Delta t = 0.004$, and at a constant temperature maintained by a Gaussian isokinetic thermostat [7]. Figure 3 shows four snapshots taken at post-quench times t = 8, 40, 200, and 1000. At t = 8, the system, which was in an initial, disordered state at $T = 1.0$ before the quench, has formed two distinct phases – a solid (black regions formed of dense particle clusters) and an extremely dilute gas (white regions essentially devoid of particles). The microstructure is characterized by finely dispersed clusters of particles that form thick filaments and is reminiscent of the structures observed in simulations of spinodal decomposition in liquids [8,9] and solids [10].

Figure 4 shows the corresponding computations of $S(q,t)$. A peak in $S(q)$ at low angles results from correlations in the positions of neighboring clusters, and its location provides a rough measure of the average cluster-cluster separation at a given time. As the simulation evolves, this peak moves to lower q and grows in height. The shift to lower q indicates increasing cluster-cluster separation; the height is related both to the degree of correlation between clusters and to the number of particles contained in an average cluster. This behavior mimics, at least qualitatively, the experimental results presented in Fig. 1.

In a previous paper [2], we have shown that the evolution of $S(q)$ in this quenched Lennard-Jones system obeys a dynamic scaling relation from which a characteristic fractal

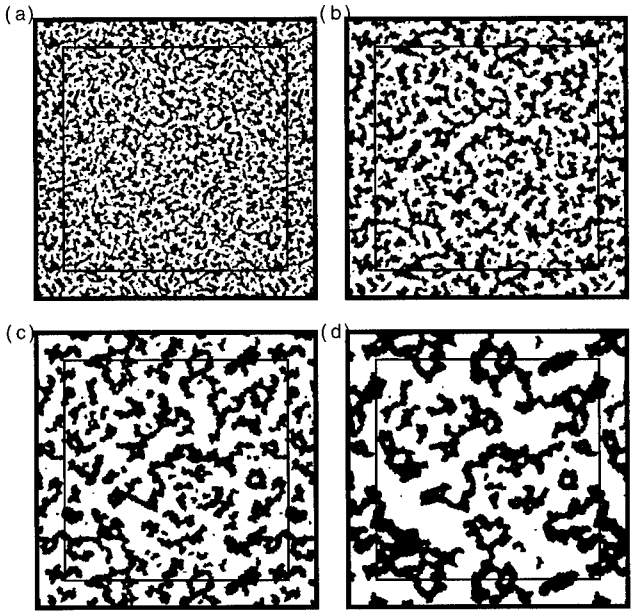


Figure 3: Molecular dynamics simulation of a 2D, 14 336 particle, Lennard-Jones system quenched from above the critical temperature (T = 1.0) into the vapor/solid coexistence region (T = 0.2) at a reduced density ρ = 0.325. Each figure is a snap-shot after the quench at reduced times (a) t = 8, (b) t = 40, (c) t = 200, (d) t = 1000. From Butler et al., *Phys. Rev. Lett.*, **74**, 4468 (1995).

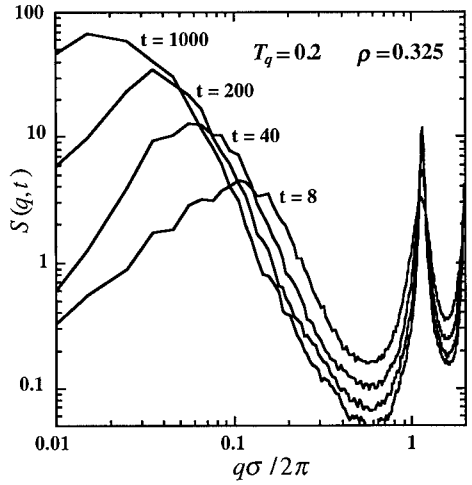


Figure 4: The structure factor *S(q,t)* computed from each of the four simulation snap-shots presented in Fig. 3. Note that as the simulation evolves the peak maximum at low *q* increases in height and moves toward smaller *q*. From Butler et al., *Phys. Rev. Lett.*, **74**, 4468 (1995).

dimension of the decomposing fluid can be derived *regardless of the density yet still in the presence of cluster-cluster correlations.* Simulations like this may thus provide valuable insight into the interpretation of experiments designed to probe the gel mechanism.

CONCLUSION

Measurements of the small angle neutron scattering from a 30 % by mass silica gel made from 7 nm diameter colloidal particles confirm the existence of a peak in the scattering at low q which indicates the presence of cluster-cluster correlations. At values of the wave vector that fall between this peak and the high-q regime (defined by the colloidal particle size), we find that the scattering falls off in a power-law fashion. We want to stress, however, that there is only a factor of 10 difference in the size of the colloids and the cluster-cluster correlation distance. Hence, the normal fractal slope analysis is not applicable. We conclude, therefore, that the power law behavior is not attributable to fractal aggregation but instead results from the particular size and arrangement of clusters in this system.

Computer simulations of quenched systems reproduce qualitatively the observed scattering features from a dense gel and may lead to a better understanding of the experimental scattering data and thus the gelation mechanism.

ACKNOWLEDGEMENTS

This work was supported in part by a grant from the Office of Basic Energy Sciences, Division of Engineering and Geosciences, US Department of Energy. BDB was supported by a National Research Council Research Associateship.

REFERENCES

1. B.D. Butler, H.J.M. Hanley, C.D. Muzny and G.C. Straty, *Mat. Res. Soc. Symp. Proc., Neutron Scattering in Materials Science* **376**, in press (1996).
2. B.D. Butler, H.J.M. Hanley, D. Hansen, and D.J. Evans, *Phys. Rev. Lett.* **74**, 4468 (1995).
3. B.D. Butler, H.J.M. Hanley, D. Hansen, and D.J. Evans, *Phys. Rev. B* (in press).
4. D.W. Schaefer, J.E. Martin, P. Wiltzius, and D.S. Cannell, *Phys. Rev. Lett.* **52**, 2371 (1984).
5. R. Vacher, T. Woignier, J. Pelous, and E. Courtens, *Phys. Rev. B* **37**, 6500 (1988).
6. G. Dietler, C. Aubert, D.S. Cannell, and P. Wiltzius, *Phys. Rev. Lett.* **57**, 3117 (1986).
7. D.J. Evans and G.P. Morriss, *Comp. Phys. Rep.* **1**, 297 (1984).
8. S.W. Koch, R.C. Desai, and F.F. Abraham, *Phys. Rev. A* **27**, 2152 (1983).
9. M.R. Mruzik, F.F. Abraham, and G.M. Pound, *J. Chem. Phys.* **69**, 3462 (1978).
10. J.W. Cahn, *J. Chem. Phys.* **42**, 93 (1964).

FORMATION OF COLLOIDAL COPPER HYDROXIDES AND OXIDES BIOPOLYMERIC INTERFACES

U. HINZE, M. THIES, H.H. PARADIES*
Märkische Fachhochschule, Biotechnology & Physical Chemistry, P.O. BOX 2061, D-58690 Iserlohn, Germany

ABSTRACT
Light sensitive colloidal particles of copper hydrous oxides were prepared at interfaces of exopolymeric materials. Dislike copper oxide or hydroxide nanoclusters were obtained which might be useful as p-type semiconductors. The colloidal $Cu_2O \cdot xH_2O$ and $Cu(OH)_2$ particles reveal fractal dimensions of $D = 2.15 \pm 0.05$ for $Cu(OH)_2$ and $D = 1.75 \pm 0.07$ for $Cu_2O \cdot xH_2O$.

INDRODUCTION

Colloidal hydrous copper oxides and hydroxides were prepared at the interfaces between Cu^{2+} ions at pH 7.2-7.5 (20°C) and exopolymeric materials (EPM), e.g. alginate, xanthan and depyruvoylated xanthan or glycolipids A&B without resorting strong basic solutions or the presence of reducing agents, e.g. hydrazine, high temperature (>100°C), or unpolar solvents or microemulsions [1,2]. Furthermore, the anionic EPM reveal at neutral pH and 20°C very low surface tensions of the order of 1-7 mN/m adhere strongly to thin Cu-metal surfaces which accelerates the deterioration of metallic Cu in the presence of O_2 by forming colloidal hydrous copper oxides [3,4].

The recently observed deterioration of Cu-surfaces by microorganisms enables us to report here on the fractal geometry of Cu-II- and Cu-I- hydrous sols of "$Cu(OH)_2$" and "$Cu_2O \cdot xH_2O$" mediated by exopolymers (EPM), mainly xanthan. The procedure offers an unprecedented aspect of the preparation of nanostructural Cu oxide particles, e.g. Cu_2O and CuO nanoparticles without using severe sample preparations, e.g. in the present of strong reduction agents [4]. We describe here to the best of our knowledge for the first time the nature of self-aggregation of Cu-hydrous oxides sols in vitro and in vivo, by monitoring the growing Cu-hydrous oxides evolution in situ in real time applying light-(LS), small-angle (SAXS)-X-ray scattering and electron-microscopic methods.

EXPERIMENTAL

The "$Cu(OH)_2$" monomers were prepared by contacting a 1 mM $CuSO_4$ solution with 1 mM NaOH at pH 7.8 (7.5 - 8.0), T = 293 K in the presence of 0.1 % (w/w) xanthan (MW $\cong 2.5 \times 10^6$ Da) for 1 hour (in vitro). This preparation was compared with Cu-metal (100 µm thick) exposed to fermentation conditions in the presence of Xanthomonas campestris among other microorganisms relevant in the environment over 8 weeks (in vivo) [3]. This fermentation procedure speeds up biologically the deterioration of Cu-surfaces. In another experiment the Cu-metal (50 - 100 µm thick) was exposed to the broth containing EPM only and aerated. SAXS-data were obtained as outlined in [7]. Since scattering experiments measure S(k) as the Fourier transform of $\rho_2(r)$, which is the two point density-density correlation function, an equivalent power law correlation to S(k) exists decaying as:

(1) $$I_{obs}(k) = S(k) \sim k^{-D}$$

Mat. Res. Soc. Symp. Proc. Vol. 407 © 1996 Materials Research Society

over the range $R_g^{-1} < k < a_p^{-1}$, with a_p the radius of the primary particle, R_g the radius of gyration of the cluster, and $k = 4\pi/\lambda \sin \theta/2$ the wave vector. Equation (1) does not obey outside the power law regime which is not of concern here. The exponent D is called the fractal dimension and describes the structure of the aggregates. LS-experiments were carried out as described previously [8], with the aim that S(k) could be measured between $0.00001 \leq k < 0.0002$ nm^{-1}, resulting in cluster sizes up to 500 - 800 nm.- The oxidation states of Cu were determined by XPS measurements and carried out with a Vacuum Generator Ltd. ESCA 3 MK II spectrometer using monochromatized AlK_α excitation. The take off angle of the signal was 70°. The binding energy scale of the instrument was calibrated using the Au $4f_{5/2}$ line of pure gold (84.0 eV).

RESULTS AND DISCUSSION

The electrolyte induced aggregation of charge-stabilized metal or metal-like colloids into fractal clusters has received a great deal of attention over the past years using LS, SAXS or neutron scattering experiments [9]., but not in the presence of polyelectrolytes. It is therefore particular noteworthy that we were able to study the time dependent clustering for "$Cu(OH)_2$" (a_p = 2.1 nm) and "Cu_2O x H_2O" (a_p = 2.8 nm) for $R_g < 10^4$ nm due to the presence of anionic polyelectrolyte, e.g. xanthan and derivates thereof. In this regime we observed a power-law behavior between $0.00001 < k < 0.01$ nm^{-1} showing fractal nature of the colloidal copper aggregates, with $I_{obs} \sim k^{-D}$ with $k < \langle R_g^2 \rangle^{1/2} > 0.1$. However, k is independent for $k < \langle R_g^2 \rangle^{1/2} \gg 0.1$. The values for D, which is universal in its value and independent of the detailed nature of the particles and reflects only the mode of aggregation [10], obtained are 2.15 ± 0.05 for the colloidal hydrous Cu-II-oxide, "$Cu(OH)_2$", which does not agree with a diffusion limited aggregation (DLA) nor a cluster-cluster aggregation (CA) model. However, the hydrous copper-I-oxide, $Cu_2O{\cdot}xH_2O$ for comparison reveals a D-value of 1.75 ± 0.07 close to the one of CA. Surprisingly, both in vitro and in vivo preparations yielded the same clustered Cu-materials having the Cu oxidation states one and two as assessed by XPS. These suspensions are stable, and the small clusters have a nominal radius of gyration of R_g = 2.1 nm. Reducing the pH to 6.5, adding xanthan to a final concentration of 0.9% ($^w/_w$) and raising the salt concentration to 5 mM NaCl, the monomers apparently aggregate in a time dependent manner. The addition of salt reduces the substantial negative charges on the particles by decreasing the Debye-Hückel screening length to a certain point where the "$Cu(OH)_2$" particles approach each other sufficiently close in order to permit van der Waals bonding.



Fig. 1 Transmission electron micrograph of $Cu_2O{\cdot}xH_2O$ grown in the presence of 0.9 % ($^w/_w$) xanthan . the bar equal 500 nm.

Fig. 1, e.g. shows an electron micrographs of and "$Cu_2O \cdot xH_2O$" clusters revealing the branching structures of the clusters. Accordingly, the "$Cu(OH)_2$"- clusters can grow to plate hexagonal particles approximately 0.5μm across, and sediment under gravity. However, treating solutions of 1 mM $CuSO_4$ with 0.1 mM NaOH, pH 7.5, (293 K), in the presence of unpyruvoylated xanthan in which the acidic pyruvoyl groups were removed by heating in 0.1M TRIS-HCl in the presence of 1 x 10^{-3}M oxalic acid at 366 K (2 h), yielded light orange solutions at concentrations of 0.5-0.6 % (w/w) EPM material. This suspension has a nominal radius of gyration of a_p = 2,9 nm, is stable and commenced to aggregate upon addition of 20 mM NaCl, pH 6.5, or by increasing the unpyruvoylated xanthan concentration to 1.0 %(w/w) [11]. The presence of the unpyruvoylated xanthan alters the form of the cluster yielding oval particles (0.25 μm). The inorganic-organic in situ synthesis of the "$Cu(OH)_2$" or "$Cu_2O \cdot xH_2O$" composites displays controlled inorganic crystal size and morphology, which are the determining features of the matrix-mediated biocomposites. However, we did not observed "$Cu_2O \cdot xH_2O$" particles in vivo. Both preparations were studied with static LS and SAXS techniques at concentrations of Cu^{2+} of 0.2 wt % and 0.5 wt % in the presence of 0.5M NaCl, and Cu^{1+} of 0.1 wt % at 1.0M NaCl, and 0.5 wt % at 1.0M NaCl, respectively (293 K). S(k) measurements using LS and SAXS were in the range of $0.00002 \leq k \leq 0.01$ nm^{-1} (Fig. 2A & B). SAXS data revealing the size of the primary particles of "$Cu(OH)_2$" sols, obtained from the slope of the scattered intensity plot at very large k-values ($a_p \cong 2,1$ nm) obeying Porod's law [12]. The fact that fractal behavior is observed up to the crossover and the limiting slope of - 4 indicates that the "$Cu(OH)_2$" or the "$Cu_2O \cdot xH_2O$"-monomers remain intact in the aggregate and the "width" of the arms of the cluster is close to the diameter of the monomers. However, on longer length scales the data indicate the formation of fractal aggregation with $D = 2.15 \pm 0.05$ (Fig. 2 A).

Fig. 2A **Fig. 2B**

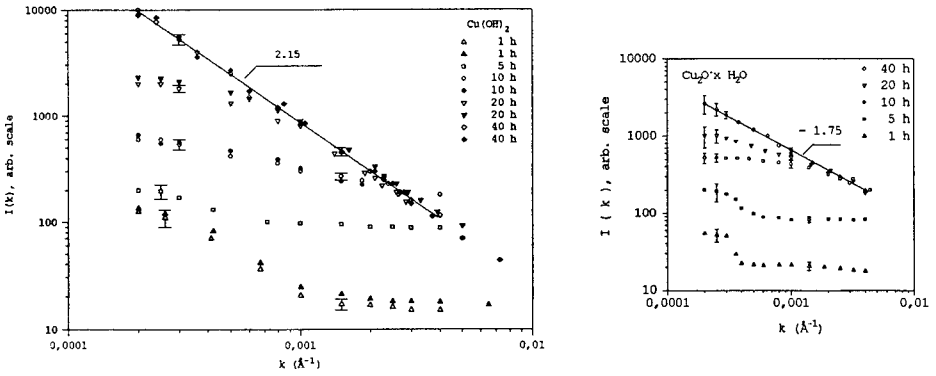


Fig. 2 Scattered light intensity profiles of "$Cu(OH)_2$" clusters as aggregation proceeds. Filled symbols correspond to in vivo, hollow symbols to in vitro experiments, respectively. (B) The same as (A) but for "$Cu_2O \cdot xH_2O$" and in vitro experiments.

The radius of gyration of these aggregates is calculated to 140 ± 25 nm. Similar values were found from in vivo experiments. The corresponding values for "$Cu_2O \cdot xH_2O$" are a_p = 2,8 nm, $\langle R_g \rangle$ of the

aggregates 190 ± 30 nm, and D = 1.75 ± 0.07. After 20 hours, $<R_g>$ of these clusters for both preparations grew beyond this limit. Fig. 2 shows the temporal development of the scattered light intensity I(k) for both preparations. The error bars in Fig. 2 decreases as the aggregation proceeds. The maximum intensity at $k < 0.00003$ nm^{-1} increases almost two decades until 40 h after initation. With respect to Fig. 2, the power law dependence of I(k), still remains after 40 h but a decrease in amplitude is observed due to sedimentation of larger aggregates. Without knowledge of the sticking probability for collision and precise information of the initial concentration of the monomers, we can infer from the D-values possible aggregation mechanisms among a large number of growth mechanisms. Furthermore, polydispersity has not seriously effected our results for D sizes, since aggregation proceeded over a large period of time, and more and more material from the minor fraction of the particle size distribution has been incorporated into the copper-cluster until they grow to a size where they sediment.

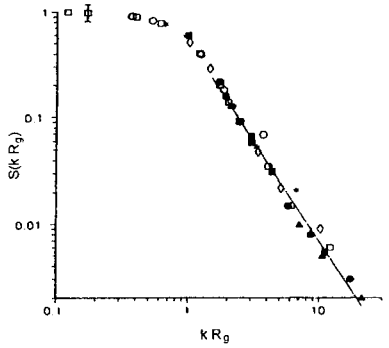


Fig. 3 Structure factor $S(kR_g)$ vs R_g for the $Cu_2O \cdot xH_2O$ clusters of different sizes masses:

⊙, 200
*, 100
◊, 150
□, 250
●, 400
▲, 800
■, 1,000

Fig. 3 is consistent with calculated values of $S(k R_g)$ for $Cu_2O \cdot xH_2O$ clusters of sizes between 20 to 1,000 particles. At present each symbol represents an assemble average of 10 different $Cu_2O \cdot xH_2O$ aggregates depending on the content of H_2O. The standard deviation is approximately the same for all data. As it is expected for fractals, at high values of h R_g the data for the structure factor from simulations satisfy the power law dependence, yielding a fractal dimension of 1.75 ± 0.10 from a least squares fit. This value is close to the values for a lattice model (= 1.75 - 1.85). However, simulations using random-walk trajectories at a density of 0.01, an effective dimensionality of D = 1.80 ± 0.07 was obtained from the density-density correlation function. The radius of gyration exponent obtained for the clusters in the size range $10<N<1{,}000$ particles per cluster was 0.575 ± 0.015 with D = 1.75 ± 0.06. These results suggest that the fractal dimensionality is slightly lower for the random-walk trajectories than for the linear trajectories. The effect is small but we cannot rule out the possibility that both random walk and linear trajectories may yield the same fractal dimensionality on the basis of these results obtained [10]. The fractal dimensions of 2.15 as found for "$Cu(OH)_2$" is not consistent for a DLA (D = 2.5) or a CA (D = 1.75) model, almost close to the one of equilibrium structures, e.g. lattice animals (LA) for which D = 2.0 [13]. The structure of "$Cu(OH)_2$" appears to be a balance of entropic effects favoring branched random - walk structures, and excluded volume forces which favor cluster expansion.

CONCLUSION

For the first time it can be shown that the microbial destruction of metallic and oxidized Cu-surfaces in the presence of exopolymers yielded defined hydrous Cu-particles dependent on the structure of EPM, solution surface tension, pH, and for in-vitro conditions the environmental consortia of

microorganisms. EPM's may be suitable for preparations of other colloidal or metal-like nanoparticles without using harsh agents or unpolar solvents.

Acknowledgment : This work was supported by a grant from Euram-Brite, Project No. BE-4088, the International Copper Research Organization (New York), and the Bundesministerium für Technologie und Forschung (Bonn, FRG)(FE-KKS #5.1/13).

REFERENCES:

[1] A. Henglein, J. Phys. Chem., 97, 5457, (1993); R. Seshardri; G.N. Subbanna; V. Vijayakrishnan; G.U. Kulkarni; G. Ananthakrishna; C.N.R. Rao, J. Phys. Chem., 99, 5639, (1995); see also: Faraday Discuss. Chem. Soc., 92, (1991)

[2] R. Kubo, A. Kawabata, S. Kobayashi, Rev. Mater. Sci., 14, 49, (1984); W.P. Halperin, Rev. Mod. Phys., 58, 533, (1986) [3]H. Siedlarek, D. Wagner, W.R. Fischer, H.H. Paradies, Corrosion Science, 36(10), 1751, (1994); H.H. Paradies, I. Haensel, D. Wagner, W.R. Fischer, in 2nd "Microbial Induced Corrosion", Eds, C. Sequeira & K. Tiller, 168-188, Materials Research Institute, London, U.K., (1992);

[4] I. Lisiecki, M.P. Pileni, J. Amer. Chem. Soc., 115, 3887 (1993)

[5] H.H. Paradies, Physico-chemical Aspects of Metal Biofilms, in "The Biology of World Resources", Vol. II, Cambridge University Press, Cambridge, U.K., pp. 197-269 (1995)

[6] C.A.C. Sequeira, Brit. Corr. Jour., 30, 137 (1995)

[7] H.H. Paradies, J. Phys. Chem., 84, 599, (1980); H.H. Paradies, Colloids & Surfaces, 74, 57, (1993);

[8] S.F. Clancy, D.A. Tanner, P.H. Steiger, M. Thies, H.H. Paradies, J. Phys. Chem., 98, 11143, (1994);

[9] D.A. Weitz, M.Y. Lin, J.S. Huang, T.A. Witten, S.K. Sinha, J.S. Genthner, R.C. Ball, "Scaling Phenomena in Disordered Systems", ed. R. Pynn & A. Skjeltorp, NATO ASI series, Plenum Press, N.Y. (1985)

[10] N.Y. Lin, H.M. Lindsay,D.A. Weitz, R.C. Ball, R. Klein, P. Meaken, Nature, 339, 360, (1989); M.F., Shlesinger, G.M. Zaslavsky, J. Klafter, Nature, 363, 31, (1993)[5]; M. Kolb, R.Botet, R. Jullien, Phys. Rev. Lett., 51, 1123, (1983); T.A. Witten, L.M. Sander, Phys. Rev. Lett., 47, 1400, (1981); & Phys. Rev. B27, 5686, (1982); P. Meakin, Phys. Rev. Lett., 51, 1119, (1983);

[11] M. Thies, U. Hinze, H.H. Paradies, Physical Behaviour of Biopolymer Artificial Models for Biofilms in Biodeterioration of Copper; in "Microbial Corrosion III", eds. C. Sequeira & K. Tiller, Materials Research Institute, London, U.K., 17-48, (1995);

[12] O. Porod, Kolloid.-Z., 125, 51, (1952);

[13] H.E. Stanley, P.J. Reynolds, S. Redner, F. Family, in "Real Space Renormalization", eds. T.W. Burkhardt, J.M.J. van Leuven, Springer Verlag, Heidelberg, (1982).

CRITICAL BEHAVIOR IN THE ULTRASONIC PROPERTIES OF SUSPENSIONS

R. ESQUIVEL-SIRVENT* and D. H. GREEN**
CMSS Program, Ohio University, Athens Ohio 45701, * Department of Physics and Astronomy, **Department of Geological Sciences.

ABSTRACT

Velocity and attenuation measurements of compressional waves at 3 and 5 MHz are presented for suspensions made of $1\mu m$ size particles of kaolinite or glass beads in water or light oil. At a critical concentration of 40%, the attenuation shows a sharp peak in attenuation as well as a sudden change in velocity. This behavior is observed in all suspensions and is independent of frequency or particle geometry. The observed behavior is consistent with the excess attenuation induced by the fluid-shearing between particles. This behavior is the first experimental evidence for the existance of the freezing point, predicted by computer simulations.

INTRODUCTION

A large body of work has appeared in recent years regarding the transition of multiphase systems from disordered to ordered states[1, 2]. Many of these studies, such as those using fluid crystals, have examined the associated changes in optical properties as a way of investigating this transition [3]. In simple two-phase systems, such as suspensions or porous media, contrasts in the mechanical properties of the two component phases can be responsible for large concentration-dependent changes in the mechanical behavior of the aggregate material [4] even when optical-property contrasts are slight. Nearly all previous reports of the acousto-mechanical properties of the fluid/solid transition have been limited to either poorly-consolidated porous solids [5, 6, 7] or dilute suspensions [8].

Optical experiments of particle ordering in suspensions have shown that as the particle concentration increases, the system goes from a fluidi state, to a phase in which fluid and solid behavior may coexist, and finally to fully rigid stucture capable of sustaining shear stresses. For dilute suspensions, Greenwood et al. [8] demonstrated that the acoustic attenuation increases linearly with concentration, consistent with the fact that the solid particles act independently when attenuating sound at low concentrations. At solid concentrations above fluid-solid transition, experiments by Blangy et al. [7] measured shear wave propagation on loosely consolidated water-saturated sands as a function of progressively lower concentrations. Their observations indicate that in the concentration range between 55% and 65%, the rigidity of the sample vanishes and the two-phase system behaves effectively as a fluid. Based on these experimental observations it is commonly assumed that the fluid-solid transition in a two-phase system occurs near a critical concentration of 60%, at which an abrupt onset of solid behavior is expected.

In this paper we report the observation of anomalous ultrasonic absorption and velocity of compressional waves at a concentration of near 40% in high concentration suspensions. This critical concentration threshold agrees well with the freezing limit predicted by random packing models for hard spheres [9, 10].

Mat. Res. Soc. Symp. Proc. Vol. 407 © 1996 Materials Research Society

EXPERIMENTAL PROCEDURE

The velocity and attenuation of compressional waves was measured in different suspensions containing kaolinite and water, glass beads and water, and glass beads and oil. Kaolinite is an aluminosilicate clay, made of hexagonal plates with a mean size of $1\mu\ m$. The measured density of kaolinite is $2500kg/m^3$. The silica glass beads have a density of $2600kg/m^3$ and also have a mean particle size of $1\mu m$. One of the fluid componenents of the suspensions was doubly destilled water and the second fluid used was a light machine oil (LPS-1) with a density of $800kg/m^3$ and a viscosity of $2.8 \times 10^{-3} Pa - sec$.

The suspensions were placed in a $10 \times 10 \times 10\ cm$ cell, and were continuosly stirred to avoid settling. The concentration was monitored with a picnometer before and after the measurement to ensure that no settling had occurred.

The pulse-trnsmission technique was used to measure the velocity and attenuation of a compressional elastic wave propagating through the suspensions. A voltage pulse was fed into an x-cut quartz transducer that acted as an acoustic source, and after propagating through the suspension, the signal was received by another x-cut quartz crystal and recorded by a digital oscilloscope. The received signal was then fed into a digital oscilloscope. The separation between the quartz transducers could be varied using a precision micrometer. This configuration allowed the accurate determination of attenuation by measuring the amplitude of the received signal as a function of transducer separation. Similarly, the velocity could be determined by measuring the propagation time as a function of transducer separation. All measurements were carried out at a constant temperature of $25^O C$. The velocity and attenuation data presented here are the average of several experimental runs and carry error bars of the order of 0.7% and 8% respectively. The procedural details of the experiment are given elsewhere [11].

RESULTS

In Figure 1 are shown the attenuation and velocity as a function of volume concentration for the kaolinite-water suspension. As discussed previously the linear monotonic increase of attenuation at low concentrations is due to the fact that the solid particles in suspension act independently when attenuating sound. With increasing concentration the attenuation exhibits a maximum at a concentration near 40%. This maximum in attenuation is accompanied by a drastic change in the overall trend of increasing velocity.

Scattering effects can be ruled out in explaining the observed phenomena at the critical concentration of 40%. Scattering is expected to produce a strong absorption when the mean separation of the particles is of the order of the wavelength [12]. While this effect will give a concentration-dependent attenuation, the position of the attenuation peak will vary with frequency (i.e. with wavelength). In Figure 1 the critical concentration is seen to be independent of the frequency.

Smectic clays, like kaolinite, show a very active surface chemistry due to cation exchange capabilities. To rule this out as the mechanism responsible for the observed behavior, the velocity and attenuation measurements were repeated using glass beads, which are relatively inert in water or hydrocarbon oils. Figures 2 and 3 show the attenuation and velocity as a function of concentration for both glass-beads suspensions. The maximum in attenuation, as well as the corresponding change in velocity, also occurs at a critical concentration of 40%, independent of the liquid matrix used.

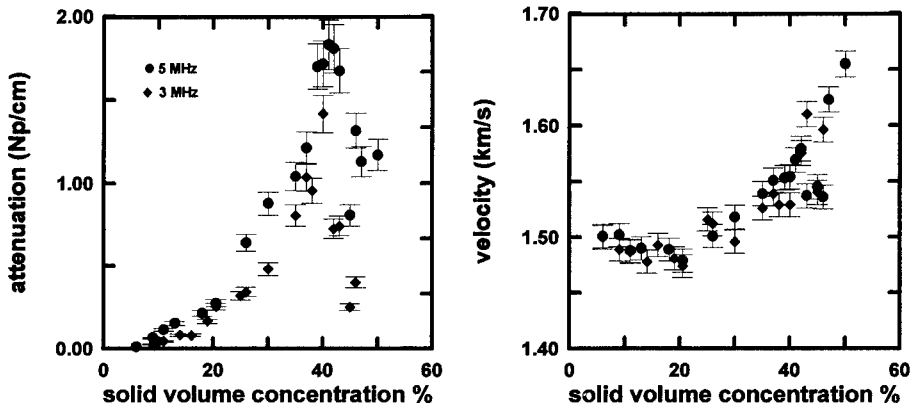


Figure 1: Attenuation and velocity as a function of concentration for the kaolinite/water suspension.

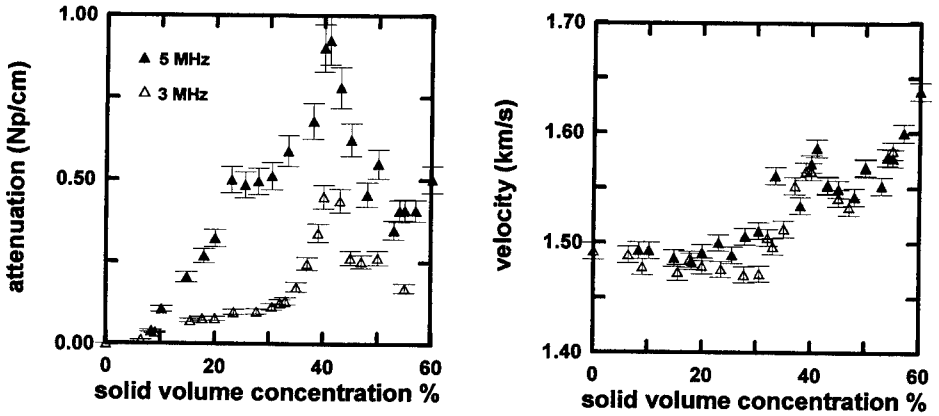


Figure 2: Attenuation and velocity for the glass beads/water suspension.

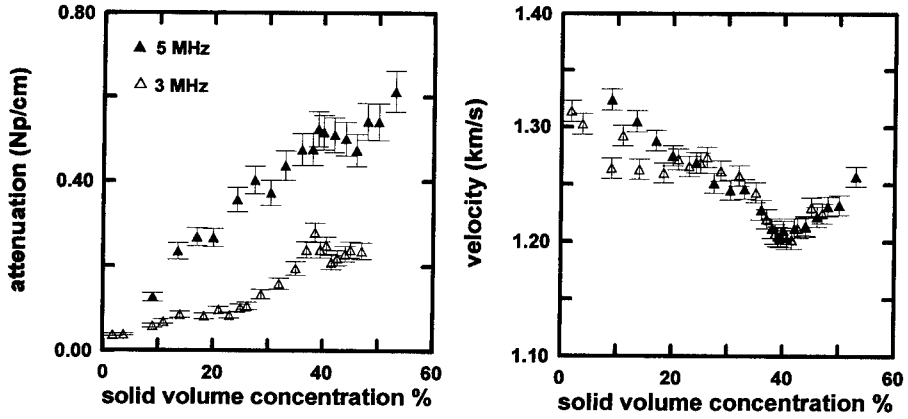


Figure 3: Attenuation and velocity for the glass beads/oil suspension.

DISCUSSION

The anomalous behavior observed at a concentration of 40%, is independent of frequency, liquid matrix or solid constituent. This suggests that the change in velocity and attenuation at the critical concentration is due to geometrical effects such as interparticle spacing. This is consistent with the "freezing" point predicted by computer simulations involving sequential packing of spheres [9]. In three dimensions the simulations predict that no more spheres can be added without significant reorderingat a concentration of 39%. We proposed that as the concentration is increased toward 40%, the shearing of the viscous fluid between adjacent particles experiencing oscillatory motion due to the passage of an acoustic wave, contributes to the attenuation processes [13]. This effect is limited at low concentrations by large inter-particle separations and at high concentrations by the increasing number of particles in contact (and therefore incapable of relative motion). This implies that there should be an optimun concentration at which this mechanism is most efficient. The fact that fluid inertia contributes to the attenuation, can be observed by comparing Figures 2 and 3. Above a concentration of around 20% the oil-based suspensions (higher viscosity) attenuates less than the water based suspensions. Thus our measurements are done in the transitional region between the visocus regime and the inertial regime, as defined by Kytomaa et al. [14, 15]. In this transition region, the viscous penetration length δ [16] is of the order of the particle radius. For example, for the water-based suspensions the ratio $R = \delta/a$ is $R = 1.6$ (3 MHz) and $R = 1.2$ (5 MHz), and similarly for the oil based suspensions: $R = 3.1$ (3 MHz) and $R = 2.4$ (5 MHz). An increasing viscosity will increase the value of R at a given frequency and the particles will cease to attenuate sound independently at a lower concentration, thus broadening the attenuation peak. Further experiments are planned to confirm this hypothesis.

Finally, the critical behavior is also independent of the particle geometry. This is due to the random orientation of the kaolinite plates, that effectively have an spherical excluded volume. If the kaolinite suspensions had been allowed to settle, then the freezing limit would

most likely have been much higher due to preferred plate orientation.

The theoretical description of two-phase systems presented in the literature, ranges from simple averaging techniques [17] to the self-consistent coherent potential approximation (CPA) [18]. The CPA model does predict a peak in attenuation at 40% concentration similar to that observed in our data. CPA attributes this peak to a liquid-solid transition after which the system is capable of sustaining shear stress at higher concentrations. However, this is not evident in our data and our samples still show a fluid-like behavior at the concentration of 40%. Hydrodynamic models like those of Harker [19] include viscous and inertial effects to describe the propagation of elastic waves through a suspension. Their model predicts a value for the velocity in accordance with our experimental data for concentrations lower than 40%. But at this critical concentation no sudden change in velocity or attenuation is predicted.

CONCLUSIONS

Attenuation and velocity measurements of compressional waves as a function of concentration have been presented for different suspensions. At a critical concentration of 40% a two-phase system undergoes a transition due to the decrease in relative motion between the solid and liquid phases. This critical concentration marks an onset to rigidity. The fluid and solid states should coexist until the system forms an interconnected elastic network capable of sustaining shear stresses on a large scale.

References

[1] Murray, C. A., and Grier, D. A., American Scientist **83**, 238-245 (1995).

[2] Paulin, S.E., and Ackerson, B.J., Phys. Rev. Lett. **64**, 2663-2666 (1990).

[3] Murray C. A., W.O. Sprenger, and R. A. Wenk, Phys.Rev. B **42**, 688 (1990).

[4] Bartlett, P. and Van Megen, W. in *Granular Matter: An Interdisciplinary Approach*, Ed. Anita Mehta (Springer-Verlag, Berlin 1993) p. 195.

[5] Digby, P. J., J. Appl. Mech., **48**, 803-808 (1981).

[6] Marion, D., and Nur, A., Physica A **157**, 575-579 (1989).

[7] Blangy, J. P., Strandenes, S. Nur, A., Geophysics, **58**, 344-356 (1993).

[8] Greenwood, M. S., Mai, Josef L., and Good, Morris S., J. Acoust. Soc. Am. **94**, 908-916 (1993).

[9] Cooper, D. W., Phys. Rev. A, **38**, 522-524 (1988).

[10] Torquato, S., Phys. Rev. Lett., **74**, 2156-2159 (1995).

[11] Esquivel-Sirvent, R., Yun, S.S. and Stumpf, F.B., J. Acoust. Soc. Am. **95**, 557-558 (1994).

[12] Sheng, P., *Introduction to Wave Scattering, Localization and Mesoscopic Phenomena*, (Academic Press, San Diego, California 1995) p.49-113.

[13] Esquivel-Sirvent, R., Green, D. H., Yun, S.S., Appl. Phys. Lett. **67**, 3087-3089 (1995).

[14] Derken, J. S. and Kytoma, H. K., *Proceedings of the 1994 ASME Fluids Engineering Division Summer Meeting*, **189** (ASME, New York 1994) p. 75-81.

[15] Atkinson, C. M. and Kytoma,H. K., Int. Journal of Multiphase Flows, **18** 577-592 (1993).

[16] Landau, L. D. and Lifshitz, E. M., *Fluid Mechanics*, (Pergammon Press, New York 1984) p. 89.

[17] Wood, A. B., *A textbook of Sound* (G. Bell & Sons, London 1930).

[18] Berryman, J. G., J. Acoust. Soc. Am. **68**, 1809-1819 (1980).

[19] Harker, A. H., and Temple, J. A. G., J. Phys. D: Appl. Phys. **21** 1576-1588 (1988).

Part III

Chemical Reactions

NON-CLASSICAL REACTION KINETICS: EXPERIMENTS

RAOUL KOPELMAN and ANNA L. LIN
Department of Chemistry, The University of Michigan, Ann Arbor, MI 48109-1055, USA

Abstract

It has been well established by theory and simulations that the reaction rates of diffusion-limited reactions can be affected by the spatial dimension in which they occur. The types of reactions $A + B \rightarrow C$, $A + A \rightarrow A$, and $A + C \rightarrow C$ have been shown, theoretically and/or by simulation, to exhibit non-classical reaction kinetics in low and fractal dimensions. We present here experimental results from several 1D and fractal systems.

An $A+B \rightarrow C$ type reaction was experimentally investigated in a long, thin capillary tube in which the reactants, A and B, are initially segregated. This initial segregation of reactants means that the net diffusion is along the length of the capillary only, making the system effectively 1D and allowing some of the properties of the resulting reaction front to be studied. The reaction rate of excitonic fusion, $A + A \rightarrow A$, as well as trapping, $A + C \rightarrow C$, reactions were observed via phosphorescence(P) and delayed fluorescence(F) of naphthalene within the channels of Vycor glass, in isotopically mixed naphthalene crystals and in the isolated chains of dilute polymer blends. In these experiments, the non-classical kinetics are measured in terms of the heterogeneity exponent, h, from the equation: $Rate \sim F = kt^{-h}P^n$, which gives the time dependence of the rate coefficient. Classically $h = 0$, while $h = 1/2$ in 1D, as well as in the fractal dimensions discussed here, for $A + A \rightarrow A$ as well as $A + C \rightarrow C$ type reactions.

1 Introduction

Non-classical, diffusion-limited reaction kinetics are of interest both in their own right and also as a tool in material sciences, catalysis, complex liquids and intracellular biochemistry [1,2]. Theoretically, the simplest cases of non-classical reactions occur for one-dimensional topologies[3–25], even though fractal, disjoint islands, two-dimensional and even three-dimensional topologies may exhibit anomalous, non-classical, reaction kinetics [18,26-28]. Subsequently, there is an abundance of theory and simulation work on reaction kinetics in one-dimensional topologies. Experimentally, 1D systems pose obvious difficulties. However, there are several experimental systems which have been utilized successfully to observe non-classical reaction kinetics in 1D. We also present results from experiments done on percolation clusters. Three types of bimolecular elementary reactions are discussed here: *one kind* ($A + A \rightarrow products$), *two kinds* ($A + B \rightarrow products$) and *pseudo-monomolecular* ($A + C \rightarrow C + products$).

The non-classical behavior of an $A+B \rightarrow C$ type reaction occurring in 1D was studied experimentally using the inorganic complexation reaction of disodium ethyl bis(5-tetrazolylazo) acetate trihydrate ('tetra') with Cu^{2+}. The reaction is carried out in long, thin, capillary tubes with the reactants A and B initially segregated in space. The reactants meet in the center of the capillary forming a reaction front. The kinetic behavior of this reaction front was predicted, via a scaling ansatz [24], to be non-classical with respect to the temporal

Mat. Res. Soc. Symp. Proc. Vol. 407 © 1996 Materials Research Society

behavior of the position of the center of the reaction front, x_f, as well as the width of the front, w, and the local reaction rate at the center of the front, r_f. The global reaction rate, R, was also determined to behave non-classically [35,36]. These predictions were borne out in an experiment which we discuss in Sec. 2.

A number of experiments have been performed which exhibit the non-classical behavior of $A + A \rightarrow products$ (homofusion) and $A + C \rightarrow C + products$ (heterofusion) type reactions in one or fractal dimensions. The photophysical fusion 'reaction' of excitons traveling through the pseudo-one-dimensional channels of Vycor glass or within the clusters of isotopically mixed molecular crystals exhibit non-classical reaction kinetics manifested in a heterogeneity coefficient, h, giving $h = 1/2$ instead of the classical value, $h = 0$, in the long-time limit. Exciton fusion studies were also performed on very dilute blends of P1VN/PMMA, where isolated chains of P1VN are insulated from exciton cross-talk by the exciton inert environment of the PMMA host [29]. Time resolved phosphorescence and delayed fluorescence intensities relate to the exciton population and the fusion rate, respectively, as a function of time. This enables the comparison of experiment with theory as well as the characterization of the polymer system and the exciton interactions.

The heterogeneity coefficient was chosen as the parameter by which to experimentally measure the non-classical reaction rates of the $A + A \rightarrow A$ and the $A + C \rightarrow C$ elementary reactions because the differential rate equations for both reactions can be written easily in terms of h. For any batch reaction, ('batch' = all reactants introduced at $t = 0$), both $A + A \rightarrow A$ and $A + C \rightarrow C$ reactions exhibit $h = 1/2$ behavior in 1D. On the other hand, the integrated rate equations of the two reactions differ in the asymptotic limit: the $A + A \rightarrow A$ reaction has an algebraic reactant density decay while the $A + C \rightarrow C$ reaction has a stretched exponential decay. However, even in the integrated cases, the time exponents are both $1 - h = 1/2$ in one dimension. Similar relations are true for the fractal systems discussed here.

We note that the 1D systems discussed here differ significantly from previously studied quasi-one-dimensional systems [30-32]. The latter are essentially two- or three-dimensional systems with highly anisotropic exciton-exchange interactions. So, for a short time, the exciton is confined in one dimension. There is a finite probability, however, of moving along other directions (interchange hopping), resulting in 2D or 3D behavior over longer and asymptotically infinite times, and thus usually limiting the measurements to ultra short times. Moreover, the phonons and exciton- phonon interactions in these systems are seldom one dimensional. In contrast, our systems are truly 1D over long times and there is no reactant (exciton) escape or tunneling out of the thin, 1D systems. Our systems may behave as 3D systems at very early times, but will cross over to 1D behavior at longer times and stay so for asymptotically infinite times.

2 $A+B \rightarrow C$ Where A and B Are Segregated Throughout the Reaction

Analytical work on an $A + B \rightarrow C$ type reaction-diffusion process in an effectively one-dimensional system was done by Galfi and Racz [24]. In their model, the reactants A, with a constant density a_o, and B, with a constant density, b_o, are initially separated. They meet

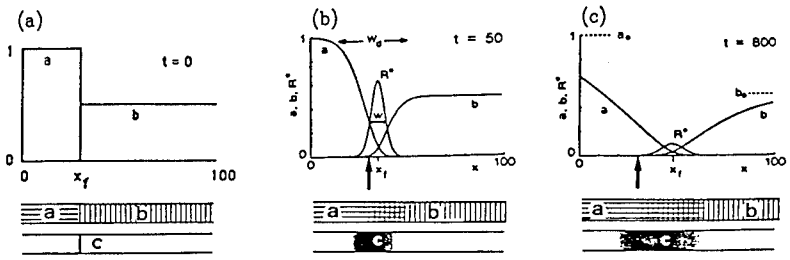


Figure 1: Motion of the reaction front with time. The length (x), time (t), densities (a,b) of reagents (A,B), and the magnified production rate ($R^* = 100R = 100kab$) of C are all scaled to be dimensionless. As an initial condition, $a = 1$, $b = 0$ for $x < 30$ and $a = 0$, $b = 0.5$ for $x > 30$. The position of the center of the reaction front, x_f, is indicated by the arrow. The top figure of (b) and (c) are from [24].

at time 0, forming a single reaction boundary, which makes the system effectively 1D. The motion of the reaction front with time is shown in Fig. 1. This model is similar to that of Weiss et al. [34] for the reaction $A + C \rightarrow C$, where A is a one-dimensional continuous solute and C is a single trap.

The results of a set of reaction-diffusion equations for a and b, which are valid in the long-time limit, show that x_f, the position of the center of the reaction front, scales as $x_f \sim t^{1/2}$, while w, the width of the reaction front, scales as $w \sim t^{1/6}$ and the reaction rate at the center of the front, r_f scales as $r_f \sim t^{-2/3}$. It was also determined[35,36] that the global reaction rate, R, scales as $R \sim t^{-1/2}$, i.e.:

$$R = \frac{dC}{dt} \sim t^{-1/2} \tag{1}$$

Such a system as is described above was investigated experimentally using the inorganic complexation reaction of disodium ethyl bis(5-tetrazolylazo)acetate trihydrate ('tetra') with Cu^{2+} [35]. This reaction produces a 1:1 complex in water. Gelatin solutions of the two reactants are introduced into opposite ends of a long, thin capillary tube (see Fig. 2). The two reactants meet in the center of the capillary, forming a reaction front. The use of gelatin allows efficient diffusion but little or no convection to occur and aids in the formation of a sharp reaction boundary. The absorbance of the product, a $1:1$ Cu^{2+} :' $tetra'$ complex, is monitored at fixed time intervals by scanning with a detector and a light source in parallel, along the reaction front domain, while the capillary reactor remains fixed in space.

Using the instantaneous reaction of Cu^{2+} with 'tetra', investigated under initially segregated reactant conditions, allowed the study of the further segregation of the reactants in time as well as other time dependent properties of the reaction front. In contrast to the classical expectation, the two reactants do not inter diffuse with time.

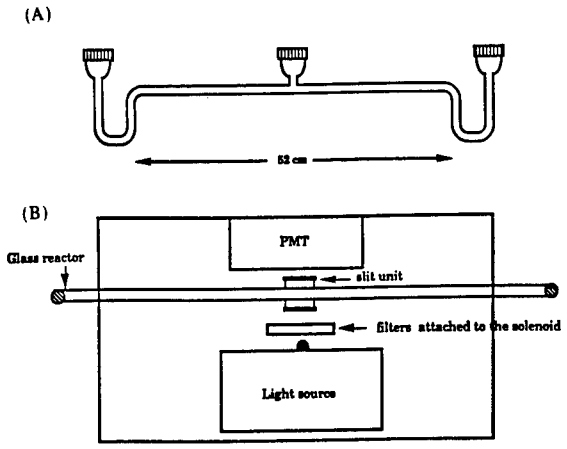


Figure 2: (A) Glass capillary reactor. (B) Top view of the experimental set-up used to obtain absorbance measurements of the reaction front.

Table 1:

Time exponents for reaction front parameters of the $A + B \rightarrow C$ reaction in a capillary.

	α	β	γ	δ	ϵ
Experiment	0.51 ± 0.03	0.17 ± 0.03	0.70^b	0.53 ± 0.02	0.45 ± 0.01
Simulation	0.52 ± 0.03	0.16 ± 0.01	0.68^b	0.52 ± 0.02	–
Theory	1/2	1/6	2/3	1/2	1/2

[a]Here $x_f \sim t^{\alpha}$, $w \sim t^{\beta}$, $r_f \sim t^{-\gamma}$, $R \sim t^{-\delta}$, and ave. distance from the origin $\sim t^{\epsilon}$. The theory and simulation values of α, β, γ, and δ are from refs. [24,39] and that of ϵ is from Einstein's diffusion theory (see refs. [37,38]).
[b]Difficult to measure experimentally and in the simulation, but derivable from the theoretical relation [24,36] $\gamma = \beta + \delta$.

Rather, a reactant gap forms and grows larger with increasing time. The concentration of A and B within the gap is very low and decreases with time as the gap size increases (see Fig. 1). Thus, the initial segregation is maintained throughout the reaction and causes the reaction rate to decrease in time as $t^{-1/2}$ (the reaction rate in the reaction-limited regime increases with time as $t^{1/2}$). The results are summarized in Tab. 1. and agree well with theoretical expectations.

Self-ordering and segregation effects have been predicted repeatedly by theory and simulations to affect the reaction rate of diffusion-limited elementary $A + B \rightarrow C$ reactions in 1D (as well as higher dimensions). However, the work discussed here was the first experimental study to show the existence and persistence of reactant segregation in low dimensional systems.

3 Homofusion vs. Heterofusion

Several of the experiments discussed in the sections below employ excited state naphthalene as the reactant, A, undergoing the process $A + A \rightarrow Products$ or $A + C \rightarrow C + Products$, where C are trapped naphthalene excitations (also designated here by A'). The excited state naphthalene participates in exciton (physical) reactions. Both the fusion (homofusion) and trapping (heterofusion) reactions that occur exhibit binary and pseudo-monomolecular kinetics, respectively. This is a result of the fact that the reactant, excited state naphthalene, exists in two forms, mobile species and trapped species.

For exciton fusion in perfect crystalline samples, the excitons move freely and at random, resulting in binary exciton-exciton fusion [9,25,41]

$$A + A \rightarrow A + h\nu \tag{2}$$

where $h\nu$ is the delayed fluorescence. The fusion rate, R, and the fluorescence rate, F, are given by

$$F \sim R = k\rho_A{}^2 \tag{3}$$

where ρ_A is the excited molecule or exciton density and k is the rate constant of the reaction. In most samples, however, a fraction of the free excitons are quickly trapped, resulting in a roughly constant density of trapped excitons, A', which gives rise to a pseudo-unary fusion reaction and rate

$$A + A' \rightarrow A' + h\nu \tag{4}$$

$$F \sim R = k'\rho_A \tag{5}$$

where $k' = k\rho_{A'}$. In addition, the triplet excitations undergo natural decay, $A \rightarrow h\nu$, with lifetime τ:

$$P \sim \tau^{-1}\rho_A. \tag{6}$$

Therefore, the overall kinetic analysis of the data should be in the form

$$k \sim \frac{F}{P^n} \tag{7}$$

with $n = 2$ for perfect, trapless samples where only homofusion occurs and $n = 1$ for samples with traps, where heterofusion prevails. For 3D samples k, and $log(k)$, is expected to be

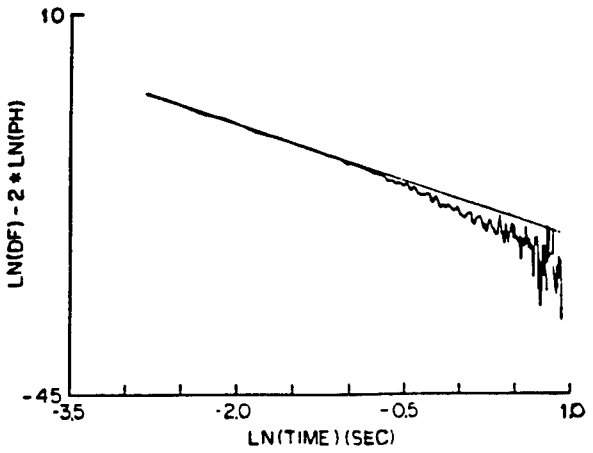


Figure 3: Exciton fusion rate coefficient in porous Vycor glass, $\frac{F}{P^n} = k_o t^{-h}$ vs. time on a ln-ln scale. $n = 2$. $T = 6K$ and $h = 0.44$.

constant in time while for 1D samples $k \sim t^{-1/2}$ and so a plot of $log(k)$ vs. $log(t)$ has a slope of $-1/2$. This relationship is tested with naphthalene exciton fusion and trapping in porous glass and porous membranes by monitoring the delayed fluorescence of the exciton-exciton collision product and the phosphorescence of the reactant triplet excitons; effectively, measuring the long-time limit kinetics. Similar one-dimensional experimental tests involve excited naphthalene molecules in solution [44,45]. The homofusion reaction is also monitored on percolation clusters in isotopic mixed crystals[9].

4 Exciton Annihilation in Porous Glass and Isotopically Mixed Crystals

In the experiments discussed in this section, exciton fusion in the 1D channels of naphthalene embedded Vycor glass and in the fractal, percolating structure of molecular crystals of isotopically mixed naphthalene was monitored via phosphorescence and delayed fluorescence. Both systems exhibit the non-classical reaction kinetics expected for a homofusion process, i.e. $k(t) \sim \frac{F}{P^2}$.

Vycor glass samples provide effective 1D structures in which to test non- classical rate laws. Preparation of the naphthalene embedded samples and the optical arrangement are described elsewhere [46,47]. The naphthalene embedded in these porous substrates forms crystalline naphthalene 'wires', the diameters of which are that of the pore size in which they are embedded. Typical results are shown in Fig. 3. The data are analyzed in the long-time limit and $n = 2$, as can be seen in Fig. 3. Thus, homofusion is the predominant reaction.

Experiments of triplet exciton homofusion in naphthalene isotopically mixed crystals, $C_{10}H_8$ in $C_{10}D_8$, demonstrate that the classical approach does not apply in general[9,42,43].

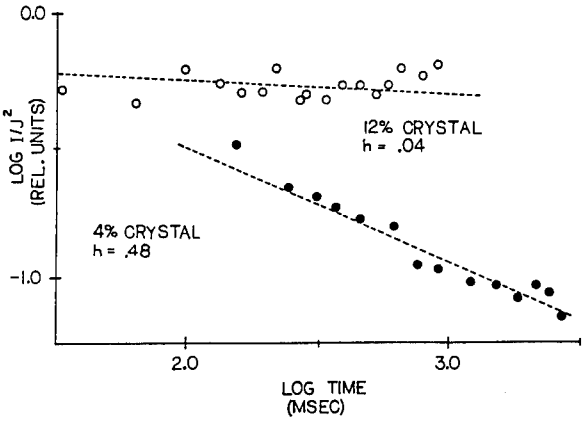


Figure 4: Exciton fusion rate coefficients[9] in two isotopically mixed naphthalene crystals, $\frac{F}{P^n} = kt^{-h}$ vs. time on a ln-ln scale. $n = 2$. The resulting slope for the 12% crystal corresponds to $h = 0.04$, in good agreement with the classical result. In contrast, the slope for the 4% crystal corresponds to $h = 0.48$.

Different concentrations of $C_{10}H_8$ in $C_{10}D_8$ result in molecular crystals with different average cluster sizes of naphthalene(guest) in perdeuteronaphthalene (host). Non-classical behavior is particularly evident for samples with less than 10% naphthalene in perdeuteronaphthalene. Fig. 4 shows that a 12% sample behaves classically, i.e. $h = 0$, while a 4% sample exhibits "fractal" behavior, $h = 0.48 \pm 0.03$, due to the cluster-limited random walks of the excitons. An 8% sample gives an intermediate h value, 0.28.

5 Exciton Annihilation and Trapping in Isolated Polymer Chains

In this section we report on studies of exciton fusion in isolated chains of poly(1-vinyl) naphthalene polymer (P1VN), molecular weight (MW) $\sim 10^5$, blended in poly(methylmethacrylate)(PMMA), MW $\sim 1.54x10^5$. Samples of 0.005 % and 0.01 % (wt/wt) P1VN-/PMMA were cast as thin films using the doctor blade technique [48]. An excimer laser was used as the pulsed excitation source. Decay data were collected about 10 milliseconds after the excitation pulse [29,49].

The exciton fusion process in P1VN/PMMA samples has been shown to be orders of magnitude more efficient than it is in naphthalene/PMMA samples [29,47], evidence that the triplet excitations migrate efficiently along the entire polymer chain, the average length of which is on the order of 100 monomers. The premise for these experiments is that chain-chain hopping can be neglected for these very dilute blends, but triplet exciton hops between adjacent naphthalene pendants on the same chain are quite efficient at the experimental temperature, $77K$. This hypothesis is corroborated by the rate law measurements.

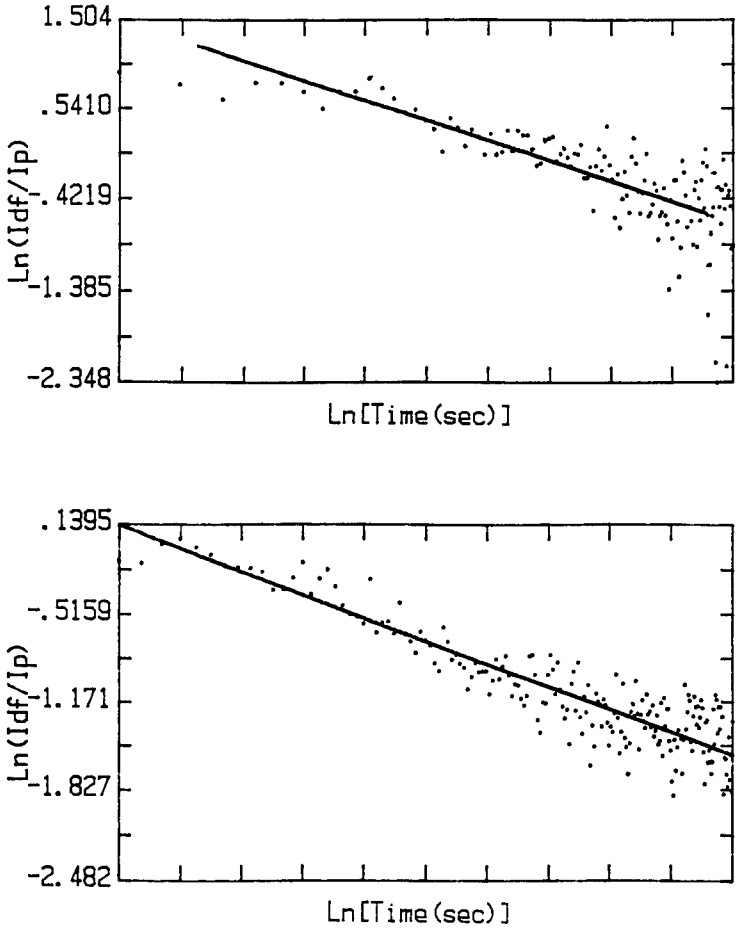


Figure 5: Exciton fusion rate coefficients [50] in (top) 0.05% and (bottom) 0.01P1VN/PMMA at $T = 77K$, $\frac{DF}{P^n} = kt^{-h}$ vs. time on an ln- ln scale. $n = 1$.

As in the previously discussed exciton fusion experiments, two fusion reactions contribute to the delayed fluorescence decay: homofusion ($A+A \rightarrow products$) and heterofusion ($A+C \rightarrow C$). We hypothesize that the reaction rate observed is that of the trapping, heterofusion reaction. The heterofusion rate law is valid after most of the traps (defects, etc.) have been discovered and occupied by freely hopping excitons. The electronic excitation is confined to the naphthalene moieties of the P1VN. The resulting triplet excitation hopping is limited to a range of approximately $5\mathring{A}$, thus in the absence of neighboring P1VN chains, exciton hopping is limited to a single chain. These chains, not being tightly coiled, are very close to true 1D systems since they have an approximate $5\mathring{A}$ diameter and the triplet exciton hopping length is on the order of $5\mathring{A}$ as well. In order to ensure 1D topology, the blends are necessarily as dilute as 0.005 % and 0.01 %. Higher P1VN concentrations, i.e. 1 %, allow cross-talk between chains, resulting in a crossover from 1D to 3D kinetics as the concentration of P1VN is increased.

Data obtained from this experiment are consistent with a heterofusion model – the data fit eqn. (7) when $n = 2$, see Fig. 5. The heterogeneity exponents for the 0.005 % and 0.01 % P1VN/PMMA samples were found to be $h = 0.47 \pm 0.05$ and 0.53 ± 0.03, respectively, in good agreement with the theoretical expectation of $h = 1/2$. On the other hand, the heterogeneity exponent for the pure (100 %)P1VN material was found to be $h = 0.02 \pm 0.02$, in good agreement with the expectation $h = 0$ for 3D (classical) systems [50].

In summary, for the 1D topology of the P1VN chains embedded within a PMMA host, the reaction is dominated by heterofusion on the time-scale in which the measurements are made and obeys the diffusion-controlled, non-classical kinetics for the pseudo-monomolecular reaction $A + C \rightarrow C + Products$ in 1D.

6 Conclusion

We have presented the results of several experimental systems which exhibit non-classical reaction kinetics in the asymptotic limit. The bimolecular reaction of Cu^{2+} with 'tetra' was observed in capillary tubes where the reactants are initially segregated in space. The non-classical behavior of some temporal properties of the reaction front are manifested in anomalous power laws. Excitonic fusion reactions were investigated using crystalline naphthalene in porous glasses and in isotopically mixed naphthalene crystals. In both cases, homofusion is the predominant process. Fusion reaction kinetics was also observed on isolated P1VN chains in P1VN/PMMA polymer blends where heterofusion was observed. The non-classical reaction kinetics observed in all of these systems was measured in terms of the heterogeneity coefficient, h. The classical value of h is $h = 0$, while the observed value was approximately 1/2 in the 1D and fractal topologies.

This work was supported by NSF grant DMR-9410709.

References

1. E. E. Fauman and R. Kopelman, *Mol. Cell. Biophys.* 6, 47 (1989).
2. *Models of Non-Classical Reaction Rates*, ed. J. L. Lebowitz, special G. Weiss issue of *J. Stat. Phys.* 65, (1991).
3. A. A. Ovchinnikov and Y. G. Zeldovich, *Chem. Phys. B}* 28, *215 (1978).*
4. *M. Bramson and D. Z. Griffeath, Wahrscheinlichskeitstheorie Gebiete 53, 183 (1980).*
5. *M. Bramson and D. Z. Griffeath, Annals of Probability 8, 183 (1980).*
6. *J. Keizer, J. Phys. Chem. 86, 5052 (1982).*
7. *J. Keizer, J. Chem. Phys. 79, 4877 (1983).*
8. *D. C. Torney and H. M. McConnel, J. Phys. Chem.} 87, 1441 (1983).*
9. *P. W. Klymko and R. Kopelman, J. Phys. Chem. 87, 4565 (1983).*
10. *D. Toussaint and F. Wilczek, J. Chem. Phys.} 78, 2642 (1983).*
11. *D. C. Torney, J. Chem. Phys. 79, 3606 (1983).*
12. *L. W. Anacker and R. Kopelman, J. Chem. Phys.} 81, 6402 (1984).*
13. *P. V. Elyutin, J. Phys. C 17, 1867 (1984).*
14. *Racz, Z., Phys. Rev. Lett. 55, 1707 (1985).*
15. *A. A. Lushnikov, Phys. Lett. A 120, 135 (1987).*
16. *L. W. Anacker and R. Kopelman, Phys. Rev. Lett. 58, 289 (1987).*
17. *C. R. Doering and D. Ben-Avraham, Phys. Rev. A 38, 3035 (1988).*
18. *R. Kopelman, S. J. Parus, and J. Prasad, in Excited State Relaxation and Transport Phenomena in Solids, eds. J. L. Skinner and M. D. Fayer, special issue of Chem. Phys. 128, 209 (1988).*
19. *K. Lindenberg, B. J. West, and R. Kopelman, Phys. Rev. Lett. 60, 1777 (1988).*
20. *E. Peacock-López and J. Keizer, J. Chem. Phys. 88, 1997 (1988).*
21. *J. L. Spouge, Phys. Rev. Lett. 60, 871 (1988).*
ibid *1885.* **22.** *C. R. Doering and D. Ben-Avraham, Phys. Rev. Lett. 62, 2563 (1989).*
23. *V. Privman, J. Stat. Phys. 69, 629 (1992).*
24. *L. Galfi and Z. Racz, Phys. Rev. A, 38, 3151 (1988).*
25. *R. Kopelman, Science 241, 1620 (1988).*
26. *V. Sundstrom, T. Gillbro, R.A. Gadonas, A. Piskarskas, sl J. Phys. Chem., 89, 2754 (1988).*
27. *V. Gulbinas, M. Chachisvilis, A. Persson, S. Svanberg, V. Sundstrom, J. Phys. Chem., 98, 8118 (1994).*
28. *S.L. Dexheimer, W.A. Vareka, D. Mittleman, A. Zettl, C.V. Shank, Chem. Phys. Lett., 235, 552 (1995).*
29. *C. S. Li, Ph. D. Thesis, University of Michigan, Ann Arbor (1988).*
30. *R. M. Hochstrasser and Whiteman, J. Chem. Phys. 56, 5945 (1972).*
31. *M. D. Fayer, in Modern Problems in Solid State Physics, Vol. 4, eds. V. M. Agranovich and R. M. Hoschstrasser, (North-Holland, Amsterdam 185 (1983)).*
32. *S. D. D. V. Rughooputh, D. Bloor, D. Phillips and B. Movaghar, Phys. Rev. B 35, 8103 (1987).*
33. *W. J. Rodriguez, R. A. Auerbach, G. L. McPherson, J. Chem. Phys. 85, 6442 (1986).*
34. *G. Weiss, R. Kopelman, S. Havlin, S. Phys. Rev. A 39, 466 (1989).*
35. *Y. E. Koo and R. Kopelman, J. Stat. Phys. 65, 893 (1991).*
36. *Y. E. Koo, L. Li, and R. Kopelman, Mol. Cryst. Liq. Cryst. 183, 187 (1990).*
37. *M. V. Smoluchowski, Z. Phys. Chem. 92, 129 (1917).*
38. *S. Chandrasekhar, Rev. Mod. Phys. 15, 1 (1943).*
39. *L. Li, Ph. D. Thesis, University of Michigan, Ann Arbor (1989).*
40. *S. Redner, in Extended Abstracts of the Materials Research Society Symposium on Dynamics in Small Confining Systems, eds. J. M. Drake, J. Klafter, and R. Kopelman, 109 (1990).*

41. *R. Kopelman, J. Stat. Phys. 42, 185 (1986).*
42. *P. W. Klymko and R. Kopelman, J. Lumin. 24/25, 457 (1981).*
43. *P. W. Klymko and R. Kopelman, J. Phys. Chem. 86, 3686 (1982).*
44. *J. Prasad and R. Kopelman, J. Phys. Chem. 91, 265 (1987).*
45. *J. Prasad and R. Kopelman, Chem. Phys. Lett. 157, 535 (1989).*
46. *R. Kopelman, S. Parus, J. Prasad, Phys. Rev. Lett. 56, 1742 (1986).*
47. *R. Kopelman, S. J. Parus, and J. Prasad, Chem. Phys. 128, 209 (1988).*
48. *E. O. Allen, Plastic Polymer Science and Technology, ed. M. D. Baijal, (New York Wiley, 600 (1982)).*
49. *Z. Y. Shi, C-S. Li and R. Kopelman, in Polymer Based Molecular Composites, Proceedings of the Materials Research Symposium, eds. J. E. Mark, D. W. Shaefer, (Pittsburgh, Pennsylvania (1989)).*
50. *Z. Y. Shi, Ph. D. Thesis, University of Michigan, Ann Arbor (1990).*

STUDY OF A+B→C and A+2B→C REACTION-DIFFUSION SYSTEM WITH INITIALLY SEPARATED COMPONENTS

Andrew Yen and Raoul Kopelman, Department of Chemistry, University of Michigan, Ann Arbor, MI 48109-1055

ABSTRACT

The presence of a reaction front is a characteristic feature of a variety of physical, chemical and biological processes. The reaction exhibits a front , provided that the diffusing reactants are separated in space. We study the reaction front dynamics of both A+B→C bimolecular and A+2B→C termolecular reactions with initially separated components in a capillary. We measure and compare with theory and simulations the dynamic quantities that characterize the kinetic behavior of the system: the global reaction rate R(t), the location of the reaction center $x_f(t)$, the front's width w(t), and the local production rate $R(x_f,t)$. The non-classical nature of this dynamical system is confirmed.

INTRODUCTION

Interest in reaction fronts has greatly increased since it was realized that pattern formation in the wake of a moving front is quite a general phenomenon. Reaction front dynamics play a crucial role in formation of patterns in the multistep Belousov-Zhabotinksii reactions[1] and Liesegang ring formation[2]. The latter is thought to be a complex interplay between the dynamics of the reaction front and the nucleation kinetics of the precipitate.

Theoretical work on the diffusion-reaction system with initially separated components was first done on the irreversible A+B→C type reaction by Galfi and Racz [3]. In this geometry reactant A of constant density a_0 and B of constant density b_0 are initially separated. They meet at time 0, forming a reaction front, which makes the system effectively one-dimensional.

The following set of mean-field type reaction-diffusion equations for the local concentrations a and b is assumed to describe the system:

$$\frac{\partial a}{\partial t} = D_a \nabla^2 a - kab$$
$$\frac{\partial b}{\partial t} = D_b \nabla^2 b - kab \qquad [1]$$

where k is the microscopic reaction constant. The equation must satisfy the initial separation condition along the separation axis x

Mat. Res. Soc. Symp. Proc. Vol. 407 © 1996 Materials Research Society

$$a=a_0H(x) \qquad b=b_0[1-H(x)] \qquad [2]$$

Where H(x) is the Heaviside step function. The long time behavior was addressed by Galfi and Racz. They assume that, in the asymptotic time domain, R(x, t) has a scaling form

$$R(x,t) \approx t^{-\beta}F(\frac{x-x_f}{t^{\alpha}}) \qquad [3]$$

where $F(\frac{x-x_f}{t^{\alpha}})$ is a scaling function. Their study shows that, in the long time limit, the center of the reaction front (x_f), and the front width (w) scale with time as $x_f \sim t^{1/2}$ and $w \sim t^{1/6}$, respectively, while the production rate of C at x_f, is proportional to $t^{-2/3}$.

Cornell, Droz and Chopard studied the generalized nA+mB→C reaction with initially separated components using a cellular automata algorithm for the reaction-diffusion of the particles[4]. Their result shows that for the A+2B→C case the time exponents in the asymptotic regime for the center of the reaction front (x_f) and the width (w) of the front scale with time as $x_f \sim t^{1/2}$ and $w \sim t^{1/4}$, respectively, and that the production rate of C at x_f, is proportional to $t^{-3/4}$.

In reality, most, if not all chemical reactions are reversible. It is shown by Chopard, Droz,Karapiperis and Racz[5] that the reversible A+B<--->C reaction-diffusion process can be described in terms of a crossover between an **irreversible** regime at short times and a **reversible** regime at long times. In the **reversible** regime, due to local equilibrium, the dynamics is governed by the diffusion process and the critical exponents are correctly given by the mean-field approximation, $w \sim t^{1/2}$, $R(x_f,t) \sim$ constant (independent of the dimension). The crossover time t is inversely propotional to the backward reaction constant.

EXPERIMENT

To study the long-time behavior of the A+B→C and A+2B→C reactions, the following criteria must be met. First, the reaction must have the right stoichiometry and, second, the reaction must be diffusion-limited.

Disodium ethyl bis(5-tetrazolylazo) acetate trihydrate **tetra** forms both a 1: 1 complex and 2:1 complex with a varity of caions[6]. We use

$$Cu^{2+} + \text{tetra} \rightarrow \text{1:1 complex}$$

to study the A+B→C case and use

$$Ni^{2+} + 2tetra \rightarrow 1{:}2\ complex$$

to study the A+2B→C case.

Optical measurements are used to monitor the dynamic quantities of the reaction [7,8]. A computerized system is used for this purpose (Fig 1). The system consists of a halogen lamp, a solenoid with two filters , a PMT, and a stepping motor. The on-off of the lamp and solenoid are controlled through the parallel port of the computer and the movement of the stepping motor is controlled via a stepping motor controller. The light source, solenoid with two filters, slit unit and detector are moved together by the stepping motor and the glass reactor is fixed over the slit unit separated from all other units. The PMT is connected to the a/d board of the computer to convert the analog data into digital data and then to be stored by a computer.

Reactions were run in a 4x2 mm rectangular glass reactor at room temperature. The two reactants were injected from the opposite ends of the reactor. The reactants meet and form a sharp boundary at t=0. The first scan along the reaction front starts immediately after the reactants meet. Each scan takes about 3 seconds to complete. The spatial resolution of the experiment is 0.1 mm. Consecutive scans of the tetra and the product profiles are taken over a course of one run. The time interval between scans increases from the order of 5 minutes to the order of 30 minutes during each run. The profiles of absorbance versus position x are obtained at different times.

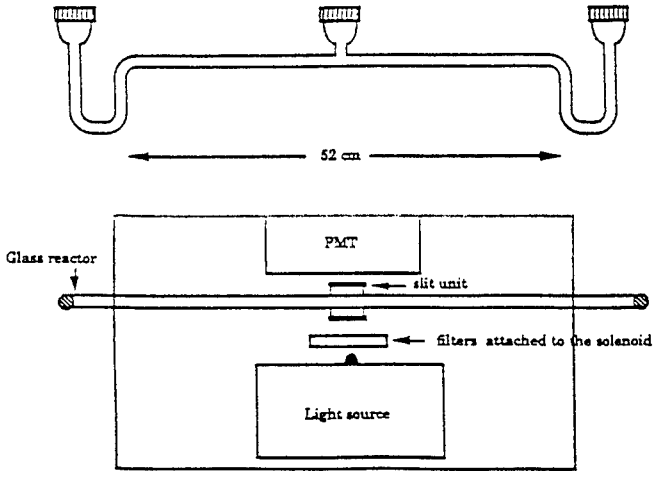


Fig. 1 Top view of the experimental set-up for absorbance measurement

RESULTS AND DISCUSSION

We obtain optical absorbance of the accumulated product measured at a fixed time interval. From the differences of absorbances of the total product measured at consective times we manipulate the time exponents. To determine the time exponent for width we plot width vs time on a log-log scale. The global rate is determined from the baseline corrected integrated area of the differential peak, divided by the appropriate time interval. We calculated the time exponent for the global rate by plotting ln (global rate) vs ln t . The local rate exponents were obtained form subtraction of the width component from the global rate component.

For the A+B→C case our data showed a clear crossover for the time exponent at around 250 minutes (Fig 2,3). The expoents are listed in Table I.

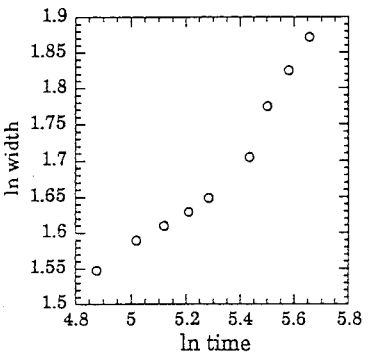


Fig.2 ln width vs ln t for A+B→C case

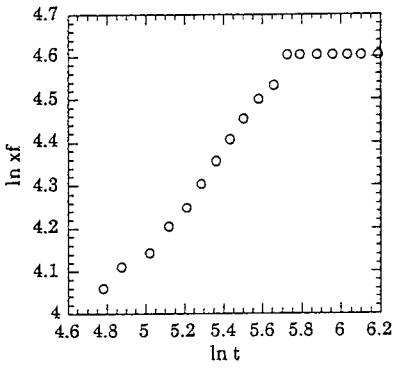


Fig.3 ln xf vs. ln t for A+B→C case

Table I

	width		center of the front		global rate	
	early	late	early	late	early	late
Experimental	0.24	0.51	0.55	0	-0.40	0.55
Theoretical	0.17	0.50	0.50	0	-0.50	0.50

For the A+2B→C case, using the linear fits for Fig 4 and Fig 5, we obtained exponents for the width and global rate to be 0.266 and 0.449, respectively, which is consistent with the prediction from the scaling argument (0.25,0.5).

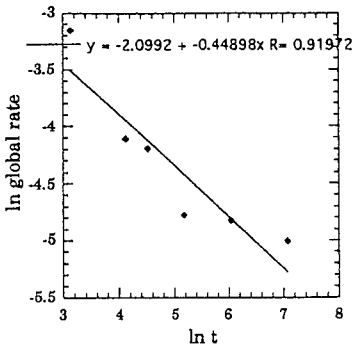


Fig.4 ln global rate vs ln t for A+2B→C case

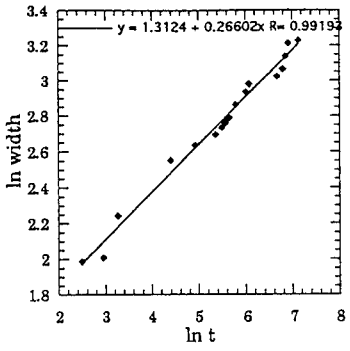


Fig. 5 ln width vs. ln t for A+2B→C case

The local rate exponent is difficult to measure directly but can be derived from the exponent of width and global rate. The experimental exponent for the local rate is 0.72 compared to 0.75 predicted by theory.

CONCLUSION

We studied experimentally the reaction front dynamics for both A+B→C and A+2B→C type reactions with initially separated components. We found both systems to have non-classical nature, they do not follow mean field behavior. Also we confirm the reversibility on the dynamics for the A+B→C case. We hope that the understanding of reaction diffusion system like this will help us to understand more complicated phenomena, such as pattern formation and oscillating chemical systems.

ACKNOWLEDGEMENT

We appreciate support from NSF Grant No. DMR-91-11622. We thank Dr. Steve Parus for helping with the experimental design and Anna Lin for helpful discussions.

REFERENCE

1. J. D. Murray, *Mathematical Biology*. Biomathematics

(Springer_Verlag, 1993), vol. 19.
2. H. K. Henisch, *Crystals in Gels and Liesegang Rings*. (Cambridge University Press, Cambridge, 1988).
3. L. Galfi, Z. Racz, *Physical Review A*, **38**, 3151-3154 (1988).
4. S. Cornell, M . Droz, B. Chopard, *Physical Review A*, **44**, 4826-4832 (1991).
5. B. Chopard, M . Droz, T. Karapiperis and Z. Racz, *Physical Review E*, R **40**, (1993)
6. H. Jonassen, V. Chamblin, V. Wagner, Jr and R.Henry, *Anal. Chem.*,**30**, 1660 (1958).
7. Y.-E. L. Koo, R. Kopelman, *Journal of Statistical Physics*, **65**, 893-918 (1991).
8. Y.-E. Koo, R. Kopelman, *Israel Journal of Chemistry*, **31**, 147-157 (1991).

DYNAMIC LIGHT SCATTERING IN 5CB CONFINED IN DISORDERED POROUS MEDIA

FOUAD M. ALIEV, VLADIMIR V. NADTOTCHI
Department of Physics and Materials Research Center, PO BOX 23343, University of Puerto Rico, San Juan, PR 00931-3343, USA

ABSTRACT

We performed dynamic and static light scattering measurements in nematic LC (5CB) confined in silica porous glasses with average pore sizes of 1000 Å (volume fraction of pores 40%) and 100 Å (27%). The experiments show significant changes in physical properties of confined LC. Nematic-isotropic phase transition temperature T_{NI} is depressed by $0.6°C$ in 1000 Å pores compared to that bulk value and this phase transition was not detected at all in 100 Å pores. We found that even about $20°C$ below bulk melting temperature the relaxational processes in confined LC were not frozen. Slow relaxation process which does not exist in the bulk LC and wide spectrum of relaxation times $(10^{-8} - 10)s$ appear in both 100 Å and 1000 Å. In 100 Å pores slow relaxation exists even at T corresponding to the bulk isotropic phase. Our data can not be described using the standard form of dynamical scaling variable (t/τ) but they obey activated dynamical scaling with the scaling variable $x = lnt/ln\tau$.

INTRODUCTION

Investigations of condensed matter in porous matrices have revealed various new properties and effects not observed in the same substances when they are in the bulk [1-8]. The difference between the surface and bulk properties, as well as finite size effects, are manifested most strikingly in the case of liquid crystals (LC) [9-13].

While the physics of the light scattering in isotropic and nematic phases of the bulk liquid crystal are well understood, the origin of fluctuations responsible for light scattering of the same liquid crystals confined in random porous matrices is very far from more or less complete explanation. In the isotropic phase of liquid crystals the intensity/intensity autocorrelation function $g_2(t)$ of depolarized component of scattered light is determined by order parameter fluctuations [14] and the corresponding decay is single exponential with relaxation time $\sim (10^{-7} - 10^{-8})s$.

In the nematic phase the main contribution to the intensity of scattered light is due to the director fluctuations [14] and in the monodomain, uniformly oriented nematic sample, there are two modes determined by these fluctuations. The first mode is determined by a combination of splay and bend distortions and the second mode by a combination of twist and bend distortions, and each of these modes is described by single exponential decay function. The corresponding relaxational processes are described [14] by the macroscopic equations of nematodynamics. The relaxation times in dynamic light scattering experiment are determined by visco-elastic properties of nematic liquid crystal, the geometry of an experiment and light polarization, and are of same order of magnitude $\sim 10^{-5}s$ for both modes. Since the investigation of the dynamics of the bulk liquid crystal is not our purpose and we discuss bulk properties only in order to stress the difference between dynamics in pores and in the bulk, we do not need rigorous consideration of the dynamic light scattering in the nematic phase. If for the simplicity we assume that six Leslie coefficients have the same order of magnitude and are $\sim \eta$ (η is an average viscosity), and three elastic constants (bend, splay and twist) are equal (K) then the relaxation time is $\tau = \eta/Kq^2$ ($q = 4\pi n \sin(\Theta/2)/\lambda$, n is refractive index, and Θ - a scattering angle).

At the moment of the completion of this paper just three papers [11-13] on the investigations of the confined liquid crystals by dynamic light scattering were published. In the first

Mat. Res. Soc. Symp. Proc. Vol. 407 © 1996 Materials Research Society

study [11] of the nematic ordering of the liquid crystal 8CB in sintered porous silica by the dynamic light scattering (and elastic light scattering) the results obtained at the nematic-isotropic phase transition in silica gel were explained on the basis of the gel imposing a random uniaxial field on the liquid crystal. The equilibrium phase transition is smeared out by the randomness, and dynamically the system exhibits [11] the kind of self-similarity that is associated with the conventional random-field behavior, it was found that liquid crystal shows orientational glasslike dynamics near the nematic-isotropic phase transition. The major mechanism which determines the observed temporal fluctuation of the intensity of scattered light is the order parameter fluctuations. These fluctuations in the nematic like state are very slow and glasslike.

In the most recent investigation [13] of the dynamic properties of 8CB in an aerogel host by dynamic light scattering the observed dynamic behavior was different from this in sintered porous silica [11], nevertheless according to Bellini *et al* [13] the spin glass interpretation given by these authors [13] and the random field interpretation given by Wu *et al* [11] are consistent if the geometrical differences between two matrices are taken into account.

There are at least two factors influencing on the dynamics of fluids or liquid crystals in confinement: surface interaction and geometrical effects. The confinement can break the symmetry of the bulk phase, and change viscosity, that can lead to a modification of dynamics.

In this paper we present the results of investigations of the influence of the confinement and interface on dynamic behavior of nematic liquid crystal impregnating random porous matrices with pore sizes of 100 Å and 1000 Å by photon correlation spectroscopy. Since the volume of this paper is limited we restrict our consideration in the main by consideration of results obtained for 100 Å pores. We present for comparison purposes some data on investigations of nematic liquid crystal in 1000 Å pores. Complete results of these investigations will be published separately.

EXPERIMENTAL

We performed photon correlation measurements using a 6328 Å He-Ne laser and the ALV-5000/Fast Digital Multiple Tau Correlator (real time) operating over delay times from 12.5 ns up to 10^3 s with the Thorn EMI 9130/100B03 photomultiplier and the ALV preamplifier. In addition we used ALV/LSE unit which allows simultaneously with photon correlation measurements monitoring of the laser beam intensity and stability of its space position as well as the intensity of scattered light integrated over all frequencies (static light scattering). Depolarized component of scattered light was investigated. Observation of the depolarized component of the scattered light makes it possible in the isotropic phase of bulk liquid crystal to detect the contribution connected with order parameter fluctuations only, and for LC in pores blocks out the scattering from the fixed matrix structure. The temperature of the samples was stabilized and measured with accuracy better than 20mK.

Porous matrices with thoroughly interconnected and randomly oriented pores with average pore size of 1000 Å (volume fraction of pores 40%) and 100 Å (27%) respectively, were prepared from the original sodium borosilicate glasses . The sodium borate phase was removed by leaching, and the matrix framework consisted of SiO_2. The nematic liquid crystal we used was pentylcianobiphenyl (5CB). The phase transition temperatures of 5CB in the bulk are $T_{CN} = 295K$ and $T_{NI} = 308.27K$. Empty matrices were heated to $450°C$ and pumped out; this was followed by the impregnation with the liquid crystals from an isotropic melt. In dynamic light scattering experiments we used a 100 Å porous glass plates of dimensions 1cm × 1cm × 0.2cm, all surfaces of the matrices were optically polished. The polishing procedure was performed in two stages: The glass plate was first polished before leaching, and then it was polished additionally after the porous structure was formed. Since the linear size of optical inhomogeneities as determined by the pore size is much smaller than the wavelength of visible light, the matrix was optically transparent. In the case of 1000 Å pore matrices, which are opaque, in order to reduce the contribution from multiple scattering, the thickness of the samples was 0.2 mm.

DYNAMIC LIGHT SCATTERING

First of all from static light scattering experiments we obtained that the nematic - isotropic phase transition in 1000Å pores is smeared out, transition is not as sharp as in the bulk LC, it occupies finite temperature region, and the temperature of this transition is depressed by $0.6°C$ compared to that bulk value. In 100 Å pores there is no well defined phase transition from ordered phase to the phase in which long range order is completely absent, or opposite from disordered phase to the phase with perfect long range orientational order.

The difference between the dynamic behavior of bulk nematic multidomain 5CB and 5CB in 1000 Å as well as in 100 Å pores can be seen by comparison of curves (1) (2) and (3) in Fig. 1.

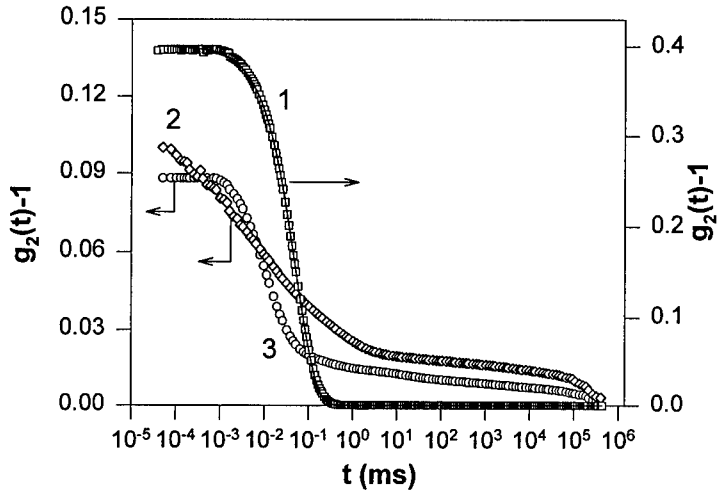


Figure 1: Intensity/intensity autocorrelation functions for 5CB: 1 - bulk nematic phase (opened squares-experimental data), 294.61 K, solid line - fitting according to the equation (1); in pores (experimental data): 2 - 5CB in 100 Å pores, 295.84 K; 3 - 5CB in 1000 Å pores, 294.77 K.

For multidomain liquid crystal in nematic phase observed correlation function slightly deviated from single exponential, and best fitting was provided by stretched exponential decay function

$$g_1(t) = a \cdot exp(-(t/\tau)^{\beta}), \tag{1}$$

with $\beta = 0.95$, and $\tau = 5.3 \cdot 10^{-5}s$. This small deviation of β from 1 is due to the fact that we used multidomain sample and the contribution from both modes is present. The relaxation time $\tau = 5.3 \cdot 10^{-5}s$ which corresponds to the curve 1 (Fig. 1) is in agreement with the theory [14]. It is clear from the Fig. 1 that the relaxation processes of 5CB in both 100 Å and 1000 Å matrices are highly nonexponential.

Slow relaxational process which does not exist in the bulk LC and broad spectrum of relaxation times $(10^{-8} - 10)s$ appear for 5CB in both 100 Å and 1000 Å (Fig. 1). It is clear that the data for 5CB in pores can not be described using the standard form of dynamical

scaling variable (t/τ). It is reasonable for so slow dynamics and such a wide spectrum to use ideas of activated dynamical scaling with the scaling variable $x = lnt/ln\tau$. We are not able to find the correlation function (or superposition of correlation functions) known from previous publications which would satisfactorily describe the whole experimental data from $t = 10^{-5}ms$ up to $t = 10^{5}ms$. However we found that in the time interval $10^{-3}ms - 10^{3}ms$ (6 decades on the time scale) and the temperature range (280 - 301)K autocorrelation function:

$$g_1(t) = a \cdot exp(-x^z), \tag{2}$$

where $x = ln(t/\tau_0)/ln(\tau/\tau_0)$, and in our case $\tau_0 = 10^{-8}s$ provides the best fitting for 5CB in micropores compared to other conventional decay functions. We assume that for 5CB in pores we measure heterodyne signal, and $(g_2(t) - 1)/f(A) = g_1(t)^2$.

The correlation functions for 5CB in 100 Å pores corresponding to different temperatures and the examples of fitting the data by decay function (2) are presented in the Fig. 2.

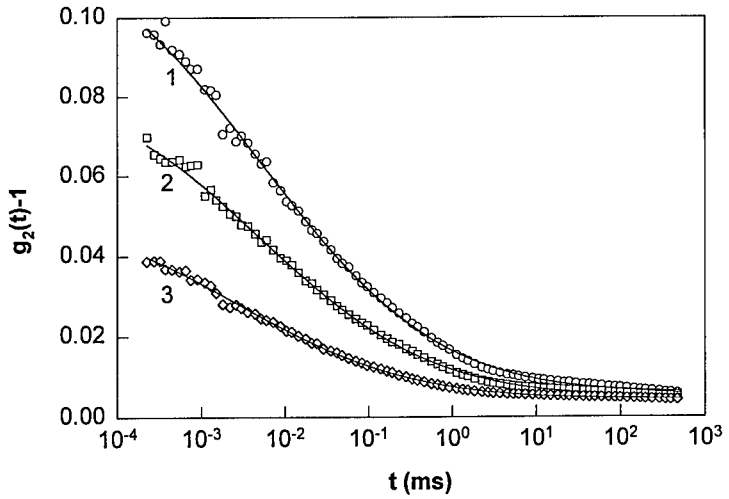


Figure 2: Autocorrelation functions for 5CB in 100 Å pores measured at different temperatures. 1 - T=296.08 K, 2 - T=297.17 K, 3 - T=299.75 K. Solid lines show fitting using the correlation function according to the equation (2) with the parameters (1): z=2.23, τ=0.49 ms; (2): 2.28, 0.42 ms; (3): 2.14, 0.26 ms.

The parameters z for the curves in the Fig. 2 are about 2. We found that even about $20°C$ below bulk melting temperature the relaxational processes in confined LC (both in 100 Å and 1000 Å pores) were not frozen while the amplitude of decay function $g_1(t)$ decreases with decreasing temperature. The relaxation time of slow process for 5CB in 100 Å pores strongly increases when temperature decreases from 300 K up to 280 K variing from 1.3×10^{-4} s to 0.08 s in this temperature range. The temperature dependence of relaxation times obtained using correlation function (2) in the temperature interval (283-301)K is described by the Vogel-Fulcher law [15]:

$$\tau = \tau_0 exp(B/(T - T_0)), \tag{3}$$

which is characteristic of glass-like behavior. These relaxation times were q independent at all temperatures under investigation.

The parameters for 5CB in 100 Å in formula (3) are: $\tau_0 = 1.45 \cdot 10^{-7}s$, $B = 469K$ and $T_0 = 247K$.

At temperatures above $\simeq 302K$ the relaxation process separates into two processes, and this separation become more clear with further temperature rise (Fig. 3).

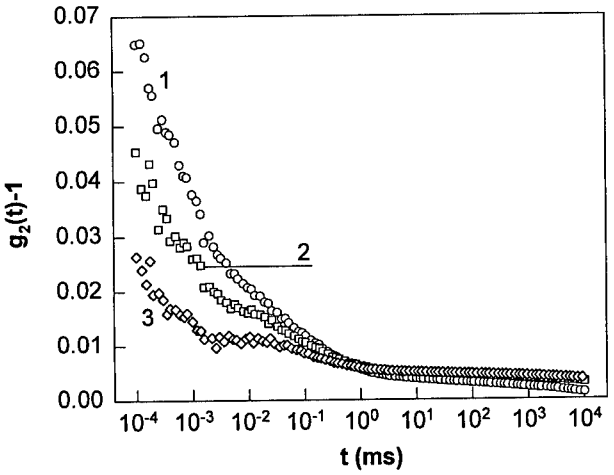


Figure 3: Autocorrelation functions for 5CB in 100 Å pores measured at different temperatures, 1 - T=301.35 K, 2 - T=302.05 K, 3 - T=303.12 K.

In 100 Å pores the slow relaxational process exists even at temperatures corresponding to the bulk isotropic phase, but first (fast) process dominates.

We attribute the first (fast) decay in 100 Å pores which is clearly seen at the temperatures above 301 K to fluctuations of order parameter. This decay dominates at high temperatures. The amplitude of the slow decay, which dominates at low temperatures decreases with increasing temperature and is almost independent at temperatures corresponding to the bulk isotropic phase.

In 1000 Å pores we observed two decays at temperatures below nematic-isotropic phase transition temperature in pores. The first part ($t \leq 1ms$) of the correlation function in Fig. 1 (curve 3) can be described by the decay function (2) with $\beta \simeq 0.9$ and $\tau \simeq 0.02ms$. This first relaxation time is weakly temperature dependent. The detailed analysis of dynamic behavior in pores of different sizes, shape and structure will be published separately. We would like to note that nevertheless first decay weakly depends on temperature it immediately vanishes when liquid crystal is in isotropic phase. The slow decay also vanishes at temperatures corresponding to isotropic phase in 1000 Å pores, and very fast decay, typical for relaxation of order parameter in the bulk isotropic phase appears, with relaxation time $\tau \sim 10^{-8}s$. Thus slow decay in both pores is connected with existence of nematic (or nematic like in 100 Å pores) ordering. Since in pores surface induced nematic ordering exists even at sufficiently high temperatures the slow decay also exists at temperatures corresponding to the bulk isotropic phase. One of additional possible explanations (together with picture suggested in [11,12] and domain picture [13]) may be formation of interfacial layers on the pore wall. The thickness (that means and volume fraction) of these layers should be temperature dependent and achieves its minimum magnitude in isotropic phase. The minimum thickness may be equal to the thickness of monolayer. In 1000 Å pores the volume fraction of first layer formed on the pore wall is very small and due to this reason it is not detected in the dynamic light scattering experiment. In 100 Å pores even if the thickness of the interfacial layer is about of molecular length $\simeq 20$ Å the volume fraction of this layer

is big enough (note that pore size is only 100 Å) to provide sufficient contribution to the intensity of scattered light and its temporal fluctuations. The temperature dependence of slow relaxation time which is typical for glass-like behavior is of that kind just simply because liquid crystal does not crystalize in 100 Å in the temperature range under investigation.

CONCLUSION

The static and dynamic light scattering experiments show significant changes in physical properties of liquid crystals confined in random porous media. Nematic-isotropic phase transition temperature T_{NI} of 5CB is depressed by $0.6°C$ in 1000 Å pores compared to that bulk value and this phase transition was not detected at all in 100 Å pores. Slow relaxation process which does not exist in the bulk LC and wide spectrum of relaxation times $(10^{-8} - 10)s$ appear in both 100 Å and 1000 Å. Temperature dependence of corresponding relaxation times is described by the Vogel-Fulcher law which is a characteristic of glass-like behavior. The slow dynamics detected by dynamic light scattering and extremely wide spectrum of relaxation times still remain unexplained and further systematic investigations are needed.

ACKNOWLEDGEMENTS

Discussions and conversations with N. Clark, D. Finotello, W. Goldburg, O.D. Lavrentovich, C. Rosenblatt, X.-l. Wu, and S. Zumer are gratefully acknowledged by F.M.A.

This work was supported by US Air Force grant F49620-95-1-0520 and DOE-EPSCoR grant DE-FG02-94ER75764.

REFERENCES

1. D.D. Awschalom, J.Warnock, Phys.Rev.,**B35**, 6779 (1987).
2. Molecular Dynamics in Restricted Geometries, edited by J. Klafter and J.M. Drake (Wiley, New York, 1989).
3. J.M. Drake, J. Klafter, Physics Today **43**(5), 46, (1990).
4. C.L. Jackson and G. McKenna, J.Chem.Phys., **93**, 9002, (1990).
5. G. Liu, Y.Li, J. Jonas, J.Chem.Phys., **95**, 6892, (1991).
6. P.A. Thompson, G.S. Grest, Phys.Rev.Lett.,**68**, 3448, (1992).
7. M.C. Goh, W.I. Goldburg, Ch.M. Knobler, Phys.Rev.Lett., **58**, 1008, (1987); S.B. Dierker, P. Wiltzius, ibid.,**66**, 1185, (1991); B.J. Frisken, D.S. Cannell, ibid.,**69**, 632, (1992).
8. F.M. Aliev, W. Goldburg, X-l. Wu, Phys.Rev.E. **47**, R3874, (1993).
9. D. Armitage, F.P. Price, Chem.Phys.Lett., **44**, 305 (1976), MCLC, **44**, 33, (1978), M. Kuzma, M.M. Labes, ibid., **44**, 100, (1983); G.S. Iannacchione, G. Crawford, S. Zumer, J.W. Doane, D. Finotello,Phys.Rev.Lett., **71**, 2595, (1993); S.Tripathi, C. Rosenblatt, and F.M. Aliev, Phys.Rev.Lett., **72**, 2725, (1994); F.M. Aliev, MCLC, **243**, 91, (1994); F.M. Aliev, J. Kelly, Ferroelectrics, **151**, 263, (1994).
10. T. Bellini, N.A. Clark, Ch.D. Muzny, L.Wu, C.W. Garland, D.W. Schaefer, B.J. Oliver, Phys. Rev.Lett., **69**, 788, (1992).
11. X-l. Wu, W.I. Goldburg, M.X .Liu, J.Z. Xue, Phys.Rev.Lett., **69**, 470, (1992).
12. W.I. Goldburg, F.M. Aliev, X-l. Wu, Physica A **213**, 61, (1995).
13. T. Bellini, N.A. Clark, D.W. Schaefer, Phys. Rev.Lett., **74**, 2740, (1995).
14. P.G. de Gennes and J. Prost, The Physics of Liquid Crystals (second ed.), Clarendon Press, Oxford, 1993.
15. G. Williams, J. Non-Cryst. Solids.**131-133**, 1 (1991).

Brillouin Light Scattering Determination of the Glass Transition in Thin, Freely-Standing Poly(styrene) Films

J.A. Forrest, K. Dalnoki-Veress, J.R. Dutcher, A.C. Rowat and J.R. Stevens

Department of Physics and Guelph-Waterloo Program for Graduate Work in Physics, University of Guelph, Guelph, Ontario, Canada N1G 2W1

Abstract

We have used Brillouin light scattering (BLS) to measure the glass transition temperature of thin, freely-standing poly(styrene) (PS) films. The freely-standing films were prepared by spincoating solutions of PS in toluene onto glass substrates, annealing the supported films in vacuum, and then using a water surface transfer technique to place the films across a 3 mm diameter orifice. Ellipsometry measurements of similar floated films transferred to Si(001) wafers allow the determination of the film thicknesses. Atomic force microscopy measurements revealed that the films have an rms roughness of less than 10 Å. With the freely-standing films placed in an optical furnace, we performed BLS measurements of the films using a high-contrast, multipassed, tandem Fabry-Perot interferometer. We obtained a reliable, reproducible measure of the glass transition temperature, T_g, from the large changes in the frequencies of the thermally-excited, viscoelastic, film-guided waves within the PS films as the films were heated above T_g. BLS results for bulk PS and a 1800 Å thick, freely-standing PS film are presented. We find the same glass transition temperature for the 1800 Å thick film as the bulk PS sample. This T_g value is the same as that obtained using differential scanning calorimetry (DSC).

Introduction

One of the fundamental properties of a polymer is its glass transition temperature, T_g. At temperatures below this value the polymer is hard and glassy, while above this temperature the material is soft and rubber-like. A number of different techniques have been employed to measure this glass-rubber transition in polymer samples. Some techniques, such as DSC and differential thermal analysis (DTA) involve measurement of changes in the thermal properties of the polymer as the temperature is varied to detect the transition. Other techniques, such as rheology and ultrasonics, involve the measurement of changes in the viscoelastic properties. Given samples with equivalent thermal histories, these methods, under the same heating or cooling rate, give the same value for T_g[1]. All of the above techniques are restricted to measure the glass transition of bulk samples.

Recently, much attention has been focussed on the properties of polymers confined to a thin film geometry. Thin films have a large surface area to volume ratio and surface energetics can play an important role in determining the physical properties of the film. Beaucage *et al.*[2] have shown that ellipsometry, traditionally used only to measure the film thickness, can also be used to measure T_g of thin polymer films. More detailed ellipsometric studies by Keddie *et al.*[3] on poly(styrene) (PS) films of varying thickness have shown that

Mat. Res. Soc. Symp. Proc. Vol. 407 © 1996 Materials Research Society

T_g of thin ($h \leq 500$Å) films spincoated onto Si substrates is lower than T_g of bulk PS. Extension of the technique to other polymers and substrate surfaces revealed that the sign and magnitude of the change in T_g relative to its bulk value depends rather strongly on the substrate used[4]. This is due to the different energetics contributed by the polymer-air, and polymer-substrate interactions. An obvious, but technically challenging, way to avoid this problem is to eliminate the substrate and measure the glass transition temperature of freely-standing films.

Brillouin light scattering (BLS) has been used previously to probe the high frequency viscoelastic properties of polymers. Study of the temperature dependence of the acoustic phonon frequencies gives rise to another successful technique for measuring the glass transition temperature of bulk samples[5]. BLS has also been used to study supported [6],[7] and freely-standing[8] thin films by observing light scattering from the various guided acoustic modes. The thin film acts as an acoustic waveguide, allowing propagation of those modes satisfying the mechanical boundary conditions at both film surfaces. By examining these modes as the temperature is varied, one can identify the glass transition of thin polymer films. The application of BLS to measure T_g for PS films supported on Si substrates has been considered previously by Dutcher *et al.*[9]. In the supported films, the glass transition is marked by a dramatic increase in the phonon linewidth as the temperature is raised above T_g. A limitation of this technique is that for films with thicknesses much less than the phonon wavelength ($\lambda \simeq 3000$ Å), the properties of the waves are dominated by the substrate, and changes in the mechanical properties of the very thin films are difficult to detect. In this paper we report using BLS to measure the glass transition temperature in thin, freely-standing films of PS. To the best of our knowledge, these are the first measurements of T_g for thin, freely-standing polymer films.

Experimental

The freely-standing polymer films were prepared using the spin coating technique. Solutions of various concentrations of PS in toluene were prepared. The anionically polymerized PS, obtained from Polymer Source Inc, had $M_w = 691,000$ with $M_w/M_n = 1.11$. A few drops of solution were placed on a cleaned glass microscope slide. The slide was then spun at 4000 rpm for 30 s. The resulting films on glass were annealed in vacuum at 110°C for 12 hours and then cooled slowly (≤ 1°C/s) by turning off the oven. While this does not produce a constant cooling rate, it is the same for all samples studied. The annealed films were then cut with a sharp blade into squares of approximately 1 cm^2 and floated off the glass slides onto a distilled water surface. A square of the floating film was deposited onto a PS coated stainless steel sample holder with a 3 mm orifice in the centre. Samples of the floating film were also transferred to Si wafers so that their thicknesses could be determined using ellipsometry. The surface roughness of the supported films was investigated using atomic force microscopy (AFM). Floated films transferred onto Si appeared to be of comparable quality to films directly spun onto Si wafers. We observed the appearance of several large cracks on these films upon transferring to the Si wafers. Optical microscopy investigations of the freely standing films reveal no such cracking. AFM investigation of films floated onto Si show no cracks at smaller length scales, and an rms surface roughness of less than 10 Å. The freely-standing films were dried in air at 50°C for up to 8 hours to remove any adsorbed water. Once dried, the films were examined visually to ensure that there were no holes.

Measurement of the high frequency, film-guided, acoustic modes in the freely-standing

films were performed using a high contrast, tandem (3+3 passes), Fabry-Perot interferometer. p-polarised light from an Ar^+ laser was focussed onto the sample using a 50 mm, f/2 camera lens. The diameter of the focussed light spot on the sample was $20\mu m$. The unpolarised scattered light was collected using the same camera lens in a 180° backscattering geometry. The angle of incidence of $\theta_i = 45°$ gives a phonon wavevector $Q_{||} = 1.73 \times 10^5$ cm^{-1}. The free spectral range of the interferometer was 10 GHz. For bulk PS samples the free spectral range was 20 GHz. The quality of the sample at the focussed light spot could be inferred from an inspection of the specularly reflected light spot. Reflections from smooth areas of the film gave a well-defined circular spot. The sample was placed in an optical furnace[9], and the sample temperature was monitored using a Copper/Constantan (type J) thermocouple junction. All data were collected by heating the films from room temperature through the glass transition temperature. Each BLS spectrum was collected at constant temperature, for about 500 s. If the temperature changed by more than 0.5 °C during the measurement, the spectrum was aborted. The maximum heating rate during the collection of a BLS spectrum is thus 0.001 °C/s. The heating rate between different temperatures used for the BLS measurements is much greater but it is still less than 1°C/min.

Results and Discussion

The use of BLS to measure the glass transition in bulk polymers is well known.[5] We studied the temperature dependence of the bulk longitudinal phonon frequency for comparison with the thin film results. In figure 1(a) we show the frequency of the longitudinal phonon in bulk PS as a function of temperature. There are clearly two different linear regions between frequency and temperature. The slope of the low temperature region is 1.3×10^{-2}GHz/°C, and that of the high temperature region is 3.7×10^{-2}GHz/°C. We take the intersection of these two lines as a measure of the glass transition temperature T_g. For this sample we find $T_g = 97 \pm 2$°C. We measured T_g for two identical bulk samples using two different laser powers to ascertain the magnitude of laser heating produced by the focussed laser light. No such heating could be detected. The T_g value determined using BLS is the same as that measured using DSC on a sample of the same polymer with the same annealing history, and heating rate.

The acoustic modes probed in BLS measurements of thin films are guided by reflections from the film surfaces. The particle displacements of these modes are of mixed polarisation, i.e. partially longitudinal, and partially transverse. For an unsupported film, the modes (called Lamb modes) are split into two groups. Antisymmetric (A) Lamb modes have a longitudinal component antisymmetric about the central plane of the film, and a symmetric transverse component. Symmetric (S) Lamb modes have the opposite symmetry. The lowest frequency mode is the first antisymmetric mode (A_0). As $Q_{||}h$ is decreased below 2, the frequency of the A_0 mode approaches zero. In contrast the frequency of the second lowest frequency mode (S_0) approaches a value determined by the longitudinal sound velocity of the film. Particle displacements for the S_0 mode are primarily longitudinal for small values of $Q_{||}h$. Because of its longitudinal character, changes in the S_0 mode frequency with temperature are likely to resemble the bulk longitudinal phonon measurements. An additional advantage of studying the first symmetric mode is that for small $Q_{||}h$, the frequency of this mode has very little variation with $Q_{||}h$. This makes the measured frequency insensitive to the occasional fluctuations in the angle of incidence which sometimes occur with thin, freely-standing films.

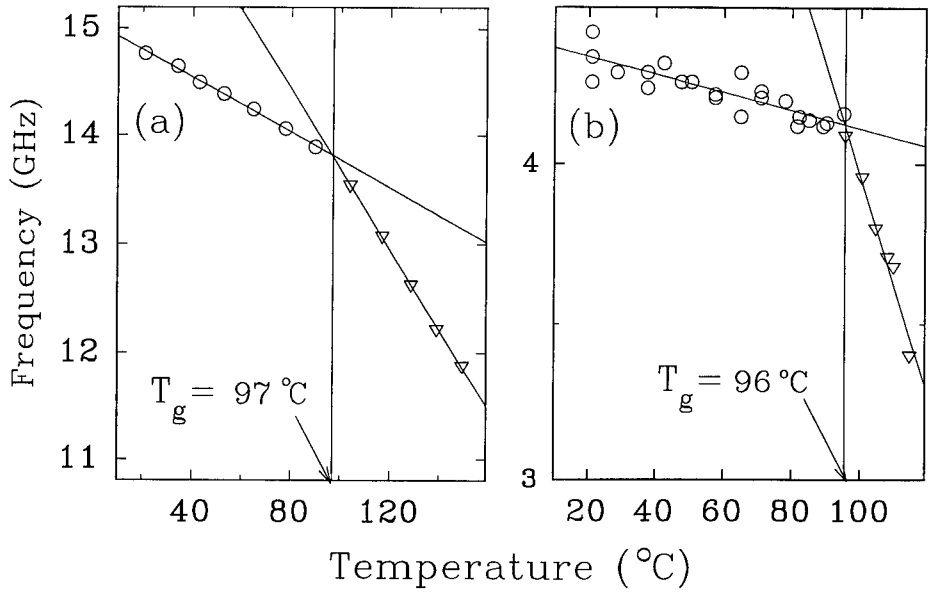


Figure 1: Temperature dependence of the longitudinal phonon frequency in bulk PS (a), and the S_0 mode frequency of a 1800 Å thick PS film (b).

The frequency shift of the first symmetric Lamb mode (S_0) as a function of temperature for a 1800 Å PS film is shown in figure 1(b). For temperatures less than 95°C there is a very small but linear shift with temperature (2.9×10^{-3}GHz/°C). To check the uniformity of the sample, BLS spectra were collected for a number of different spots on the film. The small spot-to-spot variation in the S_0 frequency is the main reason for the scatter in the low temperature data of figure 1(b). The small magnitude of this scatter implies that the thickness and mechanical properties of the film are uniform across the film plane. For $T > 96$°C, there is a much larger change in the frequency shift with temperature. The slope of this high temperature line is 3.5×10^{-2}GHz/°C. As in the case of bulk PS, the large contrast between the slopes of the two linear regions allows us to obtain an accurate measure of the glass transition temperature, T_g. For the 1800 Å film we find $T_g = 96 \pm 2$°C. This T_g value is the same as that measured for bulk PS.

Not surprisingly, we find that the films develop small holes when held at temperatures above T_g. The rate at which these holes develop increases with increasing temperature. At temperatures greater than 30°C above T_g hole formation is so rapid that BLS spectra cannot usually be acquired before film rupture. For this reason, it is necessary to collect data points with a small enough temperature difference that a sufficient number of points are obtained in the high temperature region for a convincing linear fit. For the 1800 Å thick film, BLS spectra could not be acquired for $T \geq 130$°C.

Interestingly, the ultimate rupture of the freely-standing rubber-like film is not the phenomenon limiting the collection of data at these high temperatures. For temperatures $T > T_g$ the relative intensity of the modes changes dramatically, and for $T - T_g > 20$°C , the intensity

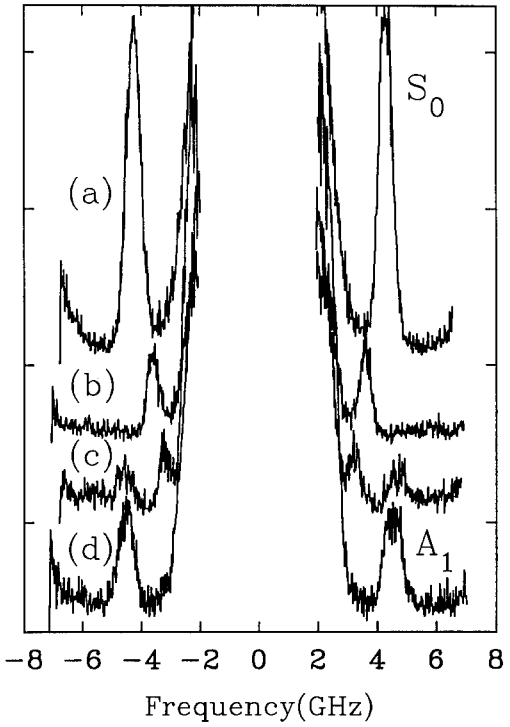


Figure 2: BLS spectra of a 1800 Å freely-standing film. Sample temperatures are from top to bottom, (a) 21 °C, (b) 109.7 °C, (c) 114.5 °C and (d) 117.5 °C.

of the S_0 mode decreases such that it is no longer observable. Representative BLS spectra at three temperatures near T_g, as well as the room temperature spectrum, are shown in figure 2. The room temperature BLS spectrum is dominated by the S_0 peak at $\simeq$ 4.5 GHz. For a 1800 Å thick film, the A_0 mode frequency is so low that it is obscured by the central elastic peak. The measured linewidth of $\simeq$ 1 GHz is substantially larger than the 0.4 GHz instrumental linewidth. The peak broadening is caused by the large spread in scattering wavevectors due to the large light collection aperture. This effect can be minimised by inserting a rectangular slit in the optical path[10]. Spectrum (b) is also dominated by the S_0 mode. The difference in intensities between spectra (a) and (b) is simply a result of shorter data acquisition times used when the sample temperature is greater than T_g. Spectrum (c) ($T - T_g \simeq 20°C$) also exhibits the S_0 mode, but the higher frequency A_1 mode is almost of equal intensity. In spectrum (d) of figure 3 ($T - T_g \simeq 22°C$) the S_0 mode has been reduced in intensity, as well as shifted downward in frequency, such that the mode is no longer observed. At all higher temperatures only the A_1 peak can be resolved.

Summary

We have succesfully made freely-standing films of PS with thicknesses $h \simeq 2000$Å. Using BLS to measure the temperature-dependent viscoelastic modes of the films allows us to obtain a well-defined, reproducible value for the glass transition temperature T_g. The value of T_g for a 1800 Å thick film was found to be the same as that of bulk PS. Extension of this technique to smaller film thicknesses is currently under investigation.

Acknowledgements

We would like to thank Paul Smith at the Xerox Research Centre of Canada for the AFM measurements, and Waterloo Digital Electronics for ellipsometry measurements. Financial support from the Natural Sciences and Engineering Research Council of Canada (NSERC) is gratefully acknowledged.

References

[1] J. Tatibouet and L. Piche, Polymer **32**, 3147-3151 (1991).

[2] G. Beaucage, R. Composto, and R.S. Stein, J. Poly. Sci: Part B: Polymer Physics, **31**, 319-326 (1993).

[3] J.L. Keddie, R.A.L. Jones and R.A. Cory Europhysics Letters **27** (1), 59-64 (1994).

[4] Joseph L. Keddie, Richard A.L. Jones and Rachel A. Cory Faraday Discussions, **98**, 219-230 (1994).

[5] J.R. Stevens, R.W. Coakely, K.W. Chau and J.L. Hunt, J. Chem. Phys. **84**, 1006-1014 (1986).

[6] G.W. Farnell and E.L. Adler, in *Physical Acoustics, Principles and methods*, edited by W.P. Mason and R.N. Thurston (Academic, New York, 1972), Vol. 9, Chap. 2.

[7] L. Sun, J.R. Dutcher, L. Giovannini, F. Nizzoli, J.R. Stevens and J.L. Ord, J. Appl. Phys. **75**, 7482 (1994).

[8] M. Grimsditch, R. Bhadra and Ivan K. Schuller, Phys. Rev. Lett. **58**, 1216-1219 (1987). R. Bhadra, M. Grimsditch, Ivan K. Schuller and F. Nizzoli, Phys. Rev. B, **39**, 12456-12459 (1989).

[9] J.R. Dutcher, Z. Wang, B.J. Neal, T. Copeland and J.R. Stevens, Effect of Annealing on High-Frequency Viscoelastic Waves in Spincoated Polymer Thin Films, Mat. Res. Soc. Symp. Proc. Vol. 356, 1995.

[10] C. Gigault and J.R. Dutcher, Submitted for publication (1995).

ANOMALOUS KINETICS OF THE TRAPPING REACTION IN ONE DIMENSION UNDER STEADY STATE CONDITIONS

ANNA L. LIN and RAOUL KOPELMAN
Department of Chemistry, The University of Michigan, Ann Arbor, MI 48109-1055, USA

Abstract

We study the $A + B \rightarrow B$ trapping reaction under steady state conditions for the case in which both A particles and traps(B) are mobile. Using Monte Carlo simulations, we follow the kinetic rate law in one dimension. Anomalies arise due to self-organization of the A particles, which results in a slower steady state reaction rate than is predicted classically. We find a partial order of reaction with respect to trap density of $X = 2$, and an overall order for the reaction of $Z = 3.2$. These results are in agreement with other works which predict an exponential rather than an algebraic decay law with respect to the A particle density.

INTRODUCTION

The diffusion limited reaction of particles in the presence of trapping centers [1, 2] is representative of many chemical and physical processes [3, 4, 5]. The kinetics of the trapping reaction, which can be represented by the equation $A + B \rightarrow B$, has been intensely investigated since the pioneering work of Smoluchowski [6]. The survival probability of a particle diffusing in a medium with a random distribution of fixed traps has been intensively studied under batch conditions on Euclidean spaces [7] and on fractal structures [8]. The steady state properties of the trapping reaction have been investigated theoretically in 3-D [9], where an anomalous dependence of the rate of reaction on trap density is found, and on fractal structures [10, 11] where an anomalously high partial order of the reaction is found for the trap density.

The trapping problem has been studied in 1,2 and 3 Euclidean dimensions [1, 2, 9, 12] as well as in fractal dimensions under various conditions [13], i.e. $A's$ move, traps sit; traps move, $A's$ sit; or both $A's$ and traps move. Previous work on $A + B \rightarrow B$ under steady state conditions focused on the reaction of A particles with a random distribution of fixed traps on percolation clusters ($d_s < 2$) [10] or on a Sierpinski gasket [14]. The effect of a hard core exclusion condition on the functional form of the rate law has recently garnered attention in the literature [15, 16] and while the trapping problem has been intensively studied under many different conditions, it is not completely understood.

We present here our results from Monte Carlo simulations of the $A + B \rightarrow B$ trapping reaction in 1D under steady state and hard core exclusion (excluded volume) conditions. Both $A's$ and $B's$ (traps) are allowed to perform random walks. The nearest neighbor distance (NNd) distribution of A particles is non- Poissonian at steady state; the A particles are more closely packed than in a random distribution. The NNd distribution of moving traps (B) is random at all times. We find that the partial orders of reaction with respect to ρ_A and ρ_B are 1.22 and 2.01, respectively, resulting in an overall order of reaction of approximately 3 instead of the classical overall order of 2.

Mat. Res. Soc. Symp. Proc. Vol. 407 © 1996 Materials Research Society

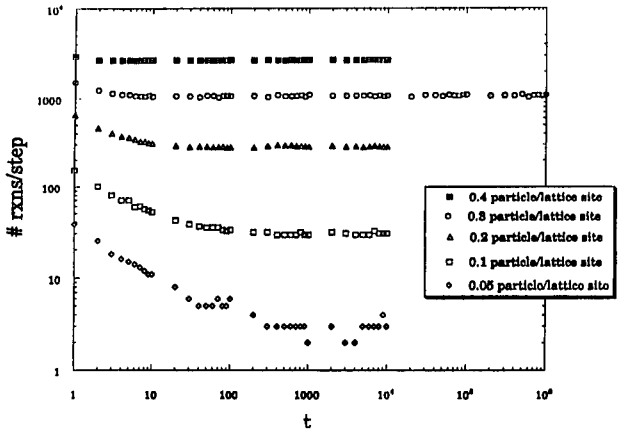


Figure 1: Approach to the steady state reaction rate for different particle densities on a 10,000 site 1D lattice. $\rho_A = \rho_B$ in all cases. Top curve to bottom curve, respectively, densities are 0.4, 0.3, 0.2, 0.1, 0.05 particle/site for both A particles and B traps.

METHOD OF SIMULATION

Monte Carlo computer simulations are often used to model random processes involving random Brownian motion [11, 17, 18]. Our computer simulations for diffusion-controlled chemical reactions are performed according to the following algorithm: A population of reacting particles is initially placed on a lattice by randomly choosing the coordinates for each particle. The diffusive motion of the reactive particles is modeled by independent random walks of the individual particles. The coordinates of all particles are monitored as a function of time. Steps are to nearest-neighbor sites only. There is no interparticle interaction.

Reaction occurs when an A and a B particle collide. No reaction occurs if two A particles (or two B particles) collide. If an $A(B)$ particle attempts to land on a site already occupied by another $A(B)$ particle, the particle does not move in that time step (excluded volume condition). Every collision of an A particle with a B particle leads to a reaction with probability one. In the event of a reaction, the B particle remains on its site while the A particle is removed from the lattice and randomly re-landed before any other particle attempts a move. The density of particles remains constant at all times since the B particles are never removed and the A particles are randomly relanded as soon as they react. The rate of reaction and the NNd's of the A particles and the B traps are monitored.

RESULTS AND DISCUSSION

For the system under study the total number of particles on the lattice is the same at all times; for every reaction, the B particles (traps) are not affected while the A particles are removed from the lattice and randomly relanded. As a consequence of this condition, the source term equals the rate term at *all* times. We observe an initial drop in the reaction

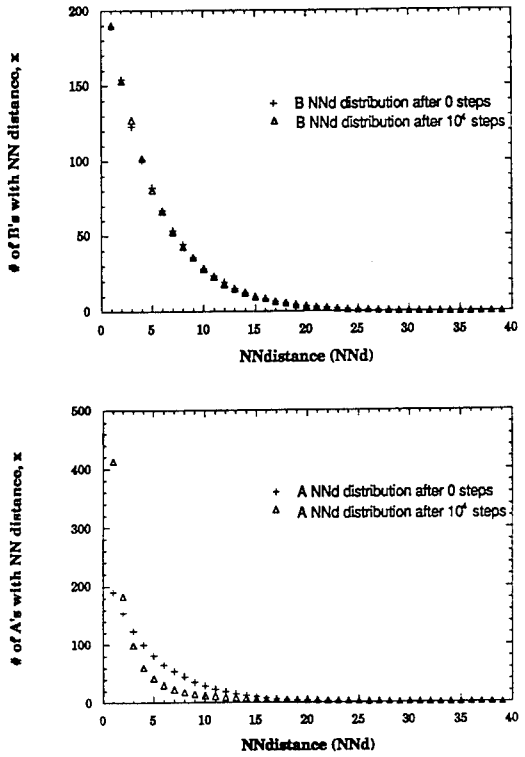


Figure 2: Distribution of nearest neighbor distances (NNd) between like species, at time, $t = 0$ and $t = 10^4$ steps. The trap NNd distribution remains random (top) while the A particle distribution becomes more compact (bottom).

rate (see Fig. 1) as the system shifts from a random distribution in both particle types to its more ordered state. We use the time averaged rate of reaction at steady state to determine the density dependence of the rate law.

We measure the distribution of particles in terms of a nearest neighbor distance (NNd) distribution of same type particles [18]. Fig. 2 shows the NNd distribution of A particles and B traps at $t = 0$ and $t = 10^4$ steps. As can be seen from this figure, the trap distribution obviously remains Poissonian but the A particles become more tightly packed, a configuration which results in a higher survival probability of A particles, and thus lowers the reaction rate.

The steady state reaction rate, R_{ss}, can be expressed by the equation

$$Rate_{ss} = k_{o,ss}[A]^X[B]^Y = k_{o,ss}([A][B])^Z \tag{1}$$

where $k_{o,ss}$ is the steady state rate constant. Alternatively, we could express R_{ss} in terms of the density dependent rate coefficient, $k_{ss}(c) = k_{o,ss}\rho_B^{(1-\frac{2}{d})}$ where d is the dimension of the space in which the reaction occurs. Figs. 3 and 4 plot the results of the Monte Carlo

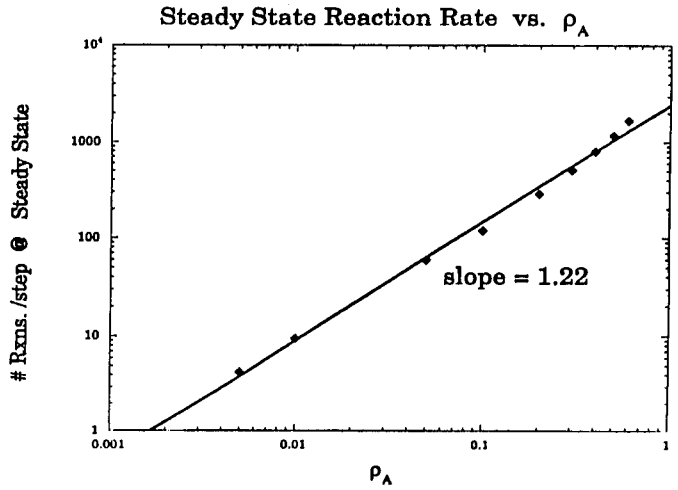


Figure 3: R_{ss} vs. ρ_A on a 10,000 site 1D lattice. The trap density is $\rho_B = 0.2$ particle/site. The slope of the line represents the partial order of the reaction with respect to A particle density.

simulations in which the steady state reaction rate is monitored for varying densities of the A particles and the B traps. In Fig. 3, the trap density is fixed at $\rho_B = 0.2$ *particle/site* and the A particle density is varied. In Fig. 4, the A particle density is fixed at $\rho_A = 0.2$ *particle/site* and the trap density is varied. The slopes of these log-log plots yield the power law dependence of the reaction rate as a function of A density (Fig. 3) and B trap density (Fig. 4), i.e. the partial orders of the reaction rate equation.

From this analysis of the $A+B \rightarrow B$ reaction occurring in 1D where we have allowed both trap and target particles to be mobile and where we have imposed steady state conditions, we determine that the partial order of reaction with respect to the A particle density is $X = 1.22$, approximately the classical expectation. The partial order of reaction with respect to the B trap density is $Y = 2.01$, an anomalous result. We therefore observe an exponential [1, 16] rather than an algebraic [15] decay law (analog to our R_{ss}) as a function of A particle density. Simulations of $A + B \rightarrow B$ in 1D under steady state conditions with equal particle and trap densities (see Fig. 5) yields an overall rate of reaction, $Z = 3.29$. All of the orders of reaction recovered with this method have a $\pm$ associated with the uncertainty due to statistical fluctuations. We find that higher densities of A and/or B (ρ_A and/or $\rho_B > 0.2$ *particle/site*) result in slightly higher valued exponents.

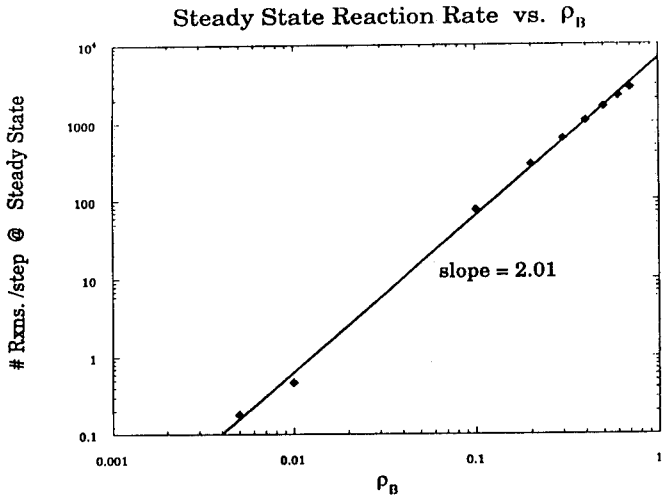


Figure 4: R_{ss} vs. ρ_B on a 10,000 site 1-D lattice. The trap density is $\rho_A = 0.2$ particle/site. The slope of the line represents the partial order of the reaction with respect to the trap density, ρ_B.

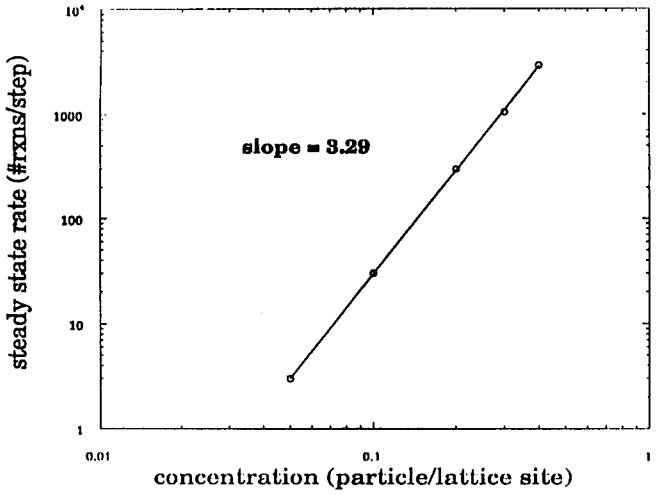


Figure 5: R_{ss} vs. $\rho_{A,B}$ on a 10,000 site 1-D lattice. For each data point, $\rho_A = \rho_B$ and the overall order of the reaction is found to be 3.29.

This work was supported by NSF grant DMR-9410709.

References

[1] V.M. Agranovich and M.D. Galanin, Modern Problems in Condensed Matter Sciences, vol. 3, V.M Agranovich and M.D. Galanin eds. (North Holland Publishing Company, Amsterdam) 254 (1982).

[2] G. Weiss, R. Kopelman and S. Havlin, Phys. Rev. A **39** 466 (1989).

[3] R. Kopelman, Topics Appl. Phys. **15** 298 (1976).

[4] R. Kopelman, Science **241** 1620 (1988).

[5] A. Blumen, J. Klafter and G. Zumofen, Optical Spectroscopy of Glasses, I. Zschokke, ed. (Reidel Publ. Co., Dordrecht) 1986.

[6] Z. Smoluckowski, Z. Phys. Chem. **29** 129 (1917).

[7] M.D. Donsker and S.R.S. Varadhan, Commun. Pure Appl. Math. **32** 721 (1979).

[8] J. Klafter, A. Blumen and G. Zumofen, J. Stat. Phys. **36** 561 (1984).

[9] B.U. Felderhof and J.M. Deutch, J. Chem. Phys. **64** 4551 (1976).

[10] E. Clement, R. Kopelman and L.M. Sander, Europhys. Lett. **11** 707 (1990).

[11] L.W. Anacker and R. Kopelman, in Science at the John von Neumann National Supercomputer Center, 1988, Consortium for Scientific Computing, Princeton, NJ 11 (1989).

[12] G. Zumofen, J. Klafter and A. Blumen, J. Phys. A / **17** L- 49 (1984).

[13] R. Schoonover and R. Kopelman, Mat. Res. Symp. Proc. **290** 255 (1993).

[14] L.W. Anacker, E. Clement, R. Kopelman, in Fractal Aspects of Materials, eds. J.H. Kaufman, J.E. Martin, P.W. Schmidt, Materials Research Society Extended Abstracts, Pittsburgh 271 (1989).

[15] V. Kuzovkov and E. Kotomin, Phys. Rev. Lett. **72** 2105 (1994).

[16] S.F. Burlatsky, M. Moreau, G. Oshanin and A. Blumen, Phys. Rev. Lett. **75** 585 (1995) *and* D.P. Bhatia, M.A. Prasad, and D. Arora, Phys. Rev. Lett. **75** 586 (1995).

[17] P. Argyrakis, Computers in Physics **6**, 525 (1992).

[18] R. Schoonover, Ph. D. Thesis, University of Michigan, Ann Arbor (1993).

Part IV

Dynamical Aspects of the Liquid-Gas Transition

RELAXATIONAL DYNAMICS AND STRENGTH IN SUPERCOOLED LIQUIDS FROM IMPULSIVE STIMULATED THERMAL SCATTERING

Yongwu Yang[1], Laura J. Muller[1,2], and Keith A. Nelson[1]
[1]Department of Chemistry , Massachusetts Institute of Technology, Cambridge, MA 02139
[2]Department of Chemistry and Biochemistry, University of Texas at Austin, Austin ,TX 78712

ABSTRACT

Impulsive stimulated thermal scattering (ISTS), a time-domain light scattering technique, provides a more than 6-decade time range from sub-ns to many ms. It permits characterization of the structural relaxation dynamics and determination of the relaxation strength or Debye-Waller factor in supercooled liquids, and thus allows testing of the mode coupling theory of the liquid-glass transition. ISTS experiments were performed on glass formers salol, butylbenzene, and the molten salt $[Ca(NO_3)]_{0.4}[KNO_3]_{0.6}$. The relaxational dynamics and the Debye-Waller factor $f_{q=0}$ were obtained. A square-root anomaly was observed in $f_{q=0}(T)$ at a crossover temperature T_c for all three materials, consistent with the prediction of mode coupling theory.

INTRODUCTION

Much recent experimental research has been focused on complex relaxation dynamics in glass-forming systems. Extensive effort has been aimed at examination of relaxation dynamics over the broadest possible ranges of time scales and sample temperatures to permit reliable description of material behavior in terms of empirical functional forms and to test the predictions of theoretical models. In particular, the recently developed mode coupling theory (MCT) of the liquid-glass transition [1], which provides detailed predictions for supercooled liquid dynamics, has stimulated many recent experiments. Impulsive stimulated thermal scattering (ISTS) has a dynamical range of more than 6 decades, from sub-nanoseconds to many milliseconds, which makes it well suited for investigation of the dynamics in supercooled liquids. It has been shown that complex elastic modulus spectrum can be constructed in the 10 MHz - 10 GHz range, and used to examine relaxation dynamics in this range, from ISTS measurements of acoustic frequencies and damping rates [2-4]. It has also been demonstrated in ISTS experiments on a molecular glass former, salol, that the relaxation dynamics and the relaxation strength or Debye-Waller factor $f_{q=0}$ can be obtained [4-7]. The Debye-Waller factor $f_{q=0}(T)$ of salol was found to exhibit a square-root cusp anomaly at a crossover temperature T_c, as predicted by MCT.

To determine whether there exists a crossover temperature in $f_{q=0}(T)$ for other materials, as observed in salol, we have performed similar ISTS experiments on a molecular glass-former butylbenzene and an ionic glass-former $[Ca(NO_3)]_{0.4}[KNO_3]_{0.6}$ (CKN). In this paper, we review results on salol and report new experimental results on these two glass formers.

REVIEW OF THEORY

A. Mode coupling theory

MCT starts from a closed set of generalized kinetic (Mori-Zwanzig) equations for the normalized density autocorrelation functions with the relaxation kernel expressed in terms of the nonlinear interactions between the density fluctuations. In its original version, MCT describes a transition at a crossover temperature T_c from a weak-coupling ergodic or liquid-like state to a strong-coupling non-ergodic state which is considered representative of a glass. Above T_c, the density fluctuations relax via a two-step process: a mesoscopic-frequency β relaxation and a low-frequency α relaxation. While the β relaxation dynamics show a weak temperature dependence,

Mat. Res. Soc. Symp. Proc. Vol. 407 © 1996 Materials Research Society

the α relaxation exhibits critical slowing down with decreasing temperature and finally arrests (no further α relaxation) at T_C. The α relaxation dynamics above T_C show non-Debye behavior and can be described reasonably well by the stretched exponential or Kohlrausch-Williams-Watts (KWW) function $\phi(t) \propto \exp[t/\tau_R]^{\beta}$, with $0 < \beta \leq 1$, even though this is not an exact solution of the MCT equation [8]. The T-dependent α relaxation $\phi(t,T)$ above T_C obeys scaling laws, or time-temperature superposition, with the scaling of the relaxation times $\tau_R(T)$ given by

$$\tau_R = \tau_R^0 |\sigma|^{-\gamma} \tag{1}$$

and with T-independent stretching parameter β. Here $\sigma=(T_C - T)/T_C$ and τ_R^0 is the relaxation time at $T = 2T_C$.

Another characteristic of α relaxation is the total relaxation strength or Debye-Waller factor $f_q(T)$, which is defined as the integrated area of the α relaxation spectrum in the frequency domain, or equivalently, the amplitude of the α relaxation function in the time domain [1,5]. The Debye-Waller factor $f_q(T)$ is expected in mode coupling theory to show a square-root cusp at T_C, i.e.

$$f_q(T) = \begin{cases} f_q^c + O(\sigma) & (T > T_c), \\ f_q^c + h_q(\sigma)^{1/2} + O(\sigma) & (T < T_c), \end{cases} \tag{2}$$

where f_q^c varies smoothly with temperature. Note that although the value of the Debye-Waller factor at any temperature is wavevector-dependent, the crossover temperature T_C is q-independent.

With thermally activated hopping processes included in "extended" MCT, both ergodicity and α relaxation are restored below T_C. Thus, the transition is smeared out by these processes. The crossover temperature T_C then marks a change in the nature of α relaxation. The α relaxation dynamics are controlled primarily by anharmonic processes above T_C and by activated hopping processes below T_C. Although new features appear below T_C, the main features of the idealized version of the theory are retained above T_C. However, the T-independence of β cannot be expected to persist near or below T_C.

B. Impulsive Stimulated Thermal Scattering

Impulsive stimulated thermal scattering is a time-delayed four-wave mixing or "transient grating" experiment in which two picosecond excitation pulses are overlapped spatially and temporally to form an optical interference pattern inside the sample. Optical absorption at the interference maxima (the grating "peaks") and subsequent rapid radiationless decay give rise to sudden, spatially periodic heating which images the interference pattern. Thermal expansion at the peaks leads to time-dependent modulation of the sample density, including transient (acoustic) as well as steady-state responses. The time dependence of the material response is monitored through time-resolved diffraction of probe light which is incident upon the grating at the Bragg angle.

The ISTS signal gives the time-dependent density response $G_{\rho T}(q,t)$ to sudden, spatially periodic heating. Neglecting β relaxation (which occurs on time scales shorter than our measurements) and describing α relaxation in terms of the stretched exponential function, the measured intensity is given by [5]

$$I(q,t) = \left|G_{pT}(q,t)\right|^2 = \left\{A\left[e^{-\Gamma_H t} - e^{-\Gamma_A t}\cos(\omega_A t)\right] + B\left[e^{-\Gamma_H t} - e^{-(\Gamma_R t)^{\beta}}\right]\right\}^2, \qquad (3)$$

where ω_A and Γ_A denote the acoustic frequency and damping rate, Γ_H is the thermal diffusion rate, and $\Gamma_R = 1/\tau_R$ and β are the characteristic structural relaxation rate and stretching exponent respectively.

The first ("A") term in Eq. (3) describes ISTS signal from simple liquids or glass-forming liquids at high temperatures in which the structural relaxation dynamics are much faster than the acoustic oscillation period. Following sudden, spatially periodic heating, thermal expansion at the grating peaks leads to a density modulation which overshoots and oscillates about the steady-state level. After the acoustic oscillations are fully damped, the steady-state density modulation decays due to thermal diffusion.

The second ("B") term in Eq. (3) describes the modifications to this time-dependent behavior for complex fluids. In such fluids the density response to sudden heating includes slow components, which do not contribute to the transient overshoot of the steady-state thermal expansion level and the resultant acoustic oscillations. Instead the slow components yield a gradual approach of the density to its steady-state level, observed in ISTS data as a gradual, nonoscillatory rise in signal toward its corresponding steady-state value. This nonoscillatory rise is often described well on nanosecond-millisecond time scales by the stretched exponential function.

In summary, the complete time-dependent density response observed through ISTS can be described in terms of acoustic, structural relaxation, and thermal diffusion modes. When all three modes are well separated temporally from each other, i.e., when $\omega_A >> \Gamma_R >> \Gamma_H$, the amplitude ratio of the relaxation mode and thermal diffusion mode gives the Debye-Waller factor f_q in the q=0 limit [5] according to

$$f_{q=0} = \frac{B}{A+B}. \qquad (4)$$

EXPERIMENT

Experimental implementation of the ISTS technique has been described elsewhere [7]. Briefly, a 100-picosecond pulse derived from a Q-switched, mode-locked, and cavity-dumped Nd:YAG laser is split with a 50% beamsplitter into two excitation pulses that are cylindrically focused and crossed at an angle θ_E. Typically, the laser spots are about 100 μm high and 5 mm wide at the focus. The large width is necessary to avoid "walk-off" of the acoustic waves before they are fully damped. The quasi-cw probe beam, derived from a single-mode Argon laser at 514 nm whose cw output is electro-optically gated, is incident at the Bragg angle for diffraction from the transient grating induced by the excitation pulses. Diffracted signal is directed into an amplified fast photodiode and temporally resolved with a digitizing oscilloscope. The digitized signal is transferred to a computer for storage and subsequent analysis.

The ISTS system offers several useful features for study of complex relaxation and the liquid-glass transition. Of primary importance are the wide ranges of time scales and excitation wave vectors q which are accessible. Since the diffracted signal is against dark background, it has high signal-to-noise ratio. Also important in practice are short data acquisition times, usually at about 10 seconds for 1000 repetitions.

Typical ISTS data are shown in Fig. 1 for salol at q=0.743 μm^{-1} and T=258.5K. In Part A the damped oscillatory features at short times represents the acoustic mode, and the signal intensity slowly reaches a steady-state level on a longer time scale which reveals the slow structural relaxation dynamics. On an even slower time scale, the signal intensity decays through thermal diffusion as displayed in Part B. Thus the data show the acoustic, α relaxation, and thermal

diffusion modes discussed in the previous section. In this paper, we are interested in characterization of the α relaxation mode (the slow rise in ISTS signal) and determination of the Debye-Waller factor. Because the α relaxation mode can only be well characterized when its time scale is larger than the acoustic period and shorter than the thermal diffusion time, the structural relaxation dynamics can only be determined in a narrow temperature range with one single wave vector. This can be overcome by realizing that the acoustic frequency ($\propto q$) and thermal diffusion rate ($\propto q^2$) are q-dependent while in the ISTS wave vector range the structural relaxation dynamics are not. Thus the temperature range over which the structural relaxation mode can be observed through ISTS can be extended by varying the wave vector. The acoustic period is shortened at large excitation angles permitting characterization of the relaxation mode at higher T. To permit observation of the very slow relaxation dynamics at lower T, very small excitation angles (less than 0.5°) are used to reach very low wave vectors and thereby to slow the thermal diffusion dynamics. Therefore the data for salol, butylbenzene, and CKN were collected at multiple excitation angles which permit characterization of the relaxation dynamics from ns to ms.

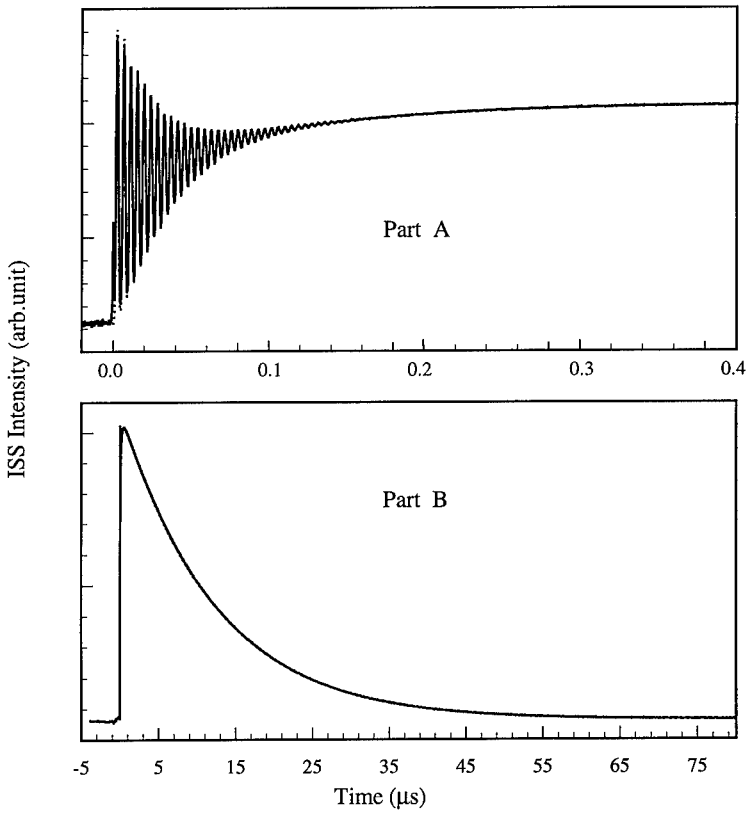


Fig.1. ISTS data (solid curves) and fits (dotted curves) to Eq. (1) of salol at 258.5K at q = 0.743 μm^{-1}. (A) Damped acoustic oscillations at short time scales and the nonoscillatory, gradually rising signal due to the structural relaxation mode on longer time scales. (B) Thermal diffusion dynamics at long times.

RESULTS

Raw data such as that displayed in Parts A and B were joined by matching the signal intensities in their overlapping temporal region. The connected data were fitted to Eq. (3). Fits to the data yielded the dynamical parameters describing the acoustic, thermal diffusion, and α relaxation modes as well as the relative amplitude B/A. With good temporal separation of the acoustic, relaxation, and thermal diffusion modes, the fitting parameters were determined uniquely with reasonable accuracy and the Debye-Waller factor was determined through Eq. (4).

In what follows we present detailed analyses of the α relaxation dynamics and strength, and compare the results with MCT predictions.

1. Salol

The average relaxation time $<\tau_R> = \Gamma(1/\beta)/(\beta\Gamma_R)$ ($\Gamma(x)$ denoting the gamma function), stretching parameter β, and Debye-Waller factor $f_{q=0}$ are plotted as a function of temperature in Fig. 2 [6,7]. The T-dependent Debye-Waller factor $f_{q=0}(T)$ (symbols in Part C) clearly shows a

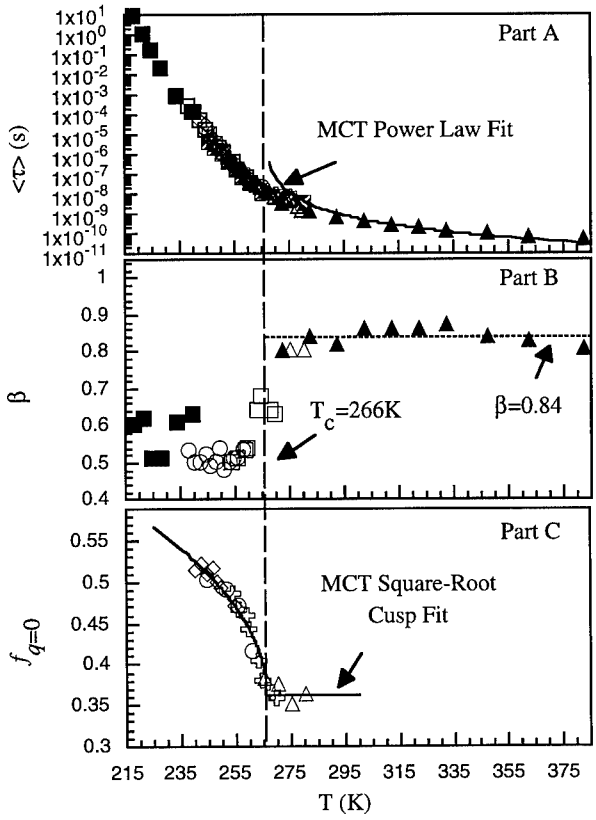


Fig. 2 The T-dependences of the average relaxation times $<\tau_R>$, stretching parameters β and Debye-Waller factor $f_{q=0}$ of salol from ISTS (open symbols), together with the results measured from DLS (▲) and PCS (■).

square-root cusp at a crossover temperature of 266K. The solid curve in Part C represents the best fit to Eq. (2). This T_c value is in good agreement with neutron scattering [9] and depolarized light scattering (DLS) [10] results.

Part B shows the T-dependence of the stretching parameters for ISTS (open symbols), along with the values obtained from DLS [10] at high T and photon correlation spectroscopy (PCS) [11] at low T. The β values determined through ISTS are in agreement with those determined through DLS and PCS measurements in their overlapping regions. Combining all the results of DLS, ISTS, and PCS, the T-dependent β values show a sigmoidal shape with most of the variation at temperatures around T_c. MCT predicts T-independent α relaxation stretching above T_c, which is supported by the results of DLS with an approximately constant value of β=0.84. MCT makes no explicit predictions on the T-dependence of β around and below T_c. However, the observed rapid change of the stretching parameter β(T) around T_c does not contradict MCT. On the contrary, it qualitatively supports the MCT picture of different α relaxation mechanisms above and below T_c.

The average relaxation times from DLS, ISTS, and PCS measurements form a smooth curve in the whole temperature range and do not show a power-law divergence at the crossover temperature T_c. This is presumably due to activated thermal hopping processes which prefer smooth crossover. In the extended MCT, these processes are accounted for, but predictions for T-dependence of the relaxation times around and below T_c are not yet available.

Note that in Fig. 2 different open symbols represent results from data collected at different wave vectors. They coincide with each other at their overlapping regions, which supports our claim that the α relaxation dynamics are wave vector independent in the wave vector ranges accessible to ISTS.

2. CKN

The mixture of ionic salts [$Ca(NO_3)$] and [KNO_3] with molar ratio of 2:3 has been investigated extensively with a variety of experimental techniques. We have recently performed ISTS experiments on this glass-former to study the relaxation in the supercooled state [12].

Following the same line as salol, we present the T-dependence of the α relaxation dynamics (stretching exponent β and relaxation time $\tau_R=1/\Gamma_R$), and the Debye-Waller factor $f_{q=0}$, the crossover temperature T_c determined therefrom. Their temperature-dependences are shown in Fig. 3. In Part C, the Debye-Waller factor values $f_{q=0}$(T) (symbols) obtained with different wave vectors are plotted. It is evident that $f_{q=0}$(T) shows a weak cusp-like anomaly as predicted by MCT. The solid curve in Part C represents the best fit to Eq. (2) which gives a crossover temperature T_c =378K. This T_c value is in good agreement with the results from neutron scattering [13], DLS [14, 15], and Brillouin scattering [16].

The dynamical parameters Γ_R and β describing α relaxation were obtained at various wave vectors in the temperature range 362.7-411.1K. The T-dependent average relaxation times $<\tau_R>$ and the stretching parameters β are shown in Parts A and B of Fig. 3 separately. We also show the results from neutron scattering [13], DLS [14], and PCS [17, 18] for comparison. The β values above T_c obtained from ISTS are approximately constant with β =0.58. Considering their uncertainties, the β values from ISTS, neutron scattering, and DLS show no temperature dependence from above T_c to 468.2K. This finding provides support for the MCT prediction of constant α relaxation stretching above T_c. Similar to salol, the β values decrease as the temperature is reduced below T_c. Again, this is consistent with the physical picture of very different mechanisms for α relaxation above and below T_c.

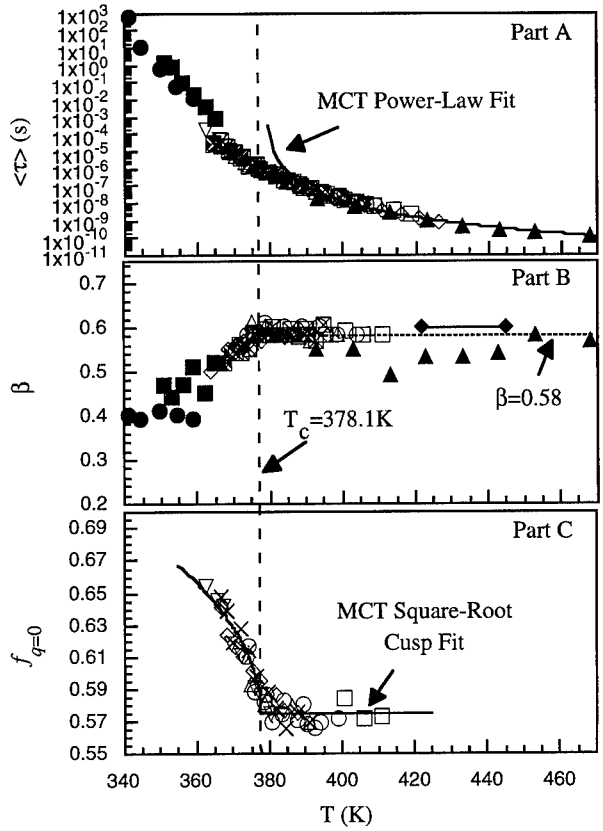


Fig. 3 The T-dependences of the average relaxation times $<\tau_R>$, stretching parameters β and Debye-Waller factor $f_{q=0}$ of CKN from ISTS (open symbols), together with the values measured from DLS (▲), neutron scattering (◆), and PCS (■, ●).

The average relaxation times shown in Part A show similar behavior as for salol. The relaxation times well above T_c show a power law dependence, as indicated by Eq. (1), but the divergence at T_c predicted by Eq. (1) is moderated, presumably by thermally assisted hopping which allows α relaxation to continue through and below T_c.

3. Butylbenzene

Recent transient holeburning studies of dimethyl-*s*-tetrazine (DMST) in *n*-butylbenzene indicated stretched exponential (KWW) local structural relaxation dynamics associated with solvation, characteristic of mechanical relaxation dynamics expected for the solvent [19, 20]. Direct ISTS measurements of the structural relaxation dynamics in supercooled *n*-butylbenzene present a basis for comparison to these results.

The temperature dependences of the average relaxation time $<\tau_R>$, the stretching parameter β, and the Debye-Waller factor $f_{q=0}$, are plotted in Fig. 4. In Part C, the symbols representing the values of $f_{q=0}$ for various wave vectors show the MCT-predicted square-root cusp at a crossover temperature of 150 K.

It is interesting to notice that the ratio $(T_c - T_g)/T_g$=0.18 found for *n*-butylbenzene by the ISTS method matches that found for salol, a liquid with a lower fragility [21], within experimental uncertainty. MCT makes no prediction regarding this relationship. In fact, the reduced temperatures of T_c for other systems that have been compared to MCT are distinctly different from 0.2 [22].

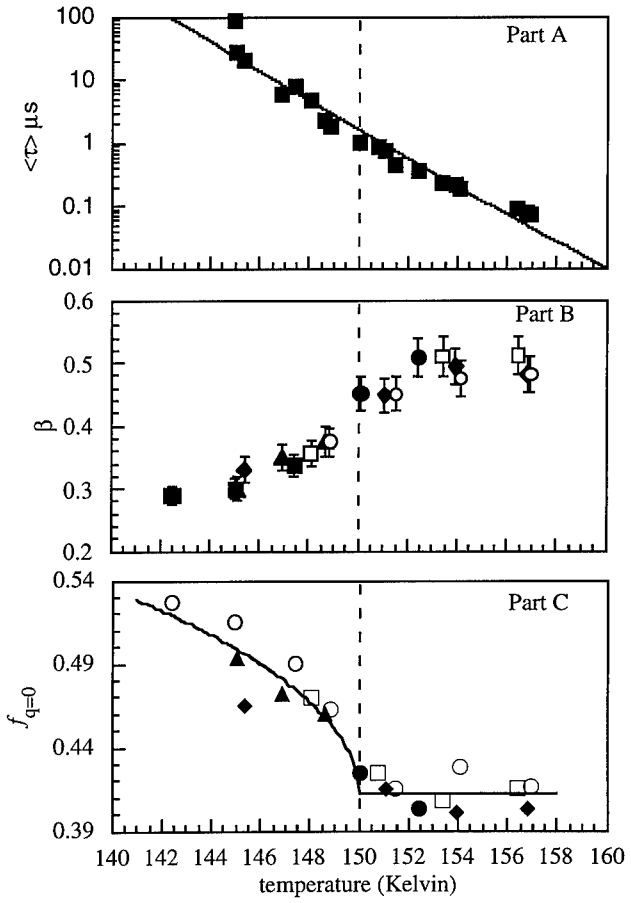


Fig. 4 The T-dependences of the average relaxation times $<\tau_R>$, stretching parameters β and Debye-Waller factor $f_{q=0}$ of *n*-butylbenzene from ISTS.

The temperature dependence of the stretching parameter β is plotted in Part B. At T_c, β=0.45 ± 0.05 in good approximation to the value found through transient holeburning [19]. ISTS, photon correlation and depolarized light scattering measurements of β in salol described earlier exhibit similar changes at about T_c but these measurements have not been reported for *n*-butylbenzene. The relatively constant value of β above T_c appears to support the idealized MCT prediction, although more data are needed for a definitive characterization.

In Part A, the temperature dependence of the average relaxation times is plotted. These relaxation times for the bulk liquid *n*-butylbenzene match those found by Fourkas *et al.* and support their conclusion that a component of the solvation dynamics they observed in the transient hole-burning study of DMST in *n*-butylbezene is due to structural relaxation of the solvent around the solvent [19, 20]. Although it is somewhat surprising that the local (i.e. high wave vector) shear relaxation measured by transient hole-burning matches the low-wavevector longitudinal relaxation measured by ISTS, earlier ISTS experiments in triphenylphosphite found identical low-q shear and longitudinal relaxation dynamics [2].

CONCLUSIONS

ISTS experiments permit characterization of the α relaxation dynamics and determination of the relaxation strength, or the Debye-Waller factor $f_{q=0}$. The temperature dependent Debye-Waller factors $f_{q=0}(T)$ in salol, CKN, and butylbenzene all show weak square-root cusp-like anomalies at distinct crossover temperatures T_c. Well above T_c, the α relaxation dynamics obey scaling laws and the relaxation times show power-law T-dependences. Our findings are largely consistent with the predictions of the MCT.

ACKNOWLEDGMENTS

This work was supported in part by NSF Grant No. DMR-9317198.

REFERENCES

[1] W. Götze, in: Liquids, Freezing and the Glass Transition, ed. J.P. Hansen, D. Levesque and J. Zimm-Justin (North Holland, Amsterdam, 1991) p. 287; and W. Götze and L. Sjögren, Rep. Prog. Phys. **55**, 241 (1992).

[2] Y.-X. Yan, L.-T. Cheng, and K. A. Nelson, J. Chem. Phys. **88**, 6477 (1988); L.-T. Cheng, Y.-X. Yan, and K. A. Nelson, J. Chem. Phys. **91,** 6052 (1989); S. M. Silence, S. R. Goates, and K. A. Nelson, Chem. Phys. **149**, 233 (1990); A. R. Duggal, and K. A. Nelson, J. Chem. Phys. **94** (1991); S. M. Silence, A. R. Duggal, L. Dhar, and K. A. Nelson, *ibid.* **96**, 5448 (1992).

[3] I. C. Halalay, and K. A. Nelson, J. Chem. Phys. **97**, 3557 (1992); I. C. Halalay, Y. Yang, and K. A. Nelson, J. Non-Cryst. Solids 172–174, 175 (1994).

[4] I. C. Halalay, Y. Yang, and K. A. Nelson, Transport Theory and Statistical Physics, **24**, 1053 (1995).

[5] Y. Yang and K. A. Nelson, J. Chem. Phys. **103**, 7722 (1995).

[6] Y. Yang and K. A. Nelson, Phys. Rev. Lett. **74**, 4883 (1995).

[7] Y. Yang and K. A. Nelson, J. Chem. Phys. **103**, 7732 (1995).

[8] M. Fuchs, W. Götze, I. Hofacker, and A. Latz, J. Phys. Condens. Matter **3**, 5047 (1991).

[9] J. Toulouse, G. Coddens, and R. Pattnaik, Phys. A **201**, 305 (1993).

[10] G. Li, W. M. Du; A. Sakai, and H. Z. Cummins, Phys. Rev. A. **46**, 3343 (1992).

[11] D. L. Sidebottom and C. M. Sorensen, Phys. Rev. B **40**, 461 (1988).

[12] Y. Yang and K. A. Nelson, J. Chem. Phys. (submitted).

[13] F. Mezei, W. Knaak and B. Farago, Phys. Scr. **19**, 363 (1987).
[14] G. Li, W. M. Du, X. K. Chen, and H. Z. Cummins, Phys. Rev. A. **45**, 3867 (1992).
[15] H. Z. Cummins, W. M. Du, M. Fuchs, W. Götze, S. Hildebrand, A. Latz, G. Li, and N. J. Tao, Phys. Rev. E. **47**, 4223 (1993).
[16] G. Li, W. M. Du, J. Hernandez, and H. Z. Cummins, Phys. Rev. E. **48**, 1192 (1993).
[17] D. L. Sidebottom and C. M. Sorensen, J. Chem. Phys. **91**, 7153 (1989).
[18] E. A. Pavlatou, A.K. Rizos, G. N. Papatheodorou, and G. Fytas, J. Chem. Phys. **94**, 224 (1991).
[19] J. T. Fourkas and M. Berg, J. Chem. Phys. **98**, 7773 (1993).
[20] J. T. Fourkas, A. Benigno, and M. Berg, J. Chem. Phys. **99**, 8552 (1993).
[21] C. A. Angell, J. Phys. Chem. Sol. **49**, 863 (1988).
[22] H. Z. Cummins, G. Li, W. M. Du, and J. Hernandez, Phys. A **204**, 169 (1994).

EXPERIMENTAL STUDY OF THE LIQUID-GLASS TRANSITION IN AN INORGANIC POLYMER $Li_{0.5}Na_{0.5}PO_3$

B. RUFFLÉ*, S. BEAUFILS*, Y. DÉLUGEARD*, G. CODDENS**, J. ETRILLARD*, B. TOUDIC*, M. BERTAULT*, J. EVEN*, J. GALLIER*, C. ÉCOLIVET*
*G.M.C.M., URA CNRS 804, Université de Rennes 1, 35042 Rennes Cedex, France
**Laboratoire Léon Brillouin, CE Saclay, 91191 Gif Sur Yvette Cedex, France

ABSTRACT

New experimental results obtained with various techniques on a less-studied glass-forming system are presented. At low frequency, a secondary β_{slow}-process, decoupled from the viscous flow, is observed by ^{31}P NMR. Raman scattering spectra and coherent neutron scattering spectra has been obtained in wide frequency and temperature ranges showing the same qualitative features for the Boson peak while the quasielastic contribution seems to differ markedly.

INTRODUCTION

Recently, the discussion concerning the microscopic origin of the glass transition has been stimulated by the application of the mode-coupling formalism (MCT). In its idealized form, this theory predicts a dynamical phase transition from an ergodic to a non ergodic behavior at a critical temperature T_c, located above the calorimetric glass transition temperature T_g, where non-linear interactions, which become stronger with decreasing temperatures, induce a structural relaxation arrest. The mode coupling theory predicts that anomalies occur at T_c for all variables that couple to density fluctuations. Between the microscopic time scale and the structural relaxation α-process, a secondary relaxation, the β_{fast}-process, is always observed by neutron and light scattering. Both processes are expected to exhibit scaling laws with diverging time scales at T_c [1].

Mode coupling theory has obtained some success on glass-forming systems that are classified as fragile liquids in Angell's classification [2]. So it is an open question how far this behavior depends on the degree of fragility of the system under study. However, as the spectra of these less fragile systems are characterized by a stronger vibrational contribution, the so-called Boson peak, a complete description of the dynamical structure factor $S(q,\omega)$ should include this inelastic feature.

MATERIAL AND METHODS

In this framework, we are studying the dynamical behavior of an alkali phosphate glass. $Na_{0.5}Li_{0.5}PO_3$ is an inorganic polymer based on the phosphorus oxygen backbone. The basic structural unit is the PO_4 group linked with two neighboring tetrahedra forming, for this alkali concentration, an infinite twisted chain. Due to the eutectic composition, the melting temperature T_m is lowered to 749 K and the calorimetric glass transition temperature T_g to 515 K.

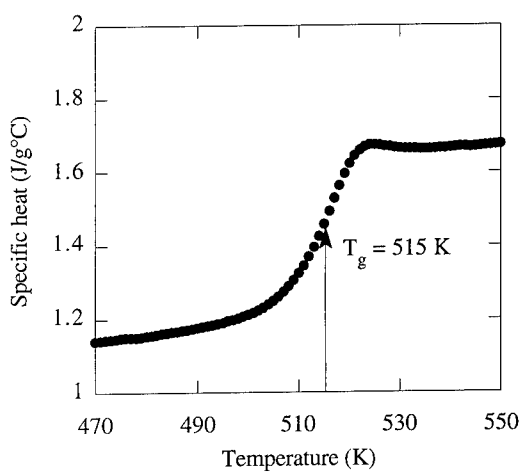
It is well known that in order to understand the complex dynamical processes which take place at the liquid-glass transition, several different techniques must be used trying to cover the widest frequency range as possible so $Na_{0.5}Li_{0.5}PO_3$ is studied by means of mechanical, calorimetric and dielectric spectroscopies and also by nuclear magnetic resonance [3], light and neutron scattering.

EXPERIMENTAL RESULTS

Bulk properties

First, the temperature dependence of the specific heat C_p has been measured in this phosphate glass by conventional differential scanning calorimetry (Perkin-Elmer DSC7, heating rate 10 K/min) leading to a calorimetric glass temperature T_g of 515 K as shown in Fig. 1. It is interesting to note the relative magnitude of $\Delta C_p/C_p$ which is often proposed as an indication of the fragility of the liquid. In the case of this phosphate glass, it amounts to 40% like in ortho-terphenyl, one of the most fragile liquids.

Mat. Res. Soc. Symp. Proc. Vol. 407 © 1996 Materials Research Society



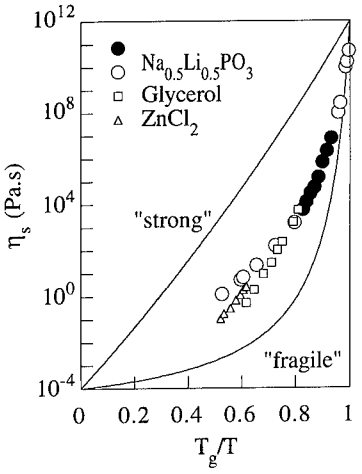


Fig. 1. (left) Temperature dependence of the specific heat in $Na_{0.5}Li_{0.5}PO_3$ leading to T_g=515K with a relative jump $\Delta C_p/C_p$ of about 40%

Fig. 2. (right) Temperature dependence of the viscosity for $Na_{0.5}Li_{0.5}PO_3$ (○ from [4,5], ● from [6]) as compared to glycerol (□) and $ZnCl_2$ (△) from [1].

In order to better characterize the temperature dependence of the structural process, shear viscosity data have been obtained in an intermediate temperature range between those near T_g [4] and those around T_m [5]. As shown in Fig. 2, this eutectic composition occupies an interesting position among known glass-forming systems between strong and fragile liquid just as two others, glycerol and $ZnCl_2$. However, the strong apparent activation energy of the viscosity at T_g leads to a fragility parameter

$$m = \left.\frac{d\log\langle\eta_s\rangle}{d(T_g/T)}\right|_{T=T_g} = 79. \qquad (1)$$

Again, this value is very close to m=81 found in ortho-terphenyl [7].

Low frequency dynamics

Applying ^{31}P and ^{7}Li NMR on this phosphate glass [3], it has been shown that below T_g, the NMR parameters are mainly determined by the lithium diffusion in the amorphous structure. This motion seems unaffected by the glass transition and its spectral density is linearly frequency dependent in the two probed frequency ranges (MHz and KHz). Above T_g, the PO_4 units of the phosphate chains move isotropically, giving rise to the so-called secondary relaxation in glasses (β_{slow}-process) while the primary or structural relaxation (α-process) is only effective on the NMR parameters near 600 K, well above T_g. In Fig. 3 are plotted the relaxation time of this β_{slow}-process deduced from the NMR study and the timescale τ_s of the structural relaxation simply calculated with the Maxwell relation ($\tau_s = \eta_s / G_\infty$). It seems that below 600 K, the time scales of these two processes are strongly decoupled, giving rise to a primary slow relaxation and to a secondary one. Such motion decoupling has been recently reported on another phosphate glass [8]

(*m*-tricresyl phosphate) at the critical temperature T_c of the MCT determined by scaling laws analysis of the light scattering susceptibilities. Well under T_g, the relaxation times measured by Dynamical Mechanical Analysis (DMA) [9] in $Na_{0.5}Li_{0.5}PO_3$ are also shown in Fig. 3. Obviously, the same secondary relaxation is probed in these macroscopic measurements of the dynamical Young modulus.

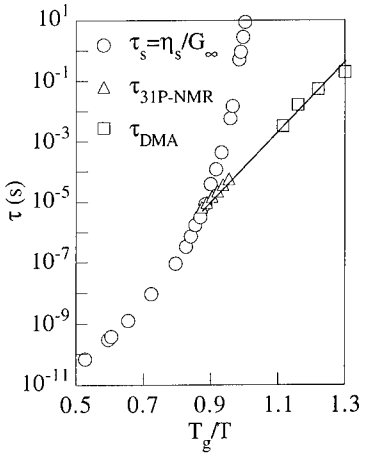


Fig. 3. Temperature dependence of the structural relaxation timescale τ_s (○ from [4,5,6]) calculated with the Maxwell relation and relaxation times obtained by ^{31}P NMR (△ [3]) and DMA (□ [9]) probing the same secondary β_{slow}-process.

High frequency dynamics

Neutron scattering experiments have been carried out on the time-of-flight spectrometer MIBEMOL at the LLB (Saclay, France) with a closed hollow niobium cell in the temperature range 300-773 K. The incident wavelength was set to 6.2 Å, allowing scattering vectors up to q=1.9 $Å^{-1}$ at zero energy transfer. The full width at half height of the energy resolution was about 84 μeV with a very clean triangular shape without wings. In $Na_{0.5}Li_{0.5}PO_3$, scattering is mainly coherent and furthermore, 87% of the signal is due to the PO_4 tetrahedra. After usual corrections (detector efficiencies, sample container and instrumental background), the TOF spectra were converted in S(q,ω). Because of the high sample transmission (90%), multiple scattering corrections were not necessary.

If the β_{fast} process and the Boson peak are correlated, factorization of the dynamic susceptiblity ($\chi''(q,\omega) = S(q,\omega) / n(\omega)$) in q and ω functions should be correct for the entire spectrum except at low frequencies where the q-dependent structural relaxation appears,

$$\chi''(q,\omega) = \chi''(\omega).S^{inel}(q) \ . \qquad (2)$$

It has been found that the data between $1.0 \leq q \leq 5.0$ $Å^{-1}$ are shown to overlap within experimental accuracy as well in the β_{fast} relaxation region as for the Boson peak. Furthermore, the shape of the inelastic structure factor $S^{inel}(q)$ is not temperature dependent, i.e. whatever the relative weight of the β_{fast} relaxation with respect to the Boson peak.

Following an approach to the description of the low frequency Raman spectra in glasses proposed by Gochiyaev [10], these q-rescaled neutron spectra ($S(\omega) = S(q,\omega) / S^{inel}(q)$) have been analysed with this model. In this approach, it is assumed that the Boson peak and the quasielastic scattering are due to a broad distribution of vibrational modes coupled with a coupling strength parameter δ to a localized relaxation process defined by its relaxation time τ. The distribution is given by the low temperature spectra without any relaxation where $\delta \ll \omega_{bp}$ (ω_{bp} is the frequency of

the maximum of the Boson peak). In this phosphate glass, the shape of the Boson peak in neutron scattering is well described by the following phenomenological expression which contains only one unknown temperature dependent parameter: the frequency of the maximum of the Boson peak $\omega_{bp}(T)$:

$$S_{vib}(\omega,T) = \frac{n(\omega,T)\,\omega^3}{(\omega_{bp}^2(T)+\omega^2)^2}. \qquad (3)$$

On increasing temperatures, δ increases towards ω_{bp} leading to an overdamping and an instability of the Boson peak. In Fig. 4 are plotted some spectra together with this model showing a good agreement at all temperatures in the whole frequency range. The insert presents the temperature dependence of the renormalized frequency of the Boson peak maximum, $\omega_{bp}^2 - \delta^2$, leading to a crossover temperature $T^* > T_g$ as already found in some glass-forming materials but from low frequency Raman spectra [11]. For these systems previously analysed within the MCT framework, T^* was found to be close to T_c.

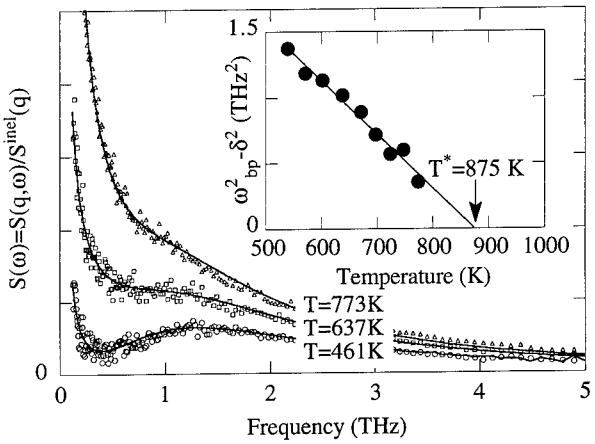


Fig. 4. Coherent neutron scattering spectra at three different temperatures for $Na_{0.5}Li_{0.5}PO_3$. Solids lines are fits with the convolution model of Gochiyaev [10]. The insert shows the temperature dependence of the renormalized frequency of the Boson peak maximum leading to an unstable mode at T^*=875 K.

So in this temperature region, it seems that there is a transition from a "liquid-like" or relaxational behavior to a "solid-like" or vibrational one. However, the temperature T^* found in this compound is higher than the melting temperature T_m=749 K so in order to give more reliability to these results and to their eventual relation with the MCT, light scattering experiments were carried out on this glass former and first analysed within the same frame.

Low-frequency Raman spectra have been obtained between 90 K and 923 K with a triple grating spectrometer using a 90° scattering geometry. Fig. 5 shows the room temperature depolarized spectrum on a reduced intensity scale [12]

$$I_R(\omega) = I(\omega)/(\omega(n(\omega)+1)) = C(\omega)g(\omega)/\omega^2 \qquad (4)$$

with its two contributions and as the neutron spectrum also on a reduced intensity scale

$$S_R(\omega) = S(\omega) / (\omega.n(\omega)) = g(\omega) / \omega^2 \qquad (5)$$

at the same temperature. In these two expressions, $g(\omega)$ is the vibrational density of states while $C(\omega)$ is the unknown light to excitation coupling function. It shows clearly that the shape of the Boson peak is almost independent of the scattering technique in this glass. In other words, the coupling coefficient $C(\omega)$ appearing in the scattering formula for low frequency light scattering mechanism can only be weakly frequency dependent. This is confirmed by the frequency of the Boson peak maximum which is seen at nearly the same value in both spectra.

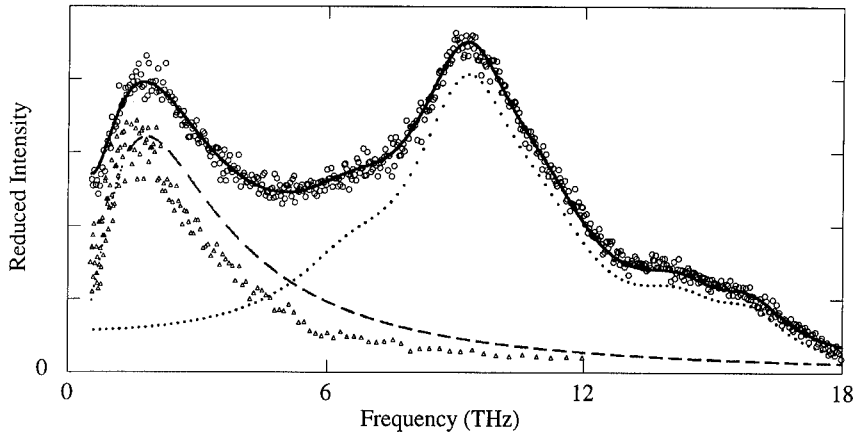


Fig. 5. (○, upper data) Low-frequency Raman spectrum in reduced intensity at 300 K. (△, lower data) Neutron spectrum in reduced intensity at 300 K. The Raman spectrum is fitted (full line) by the superposition of two contributions: sum of optical modes (dotted line) and the Boson peak (dashed line) described by the same formula as in neutron scattering (3) except for a slightly higher frequency maximum of the Boson peak ω_{bp}.

In summary, it has been verified first that the depolarization ratio was not frequency dependent in the low-frequency region around the Boson peak. Furthemore it has been found independent of temperature, i.e. whatever the relative weight of the β_{fast} relaxation with respect to the Boson peak. Again, this suggests a possible correlation between the quasielastic contribution and the inelastic one. Taking the same formula for the shape of the Boson peak (3) as in neutron scattering, these low-frequency Raman spectra have been fitted with this convolution model of Gochiyaev and while the temperature dependence of the frequency of the maximum of the Boson peak follows the same trend in both techniques, the coupling parameter δ is notably stronger in light scattering results than in neutron ones, leading to a lower crossover temperature T^* (775 K) but still slightly above T_m. This larger contribution of the β_{fast} relaxation in light scattering spectra would require a very different coupling function $C(\omega)$ for the scattering by relaxational excitations and vibrational ones in this glass-former. Moreover, these crossover temperatures pose the problem of the physical meaning of this temperature if it is the one where the glass falls out of equilibrium.

ACKNOWLEDGEMENTS

Authors are very grateful to Dr. E. Guéguen and Dr. R. Marchand from the "Verres et Céramiques" laboratory of Rennes I University for providing them with many excellent quality samples.

REFERENCES

1. W. Götze, in *Liquids Freezing and the glass transition,* edited by D. Levesque, J.P. Hansen and J. Zinn-Justin (Elsevier, New-York, 1991), p 287.

2. C.A. Angell and W. Sichina, Ann. N.Y. Acad. Sci., **279**, 53 (1976).

3. B. Rufflé, S. Beaufils, J. Gallier, Chem. Phys., **195**, 339 (1995).

4. R. Wäsche and R. Brückner, *Phys. Chem. Glasses*, **27**, 87 (1986).

5. R. Wäsche and R. Brückner, *Phys. Chem. Glasses*, **27**, 80 (1986).

6. B. Rufflé, unpublished viscosity data.

7. R. Böhmer, K.L. Ngai, C.A. Angell and D.J. Plazek, J. Chem. Phys., **99**, 4201 (1993).

8. E. Rössler and P. Eierman, J. Chem. Phys., **100**, 5237 (1994).

9. P.F. Green, D. Sidebottom and R.K. Brow, J. Non-Cryst. Solids, **172-174**, 1353 (1994).

10. V.Z. Gochiyaev, V.K. Malinovsky, V.N. Navikov and A.P. Sokolov, Philo. Mag. B, **63**, 777 (1991).

11. A.P. Sokolov, A. Kisliuk, D. Quitmann, A. Kudlik, E. Rössler, J. Non-Cryst. Solids, **172-174**, 138 (1994).

12. R. Shuker and R. Gammon, Phys. Rev. Lett., **25**, 222 (1970).

QUASI-ELASTIC NEUTRON SCATTERING STUDY OF THE FRAGILE GLASS-FORMER SALOL

J. Toulouse
Department of Physics, Lehigh University, Bethlehem, PA 18018, USA
R. Pick and C. Dreyfus
LDMC,ERS 115, Université Pierre et Marie Curie, 4 Place Jussieu, 75252 Paris, France

ABSTRACT

Quasi-elastic neutron scattering (NS) measurements of Salol have been carried out in order to study the α and β relaxations near the liquid-glass transition. The results are presented in the form of a susceptibility spectrum that is compared with the corresponding spectrum obtained from light scattering (LS) and with the predictions from the Mode Coupling Theory. The differences between the NS and LS results are due to the different correlators contributing to the susceptibility in the two types of scattering. The possible origin of these differences are discussed in the framework of the Mode Coupling Theory.

INTRODUCTION

SALOL is an organic substance with formula $C_{13}H_{10}O_3$ that undergoes a liquid-glass transition. In the last few years it has been the object of several experimental studies including Brillouin and Raman scattering[1], dielectric spectroscopy[2], specific heat[3] and inelastic neutron scattering[4]. The reason for this interest is that SALOL belongs to the class of fragile glasses, according to Angell's classification[5], and is therefore a good candidate to test the Mode Coupling Theory[6] (MCT) which has lately been the dominant theoretical approach used to understand the liquid-glass transition. In particular, MCT predicts the existence of two relaxations, a structural or α relaxation observed at low frequencies and another one at higher frequency, labeled β, often attributed to a cage effect. MCT also predicts the existence of a transition temperature, T_c, at which the system becomes non-ergodic. Upon approaching T_c, the α relaxation progressively slows down and finally comes to an arrest such that the system no longer reaches thermal equilibrium. Finally, MCT predicts[6] the existence of an effective Debye-Waller factor which
should already exist above T_c and should exhibit a $(T-T_c)^{1/2}$ singularity below T_c.

The previous quasi-elastic neutron scattering study[4] was carried out at Saclay on the Mibemol time-of-flight spectrometer with a wavelength of 5.5Å giving an energy resolution of 60μeV. Although it mostly focused on the effective Debye-Waller factor, revealing the square-root singularity below T_c=263±7K, it also showed the existence of a low frequency peak corresponding to the α relaxation, of a high frequency peak usually called "the microscopic peak" and of a minimum between the two, in the region of the β relaxation process. However, upon analyzing the results, the resolution of this experiment proved too coarse to follow even the latter, close to the transition. Consequently, we repeated the experiment, using a wavelength of 10Å giving a resolution of 20μeV. This second experiment was also more specifically designed to study the α and β relaxations and to compare the neutron scattering results with light scattering results[1] and MCT predictions. Such a comparison was recently made for glycerol[7] but it did not lead to quantitative or even entirely consistent conclusions.

Mat. Res. Soc. Symp. Proc. Vol. 407 © 1996 Materials Research Society

SCALING LAWS

In the Mode Coupling theory,[6] both α and β relaxations are tied to the resonant dynamics of a damped harmonic oscillator characterized by a microscopic frequency, Ω_o and are also related to each other. More specifically, MCT predicts that the dynamic susceptibility related to the density correlator should exhibit a wavevector-independent minimum that follows scaling laws with temperature. In the vicinity of this minimum the susceptibility should be expressed as:

$$\chi''(\omega) = \chi''_{min}[b(\omega/\Omega_{min})^a + a(\Omega_{min}/\omega)^b]/(a+b) \qquad (1)$$

where χ''_{min} and Ω_{min} are respectively the magnitude and the frequency of the susceptibility minimum and where **a** and **b** are temperature-independent coefficients related by the relation:

$$\lambda = \Gamma^2(1-a)/\Gamma(1-2a) = \Gamma^2(1+b)/\Gamma(1+2b) \qquad (2)$$

where Γ designates the gamma function. Both χ''_{min} and Ω_{min} should display a pseudo-critical behavior,

$$\text{a) } \chi''_{min} \sim (T-T_c)^{1/2} \qquad \text{b) } \Omega_{min} \sim (T-T_c)^{1/2a} \qquad (3)$$

where **a** is the coefficient introduced above and is related to the slope of the susceptibility spectrum on the high frequency side of the minimum. Finally, according to MCT, all physical quantities coupled to density fluctuations should display the same behavior.

EXPERIMENTAL RESULTS

The neutron experiment was performed on the Mibemol spectrometer at the Leon Brillouin Laboratory in Saclay (France). As in the first neutron on SALOL, the liquid sample was contained in a cell made up of two planes of staggered narrow silica tubes. The transmission of the cell was approximately 75%. The cell was placed in a double wall water-heated container for measurements down to 240K and then transferred into a displex for lower temperature measurements. The scattered intensity was measured with 57 detectors distributed over an arc of a circle and covering 150^o. Each detector had 512 channels, each channel corresponding to a time interval of arrival with respect to a common time origin.

For simplicity, the analysis of the experimental data was done for groups of 10 detectors each (1-10, 11-20, 21-30, 31-40, 41-50 and 51-57) with the lower number detectors corresponding to smaller scattering angles or wavevectors. Here we primarily present the results from the middle group of detectors, 31-40, that corresponded to a mean scattering vector Q of 0.87Å^{-1}.

Once acquired, the data were corrected for the empty sample cell, normalized to the elastic intensity from a vanadium sample and converted from time-of-flight to energy. In order to compare the neutron scattering results with the light scattering results and with the MCT predictions, it is more convenient to represent the data in the form of a generalized susceptibility:

$$\chi''(\omega) = I(\omega) / [n(\omega, T)] \qquad (4)$$

In Fig. 1 we present the neutron scattering susceptibility for the 31-40 group of detectors. For the sake of clarity, curves are only presented for selected temperatures over the whole range covered and the 20μeV cut-off shown on that figure corresponds t th energy resulution of the spectrometer. The α peak maximum is only visible at the highest temperature, T=353K, and moves into the instrumental resolution at lower temperatures. However, because the β minimum appears at higher energies, it can be followed down to lower temperature. Below 265K, it is not clear from the figure whether this minimum falls within the resolution or it disappears altogether to be replaced by a monotonic decrease of the susceptibility towards lower energies. We will argue later that the minimum does disappear at T_c.

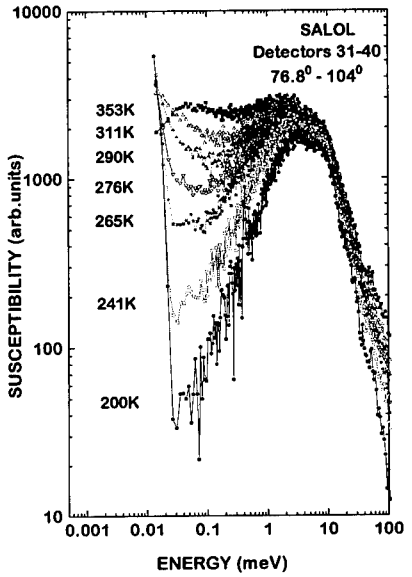


Fig.1 **Susceptibility, χ"=I(ω)/n(ω,T), vs. Energy for Q=0.89Å at different temperatures**

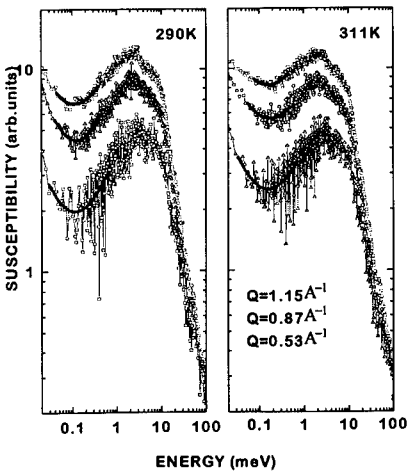


Fig.2 **Susceptibility curves for three groups of detectors. The solid curves represent fits obtained using Eq.(1) with b=0.64**

In order to compare the present neutron results with MCT predictions, we fitted the experimental spectra in the vicinity of the β minimum using Eq. (2) and thus extracted best values for χ''_{min}, Ω_{min}, **a** and **b**. In practice, we found that a good fit could not be obtained if the latter two coefficients were constrained by Eq. (3). We therefore chose to fix **b** at the value of 0.641 taken from the analysis of the light scattering results and verified that fixing **b** had little effect on the values obtained for χ''_{min} and Ω_{min} but obviously affected that of **a**. In order to verify the MCT prediction of Q-independence, the fitting procedure was carried out successively for three groups of detectors at each temperature. The results of the fitting at three temperatures are shown in Fig. 2. Within the experimental uncertainty, which increases with decreasing scattering angle, there does not seem to be any angular or Q dependence in the position of the β minimum, Ω_{min}. At 265K, i.e. close to T_c, the minimum appears to become flatter and the fits are not as good as those at higher temperatures. This might suggest that the minimum is disappearing altogether (see earlier remark). The comparison between the neutron and light scattering results is made in Fig.3 where we show the susceptibility curves for both scattering techniques at several temperatures. The overall shapes of the two

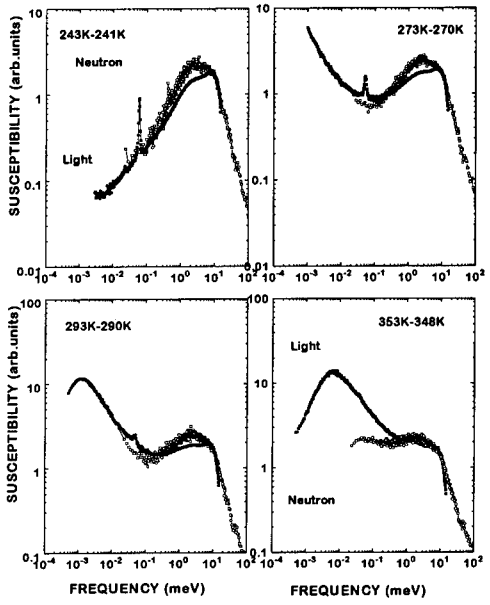


Fig.3 **Susceptibility vs. Energy at four different temperatures respectively from neutron scattering (Q=0.89Å^{-1}) and light scattering (Q=0.0016Å^{-1}). The first temperature corresponds to NS and the second one to LS. The neutron curves have been cut-off at the resolution limit of the spectrometer (20μeV).**

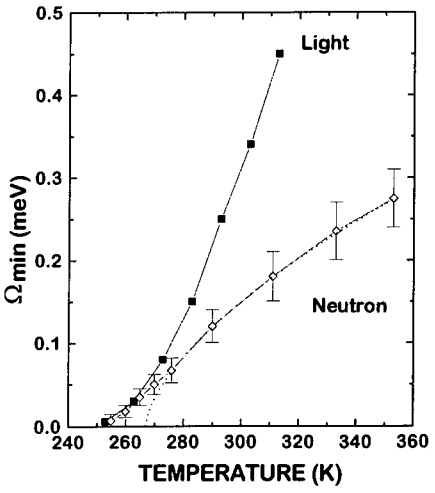


Fig.4 Ω_{min} **vs.T from neutron and light scattering. The dotted line represents the fit with Eq.(3b).**

spectra are similar: both exhibit a β minimum at intermediate frequencies and a microscopic peak (possibly two) at the highest frequencies; the α relaxation appears clearly only in the 353K NS spectrum while it is clear in all the LS spectra, due to a better energy resolution. From a comparison at this highest temperature, it nevertheless appears that the α peak is much more intense in the LS than in the NS . More important for our present discussion, the β minimum spectra is found at a lower frequency in the NS than in the LS spectrum. This latter difference is well illustrated in Fig. 4. As mentioned earlier, we did not detect any systematic Q dependence of Ω_{min} and error bars on the neutron data points represent the experimental uncertainty which initially decreases with temperature as the minimum becomes more pronounced. Below 265K, it is no longer possible to precisely determine the position of the neutron minimum. Nevertheless, based on the estimates obtained from the fitting and on the comparison of the spectra themselves, it appears that the two minima, obtained respectively from neutron and light scattering, converge as T approaches T_c. The temperature dependence of the neutron minimum can be fitted reasonably well by Eq. 3b) giving $T_c \cong 267K$ and $a_{NS} = 0.78$ (dotted curve). This T_c value is close to that obtained from a similar fit of the LS curve ($T_c \cong 256K$). However, the value of the coefficient a_{NS} differs significantly from the LS value (a_{LS} = 0.327) and, accordingly, the two curves exhibit opposite curvatures.

DISCUSSION

In order to better understand the meaning of the present neutron results and their departure from the light scattering results, it is useful to consider the theoretical expressions for the

relevant susceptibilities in the two types of experiments. In both cases, following the fluctuation-dissipation theorem, the susceptibility is proportional to a correlation function. In the case of incoherent NS and for a single particle, this function is written[8]:

$$\chi''(\omega) \sim \left\langle \exp(-i\vec{Q} \bullet [\vec{R}(t) - \vec{R}(o)]) \right\rangle \qquad (5)$$

and describes density-density correlations in which $\vec{Q}$ is the scattering wavevector and $\vec{R}$ the position of a hydrogen atom. It can be shown that this spectrum essentially reflects the self-correlation of the position of the molecular centers of mass. By contrast, in LS from Salol, it has recently been demonstrated[9] that the main scattering mechanism is the reorientation of the molecular polarizability tensor; assuming for simplicity, linear molecules oriented along a direction $\hat{u}$, and no coherence in the reorientation of different molecules, one finds[10]:

$$\chi''(\omega) \propto \tfrac{1}{2}\langle 3[\hat{u}(0) \cdot \hat{u}(t)]^2 - 1 \rangle \qquad (6)$$

One is thus probing different dynamics in the two experiments and we now suggest that this can lead to different positions of the susceptibility minimum.

The idealized MCT master equation is an equation of motion for the density-density correlator in the β relaxation regime but it does not preclude the existence of other dynamic correlators such as rotation-rotation. The theory makes predictions for the correlators of all variables that linearly couple to the density. In the asymptotic region, i.e. close to T_c, the β relaxation dynamics of all these correlators should be the same. Our findings do not contradict this result; the Ω_{min} values, obtained from NS and LS respectively, converge for $(T - T_c) < 20K$. However, the situation becomes more complex further away from T_c because the two types of variables probed in these experiments may be characterized by significantly different microscopic frequencies. Since Ω_{min} increases rapidly with temperature, the correlator of the variable with the lower microscopic frequency should depart from the asymptotic regime sooner (i.e. at a lower temperature) than the other one. In fact, a preliminary two-correlator MCT calculation[11], in which the density correlator imposes its retardation effect on the orientational correlator, has recently produced susceptibility curves in semi-quantitative agreement with those presented in Figs.3 and 4.

CONCLUSION

Quasi-elastic incoherent neutron scattering results from Salol, when compared with the light scattering results, reveal the different contributions made by density and orientational correlations respectively. Their β relaxation dynamics, which are quite similar for $(T - T_c) < 20K$, exhibit minima that depart from each other above that temperature. The density correlator then no longer follows the MCT asymptotic predictions while the orientational correlator still does. These findings may be explained by various effects that had not been taken into account in the simplest MCT models studied so far. In particular, a recent two-correlator MCT model may be able to reproduce our experimental results, an extended version of which, including $\chi''_{min}(T)$ curves, will be published elsewhere. Further study of the different contributions to the susceptibility of fragile glasses is clearly needed.

ACKNOWLEDGMENTS

We acknowledge the invaluable help of G. Coddens (LLB, Saclay) with the neutron experiment. Particular thanks go to Prof. H.Z. Cummins for providing us with the light scattering results as well as for useful discussions.

REFERENCES

1. G. Li, W.M. Du, A. Sakai, H.Z. Cummins, Phys. Rev. A46, 3343 (1992).
2. P.K. Dixon, L. Wu, S.R. Nagel, B.D. Williams, J.P. Carini, Phys. Rev. Lett. 65, 1108 (1990).
3. P.K. Dixon, Phys. Rev.. B42, 8179 (1990).
4. J. Toulouse, G. Coddens, R. Pattnaik, Physica A201, 305 (1993).
5. C.A. Angell, in Proceedings of the Workshop on Relaxations in Complex Systems, eds. K.L. Ngai and G.B. Wright (National Technical Information Service, US Dpt. of Commerce, Springfield, VA, 1984).
6. W. Gotze and L. Sjogren, Rep. Prog. Phys. 55, 241 (1992).
7. J. Wuttke et al., Phys. Rev. Lett. 72, 3052 (1994).
8. S.W. Lovesey, in Theory of Neutron Scattering from Condensed Matter, Oxford (1984) p.177.
9. H.Z. Cummins et al., Phys. Rev. E53, January 1st, 1996.
10. B. Berne and R. Pecora, in Dynamic Light Scattering, R.E. Krieger (1990) p.151.
11. W. Gotze, T. Franosch, A. Singh (private communication).

STRUCTURAL RELAXATIONS IN A SIMPLE MODEL MOLTEN SALT

Matthias Fuchs
Department of Materials Science, University of Illinois, Urbana, Il 61801

Abstract

The structural relaxations of a dense, binary mixture of charged hard spheres are studied using the Mode Coupling Theory (MCT). Qualitative differences to non–ionic systems are shown to result from the long–range Coulomb interaction and charge ordering in dense molten salts. The presented non–equilibrium results are determined by the equilibrium structure, which is input using the well studied Mean Spherical Approximation.

Introduction

The equilibrium structure of ionic liquids is strongly affected by the long–range nature of the Coulomb interaction [1]. One aspect is the screening of external charges familiar from the Debye-Hückel theory of ionic solutions. Another aspect are oscillations in the charge density around a given ion. These oscillations result from the competition between local charge neutrality and the excluded volume restriction due to the finite diameter of the ions. Also the dynamics of equilibrium ionic liquids in the hydrodynamic regime differs from the one of uncharged mixtures. Coulombic restoring forces lead to a non–diffusive and non–propagating relaxation of charge fluctuations [1]. The MCT determines the slow structural relaxations of dense (supercooled) liquids from their equilibrium structure [2]. In this paper we discuss the most salient features of these results arising from the long–range Coulombic interactions. These will be seen to be directly connected to the familiar effects in the static structure mentioned above: screening and charge ordering.

Theory

One of the most simple models of an molten salt is a binary mixture of hard spheres with radii d_i and charges z_i, $i = 1, 2$. Global charge neutrality fixes $z_1\varrho_1 + z_2\varrho_2 = 0$, where ϱ_i denotes the density of species i. The mean spherical approximation [3] gives a satisfactory description of the equilibrium structure of this system, which depends on the parameters d_1/d_2, z_1/z_2, packing fraction φ and coupling constant Γ. The packing fraction is the ratio of volume occupied by spheres to the total volume. Γ is a generalized inverse Debye screening length and a measure of the Coulomb interaction compared to the thermal energy. At the values of these parameters chosen in our study and collected in table I one observes a liquid to glass transition in the MCT equations. This transition is the topic of the work reported. It is worth noting that the density at the transition can be chosen to be lower than in the uncharged system [4]. Obviously, the charges increase the interactions of the particles. Asymmetric parameters ($d_1/d_2 \neq 1$) were first chosen in order to study experimentally more realistic non–symmetric salts. The charge asymmetry z_1/z_2, however, was then adjusted to obtain the value $\lambda = 0.85$ for the exponent parameter λ; see the discussion. The MCT for binary mixtures formulates a closed set of equations for the time and wave vector dependent density fluctuation functions, $F_q^{ab}(t) = \frac{1}{N}\langle \delta\varrho_q^{a*}(t)\delta\varrho_q^b(0)\rangle$ [5,2]. Of particular interest are the fluctuations of the total– or mass–, $\varrho^n = \varrho^1 + \varrho^2$, and the charge–density, $\varrho^c = z_1\varrho^1 + z_2\varrho^2$.

Mat. Res. Soc. Symp. Proc. Vol. 407 © 1996 Materials Research Society

Table I: Molten salt equilibrium parameters and results from MCT calculation.

d_2/d_1	z_1/z_2	φ	Γ	$k_BT\epsilon d_2/e^2$	λ	b	γ	σ/τ	ε'_o	ε'_∞
1.2	-3	0.475	1.68	0.113 (from Γ)	0.845	0.40	3.24	0.49	14.9	3.56

The initial values, $F_q^{ab}(t=0) = S_q^{ab}$, are the static structure factors which are the only input determining the $F_q^{ab}(t)$ via the MCT equations.

MCT shows that these equations exhibit bifurcations which are identified as idealized liquid to glass transitions. Close to these transitions the long time dynamics is predicted to follow from

$$q^2 F_q(t) = S_q\{M_q(t)S_q - \frac{d}{dt}\int_0^t dt' M_q(t-t')F_q(t')\}\,, \qquad (1)$$

where matrix notation is used and the memory functions are quadratic polynomials in the $F_q(t)$ correlators with coefficients determined by the static structure factors S_q [2,5]. Thermally activated transport is neglected in (1) leading to its breakdown at low temperatures. Only aspects which are not affected by this simplification will be discussed in this article.

Results

In order to screen an external charge the charge structure factor S_q^{cc} has to vanish for small q, $S_q^{cc} \propto (q\Lambda_D)^2$, where Λ_D is the Debye screening length [1,3]. This leads to a decoupling of the MCT equations (1) for small wave vector. Whereas the mass-density fluctuations are determined by a frequency dependent longitudinal viscosity $N^l(z=\omega+i\epsilon)$,

$$F_q^{nn}(z)/S_q^{nn} \to \frac{-1}{z - \frac{1}{S_0^{nn}N_0^l(z)}} \qquad \text{for } q\to 0, \text{ where} \qquad N_q^l(z) = \frac{1}{q^2}M_q^{nn}(z)\,, \qquad (2)$$

the charge fluctuations couple to the generalized conductivity $\sigma(z)$

$$F_q^{cc}(z)/S_q^{cc} \to \frac{-1}{z + 4\pi i\sigma(z)} \qquad \text{for } q\to 0, \text{ where} \qquad \sigma(z) = \lim_{q\to 0}\frac{i}{4\pi}\frac{q^2}{S_q^{cc}M_q^{cc}(z)}\,. \qquad (3)$$

These equations simplify further in two frequency windows reached close to a transition. From the well known MCT results let us only mention the von Schweidler decay which describes the onset of the α–relaxation, i.e. the final decay into equilibrium [2]:

$$F_q^{ab}(t)/S_q^{ab} = f_q^{ab} - h_q^{ab}\,(t/\tau)^b \qquad \text{for intermediate times}\,. \qquad (4)$$

The von Schweidler exponent b and the exponent γ determining the increase of the α–relaxation time τ are functions of the exponent parameter λ and uniquely determined at the chosen transition. Their values are included in table I. Eq. (4) shows that the density fluctuations exhibit a two–step relaxation. The amplitudes f_q^{ab} of the final or α–relaxation is smaller than unity. The relaxation is non–exponential in general and the α–relaxation times τ_q^{ab} depend sensitively on temperature or density and on wave vector by a multiplicative factor, which roughly equals $(f_q^{ab}/h_q^{ab})^{1/b}$. The mass–density correlation functions qualitatively agree with the results obtained for neutral one–component liquids [2,6]. Fig. 1 shows the α–amplitudes, f_q^{nn}, which describe the frozen–in mass–density structure at the glass transition.

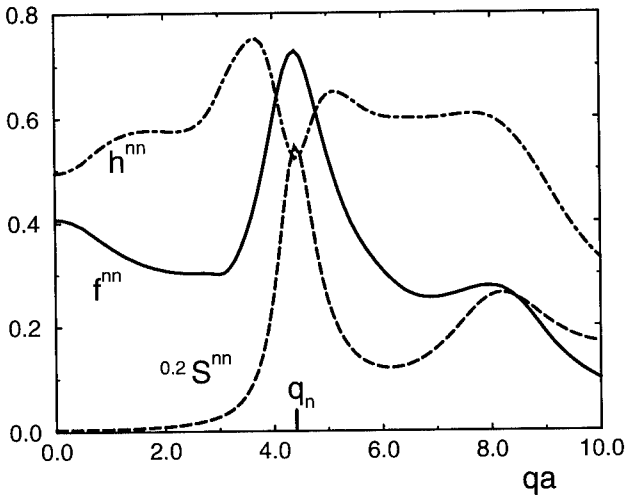


Figure 1: Mass–density α–amplitude f_q^{nn}, critical amplitude h_q^{nn} and structure factor S_q^{nn}.

The known local packing on shells separated by the mean average interparticle spacing, $a \approx q_n/4.4$, is seen in f_q^{nn} as a consequence of the one in S_q^{nn} [2,6]. Local neutrality and excluded volume effects lead to charge ordering and a prominent peak in the charge structure factor, S_q^{cc}. The average spacing between ion–shells of equal sign is larger than the average particle spacing resulting in the peak in S_q^{cc} to lie at q_c, where $q_c < q_n$. The charge–density fluctuations f_q^{cc}, which are arrested at the transition, reflect this ordering [4]; see Fig. 2.

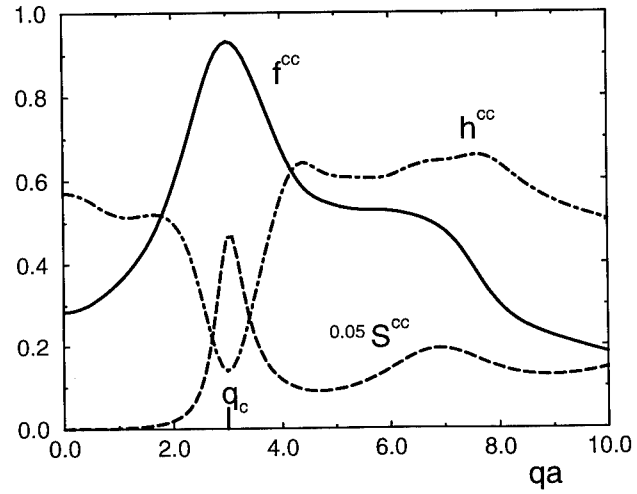


Figure 2: Charge–density α–amplitude f_q^{cc}, critical amplitude h_q^{cc} and structure factor S_q^{cc}.

The different mass– and charge–density ordering also leads to specific variations in the wave vector dependent prefactors of the α–relaxation times τ_q^{nn} and τ_q^{cc}. Fig. 3 shows these variations as estimated from the peak positions in the corresponding susceptibilities, $\tau\omega_{max} = 1$. A q–dependent slowing down at the maximal amplitudes of the α–process is observed. Superficially, this mimics the known De Gennes narrowing, as the τ_q vary in phase with the static structure factors [1]. However, this correlation only holds, because the α–relaxation amplitudes, f_q, vary in phase and the critical amplitudes, h_q, vary out of phase with the structure factors, S_q [2]; see Figs. 1 and 2.

The results presented thus far specify the structural relaxations on length scales of the order of interparticle distances. Analyzing Eq. (1) more closely, it is seen that it also is the static structure on these length scales which determines the results. The quantitative results therefore depend on the appropriateness of the underlying microscopic model, i.e. the liquid of charged hard spheres with the choice of parameters. From Eqs. (1,3) one can also obtain macroscopic transport coefficients like the conductivity σ and the dielectric constant ε' of the ionic melt. Their values are included in table I. The frequency dependent conductivity determines the dielectric "constant" via

$$\varepsilon(z) = 1 + 4\pi i \frac{\sigma(z)}{z} \,. \tag{5}$$

The liquid molten salt is characterized by a conductivity and dielectric constant measured at low frequencies, $\omega\tau \ll 1$. In the idealized glassy state the particles are arrested and ionic transport over macroscopic distances is not possible. The α–relaxation time τ diverges and the conductivity vanishes. Eq. (5) then results in a dielectric constant ε_∞ which can also be observed in the liquid state at high frequencies, $\omega\tau \gg 1$. Fig. 4 shows the dispersion of the dielectric constant versus $\omega\tau$. In the same plot, the conductivity crosses over from its low frequency value to a power law behavior, $\sigma(\omega\tau \gg 1) \propto (\omega\tau)^{1-b}$, at intermediate frequencies.

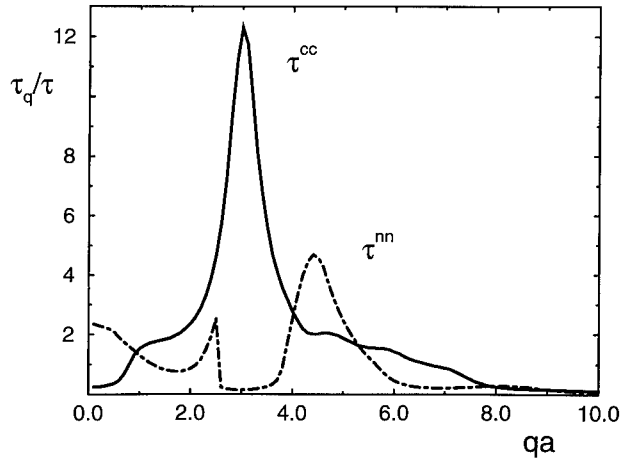


Figure 3: Wave vector dependent factors of the α–relaxation times τ_q^{nn}/τ and τ_q^{cc}/τ.

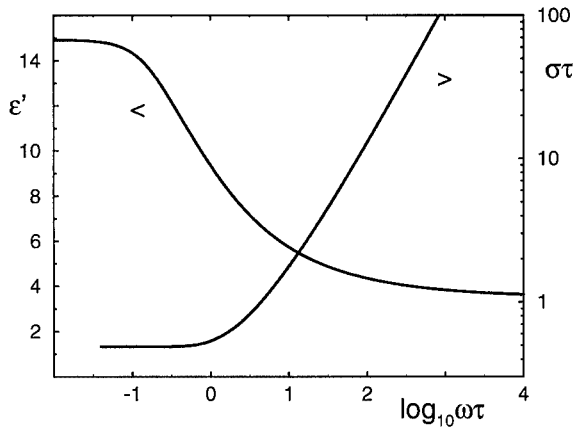


Figure 4: Scaled conductivity $\sigma\tau$ and real part of the dielectric constant ε versus $\omega\tau$.

Discussion

The mixed salt CKN [40% $Ca(NO_3)_2$- 60% KNO_3] is a well studied glassforming melt; see [7,8] and references therein. Its dynamics in a wide temperature range has been studied by neutron [7] and by depolarized light scattering [8]. In the latter work it was found that the exponent parameter $\lambda \approx 0.85$ describes the dynamics in an intermediate time window. These findings lead to the choice of parameters in our model reproducing this λ–value. This assures that the asymptotic dynamics in the intermediate time window is described by the correct asymptotic master function exhibiting, for example, the von Schweidler asymptote of Eq. (4) or Fig. 4.

The wave vector dependent prefactors, like f_q, h_q and τ_q, are strongly coupled to the structural input as specified by our model and discussed in the previous chapter. It cannot be expected that the simple model reproduces these amplitudes quantitatively. However, the variations of the α–amplitude f_q^{cc} and relaxation time τ_q^{cc} in phase with S_q^{cc} and of the critical amplitude h_q^{cc} out of phase with it, are expected to be general findings applicable to molten salts. The corresponding variations in the mass–density quantities shown in Fig. 1 have been found in MCT calculations for different simple liquids [2,6]. They have been compared to dynamic light scattering spectra in colloidal suspensions; general agreement with errors of the order of 15% was observed [9]. Neutron scattering from CKN measures a combination of charge– and mass–density fluctuations determined by the different atomic neutron scattering cross sections. Our findings of peaks in the α–amplitudes and in the α–times at the wave vectors, q_c and q_n, characterizing charge and density fluctuations in the equilibrium structure, are in qualitative agreement with the reported measurements [7]. The results show that charge ordering and local packing are the underlying mechanism.

Let us restate, that the increase of the time scales at peaks in the static structure factors is not a simple example of de Gennes narrowing and cannot be explained by short time sum rules but is a consequence of the MCT equations (1) [2]. Eqs. (1) do not include the short time dynamics and consequently violate the short time sum rules. The shown variations result from the specific magnitudes of the coupling of different modes in the

memory functions; the couplings are determined by S_q.

The MCT equations (1) correctly describe non–propagating and non–diffusive charge fluctuations in the long–wavelength limit (3). This is a consequence of screening in ionic melts which requires finite restoring forces for charge fluctuations even on long wavelengths. The generalized conductivity changes from a low frequency constant, $\sigma \propto 1/\tau$, to a power law behavior at large $\omega\tau$.

In a cursory search liquid glass transitions were located for different parameters in this model. The parameter of table I lead to a rather strong peak in the charge structure factor, S_q^{cc}. The origin of this is the large charge asymmetry z_2/z_2 =-3 which entails a corresponding concentration ratio due to the requirement of global neutrality. The overestimated charge oscillations lead to two special features in our results. First, the maxima in the q–dependent amplitudes of the charge fluctuations are quite pronounced. This prevents any quantitative comparisons with the neutron or light scattering data of [7,8]. This failure emphasizes that quantitative comparisons between MCT calculations for simple liquids and experimental data require appropriate microscopic models if non–universal features of the theory are tested; see [6,9]. Second, comparing Fig. 1 to the corresponding results for one–component liquids, shows that the frozen–in mass-density structure of the formed glass is similar but somewhat distorted. Inspection of other parameter values in this model reveals that another glassy structure becomes stable if the charge asymmetry is increased some more. The small stability of the studied glass to another amorphous structure is the origin of the large exponent parameter. This second glass differs in the frozen–in mass–density but not in the charge–density structure. A striking consequence of the proximity of the two glassy states is the splitting of the α–relaxation in $F_q^{nn}(t)$ for some wave vectors into two processes. This effect is indicated in Fig. 3, where the inverse α–peak position frequency jumps from one process to the other at $qa \approx 2.5$. This phenomenon has been discussed in schematic MCT models [10] and will be studied further in this microscopic model.

Acknowledgments

Financial support from the Deutsche Forschungsgemeinschaft under contract Fu 309/1-1 is acknowledged.

References

1. J.P. Hansen and I.R. McDonald, *Theory of Simple Liquids*, 2nd edn. (Academic Press, London, 1986), p.364.
2. W. Götze and L. Sjögren, Rep. Prog. Phys. **55**, 241 (1992); and references therein.
3. L. Blum and J.S. Høye, J.Phys.Chem. **81**, 1311 (1977).
4. J.S. Thakur and J. Bosse, J.Non-Cryst.Solids **117/118**, 898 (1990).
5. J. Bosse and T. Munakata, Phys.Rev. **A 25**, 2763 (1982); L. Sjögren and F. Yoshida, J.Chem.Phys. **77**, 3703 (1982).
6. M. Fuchs, I. Hofacker and A. Latz, Phys.Rev. **A 45**, 898 (1992); and references therein.
7. F. Mezei, W. Knaak and B. Farago, Physica Scripta **T 49**, 363 (1987).
8. H.Z. Cummins, W.M. Du, M. Fuchs, W. Götze, S. Hildebrand, A. Latz, G. Li and N.J. Tao, Phys.Rev. **E 47**, 4223 (1993).
9. W. van Megen and S.M. Underwood, Phys.Rev. **E 49**, 4206 (1994).
10. M. Fuchs, W. Götze, I. Hofacker and A. Latz, J.Phys.:Condens.Matter **3**, 5047 (1991).

RELAXATION BEHAVIOR IN POLYSTYRENE NEAR AND ABOVE THE GLASS TRANSITON STUDIED BY ULTRASONIC TECHNIQUE

A. SAHNOUNE, L. PICHÉ
National Research Council Canada, Industrial Materials Institute, 75, De Mortagne, Boucherville, Québec J4B 6Y4 CANADA

ABSTRACT

We report measurements of the temperature and pressure dependence of ultrasonic modulus in polystyrene between 340 and 550 K and applied pressures up to 775 bar. The real and imaginary parts of the modulus are analyzed within the Havriliak-Negami model and very good agreement is found over the entire temperature and pressure ranges. Using the Vogel-Tammann-Fulcher equation for the relaxation time, the Kauzmann temperature T_K and the fragility parameter D of polystyrene were determined. The value of D indicates that polystyrene is a fragile-glass former.

INTRODUCTION

Relaxation of glass-forming substances is a quite complex problem and is still a subject of intensive research, both theoretical and experimental [1, 2]. Numerous efforts have been made to build comprehensive theories to account quantitatively for the various properties observed but in general their success has been limited [3]. Instead, the experimental observations are often analyzed using phenomenological expressions. The most successful among them are the Kohlrausch-Williams-Watts (KWW) stretched exponential time decay function [4] and the Havriliak-Negami (HN) model in the frequency domain [5]. The KWW expression has been found to emerge naturally from a hierarchy relaxation model proposed by Palmer *et al.* [6]. On the other hand, Alvarez *et al.* [7] have recently demonstrated the close relationship between KWW and HN functions. One of the widest application of these expressions has been to polymer glasses. The aim of this work is to present a new approach to the analysis of ultrasonic measurements that will allow us, using the HN relaxation model, to extract fundamental information about the viscoelastic behavior of glass-forming substances. A complete analysis of the longitudinal modulus measured at a frequency of 2.5 MHz as function of temperature and pressure in a model polymer glass, namely polystyrene, is presented. The fragility parameter D and the relaxation time, τ, are extracted from fits to the data using the Vogel-Tammann-Fulcher equation (VTF) [8].

EXPERIMENTAL METHODS

The polymer used in this study is atactic polystyrene (PS) manufactured by Dow Chemical of Canada. The molecular weight is $M_w = 258{,}000\ g/mole$ and $M_n = 130{,}000\ g/mole$, $(M_w / M_n = 1.98)$. The samples consist of disks (3.0 cm diameter) held in confinement between two steel buffer rods at the opposite end of which are attached an emitting and a receiving ultrasonic transducer. A pressure up to 1 kbar can be applied and the sample thickness monitored to $\pm 1\,\mu m$. The temperature of the sample can be varied from room temperature up to 600 K using heaters attached to the steel rods. More details about the experimental set-up have been reported elsewhere [9]. All samples were prepared following the same thermal path so that systematic effects of pressure could be compared. The starting material ($\approx$ 3 g) is melted under a

Mat. Res. Soc. Symp. Proc. Vol. 407 © 1996 Materials Research Society

pressure of 200 bar and the formed disk (~ 3 mm thick) is annealed for 30 min at 490 K. The working pressure is then applied and the sample quenched to room temperature. All measurements of the specific volume V (hence mass density $\rho \equiv 1/V$), sound velocity v, and the attenuation a were taken at a heating rate of 2 K/min. These quantities are then translated in terms of a complex modulus, $M^* = M' + iM''$, by the following expressions [10]:

$$M' = \frac{v^2}{V} \qquad (1.a)$$

$$M'' = \frac{2av^3}{V\omega} \qquad (1.b)$$

where $\omega = 2\pi f$ is the angular frequency. The real and imaginary parts are called the storage (elastic) and loss (viscous) moduli, respectively, and are a measure of the material's ability to store and/or dissipate energy.

RESULTS AND DISCUSSION

The longitudinal storage, L', and loss, L'', moduli of PS are shown in Figure 1 as a function of temperature between 340 and 550 K and at different pressures up to 775 bar. The symbols represent the experimental data and the solid lines are fits to the theoretical expressions, as explained below. The storage modulus scales with increasing pressure reflecting the more dense structure at high pressures, as expected. At low temperatures, L' is large and decreases with increasing temperature. However, at the glass transition temperature, T_g, it bends over and decreases more rapidly due to the fast relaxation in this temperature range to finally reach its value of the relaxed state at high temperatures. Similarly, L'' is small below T_g and passed this characteristic point it rises sharply and goes through a strong maximum. Notice that the peak maximum shifts to higher temperatures with increasing pressure. However, the shape and width remain constant reflecting the fact that the relaxation processes are the same at low and high pressures. In turn, this suggests that the microscopic mechanisms responsible for the relaxation are pressure independent, at least in the pressure range considered here.

The frequency dependent viscoelastic modulus can be written in terms of a relaxed modulus, M_R, and an unrelaxed modulus, M_U, as:

$$M^* = M_R + (M_U - M_R) M(\omega) \qquad (2)$$

with $M_U = \rho v_U^2$ and $M_R = \rho v_R^2$, v_R and v_U are the low and high temperature limits of the velocity and ρ the corresponding mass density. $M(\omega) = \left(1 + (i\omega\tau)^{\alpha}\right)^{-\gamma}$ is the HN relaxation function [5] where τ is the average relaxation time. The exponents, $0 < \alpha, \gamma \leq 1$ are shape parameters characterizing the degree of asymmetry of the loss peaks. For polymers, the temperature dependence of τ is usually expressed by VTF equation [8]: $\tau = \tau_0 \exp(B/(T - T_0))$; where τ_0 is a

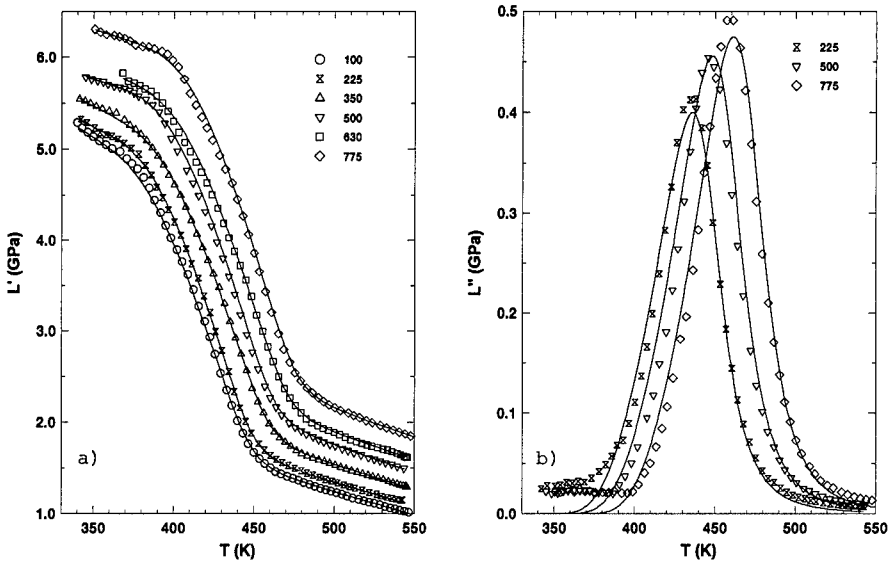


Figure 1: Longitudinal storage, L', and loss, L'', moduli as a function of temperature at several pressures. The symbols are the data and the solid lines are fits to HN model, as explained in the text. The applied pressures (in bar) are indicated in the figure.

microscopic time scale, B and T_0 are parameters specific to the material. The factor B is related to the glass-forming ability of the system and T_0 is the Vogel temperature, usually located 40 to 60 K below the glass transition temperature.

The data are fitted to the real and imaginary parts of the complex modulus derived from Eq. 2. The unrelaxed, L_U , and relaxed, L_R, moduli needed in the theoretical expressions are determined independently from the linear region of the low and high temperature data of the storage modulus. The unkown parameters are B, T_0, τ_0, α, and γ. Hence, as a first step, all parameters are kept free in a multiparameter least-squares fitting routine. The fitting process stops when the deviation between the data and the theoretical expressions is minimum. In carrying out the fits at different pressures we found that τ_0, α, and γ are pressure independent in agreement with the observation made above that the shape and width of the loss peaks remain constant as the pressure is increased. To ensure an internally consistent fit, we then fix τ_0, α, and γ to their average values and repeat the analysis. B and T_0 are now the only adjustable parameters. Thus, our analysis effectively involves only two variables. The results of the fit are shown by the solid lines in Figure 1a-b and the numerical values of the parameters are given in Table I. The agreement is very good in all cases over the temperature range from T_g to the highest temperatures for both the storage and the loss parts of the longitudinal modulus. The discrepancy below T_g for L'' is due to secondary (β) relaxation losses not considered in this work. Therefore we conclude that relaxation in polystyrene is well described by HN model. The

TABLE I: The glass transition temperature and the fitting parameters using Vogel-Tammann-Fulcher equation in polystyrene.

Pressure (bar)	T_g (K)	T_0 (K)	B (K)	D	T_g/T_0
100	372	327	1878	5.74	1.14
225	378	327	1890	5.78	1.16
350	383	335	1929	5.76	1.14
500	388	336	1970	5.86	1.15
630	395	343	1977	5.76	1.15
775	400	347	1990	5.73	1.15

Errors: T_g, ±1K; T_0, ±3K; B, ±10K.

values of $\tau_0 \approx 10^{-14}$ sec, $\alpha = 0.78 \pm 0.03$ and $\gamma = 0.19 \pm 0.02$ are within the expected range and compare well with the literature [11, 12, 13].

The temperature T_0 is plotted in Figure 2, together with the glass transition temperature as determined from velocity of sound and specific volume measurement [14]. Both quantities increase linearly with pressure. However, it is worth to mention that T_g increases at a faster rate than T_0 in such a way that the ratio $T_g/T_0 \approx 1.15$, remains constant (see Table I). A similar result has also been found for a number of other substances [15, 16] and is believed to be a simple manifestation of the validity of time-temperature superposition principle [17]. On the other hand, according to Angell [2,18], T_0 is closely related to the Kauzmann temperature T_K at which the viscosity diverges and the excess configurational entropy vanishes. Therefore, our analysis provides an alternative and simple way to determine this fundamental parameter.

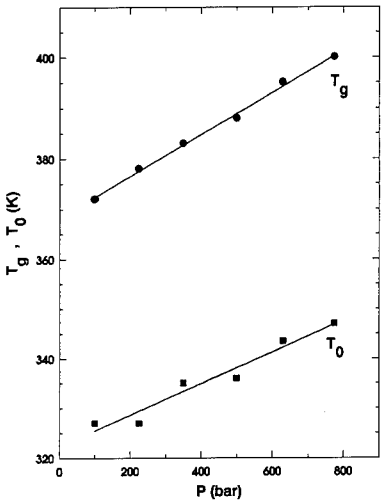


Figure 2: The glass transition temperature T_g and the Vogel temperature T_0 as a function of pressure.

The parameter B can be written as: $B = DT_0$, where D is called the fragility parameter [2, 18]. Using the values of T_0 and B one can easily extract D (see Table I). Notice that within error, $D \approx 5.8$, remains constant over the entire pressure range. Qualitatively, D is related to the topology of the potential energy surface of the system. For fragile glasses ($D \leq 6$), the density of energy minima is high whereas so-called strong glasses ($D \geq 15$) are characterized by a relatively low density of such minima [18]. It is relatively more difficult for a strong glass former to find a minimum than its counterpart and this will be reflected in the relaxation spectrum. The relaxation of strong glasses is Arrhenius like in contrast to that of fragile systems which is strongly non-Arrhenius [18,19]. Based on our results, polystyrene can therefore be classified as

a fragile glass; consistent with the non-Arrhenius dependence of the relaxation time as displayed in Figure 3.

Finally, it is useful to briefly compare the values obtained from our fits to those obtained using the Williams-Lendel-Ferry (WLF) time-temperature superposition principle [17]. WLF is a very practical tool to represent experimental data measured, for example as a function of frequency, at different fixed temperature on a same "universal" curve hence greatly simplifying their analysis [20]. The expression of the temperature superposition factor a_T is given by [17, 20]:

$$\log a_T = \frac{-C_1(T-T^*)}{C_2+(T-T^*)} \qquad (3)$$

where C_1 and C_2 are constants that depend on the reference temperature T^*. For comparison purposes, the glass transition temperature is usually selected. Equation 3 and VTF expression are equivalent if $C_1 = B/2.3(T_g - T_0)$ and $C_2 = T_g - T_0$. Using our values in Table I, we find that C_1 varies between 16-18 and $C_2 \approx 48-53$ K. These values compare very well with $C_1 \approx 17.1$ and $C_2 = 51.6$ K, reported in the literature [21, 22]. This remarkable agreement lends another strong support to our measurements and analysis.

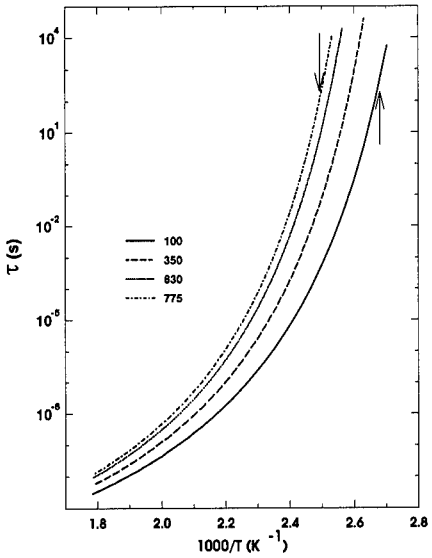


Figure 3: The relaxation time of polystyrene as determined from fits to the longitudinal modulus at different pressures as indicated in the figure (in bar). The arrows point to the value of τ at the glass transition temperature.

CONCLUSION

We have studied in detail the mechanical relaxation of PS as a function of temperature and pressure using ultrasonic techniques. We have shown that the relaxation behavior is in very good agreement with the predictions of HN model. Furthermore, with our approach we were able to obtain the Kauzmann temperature T_K and the fragility parameter D. The value of D is comparable to those of fragile glasses with a strong non-Arrhenius relaxation time. We also compared our values of the different parameters with the ones obtained from WLF time-temperature superposition method and found very good agreement.

REFERENCES

1. Relaxation in Complex Systems, edited by K. L. Ngai and G. B. Wright (North Holland, Amesterdam, 1991).
2. R. Bohmer and C. A. Angell in Disorder Effects on Relaxational Processes, edited by R. Richert and A. Blumen (Springer, Berlin, 1994), p. 11.
3. G. W. Scherer, J. Non-Cryst. Solids, **123**, 75 (1990).

4. G. W. Williams and D. C. Watts, Trans. Faraday Soc. **66**, 80 (1970).
5. S. Havriliak and S. Negami, Polymer **8**, 161 (1967).
6. R. G. Plamer, D. L. Stein, E. Abrahams, and P. W. Anderson, Phys. Rev. Lett., **53**, 958 (1984).
7. F. Alvarez, A. Alegria, and J. Colmenero, Phys. Rev. B, **44**, 7306 (1991).
8. H. Vogel, *Phys. Z.* **22**, 645 (1921); G. S. Fulcher, J. Am. Chem. Soc. **8**, 789 (1925).
9. F. Massines, L. Piché, and C. Lacabanne, Makromol. Chem. Macromol. Symp. **23**, 121 (1989).
10. G. J. Gruber and T. A. Litovitz, J. Chem. Phys. **40**, 13 (1964).
11. Y. H. Jeong, S. R. Nagel, and S. Bhattacharya, Phys. Rev. A, **34**, 602 (1986).
12. B. Hartmann, G. F. Lee, and J. D. Lee, J. Acoust. Soc. Am. **95**, 226 (1994).
13. M. Cutroni, P. Migliardo, A. Piccolo, and C. Alba-Simionesco, J. Non-Cryst. Solids, **172-174**, 201 (1994).
14. A. Sahnoune, F. Massines, and L. Piché, J. Polym. Sci., Part B: Polym. Phys. (in print, 1996).
15. G. Adam and J. H. Gibbs, J. Chem. Phys., **43,** 139 (1965).
16. G. A. Samara, J. Polym. Sci., Part B: Polym. Phys., **30**, 669 (1992).
17. N. G. McCrum, B. E. Read, and G. Williams, Anelastic and Dielectric Effects in Polymeric Solids (Wiley & Sons, New York, 1967).
18. C. A. Angell, J. Non-Cryst. Solids, **131-132**, 13 (1991).
19. R. Böhmer, K. L. Ngai, C. A. Angell, and D. J. Plazek, J. Chem. Phys., **99,** 4201 (1993).
20. D. J. Plazek and K. L. Ngai, Macromolecules **24**, 1222 (1991).
21. S. Onogi, T. Matsuda, K. Kitagawa, Macromolecules **3**, 109 (1970).
22. A. Eisenberg, in Physical Properties of Polymers, 2nd ed. (American Chemical Society, Washington, 1993), p. 61.

STRUCTURAL RELAXATION OF DENSIFIED SILICA GLASS BY THERMAL ANNEALING

Naoyuki Kitamura, Kohei Fukumi, Masaki Makihara and Hiroshi Yamashita
Osaka National Research Institute, AIST, Ikeda, Osaka 563, JAPAN.

ABSTRACT

Thermal relaxation of glass structure has been studied on silica glasses densified by hot isostatic pressing. Density of the glasses relaxed toward the value of an undensified glass by thermal annealing. Relaxation rates of density of the glasses were measured after the annealing at several temperatures. Fast and slow relaxation processes were found from the analysis by using a stretched exponential relaxation function $\Phi(t)=\exp\{-(t/\tau_{eff})^{\beta}\}$. The slow process becomes dominant after the fast process. Raman scattering spectrum also has been measured through the thermal relaxation. The width of the main band at 450cm^{-1} increased by the annealing and recovered the value for the undensified glass after the fast process. The bands at 1060 and 1200 cm^{-1} shifted back to the positions for the undensified glass. The high density state($\Delta\rho/\rho\sim0.5\%$), however, was maintained even after the fast process. From these results, it is deduced that the fast process is due to the recovery of the O_3Si-O-SiO_3 tilt angle and Si-O-Si bond angle to the mean values for the undensified glass.

INTRODUCTION

Amorphous silica (a-SiO_2) attracts many researchers who wish to understand the structure and properties of amorphous materials because of its simple compositions and its many polymorphous crystal phases compared with the amorphous state. As is known from neutron/X-ray diffraction and infrared/Raman spectra of silica glass, the glass is formed by a structural unit consisting of four oxygen atoms located at the corners of a tetrahedron with a silicon atom at the center (SiO_4 tetrahedron). The tetrahedra are linked at the corners to form the glass network, but the structure itself is not yet entirely clear. Several models have been proposed for the medium-range scale structure of the glass network. Fig. 1 shows a possible structure model consisting of a linking random network of SiO_4 tetrahedra. In this model, ring structures formed by several structural units also exist. The average bond angle between connected SiO_4 tetrahedra, i.e., the Si-O-Si bond angle, is calculated to be 144°.

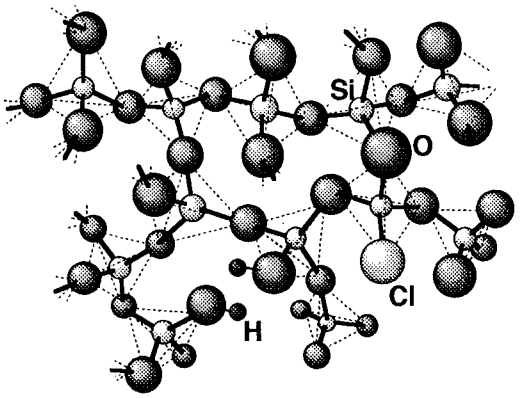


Fig. 1 Schimatic model of silica glass structure.

Densification of the a-SiO_2 [1-3] is an interesting phenomenon for understanding the amorphous structure. The structure of dense a-SiO_2 has been studied by infrared (ir) absorption and/or reflection, [4-8] Raman-scattering [7-12] spectra, and x-ray and/or neutron diffraction [13-16] measurements. In these studies, it was interpreted that the densification of the a-SiO_2 is due to a decrease in average Si-O-Si bond angle between connecting SiO_4

Mat. Res. Soc. Symp. Proc. Vol. 407 © 1996 Materials Research Society

tetrahedra, [4-11,17-19], or due to decreasing the mean number of members constituting ring structure.[12,17-18] Since a high density state should be unstable at an atmospheric pressure, the density of the glass will recover toward that of the undensified glass at high temperature, while maintaining its density at room temperature due to the rigidity of the structure on a finite time scale. The history of temperatures and pressures during densification affects this thermal relaxation process. [3, 20-21] Under pressing at high temperatures, the glass network readily rearranges and reaches a stable state under the pressure. At low temperatures or under shearing stress, however, many strained linkages may be introduced into the glass. This internal strain gives rise to structural relaxation at relatively low temperatures. Hydroxyl impurity in the glass also affects the relaxation process. Recently, Kitamura et al. [22] reported a relaxation of the 0.6% densified silica glass which contains hydroxyl impurity of 1200 wt. ppm. It was found that the relaxation process is complex and dependent on the annealing temperature. However structure analysis or dependence of the initial density under thermal annealing is not reported yet, although the analysis is important and of interest for understanding the relaxation processes.

In this paper, we shall deal with silica glasses densified at around glass transition temperature under high pressures. Isothermal relaxation of its densities has been performed, and a mechanism of the relaxation has been studied by using Raman scattering and infrared spectroscopy.

EXPERIMENT

Silica glass synthesized directly by hydrogen-oxygen flame hydrolysis was used as the starting material. The OH content of this glass was about 1200 wt. ppm, which was estimated from the ir absorption of *X*-OH(*X* is Si or H) at 3650 cm^{-1}.[23] Clear glass blocks were densified by hot isostatic pressing(HIP) in an argon gas atmosphere at 1200°C(near glass transition temperature) under 1GPa for 2 hours. The densified glasses were cut into small plates with 15x15x3mm for annealing experiment. The glass was annealed isothermally for various times at 100°C intervals from 800°C to 1100°C in air. Density of the glass was measured by Archimedes' method within an error of $\pm 5 \times 10^{-4}$ g/cm^3. Raman scattering and infrared reflection spectra have been measured in the glass annealed at 900°C. Isothermal annealing and density measurement were repeated until total annealing time of 64 hours.

RESULTS AND DISCUSSION

Density of the undensified glass was 2.1998 g/cm^{-3}. The density increased by about 3.6% ($\Delta\rho/\rho$) after hot isostatic pressing under 1GPa at 1200°C. The OH content in the glass was not changed after the densification. Non-exponential decay of the density against annealing time was found for all the isothermal annealings. The non-exponential relaxation processes were expressed well by the following stretched exponential relaxation function [20,21]:

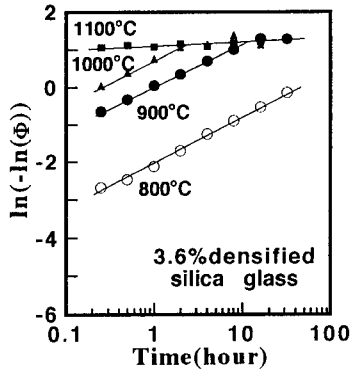


Fig. 2 Relaxation function versus annealing time for 3.6% densified silica glass.

$$\Phi(T,t) = \exp\{-(t/\tau_{eff})^{\beta}\}, \quad (1)$$

where $\Phi(T,t)$ is the relaxation function defined by

$$\Phi(T,t) \equiv (\rho(T,t)-\rho_\infty)/(\rho_0-\rho_\infty). \quad (2)$$

The constant values, ρ_∞ and ρ_0, are densities of undensified (or fully relaxed) glass and unrelaxed glass before the annealing, respectively. $\rho(T,t)$ is the density after annealing at T K for t hours. β is a constant value associated with the relaxation process. τ_{eff} is the effective relaxation time. Double logarithm of the relaxation function $\ln(-\ln\Phi)$ is plotted against annealing time in fig. 2. Fast and slow relaxation processes were found in this annealing. In the fast process which appears in relatively short time region, the relaxation function increased monotonically and is considered to have already finished in this time scale under annealing at 1100°C. At the end of the fast process, the density maintains about 0.5% higher value than that of the undensified glass. The relaxation function increased slightly in the slow process. The stretched exponential relaxation function (1) has fitted to the experimental data of the fast process and the optimized parameters, β and τ_{eff}, are listed in table 1. The β value, which corresponds to slopes of the straight lines, is independent of the annealing temperature for the 3.6% densified glass, while the value decreased with the increase of annealing temperature for the 0.6% densified glass.[22] For the 0.6% densified glass, the temperature dependent relaxation process may be due to the diffusion of hydroxyl (via protons or H_2O molecules), because the glass has many hydroxyl impurities and the diffusion should be enhanced at higher

Table 1. Optimized parameters in stretched exponential relaxation function under annealing at several temperatures for 3.6% densified silica glass.

Temperature (°C)	3.6% densified	
	β	τ_{eff} (h)
800	0.54	43
900	0.48	0.96
1000	0.49	0.23
1100	-	-

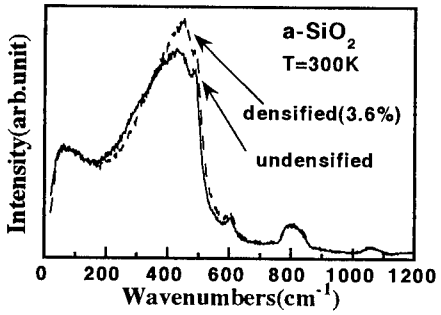


Fig. 3 Raman scattering spectra from 3.6% densified silica glass and undensified glass.

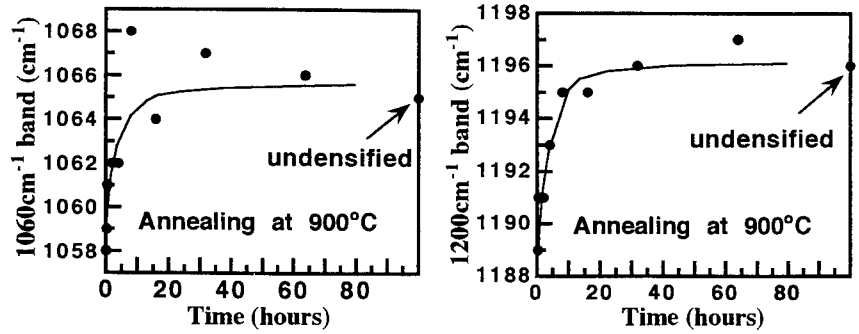


Fig. 4 Peak positions of 1060 cm^{-1} and 1200 cm^{-1} Raman bands versus time under annealing at 900°C.

temperatures. For the 3.6% densified glass, the independence of the parameter β from annealing temperature may be due to the suppression of the hydroxyl diffusion owing to a reduction in geometric space in the glass network. Another relaxation process with quite longer relaxation time becomes dominant after the fast relaxation. This slow relaxation process has the β value of one order smaller than that for the fast process. Fig. 3 shows Raman scattering spectra for the densified and undensified silica glasses. Bands at wevenumbers 460, 490, 600, 800, 1060 and 1200 cm^{-1} are caused by localized vibration modes in the glass network.[10, 24-26] Bands near 1060 and 1200 cm^{-1} due to the antisymmetric stretching vibration in Si-O-Si linkage [10,26] shifted toward lower wavenumbers after the densification. Contrary to this, a band at 800cm^{-1} assigned to the symmetric stretching vibration in O-Si-O linkage shifted toward higher wavenumbers. The central force model predicts that, as the Si-O-Si bond angle decreased, the adjacent Si-O stretching contributions become less coupled, and the symmetric and antisymmetric components converge in frequency. [27,28] This corresponds to the observed behavior of the silica glass on densification. In addition, the narrowing of the 460 cm^{-1} band would correspond to an increase in the mean dihedral angle $O_3Si\text{-}O\text{-}SiO_3$ in the densified glass.[24]

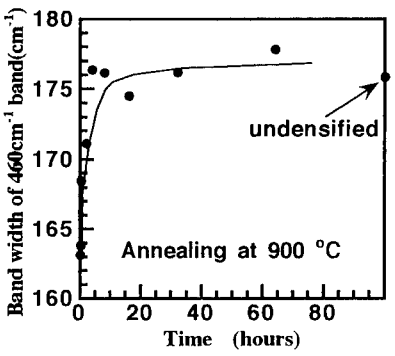


Fig. 5 Band width of 460 cm^{-1} Raman band versus time under annealing at 900°C.

Annealing at 900°C changed the positions of 1060 and 1200 cm^{-1} bands back toward the positions for the undensified glass. Fig. 4 shows the peak positions of the two bands against annealing time. The shift of the both bands in Raman spectra almost saturates within about 10 hours. As seen in fig. 2, a fast process gives place to a slow process after about 10 hours under the 900°C annealing. This alternation corresponds well to the relaxation behavior of the Raman bands. The relaxation of a width of the 460 cm^{-1} Raman band is shown in fig. 5. The width of the band recovered to the value of undensified glass within the same time scale (10 hours). These results show that the dominant fast relaxation process is attributed to the recovers of the Si-O-Si bond angle (1060 and 1200 cm^{-1} band) and the $O_3Si\text{-}O\text{-}SiO_3$ dihedral angle to the values of undensified glass. In the Infrared reflection spectra, a main band at 1120 cm^{-1} was shifted toward lower energies by the 3.6% densification. Peak position of the 1120 cm^{-1} band is shown against annealing time in fig. 6. The 1120 cm^{-1} band shifted back in a few hours by the same annealing. This behavior is not consistent with the fast process. However, the reflection measurement observes only the surface portion of the glass, because infrared light penetrates only less than

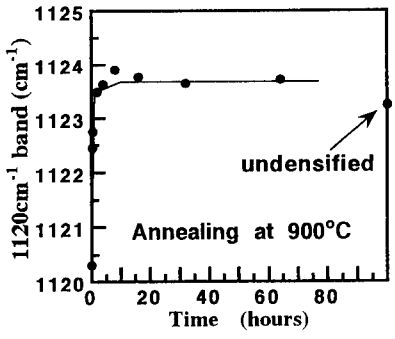


Fig. 6 Peak position of 1120 cm^{-1} infrared reflection band versus time under annealing at 900°C.

micrometers. Therefore, this different behavior from the Raman spectra is due to inhomogeneous relaxation around the surface portion.

It is interesting that Raman scattering and ir reflection spectra fully recovered after the fast process, while the high density state remains slightly (about 0.5%). The difference in glass structure between the glass under relaxing in the slow process and the undensified glass is not found in this structure analysis. The slow relaxation process might be due to a structural change of medium/long range order. For example, rearrangement from small to large membered ring structures or release of entanglement of glass network, are possible structural changes without affecting the average bond angle or dihedral angle. Measurement of glass structure by using neutron diffraction or XAFS will be needed for analyzing these structural changes.

CONCLUSIONS

Fast and slow relaxation processes were found in 3.6% densified silica glass under annealing at several temperatures from the analysis by using a stretched exponential relaxation function. Main relaxation process, i.e., the fast process is due to the recovers of Si-O-Si bond angle and dihedral angle between two SiO_4 tetrahedra toward the values for the undensified glass. The slow process is possibly due to structural changes in medium or long range order.

ACKNOWLEDGMENT

The authors express their sincere gratitude to the Nippon Silica Glass Co. for supplying the silica glass samples.

REFERENCES

1. P. W. Bridgman and I. Simmon, J. Appl. Phys. 24, 405(1953).
2. H. M. Cohen and R. Roy, J. Amer. Ceram. Soc. 44,523(1961).
3. J. D. Mackenzie, J. Amer. Ceram. Soc. 46,461(1963).
4. J. R. Ferraro, M. H. Manghnami and A. Quattrochi, Phys. Chem. Glasses 13,116(1972).
5. B. Velde and R. Couty, J. Non-Cryst. Solids 94,238(1987).
6. Q. Williams and R. Jeanloz, Science 239, 902(1988).
7. S. Mochizuki and N. Kawai, Solid State Commun. 11, 763(1972).
8. R. A. B. Devine, J. Vac. Sci. Tehnol. A 6, 3154(1988).
9. F. A. Seifert, B. O. Mysen and D. Virgo, Phys. Chem. Glasses 24, 141(1983).
10. P. McMillan, B. Piriou and R. Couty, J. Chem. Phys. 81, 4234(1984).
11. R. J. Hemly, H. K. Mao, P. M. Bell and B. O. Mysen, Phys. Rev. Lett. 57, 747(1986).
12. A. E. Geissberger and F. L. Galeener, Phys. Rev. B 28, 3266(1983).
13. R. L. Mozzi and B. E. Warren, J. Appl. Crystollagr. 2, 164(1969).
14. J. D. Jorgensen, J. Appl. Phys. 49, 5473(1978).
15. S. Susman, K. J. Volin, R. C. Liebermann, g. D. Gwanmesia and Y. Wang, Phys. Chem. Glasses 31.144(1990).
16. S. Susman, K. J. Volin, D. L. Price, M. Grimsditch, J. P. Rino, R. K. Kalia, P. Vashishta, G. Gwanmesia, Y. Wang and R. C. Liebermann, Phys. Rev. B43, 1194(1991).
17. R. A. B. Devine and J. Arndt, Phys. Rev. B 35, 9376(1987).
18. R. A. B. Devine and J. Arndt, Phys. Rev. B 39, 5132(1989).
19. R. A. B. Devine, R. Dupree, I. Farnan and J. J. Capponi, Phys. Rev. B 35, 2560(1987).
20. R. M. Kimmel and D. R. Uhlmann, Phys. Chem. Glasses 10, 12(1969).
21. J. Arndt, R. A. B. Devine and A. G. Revesz, J. Non-Cryst. Solids 131-133, 1206(1991).
22. N. Kitamura and H.Yamashita, Hot Isostatic Pressing '93, Ed. by L. Delaey and H. Tas,

p.471, Elsevier, Amsterdam, 1994.
23. G. Hetherington and K. H. Jack, Phys. Chem. Glasses 3,129(1962).
24. G.E. Walrafen and M. S. Hokmabadi, Structure and Bonding in Non-Crystalline Solids, Ed. by G. E. Walrafen and A. G. Revesz, p.185, Plenum Press, New York, 1986.
25. R. H. Stolen and G. E. Walrafen, J. Chem. Phys. 64, 2623(1976).
26. G. E. Walrafen and P. N. Kristnan, J. Chem. Phys. 74,5328(1981).
27. P. N. Sen and M. F. Thorpe, Phys. Rev. B 15,4030(1977).
28. F. L. Galeener, Phys. Rev. B 19, 4292(1979); M. F. Thorpe and F. L. Galeener, J. Non-Cryst. Solids 38/39, 1197(1980).

SIMULATION OF DYNAMICS OF LIQUID-GLASS TRANSITION

Y. KOGURE, K. KUNITOMI, Y. NAKAMURA, and M. DOYAMA
The Nishi-Tokyo University, Uenohara, Yamanashi 409-01, Japan

ABSTRACT

Glass transition of of copper is simulated by the molecular dynamics method. Embedded atom method potential is used. The glass state was produced by quenching the liquid sample, which was produced by melting a crystal. The split second peak in RDF was observed in the glass state.

INTRODUCTION

The glass transition is one of the most important problems in the condensed matter physics[1]. In the glass state, especially at low temperatures, materials shows abnormal behaviors in the mechanical (acoustic) and the thermal properties. These abnormality is considered to be related to the disordered structure of the glass state. The characteristic structure of glass may be formed at the glass transition, where the dynamics of atoms plays an important role. A computer simulation study on the glass transition of copper is described in this paper.

METHOD OF SIMULATION

The process of the simulation for glass transition is as follows. Firstly, a model copper crystal was melted by giving the particle velocity to make a liquid state. Secondly, the liquid state was quenchd by setting the particle velocity to be zero. Then the configulation of atoms were relaxed to obtain a quasi-equiliblium state.

The geometry of the starting model crystal to be melted is shown in Fig. 1, which has a cubic shape with edges along [100] axes. The numbers of atoms involved in the crystals are 1099. The configulation of atoms, which is initially located in a middle plane (shaded plane in the figure) are monitored.

The embedded atom method potential developed by the present authors[2] was used to express the interaction between copper atoms. The total energy is expressed as

$$E_{\rm tot} = \sum_i F(\rho) + \frac{1}{2}\sum_{ij}\phi(r_{ij}), \tag{1}$$

$$F(\rho) = D\rho\ln\rho, \quad \rho = \sum_{j\neq i} f(r_{ij}) \tag{2}$$

Mat. Res. Soc. Symp. Proc. Vol. 407 © 1996 Materials Research Society

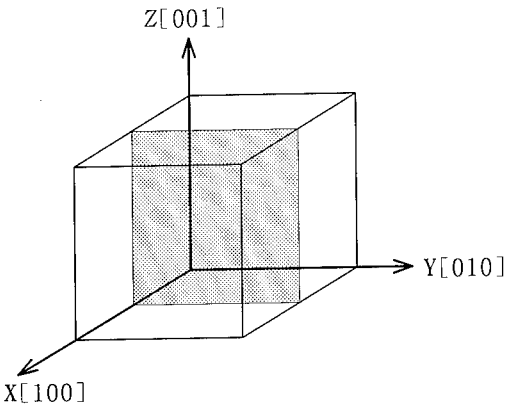


Fig. 1. Model crystal

where, $F(\rho)$ is the embedding energy for i-th atom, ρ is the electron density function, ϕ is the pairwise interaction energy and r_{ij} is the distance between i-th and j-th atoms. For the functional forms of ϕ and f, we assume

$$\phi(r) = A(r_C - r)\exp(-C_1 r), \tag{3}$$

$$\phi(r) = B(r_C - r)\exp(-C_2 r). \tag{4}$$

Here r_C is the cut off length of the interaction, and r and r_C are nomalized by the nearest neighbor distance.

As a initial condition before the melting, atoms are placed in the perfect crystal positions of fcc structure and the random velocity, v_i is given to each i-th atom. After 500 time steps liquid state is produced. The relation of the mean velocity v_m and the reference temperature of the liquid T^* is

$$mv_m^2 = 3k_B T^*, \tag{5}$$

where m is the atomic mass and k_B is the Boltzmann's constant.

After the system attained a liquid state, velocities of all the atoms were removed and molecular dynamics relaxation was started. The time interval Δt of the difference equation was set to be 5×10^{-15} sec. The atomic configulation and the radial distribution function (RDF) were calculated every hundred time steps.

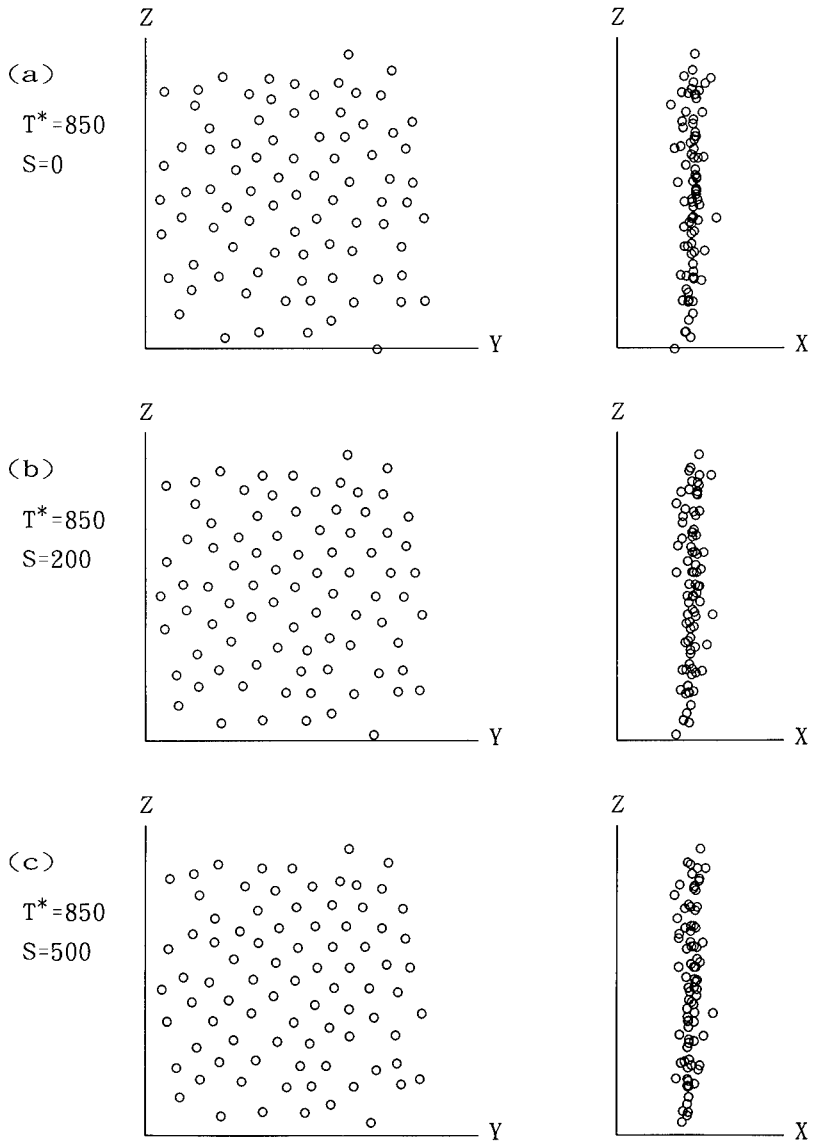


Fig. 2. Motion of atoms in a sample quenched at 850 [K].

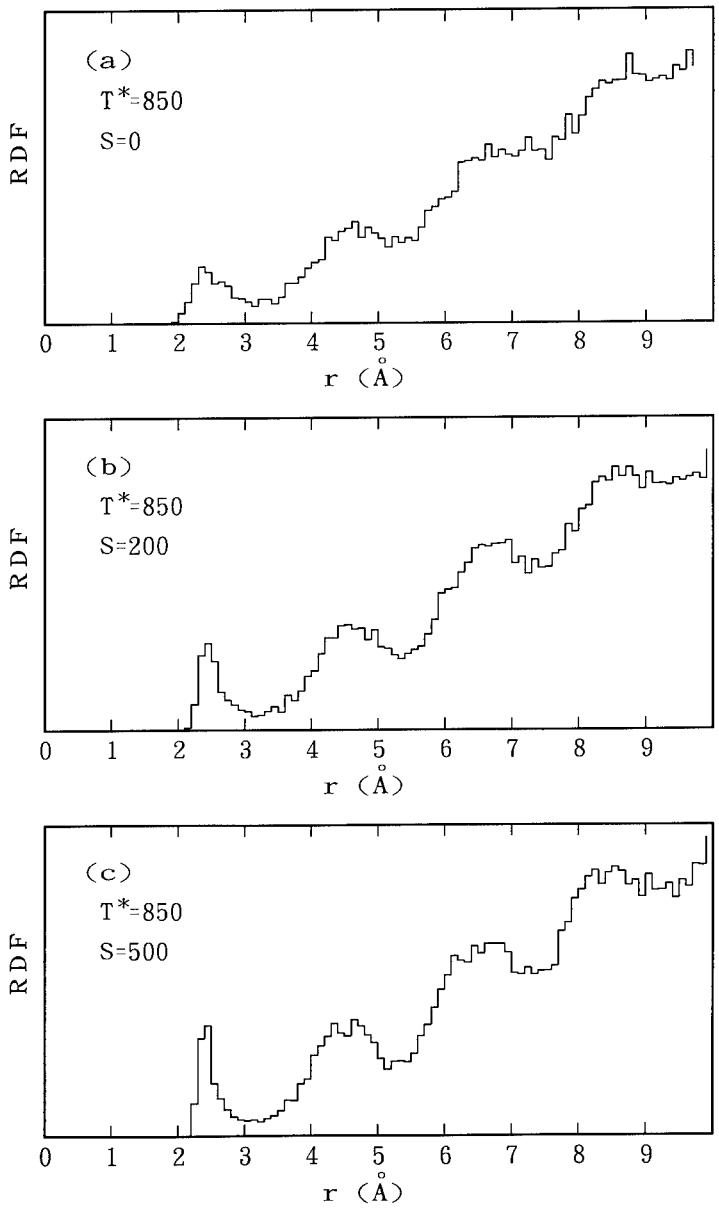


Fig. 3. Change of RDF in a sample quenched at 850 [K].

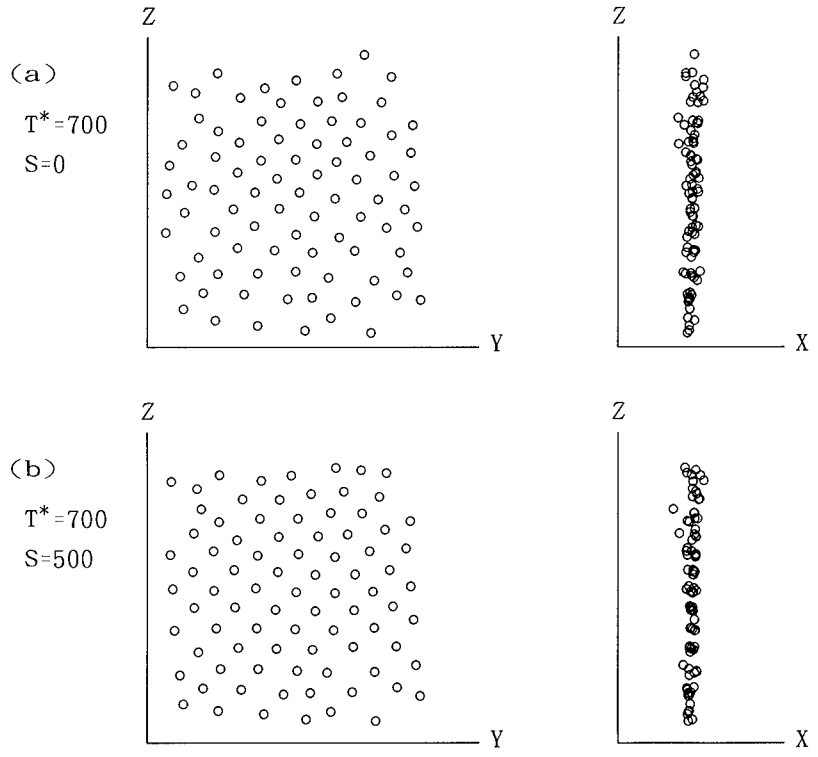


Fig. 4. Motion of atoms in a sample quenched at 700 [K].

RESULTS AND DISCUSSION

A model crystal kept at T = 850K was quenched and relaxed. The configulation of atoms initially located on a middle plane of the crystal is shown in Fig. 2 as a function of molecular dynamics time steps. The radial distribution function (RDF) is also shown in Fig. 3. It can be seen that the broad peaks in RDF becomes narrow and the second peak splits to two peaks. This phenomenon is well known and is observed experimentally in amorphous metals [3]. The relaxation was continued up to 1000 steps, but no appreciable change of the RDF was observed.

Another example of the relaxation at lower temperature (T^* = 700K) is shown in Fig. 4 and Fig. 5. At the starting point the configulation is disordered and the RDF is liquid-like. After the relaxation an ordered structure in configulation and sharp peaks in RDF are seen

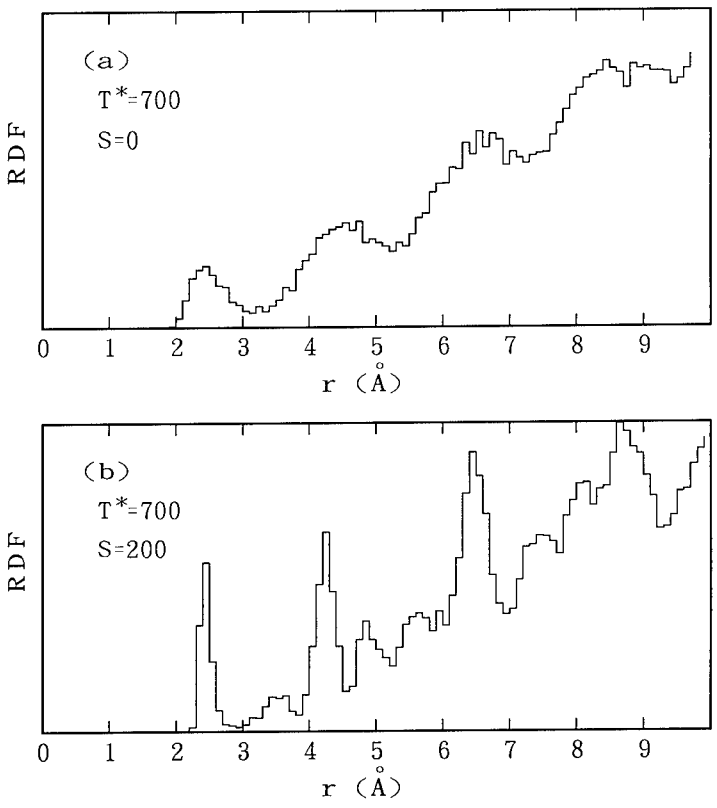


Fig. 5. Change of RDF in a sample quenched at 700 [K].

to be recovered. Namely, the crystal is not melted at this temperature. Further study on the effects of quenching rate is in progress.

REFERENCES

1. R. Zallen in The Physics of Amorphous Solids (John Wiley and Sons, New York), p. 73.

2. Y. Kogure, M. Miyazaki, T. Uzaki and M. Doyama, presented in this conference.

3. R. Yamamoto, H. Matsuoka and M. Doyama, Phys. Status Solidi A **45**, 305 (1978)

ENTHALPY RELAXATION NEAR THE GLASS TRANSITION OF A SUPERCOOLED LIQUID $[Ca(NO_3)_2]_{0.4}[KNO_3]_{0.6}$

I. K. MOON, Yoon-Hee JEONG
Department of Physics, Pohang University of Science and Technology, Pohang, Kyungbuk, 790-784, Korea

ABSTRACT

We have investigated the slow dynamics in the glass transition region of a supercooled liquid $[Ca(NO_3)_2]_{0.4}[KNO_3]_{0.6}$ by measuring the dynamic specific heat in the frequency range from 0.01 Hz to 5 kHz. The equilibrium dynamics of the system in this range is well described by the stretched exponential function, $\exp[-(t/\tau)^{\beta}]$, and the Vogel-Fulcher type relaxation time, $\tau = \tau_0 \exp[\Delta/(T - T_0)]$.

INTRODUCTION

Of the possible phases of condensed matter, the disordered phases, liquids and glasses, are not understood as well as its crystalline counterparts are. In recent years particular interest has been focused on the nature of the glass transition from a liquid to an amorphous solid. Although liquids under equilibrium conditions are considered as disordered arrangements, lacking a long-range order, of molecules, they still possess structures in the short or medium range.[1] However, these orders are not of static nature and consequently they appear as structural fluctuations. When the temperature of a liquid, for example, is changed, the structure of a liquid changes accordingly to the new equilibrium condition and this phenomenon is often called *structural relaxation*. While this structural relaxation occurs on a microscopic time scale in ordinary situations, extremely slow relaxation manifests itself when a liquid is sufficiently cooled below the freezing temperature. It is the purpose of this paper to report the results of our investigation on the slow enthalpy relaxation in the supercooled state of $[Ca(NO_3)_2]_{0.4}[KNO_3]_{0.6}$ mixture (CKN).

Of course, a liquid generally undergoes a first-order phase transition into a crystal when it is supercooled; however, there are materials which can be easily supercooled without being crystallized mainly due to the fact that they have a large viscosity at the freezing temperature.[2] One such example is CKN, which forms an ionic liquid when melted. CKN was chosen for the present study for two reasons: its good glass-forming ability and simple structure. First, the ability for CKN to stay supercooled for days without crystallization was essential in carrying out time-consuming dynamic (or frequency dependent) specific heat measurements to study the slow enthalpy relaxation in the supercooled state. Second, one may hope that the structural simplicity of CKN, that is, the fact that potassium and calcium ions have spherical charge distribution of argon and nitrate ions are of trigon shape would perhaps allow microscopic interpretation of the macroscopic enthalpy relaxation.

In the dynamic specific heat measurements, one probes the linear response of the system to a very small ac heat variation.[3,4] While the situation associated with more common rate-scanning experiments (heating and cooling) must be described as a nonstationary, viz. nonequilibrium and nonlinear, relaxation, the dynamic specific heat measurements are always carried out both in *equilibrium* and in the linear response regime. In other words the system would be in full equilibrium as soon as the ac heat were turned off. Thus the dynamic specific heat measurements yield information on the dynamic nature of the system in equilibrium in contrast to the rate-scanning method which probes the system falling out of equilibrium.

DYNAMIC SPECIFIC HEAT

Specific heat[5] is one of the fundamental quantities characterizing a condensed matter

Mat. Res. Soc. Symp. Proc. Vol. 407 © 1996 Materials Research Society

system. While specific heat is ordinarily considered to be a static thermodynamic quantity, one can generalize it as a dynamic quantity. The concept of dynamic specific heat appears natural if one recalls that static thermodynamic quantities are time-averaged (or ensemble-averaged) ones. They are static not because they do not change in time, but because they change too rapidly on the experimental time scale which, in our case, is larger than 10^{-4} sec.

For the isobaric thermal responses, the enthalpy deviation of a system from the equilibirum value, δH, per unit volume can be phenomenologically written as

$$\delta H(t)/V = \int_{-\infty}^{t} K_H(t,t')\delta T(t')dt' + C_p^{\infty}\delta T(t) \tag{1}$$

where V is the volume and δT denotes an external perturbation. C_p^{∞} represents the contribution from the degrees of freedom such as phonons which can respond instantaneously and K_H is the response function due to the slow relaxation. One may also write Eq. (1) in terms of the relaxation function $R(t,t')$ defined as $R(t,t') = \int_{-\infty}^{t'} K_H(t,t'')dt''$. For the system in equilibrium the relaxation function has the additional property of being stationary, *i.e.*, $R(t,t') = R(t-t')$.

From the statistical mechanical point of view, all the equilibrium or near-equilibrium properties of a system is described as a function of $\mathcal{H}_0/k_BT$, where $\mathcal{H}_0$, k_B, and T are the Hamiltonian of the system, the Boltzmann constant, and the temperature respectively. For the temperature variation δT, the perturbing term in the Hamiltonian is obtained from

$$\mathcal{H}_0/k_B(T+\delta T) = \mathcal{H}_0/k_BT(1+\delta T/T) = \mathcal{H}_0(1-\delta T/T)/k_BT\,. \tag{2}$$

Thus, δT couples to the Hamiltonian of the system and $R(t)$ is obtained, considering that one is dealing with the isobaric situation, from the linear response theory[6]

$$R(t) = (1/k_BT^2V) < \delta H_R(t)\,\delta H_R(0) > \tag{3}$$

where δH_R represents the enthalpy fluctuation associated with the slow relaxation.

The complex dynamic specific heat, $C_p(\omega) \equiv C_p{}'(\omega) + i\,C_p{}''(\omega)$, may be expressed in terms of the Fourier transform of the time derivative of the relaxation function $R(t)$:

$$\begin{aligned} C_p(\omega) &= C_p^{\infty} + \int_0^{\infty}[-dR(t)/dt]\,e^{i\omega t}\,dt \\ &= C_p^0 + (i\omega/k_BT^2V)\int_0^{\infty} dt\,e^{i\omega t} < \delta H_R(t)\delta H_R(0) > \end{aligned} \tag{4}$$

where C_p^0 is the static specific heat which includes contributions from both fast and slow degrees of freedom. Thus slow relaxation of enthalpy governed by the system dynamics is the origin of the frequency-dependent specific heat and therefore one can probe the slow dynamics of the system by measuring the dynamic specific heat. On the other hand, when the dynamics of the system occurs at a rate faster than the probing frequencies, the dynamic specific heat becomes the usual static specific heat.

EXPERIMENT

In measuring the dynamic specific heat of CKN, the 3ω-technique was adopted.[4] The essence of the technqiue lies in using either a planar or a line resistive element in contact with a sample as a heater and sensor *simultaneously*. When the ac current at angular frequency ω flows into the heater, heat is generated at 2ω and the temperature oscillation at the same frequency will result. The amplitude of this oscillation is determined by how well the heat from the heater is diffused into the sample which is in intimate contact with the heater and thus reflects the thermal properties of the sample. Since the sample in this

case is a liquid, we deposited by thermal evaporation a metallic heater on a glass substrate. Then a liquid sample was placed on top of the substrate.

As was shown in Ref. [4] in detail, the temperature oscillation at the heater, δT, in the present configuration is given for the planar case by

$$\delta T = [P_0/(\sqrt{2\omega C_p(2\omega)\kappa} + \sqrt{2\omega C_g(2\omega)\kappa_g})]e^{-i\pi/4} \equiv T_{mag}e^{i\phi} \quad (5)$$

where P_0 is the power per unit area generated at the heater and κ is the thermal conductivity of the sample. The behavior of a thin wire heater at low frequencies is

$$\delta T = [-P/2\pi(\kappa + \kappa_g)] \ln 2\omega + constant \equiv T_{mag}e^{i\phi} \quad (6)$$

where P is the power per unit length. The subscript g's in Eq. (5) and (6) stand for the glass substrates and they represent the background values of δT which can be calibrated away. Eq. (5) and (6) indicate that one can obtain $C_p(\omega)$ and κ separately by measuring δT as a function of frequency in both cases.

Detection of this temperature oscillation at the heater is done as follows. An ac current through the heater, $I(t) = I_0 cos\omega t$, generates the Joule-heating at 2ω, $P(t) = I^2R = (1/2)I_0{}^2R(1 + cos2\omega t)$.[7] The ac power causes the temperature oscillation of the heater according to Eq. (5) or (6) and the temperature oscillation in turn generates the resistance oscillation at the same frequency: $R(t) = R_0[1 + \alpha T_{mag} cos(2\omega t - \phi)]$ where α is the temperature coefficient of resistivity of the heater. Then the voltage across the heater, $V(t) = I(t)R(t)$, appears as

$$V(t) = I_0 \cos\omega t \cdot R_0[1 + \alpha T_{mag} \cos(2\omega t - \phi)] = I_0 R_0 \cos\omega t + (1/2)I_0 R_0 \alpha T_{mag} \cos(\omega t - \phi) + (1/2)I_0 R_0 \alpha T_{mag} \cos(3\omega t - \phi)\,. \quad (7)$$

It is the second and third terms that contain the thermal information of the sample we want to measure. These terms are very small compared to the first term, the normal ac voltage, since $\alpha \approx 0.004$ K^{-1} and T_{mag} is kept small to stay in the linear regime. However, one can take advantage of the fact that the last term appears at 3ω by using a Wheatstone bridge to balance out the large unwanted signal.

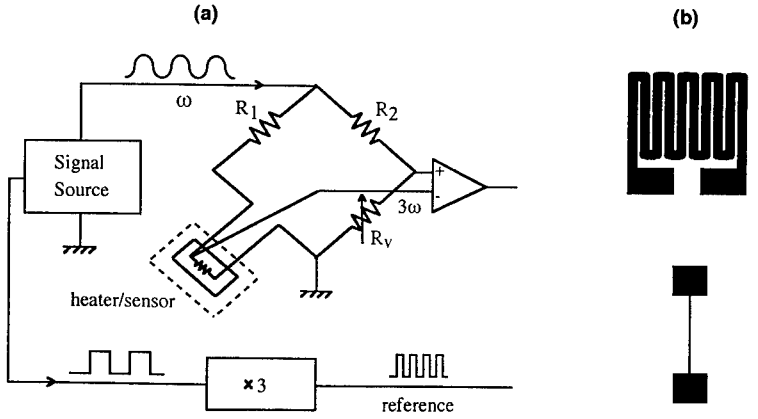


FIGURE 1. (a) Schematic diagram of the Wheatstone bridge. R_1 is a manganin wire and resistances of R_2 and R_v are much larger than those of the left arm. The sync-out signal of the synthesizer is tripled by a home-made circuit. (b) The mask patterns used to produce planar (top) and line (bottom) heaters.

Fig. 1(a) is the experimental setup. The resistors, R_2 and R_v, in the right arm of the bridge had the values in the range of kΩ, which were much larger compared to 20 $\sim$ 30 Ω of R_1 and the heater, to inhibit the current flowing into this side. A manganin wire with a small α was used as a R_1 to suppress the third harmonic generation. By balancing the bridge, we removed the large fundamental signal and detected 3ω signal with a lock-in amplifier. Also shown in Fig. 1(b) are the mask patterns used in evaporating metallic heaters of thickness $\sim$ 1000 Å on glass substrates on top of which liquids were placed. The width and length of a line heater were typically 60 μm and 6 mm respectively, while the sides of a zigzag-shaped planar heater were 6 mm long.

RESULTS

The frequency range we were able to cover was from 0.01 Hz to 5 kHz and it means that we had a frequency window of more than 5 decades.(The frequency in this section refers to the heating frequency $2\omega/2\pi$ in the previous section.) This frequency window turned out to be adequate in studying the dynamics associated with the glass transition of CKN. By using the two types of heaters, we obtained the specific heat and the thermal conductivity of CKN independently. As far as the thermal conductivity of CKN is concerned, we could not detect any appreciable change or any frequency dependence in the whole glass transition region.[8] This suggests that the heat carrying modes, probably high frequency phonons, are not affected at all by the glass transition.

In Fig. 2 shown are the real (C_p') and imaginary (C_p'') parts of the dynamic specific heat of CKN against the logarithm of frequencies. As is easily seen from the data, the dynamics of the system slows down with decreasing temperature and the shape of C_p'' is asymmetrical. These features are typical of many glass formers; since it has been found that the stretched exponential or KWW (Kohlrausch-Williams-Watts) function adequately describes the dynamics for them, the data at each temperature were fitted to Eq. (4) with $R(t) = \Delta C_p \exp[-(t/\tau)^\beta]$ where ΔC_p is a parameter representing the relaxation strength.

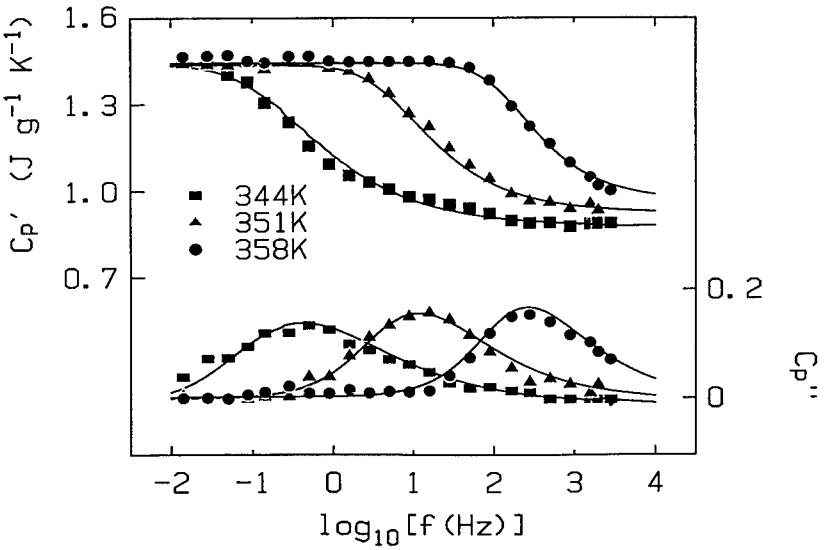


FIGURE 2. The real and imaginary parts of $C_p(\omega)$ of CKN as a function of frequency. The solid lines are fits to the data with a KWW function, $\exp[-(t/\tau)^\beta]$, with β=0.53 (344 K), 0.57 (351 K), and 0.62 (358 K).

To enhance the precision we used the set of real and imaginary data simultaneously in fitting; it is noted that since C_p^0 does not vary as a function of temperature, the fitting was done with three parameters,*i.e.*, ΔC_p, τ, and β. The best-fit curves drawn through the data indicate that the KWW function is indeed good in describing the slowing down of the enthalpy of CKN in the glass transition region.

In the upper inset of Fig. 3, the relaxation time, τ, obtained from the fitting is shown against $1/T$. We can easily see from the data points that the relaxation time is not behaving in an Arrehnius fashion, but in a Vogel-Fulcher one. The solid line represents the best fit to the data using the Vogel-Fulcher form, $\tau = \tau_0 exp[\Delta/(T - T_0)]$. The fitting procedures yielded the values for parameters: $\tau_0 = 10^{-14.6}\, sec$, $\Delta = 1800\, K$, $T_0 = 288 \pm 8\, K$. These are reasonable physical values and T_0 is probably close to the Kauzmann temperature T_K. Although the crossover of the relaxation time from an Vogel-Fulcher to an Arrhenius behavior at low temperatures was noted from the viscosity data,[9] our data, which represent the lowest-frequency dynamic characterization of CKN to date, obey well the Vogel-Fulcher law in the whole temperature range. In the lower inset of Fig. 3 shown is the KWW fitting parameter β versus T. From the data it is obvious that β is changing linearly as a function of temperature. The significance of this behavior is that the width of $C_p''(\omega)$ increases as T decreases and thus any analysis based upon the fact that $\beta = constant$, for instance time-temperature superposition, is not correct. This will also be of paramount importance in analyzing the rate-scanning results.[8] It is of value to note that if we attempt the linear fitting of β versus T, we obtain, within experimental error, $\beta = a(T - T_0)$ where a is a constant. Considering that the temperature range for the data is far off from T_0, it may not be appropriate to place too much physical meaning on this behavior; however, we mention that there exists a theory predicting such a behavior.[10]

Now that we have the full characterization of the enthalpy relaxation in CKN, we can test a very interesting idea of serial decoupling of modes in the glass transition region;

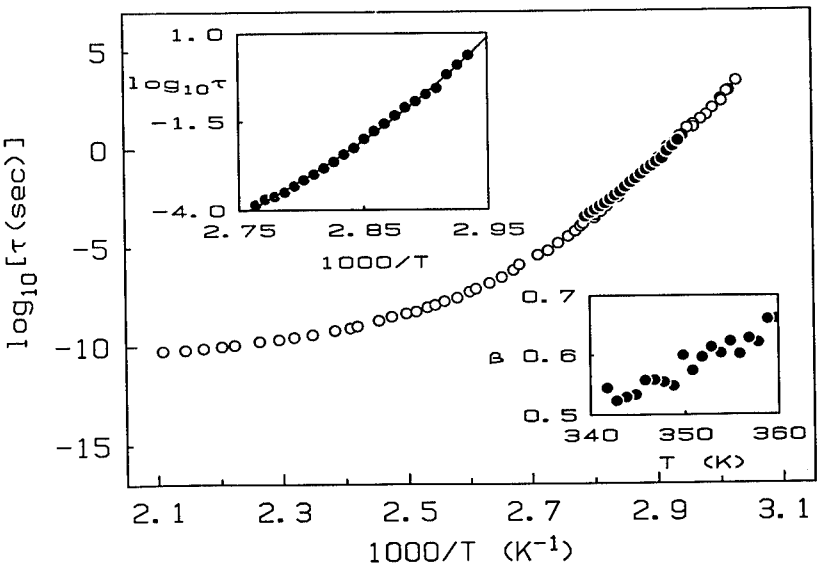


FIGURE 3. The relaxation times of CKN vs T^{-1}. The solid circles denote enthalpy relaxation times from this work, while the open circles denote the shear times from Ref. [9]. The upper inset diplays the Vogel-Fulcher fit of τ from the dynamic specific heat data and the lower inset shows β as a function of T.

CKN is often cited as an example of this decoupling.[11] The essence of the idea is that while on short time scales (or at high temperatures) the shear, volume, and enthalpy relaxation times are all the same, the shear modes decouple from the rest and the shear relaxation occurs at a faster rate as the temperature is reduced toward the glass transition. To test if decoupling really occurs, we plotted simultanesously, in Fig. 3, the average enthalpy relaxation time $< \tau >$ (solid circles) and the shear relaxation time τ_S (open circles). The average relaxation time is defined as $< \tau >= \tau\Gamma(1/\beta)/\beta$ where Γ is the usual gamma function, while τ_S is defined as $\tau_S = \eta/G_\infty$ where η is the shear viscosity and G_∞ is the high-frequency limit of the shear modulus. Values of η and G_∞ were taken from Ref. [9]. As can be seen in the figure, the two kinds of relaxation times coincide and we do not find any evidence of decoupling. Thus if decoupling indeed did occur, it should do so at longer times than $\sim 10\,sec$ which is the inverse of our lowest measuring frequency.

CONCLUSIONS

We have measured the dynamic specific heat, characterizing the equilibrium behavior, of a supercooled liquid CKN in the frequency range from 0.01 Hz to 5 kHz. It was shown that the enthalpy relaxation near the glass transition of CKN is well described by the stretched exponential function, $\exp[-(t/\tau)^\beta]$, and the Vogel-Fulcher type relaxation time, $\tau = \tau_0 \exp[\Delta/(T - T_0)]$. Currently investigation on the nonlinear relaxation is in progress.

ACKNOWLEDGMENTS

This work was supported by KOSEF (941-0200-018-2), RCDAMP of Pusan National University, and BSRI program of POSTECH (95-2438).

REFERENCES

1. See, for example, R. Zallen, *The Physics of Amorphous Solids* (John Wiley and Sons, New York, 1983), Chap. 1.

2. A supercooled liquid is said to be in *equilibrium*, even though the true ground state is crystalline below the freezing temperature. It is assumed that the escape time to the crystalline state is much longer than the internal equilibration time of the supercooled liquid and therefore one can disregard the crystalline state in the phase space and speak of the equilibrium liquid. This is presumably the case with supercooled CKN.

3. N. O. Birge and S. R. Nagel, Rev. Sci. Instrum. **58**, 1464 (1987).

4. D. H. Jung, T. W. Kwon, D. J. Bae, I. K. Moon, and Y. H. Jeong, Meas. Sci. Technol. **3**, 475 (1992); I. K. Moon, Y. H. Jeong, and S. I. Kwun, Rev. Sci. Instrum., Jan. 1996 (unpublished).

5. The term *specific heat* is used here to mean the heat capacity per unit volume at constant pressure.

6. R. Kubo, Rep. Prog. Phys. **29**, 255 (1966).

7. The sole effect of the dc component of power is its giving rise to the fixed amount of the sample temperature shift with respect to the bath temperature.

8. Y. H. Jeong and I. K. Moon, Phys. Rev. **B52**, 6381 (1995).

9. H. Tweer, N. Laberge, and P. B. Macedo, J. Amer. Cer. Soc. **54**, 121 (1971)

10. M. Papoular, Phil. Mag. Lett. **64**, 421 (1991).

11. C. A. Angell, J. Noncryst. Solids **131-133**, 13 (1991).

VARIATION OF THE STRUCTURAL UNIT IN TELLURITE GLASSES

Shigeru Suehara, Kazuo Yamamoto, Shunichi Hishita, Takashi Aizawa,
Satoru Inoue, and Akihiko Nukui
National Institute for Research in Inorganic Materials, 1-1 Namiki, Tsukuba, Ibaraki 305, Japan;
suehara@nirim.go.jp

ABSTRACT

We show that the variation of the structural unit in tellurite glasses is due to the charge transfer from modifier atoms to TeO_6 octahedra with use of first-principles molecular orbital calculations. Orbital overlap population analysis reveals that the transferred electrons to the Te-O antibonding orbital cause breaking Te-O bonds and lead to reducing the coordination number of the Te atom.

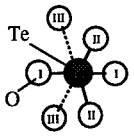
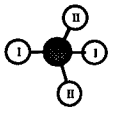
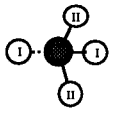
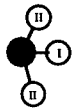
INTRODUCTION

Structural units of tellurite glasses are reported to be TeOx (x=3-6) polyhedra [1-6]. It is in contrast with the structural unit of silicate glasses (an SiO_4 tetrahedron) which is not affected by modifier atoms. Usually, modifier atoms are added to enhance glass formation, as a result of network breaking (breaking the chains of structural units) and increment of entropy (decreasing liquidus temperature). In tellurite glasses, however, the modifier atoms play one more important role: causing the variation of the structural unit itself. In order to elucidate this variation induced by modifiers, we have investigated the chemical bonding in tellurite glasses with use of first-principles molecular orbital calculations.

CALCULATION

Glass has the structural units similar to the short range order in the analogous crystalline compounds. Table I shows the examples of the structural unit for the crystalline compounds

Table I Coordination number and structural unit of some tellurite compounds.

Coordination Number	Structural Unit	Compounds
4+2		α-TeO_2 (Paratellurite)
4		$Zn_2Te_3O_8$ $CuTeO_3$
3+1		$BaTeO_3$
3		Li_2TeO_3

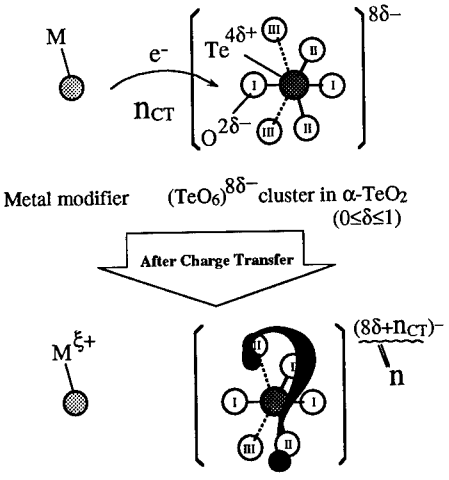


Figure 1 Schematic illustration of charge transfer from a metal modifier to TeO_6 cluster. The parameter δ ($0 \le \delta \le 1$) which represents the fractional ionic character in a Te-O bond.

Mat. Res. Soc. Symp. Proc. Vol. 407 © 1996 Materials Research Society

(M-Te-O; M=Zn, Cu, Ba, Li). On the analogy of these structures, the structural units of the tellurite glasses should be TeOx (x=3-6) polyhedra as derived forms of the TeO_6 structural unit found in paratellurite.

Since the electronegativity of M (metal modifier atoms such as Zn, Cu, Ba, Li, etc.) is smaller than those of Te and O (0.8-1.9, 2.1, and 3.5 for M, Te, and O on the Pauling scale, respectively [7]), the charge should transfer from M to TeO_6. In general, a bond in a compound is partly covalent and partly ionic. In paratellurite, the charge states of a Te atom and an O atom are $Te^{4\delta+}$ and $O^{2\delta-}$ using the parameter δ ($0 \le \delta \le 1$) which represents the fractional ionic character in a Te-O bond. Thus, the initial charge state for the TeO_6 octahedron should be $(TeO_6)^{8\delta-}$. The parameter d can not be easily determined. Despite a considerable research effort, ionicity even of simple alkaline-earth oxides is still controversial [8]. The ionicity δ in paratellurite will be discussed later. In tellurite glasses, the net charge n for $(TeO_6)^{n-}$ cluster can be defined by $8d+n_{CT}$, where n_{CT} is the amount of the charge transferred from M to TeO_6. Figure 1 shows the schematic illustration of the charge transfer.

We reveal how the parameter n affect the electronic structure and Te-O bonding in the TeO_6 octahedron. The electronic structure of $(TeO_6)^{n-}$ clusters are calculated with use of the self-consistent-charge discrete variational Xα (SCC-DV-Xα) method [9]. The SCC-DV-Xα method has been successfully applied to the interpretation of x-ray-photoemission spectra for crystalline paratellurite[10]. In this method, the Hartree-Fock-Slater (HFS) equation for a cluster is self-consistently solved with use of a localized exchange potential (Xα potential). The adjustable (exchange-correlation) parameter a was taken to be 0.7 as usual. Numerical tellurium 1s-5p and oxygen 1s-2p atomic orbitals, which were obtained as solutions of the atomic HFS equations, were utilized as basis sets.

In order to shed light on what occurs in the chemical bonding of the TeO_6 cluster due to the charge transfer, we assumed the same structure as the TeO_6 octahedron found in paratellurite. Figure 2 shows the crystal structure of paratellurite including the octahedral TeO_6 cluster employed in this calculation. The TeO_6 cluster is made of one central Te atom and six octahedral O atoms which can be divided into following three types: The first is axial type (O_I) found at a distance of 3.84 a.u. from central Te atom; The second is equatorial type (O_{II}) at a distance of 3.84 a.u.; The third is also equatorial type (O_{III}) found at a distance of 5.05 a.u.[11]. Calculations on this cluster were performed with C_2 point-group symmetry.

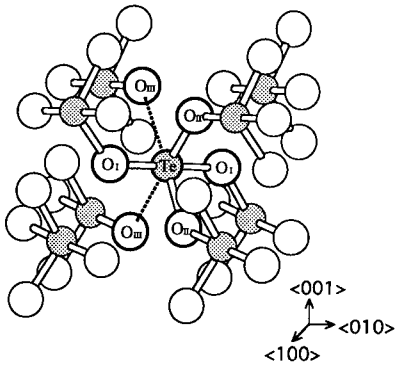


Figure 2 Schematic illustration of a TeO_6 cluster in paratellurite.

RESULTS AND DISCUSSION

Figure 3 shows the results for Mulliken overlap populations, which scale bond order in simple meaning, versus net charge n for the $(TeO_6)^{n-}$ clusters [12]. While the overlap population of Te-O_{II} bond increases slightly as n increases, those of bonds Te-O_{III} and Te-O_I decrease drastically to negative values at n=7 and 8, respectively. As no bonding is expected in the regions of the negative overlap population, the bonds Te-O_{III} and Te-O_I should break, and consequently the coordination number of the Te atom reduces from 6 via 4 to 2 as n increases from 6 to 8. While odd coordination numbers do not appear essentially in our present calculations because of C_2 point-group symmetry, the trend that the bonds Te-O_{III} break first and secondly the Te-O_I break as the coordination number reduces is consistent with the experiments. For example, the structural unit TeO_6 (more strictly, TeO_{4+2}) in paratellurite changes to TeO_4 in $Zn_2Te_3O_8$ and $CuTeO_3$ due to the modifier atoms with bond breaking of Te-O_{III}; The reduction in the coordination number from 4 to 2 is consistent with Raman investigation of alkali tellurite glasses which indicated that the coordination state of tellurium atom changes from TeO_4 through TeO_{3+1} to TeO_3 with the bond breaking between Te and axial O, which corresponds to O_I in present calculation, as increasing alkali oxide [6]. Actual tellurite glasses are made up of not one structural unit but the mixture of TeO_4, TeO_{3+1}, and/or TeO_3 [6,13]. This is due to local inhomogenuity. The electrons do not transfer from the modifier atoms to all the structural units, and consequently two or more states of the structural unit exist.

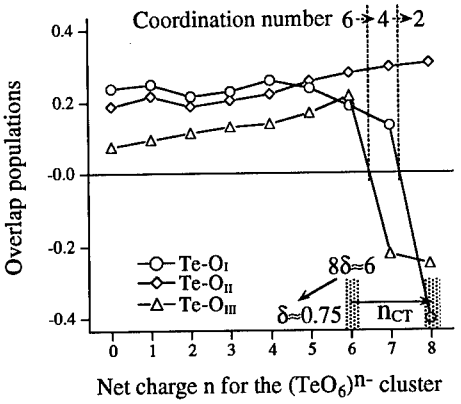


Figure 3 Mulliken overlap populations for bonds Te-O_I, Te-O_{II}, and Te-O_{III} versus net charge n for the $(TeO_6)^{n-}$ cluster.

Figure 4 shows orbital overlap populations (OOPs) for each Te-O bond in the neutral $(TeO_6)^{0-}$ cluster with the energy level structure. Positive (negative) OOP means bonding (antibonding) feature of that orbital. An electron in bonding (antibonding) state contributes to making (breaking) the bonds, hence the integral of the OOP below the highest occupied molecular orbital (HOMO) gives bond order, namely, the Mulliken overlap population [14]. There are five well-separated bands in the occupied state region. The bands A and B are mainly composed of O 2s with small amount of Te 5s and 5p bonding characters, respectively. The band C is made up of the Te 5s orbital admixed with O 2s antibonding states. The band D is bonding orbitals between Te 5p and O 2p containing a small amount of the O 2s antibonding character. The band E originates from the O 2p states [10]. In the rigid band scheme, electrons occupy the levels marked 1, 2, 3, and 4 in order as n increases. Each level can contain 2 electrons. The occupation of the levels 1, 2, and 3 hardly contribute to the Te-O bonding judging from the small OOPs.

These levels are of O 2p character and merely make lone pairs. Therefore, the bonding nature does not change up to n=6. When n exceeds 7, electrons occupy the marked 4 level and then the overlap populations of each bond decrease because of the large antibonding character of this level. In this case, Te-O_I bond is most weakened. However, Te-O_{III} bond is first broken since Te-O_{III} bond has smaller overlap population than Te-O_I from the beginning. The OOP at the marked 4 level for Te-O_{II} bond is the smallest antibonding character, and therefore, this bond remains in bonding state. Thus, the variation of the structural unit in tellurite glasses is most likely caused by the electrons in the marked 4 level.

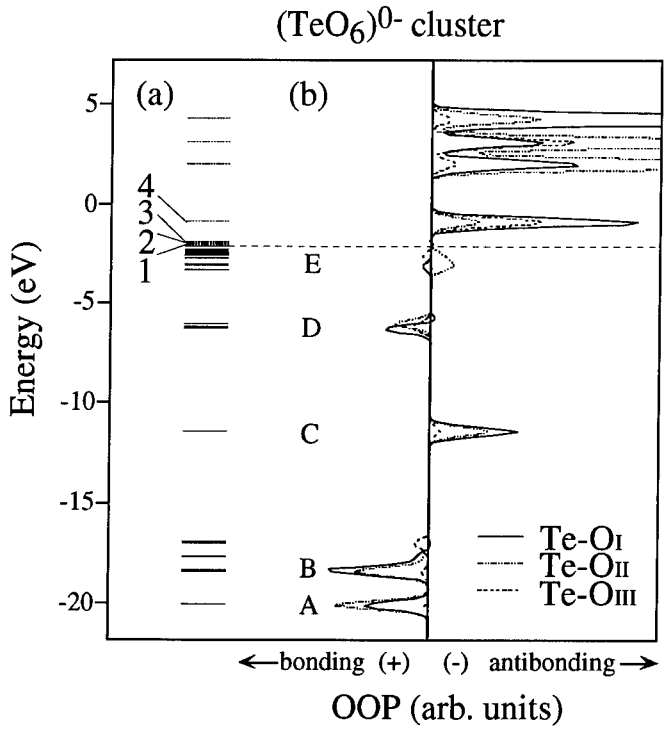


Figure 4 (a) Energy-level structure of $(TeO_6)^{0-}$ cluster. Solid and dotted lines show occupied and unoccupied levels, respectively. Levels marked 1, 2, and 3 are of O 2p character and marked level 4 is of Te 5s and 5p, and O 2p characters. (b) Orbital overlap populations (OOP's) for bonds Te-O_I, Te-O_{II}, and Te-O_{III} in the $(TeO_6)^{0-}$ cluster. The OOP curves are obtained by convolution of the OOP and a Gaussian function with 0.5 eV full width half maximum.

Finally, we estimate the initital charge state and the bond ionicity δ of paratellurite. As dicussed above, the variation of the structural unit is caused by 2 or less electrons in the marked 4 level. This is consistent with the crystalline compounds. Namely, even assuming that all modifier atoms are completely ionized, the transfer charge n_{CT} par one cluster is 2 or less; For example, n_{CT}=0 for paratellurite, n_{CT}=2 for Li_2TeO_3, $BaTeO_3$, $CuTeO_3$, and n_{CT}=4/3 for $Zn_2Te_3O_8$. Thus, we may estimate n_{CT} to be 2 or less. It follows from this estimation that the initial net charge 8δ must be ca. 6, i.e. $\delta \approx 0.75$, for structural unit changing by n_{CT} as shown in figure 3. In paratellurite, therefore, the net charge of a Te atom and an O atom should be ca. +3 and ca. -1.5, respectively.

CONCLUSION

We have shown that the variation of the structural unit in tellurite glasses is due to the charge transfer from modifier atoms to TeO_6 octahedra with use of first-principles molecular orbital calculations. Mulliken overlap populations indicate that the oxygen coordniation number of a Te atom reduces as the charge transfer progresses. This is consistent with the trend found in metal tellurite structures. Orbital overlap population analysis reveals that the transferred electrons to the Te-O antibonding orbital cause breaking Te-O bonds and lead to reducing the coordination number of the Te atom.

ACKNOWLEDGMENTS

We thank Prof. H. Adachi (Kyoto Univ.) for use of the DV-Xα calculation program.

REFERENCES

1. O. Lindqvist, Acta Chem. Scand. **22**, 977 (1968).
2. I. D. Brown, J. Solid State. Chem. **11**, 214 (1974).
3. G. W. Brady, J. Chem. Phys. **27**, 300 (1957).
4. M. Arnaudov, V. Dimitrov, Y. Dimitrov, and L. Markova, Mater. Res. Bull. **17**,1121 (1982).
5. R. V. Adams, Phys. Chem. Glasses **2**, 101 (1961).
6. T. Sekiya, N. Mochida, A. Ohtsuka, and M. Tonokawa, J. Non-Cryst. Solids **144**, 128 (1992).
7. L. Pauling, The Nature of the Chemical Bond Cornell Univ. Press, 1960.
8. R.Souda, K. Yamamoto, W. Hayami, T.Aizawa, and Y. Ishizawa, Phys. Rev. **B50**, 4733 (1994).
9. H. Adachi, M. Tsukada, and C. Satoko, J. Phys. Soc. Jpn. **45**, 875 (1978).
10. S. Suehara, K. Yamamoto, S. Hishita, and A. Nukui, Phys. Rev. **B50**, 7981 (1994).
11. R. W. G. Wyckoff, Crystal Structures 2nd ed., Interscience, New York, 1963.
12. R. S. Mulliken, J. Chem. Phys. **23**, 1833 (1955).
13. S. Noev, V. Kozhukharov, I. Gerasimova, K. Krezhov, and B. Sidzhimov, J. Phys. C.-Solid State Phys. **12**, 2475 (1979).
14. R. Hoffmann, Rev. Mod. Phys. **60**, 601 (1988).

THE ROLE OF STOCHASTIC NOISE ON THE GLASS TRANSITION

Fernando C. Perez-Cardenas and Hao Gan
Vitreous State Laboratory, The Catholic University of America, Washington, D.C. 20064

ABSTRACT

Glasses are amorphous solids that exhibit an intricate structural relaxation. A broad relaxation time spectrum always emerges when these systems are perturbed. By using a Langevin-type differential equation to describe the structure dynamics of these materials, it is depicted how the broad relaxation time spectrum arises due to the stochastic noise and how this affects the system's structure evolution as it is cooled down into the glass transition region. This stochastic model provides a macroscopic as well a microscopic view of the glass relaxation process.

INTRODUCTION

The structural rearrangement following a thermal perturbation to a glass-forming liquid is called structural relaxation. At low viscosities, the relaxation times involved in the process are very short, and become longer as the system cools down. Glass transition region (GTR) of a liquid refers to the temperature range in which the relaxation times are of the order of the observation time. Below the GTR, the liquid appears *frozen* in an out-of-equilibrium configuration.

The concept of *fictive temperature*, T_f, has been widely used to account for the structural state of glasses. It was introduced by Tool to describe the relaxation of stresses in annealing glasses [1]. By using the expression

$$\frac{dT_f}{dt}=\frac{1}{\tau}(T-T_f) \qquad (1)$$

(known today as Tool's equation), where τ is a relaxation time and T is the temperature, he was successful in accounting for the nonlinearity of the glassy relaxation process. However, this equation neglects the properties fluctuations observed in glasses and fails to explain the memory effects. In general, a comprehensive glass relaxation model must explain properties such as nonexponential decay, nonlinearity, memory effects, etc. The models proposed so far tend to take a somewhat pragmatic approach and are short in sound physical meanings, if judged from a theoretical view point. In this paper, we propose a stochastic model for glass relaxation processes. We will show how a stochastic term in our formulation influences the structure evolution of glass-forming liquids, and what physical insight we can gain about glass transition phenomena from the modeling results.

THE STOCHASTIC MODEL

The physical properties (e.g., density, refractive index, etc.) of glasses fluctuate from point to point in space. In this theory, we partition a macroscopic glass sample into microscopic subsystems, or cells. If the dimensions of such cells are small compared to the characteristic fluctuation length, a *fictive temperature* can be ascribed to each cell. This is the *local fictive temperature*, $z(r, t)$, which is a function of position, r, and time. We can redefine T_f as the spatial average of z:

$$T_f=\frac{1}{V}\int_V z(r,t)d^3r. \qquad (2)$$

Mat. Res. Soc. Symp. Proc. Vol. 407 © 1996 Materials Research Society

We propose a differential equation for the structural evolution of a glass-forming liquid that is controlled by three competing factors: (1) a *global thermodynamic driving force* of the Tool type, proportional to *(T - z(r))*, which tends to restore equilibrium between the system and its surroundings (thermal bath) whenever $z \neq T$; *(2)* a *local structural driving force*, due to inhomogeneities within the system, which can be accounted by the gradient term, $|\nabla z|$; and, (3) a *stochastic force*, originated from thermal fluctuations.

Considering the first two factors, a free-energy density functional can be expressed as

$$f(r)=\alpha(T-z)^2+\beta|\nabla z|^2, \tag{3}$$

where α and β are constants. *f(r)* has the Ginzburg-Landau form [2]. Applying the *force-flux relations* [3] we have a deterministic model:

$$\frac{\partial z}{\partial t}=-K\frac{\delta f(z)}{\delta z}, \tag{4}$$

where K is constant. If we add a stochastic term, $\theta(t)$, that accounts for the thermal fluctuations:

$$\frac{\partial z}{\partial t}=-K\frac{\delta f(z)}{\delta z}+\theta(t). \tag{5}$$

Substituting (3) in (5), and renaming constants, we get the sought stochastic differential equation:

$$\frac{\partial z}{\partial t}=\frac{1}{\tau_R}(T-z)+\frac{1}{\tau_D}\nabla^2 z+\theta(t). \tag{6}$$

The RHS consists of a relaxation, a diffusion-like and a stochastic term. Solutions to Eq. (6) describe the evolution of z as a function of r and t. τ_T and τ_D are relaxation times that depend on z, $|\nabla z|$, T and other factors, and their form will be considered below. Without the stochastic term, equation (6) is identical to the equation derived by Gupta by applying the gradient energy formalism [4]. The first term of equation (6) describes the tendency of a system to relax toward thermal equilibrium with its surrounding at temperature T; the second term accounts for the influence of the nearest neighbors of a cell and, therefore, determines the cooperative dynamics in GTR; and the last term considers the thermal noise.

We assume that the *stochastic force*, θ, satisfies the next correlations:

$$\langle\theta(t)\rangle=0 \qquad \textit{and} \qquad \langle\theta(t)\theta(t')\rangle=\Gamma\delta(t-t'), \tag{7}$$

where the brackets indicate time averaged quantities and Γ gives the *size* of the driving force generating the fluctuations.

At temperatures well above the GTR, a liquid is in equilibrium and the cooperative dynamics present in glasses and viscous liquids (produced by the strong mutual interaction between adjacent regions of the system) is very weak. Therefore, as a good approximation, we can neglect the second term:

$$\frac{dz}{dt}=\frac{1}{\tau_R}(T-z)+\theta(t). \tag{8}$$

If T does not change abruptly:

$$\frac{d\Delta}{dt} = -\frac{\Delta}{\tau_R} + \theta(t), \tag{9}$$

where $\Delta = z - T$. This is simply a Langevin equation [5] in which the *stochastic force*, $\theta(t)$, is responsible for the fluctuations, Δ, and $-\Delta/\tau_R$ is a *damping force*. Integrating (9) and using (7):

$$\langle\{\Delta(t=\infty)\}^2\rangle = \frac{\tau_R \Gamma}{2}. \tag{10}$$

If we further assume that the temperature fluctuations are of the same order as the deviations of the local fictive temperature, z, and make use of the fluctuation-dissipation theorem [6], we find that

$$\Gamma \sim \frac{2k_B T^2}{c_v \tau_R}, \tag{11}$$

where k_B is the Boltzmann constant and c_v is the heat capacity at constant volume. This expression, which indicates that Γ decreases as the relaxation time increases, is only valid in an equilibrium situation; however, we expect that as temperature drops and the liquid becomes increasingly more viscous, the role of the stochastic force diminishes in a similar way.

In the GTR, the atomic/molecular dynamics is highly cooperative and, as inhomogeneities within the system grow, the relaxation and diffusion-like terms overwhelmingly predominate over $\theta(t)$ in Eq. (6). This is true because even though the first two terms on RHS of Eq. (6) are multiplied by either $1/\tau_R$ or $1/\tau_D$ (which are small for viscous or supercooled liquids), the factors $(T-z)$ and $\nabla^2 z$ become much larger than $\theta(t)$, which in addition changes direction constant and randomly, and, for timescales of the order of τ_R or τ_D, its average is zero. *At temperatures where liquids are viscous, the atomic/molecular dynamics will be governed, mainly, by structural and relaxation factors; however, the inhomogeneities that the stochastic noise has sowed at higher temperatures grow in size and play a very important role as the temperature goes through the GTR.* Thus, for temperature in or near the GTR:

$$\frac{\partial z}{\partial t} = \frac{1}{\tau_R}(T - z) + \frac{1}{\tau_D}\nabla^2 z. \tag{12}$$

SOLUTION OF THE STOCHASTIC MODEL

The stochastic model is constructed on the basis of our current understanding on physics of glasses. Each model parameter has its clear physical meaning. We could thus make sensible simplification for a numerical solution of the differential equation. Let us subdivide the system into N identical cubic subsystems or cells, whose dimensions are small compared to the characteristic length of the fluctuations, so that a local fictive temperature can be ascribed to each cell. In this three-dimensional arrangement of cells, $z_{i,j,k}$ denotes the z of the cell (i, j, k). The *cell's environment structural state* can be estimated by defining $\overline{z_{i,j,k}}$: its neighbors' z-average. Considering only the six nearest neighboring cells, those, with which faces are shared:

$$\overline{z_{i,j,k}} = \frac{1}{6}(z_{i-1,j,k} + z_{i+1,j,k} + z_{i,j-1,k} + z_{i,j+1,k} + z_{i,j,k-1} + z_{i,j,k+1}). \tag{13}$$

For cells on the sides, edges or corners of the system, the number of nearest neighbors is different, and (13) is modified accordingly. For computational convenience, we approximate (6) by:

$$\frac{\partial z_\alpha}{\partial t} = \frac{1}{\tau_R}(T - z_\alpha) + \frac{1}{\tau_D}(\overline{z_\alpha} - z_\alpha) + \theta(t), \tag{14}$$

where $\alpha \equiv (i, j, k)$. The relaxation times τ_T and τ_D are functions of the properties of each particular cell and its environment; no subscript α is used in this case for simplicity. The first two terms on the RHS have the same form; T and $\overline{z}_\alpha$ play similar roles. If the first term stands alone, the free-energy functional (3) decreases as z_α approaches T; on the other hand, considering solely the second term, a homogeneous structure ($z_\alpha = \overline{z}_\alpha$) is energetically favorable. There is a competition between the thermal (first term) and the structural (second term) contributions.

Mathematically, it is very difficult to solve a dynamic system of such complexity. Nevertheless, the problem can be solved by using our *screened dynamics model* [7]. The basic idea of this model is that when Eq. (14) is applied to a cell, it can be assumed that one of the first two terms predominates over the other, according to the state of the cell and its nearest neighbors. In some cases, the structure of a cell readily relaxes toward a state of lower energy (global minimum), but in most of the cases, the cell's structure is *trapped* in a far-from-equilibrium situation (local minimum), and it would relax only if some of its neighbors do it first. The dynamics described by this model is similar to that depicted by the models of *hierarchically constrained dynamics*[8]. By applying the *screened dynamics* model, (14) becomes

$$\frac{\partial z_\alpha}{\partial t} = \frac{h}{\tau_R}(T - z_\alpha) + \frac{(1-h)}{\tau_D}(\overline{z}_\alpha - z_\alpha) + \theta(t), \qquad \textbf{(15)}$$

where

$$h = H((T - z_\alpha)(z_\alpha - z_\alpha)). \qquad \textbf{(16)}$$

$H(x)$ is the *Heaviside's unit step function*, defined by

$$H(x) = \begin{cases} 1 & for \quad x \geq 0 \\ 0 & for \quad x < 0. \end{cases}$$

The global minimum in a thermally agitated system is $z_\alpha = T$ for all the cells; any deviation from this state triggers *restoring forces*. The trend, throughout the system, is the cells, on average, being impelled to achieve a structural state of lower energy. At temperatures near the GTR, the cells are strongly influenced by the structure of its immediate surroundings. If a cell is in a structural state which energy level is higher than that of its immediate environment, the restoring force acting on that cell will be on the direction of equalizing both structural states; locally, the free energy is reduced by getting a more homogeneous structure: cells in high energy states, relax toward their environments' state (local minimum). Most of the times, they get *trapped* by their environments in high energy states. Glass relaxation toward a global minimum is a hindered event. The fact that the relaxation process depends on both the structural state of each cell and its environment, results in the wide relaxation time spectrum observed in glassy materials, because physical properties vary from cell to cell.

By applying the Adam-Gibbs theory [9] to each cell, the next expressions can be obtained [7]:

$$\tau_R = A\exp\left(\frac{B}{T(1 - \frac{T_K}{z_\alpha})}\right) \qquad and \qquad \tau_D = C\exp\left(\frac{D}{T(1 - \frac{T_K}{z_\alpha})}\right), \qquad \textbf{(17)}$$

where A, B, C and D are empirical constants and T_K can be identified with the Kauzmann temperature.

By making use of (16) and (17), we solved Eq. (15), numerically.

BEHAVIOR OF THE STOCHASTIC MODEL

We studied the structural relaxation of a system consisting of 30X20X20 identical cubic cells for different thermal histories.

Suppose that the system is initially in equilibrium at temperature T_1=790 K and, then, at time t=0, the temperature is stepped down to T_2=770 K. We define the normalized relaxation function as

$$\phi(t)=\frac{T_f(t)-T_2}{T_1-T_2}. \qquad (19)$$

In Fig.1 we plot $log_{10}t$ vs. $log_{10}(-ln\phi)$. As we can see, for long times, the relaxation follows the stretched exponential function $\phi=\exp[-(t/\tau)^{\beta}]$; whereas for short times, it is described by an exponential decay (β=1).

Fig. 2 illustrates the memory effects. Squares represent experimental fictive temperatures obtained by DeBolt in a crossover experiment[10]. Initially, a sample of standard glass *NBS-710* was allowed to reach equilibrium at temperature $T_0 = 830.3\ K$; that is, $T_f = 830.3\ K$. Then, at time $t_1 = 0$, the temperature was stepped down to $T_1 = 704.0\ K$. The glass started relaxing toward a state corresponding to T_1. At time $t_2 = 2687\ min$, when $T_f = 797.9\ K$, temperature was reset to this same value $T_2 = 797.9\ K$. If the sample were in equilibrium, the fictive temperature would remain fixed at this value. However, it is shown that the crossover effect shows up as a well-defined hump for times $t > t_2$. The solid line represents the fit obtained by using the stochastic model for that same thermal history. The values for the empirical constants are the same as those of Fig. 1. The agreement between theory and experiment is excellent.

In addition to the spatially averaged macroscopic properties shown in Figs.1 and 2, the stochastic model also describes relaxation processes on a microscopic scale. Fig. 3 is a two-dimensional cross-section (30X20 cells) of z's from the same three-dimensional system, and under the same thermal history as in the crossover experiment, at t=2000 min. The fictive temperature, z, is given by the vertical axis. It is easy to recognize *domains* of *fast* and *slow* relaxing cells. Fast relaxing cells relax readily toward the global equilibrium, while slow relaxing cells appear frozen in high energy states.

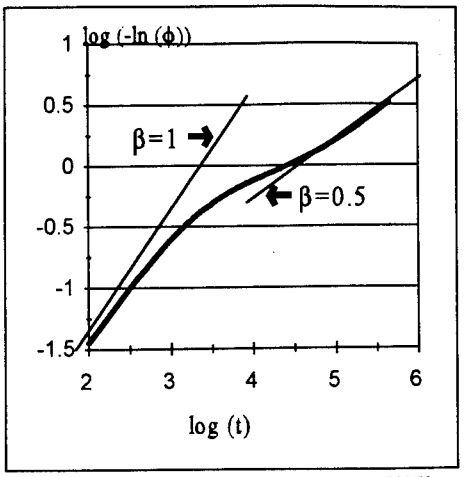


Fig 1. Relaxation function for the temperature jump 790 K --> 770 K, by using the stochastic model with A=3.45X10^{-17}, B=11000, C=5.00X10^{-22}, D=14000, T_K=540 K.

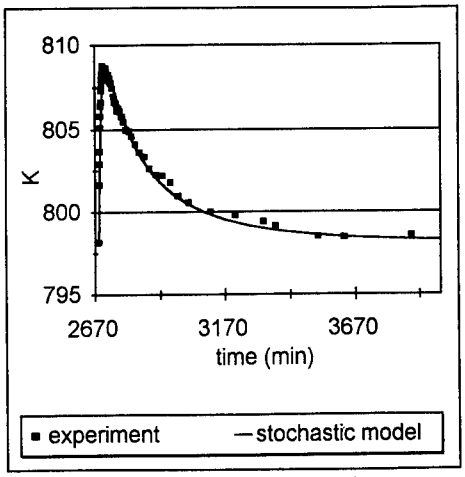


Fig. 2. Squares represent the experimental T_f for a crossover experiment [10].Initially, the system is in equilibrium at T= *830.3 K; at* t=0, temperature is stepped down to T=704 K; at t=2687 *min*, temperature is raised to T=797.9. Solid line represent the prediction of the stochastic model, using the same values for the empircal constants as in Fig. 1.

CONCLUSIONS

The stochastic force plays a key role in shaping the relaxation phenomena associated with glasses. The stochastic model presented in this paper takes into account the fluctuations as well as the cooperative structural dynamics present in glass-forming liquids. By using the stochastic noise term and sensible treatment of competing forces (screened dynamics), the typical glass relaxation phenomena (e.g., nonlinearity, nonexponential decay and memory effects) emerge as a consequence of the complex microscopic dynamics of the model. Modeling results reveal the nature of glass transition phenomena from a dynamic view point.

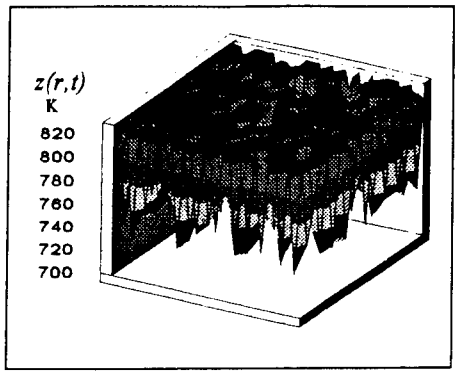


Fig. 3. Microscopic view. Two-dimensional cross section of z's from the same three-dimensional system. The thermal history is the same as in Fig. 2 and t=2000 *min.* z's are represented by the vertical axis.

ACKNOWLEDGMENTS

The authors wish to thank Pedro B. Macedo, Ian L. Pegg and Charles J. Montrose for their helpful commentaries.

REFERENCES

1. Tool, A. Q., *J. Res. Nat. Bur. Stand.* **34**, 199(1945).
2. Ma, S., *Modern Theory of Critical Phenomena*, W. A. Benjamin, London (1976).
3. de Groot, S. R. and Mazur, P., *Non-Equilibrium Thermodynamics*, Dover Publications, New York (1984).
4. Gupta, P. K., *J. Non-Cryst. Solids* **102**, 250(1988).
5. Van Kampen, N. G., *Stochastic Processes in Physics and Chemistry*, North-Holland, Amsterdam (1992).
6. Landau, L. D. and Lifshitz, E. M., *Statistical Physics*, Third Edition, Pergamon Press, Oxford (1980).
7. Perez-Cardenas, F. C., *Ph. D. Dissertation*, The Catholic University of America (to be published).
8. Palmer, R. G., Stein, D. L., Abrahams, E. and Anderson, P. W., *Phys. Rev. Lett.* **53**, 958(1984).
9. Adam, G. and Gibbs, J. H., *J. Chem. Phys.* **43**, 139(1965).
10. DeBolt, M. A., *Ph. D. Dissertation*, The Catholic University of America (1976).

STRUCTURAL DEVELOPMENTS IN FRAGILE GLASS FORMING OXIDES

J.E. MASNIK,* O. NICKOLAYEV,* J. KIEFFER* AND J.D. BASS,**
Department of Materials Science and Engineering, University of Illinois, Urbana, IL 61801
Department of Geology and Department of Materials Science and Engineering, University of Illinois, Urbana, IL 61801

ABSTRACT

Brillouin light has been used to measure the complex mechanical modulus of the molecular scale structure in oxide melts. The storage modulus reflects the degree of networking and structural integrity, while the loss modulus, which can be attributed to aperiodic motions of structural components, provides a measure of the mobility of these entities. From the loss modulus it is possible to derive the zero-shear rate viscosity, which is characteristic of a structure in thermodynamic equilibrium, and thereby provide a less encumbered insight into the molecular scale mechanisms that are underlying to the viscous momentum transport.

In this paper we compare the visco-elastic behavior of alkali borates and alkali tellurites, particularly in the temperature range between T_g and the equilibrium melting point. While in borates several mechanisms can be identified as contributing to structural relaxation, in tellurites a single mechanism dominates. The assumption of thermo-rheological simplicity, however, is invalid, and a new visco-elastic model has been developed for the description of our results.

INTRODUCTION

The tendency to form an amorphous solid is the result of the impediment which keeps the molecular structure of a substance from reaching a state of lowest free energy. In oxide systems this is attributed to strong bonds that can form between building blocks with high functionality, and which leads to a relatively immobile continuous random network. The effort required by structural components to disengage from a local potential minimum, is conveniently assessed by means of the temperature dependence of their transport properties, as expressed by diffusivities or viscosity.

Angell has categorized liquids in terms of their glass forming ability into 'strong' and 'fragile' ones.[1] Accordingly, the logarithm of the viscosity vs. the reciprocal temperature for a strong liquid appears linear over a wide temperature range, and can be well described by the Arrhenius relationship. For a fragile liquid, on the other hand, this dependency is curved, with the steepest slope near T_g. Such curvature suggests that several activated processes are invoked during the structural evolution between liquid and glass, and that those processes which require the highest activation energy dominate the relaxation near the glass transition.

Besides being of fundamental interest with regard to the glass formation process, the temperature dependence of the viscosity near T_g has also important practical implications. For example, a number of novel inorganic compounds have been identified which exhibit superior performance in applications such as optical fibers and amplifiers.[2,3] Fragility in these compounds, however, translates into large viscosity changes over a small temperature range, and makes the fiber drawing process difficult to control. To improve our understanding of the molecular level processes involved in glass formation, we have used the Brillouin scattering method to determine the mechanical properties of oxide melts on this length scale. In the following we present results for two types of glass forming liquids, alkali borates and tellurites, one relatively strong, the other one fragile. Comparison of their behaviors under similar conditions allows us to discern certain characteristics associated with each type of liquid.

EXPERIMENTAL

Glasses were prepared from powders alkali carbonates and either boric acid or tellurium oxide. The total impurity content was less than 0.2 weight-%. The powders were intimately mixed and melted. The crucible material was platinum in case of the borates and silica glass in case

Mat. Res. Soc. Symp. Proc. Vol. 407 © 1996 Materials Research Society

of the tellurites. After about one hour of homogenization in dried air, the melts were quenched and crushed. The glasses were then remelted and the Brillouin sample holders were filled with material by simply immersing these into the molten glasses. In case of borates the sample holders consisted of platinum-rhodium wire bent in the form of a double-loop spiral, while in case of the tellurites an open-ended silica capillary was used. Suspended by surface forces, the liquid assumed the shape of a slightly bulged cylinder of about 2.5 mm height and 2 mm diameter.

Samples were mounted in a small furnace which was heated by a platinum coil. The furnace has a cylindrical bore in the bottom and top part of the insulation material, and a conical orifice oriented horizontally in the side wall. The furnace housing was stainless steel and all orifices were sealed by means of fused silica windows, which allowed us to control the gas atmosphere during the experiments. The light beam entered through the bottom of the sample and the scattered light was collected laterally. The position of the specimen in the beam was carefully adjusted such that the light passed perpendicular to any curved surfaces, and a 90° scattering geometry was preserved.

The incident light was produced by a single-mode Argon laser at a wavelength of 0.5145 μm. The line width of the incident light is approximately 100 MHz. The scattered light was analyzed using a six-pass tandem Fabry-Perot interferometer.[4] The quality of mirrors used in the current setup produces a reflectivity finesse of about 150.

The collection of spectra occurred, for the most part, upon cooling of the samples. The samples were held at intervals of approximately 20°C for a few minutes, to assure thermal adjustment, before spectra were measured. This adjustment period also allowed for relatively relaxed structures in the undercooled liquids. Consequently, the fictive temperatures of the glasses was low, and comparison of measurements taken upon heating or cooling showed no significant difference. Since all measured systems are strong scatterers, the collection of the spectra typically took only 2 to 3 minutes. The data was downloaded to a computer workstation for further processing.

The shapes of the lines in the Brillouin spectrum are described by a dynamic structure factor, $S(q,\omega)$ (multiplied by a population probability function). For fluids, an expression for the dynamic structure factor can be derived using the generalized hydrodynamic formalism[5,6], which is based on the simultaneous solution of the equations of balance for mass, momentum and energy. Accordingly, the normalized scattering intensity is given by the expression

$$\frac{S(\mathbf{q},\omega)}{S(\mathbf{q})} = \frac{2(\gamma-1)}{\gamma}\cdot\frac{q^2\cdot\kappa/\rho_0 c_p}{\omega^2+\left(q^2\cdot\kappa/\rho_0 c_p\right)^2}+\frac{1}{\gamma}\left[\frac{q^2\Gamma}{(\omega+c_0 q)^2+\left(q^2\Gamma\right)^2}+\frac{q^2\Gamma}{(\omega-c_0 q)^2+\left(q^2\Gamma\right)^2}\right] + \frac{q}{\gamma c_0}\left[\Gamma+\kappa/\rho_0 c_p(\gamma-1)\right]\left[\frac{\omega+c_0 q}{(\omega+c_0 q)^2+\left(q^2\Gamma\right)^2}+\frac{\omega-c_0 q}{(\omega-c_0 q)^2+\left(q^2\Gamma\right)^2}\right], \quad (1)$$

where $\gamma=\frac{c_p}{c_v}$, $\Gamma=\frac{1}{2}\left[\frac{\eta'(\omega)}{\rho_0}+\left(\frac{\kappa}{\rho_0 c_p}\right)\cdot(\gamma-1)\right]$, ρ_0 is the average density, κ is the thermal conductivity, c_v is the heat capacity at constant volume, and c_p that at constant pressure. The viscosity coefficient $\eta'(\omega)$ is the real part of the Fourier transform of the time dependent viscosity, $\eta(t)$. The ratio $\left(\kappa/\rho_0 c_p\right)$ is the thermal diffusivity.

To eliminate instrumental broadening from the spectra these were fitted with the result of the convolution of a Lorentzian spectral function and a Gaussian broadening function. Three parameters, the widths at half maximum, $\Delta\omega$, the intensity I, and the frequency shift with respect to the Rayleigh central peak, $|\omega_B-\omega_R|$, were optimized simultaneously for every peak in the spectrum. The width of the Gaussian broadening function was determined in a separate experiment, where the sample was replaced by a mirror. When appropriately combined, this set of parameters yields the storage- and loss modulus according to

$$M' = \frac{\rho_0}{q^2}|\omega_B - \omega_R|^2 \qquad (2)$$

and

$$M'' = |\omega_B - \omega_R|\eta'(\omega) = \frac{\rho_0|\omega_B - \omega_R|}{q^2} \cdot \left[\Delta\omega_B - \frac{\Delta\omega_R}{2} \cdot \frac{I_R}{2I_B}\right] \qquad (3)$$

respectively. These are either longitudinal- or shear moduli, depending on whether the widths and shifts are taken for the longitudinal or transverse peaks of the spectra.

RESULTS AND DISCUSSION

The basic building block in borate glasses is the BO_3 planar trigonal unit. Individual units are connected by sharing oxygens, to form a continuous network. Although, based on the geometry of the basic unit, sheet-like structures would be possible, disorder in the orientation of the BO_3 triangles results in network connectivity in three dimensions. At low temperatures, however, infrared and Raman spectroscopy have shown that a large fraction of the borons are grouped into boroxol rings, a planar hexagonal structure composed of three BO_3 units. With increasing temperature, the concentration of boroxol rings decreases.[7]

When added to B_2O_3, alkali oxides dissociate and the oxygen introduced into the system is to a large degree incorporated into the network in form of B-O-B cross-links. The boron atoms involved find themselves in fourfold coordination by oxygen. This formation of cross-links is held responsible for the strengthening effect in borates by alkali oxides, a behavior which can be seen in Fig. 1. Here the longitudinal elastic (or storage) modulus is plotted as a function of temperature for sodium borates with various alkali concentrations. The room-temperature value of this modulus increases steadily with increasing alkali concentration. While the modulus does not vary much at low temperatures, the glass transition is marked by a discontinuity in this temperature dependence, and above Tg the modulus drops precipitously. The rate of decrease is higher, the higher the alkali concentration and the more fragile the liquid. This rate of decrease actually provides a credible quantitative measure to the denotation of fragility in a liquid.

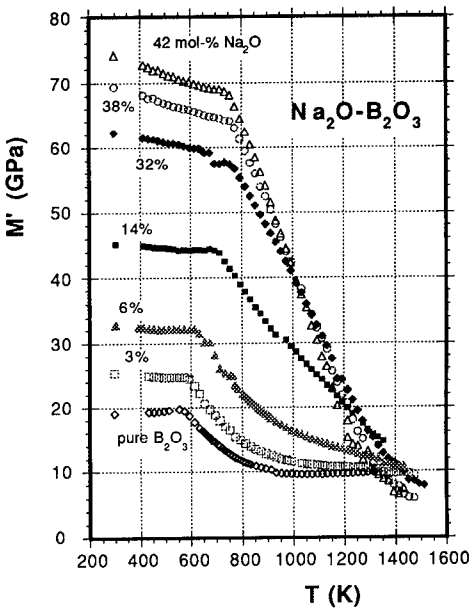


Fig.1 Longitudinal elastic modulus as a function of temperature for sodium borates with various alkali concentrations.

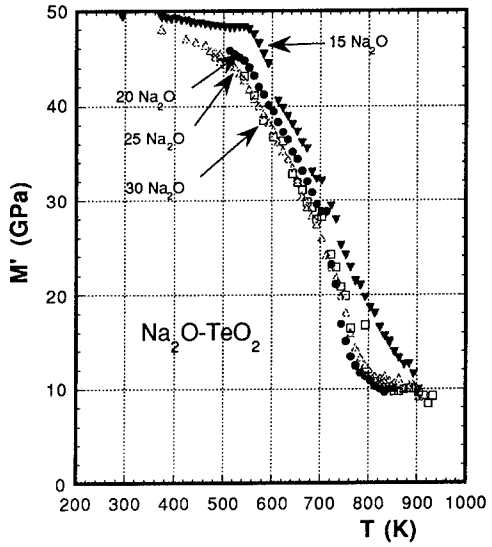


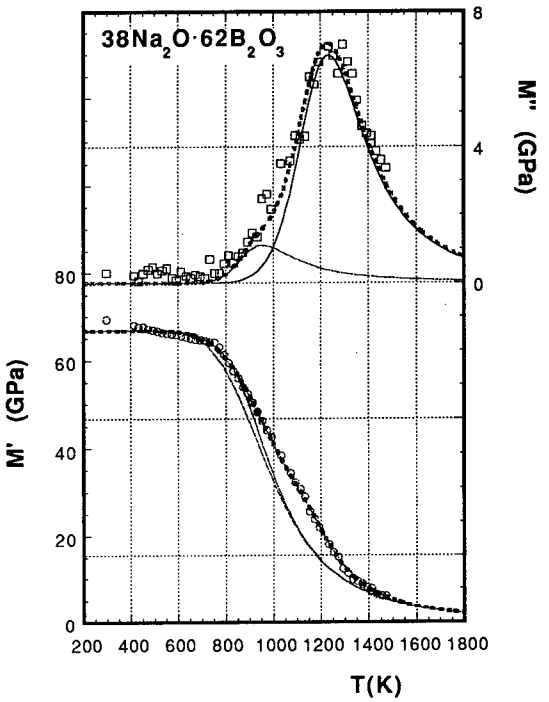
Fig.2 Longitudinal elastic modulus as a function of temperature for sodium tellurites with various alkali concentrations.

As of yet, investigations of tellurite glasses have been scarce. Based on infrared and Raman investigations, the following model for the structure of alkali tellurites has been proposed.[8] The basic network building block is the TeO_4 trigonal bipyramid (tbp), in which one of the equatorial sites is occupied by a lone pair of electrons, so that the angle between equatorial oxygens is much smaller than 180°. A continuous three-dimensional network is formed, again, by sharing oxygens between these units, but now the shared oxygen is equatorial to one unit and axial to the other one. The introduction of oxygen by alkali oxide causes these bonds to break, replacing one bridging oxygen with two non-bridging ones. The two alkali cation, however, remain closely associated with these network defects, and provide a stabilizing influence. The bond between tellurium and the axial oxygen opposite of the non-bridging one, on the other hand, becomes over-extended and ruptures with little effort. Trigonal pyramids (TeO_3) and trigonal pyramids with a loosely bonded axial oxygen (TeO_{3+1}) form. At higher alkali concentrations, isolated structures such as $(Te_2O_5)^{2-}$ and $(TeO_3)^{2-}$ develop.

Because of its stabilizing action, the addition of alkali oxide has little effect on the elastic modulus of these tellurites. This is apparent from the data shown in Fig. 2, where the longitudinal storage moduli of sodium tellurites with different alkali concentrations are plotted as a function of temperature. The glass transition is again reflected by a change in slope of this data. Over almost the entire temperature range, the modulus decreases only slightly with increasing alkali content. The rate of decrease of the modulus is also very similar in the different compositions, except the high-alkali compositions exhibit a second discontinuity in the temperature dependence of the modulus at around 700 K. This second kink in the modulus data, which indicates that a significant structural change occurs between the glass transition and the equilibrium melting temperature, inspired the development of a modified Maxwell model for the description of the modulus data in tellurites as well as in borates. Although it would not compromise the basic assumptions of this model, at this point we rule out that the kink is due to crystallization, based on TEM analysis.

Any model for the visco-elastic properties of a liquid has to describe both, the real and the imaginary component of the mechanical modulus. So, before outlining the details of the model, let us examine the loss moduli, which are plotted as a function of temperature in Figs. 3 and 4, for alkali borates and tellurites respectively. Data for only one composition in each system is shown for the sake of clarity. We notice that the loss moduli, in both cases go through a maximum as the storage moduli decrease with increasing temperature. At first sight this is what one would expect for a linear visco-elastic system. However, the position of the maximum is displaced to a higher temperature relative to the one at which the storage modulus exhibits its steepest slope. Furthermore, the difference between the low- and high-temperature elastic modulus is much larger than twice the magnitude of the loss modulus maximum. Hence, application of Maxwell's model, assuming the equivalence between time and temperature (thermo-rheological simplicity) fails.

Fig. 3



Complex mechanical modulus of sodium borate as a function of temperature. The top portion of the diagram shows the loss modulus, and the lower portion the elastic modulus. The lowest line represents the temperature dependent static modulus; the magnitudes of the various relaxational components are given by the vertical distances between each pair of consecutive lines.

A better fit of the data can however be achieved when assuming that not only the relaxational, but also the static modulus is temperature dependent. Since the static reflects the property of a system at rest, hence in thermal and mechanical equilibrium, one way to introduce a temperature dependence is by assuming the existence of two structural states, one being ideally elastic and representative of a room-temperature glass, and the other one being visco-elastic, as is the case for the melt. The volume fraction of structure found in the rigid state, $\phi(T)$, can be estimated using Boltzman statistics, with knowledge of the free energy difference between the structural states,

$$\phi(T) = \left[1 + e^{-Q(1-T/T_c)/k_BT}\right]^{-1} \qquad (4)$$

where Q is an energy comparable to the enthalpy of fusion, and T_c a critical temperature intermediate to the glass transition and equilibrium melting temperatures of the substance. Multiplying $\phi(T)$ with a constant M_0, corresponding to the static modulus at 0 K, yields the temperature dependent static modulus, and the expression for the modified Maxwell model is[9]

$$M^*(\omega,T) = M_0\phi(T) + \sum_j \left(M_{2,j}(1-\phi(T)) \frac{\omega^2\tau_{0,j}^2 e^{2E_{A,j}/k_BT} + i\omega\tau_{0,j}e^{E_{A,j}/k_BT}}{1+\omega^2\tau_{0,j}^2 e^{2E_{A,j}/k_BT}} \right), \qquad (5)$$

where τ_0 is the fundamental time constant of the relaxation process, and E_A its activation energy. These parameters are the same for real and imaginary components of the modulus. The summation in Eq. (4) allows for several independent processes (or a distribution thereof) to be active simultaneously. The solid lines in Figs. 3 and 4 represent best fits of this equation to the experimental data. Notice that in case of alkali borates more than one term is necessary to describe the data, whereas for the tellurites one term suffices. Accordingly, in the visco-elastic regime, strong liquids possess more structural complexity than fragile ones.

CONCLUSION

The Brillouin light scattering technique was used to determine the high-frequency complex mechanical modulus of glass forming melts. This modulus describes the dynamic response of molecular scale structures. The storage modulus reflects the structural integrity of the glassy network, whereas the loss modulus gives a measure of the energy dissipated in aperiodic motions of small structural components.

The temperature dependence of the storage modulus, therefore, provides insights into the structural developments between the room-temperature glass and the melt. Accordingly, the glass transition can be associated with the onset of structural degradation, and the fragility of a liquid can be assessed by the rate of decrease of the storage modulus. Structural decay involves thermally activated motion of its constituents. However, entities requiring the same activation energy are not all released at the same temperature, but sequentially while maintaining a dynamic equilibrium between the low- and high-temperature structural states. Comparison between alkali borates and tellurites show that, in the former, several distinct relaxation processes contribute to the structural changes, whereas in the latter typically only one can be detected.

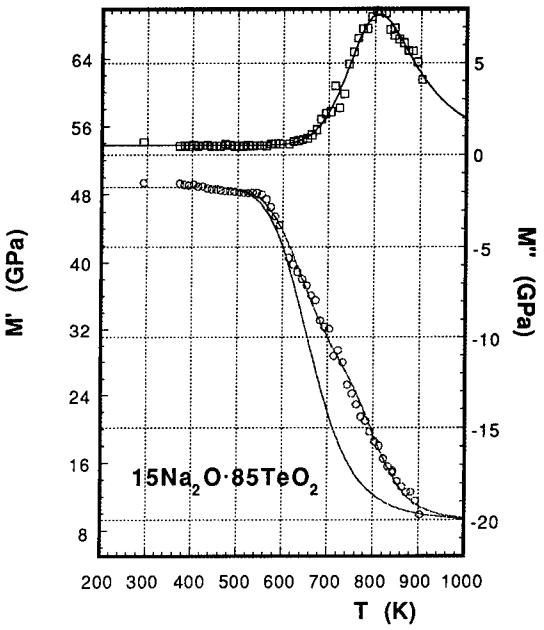


Fig.4 Complex mechanical modulus of sodium tellurite as a function of temperature.

Acknowledgment: This work was supported by the National Science Foundation (DMR 93-15779)

1 C.A. Angell, *J. Non-Cryst. Solids* **131-133**, 13 (1991)

2 J.B. MacChesney and D.J. DiGiovanni, *J. Am. Ceram. Soc.* **73**, 3537 (1990)

3 E.V. Uhlmann, M.C. Weinberg, N.J. Kreidl and A.A. Goktas, *J. Am. Ceram. Soc.* **76**, 449 (1993)

4 J.R. Sandercock in "*Light Scattering in Solids III*", Topics in Applied Physics Vol. **51**, M. Cardona and G. Güntherodt, eds., p. 173 (Springer)

5 R.D. Mountain, *Journal of Research of the NBS* **70A**, 207 (1966)

6 J.P . Boon and S. Yip, "*Molecular Hydrodynamics*" Dover Publ. (1991)

7 A.K. Hassan, L.M. Torell, L. Börjesson ad H. Doweidar, *Phys. Rev.* **B45**, 12797

8 Sekiya, Takao, Mochida, Norio, Ohtsuka, Atsushi, Tonokawa, Mamoru, *J. Non-Cryst. Solids* **144** (1992) 128

9 J.E. Masnik, J. Kieffer, and J.D. Bass, *J. Chem. Phys*, in press (Dec. 1995)

A LOW FREQUENCY STUDY OF THE VIBRATIONAL MODES IN ALKALI-SILICATE GLASSES BY RAMAN SPECTROSCOPY

R. SOMMER*, J.TOULOUSE* and H. JAIN+
* Department of Physics, Lehigh University, Bethlehem, PA 18015
+ Department of Materials Science and Engineering, Lehigh University, Bethlehem, PA 18015

ABSTRACT

We have performed a study on low frequency modes in several alkali silicate glasses by Raman spectroscopy. The Boson peak region is analyzed with a single parameter ω_0 which is believed to characterize the density of states of the system. Analysis of the dependence of ω_0 on the nature and concentration of the alkali suggests that the position of the Boson peak is essentially governed by the ratio "force constant" over "mass" of localized oscillator modes. At lower frequency (below 30 cm^{-1}), the "excess" intensity can be explained by considering second-order processes of the same vibrational modes, superimposed on other (possibly relaxational) modes.

INTRODUCTION

For more than twenty years, amorphous materials have been investigated, but there is still no complete understanding of the nature of the low frequency modes that appear in the Raman spectra. These modes are also responsible for the peculiar behavior of other physical properties, such as the heat capacity and the thermal conductivity at low temperature (2 to 20 K). Several models have been suggested to explain the universal behavior of glassy materials. In the continuum model, acoustic modes are allowed to contribute to the scattering intensity, because of the breaking of the momentum selection rule by the spatial disorder[1]. However, they become strongly attenuated at higher frequencies, when their wavelength becomes comparable to the length over which the fluctuations of the dielectric susceptibility are correlated., leading to a decrease of the scattered intensity. The soft potential model is based on localized oscillators in anharmonic double well potentials[2]. The resulting density of states then depends on the depth and distribution of these potentials. A fractal model has also been suggested, in glasses for which the dimensionality is believed to be lower than 3[3].

At low frequency (below ~20 cm^{-1}), Raman spectra of almost every glasses show additional intensity, which doesn't scale with the thermal population factor. This "excess light scattering" (ELS), reported by Winterling[4], is usually believed to arise from relaxational modes.

EXPERIMENTAL

Stokes and Anti-Stokes spectra were recorded on glass samples with a U1000 spectrometer (& Jobin-Yvon) in a 90° geometry. An argon-ion laser, tuned to 488 nm, provided the incident beam (~195 mW at the sample), with polarization perpendicular to the scattering plane (denoted by subscript V later in this paper). In order to get enough intensity at low temperature and low frequency, only polarized spectra (I_{VV}) were recorded below 80 K. Unless specified, the spectral slit width was set at 1.5 cm^{-1} for all the spectra so that the measurements could be done down to ~3 cm^{-1} from the Rayleigh line. The investigated temperature range lay between 5 K and room temperature. The temperature was measured with a silicon diode and compared with that

Mat. Res. Soc. Symp. Proc. Vol. 407 © 1996 Materials Research Society

deduced from the Anti-Stokes to Stokes ratio in the Boson range (20 to 100 cm^{-1}), which is simply given by $\exp(-\hbar\omega/kT)$.

RESULTS

First and Second Order Processes

In an amorphous material, the total first-order scattered intensity I_S can be written as[1]:

$$I(\omega,T) \propto c(\omega)g(\omega)\frac{n(\omega,T)+\frac{0}{1}}{\omega} \tag{1}$$

$g(\omega)$ and $c(\omega)$ are respectively the density of vibrational states and the coupling coefficient between the incident light and the modes of vibration in the medium. The temperature dependence is solely determined by the population factor of the modes and the order of the process. The thermal factor for a first-order process is $n(\omega,T)+1$ for the Stokes side (creation) of the spectrum and $n(\omega,T)$ for the anti-Stokes side (annihilation), where $n(\omega,T)$ is the Planck's distribution. It is convenient to define a temperature-independent quantity, the reduced intensity ${}^{R}I(\omega)$ obtained by dividing the total intensity by the thermal factor:

$${}^{R}I(\omega) = \frac{I(\omega,T)}{n(\omega,T)+\frac{0}{1}} = \frac{c(\omega)g(\omega)}{\omega} \tag{2}$$

Fig. 1 shows a plot of the reduced intensity of Na_2O-$2SiO_2$ measured at different temperatures. Above ~30 cm^{-1}, all the curves superimpose, as expected for a first-order process. At lower frequency, however, the high temperature curves show additional intensity, the so-called excess light scattering (ELS). A natural way to account for the extra temperature dependence is to include the contribution of second-order processes. Because ELS occurs only at high temperature and low frequency, these most likely come from phonon differences (creation of a phonon ω_1 and annihilation of a phonon $\omega_2 < \omega_1$). The total Stokes intensity can then be written as a sum of a first order and a second-order term:

$$I_S(\omega,T) = I_{S1}(\omega,T) + I_{S2}(\omega,T) = c(\omega)g(\omega)\frac{n(\omega,T)+1}{\omega} + \\ + \sum_{\omega_i-\omega_j=\omega} c_2(\omega_i,\omega_j)g_2(\omega_i,\omega_j)\left(n(\omega_i,T)+1\right)n(\omega_j,T) \tag{3}$$

$c_2(\omega_i,\omega_j)$ and $g_2(\omega_i,\omega_j)$ are defined as a two-phonon coupling coefficient and a two-phonon density of states. At low temperature ($T < 40$ K), the population factor $n(\omega_j,T)$ is very small, so that the second order contribution becomes negligible. As mentioned above, the ELS occurs mainly at low frequency and high temperature. Therefore, only modes for which $\hbar\omega_i/kT < 1$ are involved and their thermal population factor can be approximated by $kT/\hbar\omega_i$. The second order contribution $I_{S2}(\omega,T)$ can be rewritten as:

$$I_{S2}(\omega,T) \cong T^2 \sum_{\omega_i-\omega_j=\omega} c_2(\omega_i,\omega_j)g_2(\omega_i,\omega_j)\frac{k^2}{\hbar^2\omega_i\omega_j} \tag{4}$$

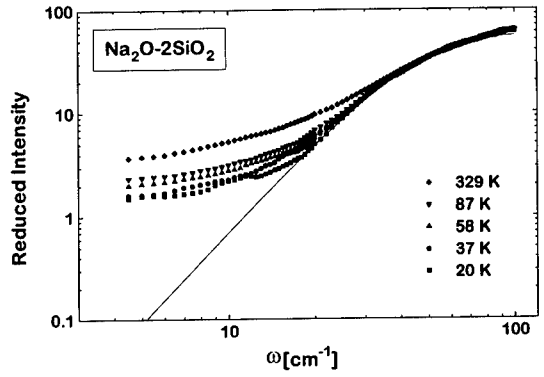


Fig. 1: Reduced intensity of Na_2O-$2SiO_2$ at different temperatures showing that the ELS intensity does not scale to a first order process. The solid line is a fit of the Boson peak using Eq. (5) in the text.

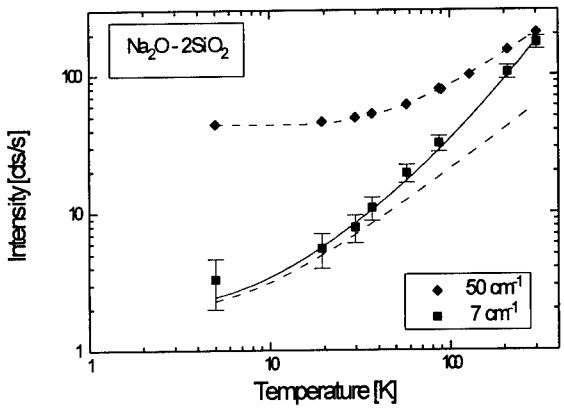


Fig. 2: Raman intensity versus temperature in Na_2O-$2SiO_2$. The dashed lines are fits using a first-order process only, the solid line is a fit using first-order and second-order processes. In the Boson range, second-order processes are insignificant (50 cm^{-1} data points) while they are able to explain the "excess" intensity at low frequency (7 cm^{-1} data points).

The advantage of (4) is that the temperature dependence can be taken out from the summation, allowing a direct comparison to the experimental data. Fig. 2 shows the Raman intensity versus temperature, at two particular frequencies in Na_2O-$2SiO_2$. The solid line is a fit obtained by substituting (4) in (3), the dashed line is the expected behavior for a pure first-order process. This shows that two-phonon processes can indeed account for the extra temperature dependence observed in the ELS region of the spectrum.

The Boson peak

The Boson peak is the part of the spectrum located above the ELS region and in which only first-order processes are relevant. To date, many theoretical expressions based on the continuum theory of Martin & Brenig[5] have been proposed in order to describe the Boson peak. Here we use an expression proposed by Sokolov[6], and show that it fits very well the depolarized spectrum of v-SiO_2:

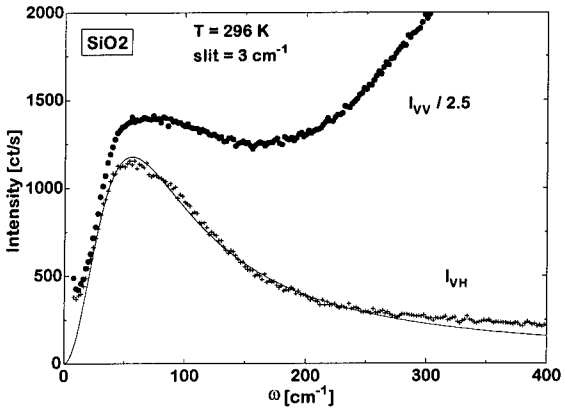


Fig. 3: Depolarized I_{VH} and polarized I_{VV} (scaled down by a factor of 2.5) spectra of silicate at room temperature. The solid line is a fit using expression (5), which shows that the fully polarized broad band gives a contribution to the intensity I_{VV} down to the Boson range.

$$I_S(\omega,T) = A\frac{\omega^3}{\left(\omega^2+4\omega_0^2\right)^2}\left(n(\omega,T)+1\right) \qquad (5)$$

The depolarized spectrum I_{VH} and the polarized spectrum I_{VV} of v-SiO_2 are plotted in fig. 3. I_{VH} can be fitted very well with expression (5) up to 200 cm^{-1} while, for I_{VH} , the situation is complicated by the presence of the "broad band" (fully polarized modes) centered at higher frequencies (~450cm^{-1}) but extending into the Boson range. In alkali-modified SiO_2, additional modes appear on the high frequency side of the Boson peak in the *VH* spectrum but the broad band is depressed in the *VV* spectrum. Consequently, we have focused our analysis on the latter spectrum.

Fig. 4 shows the reduced intensity ${}^{R}I(\omega)$ for some of the alkali-silicates. Below ~30 cm^{-1},

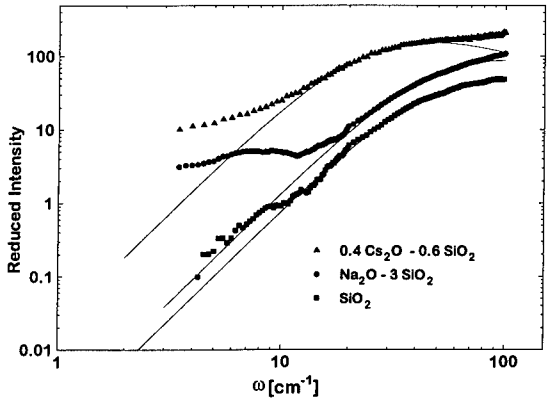


Fig. 4: Reduced intensity ${}^{R}I$ for some of alkali silicates. Pure silicate and sodium-silicate spectra were recorded at 5 K. The cesium-silicate spectrum was recorded at room temperature.

deviations occur due to the ELS, and for $\omega > 80$ cm^{-1}, the broad band or other alkali modes add to the Boson peak intensity on the polarized spectrum. Table 1 summarizes the value of ω_0 for all the investigated alkali oxides. In xNa$_2$O-(1-x)SiO$_2$, ω_0 increases slightly with the concentration x of sodium oxide. The opposite trend is observed, when adding Cs$_2$O instead of Na$_2$O.

With regards to the origin of the Boson peak, the central question of the present paper is whether ω_0 is related to the network connectivity or to the force constant and mass of localized oscillators. In the case of sodium silicate, it is well established that the sodium ions occupies an interstitial site in the network and that each ions breaks one Si-O-Si bond[7], giving rise to the formation of a non-bridging oxygen. As the concentration of sodium increases, the network connectivity decreases, the glass becomes more fragile and the Boson peak as well as ω_0 should move to lower frequencies. Instead, ω_0 increases with x. This result by itself suggests that the connectivity is not the dominant factor in determining ω_0 or the position of the Boson peak and that the latter is not likely due to acoustic modes in a disordered network (see continuum model above). This interpretation appears to be confirmed by the results obtained on Cs-modified SiO$_2$. Because it has the same valence as sodium, each cesium ion is also expected to give rise to the formation of one non-bridging oxygen and, therefore, to have the same effect as sodium on the connectivity of the glass. Yet ω_0 is found to be approximately one half what it is in sodium silicate and to further decrease with indreasing Cs concentration. The connectivity cannot be the common cause of these very different results. It is more likely that the Boson peak is due to localized oscillators, ω_0 being determined primarily by their force constant and their mass. In further support of this interpretation, it is interesting to note that the mass of cesium is 6 times that of sodium which should lead to a natural frequency of the Cs-containing oscillator 2.4 times lower than that of the corresponding Na-containing one, in reasonable agreement with the ratio of the ω_0 values found experimentally.

Comparing expression (2) and (5), one may further ask whether ω_0 is a feature of the coupling coefficient $c(\omega)$ or of the density of states $g(\omega)$. A Raman experiment alone cannot help answer this question. Nevertheless, by comparing neutron data with Raman data on pure SiO$_2$, $c(\omega)$ has been shown to vary linearly with frequency in the Boson range[8]. This would indicate that ω_0 is a feature of the density of states of the system.

The Excess Light Scattering

As mentioned previously, the excess light scattering could arise from a second-order difference process, which adds to the first-order one. At very low temperature, the population factor $n(\omega,T)$ is almost zero and the second-order contribution is negligible. The 5 K curves therefore are close to the sole first-order process. In SiO$_2$, the low temperature curves tend to the

Table I: value of ω_0 [cm^{-1}] for pure silica and for several concentrations x of sodium-silicate and cesium-silicate.

	SiO$_2$	xNa$_2$O-(1-x)SiO$_2$	xCs$_2$O-(1-x)SiO$_2$
x = 0.25	27.6	28.8	
x = 0.30			16
x = 0.33		30.3	
x = 0.40			13.7

theoretical line given by expression (5), which seems to be valid down to the lower achievable frequencies. On the other hand, the alkali-modified samples still show a marked deviation from the theoretical line even at the lowest temperature, suggesting the existence of additional modes, possibly relaxational.

CONCLUSION

This study on alkali-silicate samples shows that the "excess" light scattering in amorphous materials can be understood as a combination of first- and second-order processes. The modes involved in the second-order scattering are those corresponding to $(\omega_i - \omega_j) < 30\ cm^{-1}$ with $\hbar\omega_j/kT < 1$. The only highly populated modes satisfying these criteria are those giving rise to the Boson peak. We may therefore conclude that the ELS and the Boson peak are essentially related, the former being a second-order manifestation of the latter. The Boson peak has been characterized by a single parameter, ω_0, which is believed to be a feature of the density of states of the medium. Based on the dependence of ω_0 on the nature and concentration of the alkali, we conclude that the network connectivity has little effect on the position of the Boson peak which, thence, is more likely due to localized oscillators.

ACKNOWLEDGMENTS

Particular thanks go to Dr. P. Tick (Corning Inc.) for supplying the Cs- silicate glass sample.

REFERENCES

[1] R. Shuker and R.W. Gammon, Phys. Rev. Lett. **25**, 222 (1970)
[2] V.L. Gurevich, D.A. Parshin, J. Pelous and H.R. Schober, Phys. Rev. B **48**, 16318 (1993)
[3] A. Fontana, F. Rocca, M.P. Fontana, B. Rosi and A.J. Dianoux, Phys. Rev. B **41**, 3778 (1990)
[4] G. Winterling, Phys. Rev. B **12**, 2432 (1975)
[5] A.J. Martin and W. Brenig, Phys. Stat. Sol. (b) **64**, 163 (1974)
[6] V.K. Manilovsky and A.P. Sokolov, Solid State Commun. **57**, 757 (1986)
[7] E.I Kamitsos, J.A. Kapoutsis, H. Jain and C.H. Hsieh, J. Non-cryst. Solids **171**, 31 (1994)
[8] T. Achibat, A. Boukenter and E. Duval, J. Chem. Phys. **99**, 2046 (1993)

DIFFUSIONAL DYNAMICS NEAR THE GLASS TRANSITION IN AMORPHOUS POLYMER THIN FILMS

Denise D. Deppe[§] and John M. Torkelson[§‡]
Departments of Materials Science and Engineering[§] and Chemical Engineering[‡]
Northwestern University, Evanston, IL 60208

ABSTRACT

A novel experimental approach involving the fluorescence nonradiative energy transfer technique is employed to study transport processes in thin polymer films near the glass transition through the measurement of energy transfer efficiency, E. Using a layered thin film sample geometry, values of the small molecule diffusion coefficient, $\mathcal{D}$, as low as 8 x 10^{-16} cm^2/sec are measured within diffusion times of 3.5 hours. These studies reveal a significant dependence of both the magnitude and temperature dependence of $\mathcal{D}$ on diffusant size.

INTRODUCTION

There has been significant study recently concerning the diffusion of small molecules in polymeric matrices. In these studies a small molecule is considered to be the size of or larger than a benzene ring, but not polymeric. Technologically, there is interest in understanding diffusion-controlled phenomena such as those found in controlled drug release and thermal printing applications. Additionally of great scientific interest is the understanding of how the motion of small molecules may be coupled to or decoupled from various relaxation processes in polymers, such as the α-relaxation process associated with cooperative segmental motions occurring near the glass transition temperature, T_g. Numerous techniques have been used to measure small molecule diffusion coefficients on the order of 10^{-10} cm^2/sec and higher; however, only one technique, forced Rayleigh scattering (FRS) [1-3], has been reported to be able to measure significantly lower diffusion coefficients, such as those encountered near T_g in amorphous polymers.

Here we present a new approach which allows measurement of small molecule diffusion coefficients of magnitude comparable to those measured by FRS. This technique involves fluorescence nonradiative energy transfer (NRET), a process that occurs when an excited donor chromophore transfers its energy to an acceptor via coulombic dipole-dipole interactions over distances of a few nm. The approach employs a "sandwich" of two thin polymer films, one lightly labeled with either NRET donor or acceptor chromophores, and the other doped at low levels with the complementary chromophore. Since sufficient fluorescence intensity can be obtained from extremely thin polymer films, diffusion coefficients as low as 10^{-16} cm^2/sec can be obtained in reasonable experimental times.

EXPERIMENTAL

Pyrene (Aldrich) was used as the NRET donor, [N-(2-hydroxyethyl)-N-ethyl]-4-(tricyanovinyl) aniline (TC1, synthesized in this laboratory following the procedure outlined by McKusick, et al. [4]) and decacyclene (Aldrich) were used as acceptors, and the matrix polymer was poly(isobutyl methacrylate) (PiBMA). Polymers were prepared by copolymerization of either pyrene-labeled monomer or TC1-labeled monomer with iBMA, as described previously [5], to produce chromophore-labeled polymer, or by homopolymerization of only iBMA under the same conditions. Onset T_g's of the pure PiBMA, doped PiBMA, and labeled PiBMA were measured using a Perkin-Elmer DSC-7 at a heating rate of 10°C/min, with all samples yielding T_g's of 64°C. Typical chromophore concentrations were 0.25 mole% acceptor per iBMA unit, and 0.12 mole% donor. Förster radii (R_0, the donor-acceptor separation distance at which there

Mat. Res. Soc. Symp. Proc. Vol. 407 © 1996 Materials Research Society

is a 50% probability of energy transfer to acceptor [6]) of 3.0 nm for the pyrene/TC1 donor/acceptor pair and 2.5 nm for pyrene/decacyclene were determined.[7]

Films were spun cast onto quartz slides from chloroform solution and allowed to dry overnight at room temperature. Film thicknesses, ranging from 0.38 to 3.0 μm, were characterized using a Tencor P10 Profilometer. Layered samples were prepared by floating the chromophore-labeled polymer film off the slide onto the surface of a distilled water bath and placing this film on top of a slide coated with chromophore-doped polymer. Excess water was removed, and the polymer sandwich was allowed to dry for at least 24 hr at room temperature, and was then placed in a vacuum oven at room temperature for several hours to promote contact between layers. Further experimental details can be found in reference [8].

RESULTS AND DISCUSSION

In this study, NRET has been utilized via a simple geometry involving a "sandwich" of two thin polymer films. A film of polymer which is chemically labeled with one type of chromophore is layered on top of a polymer film doped with the complementary chromophore. Initially, the chromophores lie on opposite sides of the interface and little donor-acceptor interaction occurs. Because polymeric self-diffusion coefficients are many orders of magnitude lower than small molecule diffusion coefficients [1,9], the polymer matrix is considered to be stationary, while the dopant chromophores diffuse through it according to Fick's law. Upon heating to a temperature near T_g, the free dopant chromophores diffuse into the chromophore-labeled polymer, the number of donor and acceptor chromophores in close proximity increases, and the probability for NRET increases. Experimentally, the sample is illuminated by light of a wavelength preferentially absorbed by the donor, and decreases in the steady-state donor fluorescence intensity, I_D, are observed as a function of annealing time. Assuming that both donor-to-donor energy transfer and energy transfer across the interface before diffusion are negligible, these decreases in intensity can be related to the efficiency of energy transfer, E(t): [10]

$$E(t) = \left(\frac{K}{w}\right)\sqrt{\mathcal{D}t} = \frac{I_D(0) - I_D(t)}{I_D(0) - I_D(\infty)} \qquad (1)$$

where t refers to annealing time, w is the thickness of the donor film, $\mathcal{D}$ is the tracer diffusion coefficient of the dopant chromophore, and $I_D(\infty)$ is the donor intensity of a fully diffused sample. For diffusion times, $t \leq w^2/(16\mathcal{D})$, K is a function of only the initial acceptor concentration, and $E(t) \sim t^{1/2}$. In these studies, K=1.13 for donor diffusion measurements and K≈1.4 for acceptor diffusion. $\mathcal{D}$ at a particular temperature can be easily determined by monitoring donor fluorescence as a function of annealing time.

An example of how the pyrene steady-state fluorescence intensity of a thin-film "sandwich" sample may vary upon annealing is presented in Fig. 1. *In situ* measurements are shown for a sandwich consisting of a TC1-labeled PiBMA film layered on top of a pyrene-doped PiBMA film and annealed at 70°C, only a few degrees above the polymer T_g. Given the relatively high quantum yield of pyrene [11], well-structured fluorescence spectra are obtained even at a low doping concentration of 0.12 mole% pyrene in the thin PiBMA films. The fractional decrease in intensity is uniform across the spectrum, resulting in a loss of signal of almost 15% after 2 hr of annealing. From these decreases in fluorescence intensity, values of the energy transfer efficiency, E(t), for pyrene diffusion in PiBMA at several temperatures have been calculated using Eq. (1) and are plotted as a function of $(K/w)\sqrt{t}$ in Fig. 2. The linearity of each plot is consistent with Eq. (1), with the slope and thereby $\mathcal{D}$ increasing dramatically with temperature. Similar plots were obtained in determining diffusion coefficients for decacyclene in PiBMA.

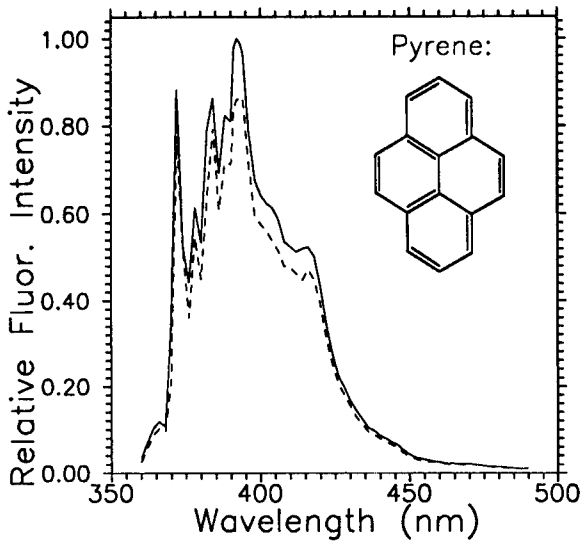


Figure 1. Measurement of pyrene diffusion in PiBMA using layered pyrene-doped PiBMA/TC1-labeled PiBMA samples. Steady-state fluorescence spectra of pyrene at 70°C at annealing times of 3 min. (solid) and 120 min. (dashed). λ_{cx}= 336 nm, K= 1.13, w = 1.6 μm.

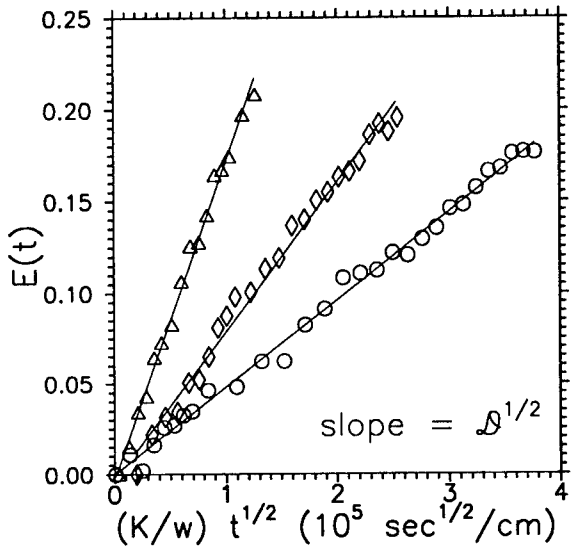


Figure 2. Measurement of pyrene diffusion in PiBMA using layered pyrene-doped PiBMA/TC1-labeled PiBMA samples. Energy transfer efficiency calculated from Eq. (1) at (○) 65°C, (◊) 70°C, and (Δ) 81°C. λ_{ex}= 336 nm, K= 1.13, w ranges from 1.3 to 2.0 μm.

Fig. 3 illustrates values of $\mathcal{D}$ for pyrene and decacyclene at several temperatures in PiBMA. A $\mathcal{D}$ value of 8×10^{-16} cm^2/sec has been determined within a diffusion time of 3.5 hr, employing films 0.51 μm thick. Evident is the significant difference in magnitude between diffusion coefficients for the two chromophores, with significantly higher $\mathcal{D}$ values observed for the smaller molecule, pyrene. In addition, the temperature dependence appears to increase with increasing chromophore size. Also shown are results for the diffusion of TTI in poly(ethyl methacrylate) (PEMA) from [1]. (Although this work was done in PiBMA, the comparison is made to literature values using a PEMA matrix because no previous studies of translational diffusion have been done using PiBMA. In any case, the α-relaxation processes in PEMA and PiBMA have been demonstrated to follow a similar temperature dependence, as demonstrated using second harmonic generation (SHG). [12,13])

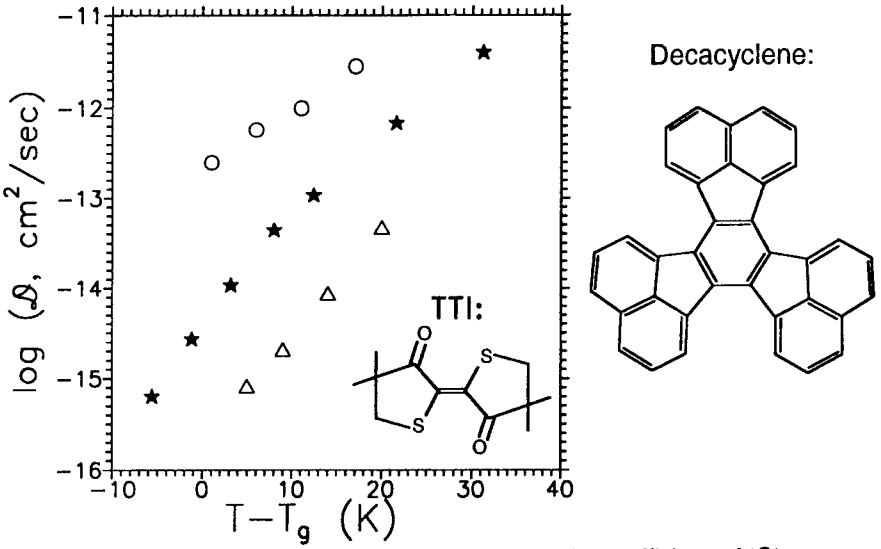


Figure 3. Temperature dependence of the translational diffusion coefficients of (O) pyrene and (Δ) decacyclene in PiBMA, T_g = 64°C, from this study, compared to that of (★) TTI in PEMA, T_g = 69°C, as determined by Ehlich and Sillescu [1].

The results shown in Fig. 3 can be examined using a modification of the Williams-Landel-Ferry (WLF) relation [14], which Ehlich and Sillescu [1] used to describe the temperature dependence of small molecule motions above T_g:

$$\log\left[\frac{\mathcal{D}(T)}{\mathcal{D}(T_g)}\right] = \frac{\xi C_{1g}(T - T_g)}{(C_{2g} + T - T_g)} \qquad (2)$$

where C_{1g} and C_{2g} are the familiar WLF parameters, and ξ is a coupling parameter for which $0 \le \xi \le 1$. Ehlich and Sillescu [1] interpreted $\xi = 1$ as corresponding to the limit of maximum coupling to the polymer α-relaxation, and $\xi = 0$ as corresponding to no coupling, or no temperature dependence. The diffusion data for pyrene and decacyclene in PiBMA (from this study) and for TTI in PEMA (from [1], determined using FRS) were fit to Eq. (2), and the results

are listed in Table I. The size of each molecule, calculated as the molar volume at absolute zero using the Sugden group contribution method [15] is also given. For each WLF fit, C_{1g} and C_{2g} were held constant, while the values of ξ and $\mathcal{D}(T_g)$ were varied. Two sets of parameters were used: C_{1g} = 13 and C_{2g} = 58K, as determined from dielectric and SHG studies in PiBMA [13], and C_{1g} = 15 and C_{2g} = 90K, from dynamic mechanical analysis of PEMA [1]. As Ehlich and Sillescu performed measurements over a much larger temperature range than was used here, their results were truncated to a 23°C temperature range near T_g. A small difference is observed between ξ values determined using the two sets of WLF parameters; however, both sets of parameters give very good fits, with correlation coefficients, $R^2 > 0.996$, demonstrating that either set of parameters results in a reasonable representation of the data. Because the temperature range of 15°C used here is fairly narrow, data that would follow a WLF-type relation over a wider temperature range could be fit very well to a simple Arrhenius relationship. From these activation energies, E_a, effective apparent coupling parameters, $E_a/(E_a)_\alpha$, were calculated and are listed in Table I. $(E_a)_\alpha$ is considered to be the effective activation energy of the α-relaxation and is calculated at T_g+8K, the middle of the temperature range, from the WLF parameters: [14]

$$(E_a)_\alpha(T) = \frac{2.303 R C_{1g} C_{2g} T^2}{(C_{2g} + T - T_g)^2} \qquad (3)$$

in which R is the gas constant. For both sets of WLF parameters and for all three probes, each value of the ratio $E_a/(E_a)_\alpha$ calculated in this manner is in excellent agreement with the values of its corresponding coupling parameter ξ, as determined from the constrained WLF fits.

Table I. Analysis of Small Molecule Diffusion in PiBMA, T_g=64°C, and PEMA, T_g=69°C.

	Size	E_a	C_{1g}=13, C_{2g}=58K[b]			C_{1g}=15, C_{2g}=90K[c]		
Probe	cm³/mol	kJ/mol	ξ	$\log(\mathcal{D}(T_g))$	$E_a/(E_a)_\alpha$	ξ	$\log(\mathcal{D}(T_g))$	$E_a/(E_a)_\alpha$
pyrene	151	147	0.38	-12.7	0.40	0.45	-12.7	0.43
decacyclene	314	276	0.77	-15.9	0.79	0.88	-15.9	0.81
TTI[d]	185	--	--	--	--	0.81[e]	-14.2[e]	--
TTI[f]	185	248	0.64	-14.4	0.67	0.75	-14.4	0.73

[a]Molar volumes at 0 K calculated using the Sugden group contribution method [15]. [b]WLF parameters for PiBMA from [13]. $(E_a)_\alpha$=370 kJ/mole, from eq (3) at T_g+8K. [c]WLF parameters for PEMA from [1]. $(E_a)_\alpha$=340 kJ/mole, from (3) at T_g+8K. [d]Fit to data over the temperature range T_g-1°C <T < T_g+89°C. [f]Fit to data over the range T_g-1°C < T < T_g+22°C. [e]Value from [1].

It may be concluded from Table I that increasing the chromophore size results in greater apparent fractional coupling of translational motion to polymer α-relaxation dynamics. Pyrene, the smallest molecule studied here, with a molar volume of 151 cm³/mole, exhibits values of ξ and $E_a/(E_a)_\alpha$ between 0.40 and 0.45, with $\mathcal{D}(T_g) = 2.0 \times 10^{-13}$ cm²/sec. TTI is intermediate in size, 185 cm³/mole, and exhibits ξ and $E_a/(E_a)_\alpha$ values of approximately 0.7 and $\mathcal{D}(T_g) = 4.0 \times 10^{-15}$ cm²/sec. Decacyclene is by far the largest probe studied here, 314 cm³/mole, and exhibits ξ and $E_a/(E_a)_\alpha$ values between 0.8 and 0.9 and $\mathcal{D}(T_g) = 1.3 \times 10^{-16}$ cm²/sec. However, the obvious conclusion that increased chromophore size results in greater coupling may be too simple. Another possibility is that the translational motions measured here may still be completely coupled to the α-relaxation even though the temperature dependence is not as strong. The distribution of α-relaxation times near T_g can be very broad, i.e., many orders of magnitude

[14,16]. As a result, average α-relaxation times reflect long-time relaxation behavior, and short-time relaxations affect the average times by only a small fraction of a percent. In contrast, the translational diffusion coefficients measured here are dominated by the largest values of $\mathcal{D}$, which correspond to the shortest relaxation times. Those regions with shorter relaxation times require the cooperative segmental mobility of fewer polymer chain segments than do regions which are characterized by longer relaxation times, likely resulting in a smaller dependence on temperature. Studies are underway to test these hypotheses, as well as the possibility that molecules such as pyrene may have translational modes of motion not requiring cooperative segmental mobility.

CONCLUSIONS

A novel fluorescence NRET technique has been used to measure extremely low diffusion coefficients of small molecules in polymers near T_g, as low as 8×10^{-16} cm^2/sec, within several hours, employing simple donor fluorescence intensity measurements. Energy transfer efficiency, E(t), was shown to increase proportionally with the square root of annealing time, as predicted by the quantitative formalism developed by Dhinojwala and Torkelson [10], resulting in the straightforward determination of diffusion coefficients. As hundreds of NRET donor/acceptor pairs exist, this NRET approach will allow for the study of how size, shape, and flexibility of a small molecule affect its translational motion in a polymer matrix, especially its apparent coupling to polymer dynamics. Current research involves study of the diffusion of highly nonplanar molecules, comparisons of rotational reorientation and translational dynamics of small molecules, and the effects of different polymer types. Small molecule diffusion in glassy polymers that are quenched from the rubbery state immediately prior to analysis is also being examined.

REFERENCES

1. D. Ehlich and H. Sillescu, Macromolecules **23**, 1600 (1990).
2. J. Xia and C. H. Wang, J. Polym. Sci. B: Polym. Phys. **33**, 899 (1995), and references therein.
3. H. Kim, D. A. Waldow, C. C. Han, Q. Tran-Cong, and M. Yamamoto, Polym. Commun. **32**, 108 (1991).
4. B. C. McKusick, R. E. Heckert, T. L. Clairns, D. D. Coffman, and H. F. Mower, J. Am. Chem. Soc. **80**, 2806 (1958).
5. A. Dhinojwala, J. C. Hooker, and J. M. Torkelson, J. Non-Cryst. Solids **172-174**, 286 (1994).
6. I. B. Berlman, Energy Transfer Parameters of Aromatic Compounds (Academic Press, New York, 1973), p. 28.
7. J. R. Lakowicz, Principles of Fluorescence Spectroscopy (Plenum Press, New York, 1983), p. 306.
8. D. D. Deppe, A. Dhinojwala, and J. M. Torkelson, Macromolecules, submitted.
9. A. Karim, G. P. Felcher, and T. P. Russell, Macromolecules **27**, 6973 (1994); S. J. Whitlow and R. P. Wool, Macromolecules **24**, 5926 (1991); P. F. Green and E. J. Kramer, Macromolecules **19**, 1108 (1986); H. H. Kausch and M. Tirrell, Ann. Rev. Mat. Sci. **19**, 341 (1989); and references contained therein.
10. A. Dhinojwala and J. M. Torkelson, Macromolecules **27**, 4817 (1994).
11. I. B. Berlman, Handbook of Fluorescence Spectra of Aromatic Molecules (Academic Press, New York, 1971), p. 383.
12. A. Dhinojwala, Ph.D. Thesis, Northwestern University (1994).
13. A. Dhinojwala, G. K. Wong, and J. M. Torkelson, Macromolecules **26**, 5943 (1993).
14. J. D. Ferry, Viscoelastic Properties of Polymers, 3rd ed. (Wiley, New York, 1980), pp. 287-301.
15. R. N. Haward, J. Macromol. Sci. - Rev. Macromol. Chem. **C42** (2),191 (1970).
16. A. Dhinojwala, J. C. Hooker, and J. M. Torkelson, ACS Symposium Ser. **601**, 318 (1995).

DYNAMICS OF STRUCTURAL RECOVERY AND MECHANICAL RESPONSE OF POLYMERIC LIQUIDS NEAR TO THE GLASS TRANSITION

D.M. COLUCCI, C.R. SCHULTHEISZ, and G.B. MCKENNA
National Institute of Standards and Technology, Gaithersburg, MD 20899

ABSTRACT

Results from the NIST torsional dilatometer have indicated that after a temperature step from equilibrium, the volume (structure) and mechanical response (physical aging) can evolve at different rates, depending on the temperature history. The torsional dilatometer results have been modeled in two ways. First, it was assumed that the volume and mechanical response are governed by different clocks, with the principle of time-aging time superposition employed to evaluate an aging time shift factor a_{te} from the torsional response, which was then compared to a structural shift factor a_δ calculated from the evolution of the volume. These results were also investigated using a thermoviscoelastic model based on rational thermodynamics and configurational entropy; this model does not include an explicit assumption of separate time scales, but different time scales for the structure and mechanical properties appear to arise naturally from the formulation. The results from the thermoviscoelastic model show good qualitative agreement with the torsional dilatometer results, although more material data is needed to make an exact comparison.

INTRODUCTION

Upon cooling a polymer melt through the glass transition T_g range the thermodynamic state (structure) of the newly formed glass evolves spontaneously towards a temporally distant equilibrium. Associated with the changes in glassy structure are changes in the mechanical response of the polymer that have come to be referred to as 'physical aging'. The changes in the viscoelastic response during physical aging were extensively explored by Struik (1978) and he found that, to first order, the behavior could be described using a time-aging time equivalence similar to time-temperature superposition used successfully in the description of the temperature dependence of the viscoelastic response of polymer melts (Ferry, 1980). Therefore, the viscoelastic response of the polymer depends on the time after the change in temperature was applied (the aging time t_e) and is related to some arbitrary reference state by a shift of the characteristic relaxation times denoted by the a_{te} shift factor. Struik (1978) also showed that the progression of a_{te} as t_e increases is independent of the mode of deformation, i.e., extension, compression and shear experiments give the same values of a_{te}.

Another aspect of the physical aging process is the kinetics of the structural recovery itself. One representation of the structural recovery is in terms of the departure of the structure from equilibrium $\delta(t)$, which exhibits a non-exponential response. The second aspect of the representation is that the characteristic relaxation time depends upon both structure δ and temperature T and can be related to the structure shift factor a_δ.

In the literature on physical aging a point that is seldom addressed is the relative values of a_δ and a_{te}. However, there have been observations that volume and enthalpy recovery proceed at different rates (Scherer, 1986). Furthermore, Moynihan (1976), Roe and Millman (1983), Scherer (1986), Santore et al. (1991), Schultheisz et al. (1995) have reported that the time required for different properties to reach equilibrium are different. Another approach is to use the 'Rational Thermodynamics' framework in its Coleman and Noll (1961) formulation and as further developed by Shay and Caruthers (1988, 1989) which results in a 'natural' separation of time-scales for different processes. In the following we will review the experimental findings of McKenna et al. (1995) and Schultheisz, et al. (1995) in which different time scales are found for volume recovery and mechanical responses in the same experiments. We then review the essentials of the Tool-Narayanaswamy-Moynihan Kovacs-Aklonis-Hutchinson-Ramos (Narayanaswamy, 1971; Tool, 1946; Moynihan et al. 1976; and Kovacs et al. 1979) TNMKAHR equations used to analyze the data. This

Mat. Res. Soc. Symp. Proc. Vol. 407 © 1996 Materials Research Society

is followed by a description of the thermoviscoelastic model of Shay and Caruthers (1988, 1989), showing also that they contain the 'essential' ingredients described above for the structural recovery. Finally we compare the model calculations with the experimental results and discuss their significance.

EXPERIMENTAL

Experiments were performed with the NIST torsional dilatometer (Duran and McKenna, 1990) which allows simultaneous real-time measurements of temperature, volume change, torque and normal force in cylindrical samples subjected to arbitrary torsional deformation histories subsequent to rapid temperature changes (T-jump histories). The single sample used for all experiments had a length l of 115 mm and a diameter d of 15.3 mm. The material was a model epoxy (DGEBA/polypropylene oxide) that is fully described elsewhere (Lee and McKenna, 1990). The glass transition temperature of the epoxy is 42.4 °C as measured by differential scanning calorimetry at 20 °C/min. Details of the experimental procedure and thermal control can be found in McKenna et al., 1995. The origin of the aging time t_e is taken at 450 s after the jump to correct for the time required for the dilatometer to achieve the final temperature (Duran and McKenna, 1990). Sequential torsional strains were applied following Struik's (1978) protocol. A constant angle of twist (ϕ) was first applied at one end of the specimen for a time t_1 and then removed for $10t_1$; each successive twist application was for twice as long as the previous twist, and the post-twist relaxation time was always ten times as long as the twist itself. The torsional strain reported here has a maximum strain γ given by (ϕ d)/(2 l) and experiments were performed at values of γ = 0.03 and 0.05.

RESULTS

In order to address the potentially different volume and mechanical timescales, the torsional relaxation modulus was determined at various aging times. Using the principle of time-aging time superposition, each response was first fit to the KWW function then horizontally shifted along the log time axis to form a single master curve. A plot of log a_{t_e} versus $\delta=(V-V_\infty)/V_\infty$ revealed three different types of behavior: (i) the dependence is linear with no further aging behavior observed at small δ values, (ii) the dependence is linear with further aging observed at small δ values near zero, (iii) the dependence is curved or bilinear with the log a_{t_e} values becoming relatively constant before δ becomes zero.

TNMKAHR Model

McKenna and coworkers (1994, 1995) originally attributed their findings to the existence of two different clocks, a mechanical and a volume clock, that "tick" at different rates, each depending upon the time after the applied temperature jump. This suggestion contradicts the original hypothesis by Struik (1978) that the volume clock and the mechanical deformation clock run at the same rate. In order to test the hypothesis, Schultheisz et al. (1995) used the TNMKAHR model to directly determine the change in the reduced time t* using the following relations valid for a single step

$$\delta(t^*)=-\Delta\alpha\ (t^*)(T_0-T_1) \tag{1}$$

$$t^*=\int_0^t \frac{d\xi}{(a_T, a_\delta)} \tag{2}$$

where $\Delta\alpha$ is the rubbery minus glassy change in the thermal expansion coefficient, T is the temperature, a_T the temperature dependent shift factor, and a_δ is the volume (structural) recovery shift factor. The volume recovery response function R(t*) is represented by the KWW function

$$R(t^*)=e^{-(t^*/\tau_r)^\beta} \tag{3}$$

where τ_r is the mean retardation time and β is a parameter which describes the breadth of the retardation spectrum. The volume recovery shift factor a_δ as a function of time was determined for each of the T-jumps using Equations 1, 2, and 3 assuming that a_T and a_δ have the following forms proposed by Kovacs, Aklonis, Hutchinson, and Ramos (1979)

$$a_T=e^{-\theta(T-T_r)} \tag{4}$$

$$a_\delta=e^{\frac{-(1-x)\theta\delta}{\Delta\alpha}} \tag{5}$$

The a_δ and a_{te} values as functions of δ can then be compared. If Struik's hypothesis were correct, one would expect a plot of a_{te} versus a_δ to result in a straight line with a slope equal to 1. In their work, Schultheisz et al. (1995) found that the slope of the log a_{te} versus log a_δ values ranged anywhere from 2-5 depending upon thermal history.

Thermoviscoelastic Model

While the data analysis used by Schultheisz et. al. (1995) indicates that the mechanical and volumetric responses are governed by different shift factors, the building block approach required to describe such behavior is at a minimum awkward. In addition, multiple parameter sets are needed to describe the complete set of torsional relaxation and structural recovery data. The thermoviscoelastic constitutive model is derived using a rational thermodynamics framework first proposed by Coleman (1964) for simple materials with fading memory. The method incorporates in the derivation the conservation of mass, energy, linear and angular momentum, and the Clausius-Duhem inequality as required by Coleman, but where (i) the standard laboratory time is replaced by the reduced time t* and (ii) a form of the entropy is assumed to control the rate of relaxation. The derivation of the model begins by assuming a free energy functional which is a function of both the instantaneous state of temperature and deformation as well as the temperature and deformation histories. The resulting general form of the constitutive model is as follows:

$$T=-p^\infty I+\frac{V_r}{V}\int_0^t G_\Delta(t^*-\xi^*)\left(\frac{dC_t}{d\xi}-\frac{1}{3}I\frac{dI_{t1}}{d\xi}\right)d\xi$$
$$+\frac{V_r}{2V}I\int_0^t K_\Delta(t^*-\xi^*)\frac{dI_{t1}}{d\xi}d\xi+\frac{2I}{V}\int_0^t A_\Delta(t^*-\xi^*)\frac{d\Theta}{d\xi}d\xi \tag{6}$$

where T is the stress, Θ is the temperature, G_Δ the linear viscoelastic shear contribution related to the linear viscoelastic shear modulus, K_Δ the linear viscoelastic bulk contribution related to the linear viscoelastic bulk modulus, A_Δ is the thermal stress, V_r is the reference volume, I_{t1} is the first invariant of the relative right Cauchy-Green deformation tensor $C_t=F_t^T.F_t$, F_t is the relative deformation gradient, and p^∞ is the equilibrium pressure determined by using the Tait equation. The material time is defined as

$$(t^*-\xi^*)=\int_\xi^t\frac{d\varsigma}{a(\varsigma)} \tag{7}$$

where $a(\varsigma)$ is a generalized shift factor. The Adam and Gibbs (1965) form of $a(\varsigma)$ is used

$$\log a = B\left(\frac{1}{\eta_c\Theta}-\frac{1}{\eta_{cr}\Theta_r}\right) \tag{8}$$

where the rate of viscoelastic relaxation controlled by the configurational entropy η_c given by

$$\eta_c=\eta_c^{\infty}-\int_0^t A_\Delta(t^*-\xi^*)\frac{dI_{tl}}{d\xi}d\xi-2\int_0^t C_\Delta(t^*-\xi^*)\frac{d\Theta}{d\xi}d\xi \tag{9}$$

where η_c^{∞} is the equilibrium configurational entropy and C_Δ is a material function related to the constant pressure heat capacity.

In order to use the thermoviscoelastic constituitve model, the G_Δ, K_Δ, A_Δ, and C_Δ material functions as well as the B parameter in the shift factor and p^∞ must be determined. Rubbery isobaric constant rate of cooling PVT experiments or rubbery Tait parameters are needed to obtain p^∞. Using the principle of pseudo-time shift invariance allows for the time dependent portion $k_\Delta(t^*)$ to be separated from the limiting glassy minus rubbery portion ΔK given by the following relations for the bulk material function K_Δ

$$K_\Delta=\Delta K(V,\Theta)\ k_\Delta(t^*) \tag{10}$$

Similar relationships exist for the G_Δ, A_Δ, and C_Δ material functions. The limiting ΔK and ΔA are determined from glassy PVT data and ΔC is obtained from the change in heat capacity ΔC_p obtained from a simple differential scanning calorimetry DSC experiment. A linear viscoelastic shear modulus master curve from viscoelastic measurements at different temperatues is used to determine ΔG, $g_\Delta(t^*)$ and B. Optimization of Kovacs' (1964) volume recovery data (McWilliams and Caruthers, 1993) for poly(vinyl acetate) PVAc provided the $k_\Delta(t^*)$, $a_\Delta(t^*)$, and $c_\Delta(t^*)$ time dependent contributions.

Since Struik (1978) found the linear viscoelastic aging time behavior to be independent of deformation type, and currently, computer code is not available to predict the nonuniform (torsional) deformations used in the NIST torsional dilatometer, the model simulations were conducted using tensile creep compliance as the mode of deformation. Also since model parameters are only available for PVAc, the thermal histories used were normalized to the different T_g's of the model epoxy and PVAc systems obtained at the same cooling rate; in other words, the thermal histories used in the simulations are performed at the same $T-T_g$ difference.

Creep compliance simulations for PVAc were performed for aging times from 0.5 to 1×10^6 hours. Much longer aging times were required in the simulations of the prescribed thermal histories than were needed in the experiments to achieve structural equilibrium. Since the same set of parameters can quantitatively represent the Kovacs (1964) volume relaxation experiments, the need to employ longer aging times in the simulation is attributed to material differences in using the PVAc parameters instead of those needed for epoxy. The resulting simulated compliance curves were then shifted horizontally a distance $\log a_{te}$ for each aging time as performed in the work of Struik (1978).

In order to compare the thermoviscoelastic model simulation results to the experimental epoxy results, the $\log a_{te}$ reference state was chosen at the same δ value as observed experimentally. The resulting $\log a_{te}$ versus δ dependences are shown in Figures 1 and 2. The symbols represent the experimental torsional dilatometry data while the solid lines are the thermoviscoelastic model predictions. The model was able to predict the qualitative differences in the aging and volume relaxation responses. As shown in Figure 1 for the lower temperature jump cases the model was able to discriminate between the two different types of behaviors observed. As shown in Figure 2, the model was able to predict the further aging after thermodynamic equilibrium was obtained.

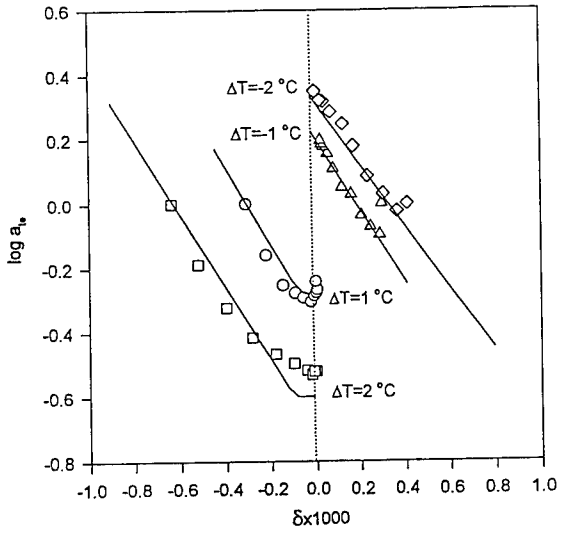


Figure 1: Result of Time-Aging-Time Superposition of the Thermoviscoelastic Constitutive Model Creep Simulations. The symbols are the experimental results of up and down jumps to 32.8 °C and the solid lines are the thermoviscoelastic model predictions.

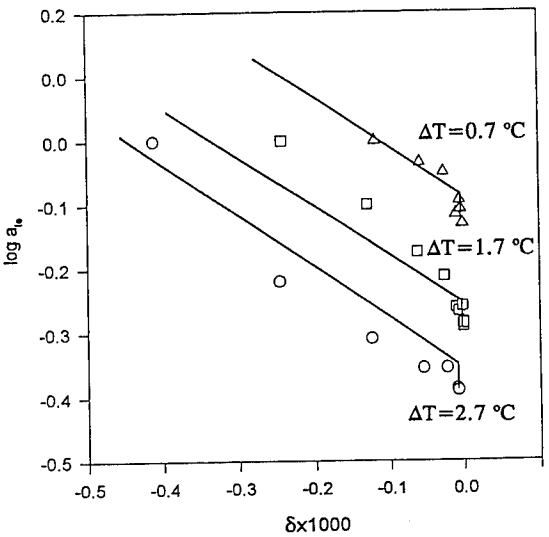


Figure 2: Result of Time-Aging-Time Superposition of the Thermoviscoelastic Constitutive Model Creep Simulations. The symbols are the experimental results of up jumps to 35.5 °C and the solid lines are the thermoviscoelastic model predictions.

CONCLUSIONS

Preliminary results reveal that the thermoviscoelastic constitutive model contains the appropriate physics to predict the three different types of mechanical and volume relaxation responses found by McKenna and coworkers in their torsional dilatometry studies. Comparison of these results with those in the paper by McKenna et al. (1994) show that the thermoviscoelastic model can qualitatively account for the effect of thermal history on the relaxation. Instead of attributing these findings to different mechanical and volume timescales, the agreement of the model with the data suggests that the coupling between the deformation and thermal histories inherent in the thermoviscoelastic constitutive model explains the experimentally observed phenomena in a natural way. These results indicate that the thermoviscoelastic model contains the appropriate physics to account for different rates of relaxation dependent upon thermal history and could unify a large variety of polymeric relaxation phenomena.

REFERENCES

Adam G. and Gibbs J.H., J. Chem. Phys., 43, 139, 1965

Coleman B.D. and Noll W., Rev. Mod. Phys., 33, 239, 1961

Coleman B.D., Arch. Rat. Mech. Anal., 17, 1, 1964

Coleman B.D., Arch. Rat. Mech. Anal., 17, 230, 1964

Duran R.S. and McKenna G.B., J. Rheol., 34, 813, 1990

Ferry J.D., Viscoelastic Properties of Polymers, 3rd Edition, John Wiley, New York, 1980

Kovacs A.J., Fortsch. Hochpolym. Forsch., 3, 394, 1964

Kovacs A.J., Aklonis J.J. Hutchinson J.M., and Ramos A.R., J. Poly. Sci., Polym. Phys. Ed., 17, 1097, 1979

Lee A. and McKenna G.B., Polymer, 31, 423, 1990

McKenna G.B., Schultheisz C.R., Leterrier Y., "Volume Recovery and Physical Aging: Dilatometric Evidence for Different Kinetics,." Deformation, Yield, and Fracture in Polymers, 9, 31/1, Institute of Materials, London, 1994

McKenna G.B., Leterrier Y., and Schultheisz C.R., Poly. Eng. and Science, 35, 403, 1995

McWilliams D.S. and Caruthers J.M., Society of Rheology Annual Meeting, Boston, MA, October 1993

Moynihan C.T., Macedo P.B., Montrose C.J., Gupta P.K., DeBolt M.A., Dill J.F., Dom B.E., Drake P.W., Easteal A.J., Elterman P.B., Moeller R.P., Sasabe H., and Wilder J.A., Ann. N.Y. Acad. Sci., 279, 15, 1976

Narayanaswamy O.S., J. Amer. Ceram. Soc., 54, 491, 1971

Roe R.J. and Millman G.M., Poly. Eng. Science., 23, 318, 1983

Santore M.M., Duran R.S., and McKenna, Polymer, 32, 2377, 1991

Scherer G.W., Relaxation in Glass and Composites, John Wiley and Sons Inc., New York, 1986

Schultheisz C.R., McKenna G.B., Leterrier Y., and Stefanis E.A., Proc. Soc. for Exp. Mech., Grand Rapids, MI, June 1995

Shay R.M. Jr. and Caruthers J.M., Proc. North Amer. Thermal Anal. Soc., Orlando, 1988

Shay R.M. Jr. and Caruthers J.M., Mechanics of Plastics and Composites, V.K. Stokes, ed., AMD-Vol 104, ASME, 1989

Struik L.C.E., Physical Aging in Amorphous Polymers and Other Materials, Elsevier, New York, 1978

Tool A.Q., J. Res. NBS, 37, 73, 1946

Tool A.Q., J. Amer. Ceram. Soc., 29, 240, 1946

FRACTIONAL DEBYE-STOKES-EINSTEIN LAW IN POLYMERIC LIQUID CRYSTALS

L.ANDREOZZI [1], C.DONATI [2], M.GIORDANO [1], D.LEPORINI [1]
[1] Dipartimento di Fisica, Universita' di Pisa, Piazza Torricelli 2, I-56100 Pisa ITALY
leporini@ipifidpt.difi.unipi.it
[2] Scuola Normale Superiore, Piazza dei Cavalieri, I-56100 Pisa ITALY
donati@ipifidpt.difi.unipi.it

ABSTRACT
The viscosities of amorphous and semicrystalline polymeric liquid crystals η have been measured by dynamic mechanical analysis. They have been compared with the rotational correlation times of molecular probes, as drawn by Electron Spin Resonance spectroscopy on two different time scales. In all the cases the correlation times of the spinning motion of a cigar-like probes $\tau_{\parallel}$ and η are related by a fractional Debye-Stokes-Einstein law, *i.e.* $\tau_{\parallel} \propto \eta^{\xi}$, $\xi \leq 1$.

INTRODUCTION

The Debye-Stokes-Einstein law (DSE) relates the rotational correlation times of a tagged particle to the shear viscosity of the host medium. The DSE law is the rotational counterpart of the Stokes-Einstein law (SE) relating the translational diffusion coefficient D and the shear viscosity.

Both laws are derived in the framework of the hydrodynamic theory and for a cylindrical molecule the DSE law takes the form [1]:

$$\tau_i = v_i \eta / kT + \tau_{0i} \qquad i = \parallel, \perp \tag{1}$$

where η, k and T are the shear viscosity, the Boltzmann constant and the temperature, respectively. $\tau_{\parallel}$ and $\tau_{\perp}$ are the correlation times of rotations around the symmetry axis and of the symmetry axis itself, respectively. τ_{0i} is important only in the low-viscosity region of the fluid and will be ignored henceforth. v_i is related to the molecular effective volume and to the boundary conditions between the fluid and the surface of the tagged particle.

The success of DSE is impressive in low viscosity fluids, even in cases where the tagged particle is not a large brownian particle and is identical to the host molecules [2]. In particular, even if small discrepancies have been observed, usually reduced by considering v_i as one adjustable parameter, the linearity in η / T has been always demonstrated [3].

In the last few years a considerable amount of experimental work provided evidence of a failure of both the DSE and SE laws in the supercooled phases of polymers [4], liquid crystals [5] and molecular fluids [6,7]. Careful compilation of the available data evidence that the DSE and the SE laws break down close to the critical temperature T_c predicted by the so called mode coupling theory of the glass transition [8,9]. The breakdown manifests itself as a decoupling between the viscosity and the rotational/translational diffusion constants, the latter being much less temperature dependent. In many cases it is found that the decoupling may be expressed by fractional SE, DSE laws [4,6,8]

$$\tau_i, D^{-1} \propto \left(\eta / T\right)^{\xi} \quad \xi \leq 1 \tag{2}$$

A number of theoretical papers have discussed the above decoupling [10-12]. However, in spite of the increasing evidence in favor of eq.2 a satisfactory derivation of it still lacks. Elementary free

Mat. Res. Soc. Symp. Proc. Vol. 407 © 1996 Materials Research Society

volume arguments lead to Eq.2 with $\xi = V_g/V_h$ where V_g and V_h are the volume of the guest molecule and the critical volume of the host phase involved in the diffusion process, respectively [4]. The result is suggestive, since it provides a way to measure the cooperative volume expected in supercooled phases [7]. Nonetheless, it fails to recover the SE form in the hydrodynamic limit, since it predicts $\xi \to \infty$. Furthermore, it is known that V_g is solvent-dependent [4].

In the present paper it will be shown that comparing the rotational correlation times of guest molecules, as drawn by Electron Spin Resonance spectroscopy on two different time scales, with the viscosity of amorphous and partially crystalline polymeric liquid crystals yields new evidence of the fractional Debye-Stokes-Einstein law (FDSE). Differently from previous studies the anisotropic character of the diffusion is taken into account explicitely [7].

EXPERIMENT

Viscosity: Dynamic mechanical measurements

Dynamic mechanical measurements were performed by a dynamic-mechanical analyzer Perkin Elmer DMA7 equipped with a control system TAC7/DX. A DEC station 325c is on-line committed to the data management. In the investigated frequency range *0.01÷50 Hz* the three-point bending geometry is used. The sample was prepared as a rectangular *18x5x1 mm* sheet, according to the procedure described elsewhere [13]. Frequency scans were carried out after having equilibrated the sample for *30 min* at the temperature of interest. By the usual frequency shift procedure master curves and shift factors a_T were obtained for an appropriate reference temperature. It is known that the polymer viscosity is proportional to the shift factor a_T [13].

Rotational Diffusion: Linear and non-linear Electron Spin Resonance Spectroscopies

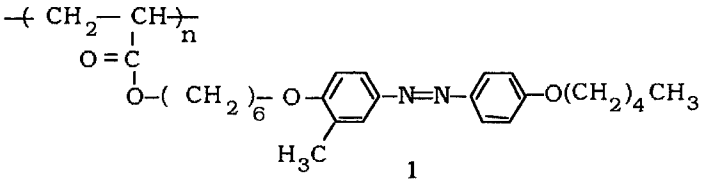
The Electron Spin Resonance spectroscopy is extensively used to study the rotational motion of guest paramagnetic molecules , so called *spin probes*, dissolved in simple fluids, liquid crystals and polymeric materials [14]. It must be noted that the signal is a sum of single particle contributions. In the present study in addition to the customary linear Electron Spin Resonance experiment (ESR) we have also employed the Longitudinally Detected ESR technique (LODESR) which is based on the non linear response of the paramagnetic system. Details on both the spectroscopies are given elsewhere [15]. The linear ESR measurement were carried out on a Bruker ER 200D SRL spectrometer equipped with an X-band microwave bridge. The home-made LODESR spectrometer is described elsewhere [15].The two techniques offer complementary information on the power spectrum of the random orientation of the probe molecule $J(\omega)$. The ESR spectroscopy is sensitive to $J(0)$, whereas the LODESR spectroscopy measures the electron longitudinal relaxation time T_1 and then $J(\omega_0)$, where ω_0 is the electron Larmor angular frequency ($\omega_0 = 2\pi 10^{10}$ *Hz rad*) . Combining the ESR and LODESR measurements draw information on both the high- and low-frequency behaviour of $J(\omega)$, namely on both the short- and long-time behaviour of the correlation function of the orientation of the probe molecule. The time scales investigated by linear ESR are in the range $10^{-12}\,s < \tau < 10^{-7}\,s$. This interval covers the relevant range for fluids of low or intermediate viscosity. The lower time scales of polymeric materials are accessible to LODESR which explores the range $10^{-11}\,s < \tau < 10^{-5}\,s$.

The interpretation of both the ESR and LODESR signals is detailed elsewhere [16]. The model pictures the probe reorientation as a two-step process. This character is expected in viscous materials and may be ascribed to the fast, restricted reorientation of the probe inside the cage where it is embedded and the slower reorientation of the cage itself. Evidence in favour of this model has been recently reported [17]. The two components are described in terms of the anisotropic

diffusion model and characterized by two different pairs of correlation times $\tau_{i\parallel}$ and $\tau_{i\perp}$ ($i = f, s$). $\tau_{i\parallel}$ refers to the rotation around the symmetry axis, whereas $\tau_{i\perp}$ to the rotation of the symmetry axis. The time scales of the two components are well separated. Then, $J(\omega_0)$ and $J(0)$ will be dominated by the pairs $\{\tau_{f\parallel}, \tau_{f\perp}\}$ and $\{\tau_{s\parallel}, \tau_{s\perp}\}$, respectively. In conclusion, the LODESR and the ESR measurements provide information on the pairs $\{\tau_{f\parallel}, \tau_{f\perp}\}$ and $\{\tau_{s\parallel}, \tau_{s\perp}\}$, respectively. In the present paper only the results on $\tau_{f\parallel}$ and $\tau_{s\parallel}$ are discussed.

Materials

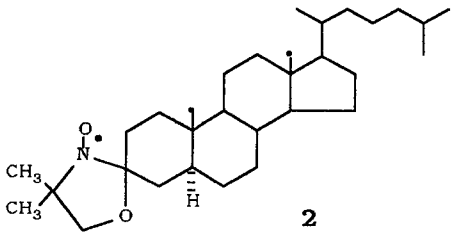
The PLC under investigation is the azobenzene-containing polyacrylate **1**, characterized by repeating units reported in the formula:



1

Polymer **1** was prepared by free radical polymerization (polymerization degree : 100÷200). Amorphous samples of the polymer **1** were prepared by quench-cooling into water at *273 K*, whereas partly crystallized samples were subsequently annealed at *303K* for *16 h*. The transition temperatures, as measured by calorimetry, are $Tg = 293\ K$, $Tm = 353\ K$, $Ti = 365\ K$

In the ESR study the spin probe of choice is cholestane which has the following structure



2

The rod-like shape of the radical **2** makes it suitable to probe anisotropic environments. The concentration of the spin probe *C* referred to the monomeric unit was $C = 10^{-2}$. The magnetic parameters of the probe **2** were optimized by careful simulation of the linear ESR lineshape , according to the procedure detailed elsewhere [16]. The best fit set for the components of the Zeeman and hyperfine tensors in the magnetic frame are $g_x = 2.0090$, $g_y = 2.0075$, $g_z = 2.0030$, $A_x = 6$ *Gauss*, $A_y = 4.9$ *Gauss*, $A_z = 33.9$ *Gauss*, respectively. Experimental evidence shows that the spin probe molecules, even in a partially cristallized sample, remain confined in the amorphous phase [14]. It has been checked that the presence of the spin probe does not lead to any observable change in the DSC thermograms of the polymer **1**.

RESULTS

In fig.1 the temperature dependences of $\tau_{f\parallel}$, $\tau_{s\parallel}$ and the shift factor a_T are shown for the

amorphous polymer. An apparent increase of the activation energy is observed by lowering the temperature. Fig.1 shows that at T_g $\tau_{s\|}$ / $\tau_{f\|} \approx 300$ confirming that the decay of the correlation function occurs with very different rates at short - and long- times. Fig.2 tests the FDSE law for

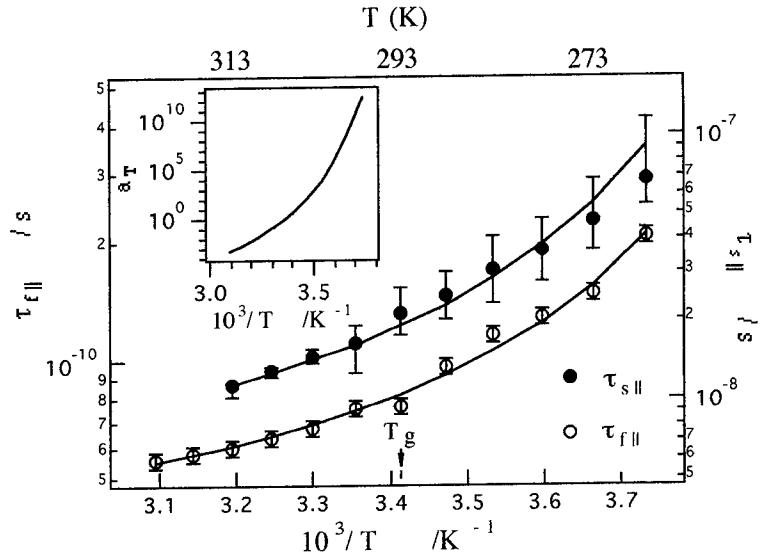


Fig.1. Amorphous polymer. Temperature dependence of the correlation times $\tau_{f\|}$, $\tau_{s\|}$ and the shift factor a_T. The lines are guides for the eye.

the cholestane probe in the amorphous polymer. The deviation from the DSE law is marked. Furthermore, new evidence in favour of the fractional DSE law is provided. The deviation from the DSE law are stronger for $\tau_{f\|}$, *i.e.* a smaller exponent ξ is found.

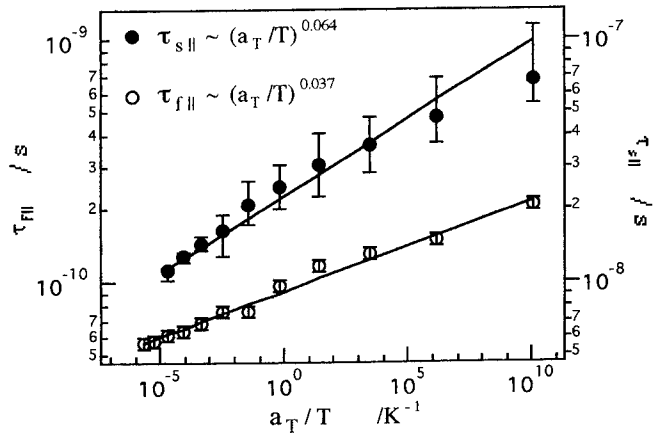


Fig.2 Test of the FDSE law for the cholestane probe in the amorphous polymer.

In fig.3 the temperature dependences of $\tau_{f\parallel}$, $\tau_{s\parallel}$ and the shift factor a_T are shown for the semicrystalline polymer. Differently from the amorphous case the activation energy decreases by lowering the temperature with a knee at T_g. It is found that $\tau_{s\parallel} / \tau_{f\parallel} \approx 200$ at T_g confirming the non-exponential decay of the rotational correlation functions also in this case .

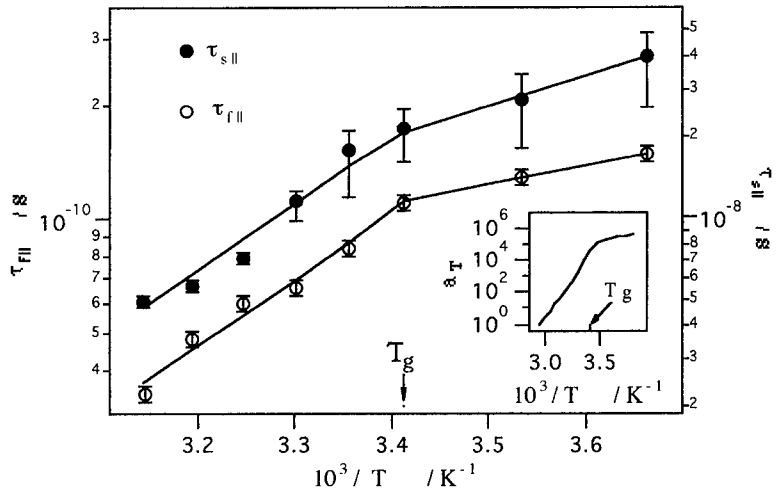


Fig.3. Semicrystalline polymer. Temperature dependence of the correlation times $\tau_{f\parallel}$, $\tau_{s\parallel}$ and the shift factor a_T. The lines are guides for the eye.

It is known that the cholestane probe is confined in the amorphous fraction of the semicrystalline polymer (≈ 80%) [14]. Therefore, since the low-frequency viscoelastic properties measured by DMA are essentially governed by the amorphous fraction disturbed by the crystalline nuclei, a comparison of $\tau_{f\parallel}$ and $\tau_{s\parallel}$ with a_T makes sense also in this heterogeneous systems. Fig.4 tests the FDSE law for the cholestane probe in the semicrystalline polymer. Even if the exponent of the

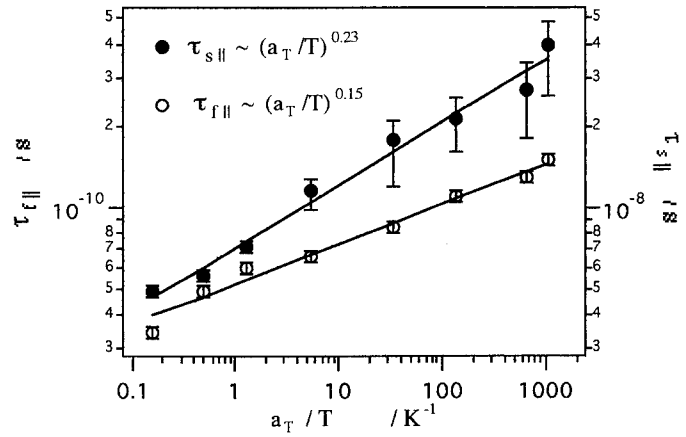


Fig.4 Test of the FDSE law for the cholestane probe in the semicrystalline polymer.

FDSE law ξ (eq.2) is higher than in the amorphous case, the deviations from the DSE law are marked on both time scales and, again, stronger for $\tau_{f\,1}$.

CONCLUSIONS

We have tested the Debye-Stokes-Einstein law by dissolving a probe molecule in the amorphous and semicrystalline phases of a polymeric liquid crystal. The reorientation process of the probe molecule has been studied by linear and non-linear ESR spectroscopies on two different time scales. The temperature curves of the correlation times and viscosity depend strongly on the amorphous fraction of the sample. Nonetheless, they can be correlated by a fractional form of the DSE law (eq.2) on both the investigated time-scales.

ACKNOWLEDGMENTS

Financially support by Istituto Nazionale di Fisica della Materia is gratefully acknowledged. The authors thank M.Laus and D.Ferri for help and assistance during the DMA measurements.

REFERENCES

1) D.Kivelson in Rotational Dynamics of Small and Macromolecules, edited by Th.Dorfmüler, R.Pecora (Springer, Berlin, 1987), p.1.
2) P.A. Egelstaff An Introduction to the Liquid State (Clarendon Press, Oxford, 1994).
3) J.L.Dote, D.Kivelson, R.N.Schwartz, J.Phys.Chem. **85**, 2169 (1981).
4) D.Ehlich and H.Sillescu, Macromolecules **23**, 1600 (1990).
5) R.Kind, O.Liechti, N.Korner, J.Hulliger, J.Dolinsek, R.Blinc, Phys.Rev.**B45**, 7697 (1992).
6) F.Fujara, B.Geil, H.Sillescu, G.Fleischer, Z.Phys.**B88**, 195 (1992).
7) M.Cicerone, F.R.Blackburn, M.D.Ediger J.Chem.Phys, **102**, 471 (1995).
8) E.Rössler, Phys.Rev.Lett. **65**, 1595 (1990).
9) W.Götze in Liquids, Freezing and the Glass Transition, J.P.Hansen, D.Levesque, J.Zinn-Justin eds. (North-Holland, Amsterdam 1991) ;
10) G.Tarjus and D.Kivelson J.Chem.Phys, **103**, 3071 (1995).
11) J.A.Hodgdon, F.H.Stillinger Phys.Rev.E **48**, 207 (1993); F.H.Stillinger, J.A.Hodgdon ibid.**50**, 2064 (1994); F.H.Stillinger, Science **267** (5206), 1935-1939 (1995).
12) U.Mohanty Adv.Chem.Phys. **89**, 89 (1995).
13) M.Laus, E.Chiellini, L.Andreozzi, D.Ferri, D.Leporini Mol.Cryst.Liq.Cryst.**266**, 179 (1995)
14) L.Andreozzi, M.P.Fontana, F.Francia, M.Giordano, D.Leporini, M.Rateo, J.Non-Cryst.Solids, **172-174**, 943 (1994) and references quoted therein.
15) M.Giordano, D.Leporini, M.Martinelli, L.Pardi, S.Santucci, C.Umeton J.Chem.Phys.**88**, 607 (1988);
16) D.Leporini Phys.Rev.A,**49**, 992 (1994).
17) J.W.Saalmüller, H.W.Long, G.G.Maresch, H.W.Spiess in press on J.Magn.Reson. ; J.W.Saalmüller, H.W.Long,T.Volkmer, U.Wiesner, G.G.Maresch, H.W.Spiess submitted to J.Polym.Sci. Part B: Polym Phys.

Kinetic Roughening of Quenched Xenon Films

Ralf K. Heilmann and Robert M. Suter
Department of Physics, Carnegie Mellon University, Pittsburgh, PA 15213

ABSTRACT

We investigate the growth of quenched Xe films formed by deposition onto a cold (15-35K) substrate via *in situ* measurements of x-ray reflectivity and diffraction. Surface roughness, film density, and crystallinity are determined as a function of Xe film thickness, substrate temperature and Xe flux in order to test for dynamic scaling behavior. Deposition of polycrystalline films with random crystallite orientations is achieved through heating of a grafoil sheet that is enclosed in the sample cell and has previously been covered with bulk Xe. At 16K the films are sufficiently quenched to be stable over several days, while at 25K annealing takes place. Differing atomic mobilities at different temperatures lead to contrasting scaling behavior. The substrate remains unchanged under repeated film deposition and desorption and therefore allows a systematic comparison of different films.

INTRODUCTION

Non-equilibrium growth of thin films is a complex process that is not well understood in detail despite its tremendous technological importance. Macroscopic properties of the final product depend on the microscopic structure of the film, which in turn is determined by the interplay of adsorption, desorption and surface diffusion probabilities, the flux and kinetic energy of impinging particles, and the interactions between individual film and substrate particles. The first three of these processes depend strongly on the substrate temperature and local surface morphology, the flux is determined by the chosen particle source, and the particle interactions vary according to their chemical composition.

Despite the multitude of both local and non local factors contributing to the growth process a very general phenomenological scaling approach for self-affine surfaces [1] has been very succesful in the description of continuum theories, discrete computer models, and experimental data on growing surfaces and interfaces (see [2] for a recent review). According to this dynamic scaling theory the interface width scales as

$$w(L,t) \sim L^{\alpha} f(t/L^{\alpha/\beta}), \text{ with } w^2(L,t) = \langle (h(r,t) - \langle h \rangle)^2 \rangle_L \qquad (1)$$

where L specifies an interval in the plane of the interface, and $h(r,t)$ parametrizes the interface as a function of in-plane distance r and time or film thickness t. The roughness exponent α describes scaling of the interface width over in-plane distances short compared to the system size, while for systems much larger than any in-plane correlations the global roughness σ scales with t according to the growth exponent β:

$$w(L) \sim L^{\alpha} \text{ (for } t >> L^{\alpha/\beta}), \text{ and } \sigma = w(\infty,t) \sim t^{\beta} \qquad (2)$$

In the experimental determination of these exponents, which represent different universality classes of growth, x-ray reflectivity (XR) is a powerful tool [3,4], since it measures spatial variations in the electron density from Ångstrom to micron lengths scales, while sampling macroscopic regions of the film. It can be applied *in situ* during film growth and concurrent with diffraction measurements, thereby correlating interface properties with information on crystal structure and even growth dynamics.

XR data allow the determination of interface roughness. In order to extract the growth exponent β, a sequence of films of different thicknesses has to be manufactured and examined. For metal or semiconductor films one must grow a number of films, using different substrates, or one can grow a single film in stages, interrupt growth in order to perform XR measurements, and then continue deposition onto the same film. An "ideal" experiment

Mat. Res. Soc. Symp. Proc. Vol. 407 © 1996 Materials Research Society

would allow repeated use of a single, unchanged substrate for *in situ* film deposition under a wide range of deposition parameters, thereby allowing a full exploration and eliminating variances not related to growth dynamics. In an attempt to come close to this situation we chose to investigate the growth of Xenon films on a SiO_2/Si substrate at low temperatures (15-35K). Xenon only interacts via van der Waals potentials, is easy to desorb from the substrate, and it might be easier than e.g. semiconductors to model in computer simulations for comparison.

SAMPLE CELL AND EXPERIMENTAL SETUP

We designed and built a sample cell (Fig. 1) with the above ideas in mind. Our substrate is suspended from a massive OFHC copper base, which is surrounded by a heater at its circumference and in good thermal contact with the cold finger of a closed-cycle displex helium refrigerator. The substrate (2x1.5 in) is backed by a heating foil and faces a sheet of grafoil of the same dimension 1.5 cm away. The grafoil sheet is mounted on a thermally insulating epoxy resin holder and also backed by a heater. A Beryllium cup seals the inner part of the sample cell, which is connected to a gas handling system/turbopump. For necessary thermal insulation the inner cell is surrounded by an aluminized mylar heat shield and an outer Beryllium cup. The volume enclosed between the two Be shells is evacuated through a diffusion pump. The temperature is measured at the copper base/cold finger junction. The cell cools down to 15-18 Kelvin. At these temperatures the walls of the cell cryopump the interior, resulting in a vacuum better than in typical UHV systems at room temperature.

After acid cleaning of the substrate [5] and outgassing of the grafoil sheet (under vacuum at 800°C) both were mounted in the sample cell, put under vacuum, and pumped on over night at ca. 50°C. The cell was then cooled down to 125K. At that temperature we filled the cell to saturation pressure for bulk Xe ($\approx$ 25Torr [6]), assuring complete coverage of the high surface area grafoil sheet with Xe. After closing off the cell we cooled to the lowest achievable temperature, while keeping the substrate at an elevated temperature and thereby minimizing condensation of Xe gas onto the substrate.

The protocol for the repeated deposition and desorption of films was the following: to desorb a film the cell was warmed as quickly as possible to about 60K with the help of both

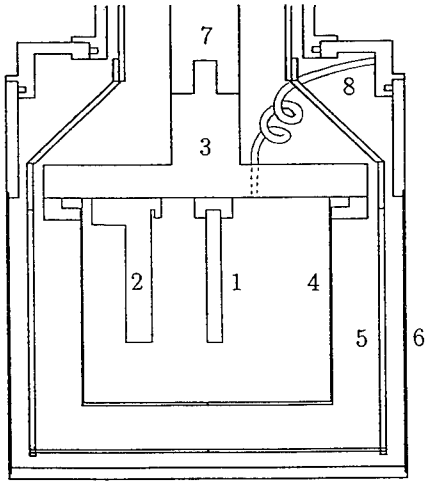


Fig. 1: *Cross section of our low temperature high vacuum sample cell for* in situ *XR measurements*

1 - Substrate
2 - Grafoil Holder
3 - Copper Base
4 - Inner Beryllium Can
5 - Heat Shield
6 - Outer Beryllium Can
7 - Cold Finger
8 - towards Turbopump/Gas Handling System

the copper heater and the substrate heater. At this temperature the XR signal of the uncovered substrate was visible. We then cooled the cell down again, leaving the substrate heater at an intermediate setting and monitoring the reflectivity at a fixed angle. This way almost all of the Xe would adsorb onto the large surface area offered by the grafoil sheet, which due to its insulation does not reach temperatures as high as the rest of the sample cell. Back at the lowest temperature with the substrate heater turned off we recovered a repeatable reflectivity curve corresponding to about 5Å of Xe on top of the substrate and no detectable Xe Bragg peaks. Films were deposited simply by turning on the grafoil heater. Unfortunately there is a significant time delay between turning on the heater and Xe adsorption on the substrate, since the grafoil has to reach a temperature close to 50K before significant Xe desorption sets in. This makes it difficult to exactly obtain a desired thickness. At a fixed angle one can watch oscillations in the XR with increasing film thickness to monitor the growth to some extent, not unlike RHEED oscillations, but with periods of about 100Å. The oscillations decay as the film roughens.

Our setup for XR is discussed in detail elsewhere [7]. Specular reflectivity is described by the momentum transfer between incoming and reflected beam $q_z = 2k\sin(2\theta/2)$, with $k = 2\pi/\lambda$ as the wavevector, $\lambda = 1.542$Å as the wavelength of the x-rays, and 2θ the scattering angle. We used a bent graphite monochromator and a scintillation detector for moderate resolution (MR) measurements on the substrate and Xe films up to 260Å thick. Our source is a rotating copper anode, which allows us to cover eight orders of magnitude in specular reflectivity and momentum transfer up to about 0.7Å^{-1} in this setup. For thicker films we used a Si(111) crystal as monochromator and a position sensitive detector (PSD) with a beam size of 0.1 mm in the scattering plane in a high resolution setup (HR). With the PSD we can record specular and off-specular reflectivity simultaneously without having to perform time consuming detector scans. Analysis of off-specular data will be presented elsewhere [8]. Due to the lower level of dark counts in the PSD we can still cover up to seven orders of magnitude in reflectivity despite the smaller x-ray flux (see Fig. 2). Fitting of our specular reflectivity data was done with a dynamically optimized simulated annealing technique [9]. The model parameters are roughness, thickness, and unit number density for each layer (see [5] for details). Interface roughness is modeled by an error function density grade, using the "q-q_t" approximation [10] to describe the reduction in specular intensity due to roughness. The calculated reflectivity takes finite resolution in q_z into account.

RESULTS

In order to obtain a clearly identifiable substrate signal we chose a Si crystal with a thick regrown SiO_2 layer on top, avoiding difficulties with the characterization of natural SiO_2 layers [5]. Fitting of MR data in the absence of Xe required the addition of a layer of unknown consistency (about 8Å thick and 3Å rough) on top of a 313Å thick and 6Å rough SiO_2 layer. We assume the top layer to be residual water and incorporate it into our model. The existence of this layer only became obvious due to the large range in q_z accessible in the MR setup. Repeated Xe ad- and desorption did not measurably affect the reflectivity of the bare substrate.

In the 15-18K temperature range specular reflectivity from a single Xe film remained virtually unchanged over the course of days, while increasing the temperature to 25 K lead to slow annealing of the films due to increased Xe mobility. Fig. 2 shows some specular reflectivity spectra and their fits. The characteristic oscillations from the regrown SiO_2 are visible in all data sets. For the thicker and rougher films the Xe oscillations die out at much lower q_z, leaving only the substrate signal. Fig. 3 is a log-log plot of roughness vs. two orders of magnitude in thickness of the Xe films. The shown points were obtained from films deposited with randomly varied fluxes, differing amounts of Xe present in the cell, and measured in MR and HR setups. The temporal sequence is indicated by the numbers. Nevertheless the points seem to fall into two distinct groups with power law fits

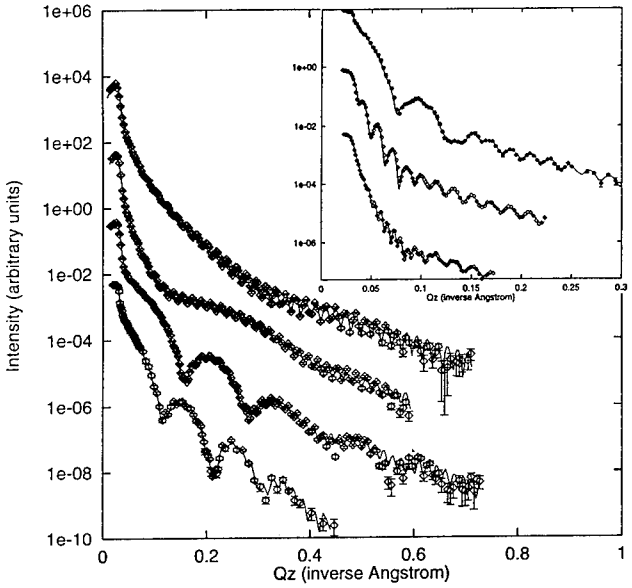


Fig. 2: *Specular reflectivity data and fits for (top to bottom) the substrate without Xe, with residual Xe, with 45Å (all in MR), and with 62Å (HR) of Xe. The inset shows the same data for films of 103, 363, and 830Å of Xe in HR. All films were deposited between 15 and 18K. The curves are shifted for clarity.*

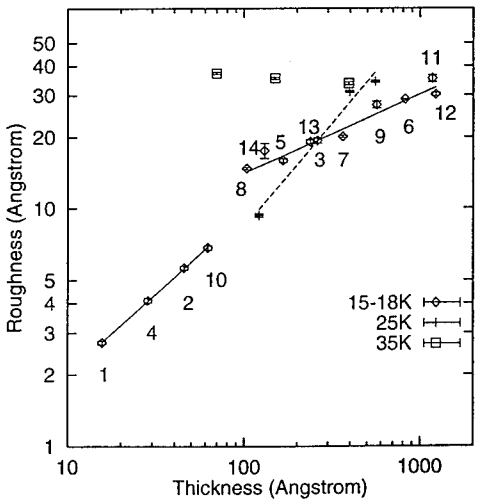


Fig. 3: *Roughness σ of Xenon films as function of thickness at three different deposition temperatures. Films deposited between 15 and 18K are numbered according to the temporal sequence in which they were made. The solid lines show separate fits to eqn. 2 for films less ($\beta = 0.66(1)$) and more ($\beta = 0.33(2)$) than 100Å thick. The dashed line is a fit to the 25K films ($\beta = 0.9(2)$).*

to $\beta = 0.33(2)$ for the thicker films and $\beta = 0.66(1)$ for the films below 100Å thickness, and with a steep increase in roughness between the groups. The fits also reveal an increase in Xe number density n with thickness, ranging from 1.0×10^{-2}Å^{-3} for a 16Å thick film to $1.7(2) \times 10^{-2}$Å^{-3} for films more than $\approx$ 60Å thick. (Bulk Xe at 58K has $n = 1.68 \times 10^{-2}$Å^{-3} and a lattice constant of 6.197Å [11]).

Xe(111) Bragg peaks are visible in all but the thinnest films in HR. Rocking curves

show the films to be polycrystalline with random crystal orientations. A weak variation in radial peak width shows crystal sizes to increase with film thickness. However for films more than 300Å thick the average crystal size remains fairly constant around 120Å. The lattice constant for Xe crystallites tends to be slightly smaller for films less than 300Å thick (6.08Å compared to 6.11Å), probably due to stress caused by interaction with the substrate.

We made some films at substrate temperatures of 25 and 30 K, cooling the cell down again immediately after the deposition. The thicker films are rougher and the thinner films are smoother than their counterparts deposited between 15 and 18K. Extracting β from only three points yields a value of 0.9(2). The distinction is also visible during deposition, as shown in Fig. 4. The reflectivity starts out in a similar fashion for both 17 and 25K, but at the second maximum ($\approx$ 160Å Xe) the 25K curve corresponds to a significantly smoother film than the 17K curve. Around the third maximum the curves cross ($\approx$ 260Å Xe) and the 17K layer becomes smoother than the 25K layer. in complete correspondence with the data shown in Fig. 3.

Depositions at 35K look strikingly different. The reflectivity falls off very quickly, corresponding to very large roughnesses for rather thin Xe layers, and then seems to oscillate without a strong increase in surface rouhgness. This behavior is mirrored as well in Fig. 3. The density of the 74Å thick and 37Å rough Xe layer is only 70% of bulk density, while the two thicker films are close to bulk density.

DISCUSSION

Fig. 3 and the real-time trends seen in Fig. 4 indicate several different deposition regimes. For the lowest temperature depositions, where we have concentrated our efforts, two different behaviors are observed as the film thickens. At low coverage the average Xe density is lower than bulk and approaches bulk as thickness increases. We suspect that near 100Å islands coalesce into a continuous film and that the growth in roughness thereafter is due to a different process. The fact that islands are able to form at such low temperatures may be due to mobility associated with the release of the roughly 10^3K of binding energy per adsor-

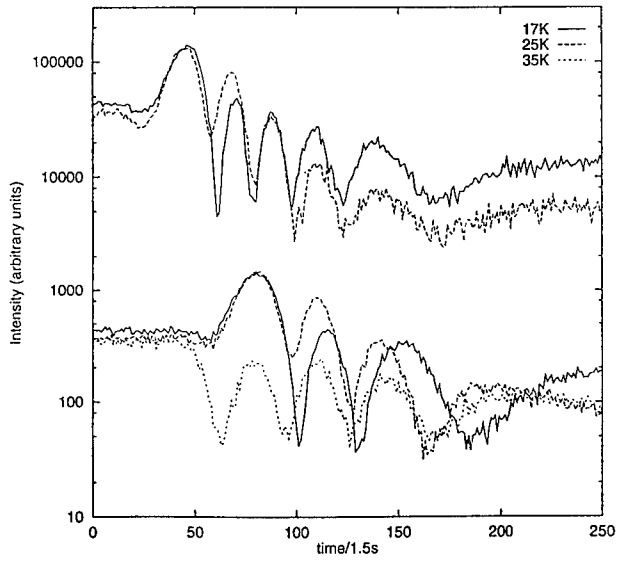


Fig. 4: *Reflected specular intensity at a fixed angle (2θ = 1.0°) during film deposition at different substrate temperatures. Two different sets of depositions resulting in similar film thicknesses are shown (top: ~ 550Å, bottom: ~ 390Å) and shifted for clarity.*

bing Xe atom; we expect finite mobility of incoming atoms even in the zero temperature limit. At slightly elevated temperatures (25K), roughness is intially reduced but then overtakes that of the low temperature films. Since at 25K we see slow annealing dynamics changing average crystallite size, surface roughness, and Xe density - all of which is not visible at 18K - it is clear that surface and maybe even bulk diffusion takes place here. Thus, initial islands may be smoother, larger, and farther apart and coalescence occurs at an increased average film thickness. At 35K our sparse data may indicate a small number of large crystallites yielding large roughnesses even for 100Å films.

The present work demonstrates the feasibility of using inert atoms and molecules as model materials in the study of deposition kinetics. With an appropriate sample cell *in situ* deposition of many films onto a repeatably prepared substrate is straightforward. Non-equilibrium, rough, but stable films of even a heavy noble gas can be generated at sufficiently low temperature. These films should mimic the behavior of more conventional non-equilibrium depositions such as metals deposited at room temperature. The ease of doing repeated measurements on a single substrate allows measurement of many samples produced under a variety of conditions, such as varied substrate temperature and deposition rate. The preliminary analysis of our data reported here illustrates that there exists a rich variety of regimes in this system (see below). This variety is probably reflected in other systems and may be responsible for the wide variation in reported exponents [2]. Continuum theories and discrete computer models that show dynamic scaling generally do not take into account the effects of crystallization, which can influence surface roughness.

We have combined XR and diffraction in order to correlate trends in the "continuum limit" parameters surface morphology, density, and thickness, with variations in atomic ordering parameters such as lattice constants and crystallite sizes and orientations. We are also able to verify that our fitting of extensive XR data after film growth is completed is consistent with the behavior of the film during deposition. Analysis of the real time deposition curves in Fig. 4 potentially could supply detailed information on the kinetic roughening process, but is complicated by the varying film density during growth and by changes in the deposition rate due to the varying grafoil temperature.

Many further developments are possible. First, we will analyse the diffuse scattering from the films reported here. This may yield information on islanding and coalescence through the in-plane length scales which dominate the roughness. Further data collection using a synchrotron source, an improved substrate, additional temperature sensing inside the sample cell, and possibly a deposition source with faster response time should yield copius information about all the deposition regimes merely hinted at in this work. Finally, we look forward to making similar measurements on more complex molecular systems.

REFERENCES

1. F. Family and T. Vicsek, J. Phys. A **18**, L75 (1985).
2. A.-L. Barabási and H.E. Stanley, Fractal Concepts in Surface Growth (Cambridge University Press, Cambridge, 1995).
3. C. Thompson, G. Palasantzas, Y.P. Feng, S.K. Sinha, and J. Krim, Phys. Rev. B **49**, 4902 (1994).
4. H. You, R.P. Chiarello, H.K. Kim, and K.G. Vandervoort, Phys. Rev. Lett. **70**, 2900 (1993).
5. W.R. Birch, M.A. Knewtson, S. Garoff, R.M. Suter, and S. Satija, Coll. and Surf. **89**, 145 (1994); Langmuir **11**, 48 (1995).
6. J.A. Venables and P.S. Schabes-Retchikman, J. Physique **38**, C4 105 (1977).
7. J.D. Shindler and R.M. Suter, Rev. Sci. Instrum. **63**, 5343 (1992).
8. R.K. Heilmann and R.M. Suter, work in progress.
9. D. Bouzida, S. Kumar, and R.H. Swendsen, Phys. Rev. A **45**, 8894 (1992) .
10. L. Nevot and P. Croce, Rev. Phys. Appl. **15**, 761 (1980).
11. G.H. Cheesman and C.M. Soane, Proc. Phys. Soc. **70 B**, 700 (1957).

SIMULATION OF DYNAMICS OF SOLID-LIQUID TRANSITION

Y. KOGURE, H. MASUYAMA, and M. DOYAMA
The Nishi-Tokyo University, Uenohara, Yamanashi 409-01, Japan

ABSTRACT

Molecular dynamics simulations on the solid-liquid transition of copper crystals have been performed. The configulation and the motion of atoms are monitored by RDF. It is seen that the height of the first peak in the RDF, which located at the nearest neighbour distance, decreased drastically as the temperature is increased.

INTRODUCTION

The melting of crystals is one of the most fundamental phenomena in the materals. A number of experimental and theoretical studies have been reported on the subject, but the microscopic mechanisms of the melting is not known. The method of computer simulation has widely been applied to the problem [1,2]. A mlecular dynamics simulation of the melting of fcc metals has been done by using a new EAM potential developed by the present authors[3]. The results for copper is presented in this paper.

METHOD OF SIMULATION

The model crystal used in the simulation is shown in Fig. 1, which has a cubic shape with edges along [100] axes. The numbers of atoms involved in the crystals are 1099 or 2457. The configulation of atoms, which is initially located in a middle plane (shaded in the figure) are monitored.

The embedded atom method potential developed by the present authors was used to express the interaction between copper atoms. The total energy is expressed as

$$E_{\rm tot} = \sum_i F(\rho) + \frac{1}{2}\sum_{ij}\phi(r_{ij}), \tag{1}$$

$$F(\rho) = D\rho\ln\rho, \quad \rho = \sum_{j\neq i} f(r_{ij}), \tag{2}$$

where, $F(\rho)$ is the embedding energy for i-th atom, ρ is the electron density function, ϕ is the pairwise interaction energy and r_{ij} is the distance between i-th and j-th atoms. For the functional forms of ϕ and f, we assume

$$\phi(r) = A(r_{\rm C} - r)\exp(-C_1 r), \tag{3}$$

$$\phi(r) = B(r_{\rm C} - r)\exp(-C_2 r). \tag{4}$$

Mat. Res. Soc. Symp. Proc. Vol. 407 © 1996 Materials Research Society

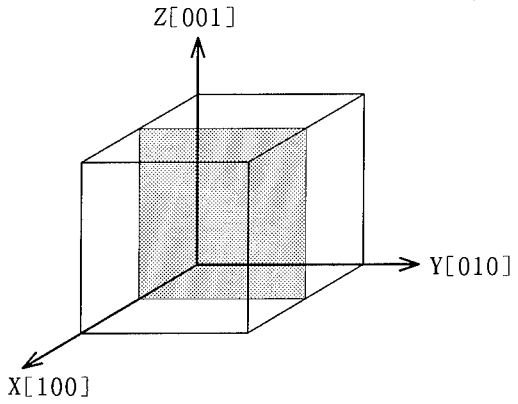


Fig. 1. Model crystal

Here r_C is the cut off length of the interaction, and r and r_C are nomalized by the nearest neighbor distance.

As a initial condition, atoms are placed in the perfect crystal positions of fcc structure and the initial velocity, v_i is given to each i-th atom. The magnitudes and the directions of v_i's are chosen by random numbers and their mean value v_m is related by the reference temperarure T^*.

$$mv_m^2 = 3k_B T^*, \tag{5}$$

where m is the atomic mass, and k_B is the Boltzmann's constant.

Under these initial conditions, molecular dynamics was started. The time interval Δt of the difference equation was set to be 5×10^{-15} sec. The atomic configulation and the radial distribution function (RDF) were calculated every hundred time steps.

RESULTS AND DISCUSSION

The result for the change of atom configuration in the crystal with 1099 atoms at the temperature $T^* = 1300$K is shown in Fig. 2, where S is the number of time steps. The displacement in $Y - Z$ plane and $X - Z$ plane are separately shown at each time steps. It is seen that the atoms are moving violently in the crystal and many holes appear with the time step. The radial distribution functions (RDF) correspondig to each time step of Fig. 2 are shown in Fig. 3. The pulse-like distribution for the crystal ($S = 0$) is quickly

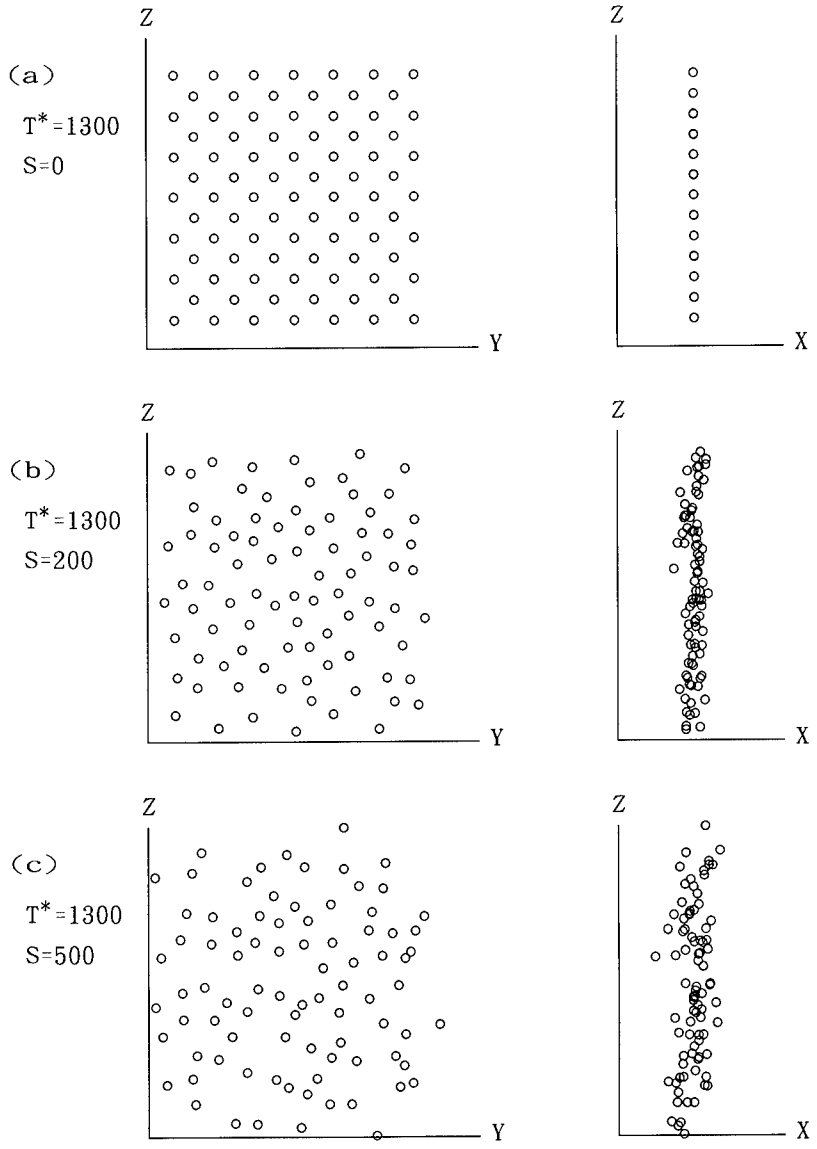


Fig. 2. Change of atomic configuration at T=1300 [K].

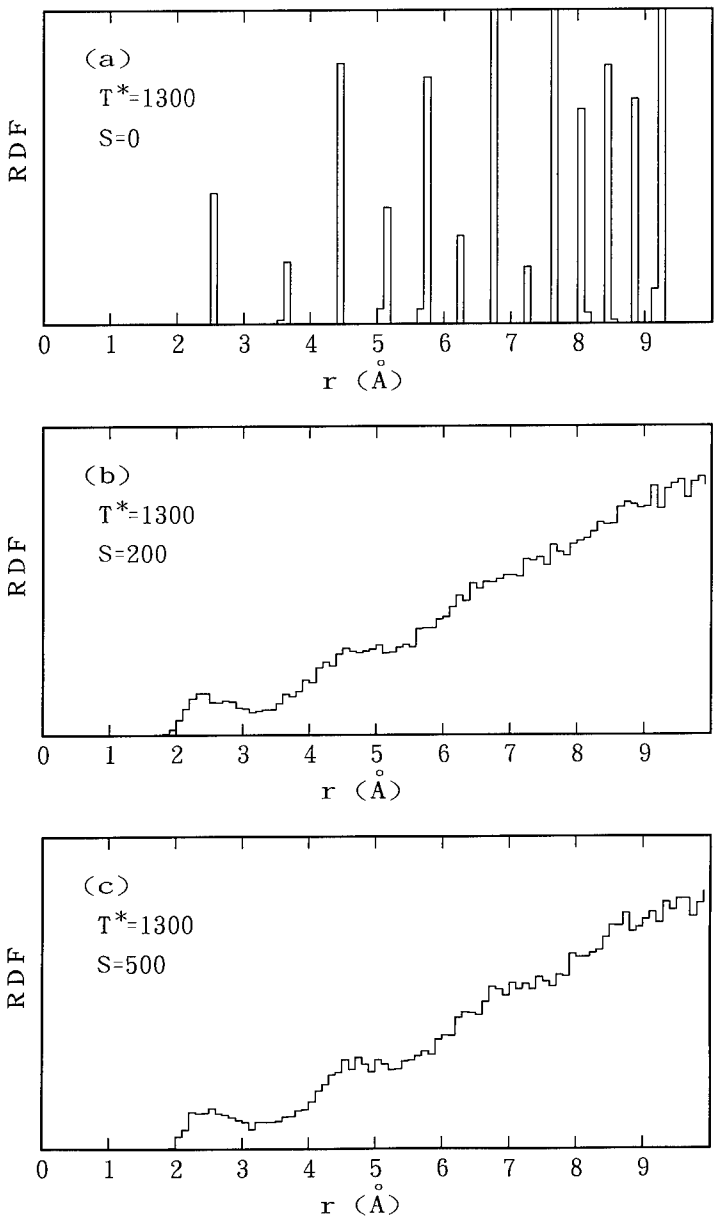


Fig. 3. Change of RDF at T=1300 [K].

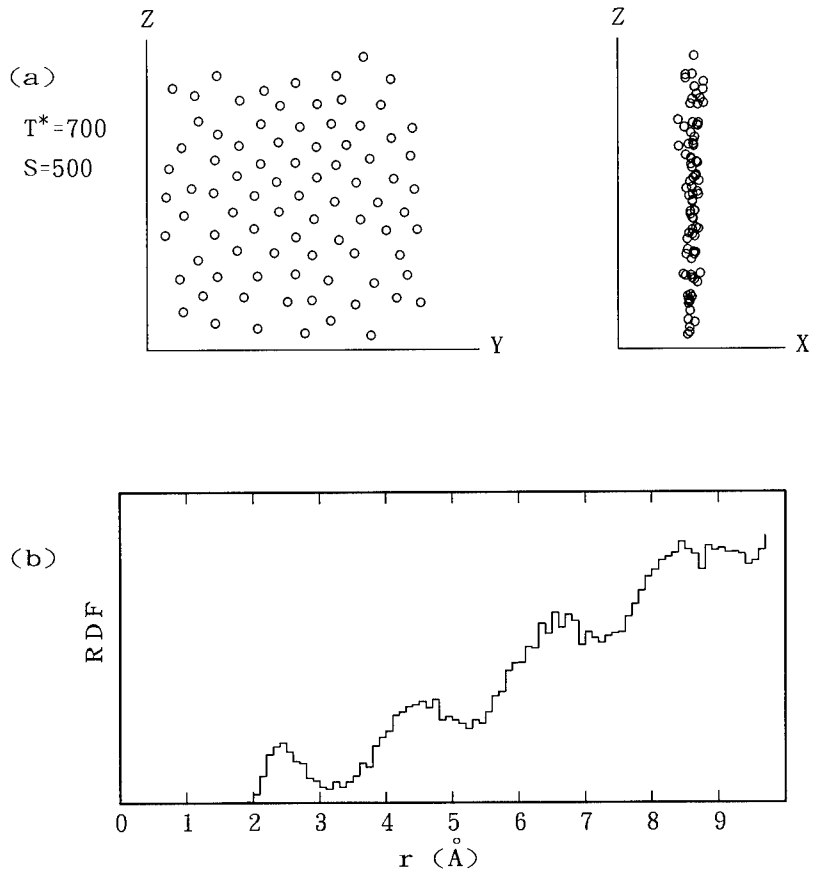


FIG. 4. Atomic configuration and RDF at T=700 [K].

smeared out at early stages of the simulation, and broad peaks are observed at the first and third neighbor distances.

The atom configulations and the RDF for different temperatures T^* are shown in Fig. 4 respectively. At the lower temperatur (T^* = 700K), atoms near the crystal surface are moving, but the fcc structure is seen inside. The RDF peaks are narrower than the T^* = 1300K. It may be suggesting that the melting initially happens at the surface.

Similar calculations were made at various temperatures. The RDF values at the first ($r = r_0$), the second ($r = \sqrt{2}r_0$) and the third ($r = \sqrt{3}r_0$) neibor distance in the crystal

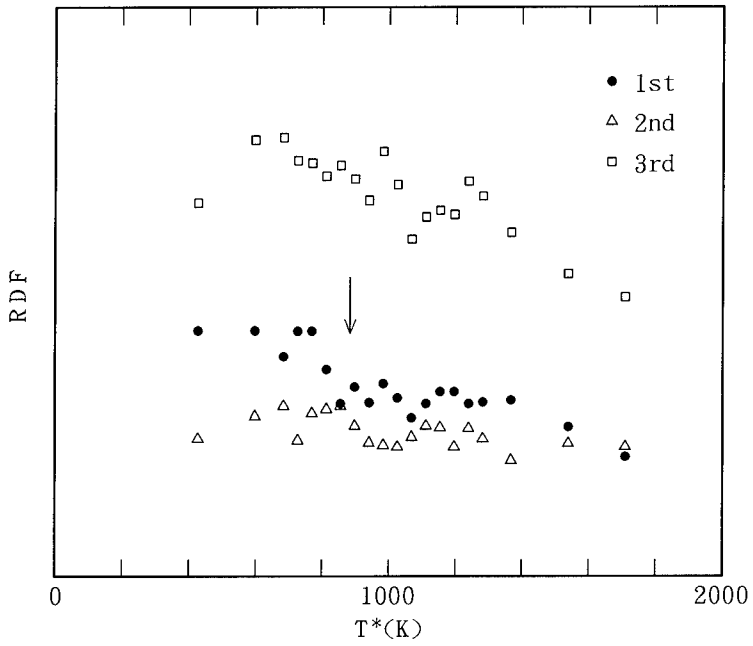


Fig. 5. Temperature dependence of RDF

are shown as a function of the temperature in fig 5. The peak height at the first neighbur distance shows clear drop at $T^* \sim 800$K, which may crrespond to the melting. More detailed investigation is in progress.

REFERENCES

1. B. J. Alder and T. E. Weinwrite, Phys. Rev **127**,359 (1962)

2. J. M. Ziman in Models of Disorder, (Syndics of Cambridge Univ. Press, 1979) §6.7.

3. Y. Kogure, M. Miyazaki, T. Uzaki and M. Doyama, presented to this conference.

Part V

Disordered Materials and Surfaces

LOCALIZATION OF ELECTRONS AND ACOUSTICAL PHONONS IN IRREGULAR OR FRACTAL CRYSTALLITES

B. Sapoval and S. Russ
Laboratoire de Physique de la Matière Condensée, C.N.R.S. Ecole Polytechnique*
91128, Palaiseau Cédex, France

ABSTRACT

The behavior of electron and phonon excitations in systems with irregular boundaries is discussed on the specific example of prefractal shapes. We show that both electron states and acoustical phonons exhibit localization properties. This effect is stronger when the fractality of the shape is increased. In consequence the electron-phonon interaction in small crystallites should be strongly dependent on their shape or roughness. This localization could play a role in the thermal properties of glasses where internal partial crytallization has no reason to build pseudo-crytalline entities which should be smooth.

INTRODUCTION

It is known that disorder can cause localization [1]. Usually disorder really means internal disorder, like impurity disorder, structural or compositional disorder. "Shape" disorder on the other hand, has not yet been considered. It is accepted that many between the essential properties of solids do not depend on their shape. This belief is justified by the fact that the density of states, for electrons or for phonons, is considered to be proportional to the volume of the solid, independently of its shape. This fact corresponds to the exact mathematical result that, in the so-called asymptotic limit, the density of states contains a dominant term proportional to the volume of the solid. Although it is known that there exist correction terms which are shape dependent, their contribution is negligible in the asymptotic limit where wavelengths are much smaller than the size of the solid [2].

If, however, one considers the physics of small clusters, dots or wires with a typical size in the order of a few nanometers, the effects of size and shape are not small. Consequently, the physical properties of these systems will depend on their shape. If one considers electron states, this is important for energies near the band edges in semi-conductor wires and dots. For the same type of crystallites, the shape will influence thermal phonon properties at relatively low temperature where the wavelength is of the order of nanometers.

In this paper we show that geometrical irregularity causes effective localization both for electrons and phonons. We use fractal geometry as a general framework for the description of irregularity. We can then apply previous work and concepts used in our studies of the vibrations of fractal drums. However, the results that will be presented here are more related to the geometrical irregularity than to scaling properties of the structure.

We consider here the two geometries which are shown in Fig. 1. It is these prefractal shapes that we use to model a concrete case of irregularity. They could represent a 2d crystallite. If we are interested in electron states we have to solve a Schrœdinger eigenvalue equation on this domains:

$$(-\hbar^2/2m)\,\Delta\Psi_N = E_N\,\Psi_N \qquad (1)$$

with the Dirichlet boundary condition $\Psi_N = 0$ on the perimeter of the system. The problem is really the problem of quantum states in irregular quantum wells. The computation of these states was made numerically in references [3-4] where the eigenmodes were called Dirichlet fractinos. These results have been tentatively used to explain the electro-optical properties of porous silicon in reference [5].

If we consider acoustical vibrations, we are lead to the same eigenvalue problem

$$\Delta\,\Psi_N = -\,(\omega_N^2/c^2)\Psi_N \qquad (2)$$

but now the Neumann condition $\partial\Psi_N/\partial n = 0$ applies along the normal to the boundary. Here c

Mat. Res. Soc. Symp. Proc. Vol. 407 © 1996 Materials Research Society

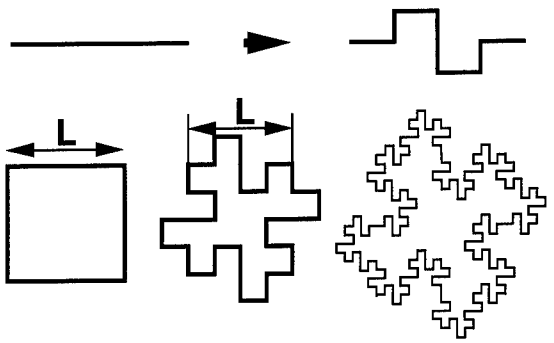


Fig. 1: The prefractal shapes under study at stage $\nu = 1$ and 2 of iteration. The square inititator has a side L.

represents the sound velocity of the transverse acoustical modes in a 2d crystal of large volume. These eigenstates have been computed and are presented in reference [6]. They are named Neumann fractinos. We do not recall here the computational method which has been used to compute Dirichlet and Neumann fractinos as it is described extensively in [3-4] and [6]. Note that discretization of (2) is not a problem concerning phonons as they represent the motion of discrete masses.

The density of states of both Dirichlet and Neumann fractinos are strongly perturbed by the irregularity but we do not discuss this aspect here and concentrate on the description of localization and its general dependence on the geometry of the system. For this we compute the size of the region where the vibrational amplitude is large.

To characterize mathematically the localization or the confinement of each state we compute, following Thouless [7], the "existence volume" S_N of a given state Ψ_N. This volume is a sum over the square lattice sites i:

$$S_N = [\Sigma_i a^2 |\Psi_{N,i}|^4]^{-1} \quad (3)$$

where a is the distance between the lattice sites. The state Ψ_N has been normalized by:

$$\Sigma_i a^2 |\Psi_{N,i}|^2 = 1. \quad (4)$$

For a normalized constant function the localization volume is equal to the surface S of the system.

LOCALIZATION OF ELECTRONS IN DIRICHLET FRACTINOS

Due to the discretization in the numerical procedure there exists a small systematic error in the numerical value that we find for the eigenvalues. This should have very little effect on the spatial distribution of the amplitudes that we discuss here. For sine functions which are the eigenstates of the square crystallite the existence volume is a constant equal to (4/9)S independently of the frequency or energy of the mode. If we find that S_N is significantly smaller than this value, we will say that the corresponding state of index N is "localized".

The values of the relative occupation volume S_N/S of the first 300 lower Dirichlet fractinos for $\nu = 1$ and $\nu = 2$ are presented in Fig. 2. They show first that the existence volume is only a fraction of the total surface of the resonator. Second, the tendency to localization is increased by the fractality of the frontier. For the second generation the smallest value of the existence volume that we found was equal to 0.043 for state index N =235/238 (a degenerated state). The averages over these 300 lower states are $\langle S_N/S \rangle = 0.33$ for generation 1 and $\langle S_N/S \rangle = 0.23$ for generation 2.

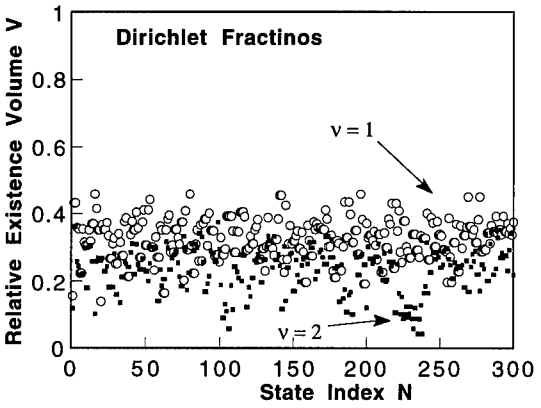


Fig. 2: Relative localization volume for Dirichlet fractinos or electron states in irregular quantum wells with the shapes of Fig. 1. For a square crystallite the value is equal to 4/9=0.444 independently of the energy.

The particular geometries that we have studied have a C_4 rotational symmetry. Eigenmodes are then basis functions of this symmetry group and therefore occupy the four quadrants of the geometry shown in Fig. 1 with the same density. In a non-symmetric geometry, this would not be true and the existence volume will be smaller by a factor between 2 and 4.

Note that the second generation has a smaller cut-off length equal to L/16 in our specific example. This smaller cut-off is then of the order of a few atomic distances for a system of a few nanometers in diameter. If one considers electrons in metal clusters, the localization effects should not be important because the Fermi wavelength is of the order of the interatomic distance. In such a case the asymptotic limit is a good approximation. On the contrary electrons and holes in semiconductors will be localized in such structures if L is of the order of a few nanometers.

The reason for the localization of these modes is the very efficient screening properties of the geometrical irregularities that were discussed extensively in [3]. It is interesting to note that increased fractality causes an increase in localization effectiveness.

LOCALIZATION OF ACOUSTICAL PHONONS IN NEUMANN FRACTINOS

The values of the relative occupation volume S_N/S of the first 200 lower Neumann states for $\nu = 1$ and $\nu = 2$ are presented in Fig. 3. Again, apart from the very first lower states, the existence volume is only a fraction of the total surface of the resonator. Here also, the tendency to localization is increased by the fractality of the frontier. For the second generation the smallest value of the relative existence volume that we found was equal to 0.031 for state index N = 62 and 63. We give a graphical representation of this mode in Fig.4. For Neumann fractinos the average over two hundred lower states is $\langle S_N/S \rangle = 0.35$ for generation 1 and $\langle S_N/S \rangle = 0.24$ for generation 2. The above remark about the influence of the symmetry is applicable to Neumann states and in nonsymmetric systems the localization effects should be stronger.

The reason for localization in this case is very different. Whereas Dirichlet fractinos decay very rapidly towards the boundary [4] and are thus located in at least some small distance from the perimeter, Neumann fractinos have the opposite tendency. As a most remarkable fact we have found that many of the localized modes have their maxima at or close to the fractal boundary. The boundary region is free to vibrate. In a region close to the boundary the spatial variation of the amplitude is constrained by the fact that the Neumann boundary condition $\partial\Psi/\partial n$ is imposed in several directions of space. In the only direction where the gradient can be large the amplitude must vary significantly over a fraction of the wavelength to satisfy the Helmholtz equation. Far from the boundary destructive interferences will make the amplitude small.

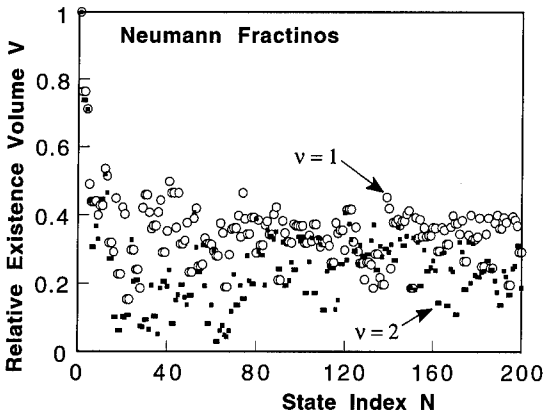


Fig. 3: Relative localization volume for Neumann fractinos or acoustical phonons in irregular crystallites having the shapes of Fig. 1. The trivial constant state has a relative localization volume equal to one and the cosine eigenstates of the square have $S_N/S = 4/9$.

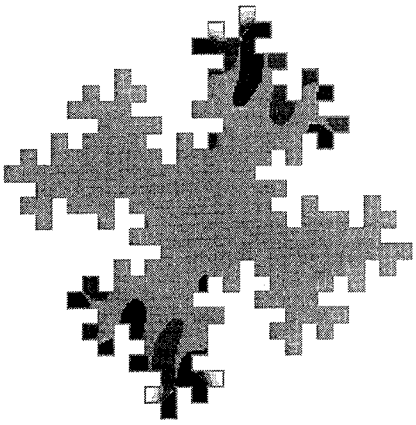


Fig. 4: Specific example of a localised (degenerated) eigenmode under Neumann boundary conditions. In this picture the amplitudes are indicated by different grey levels. The black regions stand for positive and the white regions for negative amplitudes, the neutral grey tone for nearly zero amplitude.

CONCLUSIONS AND OUTLOOK

We have shown that geometrical irregularity of the boundaries of 2d crystallites in otherwise uniform or periodic structures creates localization. There is no reason why this fact should not exist in three dimensional systems. The geometrical decoupling between the Neumann and Dirichlet fractinos corresponds to a lowering of the electron-phonon interaction effectiveness in irregular structures. In a very qualitative manner, one could say that in irregular semiconductor

crystallites electrons in the fundamental states and acoustical phonons do not occupy the same regions.

The fact that both Dirichlet and Neumann fractinos have a strong tendency to localization may have special implications in the case of glasses. Let us consider glasses as made of intermixed regions of soft and hard material with a typical range of the order of a few nanometers and irregularity in the range of 1 nanometer. Then the vibrational acoustical states should be localized in both hard and soft regions. This is true of the "hard" regions which will see a soft environment and will vibrate freely like Neumann excitations. In the same time, the "soft" regions would have their boundaries blocked by the harder regions and their vibrations should then behave as Dirichlet excitations which should also be localized if the boundaries are irregular.

Although we have not computed acoustical 3d modes with their different polarizations we see no reason why the same localization properties should not hold for these cases if geometrical irregularity is present.

ACKNOWLEDGEMENTS

One of us (S.R.) has benefited from the E.E.C program "Human Capital and Mobility". The computation was performed at the "Institut du développement et des ressources en informatique scientifique" (IDRIS) in Orsay.

*Unité associée du C.N.R.S. n° 1254

REFERENCES:

1. R. Zallen, The physics of amorphous solids, (John Wiley & Sons, New York, 1983).

2. H.P. Baltes and E. R. Hilf, Spectra of finite systems, (BI Wissenschaftsverlag, Vienne, 1976).

3. B. Sapoval, Th. Gobron and A. Margolina, Phys. Rev. Lett. **67**, 2974 (1991).

4. B. Sapoval and Th. Gobron, Phys. Rev. E **47**, 3013 (1993).

5. B. Sapoval and S. Russ, in Mater. Res. Soc. Symp. Proc. **358**, Pittsburgh, PA, 1995, p.37-42; B. Sapoval, S. Russ and J.-N. Chazalviel, submitted to Phys. Rev. B.

6. S. Russ and B. Sapoval, submitted to Phys. Rev. E.

7. D.J. Thouless, Phys. Rep. **13**, 93 (1974).

FRACTAL AND NON-FRACTAL SURFACES IN ION SPUTTERING

A.-L. BARABÁSI[†] AND R. CUERNO[‡]
[†] Department of Physics, University of Notre Dame, Notre Dame, IN 46656
[‡] Center for Polymer Studies and Dept. of Physics, Boston University, Boston, MA 02215

ABSTRACT

Recently a number of experimental studies focusing on the scaling properties of surfaces eroded by ion bombardment provided apparently contradictory results. A number of experiments report the observation of self-affine fractal surfaces, while others provide evidence about the development of a non-fractal periodic ripple structure. To explain these discrepancies, here we derive a stochastic nonlinear equation that describes the evolution and scaling properties of surfaces eroded by ion bombardment. The coefficients appearing in the equation can be calculated explicitly in terms of the physical parameters characterizing the sputtering process. We find that transitions may take place between various scaling behaviors when experimental parameters, such as the angle of incidence of the incoming ions or their average penetration depth, are varied.

Introduction

With the decreasing size of microelectronic devices, long ignored questions regarding the morphology of surfaces resulting from various growth methods and processing techniques have become the center of the attention in the research community. While for a long time attempts have been made to characterize the morphology of various surfaces, only lately, with the introduction and wide availability of high resolution observational techniques, such as STM or AFM, it has become possible to obtain quantitative results regarding the surface morphology and surface roughness. The most striking result is that for most growth processes roughness is not an exception but rather a rule, most surfaces being microscopically rough [1]. Depending on the temperature, flux, and the nature of the deposited material and substrate, the roughness of the surface can vary from a few monolayers to hundreds of monolayers. Naturally, for many applications one would need surfaces that are smooth down to the atomic level, for rough surfaces have rather poor contact properties, and roughness affects both the electronic and the magnetic properties of the system.

In the last decade we have witnessed the development of an array of theoretical tools, ideas and techniques intended to describe and characterize the growth and roughening of nonequilibrium surfaces [1, 2, 3, 4, 5]. Initiated by advances in understanding the statistical mechanics of various nonequilibrium systems, it has been observed that for most surfaces in nature the roughness follows simple scaling laws. These surfaces are self-affine fractals, being uniquely characterized by the roughness or self-affine exponent. One of the main advantage of this description is that various growth processes can be classified into universality classes that share the same scaling exponents. On the practical side this means that the scaling exponents characterizing roughness do not vary continuously, but are defined by the universality class to which they belong.

One particularly important thin film processing technique is ion beam sputtering [6, 7, 8]. Sputtering is the removal of material from the surface of solids through the impact of energetic particles. It is a very widespread technique, used in a large number of applications, with a remarkable level of sophistication. It is a basic tool in surface analysis, depth profiling, sputter cleaning, micromachining, and sputter deposition. Perhaps the largest community of users of sputtering are in the thin film and semiconductor fabrication areas. Here sputtering is used routinely for the deposition of films and the etching of patterns

Mat. Res. Soc. Symp. Proc. Vol. 407 © 1996 Materials Research Society

and features important to the production of integrated circuit devices as well as device packaging.

Dealing with such a widely used technique, one needs to ask what is the morphology of the film sputtered by energetic particles. In many cases sputtering is routinely used to smooth a surface. On the other hand, other investigations indicate that sputtering may also roughen the surface. To have a better control over this important experimental tool, we need to obtain quantitative answers on the effect of the sputtering process on the surface morphology.

Motivated by the advances in understanding growth, and by the need of having a detailed knowledge on the morphology of the sputter eroded surfaces, recently a number of experimental studies have investigated the morphological properties of surfaces eroded by ion bombardment. Briefly, the experimental results can be classified in two main classes. There exists ample evidence about the development of a periodic ripple structure in sputter etched surfaces [9, 10, 11, 12, 13, 14]. However, a number of recent investigations have provided rather detailed and convincing experimental evidence, that under certain experimental conditions ion eroded surfaces are rough and self-affine, and the roughness follows the predictions of various scaling theories [15, 16, 17, 18]. Moreover, these investigations did not find evidence of ripple formation on the surface!

The discrepancy between the results of the mentioned investigations motivated us to have a second look at the mechanisms shaping the morphology of ion eroded surfaces [19]. In this paper we investigate the large scale properties of ion-sputtered surfaces aiming to understand in an unified framework the various dynamic and scaling behaviors of the experimentally observed surfaces. For this we derive a stochastic nonlinear equation that describes the time evolution of the surface height. The coefficients appearing in the equation are functions of the physical parameters characterizing the sputtering process. We find that transitions may take place between various surface morphologies as the experimental parameters (e.g. angle of incidence, penetration depth) are varied. Namely, at short length-scales the equation describes the development of a periodic ripple structure, while at larger length-scales the surface morphology may be either logarithmically ($\alpha = 0$) or algebraically ($\alpha > 0$) rough. Usually stochastic equations describing growth models are constructed using symmetry principles and conservation laws. In contrast, here we show that for sputter eroded surfaces the growth equation can be derived directly from a simple model of the elementary processes taking place in the system.

Scaling theory

Recently there has been much interest in understanding the formation and roughening of nonequilibrium interfaces [1, 2, 3, 4, 5]. A common feature of most rough interfaces observed experimentally or in discrete models is that their roughening follows simple scaling laws. The associated scaling exponents can be obtained using numerical simulations or stochastic evolution equations. The morphology and dynamics of a rough surface can be characterized with the *interface width*, defined by the rms fluctuation in the height $h(x, y)$,

$$w(L) \equiv \sqrt{\frac{1}{L^2} \langle \sum_{x,y=1,L} [h(x,y) - \bar{h}]^2 \rangle}, \tag{1}$$

where L is the linear size of the sample, the brackets $< ... >$ denote ensemble average, and the *mean height* of the surface, $\bar{h}$, is defined by

$$\bar{h} \equiv \frac{1}{L^2} \sum_{x,y=1,L} h(x,y). \tag{2}$$

Instead of measuring the roughness of a surface over the whole sample size $L \times L$, we can choose a window of size $\ell \times \ell$, and measure $w(l)$. As we mentioned above, a general property of many rough surfaces is that the roughness depends on the length scale of observation. This can be quantified by plotting $w(\ell)$ as a function of ℓ. There are two characteristic regimes one can distinguish.

(i) For length scales smaller than $\ell_\times$, the local width increases as

$$w(\ell) = A\ell^\alpha, \tag{3}$$

where α is the *roughness exponent* and A is a proportionality constant. If we are interested in surface phenomena that take place at length scales shorter than $\ell_\times$, then we cannot neglect the roughness of the surface. In this regime the roughness is not simply a number, but it depends on the length scale available to the method probing the surface.

(ii) For $\ell >> \ell_\times$, $w(\ell)$ is independent of ℓ. For most processes that take place at length scales larger than $\ell_\times$, the surface is *smooth*, i.e. we can neglect the roughness. In this regime we can characterize the surface roughness with a single number, namely the saturation value $w_{sat}(\ell)$.

In general reporting a *number* for characterizing the surface roughness, as it is frequently done, is a misleading and unsatisfactory procedure. The concept of roughness, for many applications, has to be replaced with the length scale dependent roughness, requiring the determination of the full $w(\ell)$ curve.

Regarding the dynamics of the roughening process, at early times the total width increases as $w(L,t) \sim t^\beta$, where β is the *growth exponent.* Similarly, we can define the *dynamic exponent*, z, using $\ell_\times \sim t^{1/z}$. The dynamic exponent is related to α and β by the relation $z = \alpha/\beta$ [20].

Next we need to understand what determines the $w(\ell)$ curve. Can we develop models and theories that can provide/predict A, α, β, $\ell_\times$ and w_{sat}?

Studying scaling relations, such as (3), allows us to define *universality classes.* The universality class concept is a product of modern statistical mechanics, and codifies the fact that there are but a few essential factors that determine the exponents characterizing the scaling behavior. Thus different systems, which at first sight may appear to have no connection between them, behave in a remarkably similar fashion. For example, the values of the exponents α and β are independent of many "details" of the system, such as the details of the crystal lattice or the implementation of the model, as long as the mechanism generating the roughening does not change. In contrast, other quantities, such as A, $\ell_\times$, or w_{sat}, are non-universal, i.e. they depend on almost every detail of the system.

For understanding the roughening process, we need to develop methods to predict the value of the scaling exponents α and β. A breakthrough in this direction was the introduction of the Kardar-Parisi-Zhang (KPZ) equation [21]

$$\frac{\partial h}{\partial t} = \nu\nabla^2 h + \lambda(\nabla h)^2 + \eta(x,y,t) \qquad [KPZ]. \tag{4}$$

The first term on the rhs describes the relaxation of the interface due to the surface tension ν and the second is a generic nonlinear term incorporating lateral growth. The noise, $\eta(x,y,t)$, reflects the random fluctuations in the growth process and is an uncorrelated random number that has zero configurational average. For one dimensional interfaces the scaling exponents of the KPZ equation are known exactly, as $\alpha = 1/2$, $\beta = 1/3$, and $z = 3/2$. However, for higher dimensions they are known only from numerical simulations. For the physically most relevant two dimensional interface we have $\alpha \simeq 0.38$ and $\beta \simeq 0.18$ [22, 23, 24, 25, 26].

If $\lambda = 0$ in (4), the remaining equation describes the equilibrium fluctuations of an interface. This equation, introduced and studied in the context of interface roughening by

Edwards and Wilkinson (EW) [27], can be solved exactly due to its linear character, giving the scaling exponents $\alpha = (2-d)/2$ and $\beta = (2-d)/4$. For two dimensional interfaces we have $\alpha = \beta = 0$, leading to a logarithmic roughening of the interface.

Experimental results

The morphology of surfaces bombarded by energetic ions has long fascinated the experimental community. Lately, with the development of high resolution observation techniques, this question is living a new life. The various experimental investigations can be classified in two main classes. First, early investigations found that ion bombarded surfaces develop a ripple morphology with a rather characteristic wavelength of order of a few micrometers. These observations were supported by recent detailed studies on the ripple morphologies observed in various materials and bombarding ions [9, 10, 11, 12, 13, 14].

However, a number of research groups have found no evidence of these ripples, but rather observed the development of a random rough surface, that they characterized using the scaling theories discussed in the previous section [15, 16, 17, 18]. In the following we review in some detail these experimental observations.

We shall focus here on these two dominant morphologies (ripple formation and kinetic roughening), since these are observed in the sputtering of impurity free, amorphous materials. Impurities that bind strongly to the surface (and thus it is difficult to sputter them) may induce other dominant morphological features, such as cones or abrupt walls [9]. These will not be considered in this paper. Also, we limit ourselves to sputtering by ion bombardment, in which the ions have parallel trajectories and the same velocity. Thus we will not consider plasma etching (where the ions have a broad energy distribution and random angles of incidence) or chemical sputtering, where the yield is influenced by the chemical reactions taking place on the surface.

Ripple formation

Ripple formation on ion-sputtered surfaces have been observed by many groups in various systems and ion beams (for a review see [9]). Here we discuss a few recent investigations that characterized in great detail the observed ripple morphologies.

Evidence for the ripple structure on the surfaces of SiO_2 and Ge has been provided in a series of studies by Chason *et al.* [10, 11, 12, 13]. We shall discuss here the results obtained on SiO_2 [11, 12]. A low energy ion beam (Xe, H or He), with energies ≤ 1 KeV is directed towards a SiO_2 sample with an angle of incidence of 55° from normal. The typical incoming flux is 10^{13} $cm^{-2}s^{-1}$. The interfaces are analyzed using *in situ* energy dispersive x-ray reflectivity and *ex situ* atomic force microscopy (AFM).

Bombarding the surface with 1 KeV Xe ions, one finds that the interface roughness, determined from X-ray diffraction, increases linearly with the fluence (the fluence is the number of incoming atoms per surface area, and plays the role of time in these measurements). Thus $\beta = 1$, too large a value to be interpretable by continuum theories. Such a large value of β indicates the existence of an instability in the system. Indeed, the source of the instability is the negative surface tension. But the instability should be balanced by surface diffusion, leading to the appearance of the ripple structure. Such a ripple structure can be seen if one inspects the AFM pictures of the interface. A similar ripple structure has been observed for Ge surfaces bombarded by Xe atoms [10].

Another series of experiments on ripple formation were reported by MacLaren *et al.* [14]. They studied InP and GaAs bombardment with 5 KeV Ar^+, 17 KeV Cs^+ and 5.5 KeV O_2^+ beams in a temperature range of -50 to 200 °C. Their study revealed in detail the temperature dependence of the ripple wavelength. For example for GaAs bombarded

by Cs^+ ions the ripple spacing increased from zero 0.89 μm to 2.0 μm, as the temperature increased from 0 °C to 100 °C. Probably the most interesting finding of their study was that when lowering the temperature, the ripple spacing (wavelength) did not go continuously to zero, as one would expect, since the diffusion constant decreases exponentially with the inverse temperature, but rather at around 20 °C it stabilized at an approximately constant value. MacLaren *et al.* interpreted this as the emergence of a radiation enhanced diffusion, that gives a constant (temperature independent) contribution to the diffusion constant.

Roughening

Motivated by the advances in understanding growth, recently a number of experimental studies have focused on the scaling properties of surfaces eroded by ion bombardment. For graphite bombarded with 5 KeV Ar ions, Eklund *et al.* [15, 16] reported $\alpha \simeq 0.2 - 0.4$, and $z \simeq 1.6 - 1.8$, values consistent with the predictions of the Kardar-Parisi-Zhang (KPZ) equation in 2+1 dimensions [21, 22, 23, 24, 25, 26]. In these experiments pyrolytic graphite was bombarded by 5 KeV Ar ions, which arrived with an angle of incidence of 60°. The experiments were carried out for two flux values, 6.9×10^{13} and 3.5×10^{14} ions/cm^2, and the total fluences obtained were 10^{16}, 10^{17} and 10^{18}. The etched graphite was examined using STM. We observe that large scale features develop with continuous bombardment, the interface becoming highly correlated and rough. The scaling properties can be probed using the Fourier transform of the height–height correlation function indicating a scaling region for large q, and saturation for small q values (corresponding to large length scales). The results indicate a dynamic exponent z in the range 1.6–1.8, and a roughness exponent in the range 0.2–0.4. The exponents are consistent with the predictions of the KPZ equation for the strong coupling regime.

A somewhat larger roughness exponent has been measured for samples of iron bombarded with 5 KeV Ar arriving with angle of incidence of 25°. The interface morphology was observed using STM, and the height–height correlation function results in a roughness exponent $\alpha = 0.53 \pm 0.02$ [17]. The mechanism leading to such a roughness exponent is not yet understood in terms of the continuum theories, since for two dimensions the growth equations predict 0.38, 2/3 and 1, all values far from the observed value.

Recently Si(111) sputtered by 0.5 KeV Ar^+ ions was observed to roughen following an anomalous dynamic scaling form $w(t, \ell) \sim ln(t)\ell^{2\alpha}$, with $\alpha \simeq 1.15 \pm 0.08$ [18].

Continuum theory

Sigmund's theory of sputtering

In order to calculate the sputtering yield, and predict the surface morphology, we first need to understand the mechanism of sputtering, resulting from the interaction of the incident ion and the surface layer. The incoming ions penetrate the surface and transfer their kinetic energy to the atoms of the substrate by inducing cascades of collisions among the substrate atoms, or through other processes such as electronic excitations. Whereas most of the sputtered atoms are located at the surface, the scattering events that might lead to sputtering take place within a certain layer of average depth a.

A qualitative picture is as follows. An incoming atom undergoes a series of collisions in the target, and atoms that recoil with sufficient energy undergo secondary collisions, thereby generating another generation of recoiling atoms. A vast majority of atoms will not gain enough energy to leave their lattice position permanently. However, some are permanently removed from their sites, locally making the substrate amorphous. The atoms that are near the surface and gain enough energy to break their bonds and leave the surface will be

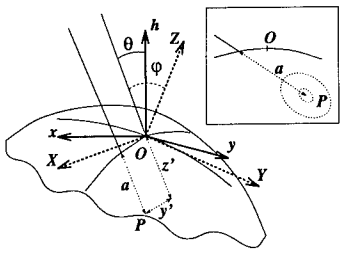


Figure 1: Reference frames for the computation of the erosion velocity at point O. Inset: Following a straigh trajectory (solid line) the ion penetrates an average distance a inside the solid (dotted line) after which it completely spreads out its kinetic energy. The dotted curves are equal energy contours. Energy released at point P contributes to erosion at O.

sputtered. Usually the number of sputtered atoms is orders of magnitudes smaller than the total number of atoms participating in the collision cascade.

A rather successful theory was introduced by Sigmund to describe the experimentally observed sputtering yields [29, 30]. His treatment considers the energy transfer from the incoming ion to the atoms of an isotropic solid by writing down a Boltzmann transport equation for the atoms. Expanding this equation in form of Legendre polynomials, he obtains a solution using the method of moments.

One of the most important result of his analysis is that for low energies the damage and energy distribution generated by the incoming ion follows a Gaussian. Thus here, following [29, 30, 31], we consider that the average energy deposited at point O due to the ion arriving at P follows the Gaussian distribution

$$E(r') = \frac{\epsilon}{(2\pi)^{3/2}\sigma\mu^2} \exp\left\{-\frac{z'^2}{2\sigma^2} - \frac{x'^2+y'^2}{2\mu^2}\right\}. \tag{5}$$

In (5) z' is the distance measured along the ion trajectory, and x', y' are measured in the plane perpendicular to it (see Fig. 1; for simplicity in the figure x' has been set to 0); ϵ denotes the total energy carried by the ion and σ and μ are the widths of the distribution in directions parallel and perpendicular to the incoming beam, respectively. However, the sample is subject to an uniform flux J of bombarding ions. A large number of ions penetrate the solid at different points simultaneously and the velocity of erosion at O depends on the total power $\mathcal{E}_O$ contributed by all the ions deposited within the range of the distribution (5). If we ignore shadowing effects among neighboring points, as well as further redeposition of the eroded material, the normal velocity of erosion at O is given by

$$v = p \int_{\mathcal{R}} dr\ \Phi(r)\ E(r), \tag{6}$$

where the integral is taken over the region $\mathcal{R}$ of all the points at which the deposited energy contributes to $\mathcal{E}_O$, $\Phi(r)$ is a local correction to the uniform flux J and p is a proportionality constant between power deposition and rate of erosion. In the following we outline the basic steps in the calculation of v; further details can be found in Refs. [19, 31, 28].

Continuum equation for the surface height

In this section, we derive an equation of motion for the surface height from the physical model of ion–sputter erosion discussed in the previous section. Since we are mainly interested in the physically relevant case of a two dimensional substrate and the one dimensional

case to linear order is very clearly explained in the work by Bradley and Harper [31], we refer the reader to that reference, and focus here in the more general 2d case.

In the following we summarize the steps in the derivation of the equation of motion.

(i) First we calculate the normal component of the velocity of erosion v_O at a generic point O of the interface. This calculation is most easily performed in a local frame of reference (X, Y, Z) defined as follows: the $\hat{Z}$ axis is identified with the normal direction to the average surface orientation at O. Now $\hat{Z}$ forms a plane with the trajectory of an ion penetrating the surface at O. We choose the $\hat{X}$ axis to lie in that plane. Finally, $\hat{Y}$ is the remaining direction which completes the local reference frame, see Fig. 1.

(ii) Next we relate the quantities measured in coordinates of the local frame to coordinates in the laboratory frame (x, y, h). The latter is defined by the experimental configuration. That is, h is the direction normal to the uneroded flat surface. The ion trajectories together with the h axis define a plane, which is taken to be the $x - h$ plane. And finally the y axis completes a right–handed reference frame, see Fig. 1. However, φ, which is the angle between the ion trajectory and the *local* normal to the surface, changes from point to point along the surface, and is a function of the local values of the slopes at O (as seen in the laboratory frame), as well as of the fixed angle θ subtended by the ion trajectories and the normal to the uneroded surface (the h direction in Fig. 1).

(iii) Finally, to obtain the equation of motion for the surface profile function $h(x, y, t)$, we will have to project the normal component of the velocity of erosion onto the global h axis.

In the absence of overhangs the surface can be described by a single valued height function $h(x, y, t)$, measured from an initial flat configuration which is taken to lie in the (x,y) plane. The ion beam is parallel to the x-h plane forming an angle $0 \leq \theta < \pi/2$ with the z axis. The time evolution of h is given by

$$\frac{\partial h(x,y,t)}{\partial t} \simeq -v(\varphi, R_X, R_Y)\sqrt{1 + (\nabla h)^2}, \tag{7}$$

where φ is the angle of the beam direction with the local normal to the surface at $h(x, y)$. Now φ is a function of the angle of incidence θ and the values of the local slopes $\partial_x h$ and $\partial_y h$, and can be expanded in powers of the latter. We will assume that the surface varies smoothly enough so that products of derivatives of h can be neglected for third or higher orders.

At this stage additional relevant physical processes must be taken into account to describe the evolution of the surface. First, the bombarding ions reach the surface at random positions and times. We account for the stochastic arrival of ions by adding to (7) a Gaussian white noise $\eta(x, y, t)$ with zero mean and variance proportional to the flux J. Second, at finite temperature atoms diffuse on the surface [10, 15, 16]. To include this surface self-diffusion we allow for a term $-K\nabla^2(\nabla^2 h)$ [32, 33, 34, 35, 36], where K is a temperature dependent positive coefficient. Expanding (7) and adding the noise and the surface-diffusion terms we obtain the equation of motion [37]

$$\begin{aligned} \frac{\partial h}{\partial t} &= -v_0 + \gamma\frac{\partial h}{\partial x} + \nu_x\frac{\partial^2 h}{\partial x^2} + \nu_y\frac{\partial^2 h}{\partial y^2} + \\ &+ \frac{\lambda_x}{2}\left(\frac{\partial h}{\partial x}\right)^2 + \frac{\lambda_y}{2}\left(\frac{\partial h}{\partial y}\right)^2 - K\nabla^2(\nabla^2 h) + \eta. \end{aligned} \tag{8}$$

From (7) we can compute the expressions for the coefficients appearing in (8) in terms of the physical parameters characterizing the sputtering process. To simplify the discussion we restrict ourselves to the symmetric case $\sigma = \mu$. The general case is discussed in [19]. If

we write $F \equiv (\epsilon J p/\sqrt{2\pi})\exp(-a_\sigma^2/2)$, $s \equiv \sin\theta$, $c \equiv \cos\theta$ and $a_\sigma \equiv a/\sigma$, we find for the coefficients in (8)

$$\begin{aligned} v_0 &= \frac{F}{\sigma}c \ , \ \gamma = \frac{F}{\sigma}s(a_\sigma^2 c^2 - 1), \\ \lambda_x &= \frac{F}{\sigma}c\left\{a_\sigma^2(3s^2 - c^2) - a_\sigma^4 s^2 c^2\right\}, \\ \lambda_y &= -\frac{F}{\sigma}c\{a_\sigma^2 c^2\}, \\ \nu_x &= \frac{F}{2}a_\sigma\left\{2s^2 - c^2 - a_\sigma^2 s^2 c^2\right\}, \\ \nu_y &= -\frac{F}{2}a_\sigma c^2. \end{aligned} \tag{9}$$

Analysis of the obtained growth equations

Consistent with the direction of the bombarding beam and the choice of coordinates, the terms in (8) are symmetric under $y \to -y$ but not under $x \to -x$, while for $\theta \to 0$ we get $\gamma = \xi_x = \xi_y = 0$, $\lambda_x = \lambda_y$ and $\nu_x = \nu_y$. The equation studied in Ref. [31] corresponds to the deterministic linear version of (8), i. e. $\lambda_x = \lambda_y = \eta = 0$.

If ν_x and ν_y are positive, the surface diffusion term is expected to contribute negligible to the relevant surface relaxation mechanism when we probe the system at increasingly large length scales. Scaling properties are then described by the anisotropic KPZ equation (AKPZ), which predicts two possible behaviors depending on the relative signs of the coefficients λ_x and λ_y [38, 39]. If $\lambda_x\lambda_y > 0$, then $\alpha = 0.38$ and $z = 1.6$, the surface width $w(L,t)$ increases algebraically, being characterized by the exponents of the KPZ equation in 2+1 dimensions [22, 23, 24, 25, 26]. For $\lambda_x\lambda_y < 0$, the nonlinear terms λ_x and λ_y become irrelevant, and the width grows only logarithmically, i.e. $\alpha = 0$.

In our case ν_x can change sign as θ and a_σ are varied, while ν_y is always negative. The negative ν causes an instability, whose origin is the faster erosion for the bottom of a trough than for the peak of a crest, as predicted by (6) (see also Fig. 3 of Ref. [31]). An instability due to a negative surface tension is also known to take place in the Kuramoto–Sivashinsky (KS) equation [40], which is the *noiseless* and isotropic version of (8). It has been argued for the KS equation that in 1+1 dimensions ν renormalizes to a positive value [41], and the large length scale behavior is described by the KPZ equation. In 2+1 dimensions it is not completely settled whether the large distance behaviors of KS and KPZ fall in the same universality class, different approaches leading to conflicting results [42].

In contrast to the KS equation, Eq. (8) is anisotropic, and explicitly contains a noise term. The competition between surface tension and surface diffusion generates a characteristic length scale in the system, $\ell_c = \sqrt{K/|\nu|}$, where ν is the largest in absolute value of the negative surface tension coefficients. Below we discuss a possible scenario for the scaling behavior predicted by (8) based primarily on the results available in the literature for some of its limits. The complete scaling picture should be provided by either a DRG analysis capable of coping with the linear instabilities present in the system, or a numerical integration of (8).

The scaling behavior depends on the relative signs of ν_x, ν_y, λ_x and λ_y [43]. The variations of these coefficients as functions of a_σ and θ lead to the phase diagram shown in Fig. 2.

Regions I and II— For small θ both ν_x and ν_y are negative. As discussed by Bradley and Harper [31] and experimentally studied by Chason *et al.* [10], a periodic structure dominates

the surface morphology, with ripples oriented along the direction (x or y) which presents the largest absolute value for its surface tension coefficient. The observed wavelength of the ripples is $\lambda_c = 2\pi\sqrt{2}\ell_c$.

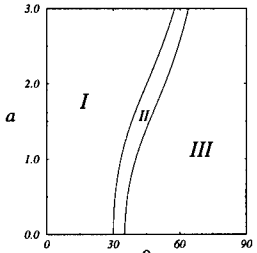


Figure 2: Phase diagram for the isotropic case $\sigma = \mu = 1$. Region I: $\nu_x < 0$, $\nu_y < 0$, $\lambda_x < 0$, $\lambda_y < 0$; Region II: $\nu_x < 0$, $\nu_y < 0$, $\lambda_x > 0$, $\lambda_y < 0$; Region III: $\nu_x > 0$, $\nu_y < 0$, $\lambda_x > 0$, $\lambda_y < 0$. Here a is measured in arbitrary units and θ is measured in degrees.

The large length scale behavior $\ell \gg \ell_c$ is expected to be different. Now both nonlinearities and the noise may become relevant. The scaling properties of the surface morphologies predicted by (8) are unknown. A possible scenario is that the ν's renormalize to positive values, as they do for the KS equation in $1+1$ dimensions, and the large scale scaling properties of the system are described by the AKPZ equation. Then one would observe algebraic scaling in region I, where both nonlinearities have the same (negative) sign, whereas scaling would become logarithmic through an AKPZ-like mechanism in region II, where λ_x and λ_y have opposite signs. Actually, the asymptotic KPZ scaling has been recently shown to occur for the $\theta = 0$ limit of Eqs. (8) and (9) by a renormalisation group analysis [44].

Region III — This region is characterized by a positive ν_x and a negative ν_y. Now the periodic structure associated with the instability is directed along the y direction and is the dominant morphology at scales $\ell \sim \ell_c$. Again, such an anisotropic and linearly unstable equation is unexplored in the context of growth equations. Assuming that ν_y renormalizes to a positive value, and that the AKPZ mechanism operates, one would expect logarithmic scaling in region III, since the nonlinear terms have opposite signs.

Even though several aspects of the scaling behavior predicted by (8) and (9) remain to be clarified, we believe that these equations contain the relevant ingredients for understanding roughening by ion bombardment [45]. To summarize, at short length scales the morphology consists of a periodic structure oriented along the direction determined by the largest in absolute value of the negative surface tension coefficients [10]. Modifying the values of a_σ or θ changes the orientation of the ripples [9, 31]. At large length scales we expect two different scaling regimes. One is characterized by the KPZ exponents, which *might* be observed in region I in Fig. 2. Indeed, the values of the exponents reported by Eklund *et al.* [15, 16] are consistent within the experimental errors with the KPZ exponents in 2+1 dimensions. The other regions (II and III) are characterized by logarithmic scaling ($\alpha = 0$), which has not been observed experimentally so far. Moreover, by tuning the values of θ and/or a_σ one may induce transitions among the different scaling behaviors. For example, fixing a_σ and increasing the value of θ would lead from KPZ scaling (region I) to logarithmic scaling (II, III) for large enough angles.

Recent numerical results on the two dimensional anisotropic KS equation indicate that the scaling regimes II and III in the *noiseless* limit of our model is dominated by exponentially growing solutions of the KS equation [46]. In those regions the ripple structure is oriented along a direction which is neither the x nor y. Further numerical simulations are needed to understand the effect of the noise on the stability of the exponential solutions.

Insight into the expected morphologies are obtained from numerical simulation of discrete models, correctly capturing the basic mechanisms taking place during sputtering. Recent simulations on discrete models indicate that the noisy KS equation indeed describes the dynamics of the sputtering generated roughening [47]. Also, now that we have a rather detailed experimental and theoretical understanding of the morphologies generated by ion sputtering, we can start investigating the effect of the roughness and in general that of the surface morphology on various experimentally relevant quantities, such as the sputtering yield. Most theoretical results on the yield were obtained assuming smooth surfaces. However, preliminary results indicate that the roughness has a nontrivial effect on the yield [48], that can be calculated using the formalism discussed in the present paper.

The experimental verification of the above possibilities would constitute an important step to elucidate the interplay between the mechanisms leading to the different morphologies and dynamics for sputter-etched surfaces. It will also provide additional insight into the scaling behaviors to be expected from equation (8).

Acknowledgment

We would like to acknowledge discussions, comments and encouragement by L. A. N. Amaral, G. Grinstein, K. B. Lauritsen, H. Makse, L. M. Sander, and H. E. Stanley. We would like to thank one of the referees for the very constructive criticisms and observations made. R. C. acknowledges a postdoctoral Fellowship of the Spanish Ministerio de Educación y Ciencia.

References

[1] A.-L. Barabási and H. E. Stanley, *Fractal Concepts in Surface Growth* (Cambridge University Press, Cambridge, 1995).

[2] *Dynamics of Fractal Surfaces*, F. Family and T. Vicsek, eds. (World Scientific, Singapore, 1991).

[3] P. Meakin, Phys. Rep. **235**, 189 (1993).

[4] T. Halpin-Healey and Y.-C. Zhang, Phys. Rep. **254**, 215 (1995).

[5] W.M. Tong, and R.S. Williams, Annu. Rev. Phys. Chem. **45**, 401 (1994).

[6] *Sputtering by Particle Bombardment*, R. Behrisch, ed. (Springer-Verlag, Heidelberg 1981, 1983), Vols. I, II, III.

[7] *Handbook of Ion Beam Processing Technology*, J.J. Cuomo, S.M. Rossnagel, and H.R. Kaufman, eds. (Noyes Publications, Park Ridge 1992).

[8] *Ion Beam Assisted Film Growth*, T. Itoh ed. (Elsevier, Amsterdam, 1989).

[9] G. Carter, B. Navinšek and J. L. Whitton in Vol. II of Ref. [6], p. 231.

[10] E. Chason *et al.*, Phys. Rev. Lett. **72**, 3040 (1994).

[11] T. M. Mayer, E. Chason and A. J. Howard, J. Appl. Phys. **76**, 1633 (1994).

[12] E. Chason, T. M. Mayer, and A. Payne, Appl. Phys. Lett. **60**, 2353 (1992).

[13] E. Chason and T. Mayer, Appl. Phys. Lett. **62**, 363 (1993).

[14] S.W. MacLaren, J.E. Baker, N.L. Finnegan, and C.M. Loxton, J. Vac. Sci. Technol. A **10**, 468 (1992).

[15] E. A. Eklund, *et al.*, Phys. Rev. Lett. **67**, 1759 (1991).

[16] E. A. Eklund, E. J. Snyder and R. S. Williams, Surf. Sci. **285**, 157 (1993).

[17] J. Krim *et al.*, Phys. Rev. Lett. **70**, 57 (1993).

[18] H.-N. Yang, G.-C. Wang, and T.-M. Lu, Phys. Rev. **B 50**, 7635 (1994).

[19] R. Cuerno and A.–L. Barabási, Phys. Rev. Lett. **74**, 4746 (1995).

[20] F. Family and T. Vicsek, J. Phys. A **18**, L75 (1985).

[21] M. Kardar, G. Parisi and Y.-C. Zhang, Phys. Rev. Lett. **56**, 889 (1986).

[22] J. M. Kim and J. M. Kosterlitz, Phys. Rev. Lett. **62**, 2289 (1989).

[23] B. M. Forrest and L. Tang, J. Stat. Phys. **60**, 181 (1990).

[24] J.G. Amar and F. Family, Phys. Rev. A **41**, 3399 (1990).

[25] K. Moser, D. E. Wolf and J. Kertész, Physica **A 178**, 215 (1991).

[26] T. Ala Nissila *et al.*, J. Stat. Phys. **72**, 207 (1993).

[27] S. F. Edwards and D. R. Wilkinson, Proc. R. Soc. London A **381**, 17 (1982).

[28] R. Cuerno and A.–L. Barabási, (unpublished).

[29] P. Sigmund, Phys. Rev. **184**, 383 (1969).

[30] P. Sigmund, J. Mat. Sci. **8**, 1545 (1973).

[31] R. M. Bradley and J. M. E. Harper, J. Vac. Sci. Technol. A **6**, 2390 (1988).

[32] C. Herring, J. Appl. Phys. **21**, 301 (1950).

[33] W.W. Mullins, J. Appl. Phys. **28**, 333 (1957).

[34] D.E. Wolf and J. Villain, Europhys. Lett. **13**, 389 (1990).

[35] S. Das Sarma and P. I. Tamborenea, Phys. Rev. Lett. **66**, 325 (1991).

[36] J. Villain, J. Phys. I **1**, 19 (1991).

[37] In the expansion of (7) two additional nonlinearities are obtained on the rhs of Eqn. (8): $\xi_x \frac{\partial h}{\partial x}\frac{\partial^2 h}{\partial x^2} + \xi_y \frac{\partial h}{\partial x}\frac{\partial^2 h}{\partial y^2}$, where ξ_x and ξ_y are functions of a, σ, μ and θ [28]. One can see that ξ_x and ξ_y are irrelevant at large length scales using the known values of α and z [22, 23, 24, 25, 26] for both the nonlinear and the linear fixed points in 2+1 dimensions.

[38] D. E. Wolf, Phys. Rev. Lett. **67**, 1783 (1991).

[39] The relevance of the AKPZ equation to sputter erosion has been suggested by R. Bruinsma in *Surface Disordering: Growth, Roughening and Phase Transitions*, R. Jullien *et al.* eds. (Nova Science, New York, 1992).

[40] Y. Kuramoto and T. Tsuzuki, Prog. Theor. Phys. **55**, 356 (1977); G. I. Sivashinsky, Acta Astronaut. **6**, 569 (1979).

[41] S. Zaleski, Physica **D 34**, 427 (1989); K. Sneppen *et al.* Phys. Rev. **A 46**, 7352 (1992); F. Hayot, C. Jayaprakash, and Ch. Josserand, Phys. Rev. **E 47**, 911 (1993); V. S. L'vov *et al.*, Nonlinearity **6**, 25 (1993).

[42] I. Procaccia *et al.* Phys. Rev. **A 46**, 3220 (1992); V. S. L'vov and I. Procaccia, Phys. Rev. Lett. **69**, 3543 (1992); *ibid.* **72**, 307 (1994); C. Jayaprakash, F. Hayot, and R. Pandit, Phys. Rev. Lett. **71**, 12 (1993); *ibid.* **72**, 308 (1994).

[43] The terms $-v_0$ and $\partial_x h$ can be reabsorbed by a change of variables to a comoving frame, and do not affect the scaling properties.

[44] R. Cuerno, and K.B. Lauritsen, Phys. Rev E **52**, 4853 (1995).

[45] Our analysis describes the roughening process in the small slope approximation. However, at late stages additional non-linear effects, such as shadowing may become relevant [For a review see G. S. Bales *et al.*, Science **249**, 264 (1990).]

[46] M. Rost, and J. Krug, Phys. Rev. Lett. **75**, 3894 (1995).

[47] R. Cuerno, H.A. Makse, S. Tomassone, S.T. Harrington, and H.E. Stanley, Phys. Rev. Lett. (in press).

[48] A.-L. Barabási and M. Makeev (to be published).

Topological Disorder and Conductance Fluctuations in Granular Thin Films

Kristin M. Abkemeier and David G. Grier
The James Franck Institute and Department of Physics
The University of Chicago
Chicago, IL 60637

Topological disorder places constraints on the local flow of currents in granular thin films of metals and semiconductors. These constraints in turn influence measurable transport properties such as conductance and conductance fluctuations for these films. We quantify disorder in the disposition of grains within real and simulated thin films by applying methods originally developed studying foam evolution. For simulated Voronoi resistor networks the overall conductance of a film with a given grain density achieves a minimum value for an intermediate degree of disorder. Films of equal conductances on either side of this minimum can have strikingly different current distributions. Short range inhomogeneities in the size and placement of grains lead to large scale conductivity inhomogeneities in disordered films. This renders the disordered films more susceptible to $1/f$ noise for systems with nonlinear intergrain coupling due to factors such as hydrogen diffusion. We discuss the results of simulations of such systems in the context of transport and scanning probe microscopy measurements on a-Si:H thin films.

The widespread phenomenon of $1/f$ noise occurring in transport measurements in many different materials has intrigued theorists and experimentalists alike over the past forty years. Within the past fifteen years, reviews on $1/f$ noise have appeared describing the multitudinous manifestations of this phenomenon for the disparate systems where it has been observed [1,2]. $1/f$ noise refers to the situation when the power spectral density $S_V(f)$ ($S_I(f)$) of voltage (current) fluctuations varies according to the relation $S(f) \propto f^{-\alpha}$, where $0.9 \leq \alpha \leq 1.4$. $S_V(f)$ is the Fourier transform of the voltage-voltage autocorrelation function $C_V(t)$ [1]:

$$S_V(f) = 4 \int_0^\infty C_V(t) \cos(2\pi t) dt,$$
$$C_V(t) = \langle V(t)V(0) \rangle - \langle V \rangle^2.$$

Besides the commonly observed $1/f$ spectrum from standard Gaussian noise processes, sometimes Lorentzian features with characteristic corner frequencies appear in the spectrum due to a particular form of correlated noise originating in two-level systems [1,2]. The action of two-level fluctuators can be manifested in a peculiar form of noise resembling a telegraph switching signal, and thermally activated telegraph signals not explainable by a simple charge trapping mechanism have been observed in several disparate disordered systems at low temperatures [3,4]. More recently, random telegraph signal noise appearing at and above room temperature has been observed in coplanar conductance measurements on a-Si:H [5–7]. In these systems, charge trapping was ruled out as a cause of the noise due to the number of electrons that would have to act in concert for the conductance fluctuations δG to be on the order of one percent of the d.c. conductance. Previous transverse conductance measurements on a-Si:H devices had also manifested telegraph noise which was attributed to charge trapping which in turn affected current microchannels flowing through the device [8,9].

A significant number of systems where $1/f$ noise is observed are structurally disordered [2]. We choose the hydrogenated amorphous silicon system (a-Si:H) as a representative experimental system with which to compare our simulation due to the presence of significant noise phenomena at room temperature and in coplanar sample geometry conducive to local probe measurements [5,6]. An example of telegraph noise from a two probe coplanar transport measurement of an n-type a-Si:H sample (doping concentration $2 \times 10^{-5}[PH_3]/[SiH_4]$ with unannealed resistance of 2 MΩ, sample current 1μA, distance between electrodes 0.5 mm, channel width 1 cm, and thickness 1 μm at $T = 300K$) is shown in Fig. 1. An example of telegraph noise observed in the n-type sample measured in our lab is shown in Fig. 1.

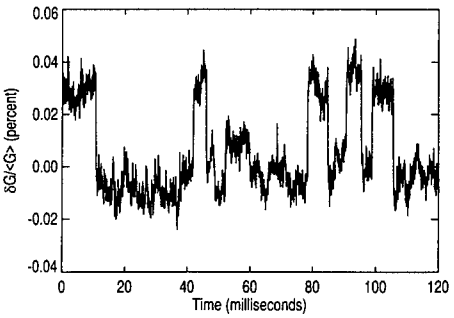


FIG. 1. Random telegraph signal in the measured sample at 1μA applied current.

We propose a model based on the analysis of the static and dynamical behavior in a topologically disordered Voronoi resistor network to explain the susceptibility of disordered granular thin films to $1/f$ and random telegraph switching noise. Previous models have

Mat. Res. Soc. Symp. Proc. Vol. 407 © 1996 Materials Research Society

demonstrated how conducting materials at the percolation threshold can manifest $1/f$ noise behavior by moving a select number of resistor bonds as time evolves [7,10]. Here we integrate the flipping conductance bond behavior into a fully interconnected resistance network where the connectivity and magnitudes of the individual resistors are determined by the topology of the material.

A two-dimensional disordered Voronoi resistor network is a good way to model conduction in granular thin films because it provides an exact analog for grain growth from nucleation sites. Since we are interested in the correlation between the complex local microstructure and the global transport properties of granular thin films, it is important to investigate a system in which the degree of disorder is controllable and isotropic. The relationship between the global conductance and topological disorder in disordered Voronoi networks has been studied previously for the d.c. case [11]. In this investigation we have furthered these results by defining an order parameter which allows direct comparison of results of visualization experiments with the model and by exploring the effects of nonlinear coupling as the system is stepped forward in time.

Conductance fluctuations originating in the topology of a Voronoi resistor network may occur by either intrinsic or extrinsic mechanisms. Intrinsic conductance fluctuations are those which may arise from nonlinear intergrain couplings, such as Schottky barriers, interfacial capacitances, and carrier traps. Many instances of telegraph switching noise observed in semiconductors has been found to be attributable to the lattermost situation [2,12]. Extrinsic mechanisms are those which have origins independent of the sample topology but which may act to influence local transport as a result of the sample structure. The most common instance of this in metals and semimetals is defect motion within the bulk of the sample [2], and in particular, hydrogen diffusion has been observed to contribute to low frequency fluctuations in metal films of Nb [13], Pd [14], and a-PdSi [15]. Additionally, hydrogen diffusion in a-Si:H has been observed to alter the defect structure in sample films and thereby alter their electrical conductivities [16]. Since defect motion as a source of $1/f$ noise appears to be a fairly general phenomenon and the cases involving hydrogen in particular are well documented, with a-Si:H being readily accessible for exploratory experimental work, we choose this extrinsic factor to motivate our dynamical simulation.

Our method of generating disordered Voronoi networks to selected degrees of disorder and solving the Kirchhoff current node equations was similar to that described in the initial work of Priolo *et al* [11]. Each disordered network was generated as a regular triangular lattice of approximately 5000 seed points inside a square of side length 66 lattice spacings whose nearest neighbor distance was set to d = 1. These dimensions were chosen as a compromise between convergence of the solutions and computational manageability. Disorder was introduced by displacing each point (x, y) by a random vector ($\Delta x \in [-\delta/2, \delta/2], \Delta y \in [-\delta/2, \delta/2]$), where $0.1 \leq \delta \leq 9.99$ lattice spacings for the data presented here. A Voronoi tessellation was performed on the resulting array of points, yielding a network of conductances g equal to the cell side lengths with connectivity according to the Delaunay triangulation of the seed points. One side of the square of conductances was set to a dimensionless potential of 1 with the opposing edge at ground. The sparse conductance matrix equations were then solved to obtain the potentials in each of the cells within the sample. From this the global conductance G was also calculated and normalized by the conductance across one of the cell interfaces in the regular network, $g_\Delta = 0.57735$.

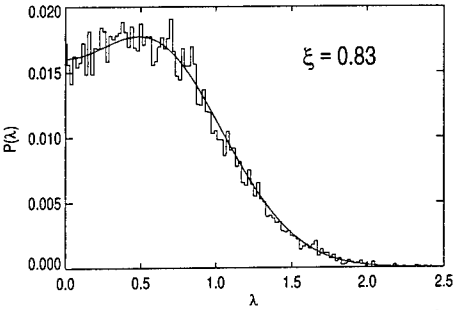


FIG. 2. Simulation cell side length λ distribution for $\xi = 0.83$ with calculated probability distribution $P(\lambda)$ overplotted as described in the text.

Defining a "disorder" parameter was crucial in order to be able to compare experimental and computational results appropriately. A study of the body of literature on two-dimensional cellular networks and their geometrical properties yielded just such a parameter to characterize our systems. In a paper investigating a method to generate realistic two-dimensional froths, Le Caër and Ho [17] noted that the distribution of cell side lengths in a random Voronoi network was accurately described by the probability density $p(\lambda)$ of the absolute value λ of a Gaussian variable of mean m and variance σ^2 given by

$$p(\lambda) = \frac{1}{\sigma\sqrt{2\pi}}\left[\exp\left(-\frac{(\lambda-m)^2}{2\sigma^2}\right) + \exp\left(-\frac{(\lambda+m)^2}{2\sigma^2}\right)\right].$$

The first two moments of $p(\lambda)$ are given by

$$\langle\lambda\rangle = \left(\frac{2}{\pi}\right)^{1/2}\sigma\exp\left(-\frac{m^2}{2\sigma^2}\right) + m\,\mathrm{erf}\left(\frac{m}{\sigma\sqrt{2}}\right) \quad (1)$$

$$\langle\lambda^2\rangle = \sigma^2 + m^2 \quad (2)$$

where erf is the error function. The quantities $\langle\lambda\rangle$ and $\langle\lambda^2\rangle$ are obtained from simple statistics of all cell side lengths in a Voronoi realization, and then the nonlinear system of equations (1) and (2) is solved to obtain m

and σ. We then choose as our disorder parameter the quotient $\xi = \sigma/m$, which measures the spread of the distribution of cell side lengths (conductances) relative to the mean. ξ therefore increases as disorder increases and the cell side lengths become uncorrelated. The probability distribution $P(\lambda)$ results from the integration of $p(\lambda)$ over the bin width for the experimental distribution, $P(\lambda) = \int_{x_i}^{x_i+0.02} p(\lambda)d\lambda$. The quality of the fit of $P(\lambda)$ thus calculated, *using no free parameters,* compared to the measured distribution for a single realization of a Voronoi network in the random limit is evident in Fig. 2.

With a disorder parameter established, global conductances for systems with $0 \leq \xi \leq 0.8$ were calculated, echoing the nonmonotonic change in the d.c. network conductance as disorder was increased found in the earlier Priolo study [11]. This result, plotted against the new order parameter, is shown in Fig. 3.

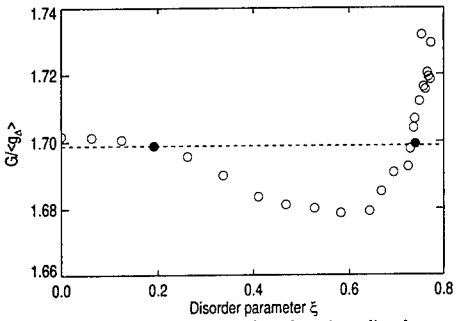


FIG. 3. Global conductance plotted against disorder parameter ξ. All conductances are normalized by the single grain boundary conductance in the regular triangular network $g_\Delta = 0.57735$. The dashed line indicates two global conductances of equal value (filled circles) at very different levels of disorder.

As in the calculations of Priolo *et al* [11], we observe a conductance minimum at an intermediate value $\xi \approx 0.6$, and although films may have equal global conductances at very different levels of disorder as the dashed line indicates, we will show that the local properties diverge greatly.

We have initiated a study of the influence of extrinsic factors in creating noise through spatial correlations of local currents. For the regular triangular network and seven other values of ξ (50 realizations each) up through the random case the system of Kirchhoff equations was solved and the approximately 15,000 individual bond currents were then calculated and ordered in magnitude. The bond carrying the most current was then removed, creating a local open circuit, and the new system of network equations was solved again to determine the new global conductance. The conductance dropped by over 0.15% in the random case. The results are plotted with error bars indicating the standard deviation in the spread of results over the 50 realizations at each ξ in Fig. 4. Note that the values for $\delta G/G$ would be comparable to those seen in Fig. 1 if scaled for the experimental sample's areal aspect ratio.

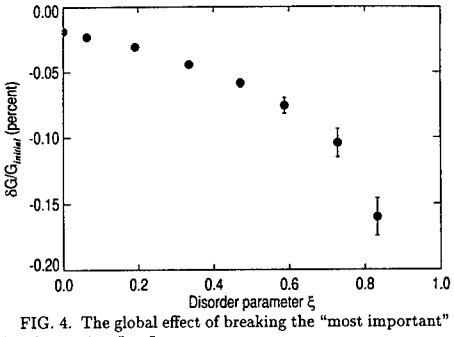


FIG. 4. The global effect of breaking the "most important" bond, carrying $I = I_{max}$.

The microscopic effect of breaking the "most important" current bond at each value of disorder can also be calculated. The absolute value of the difference in current $|I_{initial} - I_{final}|$ at each bond both before the bond carrying the greatest current was broken and after was taken for all bonds in the network and normalized by the absolute value of the initial bond current, yielding $|\Delta I|/|I_{initial}|$. This quantity was then binned up as a function of radial distance from the site of the broken bond and averaged. This operation was performed for

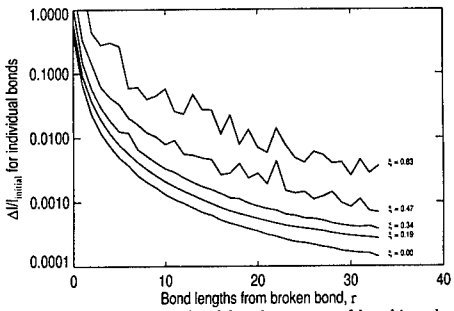


FIG. 5. The effect on local bond currents of breaking the "most important" bond, showing significant fluctuations extending to far distances in the two most disordered topologies shown.

all network realizations at each ξ in which the broken bond was a minimum of 10 lattice spacings away from all sides of the network boundaries to avoid current constriction effects. The values averaged over all relevant

realizations for $\xi = 0$ and four other values of disorder are depicted in Fig. 5. It is notable that in the most disordered systems, breaking the strongest bond influences local currents by at least 1% up to twenty bond lengths away. This suggests that a locally fluctuating cellular region in a disordered granular thin film could be observed via a visualization technique, as its influence is felt over a region over two orders of magnitude larger than the area of the fluctuator itself.

Finally, as the microscopic current redistributions drawn in Fig. 5 were all observed to have the same exponential functional dependence as a function of radius, a scaling law linking the microscopic current change $|\Delta I|/|I_{initial}|$ to ξ became apparent. We propose that $|\Delta I|/|I_{initial}| = f(\xi)g(r) \equiv \Phi(\xi, r)$. Since $g(r)$ has the same radial dependence for all disorder, then normalizing by $\Phi(0, r)$, representing the maximally ordered case, would yield

$$\frac{\Phi(\xi, r)}{\Phi(0, r)} = \frac{f(\xi)}{f(0)} \equiv f(\xi).$$

This parameter then represents the relative magnitude of the influence of the broken bond upon its local bonds, *i.e.*, the most disordered case changes local currents an average of *30 times* as much as in the triangular network. This evolution is plotted in Fig. 6.

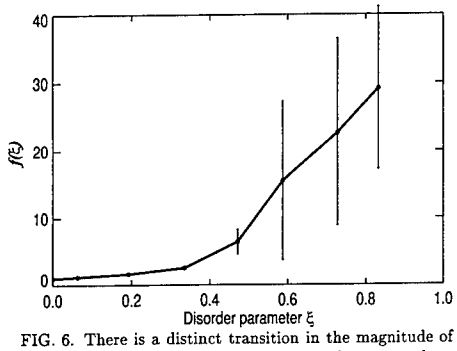


FIG. 6. There is a distinct transition in the magnitude of the local current changes at $\xi = 0.47$. The large error bars represent the fluctuations in the magnitude of the scaling factor as r varies in the most disordered cases.

In conclusion, we have discovered a disorder parameter which predicts both steady states and dynamical properties based strictly on the topology of a cellular network. Both in the experimental literature and in our phenomenological investigation thus far it has been demonstrated that topological disorder is essential in creating an environment favorable to the occurrence of significant conductance fluctuations. Our model is not specific to a particular material and does not rely upon the existence of a percolation threshold for fluctuations to be observed, although it can make percolation models more plausible if the critical fluctuating cells embedded in our system were shown to be percolative on a more microscopic scale than that of our study. Finally, the more disordered a granular thin film is, the greater the magnitude of the change in local currents surrounding a fluctuating current bond: this implies that such currents could be observed with a local probe in a visualization experiment implementing a scanning probe microscope. These results motivate planned investigation into local noise in coplanar a-Si:H films as well as further theoretical work into the dependence of $1/f$ noise on spatial current correlations.

K.M.A. was supported by an AT&T Bell Laboratories Ph.D. Fellowship while conducting this research. D.G.G. acknowledges support from the NSF MRSEC at the University of Chicago and the David and Lucille Packard Foundation.

[1] P. Dutta and P. M. Horn, Rev. Mod. Phys. **53**, 497 (1981).
[2] M. B. Weissman, Rev. Mod. Phys. **60**, 537 (1988).
[3] G. A. Garfunkel, G. B. Alers, and M. B. Weissman, Phys. Rev. B **41**, 4901, (1990).
[4] F. Coppinger, J. Genoe,D. K. Maude, U. Gennser, J. C. Portal, K. E. Singer, P. Rutter, T. Taskin, A. R. Peaker, and A. C. Wright, Phys. Rev. Lett. **75**, 3513 (1995).
[5] C. E. Parman, N. E. Israeloff, and J. Kakalios, Phys. Rev. B **44**, 8391 (1995).
[6] C. E. Parman, N. E. Israeloff, and J. Kakalios, Phys. Rev. B **47**, 12578 (1993).
[7] L. M. Lust and J. Kakalios, Phys. Rev. Lett. **75**, 2192 (1995).
[8] W. K. Choi, A. E. Owen, P. G. LeComber, and M. J. Rose, J. Appl. Phys. **68**, 120 (1990).
[9] T. Teuschler, M. Hundhausen, L. Ley, and R. Arce, Phys. Rev. B **47**, 12687 (1993).
[10] L. M. Lust and J. Kakalios, Phys. Rev. E **50**, 3431 (1994), and references therein.
[11] A. Priolo, H. M. Jaeger, A. J. Dammers, and S. Radelaar, Phys. Rev. B **46**, 14889 (1992).
[12] K. S. Ralls, W. J. Skocpol, L. D. Jackel, R. E. Howard, L. A. Fetter, R. W. Epworth, and D. M. Tennant, Phys. Rev. Lett. **52**, 228 (1984).
[13] J. H. Scofield and W. W. Webb, Phys. Rev. Lett. **54**, 353 (1985).
[14] N. M. Zimmerman and W. W. Webb, Phys. Rev. Lett. **61**, 889 (1988).
[15] N. M. Zimmerman and W. W. Webb, Phys. Rev. Lett. **65**, 1040 (1990).
[16] R. A. Street, J. Kakalios, C. C. Tsai, and T. M. Hayes, Phys. Rev. B **35**, 1316 (1987).
[17] G. Le Caër and J. S. Ho, J. Phys. A: Math. Gen. **23**, 3279 (1990).

NONEQULIBRIUM STATISTICAL MECHANICS OF AN ENSEMBLE OF VESICLES

LEONARDO GOLUBOVIĆ
Department of Physics, West Virginia University, Morgantown, WV 26506

ABSTRACT

We investigate *far-from-equilibrium* dynamics of a polydisperse ensemble of vesicles (such as liposomes). For that purpose, we construct of a Smoluchowsky-type transport equation incorporating vesicle diffusion and the processes of vesicle fusions and fissions. This approach is used to study the time evolution of an initially monodisperse vesicle ensemble and its important quantities such as the internal aqueous, encapsulated volume. We find three stages of the evolution: (i) an early stage during which EV remains nearly constant, followed by (ii) a stage with a rapid decay of the EV, and, finally (iii) a late stage in which the ensemble approaches the thermodynamic equilibrium. In the far-from-equilibrium stages (i) and (ii), the vesicle ensemble is a "two-fluid" system composed of a polydisperse fluid of small, nearly equilibrated vesicles, coexisting with a fluid of nearly monodisperse vesicles which size evolves due to evaporation-recondensation of the small vesicles. Our picture agrees with experimental data on the EV of lecithin liposomes.

INTRODUCTION

In recent years significant attention has been devoted to the equilibrium statistical mechanics of fluid membranes [1], and their phases [2]-[8]. Many of real life phenomena involving membranes are non-equilibrium in nature. Technologically important example are liposomes.[9]-[11] They are vesicles formed by bilayers contaninig amphiphilic substances like phospholipids dispersed in water. Liposomes are potential vehicles for transporting therapeutic and diagnostic agents from the site of administration to the specific targets within the body. To be effective, the liposomes must not only reach the appropriate tissue but must also release their content at the desired time.

Vesicles such as liposomes have a size distribution that is determined both by the method of preparation and by the lipid composition. During storage, fusion or fission of vesicles can occur [12] with subsequent changes in size and internal aqueus volume called "encapsulated volume" (EV). It is thus important to learn about stability of vesicles during storage in order to be able to understand their potential for use as a carrier over an extended period of time.

As the first step in this direction, here we construct a Smoluchowsky-type transport equation incorporating vesicle diffusion and the processes of vesicle fusions and fissions. It can be used to investigate *far-from-equilibrium* dynamics of a dilute polydisperse ensemble of vesicles such as liposomes. We use this approach to study the time evolution of an initially monodisperse vesicle ensemble and its important quantities such as the EV.

TRANSPORT EQUATION FOR POLYDISPERSE VESICLES

A dilute nonequilibrium polydisperse ensemble of nearly spherical vesicles can be described by a vesicle density $\rho(A, \mathbf{x}, t)$, such that $\rho(A, \mathbf{x}, t) dA d^3x$ is the number of vesicles

Mat. Res. Soc. Symp. Proc. Vol. 407 © 1996 Materials Research Society

of the area $A = 4\pi R^2$ in the interval $(A, A + dA)$ contained in a volume element d^3x. A vesicle of area A is free to diffuse and undergo fusions with other vesicles or to split into smaller vesicles. Thus, the vesicle ensemble is a diffusion-reaction system where reactions are vesicle fusion and fission processes (see Figure 1) preserving total area of vesicles (i.e., total amount of the membrane material). Thus, the time evolution of $\rho(A, \mathbf{x}, t)$ can be described by a Smoluchowsky-type transport equation (STE) of the form

$$\frac{\partial}{\partial t}\rho(A, \mathbf{x}, t) = D(A)\Delta_{\mathbf{x}}\rho(A, \mathbf{x}, t) + R_a + R_b + R_c + R_d, \tag{1}$$

where the first term is ordinary diffusion with the size dependent diffusion constant $D(A) = k_B T/6\pi\eta(A/4\pi)^{1/2}$, according to the Einstein-Stokes law, with η, the viscosity of the solvent. R_a to R_d in (1) are reaction rates associated with the reactions in the Figure (1) [fusions (a) and (b), and fissions (c) and (d)].

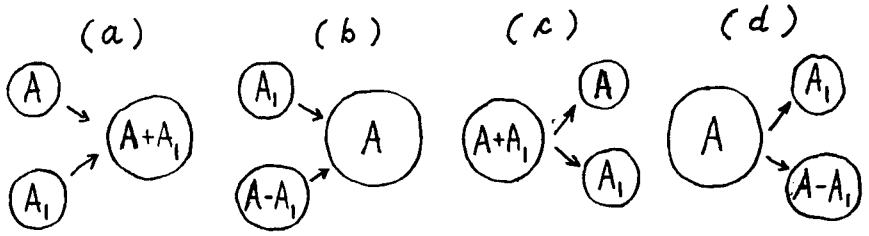


Figure 1: Reactions between vesicles.

If $\rho(A, \mathbf{x}, t)$ is slowly varying in space, these rates can be generally written in the form

$$R_a = -2\int_0^\infty dA_1\ \Gamma(A_1, A)\ \rho(A_1, \mathbf{x}, t)\ \rho(A, \mathbf{x}, t), \tag{2a}$$

$$R_b = \int_0^A dA_1\ \Gamma(A_1, A - A_1)\ \rho(A_1, \mathbf{x}, t)\ \rho(A - A_1, \mathbf{x}, t), \tag{2b}$$

$$R_c = 2\int_0^\infty dA_1\ \Pi(A_1, A)\ \rho(A + A_1, \mathbf{x}, t), \tag{2c}$$

$$R_d = -\int_0^A dA_1\ \Pi(A_1, A - A_1)\ \rho(A, \mathbf{x}, t), \tag{2d}$$

Reaction kernels Γ and Π in Eqs. (2) are related by the detailled balance between fusions in Fig. 1 (a) and fissions in (c) [fusions in (b) and fissions in (d)] in the thermodynamic equilibrium. This gives the condition

$$\Pi(A_1, A_2) = \frac{\rho_{eq}(A_1)\ \rho_{eq}(A_2)}{\rho_{eq}(A_1 + A_2)}\Gamma(A_1, A_2), \tag{3}$$

where $\rho_{eq}(A)$ is the equilibrium density. For example, for the entropically stabilized vesicles [5][6]

$$\rho_{eq} = \frac{C}{A^{5/2}}\left(\frac{A}{A_{min}}\right)^{4/3} e^{-A/A_{max}}, \tag{4}$$

with A_{min}, the minimum area of a vesicle; $C = (\kappa/k_BT)^2 exp(-E_b(A_{min})/k_BT)$, with κ, the mebrane bending rigidity, and $E_b(A_{min})$ the curvature energy of the smallest vesicles (with the area= A_{min}). A_{max} in (4) is, effectively, the area of the largest vesicles present in the system. It is determined by the total amount of the membrane material, i.e, total membrane area A_{tot} present in the system

$$A_{tot} = \int d^3x\ dA\ \rho(x, A). \tag{5}$$

Vesicle fusions and fissions processes included in our STE (1) preserve A_{tot} and drive the density $\rho(\mathbf{x}, A, t)$ towards the equilibrium density (4) at long times. We remark that the actual value of A_{max} in (4) does not explicitely enter the STE (1) [see Eqs. (3) and (4)]

To close our theory, we now derive the form of the reaction kernel Γ in Eqs. (2). To this end, consider the process in Figure 1(a), represented by the rate in Eq.(2a). The quantity $\Gamma(A_1, A)\rho(A_1)dA_1$ is the inverse of the average time $t(A_1, A)$ it takes for a vesicle of the area A to encounter with vesicles with areas in the interval $(A_1, A_1 + dA_1)$ and fuse with one of them. Let us first estimate the number of these encounters $N(t)$ during the time interval t. During an encounter, the vesicles are as close as $R + R_1 = (\sqrt{A} + \sqrt{A_a})/(4\pi)^{1/2}$. Thus, $N(t) = V(t)\rho(A_1)dA_1$, where $V(t)$ is the volume swept in space by a sphere of the radius $R + R_1$ diffusing with the diffusion constant $D(A, A_1) = D(A) + D(A_1)$(="relative" diffusion constant for the diffusion of A_1 in the reference frame co-moving with A). The volume $V(t)$ can be estimated as $V(t) \approx (4\pi/3)(R + R_1)^3(t/t_1)$, where $t_1 = (R + R_1)^2/2D(A, A_1)$(=the time it takes for the sphere to diffuse over the distance equal to its radius). Thus, $N(t) \approx (R + R_1)D(A, A_1)\ t\ \rho(A_1)dA_1$ is the number of the encounters of the vesicle of area A with vesicles with areas in the interval $(A_1, A_1 + dA_1)$. If p_{fus} is the probability that an encounter between the vesicles leads to a fusion, the average time $t(A_1, A)$ it takes for a fussion to occur satisfies $p_{fus}N(t(A_1, A)) \approx 1$. By using this, and $\Gamma(A_1, A)\rho(A_1)dA_1 = 1/t(A_1, A)$, we find that $\Gamma(A_1, A) \approx p_{fus}(D(A_1) + D(A))(R_1 + R)$. By using here the Einstein-Stokes form for $D(A)$, we find

$$\Gamma(A_1, A) \approx p_{fus}\frac{k_BT}{\eta}\left[2 + \left(\frac{A}{A_1}\right)^{1/2} + \left(\frac{A_1}{A}\right)^{1/2}\right]. \tag{6}$$

This equation completes our transport theory, Eqs. (1) to (6).

DECAY OF AN INITIALLY MONODISPERSE ENSEMBLE

Here we discuss decay of a spatially uniform, initially monodisperse ensemble of vesicles. Let n_0 be the density of these vesicles all initially, at $t = 0$, having the same area $A(0)$. Thus $\rho(A, \mathbf{x}, t = 0) = n_0\delta(A - A(0))$. The STE (1) will drive ρ to an equilibrium distribution of the form (4) with A_{max} determined by the conservation of A_{tot}, Eq.(5). This conservation law gives A_{max} through the equation $n_0A(0) = \int dA\ \rho_{eq}(A) =$

$CA_{max}^{5/6}/A_{min}^{4/3}$, yielding $A_{max} = A(0)(n_0/n^*)^{6/5}$, with $n^* = C(A(0))^{-1/6}/A_{min}^{4/3}$. In the following, we consider the dilute limit $n_0 \ll n^*$. Then $A(0) \gg A_{max}$ and the vesicle ensemble is initially *far* from equilibrium. These initially large monodisperse vesicles will decay dominantly through fissions ("evaporations") producing small vesicles with sizes $< A_{max}$. Thus, the vesicle ensemble becomes a "two-fluid" system composed of a polydisperse fluid of small, nearly equilibrated vesicles, coexisting with a fluid of nearly monodisperse vesicles which size evolves due to evaporation-recondensation of the small vesicles. $\rho(A,t)$ corresponding to this picture is sketched in Figure 2(a):

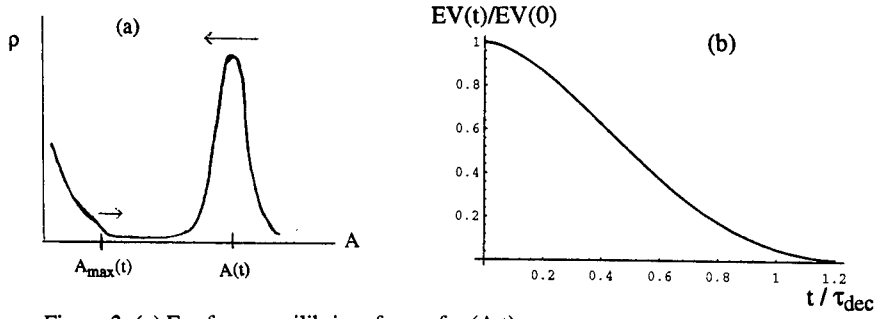


Figure 2: (a) Far-from-equilibrium form of ρ(A,t).
(b) Evolution of the encapsulated volume: EV(t) / EV(0) versus t / τ_{dec}.

There is a delta-like peak around some $A(t) \gg A_{max}$, corresponding to the large vesicles, and another peak around $A = 0$, corresponding to the small vesicles. These small vesicles get quickly equilibrated. Their number is, however, increasing with time due to their evaporations from the large vesicles (this will drive the delta-peak in Fig 2(a) towards A=0). Thus, one may write the form of the small vesicles peak in Fig. 2(a) in a form similar to the Eq. (4), $\rho(A,t) = \rho_o(A,t)$, with

$$\rho_o(A,t) = \frac{C}{A^{5/2}}\left(\frac{A}{A_{min}}\right)^{4/3} e^{-A/A_{max}(t)}, \tag{7}$$

where $A_{max}(t)$ is growing from zero, at $t = 0$ to its equilibrium value A_{max} at a long time scale when the two peaks in Fig. 2(a) merge to form a single peak corresponding to (4).This time scale is calculated below (see Eq. 12).

Before this actually happens, there is a long evolution during which the position of the delta-peak ($A(t)$) in Fig. 2(a) approaches A_{max}. Due to the condition $A(t) \gg A_{max}(t)$ satisfied during this evolution, it turns out that our Smoluchowsky equation (1)and (2) can be transformed into a Fokker-Planck equation. Indeed, for $A \sim A(t) \gg A_{max}(t)$ (i.e., arround the delta-peak) one can expand the integrands in (2) in powers of $A_1 \sim A_{max}(t)$. Thus, to the leading order, we find the Fokker-Planck equation:

$$\frac{\partial \rho}{\partial t} = \frac{\partial}{\partial A}\left(\mathcal{D}(A)\frac{\partial \rho}{\partial A} - v_d(A)\rho\right), \tag{8}$$

with a diffusion constant $\mathcal{D}(A) = C'A^{1/2}(A_{max}(t))^{4/3}$, and a "drift" velocity $v_d = -C'A^{1/2}(A_{max}(t))^{1/3}$; here $C' = CA_{min}^{-4/3}p_{fus}k_BT/\eta$. For $A \gg A_{max}(t)$, the drift term

in (8) dominates over the diffusion term. Thus, we find a simple equation for the position of the delta-peak in Fig. 2(a) ,

$$\frac{dA}{dt} = v_d = -C' A^{1/2} (A_{max}(t))^{1/3}. \tag{9}$$

The total membrane area A_{tot}, Eq. (5), contained in the large vesicles ($A \approx A(t)$) and the small vesicles (with the density given by (7)) is conserved. Thus

$$n_0 A(0) = n_0 A(t) + \int dA\ A\ \rho_o(A,t) = n_0 A(t) + C \frac{(A_{max}(t))^{5/6}}{A_{min}^{4/3}}. \tag{10}$$

Eqs. (9) and (10) can be used to extract the evolution of the $A(t)$. To this end, we introduce the dimensionless quantity $\omega(t) = \int_0^t |v_d(t)|/(A0)^{1/2}$. Then, by (9) and (10), $A(t) = A(0)(1-\omega(t))^2$ and

$$\tau_{dec} \frac{d\omega}{dt} = [\omega(2-\omega)]^{2/5}, \tag{11}$$

with

$$\tau_{dec} = C''(A(0))^{1/10} n_0^{-2/5}, \tag{12}$$

and

$$EV(t) = EV(0)(1-\omega(t))^3, \tag{13}$$

where $C'' = C^{2/5}/C' A_{min}^{8/15}$, and $EV(t)$ is the *encapsulated volume* fraction inside the the large vesicles, $EV(t) = (4\pi/3)(A(t))^{3/2} n_0$. It is easy to numerically solve (11) and find that ω grows from zero to one at $t \approx 1.35\tau_{dec}$. During this time $EV(t)/EV(0)$ drops from one to zero, see Figure 2(b). Experimental data on the EV of lecithin liposomes [13]-[16] strikingly ressemble our Figure 2(b) which indicates the presence of three stages of the evolution: (i) an early stage during which EV remains nearly constant ($t < 0.1\tau_{dec}$), followed by (ii) a stage with a rapid decay of the EV to nearly zero ($t < 1.35\tau_{dec}$), and, finally, (iii) a late stage in which the ensemble approaches the thermodynamic equilibrium and the EV is essentially zero. (i) and (ii) are far-from-equilibrium stages during which large vesicles evolve from their initial size $A(0)$ to the equilbrium size $\sim A_{max}$.

ACKNOWLEDGMENTS

This work is supported by a Mylan Pharmaceuticals Inc. research grant. We thank Mirjana Golubović for discussions.

REFERENCES

1. Statistical Mechanics of Membranes and Surfaces, edited by D. R. Nelson, T. Piran, and S. Weinberg (World Scientific, Singapore, 1989).
2. S. A. Safran, D. Roux, M. E. Cates, and D. Andelman, Phys. Rev. Lett. **57**, 491 (1986).
3. L. Golubović and T. Lubensky, Phys. Rev. B**39**, 12110 (1989).
4. L. Golubović and T. Lubensky, Phys. Rev. A**41**, 4343 (1990).
5. D. A. Huse and S. Leibler, J. Phys. (Paris) **49**, 605 (1988).
6. D. Morse and S. Milner, Europhys. Lett **26**, 565 (1994), and Phys. Rev. E in press.
7. L. Golubović, Phys. Rev. E**50**, R2419 (1994).
8. D. Morse, Phys. Rev. E**50**, R2423 (1994)
9. Liposomes in biological systems, edited by G. Gregoriades and A. C. Allison (John Wiley, Chichester, 1980).
10. Liposome: From physical structure to therapeutic applications, edited by C. K. Knight (Elsevier, Amsterdam, 1991).
11. Liposome technology, edited by G. Greogoriades (CRC Press, Boca Raton, 1984).
12. A. A. Larabee, Biochemistry **18**, 3321 (1989).
13. A. A. Hager et al., Spectrochem. Acta **49A**, 1991 (1993).
14. M. Mauk et al., Science **207**, 309 (1981).
15. M. M. Ponpipom et. al., J. Med. Chem. **24**, 1388 (1981).
16. P. S. Wu, Proc. Natl. Acad. Sci. USA **79**, 5490 (1982).

PITTING CORROSION IN TWO-DIMENSIONAL ALUMINIUM THIN LAYERS

L. BALÁZS*, **, J-F. GOUYET *
*Laboratoire de Physique de la Matière Condensée, Ecole Polytechnique, 91128 Palaiseau, France
**KFKI-Institute for Atomic Energy Research, P. O. B. 49, H—1525 Budapest, Hungary

We have investigated the influence of Cl^- and Fe^{3+} ions on the morphology of pits grown in aluminium thin films, under open circuit conditions. We observed various morphologies ranging from percolation-cluster-like patterns to dense holes with smooth perimeters. The experimental behavior has been appropriately simulated by a spreading percolation model with feed-back. This model reproduced all the morphologies observed and sustains the mechanisms proposed.

INTRODUCTION

Localized corrosion plays a very important role in industry. Pitting corrosion itself represents among 20% of the cases of corrosion of metal structures and is then of immense practical importance [1]. It is characteristic for metals (*e.g.* stainless steel, aluminium, nickel, chromium, titanium, *etc.*) possessing a thin protective oxide film which prevents the strong chemical reaction between the metal and a solution of certain anionic species. Electrode scratching experiments [2-4] revealed that following oxide breakdown, violent reaction occurs between the bare metal and water leading to the formation of a hydroxide layer on the metal surface. This layer impedes the dissolution of the metal, on the other hand in a subsequent chemical reaction it may be transformed to oxide [2] and in a few tenths of seconds the protective layer will be completely repaired [5].

The presence of aggressive anions is not a sufficient condition: actually, for all metals, it exists a lower limit of concentration in aggressive ions below which the pitting corrosion cannot develop: pitting corrosion is a *threshold phenomena*. Pit growth usually starts on chemical impurities, inclusions, or in the case of extremely pure metals, physical defects and dislocations. Once the pit growth has been started the composition of the electrolyte changes locally due to the metal dissolution. As a consequence, due to the hydrolysis of metal ions the aggressiveness of the medium increases close to the dissolution site leading to the acceleration of the corrosion process [6]. Pit propagation is controlled by the relative rate of metal dissolution and of ion transport in the liquid phase. On the other hand, if the concentration of aggressive anions decreases significantly in the vicinity of a dissolution site the bare metal surface becomes prone to oxidation which also inhibits the growth. The case of stable pit growth, when corrosion lasts indefinitely in time, needs a delicate balance between the metal dissolution and the ion transport towards and away from the active surface.

Corrosion studies usually consists in the determination of functional dependency between the corrosion rate (current density of the metal dissolution) and the parameters pertinent to the corrosion. Beside the measurement of anodic current, accurate determination of the active pit surface would be necessary to calculate current densities. Most of the investigations in this field makes the assumption that *hemispherical pits* are etched in the metal surface. This is the case only for corrosion under very aggressive conditions. In the case of less aggressiveness, corrosion pits are usually rougher and pit profiles are irregular over a broad length scale and cannot be characterized with a single radius [7]. Fractal geometry proved to be useful to describe irregularities of pit walls and to support the comparison with simplified models.

To describe the morphological aspect of pitting corrosion, several two-dimensional statistical models have been developed. Nagatani [8, 9] proposed an oversimplified anti-DLA model in which irregular profiles of corrosion pits are explained merely by the diffusion limited nature of metal degradation. Meakin *et. al* [10] assumed, that corrosion is a result of a diffusion limited reaction between mobile corrosive chemical species and the bare, unprotected metal surface. By tuning rate constants of passivation and depassivation reactions, they were able to reproduce smooth and rough pit shapes. Reigada *et. al* [11] proposed a model based on the idea that microscopic crystallographic tunnels [12] are randomly nucleated on the pit wall, which quickly penetrate the metal. The occurrence and size of tunnels is a function of local chloride concentration and of the potential. Under mild conditions the pit profile becomes rough. With increasing aggressiveness smooth, hemispherical pits are formed.

Mat. Res. Soc. Symp. Proc. Vol. 407 © 1996 Materials Research Society

To develop and test more elaborated models precise data on pit morphology is needed. Proper characterization of three-dimensional holes etched into a metal surface, however, requires enormous experimental and numerical effort [13]. Therefore it would be useful to compare the results of 2D model calculations with experiments on two-dimensional pitting [14-17]. Frankel *et. al.* studied under constant electrode potential, the corrosion of Al [14] and Permalloy [15] films. They observed extremely convoluted pits in the case of aluminium at low potentials, whereas at high potentials, *i.e.* under aggressive conditions, circular pits with smooth walls developed. The most striking feature of pitting in aluminium films is the evolution of hydrogen gas from the active metal surface which evidently affects passivation processes and pit morphology. Pits grown in Permalloy behaved similarly, but low-potential pits were significantly less ramified than pits grown in aluminium layers. This observation highlights the effect of bubbling induced convection on pit morphology, which was absent in Permalloy corrosion.

An interesting approach is to make experiments under open circuit conditions. Open circuit conditions mimic the natural circumstances of the corrosion process. In contrast to potentiostatic experiments a rich variety of pit morphologies can be observed in this case for aluminium film corrosion [16]. Pits can be initiated with the addition of some kind of oxidizing agent (*e.g.* Fe^{3+}) to the Cl^- containing corrosive medium. Preliminary experiments have shown that pit morphology is influenced by several factors, *e.g.* electrolyte composition, stirring rate of the solution, layer thickness, *etc.* One of the objectives of this work was to determine how Cl^- and Fe^{3+} ions affect pit shapes. More detailed results can be found in [18] where the noise behavior is also discussed. We shall essentially present here the main features of the experimental morphologies and their comparison with the simulation model.

EXPERIMENT

Aluminium thin layers of thickness of 50 nm were deposited by vacuum evaporation onto glass discs of 5 cm in diameter. The concentration of chloride and iron ions in the electrolyte were varied All the experiments were performed under open circuit conditions in stagnant electrolyte. Microscopic images of growing pits were taken by a video camera attached to a microscope. Pictures were digitized into a 512 × 512 pixel images. Schematic drawing of the experimental arrangement is shown in Fig. 1.

RESULTS

As expected we observe that above a certain threshold of electrolyte composition pits nucleate spontaneously on the metal surface. Pits quickly penetrate the metal film, and as soon as they reach the glass bottom a two-dimensional hole with walls perpendicular to the substrate starts to grow. The pit contour becomes ramified, peninsulas of aluminium are created which are

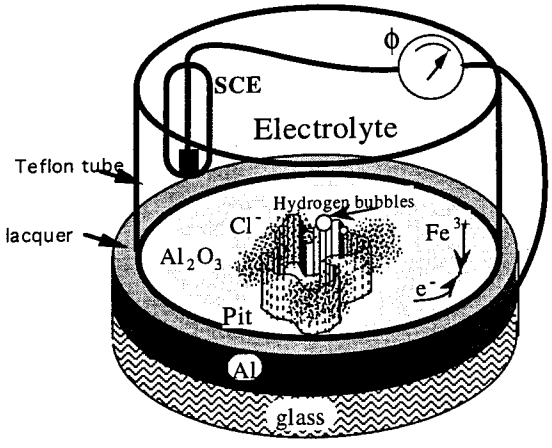


Figure 1. Schematic drawing of the experimental arrangement. The saturated calomel electrode (SCE) provides the reference for the measurement of the free corrosion potential, ϕ. The aluminium surface is covered with Al_2O_3 except the active sites on the pit perimeter. Increase of aggressiveness in the electrolyte above the active sites is indicated by dotted clouds.

transformed to islands as the dissolution front evolves. The first remarkable point is that islands, once formed, remain intact throughout the corrosion process. Further degradation of isolated islands can be obser ved only at high (>10 mM) Fe^{3+} concentration. So as to control perfectly the growth behavior, all the images discussed below are the results of single pit growth. As it is shown in Fig. 2 patterns grown at various Cl^- and Fe^{3+} concentrations can be classified into four main categories:

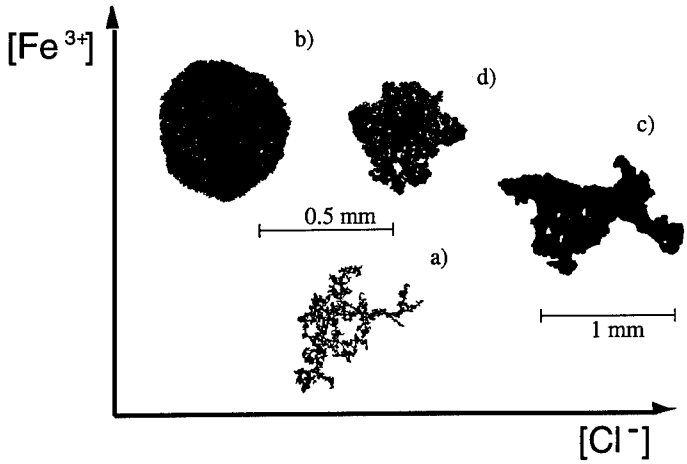


Fig.2. Characteristic pit morphologies observed at various Cl– and Fe3+ concentrations.
a) 10 mM Cl–, 0.2 mM Fe3+;
b) 1 mM Cl–, 10 mM Fe3+;
c) 1 M Cl– 0.5 mM Fe3+ ;
d) 100 mM Cl–, 5 mM Fe3+.

a) Fractal-like patterns (Fig 2(a))

At low Cl^- and Fe^{3+} content (10 mM Cl^-, 0.2 mM Fe^{3+}) patterns similar to percolation clusters in the vicinity of the percolation threshold are etched into the layer. Pit evolution terminates spontaneously and the final shape of the pattern has been analyzed. The density-density correlation function determined for the connected cluster of black pixels formed by digitalizing a pit exhibits scaling over two orders of magnitude with an exponent of 1.91±0.01, the value close to 1.89, the fractal dimension of percolation clusters at p_c in agreement with the suggestion of Sapoval et al. for an invasion-like corrosion pattern in the plane [19].

b) Homogeneous, round patterns (Fig. 2(b))

In the case of low Cl^- and high Fe^{3+} concentration (1 mM Cl^-, 10 mM Fe^{3+}) round holes containing uniformly distributed small islands are formed. These patterns are similar to a growing infinite percolation cluster with $p >> p_c$, where p is the concentration of cluster sites, *i.e.* the dissolved region, and p_c the percolation threshold.

c) Dense branches (Fig. 2(c))

With increasing Cl^- concentration the perimeter of the patterns becomes smoother. At high Cl^- content (> 100 mM Cl^-), long (≈100 mm) contiguous dissolution fronts are formed etching broad channels into the aluminium film.

d) Mixed morphology (Fig. 2(d))

At medium Cl^- and Fe^{3+} concentration (100 mM Cl^-, 5 mM Fe^{3+}) the dissolution process starts like in the case of dense structures but sooner or later the long dissolution front becomes convoluted at certain places and small individual growth regions propagate further .

To summarize, we observe the existence of two mains structures: percolation like structures with $p < p_c$ (Fig. 2(a)) or $p \gtrsim p_c$ (Fig. 2(b)), and dense structures (Fig. 2(c)); coexistence of these two structures is also observed (Fig. 2(d)).

The fact that at high Cl^- and at relatively low Fe^{3+} concentration broad channels are developed and dissolution takes place only at the tip of these branches, suggests that the active surface area becomes restricted and that the growth perimeter length attains a steady-state. To verify this assumption directly we have measured the time evolution of a single pit grown in the metallic film: pit bottom area increases linearly with time, *i.e.* the dissolution current is constant on the time scale of the experiment.

DISCUSSION

To interpret the above results we must take into account at least two processes which we expect influence pit morphologies: a) At the dissolution sites hydrogen gas bubbling can be observed. This leads to the dilution of the liquid in the vicinity of the active metal surface. This dilution may if significant cause the passivation of the metal surface.
b) The other factor to be considered is the consequence of open circuit conditions. The anodic current corresponding to the dissolution of aluminium must be compensated by cathodic processes. The anodic current density might attain a high limiting value controlled by transport in the liquid phase [9, 14]. The cathodic current is limited by the number of cations reduced on the whole oxide layer (Fig. 1). This limiting current is believed to be proportional to the size of the inactive, oxidized surface and the concentration of Fe^{3+} ions. As time elapses the anodic area and consequently the corrosion current steadily increases, it must be compensated by cathodic processes. Depending on the experimental parameters, this may limit the anodic current and consequently the size of active area since the anodic current density can be regarded as constant. Once this limit is reached the growth of the pattern area must continue linearly in time, as it is experimentally observed.

GROWTH MODEL

Coupled lattices (C-S) for the simulation the electrolyte-metal interaction: The above remarks, suggest to simulate the system by two lattices: the sample surface ($\boldsymbol{S}$) representing the metallic film where the growth takes place, and the adjacent electrolyte layer ($\boldsymbol{C}$) representing the part of the electrolyte directly in contact with the metal. The rest of the electrolyte constitutes a reservoir with a fixed ion concentration with which the ($\boldsymbol{C}$) lattice exchanges ions (by diffusion and convection).

Simulations were carried out on two 512 × 512 square lattices, representing the sample surface $\boldsymbol{S}$ and the adjacent electrolyte layer $\boldsymbol{C}$, respectively. A site on $\boldsymbol{S}$, identified by coordinates (i,j), can be empty, occupied and active, standing for microscopic areas of intact metal layer, sites from which aluminium has already been dissolved and sites at which dissolution is taking place, respectively (see Fig. 3). In the beginning of the simulation all the sites on $\boldsymbol{S}$ are empty except an active seed placed in the middle of the array. At each step the nearest empty neighbors of the active sites, called candidates, are updated. The state of other empty sites will not be changed. The previous active sites are occupied by the growing pattern at each step. If the local aggressiveness of the electrolyte, c_{ij}, exceeds a critical value, c_{cr}, a candidate site s_{ij}, may be activated. Whether the candidate is turned to an active site or not depends also on the actual number of active sites, N_a. (We describe below how the global restriction imposed on N_a influences the activation procedure.) If the site has not been turned to active it becomes empty if it has no more active

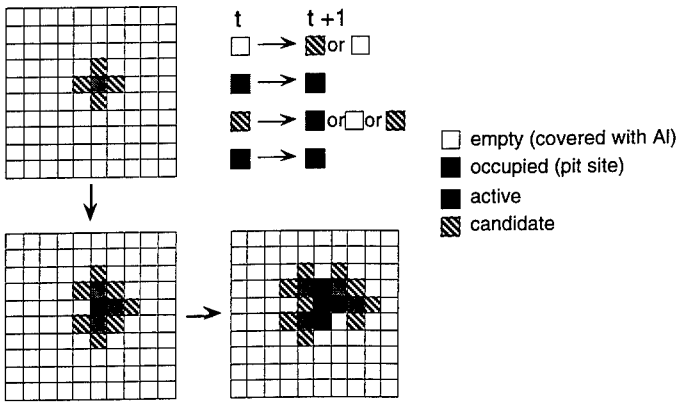


Fig. 3. The first three steps of the growth algorithm.

neighbors; else the site remains candidate if at least one of its first neighbors is an active site. Therefore an already tested but not activated site may become active later. An occupied site stays always occupied. A simple example in Fig. 3 demonstrates the evolution of the pattern.

Accumulation of the corrosion products in the active region

To determine whether a candidate can be transformed to a new active site, the local electrolyte aggressiveness c_{ij}, above the site s_{ij}, is allowed to vary between a bulk value c_0 and a limit corresponding to the saturated salt solution, c_{sat}. Initially c_0 is attributed to each cell on the electrolyteside (C). Once an active site appears on lattice S, the corresponding c_{ij} value will be incremented by a constant (Δc), in agreement with the assumption of constant anodic current density:

$$c_{ij} \longrightarrow c_{ij} + \Delta c. \qquad (1)$$

Diffusion and convection of the aggressive products

The diffusion of aggressive products parallel to the Al layer is simulated by:

$$c_{ij} \longrightarrow (c_{ij} + c_{i-1,j} + c_{i+1,j} + c_{i,j-1} + c_{i,j+1})/5, \qquad (2)$$

while the diffusion normal to the layer corresponds to decreased the aggressiveness according to

$$c_{ij} \longrightarrow c_{ij} - \eta(c_{ij} - c_0), \qquad (3)$$

resulting in an exponential relaxation towards c_0 with the relaxation time:$-1/\log(1-\eta)$. Eq. (3) formally corresponds to the diffusion into the bulk of the electrolyte

Upper limit of the corrosion current

The number of active sites, N_a, *i.e.* the number of "Al-sites" removed between two steps, corresponds to a "corrosion current" in the model which is determined as follows: We consider all the candidate sites, s_{ij}, with a local aggressiveness, c_{ij}, greater then the critical value, c_{cr}. If the number of these sites, N_a^*, is smaller then N_{th}, representing the upper limit of the "corrosion current", all the candidates with $c_{ij} > c_{cr}$ will be activated and consequently $N_a = N_a^*$. Should N_a^* exceed N_{th}, the number of new active sites will be calculated according to

$$N_a \longrightarrow \nu N_a^* \qquad (4)$$

where $\nu \in rnd[\nu_{min}, 1]$.

Stable metal islands (trapping)

In order to simulate the experimental observation that dissolution ceases immediately on a newly formed metal island, which is no more in direct electrical contact with the main Al film, the active sites not on the external perimeter of the growing cluster are transformed to occupied sites after each step, without the possibility of activating any of their empty neighbors. This feature is similar to "trapping" described in invasion percolation models [20].

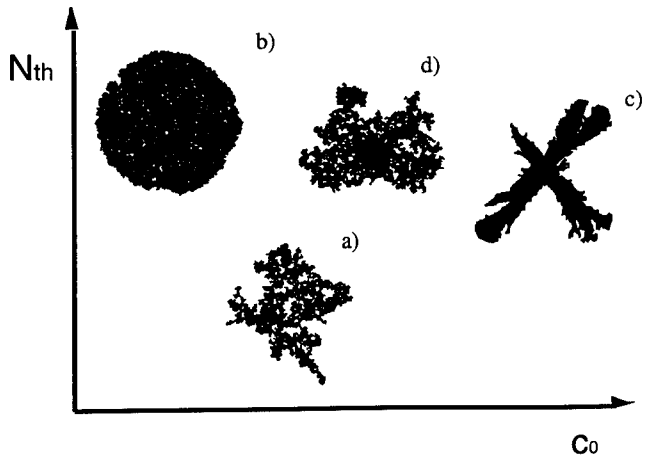


Fig. 4 Simulated pit morphologies as a function of the input parameters of the model.
(a) c0=10, Nth=100;
(b) c0=1, Nth=10000 ;
(c) c0=1000, Nth=200;
(d) c0=368, Nth=200.
Active sites are ran domly distributed over the candidates if c0 << cth, (a) and (b), whereas dense branches develop if c0 >> cth, (c). Mixed morphology is observed if c0 ≈ cth, (d). In (b) Na has not reached the limit, Nth, throughout the simulation .

Fig. 4 shows that variation of c_0 and N_{th} (corresponding to the concentrations of Cl^- and Fe^{3+} ions, respectively) results qualitatively in the same four main morphologies as those observed experimentally.

As a consequence of trapping and the global feed-back employed in Eq. (4), our model falls in the class of non-local growth models. Therefore, instead of talking about the activation of a candidate with a probability p, we define the spreading probability, p_s, globally, as the expectation value of the ratio of the number of active sites at time t, $N_a(t)$, and the number of candidates at $t-1$, $N_c(t-1)$, from which the $N_a(t)$ active sites have been selected. The spreading probability, p_s, is determined by Δc, c_{th} and h_{max} in a nontrivial way and does not appear explicitly in our model. The value of p_s defines a characteristic length, ξ, below which the growing cluster exhibits fractal properties. Above the correlation length ξ the cluster goes over to a circular structure, (see Fig. 4 (b) for which the value of ξ is of the order of a few intersite distances, *i.e.* p_s is far above the percolation threshold, p_{sc}).

The limit on the number of active sites acts as a negative feed-back on the spreading probability. If $N_a > N_{th}$, Eq. (4) comes into effect and the number of new active sites will be smaller than it would follow from the value of p_s. Formally this corresponds to an instantaneous drop in spreading probability below the percolation threshold. After N_a has been forced under N_{th} (via Eq. 4), the growth process is determined by the initial value of p_s again as long as $N_a < N_{th}$, *i.e.* until the next fall in the number of active sites.

Correlated growth (case (c) and (d))

At high c_0 diffusion is the dominating process on the electrolyte side which introduces long term memory in the growth. As it is shown in Fig. 4(c), if N_a is limited, dense branches are developed. The ratio $N_a(t)/N_c(t-1)$ undergoes large fluctuation and p_s remains in the vicinity of 1 showing that the active sites form long contiguous fronts. As long as $N_a < N_{th}$, the growth is essentially two-dimensional turning into a linear one once the upper limit, N_{th}, has been reached by the number of active sites.

Intermediate values of c_0 and N_{th} reproduce the mixed morphology in which case irregular and smooth dissolution fronts propagate simultaneously (Fig. 4(d)). The beginning of the growth is similar to the case (c) but long fronts of the active sites are not stable in this regime. This property is clearly manifested by the violent fluctuation of $N_a(t)/N_c(t-1)$. The crossover from two-dimensional to linear growth is slower than in the previous case.

REFERENCES

1. F. Mansfeld, ed., Corrosion Mechanisms (Marcel Dekker, New York, 1987).
2. F. P. Ford, G. T. Burstein and T. P. Hoar, J. Electrochem. Soc. **127,** 1325 (1980).
3. G. T. Burstein, D. H. Davis, J. Electrochem. Soc. **128,** 33 (1981).
4. G. T. Burstein, R. C. Newman,J. Electrochem. Soc. **128,** 2270 (1981).
5. G. S. Frankel, B. M. Rush, C. V. Jahnes, C.E. Farrell, A. J. Davenport and H. S. Isaacs J., Electrochem. Soc. **138,** 643 (1991).
6. Z. Szklarska-Smialowska, Corrosion **27,** 223 (1971).
7. J. M. Costa, F. Sagués and M. Vilarassa, Corros. Sci. **32,** 665 (1991).
8. T. Nagatani Phys. Rev. A, **45,** 2480 (1992).
9. T. Nagatani Phys. Rev. A, **45,** 6985 (1992)
10. P. Meakin, T. Jøssang and J. Feder, Phys. Rev. E **48,** 2906 (1993).
11. R. Reigada, F. Sagués and J. M. Costa, J.Chem.Phys. **101,** 2329 (1994).
12. M. Baumgärtner, H. Kaesche, Corros. Sci **29,** 363 (1989).
13. T. Nagatani, Phys. Rev. Lett. **68,** 1616 (1992).
14. G.S. Frankel, Corros. Sci **30,** 1203 (1990).
15. G.S. Frankel, J. O. Dukovic, V. Brusic, B. M. Rush and C. V. Jahnes, J. Electrochem. Soc. **139,** 2196 (1992).
16. L. Balázs, L. Nyikos, I. Szabó and R. Schiller, Fractals **1,** 416 (1993).
17. T. Holten, T. T. Jøssang P. Meakin and J. Feder, Phys. Rev. E **50,** 754 (1994).
18. L. Balázs, and J.F. Gouyet, Physica A **217,** 319 (1995).
19. B. Sapoval, M. Rosso, J-F. Gouyet, in: The Fractal Approach to Heterogeneous Chemistry, D. Avnir, Ed. (John Wiley & Sons, 1989) p. 227.
20. R. Chandler, J. Koplik, K. Lerman, J. Willemsen, J. Fluid Mech. **119,** 249 (1982).

FRACTAL GROWTH OF CLUSTERS AND PORES DURING ANNEALING OF ALUMINUM THIN FILMS DEPOSITED ON SILICA.

Vincent FLEURY, Lazlo BALAZS and Franck DUCLOS
Laboratoire de Physique de la Matière Condensée,
Ecole Polytechnique, Palaiseau, France.

ABSTRACT

Annealing of an Al thin-film on SiO_2 at temperatures in the range 400-660°C leads to a chemical reaction (oxidation of Al and reduction of Si) whih proceeds *via* irreversible growth of 2-D aggregates which belong to a class of clusters first described in MBE.

I.INTRODUCTION.

In the past ten years, Diffusion Limited Aggregation[1] has served as a paradigm for the study of fractal growth of branched structures driven by a Laplacian field. A recent development of the DLA model[2-8], which includes a constant flux of particules, is able to reproduce the range of shapes, -from DLA fractal to compact- which are observed in Molecular Beam Epitaxy and related «deposition-diffusion-aggregation» experiments[8-11]. We present in this article a new system in which growth of aggregates is observed, which belongs to a DLA model with an additional constant flux of "particles". The experiment consists in annealing aluminum thin films deposited on silica [temp. range 400°C-660°C]. A genuine chemical reaction, involving reduction of the silica and oxidation of the aluminum, leads to irreversible growth of aggregates which are well described by the recent models developped for MBE. A morphology diagram can be elaborated as a function of temperature and annealing time. Large DLA structures are obtained at high temperature and short annealing times. Several thousands of patterns are obtained on a single sample. At low temperature two dimensional pores are also observed, which may be related to a 2-D Kirkendall effect.

II. PATTERN FORMATION BACKGROUND.

Several authors have reported growth of branched DLA-like structures during growth or annealing of thin films. For example Radnoczi *et al* [12] have reported that, when an amorphous film of $SeGe_2$ is annealed, a crystalline phase grows, at the expense of the amorphous phase. The structure of the crystal phase is strikingly similar to DLA aggregates. Also Zhang *et al*[13] have reported that silver atoms deposited on tin oxide can form DLA-like clusters when the substrate temperature is lowered below the melting point of silver. Elam *et al* have observed the formation of DLA clusters during sputter deposition of $NbGe_2$ films[14]. Finally, Chabala[15] has reported that oxidation of liquid gallium by an external flux of oxygen occurs *via* formation of DLA clusters of gallium oxide, at least in the first stages of the process.

A different instance, still related to surface and thin-film science, in which DLA aggregates are formed, is provided by Molecular Beam Epitaxy. In MBE experiments, a supersaturated vapor is formed on top of a substrate on which a (possibly different) material nucleates and grows. In the last five years, a lot of attention has been dedicated to the very first stages of MBE, when the deposit thickness is smaller than a few atomic layers. In this instance, the film growth is controled by : i)The Diffusion of the adatoms. ii)The external flux of adatoms. iii)The critical size for homogeneous island formation. iv)Heterogeneous nucleation, if any.

The main control parameter[2-8] is the ratio D/Φ of the diffusion constant D over the external flux Φ. Depending on time, or, in a rescaled variable, depending on the surface coverage η, a morphology diagram can be constructed. Schematically, one observes DLA fractals as long as the ratio D/Φ is large and time is small. These DLA fractals grow almost up to percolation. Next they compactify, percolate and form a continuous film. If D/Φ is small, the patterns are rather compact from the very start, they remain compact while they grow, and, eventually, they percolate and form a continuous layer. Fig. 1 shows the morphology as a function of D/Φ and η, reprinted from Ref.[5]. These features have been observed experimentally by several groups[8-11].

Mat. Res. Soc. Symp. Proc. Vol. 407 © 1996 Materials Research Society

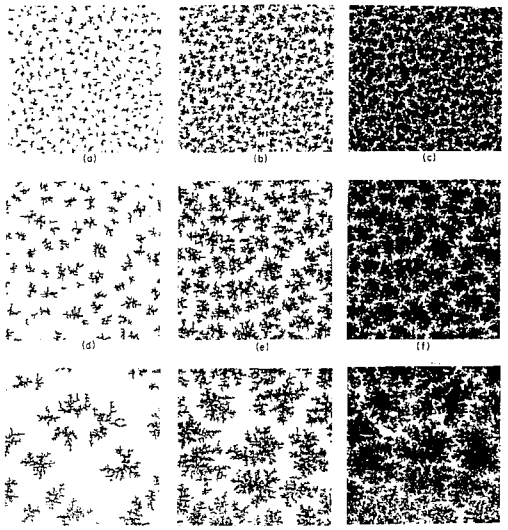


Figure.1 Morphological diagram showing the cluster shape as a function of surface coverage and ratio D/Φ (Ref[5]). large DLA-like patterns are obtained at short times and large values of D/Φ. In all cases, the patterns become compact and percolate in the late stages of the process (high coverage).

We now present a new thin-film experiment, quite different from the ones reported above, which is conceptually very close to the MBE models described above.

III. EXPERIMENTAL.

The experiment consists in annealing aluminum thin films (thickness ~1000Å) which are deposited on silica. We have used pure silica (99.999 polished to optical precision), and also soda-lime glass (microscope slides) and crystallized glass (Acticeram[16]).The aluminum film was obtained by evaporating Al 99.999% in a custom evaporator jar. The films were annealed in a custom furnace under nitrogen flow (N_2 5ppm) with annealing times ranging from 30secs. (at temperatures above 600°C) to several days (400°C). In a first series of experiments the reaction could not be observed in situ. The samples were withdrawn, photographed under a microscope Nikon Optiphot 2, and put back into the furnace.(With a more recent set up, we are able to film the sample surface during the process). Let us insist that the reaction of Al on SiO_2 has been studied by a few authors[17-22], because Al/SiO_2/Si capacitors were (and still are) extensively used in computer hardware, and because the Al/SiO_2 interface was found not to be stable. The capacitors have been reported to breakdown, especially at temperatures above 400°C. Some authors report that the breakdown tendency is due to "quite massive defects" or to "small crystallized regions"[19]. The fractal patterns that we report on here have escaped previous studies, but may well be the same thing as those «defects». The very same reaction has also been studied in the context of composite materials, because fiber-glass reinforced aluminum makes a light and strong material. Let us not forget that the reduction of silica by aluminum has long been known, and was even proposed once as a possible path for silicon production[23].

IV RESULTS.

IV.a General trends.

In the temperature range 400-660°C, the aluminum film oxidation is activated (Fig. 2), and lasts between about 3 days (400°C) and 30 seconds (660°C), the activation energy is about 1.5eV. As oxidation progresses, the aluminum film becomes more and more translucent and it loses its silverish aspect. A microscopic observation of the film reveals that a transparent phase nucleates on the film. For example, after only one hour at 440°C, a lot of transparent nuclei appear on the film, as observed by transmission illumination under an optical microscope (Fig. 3). When magnified, these nuclei appear as very irregular islands which are embedded in the film (Fig. 4).

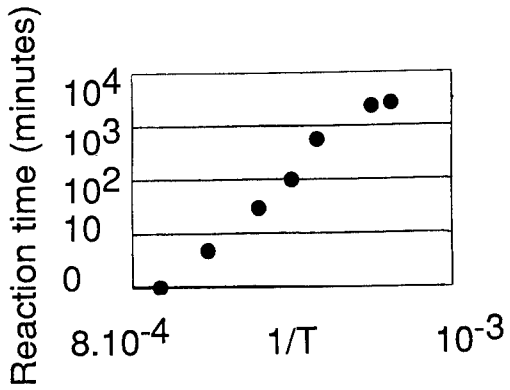


Figure 2. The reaction time as a function of temperature. The reaction is activated, and lasts between several days (400°C) and a few tens of seconds (T~640°C).

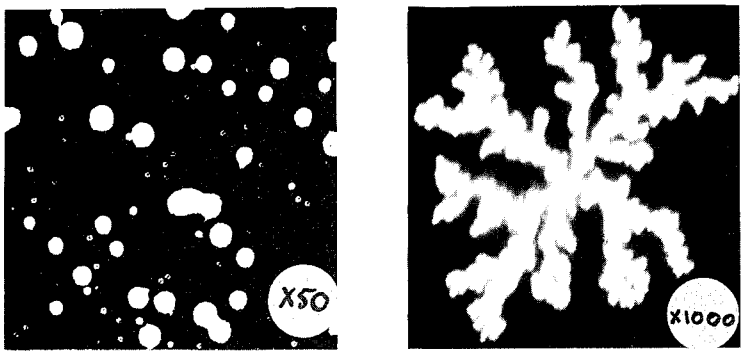


Figure 3. General aspect of the aluminum film, at low magnification. At short annealing times (very small coverages) a lot of transparent nuclei appear on the surface.
Figure 4. When magnified, the nuclei appear as irregular islands, with a shape reminiscent of small DLA patterns. Note that several thousands of patterns are formed on a sample 1cmx1cm.

As the reaction progresses, the number of nuclei and the sizes of the islands increase. Also, the aluminum film surrounding the islands becomes more and more transparent and white; as explained below, the aluminum is oxidized to alumina. The color of the irregular islands is generally yellow.

IV.b. Morphology Diagram.

The morphology of the islands is not unique, and it changes with time. It is therefore necessary to elaborate a morphology diagram. The result, as encapsulated in Fig. 5 is the following. At high temperatures (T>600°C), the patterns grow very quickly (in a few minutes) and are DLA-like almost up to percolation. In the next few minutes, the patterns compactify, and the film becomes a random distribution of compact patches surrounded by a white material (alumina). At lower temperatures, the process is much slower. The patterns are DLA-like only at very early times (small coverages). Large branched structures are not formed. Instead, the patterns become rapidly compact, though irregular, and remain compact up to percolation. Fig.6A shows the patterns at the very beginning and at the end of the process, at low temperature, Fig. 6B, shows the same thing at high temperature. The largest patterns were one millimeter in diameter (Fig.7). Fractality was observed from the micron range up to the cluster size .

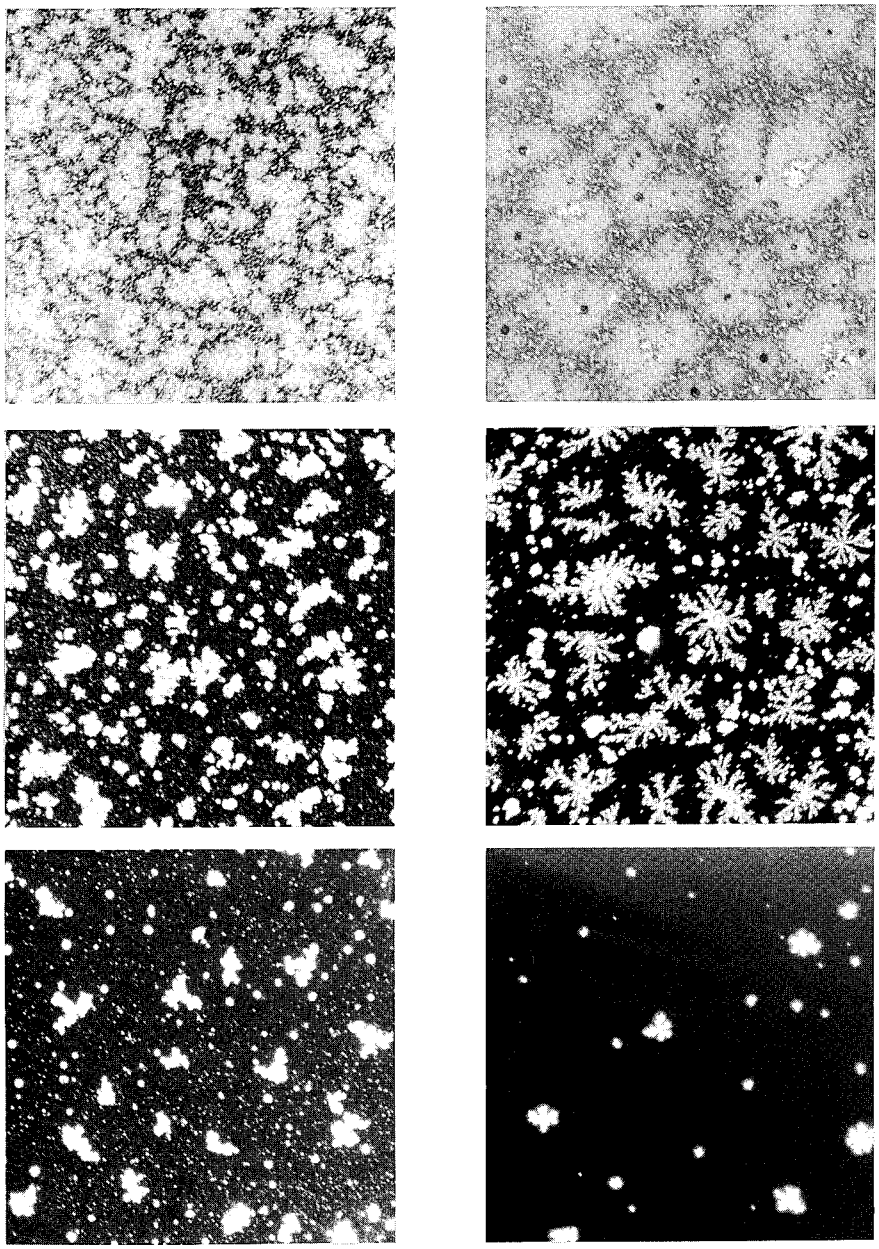
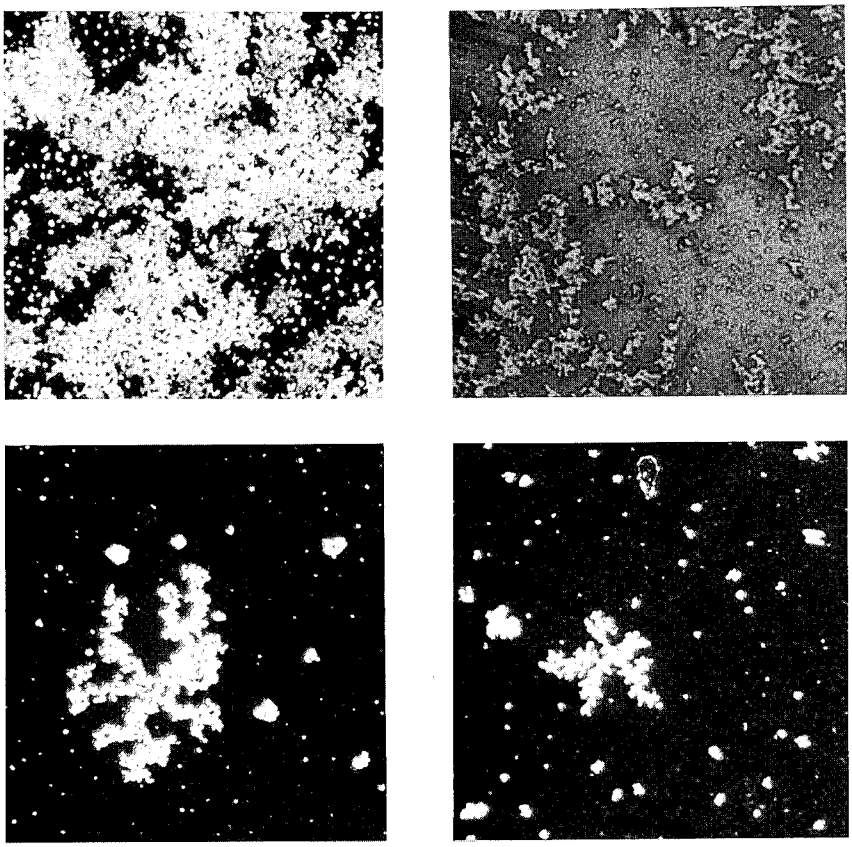


Figure 5. Morphological diagram. Magnification 200x. Left column 530°C, right column 600°C. The reaction times are 30hours at 500°C and only 30 minutes at 600°C.



A B

Figure 6. Close view (x1000) of the sample surface in early stages, and late stages of the process, at temperature 500°C (A) and 600°C (B). At small coverages, the patterns are always ramified. At high coverages, they always become compact. The patterns are surrounded by alumina. The reaction stops when metal Al is exhausted.

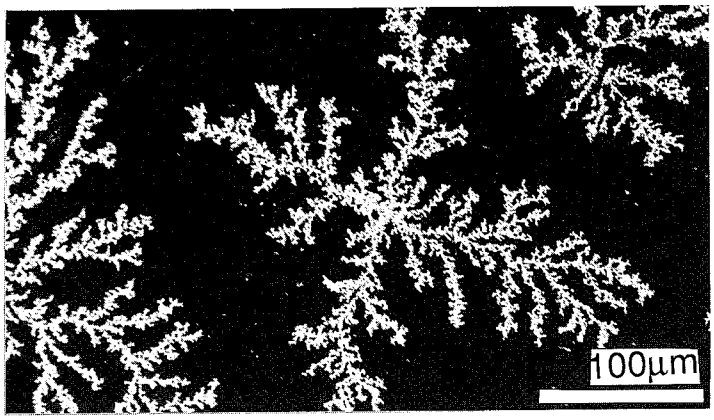
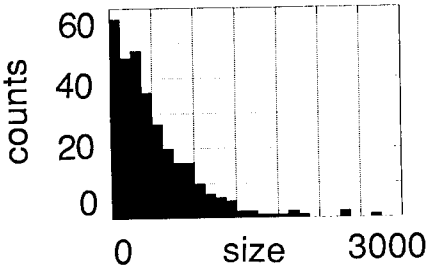


Figure 7. A typical large pattern obtained at 600°C on the ceramic. The fractal dimension was found to be 1.66 (averaged over 20 patterns).

IV. c. Nucleation.

As demonstrated by many authors[5], the distribution of island sizes as a function of surface coverage, in MBE, depends basically on whether the island growth starts by homogeneous or heterogeneous nucleation. If nucleation is homogeneous, then the distribution function possesses a minimum at small and large island sizes. If nucleation is heterogeneous, then the island size distribution has a maximum at small sizes (small islands keep on nucleating, and they are always more numerous than larger islands). In the experiment reported on here, the distribution of island sizes always corresponds to an heterogeneous nucleation (Fig. 8), a fact which needs not surprise us.



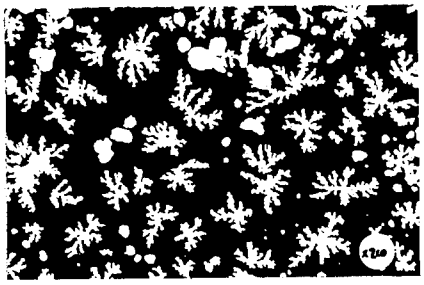


Figure 8. Distribution of sizes for a sample at temperature 640°C annealed for a few minutes. In this instance, the patterns are DLA-like almost up to percolation, while the surrounding film is only partially oxidized.The shape of the curve reveals that small clusters dominate. This feature was observed at all temperatures.

So far, we were unable to extract a «universal» function for the distribution function, from our datas. In practical instances, one is forced to analyze parameter ranges in which a reasonable number of islands is observed with a reasonable size distribution (and with a good contrast), which limits the analysis. Work is in progress on this issue.

IV.d. Chemical Analysis.

Of course, one would like to know the exact formulae of the materials which are formed. It has been shown by several authors[17-22] that in the experiment which we report on here, the only products of reaction are silicon and alumina. We have performed EDX analysis on the samples, and correlated it to the cluster morphology. The conclusions are that :
i)The aluminum film is progressively and homogeneously oxidized; ii)The clusters are silicon rich and aluminum poor; iii)There is very little silicon in the surroundings of the clusters.

We shall not enter into details here, but it should be acknowledged that we cannot yet

give a quantitative stoechiomery for the material in the patterns. The X-peaks give a similar concentration of Al and Si in the clusters, and an Al concentration 5 times as small in the patterns as in the surrounding film, but a quantitative interpretation is difficult because the EDX analysis is performed over a sphere of interaction which is larger than the film thickness. EDX maps show clearly the anti-correlation between Al and Si concentrations (Fig. 9).

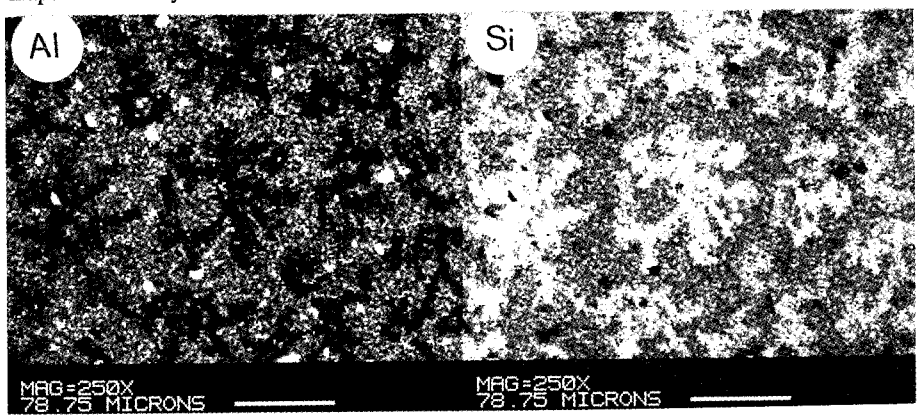


Figure 9. The concentration maps of Al and Si as measured by EDX. Rich zones appear lighter in colour. In the center of the scanned area on observes a typical cluster, which is rich in Si and Al depleted. The Al X-peak is 5 times as large in the film as in clusters. The Si and Al X-peaks in the clusters are similar.

IV.e. Pore formation

At low temperatures (400-450°C) formation of holes (pores) in the film was observed. The DLA patterns were found to grow in an anti-correlated manner, in between large white holes ressembling percolation clusters and having a fractal dimension 1.75 (Fig.10). Apparently, the formation of holes provides the diffusing species to the DLA patterns. We conjecture that the holes are linked to Al diffusion towards the substrate, which, after reacting on silica provides the diffusing Si for the DLA clusters. It should be noted that the diffusion coefficient of Si in Al is much larger than the diffusion coefficient of Al in Al (self-diffusion)[30]. Therefore, the Kirkendall interface[24,25] moves towards the substrate. It may be possible that, as a consequence of vacancy precipitation, 2-D pores are formed on the film.

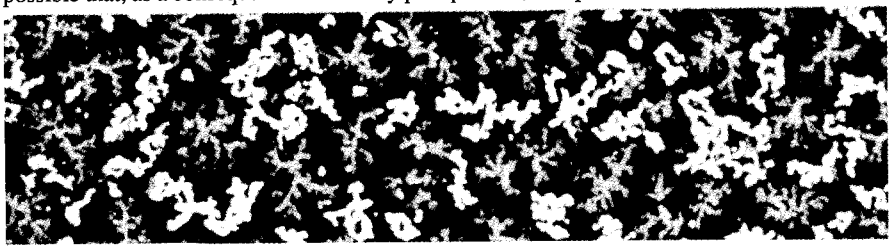


Figure 10. Clusters and pores formed at low temperature (T=440°C, substrate=soda-lime glass, annealing time 40h). The clusters and pores distributions are anti-correlated. In some sense, the pores are the outer source of a DLA process which occurs in between them. The fractal dimension of the pores was found to be close to 1.75

V. INTERPRETATION and CONCLUSION.

Existing studies of the reaction of Al on SiO_2 and our data strongly support the following reaction mechanism. On a thin layer at the Al/SiO_2 interface, interdiffusion brings Al and SiO_2 in contact, The Si--O bonds are disrupted, oxygen does not diffuse very far (a few

hundred of Ångstroms at most) and oxidizes almost immediately the aluminum (hence the homogeneity of the Al oxidation, and the progressive change of colour). The silicon which is released in the film diffuses and precipitates on the clusters which are made of a silicon-rich material which could well be crystalline silicon (hence the diffraction peaks), or a mullite. The flux of silicon into the film is determined essentially by the interdiffusion of the species across the interface in the direction perpendicular to the film, and by the reaction. It is thermally activated. Diffusion of Si in the film is also thermally activated[24,25]. The cluster growth is irreversible, and limited by the diffusion of silicon in the film towards the patterns, and possibly the diffusion of Al away from them. As long as metal Al is not exhausted there is an «external» flux of silicon around and inside the clusters provided by the reaction.

As we see, if this scenario is correct, then the reaction is, at least in principal, very close to the growth process described by the MBE models. The morphology diagrams, in particular, point to a mechanism of this sort. However, in our case we do not control independently the flux and the diffusion constant of Si. They both depend on a single parameter which is the temperature. Observation of the morphology diagram shows that the ratio D/Φ is not constant, and that it increases with temperature, since the larger DLA patterns are obtained at higher temperatures. Therefore Si diffusion in 2-D, in the film, increases more rapidly with an increase in temperature than the reaction *accross* the SiO_2/Al interface. (The activation energy of diffusion should be larger than the activation energy of reaction). Also, the data clearly show that the clusters nucleate on defects, which are often visible in the center of the patterns.

ACKNOWLEDGEMENTS.

We acknowledge the invaluable help of P.Barboux, F. Chaput, J.-P. Boileau, A. van Herpen, N. Lequeux, P. Bertrand, R. Geoffroy, A. Barbu and of the "Groupe Irregularité et Milieux Confinés" of the Laboratoire de Physique de la Matière Condensée.

REFERENCES and NOTES.

[1]T. A. Witten and L. M. Sander, Phys. Rev. Lett. **47**, 1400 (1981).
[2]M. C. Bartelt and J. W. Evans, Phys. Rev. B **46**,12675 (1992).
[3]L. H. Tang, J. Phys. (Paris) **123**, 935 (1993).
[4]G. S. Bales and D. C. Chrzan, Phys. Rev. B **50**, 6057 (1994).
[5]J. G. Amar, F. Family and P. M. Lam , Phys. Rev. B **50**, 8781 (1994).
[6]J. G. Amar and F. Family, Mat. Res. Soc. Symp. Proc. Vol. **367**, 149, (1995).
[7]P. Jensen, A.-L. Barabasi, H.Larralde, S. Havlin and H. E. Stanley, Phys. Rev B **50**, 15 316 (1994).
[8]L. Bardotti, P. Jensen, A. Hoareau, A.Treilleux and B. Cabaud, Phys. Rev. Lett. **74**, 4694 (1995) In this experiment, the diffusion specie is composed of atom clusters.
[9]R. Q. Hwang, J. Schroder, C. Gunther and R. J. Behm, Phys. Rev. Lett. **67**, 3279 (1991).
[10]T. Michely, M. Hohage, M. Bott and G.Comsa, Phys. Rev. Lett. **70**, 3943 (1993).
[11]D. D. Chambliss and R. J. Wilson, J. Vac. Sci. Technol. B **9**, 928 (1991).
[12]G. Radnoczi, T. Vicsek, L. M. Sander and D. Grier, Phys. Rev. A **35** R4012 (1987). In this experiment, the diffusing specie is not clearly identified, it is conjectured that Se is expelled from the crystal and diffuses away.
[13]J. Zhang, D. Liu and K. Colbow, Phys. Rev. B **48**, 9130 (1993).
[14]W. T. Elam, S. A. Wolf, J. Sprague, D. U. Gubser, D. Van Vechten and G. L. Barz and P. Meakin, Phys. Rev. Lett. **54**, 701 (1985).
[15]J. M. Chabala , Phys. Rev. B. **46**, 11346 (1992). In this experiment, the diffusing species is Oxygen.
[16]The ceramic used was Acticeram, purchased from Préciver (Maisons-Alfort, France). Acticeram is a slowly crystallized glass which can sustand a temperature of 850°C without significant deformation.
[17]A. E. Standage and M. S. Gani, J. Am. Ceram. Soc. **50**, 101 (1967).
[18]R. Silverman, J. Electrochem. Soc. **115**, 674 (1968).
[19]N. J. Chou and J. M. Eldridge, J. Electrochem Soc. **117**, 1287 (1970).
[20]K. Prabriputaloong and M. R. Piggott , J. Am. Ceram. Soc. **56**, 184 (1973).
[21]K. Prabriputaloong and M. R. Piggott, J. Am. Ceram. Soc. **56**, 177 (1973).
[22]K. Prabriputaloong and M. R. Piggott, J. Electrochem. Soc. (Solid State Science and Technology) **121**, 430 (1974).
[23]Vigouroux, Ann. Chim. Phys. 12-153-1897.
[24]I. Adda and P. Phillibert, La Diffusion dans les Solides, Presses Universitaires de France, Paris (1966).
[25]S.-I. Fujikawa, K.-I. Hirano and Y. Fukushima, Meta. Trans. A, **9A** 1811, (1978).

GROWTH EQUATION WITH A CONSERVATION LAW

KENT BÆKGAARD LAURITSEN
Center for Polymer Studies and Dept. of Physics, Boston University, Boston, MA 02215
Address from 1 Feb 1996: Center for Turbulence and Chaos Studies, Niels Bohr Institute, Blegdamsvej 17, 2100 Copenhagen Ø, Denmark
Email: kent@juno.bu.edu

ABSTRACT

We investigate an interface growth equation with a conservation law. The interaction is characterized by an integral kernel. The equation contains the Kardar-Parisi-Zhang, Sun-Guo-Grant, and Molecular-Beam Epitaxy growth equations as special cases and allows for a unified investigation of growth equations. We perform a dynamic renormalization-group analysis and determine the scaling behavior and universality classes for such growth models with a conservation law.

INTRODUCTION

Nine years ago Kardar, Parisi, and Zhang (KPZ) introduced a Langevin equation which now has become the paradigm for modeling nonequilibrium interface growth [1, 2, 3]. The appearance of interfaces are common in nature and many experimental results exist for the scaling properties characterized by the roughness exponent α and the dynamic exponent z [4]. The predictions obtained from the KPZ equation, however, do not in general agree with those obtained in experiments. Therefore, there is still a big need to explore other interface growth equations in order to determine universality classes.

Here, we investigate a growth equation characterized by an integral kernel. We will refer to the equation as the kernel equation. It contains the KPZ equation as a special case. In addition, the previously studied Sun-Guo-Grant (SGG) [5] and Molecular-Beam-Epitaxy (MBE) [6] equations are also contained in our general equation.

The kernel equation for a d dimensional interface $h(x,t)$ reads

$$\frac{\partial h}{\partial t} = \int d^d x' \, K(x-x') \left(\nu \nabla'^2 h + \frac{\lambda}{2} (\nabla' h)^2 \right) + \eta(x,t), \tag{1}$$

with a surface tension term described by ν, a nonlinear term with strength λ, and an additive noise $\eta(x,t)$ whose correlations will be specified below. The integral kernel $K(r)$ describes nonlocal interactions in the system [7]. Equations with such a kernel has been previously investigated in, e.g., the dynamics of Ising systems [7], fluctuating lines in quenched random environments, and domain walls subjected to quenched long-range correlated impurities [8].

Our motivation for introducing the kernel equation is to gain information on how conservation laws change the universality classes for nonequilibrium growth models, and to allow for a *unified* description of growth models studied so far. Furthermore, one can speculate whether some growth experiments, which yield exponents that do

Mat. Res. Soc. Symp. Proc. Vol. 407 © 1996 Materials Research Society

not agree with the KPZ exponents, may contain nonlocal growth effects such as, e.g., the experiments on electrochemical deposition reported in Refs. [9, 10].

The kernel $K(r)$ has the behavior

$$K(r) \sim \frac{1}{r^{d+\sigma}} \quad \text{for} \quad r \to \infty, \tag{2}$$

characterized by an exponent σ describing the long-distance decay. By Fourier transforming, one notes that $\sigma = 0$ corresponds to the kernel being a Dirac delta function, and therefore the usual KPZ equation [1]. The case $K(x - x') = -\nabla_x^2 \delta^d(x - x')$ yields the dynamics of the SGG and MBE equations [5, 6], and corresponds to $\sigma = 2$. In order to incorporate these equations, we introduce a kernel $N(r)$ in the noise correlator

$$\langle \eta(x,t)\eta(x',t') \rangle = 2D\, N(x - x')\delta(t - t'), \tag{3}$$

with the form

$$N(r) \sim \frac{1}{r^{d+\tau}} \quad \text{for} \quad r \to \infty. \tag{4}$$

Here, τ is an exponent independent of σ. Note that $\tau = 0$ means no correlations in the noise (KPZ, MBE) whereas $\tau = 2$ corresponds to conserved noise as it appears in, e.g., the SGG equation.

We want the total height $H(t) = \int d^d x h(x,t)$ to be a conserved quantity and impose the constraint $\int d^d x'\ K(x - x') = 0$. This leads to $\partial H/\partial t = 0$ (for $\tau, \sigma > 0$), since the noise satisfies $\eta(k = 0, t) = 0$ (follows from Eq. (3)). As a result, the kernel equation conserves the quantity $H(t)$.

RENORMALIZATION GROUP ANALYSIS

By performing the rescaling $x \to x' = x/b$, the parameters change as

$$\nu \to \nu' = b^{z-2-\sigma}\nu, \tag{5}$$

$$\lambda \to \lambda' = b^{z+\alpha-2-\sigma}\lambda, \tag{6}$$

$$D \to D' = b^{z-2\alpha-d-\tau} D. \tag{7}$$

For $\lambda = 0$, the solution of the kernel equation is described by the linear exponents

$$z_0 = 2 + \sigma, \qquad \alpha_0 = \frac{2 + \sigma - d - \tau}{2}. \tag{8}$$

Using these values in the rescaling for λ, we obtain $\lambda' = b^{(2+\sigma-d-\tau)/2}\lambda$, so naively we expect the critical dimension of the model to be $d_c = 2 + \sigma - \tau$. For $d > d_c$ the λ term will scale to zero, whereas for $d < d_c$ the λ term will be relevant and the scaling behavior of the kernel equation will no longer be described by the linear exponents.

Now we will carry out a dynamic renormalization group (RG) analysis in order to determine the scaling behavior of the kernel equation. We Fourier transform the kernel equation (1) and obtain in the hydrodynamic limit $k \to 0$,

$$\begin{aligned} h(k,\omega) &= G_0(k,\omega)\eta(k,\omega) - \frac{\lambda}{2} G_0(k,\omega)\, k^\sigma \int^\Lambda \frac{d^d q}{(2\pi)^d} \\ &\times \int_{-\infty}^{\infty} \frac{d\Omega}{2\pi}\, q \cdot (k - q)\, h(q,\Omega)\, h(k - q, \omega - \Omega), \end{aligned} \tag{9}$$

where $G_0(k,\omega)$ is the propagator defined by the expression $G_0(k,\omega) = 1/(\nu k^{2+\sigma} - i\omega)$. Λ is the momentum cutoff. The noise in Fourier space takes the form

$$\langle \eta(k,\omega)\eta(k',\omega')\rangle = 2D\, k^{\tau}\, (2\pi)^{d+1}\delta^d(k+k')\delta(\omega+\omega'). \tag{10}$$

The renormalization group consists of coarse-graining followed by rescaling [11]. In the coarse-graining procedure, modes with momenta $e^{-\ell} < k < 1$ ($\Lambda \equiv 1$) are eliminated from the equation of motion. After performing the coarse-graining, wavevectors are rescaled according to $k \to k' = bk$, with $b = e^{\ell}$. The RG procedure is most efficiently carried out by the means of diagrams, i.e., we represent the kernel equation (9) as shown in Fig. 1, cf. Refs. [1, 12, 13].

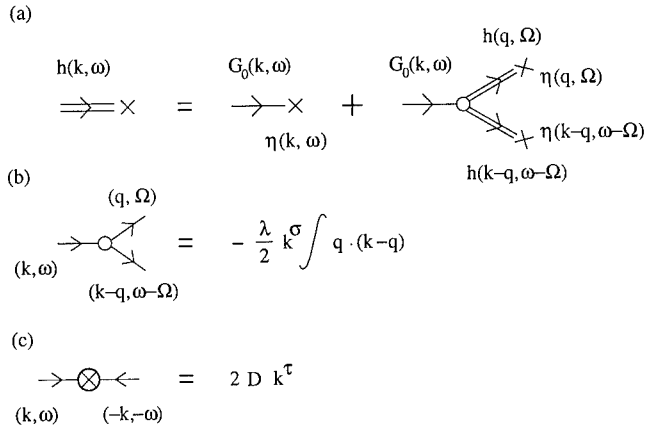


Figure 1: (a) Diagrammatic representation of the kernel equation (9). (b) The vertex λ which includes integration over (q,Ω). The $q\cdot(k-q)$ is associated with the outgoing momenta; $\int \equiv \int^{\Lambda} \frac{d^dq}{(2\pi)^d}\frac{d\Omega}{2\pi}$. (c) The contracted noise $2Dk^{\tau}$, from Eq. (10).

The one-loop RG flow for the parameters in the kernel equation reads [14, 15]

$$\frac{d\nu}{d\ell} = \nu\left(z-2-\sigma+K_d\,\frac{\lambda^2 D}{\nu^3}\,\frac{2+2\sigma-\tau-d}{4d}\right), \tag{11}$$

$$\frac{d\lambda}{d\ell} = \lambda\,(\alpha+z-2-\sigma), \tag{12}$$

$$\frac{dD}{d\ell} = \begin{cases} D\,(z-2\alpha-d-\tau), & \tau < 2\sigma, \\ D\,(z-2\alpha-d-\tau+\frac{K_d}{4}\frac{\lambda^2 D}{\nu^3}), & \tau \geq 2\sigma, \end{cases} \tag{13}$$

where $K_d = S_d/(2\pi)^d$, and $S_d = 2\pi^{d/2}/\Gamma(d/2)$ is the surface area of the d dimensional unit sphere. Due to the fact that λ does not renormalize to one-loop order, cf. Eq. (12), one obtains the exponent relation

$$\alpha + z = 2 + \sigma. \tag{14}$$

In addition, the non-renormalization of the noise for $\tau < 2\sigma$ (a result which will be valid to all orders) leads to the relation $z = 2\alpha + d + \tau$.

RESULTS

In order to study the RG flow, it is convenient to introduce the coupling constant $g = g(\ell) = K_d\lambda^2 D/4d\nu^3$. First, we identify the fixed points (FP's) for the flow of g, and next we calculate the critical exponents at the fixed points. The critical exponents are determined from $d\nu/d\ell = 0$ and $dD/d\ell = 0$.

The case $\tau \geq 2\sigma$: We note that for any $\tau > 2\sigma$ we get the behavior for $\tau = 2\sigma$, and therefore we only have to discuss the latter case [14]. The critical dimension is $d_c = 2 - \sigma$. With $\epsilon = d_c - d$, the nontrivial FP becomes for $\sigma \neq \frac{1}{2}$

$$g^* = \frac{\epsilon}{2(2\epsilon + 2\sigma - 1)} = \frac{\epsilon}{2(2\sigma - 1)} + O(\epsilon^2). \tag{15}$$

For $0 \leq \sigma \leq \frac{1}{2}$: Here, g^* is negative, and a FP expansion in powers of ϵ does not exist (which is known to be the case also for the KPZ equation). In order to obtain the exponents we can use the one-loop result of the g^* fixed point. For the KPZ equation this gives the exact exponents in $d = 1$ (cf. [1]), but despite this the method is uncontrolled due to the fact that g^* (or λ^*) is not small at the FP, which has been the underlying assumption under the whole RG calculation. The direct substitution of g^* into the expressions for the exponents results in the values

$$\alpha = \frac{(2-d)(2-\sigma-d)}{2(3-2d)}, \qquad z = 2 + \sigma - \frac{(2-d)(2-\sigma-d)}{2(3-2d)}. \tag{16}$$

In $d = 1$, this yields $\alpha = (1-\sigma)/2$, and $z = 3(1+\sigma)/2$, which for $\sigma = 0$ reduces to the KPZ exponents [1].

For $\sigma > \frac{1}{2}$: In this interval, the ϵ expansion is possible. We can obtain the exponents to first order in ϵ at the $O(\epsilon)$ fixed point (15) with the result

$$\alpha = \frac{\sigma}{2(2\sigma-1)}\epsilon + O(\epsilon^2), \qquad z = 2 + \sigma - \frac{\sigma}{2(2\sigma-1)}\epsilon + O(\epsilon^2). \tag{17}$$

The case $\tau < 2\sigma$: For $d > d_c = 2 + \sigma - \tau$ the FP associated with the linear exponents, g_0^*, is stable and describes the scaling behavior. For $d < d_c$ there is a new FP, $g^* = \epsilon/3\sigma$, with $\epsilon = d_c - d$. The exponents at this FP are

$$\alpha = \frac{\epsilon}{3} = \frac{2+\sigma-\tau-d}{3}, \qquad z = 2 + \sigma - \frac{\epsilon}{3} = \frac{d+\tau+2\sigma+4}{3}. \tag{18}$$

These values are consistent with the non-renormalization of λ and D in the case $\tau < 2\sigma$, cf. Eqs. (12) and (13) [16].

CONCLUSIONS

In summary, we have performed a renormalization group analysis of the kernel growth equation (1). This is a growth equation which describes interfaces with a conservation

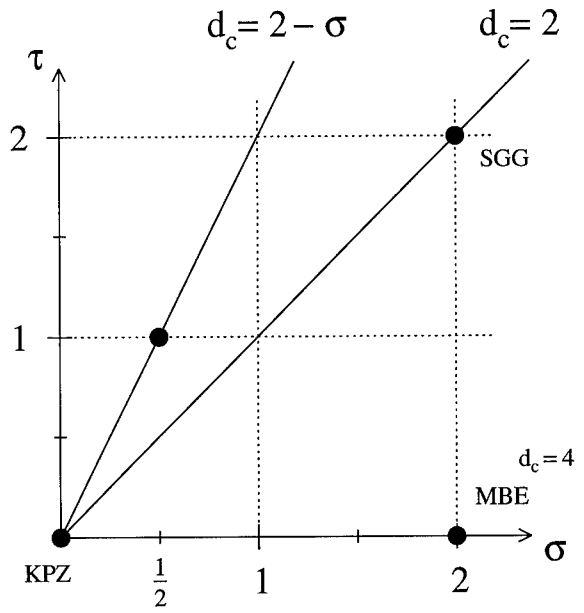


Figure 2: Universality classes and critical dimensions for the kernel equation. For $\tau < 2\sigma$ (below the line $d_c = 2 - \sigma$), every point represents a distinct universality class. For $\tau \geq 2\sigma$, every vertical line represents a different universality class. The KPZ, SGG and MBE models are shown with solid circles. The circle at $\sigma = \frac{1}{2}, \tau = 1$ divides the $\tau = 2\sigma$ line into two parts. The part with $\sigma \leq \frac{1}{2}$ where the ϵ expansion does not exist, and the part $\sigma > \frac{1}{2}$ where the ϵ expansion does exist.

law. In Fig. 2 we show that the equation encompasses a range of different universality classes which includes among others the Kardar-Parisi-Zhang equation.

For $\tau < 2\sigma$, every point represents a distinct universality class, with the SGG and MBE models belonging to this case. For these universality classes we were able to obtain the critical exponents, and the values are given in Eq. (18). Furthermore, the exponents fulfill the relation (14).

For $\tau \geq 2\sigma$, every vertical line represents a different universality class. The KPZ equation belongs to this case. Moreover, we noted the breakdown of the ϵ expansion for $\sigma < \frac{1}{2}$. As a consequence, estimates for the critical exponents could only be obtained by a direct substitution of the g^* FP value into the expressions for the exponents, resulting in the values in Eq. (16). However, for $\sigma > \frac{1}{2}$ the ϵ expansion could be used to obtain the exponent values as given in Eq. (17).

ACKNOWLEDGEMENTS

I acknowledge the financial support from the Carlsberg Foundation and discussions with R. Cuerno. The Center for Polymer Studies is supported by NSF.

References

[1] M. Kardar, G. Parisi and Y.-C. Zhang, Phys. Rev. Lett. **56**, 889 (1986).

[2] J. Krug and H. Spohn, "Kinetic Roughening of Growing Surfaces", in *Solids far from Equilibrium: Growth, Morphology and Defects*, ed. C. Godrèche, Cambridge University Press, Cambridge (1991).

[3] T. Halpin-Healey and Y.-C. Zhang, Phys. Rep. **254**, 189 (1995).

[4] A.-L. Barabási and H. E. Stanley, *Fractal Concepts in Surface Growth*, Cambridge University Press (1995).

[5] T. Sun, H. Guo and M. Grant, Phys. Rev. A **40**, 6763 (1989).

[6] D. E. Wolf and J. Villain, Europhys. Lett. **13**, 389 (1990); Z.-W. Lai and S. Das Sarma, Phys. Rev. Lett. **66**, 2348 (1991).

[7] A. J. Bray, Phys. Rev. B **41**, 6724 (1990); Phys. Rev. Lett. **66**, 2048 (1991).

[8] M. Kardar, J. Appl. Phys. **61**, 3601 (1987).

[9] G. L. M. K. S. Kahanda, X.-Q. Zou, R. Farrell and P.-Z. Wong, Phys. Rev. Lett. **68**, 3741 (1992).

[10] A. Iwamoto, T. Yoshinobu and H. Iwasaki, Phys. Rev. Lett. **72**, 4025 (1994).

[11] S.-K. Ma, *Modern Theory of Critical Phenomena*, Frontiers in Physics, Vol. 46, Benjamin (1976).

[12] E. Medina, T. Hwa, M. Kardar and Y.-C. Zhang, Phys. Rev. A **39**, 3053 (1989).

[13] D. Forster, D. R. Nelson and M. J. Stephen, Phys. Rev. A **16**, 732 (1977).

[14] K. B. Lauritsen, Ph.D. thesis, Aarhus University (1994).

[15] K. B. Lauritsen, Phys. Rev. E **52**, R1261 (1995).

[16] In A. J. Bray and M. Marsili (private communication), it has been argued that under the RG tranformation the noise can also get a white noise contribution. This implies that α will be continuous as a function of τ.

MORPHOLOGY OF THE FUNGUS *Aspergillus Oryzae* AND *Nidulans*

SASUKE MIYAZIMA* and SHU MATSUURA**
*Department of Engineering Physics, Chubu University, Kasugai, Aichi 487 Japan, miyazima@isc.chubu.ac.jp
**School of High-Technology for Human Welfare, Tokai University, Numazu, Shizuoka 410-03, Japan

ABSTRACT

A variety of growth manner of the fungus Aspergillus oryzae and nidulans under varying environmental conditions such as the nutrient concentration, and medium stiffness are investigated, ranging from a homogeneous Eden-like to a ramified DLA-like pattern. The roughness $\sigma(l, h)$ of the growth front of the band-shaped colony, where h is the mean front height within l of the horizontal range, satisfies the self-affine fractal relation under favorable environmental conditions.

1. INTRODUCTION

Mandelbrot has introduced a new concept of fractal and multifractal by surveying a great number of random growth phenomena in nature[1]. Many of these random phenomena can be understood by applying this new concept. The first simple object which was understood with satisfaction is a diffusion limited aggregation[2,3]. The fact that reasonable agreement exists between simulation and experiment provides the stimulus to the recent progresses in fractals[4-8]. A preliminary theoretical understanding of DLA has also been made using several different methods[9-11]. Soon the investigation from the fractal points of view extends to chemistry, biology, geology and so on. For example, polymerization, piling of particles, fracture pattern of soil and so on, are discussed in terms of cluster-cluster aggregations[12,13], the ballistic model[14], fracture model[15] and so on, respectively There are further more too many applications to be mentioned here.

Recently several physicist groups began morphological studies of biological objects, such as cell growth of human retinal vessel[16], as well as colony formation of bacteria[17,18]. On the other hand, the present authors has investigated the pattern formation of growh front in the fungal colony of Aspergillus oryzae.[19]

Mycelium of the filamentous fungi consists of highly branched filaments called hyphae. Individual hyphae are interconnected with each other through the cellular transportation. Further, the neighboring hyphae, or hyphal systems, interact with each other through the competitive nutrient uptake and the secretion of extracellular materials which inhibit growth.

As the fungal colony develops, the mycelium organize a beautiful texture. Although the appearance of colony is generally regarded as inherent to the strain, behaviors of patterning changes exquisitely with the environmental conditions. Manner of growth response may be, to a certain extent, inherent to the strains, and is thought to be selected through the evolutionary processes.

However, since the cells are completely exposed to the environment, hyphal growth is highly subject to the physical conditions such as the diffusion of nutrients and inhibitory materials. Provided that there exists some universal nature of growth response to the environmental conditions, this universal profile might be modelized in terms of simple dynamics.

On the other hand, the flexible nature of branch growth is pretty advantageous for the exploration of patchy nutrient distributions in natural habitats. The peculiarity of growth manner is thought to represent a positive tactics inherent to the strain.

In this study, we observe the colony morphology of some Aspergillus strains with two variables of environmental factors, the nutrient contents and the substrate stiffness, where the lower stiffness affects as an adverse condition for hyphal growth. From the morphology diagram of a wild type Aspergillus oryzae strain and a wild and some colonial mutant strains of Aspergillus nidulans, we make a first step trial to extract the underlying universality of shape responses.

Furthermore, the physiological activities may also have influences on the filament growth, and as a result, on the whole shape of colony. Thus we vary the temperature, this being the most

Mat. Res. Soc. Symp. Proc. Vol. 407 © 1996 Materials Research Society

important physical factor affecting the physiological activities of colonies. There are other factors such as the respiration conditions, autotropism among the growing filaments, and accumulation of waste products. Therefore, the mechanism of colony pattern formation is thought to be more complicated.

In the present study self affine analysis is applied to the growing surface of colonies. The height of a surface point is defined as the distance from the inoculation line. The roughness of the colony surface is estimated by the mean square deviation $\sigma(l, h)$ as a function of the measured mean height h and l within which the data of height are measured. If the surface is self-affine, $\sigma(l, h)$ is scaled with l and h as follows:

$$\sigma(l, h) \sim l^{\alpha} \qquad \text{for} \quad h >> l \qquad (1)$$

and

$$\sigma(l, h) \sim h^{\beta}, \qquad \text{for} \quad h << l. \qquad (2)$$

In the 2-dimensional Eden model[21], $\sigma = 1/2$ and $\beta = 1/3$ are obtained[22]. Vicsek et al. obtained the above characteristic exponents $\alpha = 0.78$ for bacterial colony[18]. On the other hand, $\alpha = 0.62$ is obtained for the present experiment on growth.

2. EXPERIMENTAL METHODS

2.1 Organism and Media

The strains used are wild type Aspergillus oryzae (supplied by the Institute for Fermentation Osaka, Japan), wild type Aspergillus nidulans and some colonial mutant strains of A. nidulans (supplied by the Fungal Genetics Stock Center, Dept. of Microbiol., Univ. Kansas Medical Center, Kansas City, USA. FGSC numbers of the strains are A4(wild type), A66, A232, A583 and A695(mutant strains)). Colonies of these mutant strains developed on a nutrient-rich standard media shows peculiar features different from the normal colony of wild type strain.

A. oryzae was cultivated on modified Czapek-Dox synthetic agar medium, containing $NaNO_3$(0.3%), K_2HPO_4(0.1%), $MgSO_4 \cdot H_2O$(0.05%), KCl(0.05%), $FeSO_4 \cdot H_2O$(0.001%), glucose(as a carbon source, varied from 0.01% to 5%), and Difco Bacto-Agar(which controls the stiffness of substrate, concentration varied from 0.15% to 5%). About 25ml of sterile medium is poured into Petri plates of 9cm in diameter.

Since the A. nidulans mutant strains were seen to remain almost inactive on the above Czapek-Dox medium, the strains were cultivated on modified peptone agar medium, containing K_2HPO_4(0.05%), KH_2PO_4(0.05%), Difco Neopeptone (as a source of amino acids, etc., varied from 0.05% to 1%), and Difco Bacto-Agar (varied from 0.3% to 2%), 20ml sterile medium per each 9cm Petri plates. Lastly, we set the incubation temperature, at 24°C which is favorable for the physiological activities of the fungus.

2.2 Inoculation, Cultivation and Photography

In order to make 1-dimensional colony growth for A. oryzae, spore suspension was inoculated on a line. A cover glass plate (65 or 55mm length and 0.12mm thickness) is perpendicularly inserted into the medium as a ruler for drawing. Rinsed spore suspension was drawn along the glass ruler using a sterile string. The glass ruler was immediately removed after inoculation. Medium plates are kept at 24°C packed in a polyethylene package to reduce drying of substrate.

Spores of A. nidulans strains were preserved in hydrous silica gel particles. A single grain of silica gel stock was added on the agar medium and cultivated at 24°C to develop a circular colony.

Photographs of colonies, illuminated from under the plates, were taken using a 35mm camera with black-and-white films. Dark areas seen in the photos indicates the area where conidia

(spores) were produced densely.

3. GROWTH

Generally the growth occurs at the apical tip (apical growth). Figure 1 shows how the growth occurs. The growth conditions are 0.01 wt% glucose, 0.15 wt% agar at the temperature of 24°C. In 23 days after the inoculation, one of many branches (see figure at the left and bottom of Fig.2) is observed. At the top, there are many thin branches, and they get fat without extension to the outer environments. Suddenly about 25 days after, one of the branch grows and get fat later again (see 26 days also). If you look at 28 days, you find again the sudden growth of a branch among many ones.

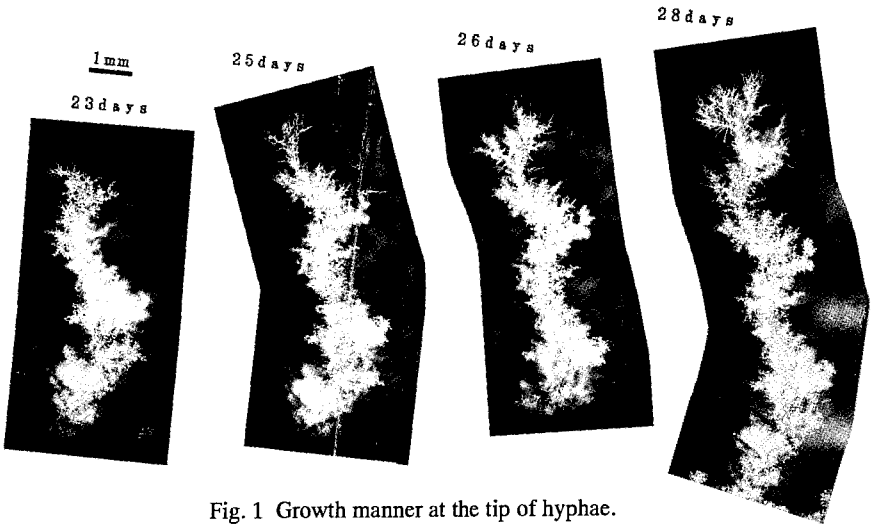


Fig. 1 Growth manner at the tip of hyphae.

4. PHASE DIAGRAM

4.1 General Morphology of *Aspergillus oryzae*

Photographs of Aspergillus oryzae colonies grown with various glucose and agar concentrations are shown in Fig.2. On the solid agar media, colonies become thick and compact. The band shaped colony is an assembly of sub-colonies as clearly seen in the photographs of low glucose cases. The front shape of the whole colony is the connection of the front lines of the sub-colonies. These sub-colonies have the most advancing portion in the middle of their fronts, exhibiting smooth arch shapes.

At high glucose concentration ($\geq$ 1 wt%), thick colonies cover the medium homogeneously, independent of the medium stiffness. The colony growth rate is, however, higher and the front is rougher for the colonies on solid medium, indicating active growth at the front.

Stiffness of the agar medium causes remarkable morphological change of the colony. Roughening of front and ramification of whole colonies appear on the soft and liquid-like media (Fig.2). On the liquid-like media, localization of growth points occurs with decreasing glucose concentration. At very low glucose condition 0.01 wt%, only strong leading hyphae continue to extend, and most secondary hyphae seem to cease growing at some physiological age. The inactive hyphae are seen to form the chains of conidia at their apical portions.

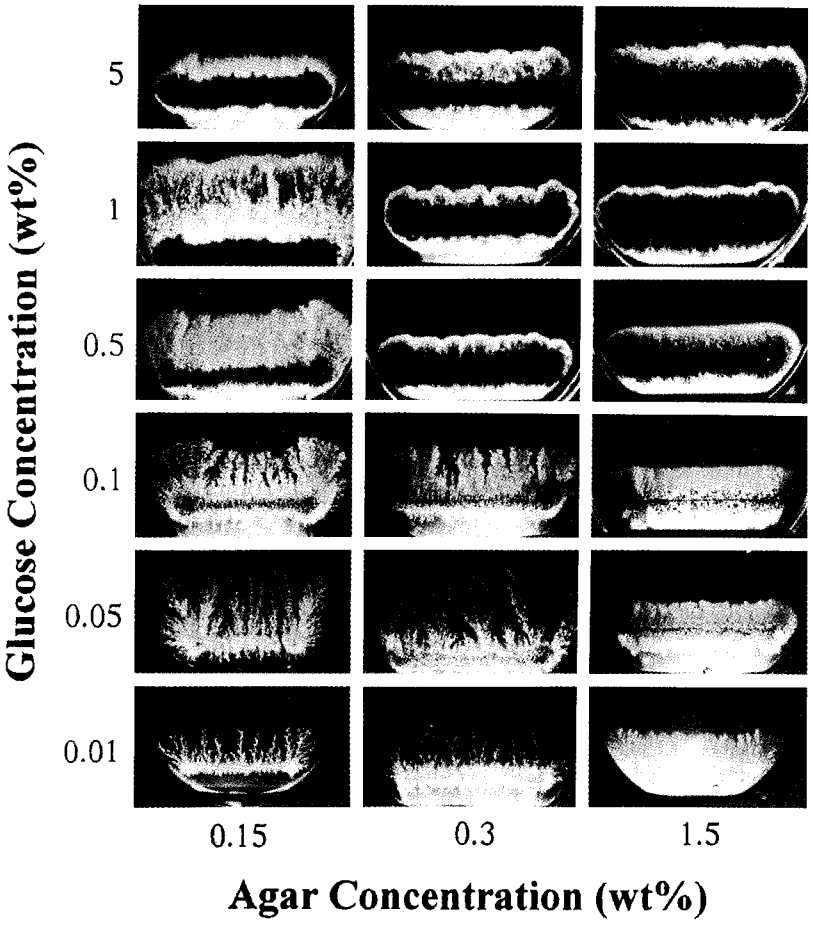


Fig. 2. Aspergillus oryzae colonies cultivated on the media with various glucose and agar concentrations. The cultivation periods for colonies on liquid-like media (0.15 wt% agar) are 10 days for 5 wt% glucose, 20 days for 1 wt% glu., 20 days for 0.5 wt% glu., 20 days for 0.1 wt% glu., 30 days for 0.05 wt% glu., and 30 days for 0.01 wt% glu., for colonies on soft media (0.3 wt% agar) are 10 days for 5 wt% glu., 10 days for 1 wt% glu., 10 days for 0.5 wt% glu., 15 days for 0.1 wt% glu., 30 days for 0.05 wt% glu., and 30 days for 0.01 wt% glu., and for colonies on solid media (1.5 wt% agar) are 8 days for 5 wt% glu., 8 days for 1 wt% glu., 8 days for 0.5 wt% glu., 8 days for 0.05 wt% glu., and 10 days for 0.01 wt% glu., respectively. The length of

inoculation line is approximately 55 mm for soft and solid media.

Hyphae secretes various enzymes to decompose and absorb nutrient materials. If the nutrients are distributed uniformly in the substrates, the diffusion of nutrient to the mycelium or the individual hypha must be one of the important factors which determine the mycelial pattern formation. In our experimental conditions, diffusion of glucose must be easier both in the medium of low agar and high glucose concentration.

However, at a fixed glucose concentration, low stiffness of the substrate seems to be unfavorable condition for mycelial growth. Selection of hyphal

4.2 General Morphology of *Aspergillus nidulans* mutant A583

One of the most interesting patterns of Aspergillus nidulans is shown in Fig.3. The ramified patterns are observed in the solid media, i.e., 1 wt% and 2 wt% agar. Although this condition is a rather favorable for A. oryzae, this is unfavorable conditions. In such a situation A. nidulans takes a growth manner of ramification as a strategy of fungi. In a poorer condition (lower agar concentration) the growth rate of A. nidulans is very slow, rather they make spore in the central region.

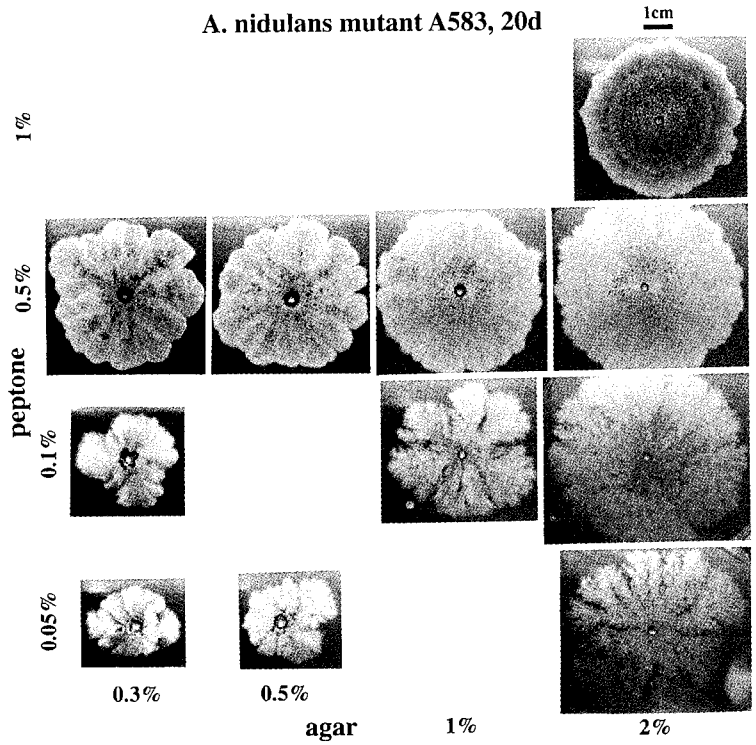


Fig. 3. Aspergillus nidulans colonies cultivated on the media with various peptone and agar

concentrations. The cultivation period for all cultivation is 20 days.

5. CONCLUDING REMARKS

We have found that the shape response of the Aspergillus oaryzae colonies to the environmental conditions ranges from Eden-like to DLA-like ramified patterns. In the glucose-rich case, the colonies generated on solid agar show a homogeneous and smooth growth front, while the colonies on a semi-liquid agar show a ramified front. In the glucose-poor case, the colony surfaces become rough even on solid agar, while the colonies show a DLA-like ramified form on the semi-liquid medium. There are many combinations of these various motive forces for growth and therefore we can find a lot of variations of growth patterns in A. oryzae. As seen in the above, we have found a conflicting force for growth, such that solid medium is advantageous for homogeneous growth and semi-liquid medium for inhomogeneous and ramified growth. The growth activities are decreased when the stiffness of the medium is reduced, though the diffusion of nutrient is active. Most of colony growth processes may be regarded as intermediate between a purely homogeneous growth, like the Eden process, and a ramified growh due to selection of growing filaments, analogous to the situation of the diffusion limited aggregation (DLA) process.

In the case of A. nidulans mutant A583, the growth activity is relatively weak comparing with the wild cell. Therefore we have observed a ramified growth even in the favorable condition 2 wt% agar for oryzae. However it must be noted that the nutrient is only peptone in this case, and we need experiments including other nutrient materials

REFERENCES

1. B. B. Mandelbrot, Nature of Fractal of Geometry (Freeman, San Francisco, 1982).
2. T. A. Witten and L. M. Sander, Phys. Rev. Lett. 47,1400 (1981).
3. M. Matsushita, M. Sano, Y. Hayakawa, H. Honjo and Y. Sawada, Phys. Rev. Lett. 53, 286 (1984).
4. F. Family and D. P. Landau, Kinetics of Aggregation and Gelation (North-Holland, Amsterdam, 1984).
5. H. E. Stanley and N. Ostrowski, On Growth and Form (Martinus Nijhoff Dordrecht, 1986).
6. J. Feder, Fractals (Plenum Press, New York, 1988).
7. T. Vicsek, Fractal Growth Phenomena (World Scientific, Singapore, 1989).
8. P. Meakin, in Phase Transitions and Critical Phenomena, Vol. 12, eds. C. Domb and L. Lebovitz (Academic Press, New York, 1990).
9. L. A. Turkevich and H. Scher, Phys. Rev. Lett. 53, 1026 (1985)
10. R. C. Ball, R. M. Brady, G. Rossi and B. Thompson, Phys. Rev. Lett. 55, 1406 (1985).
11. K. Honda, H. Toyoki and M. Matsushita, J. Phys. Soc. Jpn. 55, 707 (1986).
12. P. Meakin, Phys. Rev. Lett. 51, 1119 (1983).
13. M. Kolb, R. Botet and R. Jullien, Phys. Rev. Lett. 51, 1123 (1983).
14. M. J. Vold, J Colloid Interface Sci. 18, 684 (1963).
15. E. Charlaix, E. Guyon and N. River, Geol. Mag. 122, 157 (1985).
16. F. Family, B. R. Masters and D. F. Platt, Physica D38, 98 (1989).
17. H. Fujikawa and M. Matsushita, J. Phys. Soc. Jpn 58, L3875 (1989).
18. T. Vicsek, M. Cserzo and V. K. Horvath, Physica A167, 315 (1990).
19. S. Matsuura and S. Miyazima, in "Formation, Dynamics and Statistics of Patterns" eds K. Kawasaki and M. Suzuki, (World Scientific, Singapore, 1993).
20. M. Obert, P. Pfeifer and M. Sernetz, J. Baqteriology 172, 1180 (1990).
21. M. Eden, Proc. 4-th Berkeley Symp. on Math. Statistics and Probability, Vol. 4, ed. F. Neyman (University of California Press, Berkeley, 1961).
22. M. Kardar, G. Parisi and Y, Zhang, Phys. Rev. Lett. 56, 889 (1986).

A MODEL FOR ION-SPUTTERING: FROM PATTERN FORMATION TO ROUGH SURFACES

R. CUERNO[†] H. A. MAKSE[†], S. TOMASSONE[‡], S. T. HARRINGTON[†], AND H. E. STANLEY[†]

[†] Center for Polymer Studies and Dept. of Physics, Boston University, Boston, MA 02215

[‡] Department of Physics, Northeastern University, Boston, MA 02115

ABSTRACT

Many surfaces eroded by ion-sputtering have been observed to develop morphologies which are either periodic, or rough and non-periodic. We have introduced a discrete stochastic model that allows to interpret these experimental observations within a unified framework. A simple periodic pattern characterizes the initial stages of the surface evolution, whereas the later time regime is consistent with self-affine scaling. The continuum equation describing the surface height is a noisy version of the Kuramoto-Sivashinsky equation.

INTRODUCTION

Surface erosion by ion–sputtering is a phenomenon in which a surprisingly rich variety of surface morphologies are generated, depending on experimental conditions [1]. Topography features can be found at all length scales, and from the technological point of view it is very important to understand the mechanisms by which they are formed, and thus gain control on the final morphology of the bombarded samples. On a more fundamental level, the different morphologies observed constitute interesting examples of pattern formation [2] and rough surfaces [3] in non-equilibrium phenomena, where there exists an interesting interplay between mechanisms of deterministic and stochastic natures.

Both types of morphologies (e. g. periodic surfaces and rough surfaces) have been long known to occur in the bombardment of amorphous targets at low energies. Specifically, in many cases a pattern is generated consisting of a ripple structure [4], aligned in directions either parallel to or perpendicular to that of the bombarding beam of ions. On the other hand, one also finds in similar experimental conditions that the surfaces generated are rough and thus display self-affine scaling at long distances and long times [5]. An outstanding question is then how to reconcile these observations with the formation of the periodic ripple structure.

In this work we report on the introduction [6] of a discrete stochastic model that allows to understand the formation of a periodic pattern and the kinetic roughening of the bombarded surface in an unified framework. We argue that the continuum equation describing the evolution of the model interface is a noisy version of the Kuramoto-Sivashinsky (KS) equation. The deterministic KS equation [7] appears very frequently in studies of pattern formation, and is considered as a paradigm of spatiotemporal chaos [2]. In the KS system, an initially flat surface evolves into an almost periodic morphology. At later stages, the surface roughens in a fashion consistent with the Kardar-Parisi-Zhang [8] universality class (for a one dimensional interface) [10]. In our case, the relevant continuum equation differs from the deterministic KS in the presence of a noise term taking into account the stochastic nature processes occurring in the system. Nevertheless, the qualitative behavior is identical with that just described, thus permitting to understand the formation of the ripple structure and of the rough surfaces in the ion-sputtered system as different stages of a same dynamical evolution.

Mat. Res. Soc. Symp. Proc. Vol. 407 © 1996 Materials Research Society

PHYSICAL MECHANISMS IN ION-SPUTTERING

Here we discuss briefly the main physical mechanisms determining the evolution of an amorphous target bombarded with low energy ions (typically with kinetic energies around 1–10 keV).

As established long ago by Sigmund [11], the sputtering is induced by cascades of collisions among the atoms of the solid, triggered by the incoming ions along a finite penetration path inside the target. These collisions may eventually affect an atom living at the surface, which may be ejected leading to the sputtering event proper. The value of the average penetration depth a depends chiefly on the ion/target atom mass ratio and the energy of the ions. A typical value for a is 100 Å. On the other hand, at the energies considered, the cascades of collisions are sufficiently large to involve many atoms (the spatial extent of the cascades is also of the order of 100 Å), but sufficiently small to be accurately described by the linear cascade theory of [11], where binary collisions are supposed to take place between one atom at rest and one atom in motion. This approach describes rather succesfully the phenomenology for rates of erosion, etc. In this description, the velocity of erosion at one point of the surface can be taken to be proportional to the total amount of energy that it gains form all the collisions, thus being proportional to the amount of target solid surrounding that point. As noticed by Sigmund and later ellaborated on by Bradley and Harper [12], this leads to an instability in the system, since the bottom of troughs will be eroded *faster* than the peaks of crests. Phenomenologically, on the other hand, it is known that the velocity at which the surface recedes at a point depends also on the value of the slope of the surface there. This is a surface effect which goes beyond the approximations made in the linear cascade theory, where an infinite medium is assumed. A finite medium has the effect of a lower velocity of erosion, which is usually described by a lower sputtering yield $Y(\varphi)$, defined as the number of eroded atoms divided by the number of bombarding ions. In practice, at any given point on the surface, $Y(\varphi)$ depends on the angle of incidence φ of the ions trajectories to the normal direction at that point. The smaller φ is, the closer is $Y(\varphi)$ to the linear cascade prediction. If φ increases from zero, there's a finite maximum value for the yield, beyond which more and more ions are reflected by the surface itself, and when $\varphi = 90^0$ one has $Y(\varphi = 90^0) = 0$. For a generic point on the interface, the normal direction will not coincide with the normal to the uneroded surface, but will be determined by the value of the slope there.

There exists a physical mechanism that counterbalances the instability existing in the erosion mechanism described above. This is surface diffusion, which tends to smooth out surface features. Surface diffusion is activated by temperature, and in many cases (as typically for surfaces grown by Molecular Beam Epitaxy) can be considered as minimizing a chemical potential proportional to the surface curvature [13]. This approach is possible in a coarse grained description of the system [14], as the one we pursue here, in which the unit length is set by the finite penetration depth (or the spatial extent of the cascades), and therefore goes beyond the individual atoms.

In the above discussion, additional effects have been neglected, such as the shadowing of some surface features over others and redeposition of the eroded material. These assumptions have been shown to be consistent with the early stages of the surface evolution [4]: the late roughening is again consistent with them.

Finally, to model the sputtering phenomena, one has to take into account that in general the ion beam fluctuates in time and space. This can be described by assuming that at each time step (through which the average flux is implicitly fixed) a dynamical process takes place at a randomly chosen location along the interface.

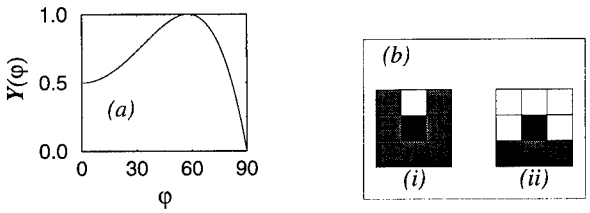


Figure 1: (a) Sputtering yield $Y(\varphi)$ as a function of the angle φ. (b) Box rule for erosion. We define p_e as the number of occupied neighboring sites (grey squares) inside the 3×3 box centered at site i (black square), normalized by 7. The examples shown correspond to (i) $p_e = 1$ and (ii) $p_e = 3/7$.

DISCRETE MODEL

To define our model, we introduce two dynamical rules, one to account for erosion and one to account for surface diffusion. The model for the case of $1+1$ dimensions is defined on a square lattice of lateral size L, with periodic boundary conditions in the horizontal direction. The initial interface is a horizontal line separating occupied sites (below) from empty sites (above). We choose randomly a site i at the interface where $i = 1, \ldots, L$. The chosen site is subject to erosion with probability p, or to diffusion with probability $1-p$, where the rules are as follows:

(i) Erosion (probability p)— We compute $\varphi \equiv \tan^{-1}[(h_{i+1} - h_{i-1})/2]$, where h_i is the height of the interface at site i, and apply the erosion rule with probability $Y(\varphi)$, as given in Fig. 1a. To erode, we count the number of occupied neighbors inside a square box of size 3×3 lattice spacings centered in the chosen site i (box rule). We empty the site with an erosion probability p_e proportional to the number of occupied cells in the box (see Fig. 1b). Thus the box rule favors the erosion of troughs as compared to the peaks of crests, and therefore is the source of the instability in the ion-sputtered system.

(ii) Surface Diffusion (probability $1-p$*)*— A diffusive move of the particle i to a nearest neighbor column is attempted with hopping probability $w_{i\to f} \equiv \left[1 + \exp\left(\Delta\mathcal{H}_{i\to f}/k_BT\right)\right]^{-1}$, where $\Delta\mathcal{H}_{i\to f}$ is the energy difference between the final and initial states of the move. Following [14], we choose $\mathcal{H} \equiv (J/2)\sum_{\langle i,j\rangle}(h_i - h_j)^2$.

The above model can be generalized in a straightforward way to the physical two dimensional case. We expect the results to be qualitatively similar to the one dimensional case discussed below. An additional ingredient in 2+1 dimensions is the anisotropy between the two substrate directions induced by the bombarding beam. This can be accounted for by imposing a finite angle of incidence, assumed in the above to be zero. For illustration, we show in Fig. 2 the result of two-dimensional simulations in which we have set $Y(\varphi) \equiv 1$. In Fig. 2a an isotropic box rule has been used, while in Fig. 2b the box does not count the number of neighbors in one of the two directions. Therefore, the surface only presents ripples with wavevector parallel to that direction in which the neighbors are counted in the corresponding box rule.

DISCUSSION

Next we consider the model with $Y(\varphi)$ shown in Fig. 1a. The results are not expected to depend strongly on the specific form of $Y(\varphi)$, so long as it preserves the existence of a maximum, and $Y(0) \neq 0$, $Y(90^0) = 0$ [15]. The initial stages of the evolution are dominated by an instability in which there exists a maximally unstable mode in the system, and the surface looks almost periodic, see Fig. 3a. Fig. 4a displays the structure factor

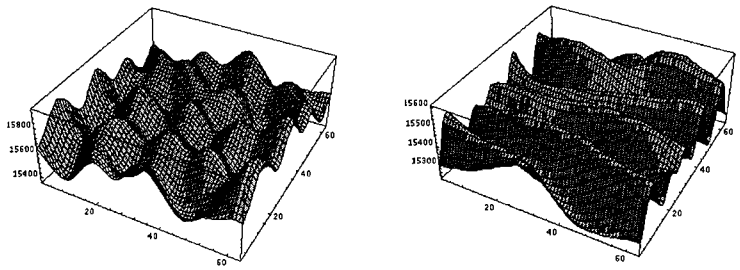


Figure 2: Two-dimensional simulations with $Y(\varphi) \equiv 1$. In Fig. 2*a* an isotropic box rule has been used, while in Fig. 2*b* the box does not count the number of neighbors in one of the 2 directions.



Figure 3: (*a*) Periodic surface morphology for initial stages (we have set $Y(\varphi) \equiv 1$) for $L = 50$ and $t = 1000$; (*b*) rough surface morphology for $L = 2048$ at late stages.

$S(\boldsymbol{k}) \equiv \langle \widehat{h}(\boldsymbol{k},t)\widehat{h}(-\boldsymbol{k},t)\rangle$ at the onset of the instability. Here $\widehat{h}(\boldsymbol{k},t)$ is the Fourier transform of $h_i(t) - \overline{h(t)}$, and $\overline{h(t)} \equiv L^{-1}\sum_{i=1}^{L} h_i(t)$. The solid line in Fig. 4*a* is a fit to the solution of the linear part of

$$\partial_t h(\boldsymbol{x},t) \;=\; \nu\nabla^2 h - \kappa\nabla^4 h + \eta(\boldsymbol{x},t) + f_Y[h(\boldsymbol{x},t)], \qquad (1)$$

where $h(\boldsymbol{x},t)$ is the height of the interface at position $\boldsymbol{x}$ and time t, ν is a *negative* surface tension coefficient, κ is a *positive* coefficient that accounts for the surface diffusion, and $\eta(\boldsymbol{x},t)$ is a Gaussian noise with short range correlations and strength $2D$, that accounts for the fluctuations in the ion beam. The functional $f_Y[h]$ takes into account the contribution of nonlinear terms, which appear in the equation of motion due to the effect of $Y(\varphi)$, itself a nonlinear function of the local slope $\nabla h \equiv \tan\varphi$ [16]. These nonlinear effects are triggered at later times by the large slopes built in by the instability, so that eventually the interface results in a rough morphology (Fig. 3*b*). In Fig. 4*b*, we present the time evolution of the total interface width $W(t) \equiv \langle L^{-1}\sum_{i=1}^{L}(h_i(t) - \overline{h(t)})^2\rangle^{1/2}$ (the brackets denote an average over realizations of the noise). We observe a first scaling regime [17] $W(t) \sim t^{\beta_1}$, with $\beta_1 = 0.38 \pm 0.03$, consistent with the linear MBE equation [13, 14] (which is (1) with $\nu = f_Y \equiv 0$). This regime is followed by unstable erosion ($\beta_2 > 0.5$). For later stages, we find $\beta_3 = 0.23 \pm 0.03$, consistent with the scaling of the EW equation [18] (Eq. (1) with $\kappa = f_Y \equiv 0$, and $\nu > 0$), after which a crossover to $\beta_4 = 0.28 \pm 0.03$ is found. Finally, the width saturates due to the finite size of the system. Note that the value of the growth exponent for the KPZ equation is $\beta_{\rm KPZ} = 1/3$ [8]. As we see in Fig. 4*b*, there is a long crossover time from EW to KPZ behavior, responsible for the difference between β_4 and β_{KPZ}, and for the narrow window in which β_4 is observed—we find that the width of this window increases systematically with L. A similar phenomenon is well known to occur in the

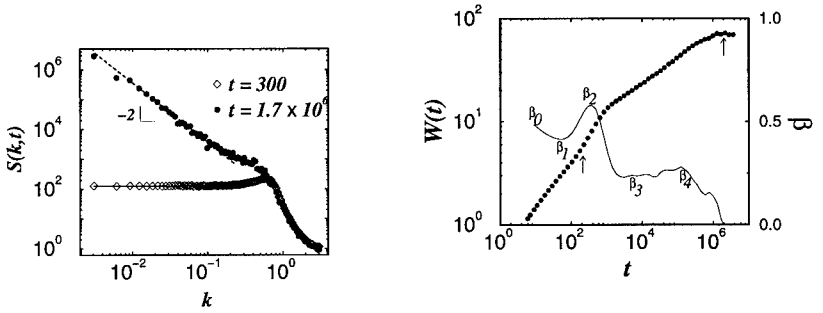


Figure 4: (a) $S(k)$ computed for a system with $L = 2048$. For $t = 300$, averaged over 2600 noise realizations ($\diamond$), and for $t = 1.7 \times 10^6$, averaged over 39 realizations ($\bullet$), see arrows in (b). The solid line is a fit to the exact solution of the discretized linear part of Eq. (1). The dashed straight line has slope -2; (b) $W(t)$ showing the regimes of the evolution for $L = 2048$. The solid line is the consecutive slope. The arrows indicate the times at which the structure factor is displayed in (a).

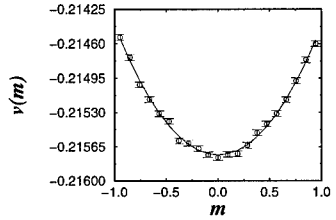


Figure 5: $v(m)$ as a function of the average tilt m of the interface, calculated in the saturated regime for $L = 128$, and averaged over 810 noise realizations. The solid line is a fit to a parabola.

deterministic KS equation in 1+1 dimensions, see Sneppen *et al.* in [10]. At saturation, $S(k)$ displays the small momenta behavior $S(k,t) \sim k^{-2}$ (Fig. 4a), consistent with the scaling of both the EW and KPZ universality classes. To determine if a KPZ nonlinearity is present in Eq. (1), we compute the mean velocity $v(m)$ of the interface in the saturated regime as a function of an average tilt $m \equiv \langle \nabla h \rangle$ imposed by using helical boundary conditions. If we assume that the relevant nonlinearity in (1) is of the KPZ type, then $f_Y[h] = (\lambda/2)(\nabla h)^2$. Taking spatial and noise averages in (1), $v = v_0 + (\lambda/2)m^2$, where v_0 is the velocity of the untilted interface [19]. The parabolic shape of $v(m)$ obtained in our simulations (see Fig. 5) leads to the conclusion that the long time and long distance behavior of the model falls into the KPZ universality class. Moreover, the continuum equation describing the model ion-sputtered surfaces is the *noisy* KS equation

$$\partial_t h = \nu \nabla^2 h - \kappa \nabla^4 h + \frac{\lambda}{2} (\nabla h)^2 + \eta(\boldsymbol{x}, t). \tag{2}$$

To compare the *dynamics* of (2) with those obtained for the discrete model, we have integrated numerically Eq. (2) in $1 + 1$ dimensions [6]. We obtain the same crossover behavior for (2) as for the discrete model. Consistent with these numerical findings, the late scaling of Eq. (2) has been shown through a renormalization-group calculation [9] to

be that of the KPZ equation in 1+1 and 2+1 dimensions. Also, recently Eq. (2) has been derived for the present model through a master equation approach [20].

Finally, we compare the results of the model with observations of recent experiments. The experimental development of a ripple structure [4] is well understood in terms of the unstable linear theory of ion-sputtering describing the early stages of the time evolution of the model presented here. Moreover, the model predicts that in the late regime the large slopes generated by the unstable growth trigger the action of nonlinearities which stabilize the surface. The nonlinearity we find is of the KPZ type, consistent with the experimental observation of KPZ scaling reported by Eklund *et al.* [5]. To confirm the above picture, it would be of interest to study experimentally if both regimes do effectively take place in the time evolution of the *same* physical system.

We would like to acknowledge discussions and comments by A. L. Barabási, G. Carter, S. Havlin, and K. B. Lauritsen. R. C. acknowledges support from Ministerio de Educación y Ciencia, Spain. The Center for Polymer Studies is funded by NSF.

References

[1] G. Carter *et al.*, B. Navinšek and J. L. Whitton in *Sputtering by Particle Bombardment*, Vol. II, edited by R. Behrisch, (Springer-Verlag, Heidelberg 1983), p. 231.
[2] M. C. Cross and P. C. Hohenberg, Rev. Mod. Phys. **65**, 851 (1993).
[3] P. Meakin, Phys. Rep. **235**, 189 (1993); T. Halpin-Healey and Y.-C. Zhang, *ibid.* **254**, 215 (1995); A.-L. Barabási and H. E. Stanley, *Fractal Concepts in Surface Growth* (Cambridge University Press, Cambridge 1995).
[4] E. Chason *et al.*, Phys. Rev. Lett. **72**, 3040 (1994); T. M. Mayer *et al.*, J. Appl. Phys. **76**, 1633 (1994).
[5] E. A. Eklund *et al.*, Phys. Rev. Lett. **67**, 1759 (1991); E. A. Eklund *et al.*, E. J. Snyder and R. S. Williams, Surf. Sci. **285**, 157 (1993); J. Krim *et al.*, Phys. Rev. Lett. **70**, 57 (1993); H.-N. Yang, G.-C. Wang, and T.-M. Lu, Phys. Rev. **B 50**, 7635 (1994).
[6] R. Cuerno, H. A. Makse, S. Tomassone, S. T. Harrington, and H. E. Stanley, Phys. Rev. Lett. in press.
[7] Y. Kuramoto and T. Tsuzuki, Prog. Theor. Phys. **55**, 356 (1977); G. I. Sivashinsky, Acta Astronaut. **6**, 569 (1979).
[8] M. Kardar, G. Parisi and Y.-C. Zhang, Phys. Rev. Lett. **56**, 889 (1986).
[9] R. Cuerno and K. B. Lauritsen, Phys. Rev. **E 52**, 4853 (1995). For $d > 2$, L. Golubović and R. Bruinsma, Phys. Rev. Lett. **66**, 321 (1991); *ibid.* **67**, 2747 (E) (1991).
[10] S. Zaleski, Physica **D 34**, 427 (1989); K. Sneppen *et al.* Phys. Rev. **A 46**, R7351 (1992); F. Hayot *et al.*, Phys. Rev. **E 47**, 911 (1993).
[11] P. Sigmund, Phys. Rev. **184**, 383 (1969).
[12] P. Sigmund, J. Mat. Sci. **8**, 1545 (1973); R. M. Bradley and J. M. E. Harper, J. Vac. Sci. Technol. **A 6**, 2390 (1988).
[13] C. Herring, J. Appl. Phys. **21**, 301 (1950); W. W. Mullins, J. Appl. Phys. **28**, 333 (1957); in the context of surface roughening, see D. E. Wolf and J. Villain, Europhys. Lett. **13**, 389 (1990); S. Das Sarma and P. I. Tamborenea, Phys. Rev. Lett. **66**, 325 (1991).
[14] M. Siegert and M. Plischke, Phys. Rev. **E 50**, 917 (1994).
[15] G. Carter *et al.*, Surf. Interface Anal. **20**, 90 (1993); A. N. Protsenko, Nucl. Instr. and Meth. **B 82**, 417 (1993).
[16] This argument can be made more precise, see [20].
[17] An initial random erosion regime ($\beta_0 = 0.5$) is also observed before correlations build up in the system.
[18] S. F. Edwards and D. R. Wilkinson, Proc. R. Soc. Lond. **A 381**, 17 (1982).
[19] J. Krug and H. Spohn, Phys. Rev. Lett. **64**, 2332 (1990).
[20] K. B. Lauritsen, R. Cuerno, and H. A. Makse, preprint.

INTERACTION OF ORGANIC ADDITIVES WITH ALUMINA SURFACES IN A CERAMIC SLURRY

W.M. SIGMUND*, G. WEGNER**, F. ALDINGER*
*University of Stuttgart, Institut für Nichtmetallische Anorganische Materialien, Heisenbergstr. 5, 70569 Stuttgart, Germany, sigmund@aldix.mpi-stuttgart.mpg.de
**Max-Planck-Institute for Polymer Research, 55128 Mainz, Germany

ABSTRACT

The interaction of organic additives with alumina surfaces was studied using a typical tape casting composition for alumina: solvent mixture trichloroethylene/ethanol, polyvinylbutyral (PVB) as binder and fish oil as dispersant.

The characterization of the single components revealed why the dispersant Menhaden fish oil has such excellent dispersing properties for colloids and slurries. Menhaden fish oil used for wet-chemical processing was found to be a chemically polydisperse polymer with a dispersity of D=45 (by GPC) and a molecular weight of M_w=28,000.

The investigation of the interaction in the highly concentrated colloidal slurry indicates that the high molecular weight fraction of fish oil is preferentially adsorbed and that an onion like supramolecular structure is formed by the ceramic particle/dispersant/binder system. The sequence in this nanostructure can be controlled by the sequence of addition of the compounds and is guided by polymer effects. The results gained on powders are supported by experimental data from surface plasmon resonance spectroscopy (SPR).

INTRODUCTION

Optimum properties of high-tech ceramics such as structural or functional ceramics can only be achieved by powder metallurgy processes when high purity powders are used. These powders with an average particle size of submicron to micron tend to agglomerate and lack plasticity. In order to increase the processability of these powders and the overall properties and reliability of the sintered high-tech ceramic, organic compounds have to be introduced. For wet-chemical processing such as tape casting and slip casting, dispersants (surfactants), binders and plastisizers amongst other organic compounds are used[1].

These compounds play an important role as they chiefly control the reliability of the sintered ceramic part as well as influencing its microstructure and therefore its properties. To further elucidate the function of these organic compounds we studied a typical tape casting composition for the preparation of alumina substrates.

In the tape casting of alumina the order of addition of the organic compounds plays an important role in the process. Keeping the order of addition as dispersant first and binder second the slurry is processable, i.e., the viscosity can be controlled in the desired range for tape casting. Changing the order of addition to binder first and dispersant second yields slurries that are too viscous to be tape cast although nothing else has been changed.

In this paper we will present experimental data that suggests that the above described macroscopic effects are very likely to be the result of a structural change at the molecular level.

Mat. Res. Soc. Symp. Proc. Vol. 407 © 1996 Materials Research Society

EXPERIMENTAL

Compounds

Menhaden fish oil was from Spencer Kellog, USA. Polyvinylbutyral (PVB) was from Hoechst AG, Frankfurt, Germany. The molecular weight distribution (dispersity D= 3.5) was determined by size exclusion chromatography (GPC) in tetrahydrofurane (THF) and the molecular weight average (M_w= 113,000) was measured by light scattering. The amount of alcohol, acetate and butyral groups were determined by ^{1}H-NMR-spectroscopy giving 34.8, 0.9 and 64.3 atom%, respectively.

The azeotropic mixture of trichloroethylene/ethanol was composed by mixing ethanol p.a. (99.9 %) (Riedel de Haen, Germany) and trichloroethylene p.a. (Merck, Darmstadt, Germany) Alumina powder A16 SG was from Alcoa (USA). XRD proved it to be pure α-alumina with a BET-surface of the as-received powder of 10.2 m^2/g.

Equipment

GPC was done in THF using a Waters system (WISP710B, Pump 590, UV-Vis-detector Soma S-3702) with a column set from PL-Gel (Germany).

FTIR\DRIFT measurements were done on a Nicolet FT 730-spectrometer using a Spectratech diffuse reflectance unit.

For surface plasmon resonance spectroscopy (SPR) a 10 nm thin layer of alumina was synthesized by evaporation of aluminum at 10^{-4} mbar of oxygen, layer thickness growth 0.2 nm/s. For the adsorption studies of organic compounds on the synthetic alumina surfaces presented in this paper, a solution of 50 mg/ml of PVB and fish oil was used. Layer thicknesses were calculated using the dielectric constants of the bulk materials and assuming a simple model in which a block of the bulk material is attached to the alumina surface containing no solvent. The properties of the synthetic alumina surface were intensively studied. Adsorption of surface probe molecules showed that comparable surface properties were achieved for the synthetic alumina as for the A16 SG alumina powder.[2]

RESULTS AND DISCUSSION

The Menhaden fish oil used in the tape casting of high-tech ceramics was characterized by GPC, FTIR and NMR. Fig. 1 A shows the GPC of the as-received fish oil. This proves that Menhaden fish oil for tape casting is a polymer and not a low molecular weight compound. The formation of polymer in this oil can be explained as follows: fish oil used for wet chemical processing is a blown oil. Blown oils are prepared by heating the freshly extracted and purified oil from the fish to about 100°C while air bubbles through for about seven days. This causes an autoxidation reaction to start, which yields oxygen rich functional groups such as carbonyls, alcohols and carboxylic acids. This autoxidation reaction process also causes polymers to be formed.[2] Therefore, as shown in Fig. 1A Menhaden fish oil is a polydisperse polymer (dispersity D=45) with a molecular weight average of M_w=28,000.

On contact of a solution of Menhaden fish oil in trichloroethylene/ethanol with alumina powder, fish oil molecules start to adsorb. Adsorption isotherms can be studied. On checking the supernatant solution with GPC we find that the high molecular weight part disappeared (Fig. 1B). Only the low molecular weight part of fish oil is still available in the solution. This

indicates that the high molecular weight fraction of fish oil is adsorbed on the surface of the alumina powder.

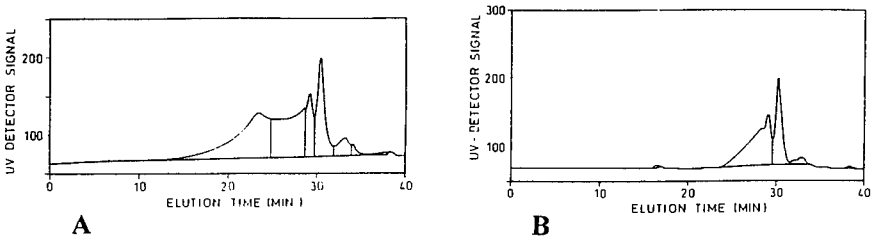


Fig. 1: GPC of Menhaden fish oil as used in tape casting for alumina A) as received and B) in the supernatant solution after adsorption onto the alumina powder.

Fractionation of the polydisperse fish oil can be explained by different sizes of the molecules. The high molecular weight fraction has a much higher number of repeat units and therefore multiple interactions with the alumina surface can occur for the larger molecules. The smaller molecules on the other hand have only a few or just one functional group available to interact with the adsorptive sites on the surface. On comparison with polystyrene standards the molecular weight average of the preferentially adsorbed high molecular weight fraction can be calculated to be M_w=80,000 with a dispersity of D=10. Additionally, it was possible to show that fish oil is not only a physically polydisperse polymer, but also a chemically polydisperse polymer containing a higher number of double bonds and carbonyl, alcohol and carboxyl groups in the high molecular weight fraction than in the low molecular weight fraction.[2]

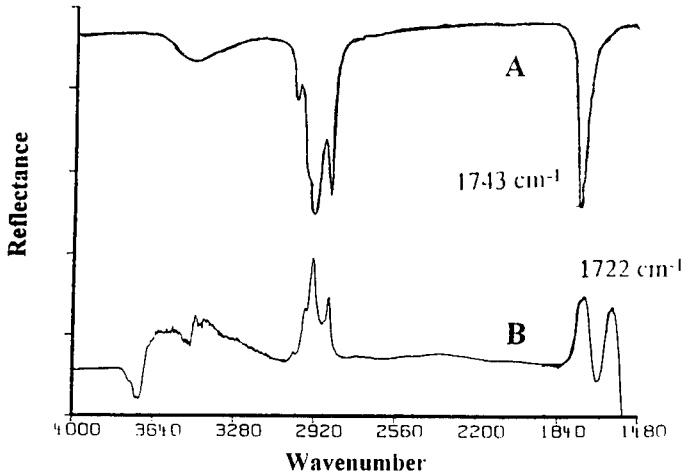


Fig. 2: IR-spectra of A) Menhaden fish oil and B) Menhaden fish oil adsorbed onto alumina. Spectrum A is in transmission. Spectrum B is a subtraction spectrum of two DRIFT spectra. The DRIFT-spectrum of alumina is subtracted from a DRIFT-spectrum of fish oil adsorbed onto alumina.

IR-spectra were run in order to elucidate the interacting moieties. Fig. 2 shows the IR-spectra of fish oil and fish oil adsorbed onto alumina. Fish oil shows bands for alcohol groups at 3500 cm^{-1}, bands for hydrocarbons between 2850 and 3100 cm^{-1} and a strong band at 1743 cm^{-1} for carbonyl and carboxyl moieties. In the DRIFT-spectrum of the adsorbed fish oil (Fig. 2B) a band shift and an increase in half-width of the carbonyl moiety is observed. This indicates the interaction of alumina with carbonyls via hydrogen bonding. The occurrence of a new band at 1585 cm^{-1} indicates the formation of carboxylates that interact with the alumina surface. The sharp aluminum hydroxyl band at 3704 cm^{-1} is shifted to a weak and broad band at lower wavenumbers. This also indicates the interaction of the surface hydroxyls of alumina with the functional groups of fish oil via hydrogen bonding and ionic interactions.

In order to further elucidate the influence of the sequence of addition of the dispersant/binder system SPR-measurements were done. Solutions of fish oil and PVB were adsorbed onto a thin layer (10 nm) of alumina on silver. The results are shown in Fig. 3.

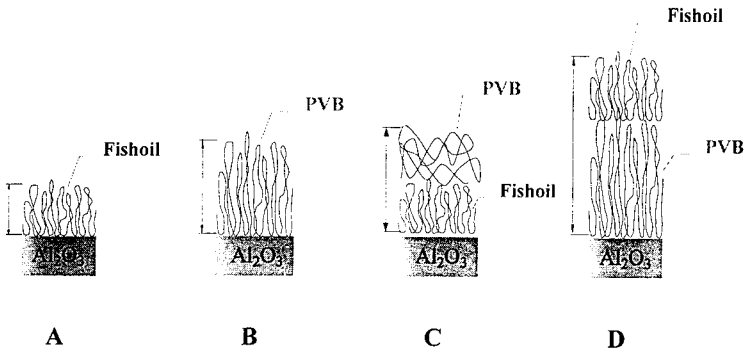


Fig. 3: Adsorbed layer thicknesses of fish oil and PVB in trichloroethylene/ethanol solution calculated by using data from SPR-measurements. A) Adsorption of fish oil, B) PVB, C) first fish oil and then PVB, D) first PVB and then fish oil.

When fish oil is adsorbed onto alumina a layer thickness of 1.6±0.5 nm is formed. Adsorbing a solution of PVB yields a layer of thickness 2.8±0.5 nm. When fish oil is adsorbed first, and PVB second, a layer thickness of 3.0±0.5 nm is achieved that is about the same thickness as for the PVB layer only. By reversing the sequence a layer of 4.5±0.5 nm thickness is achieved, i.e., the thickness equals the sum of a PVB-layer and a fish oil layer.

Fig. 3. shows a possible interpretation for the adsorbed layer structures. Reasons for this happening can be found in polymer physics: when the first polymer is adsorbed a dense layer with complete surface coverage is formed. When the second polymer is introduced into the solution there is no competition for the adsorptive sites on the alumina surface as intrusion into the first layer to reach the surface is unlikely. This is caused by the non-miscibility of two different polymers. Therefore, the polymer that is introduced secondly can only cover the first layer. Therefore, the sequence of addition causes a special supramolecular nano-structure to form that can be described similar to an onion containing two shells around the particle.

With these results in mind a model describing the wet chemical ceramic processing can be suggested as shown in Fig. 4.

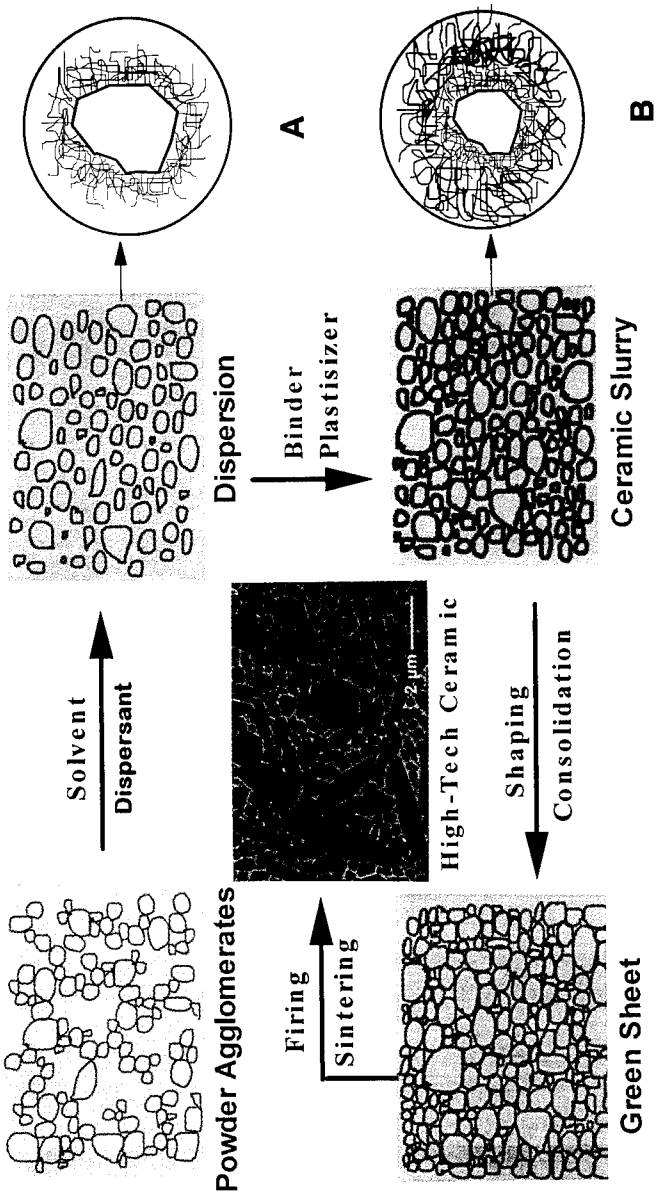


Fig. 4: Schematic model for the tape casting of high-tech ceramics. When the dispersant Menhaden fish oil is added to the slurry a first polymer shell is formed covering the surface of the particle (A). The binder which is added in the second step forms another polymer shell around the particle. Overall an onion-like nano-structure around the particle is achieved. By reversing the sequence a different, less favorable supramolecular structure is yielded.

The first step in the processing (Fig. 4) is dispersing with breaking up of agglomerates. Dispersants like fish oil help this process by covering the surfaces with a polymer monolayer, i.e., the powder particle is covered by a first onion-like shell. The dispersing polymer molecules are strongly bound to the surface in comparison to small molecules such as triglycerides. In the following step the binder PVB is added so a castable slurry is achieved. With the above explanations it is now possible to conclude that the binder forms a second layer around the particle in the slurry, i.e., a second onion shell is formed.

If the addition of the dispersant and binder is reversed, a different supramolecular structure is formed, i.e., PVB forms the first inner layer on alumina whereas fish oil forms the second outer onion shell. This supermolecular structure seems to be less favorable as tape casting with the last mentioned type of slurry does not yield ceramics of acceptable quality.

CONCLUSIONS

It could be shown that a macroscopic effect in viscosity and poor processability that is caused by reversing the sequence of addition of Menhaden fish oil and binder PVB is very likely to be caused by a change in the supramolecular structure. Whichever polymer is added first to the slurry completely covers the alumina particle surface. Due to a general poor miscibility of different polymers this first adsorbed polymer layer forms a barrier for any other polymer. Therefore, the polymer that is added secondly cannot intrude into this first layer to compete for alumina surface adsorptive sites. This then causes a supramolecular structure to form in the slurry that resembles an onion. Finally, the particle is coated by two polymer shells of nano-size thickness. The type of nano-structure can be controlled by the sequence of addition of the polymers.

REFERENCES

1. J. Böhnlein-Mauß, W.M. Sigmund, G. Wegner, W.H. Meyer, F. Heßel, K. Seitz, A. Roosen Advanced Materials, **4**, 73, (1992).
2. W.M. Sigmund, PhD thesis, Max-Planck-Institut for Polymer Research and Johannes Gutenberg-Universität in Mainz, Germany, 1992.

ATOMIC KINETICS AND DYNAMICAL PHASON DISORDER IN A QUASICRYSTAL

M. DZUGUTOV
Center for Parallel Computers, Royal Institute of Technology S-100 44 Stockholm, Sweden
e-mail: mik@pdc.kth.se

ABSTRACT

Slow relaxation dynamics in strongly coupled systems is known to be universally described by the stretched exponential Kohlrausch law. However, this phenomenon, observed in various condensed systems, still eludes a comprehensive microscopic interpretation. I discuss here the relaxation dynamics in an equilibrium dodecagonal quasicrystal which demonstrates a pronounced stretched exponential behaviour. The quasicrystal, simulated by Molecular Dynamics, reveals the presence of dynamical phason disorder, a generic form of relaxation dynamics associated with incommensurate, or phason degrees of freedom. This dynamics brings about a novel form of atomic diffusion, which is examined here by calculating the self part of intermediate scattering function $F_s(Q,t)$. The latter displays a non-exponential decay which is found to be described by the Kohlrausch law with the stretching exponent $\beta = 0.47$. I discuss here a possible similarity between the dynamics of quasicrystals observed and that of supercooled liquids and glasses.

INTRODUCTION

Kinetic theory identifies coupling between the diffusive atomic motions and the density fluctuations as the microscopic mechanism dominating dynamics of condensed systems. Due to the pronounced local ordering arising at high densities of packing, each atom finds itself in a structural cage comprised of its immediate neighbours, and its diffusive dynamics is thus defined by the topology of local structural relaxations. The constraints imposed on the atomic dynamics by the latter would manifest themselves in a deviation from the Fick's law of macroscopic diffusion observed at the time scale that is characteristic for the microscopic diffusion mechanism involved. It is found that this dynamic regime, referred to as α-relaxation, can be universally described by the Kohlrausch stretched exponential law; for the density self-correlation function, $F_s(Q,t)$, describing the tagged particle dynamics, it reads

$$F_s(Q,t) = Aexp[-(t/\tau)^{\beta}] \qquad (1)$$

Scaling behaviour displayed by most of the systems [1] confines the temperature dependence to the scaling parameter τ, whereas β, which quantifies the degree of stretching, is a constant entirely defined by the diffusion mechanism involved. Indeed, the variations of β observed in liquids approaching the slow dynamics regime are accompanied by non-Arrhenius behaviour. The presence of activated hopping was found to considerably reduce β as compared to the hydrodynamic-like diffusion [2]. However, a quantitative microscopic interpretation of the value of β in terms of the topology of local fluctuations

Mat. Res. Soc. Symp. Proc. Vol. 407 © 1996 Materials Research Society

remains a challenging problem.

I present here a detailed description of the atomic kinetics in a quasicrystal simulated by the Molecular Dynamics (MD), which demonstrates a pronounced stretching behaviour. Quasicrystals possess a generic form of structural relaxation dynamics associated with incommensurate or phason degrees of freedom [3]. A uniform phason shift results in a set of configurations which belong to the same local isomorphism class. Therefore, it is a continuous macroscopic symmetry, and its breaking leads to dynamical modes (phasons). The phason dynamics can arise in the entropic scenario as postulated by random tiling model [4]. It assumes that phason flips connect degenerate structural units, thus producing a large configurational entropy with the maximum at zero phason strain. This stabilizes the quasicrystal structure as long as the rate of phason dynamics is high enough.

An important aspect of phason dynamics is that the local atomic motions involved give rise to a novel form of diffusion [5,6], which, due to small activation energy of a phason flip, is expected to be much faster than the conventional vacancy driven diffusion in crystals and glasses. An intellectual appeal of this phenomenon is in that the transparent geometry of phason fluctuations provides a clear interpretation of the relevant modes in terms of local atomic motion. In this study, phason mediated structural relaxations as well as the related atomic diffusion are reported, observed in a Molecular Dynamics simulation (MD) of a realistic model of a dodecagonal quasicrystal [7]. This report concentrates on the analysis of the tagged particle dynamics in the α-relaxation regime in terms of geometric constraints imposed on the relevant modes by the structure of the quasicrystal.

MOLECULAR DYNAMICS MODEL

The results presented here have been obtained in a MD simulation using a model of a dodecagonal quasicrystal [7] comprised of 16384 identical particles. It is based on a short-range pair potential, conceived to favour icosahedral local order in the first coordination shell [8]. The quasicrystal has been formed by this model from the liquid state as it was undercooled at constant density $\rho = 0.84$ below its apparent melting point at T=0.5 (the Lennard-Jones reduced units are adopted in this simulation). It represents a uniaxial stacked layered structure with 12-fold symmetry. Fig. 1a depicts the projected configuration of a structural layer; It is composed of CN14 blocks (hexagonal antiprisms), seen as dodecagons at the projection, and, by connecting their adjacent centers, a characteristic tiling is produced. Besides squares and triangles, characteristic of the related Frank-Kasper phases, it includes 30° rhombi and 3-fold hexagons (shields). The structure observed demonstrates a close consistency with the dodecagonal phases formed by Ni-Cr and V-Ni-Si alloys [9].

RESULTS

Fig. 1 presents the dynamics which the model displays at reduced temperature $T = 0.48$, where it is found to remain in apparent thermodynamical equilibrium. The principal observation is a considerable rate of spontaneous local structural rearrangements resulting in tile flips, which can be seen as mutual transformations of the rhombi and the shields. Al-

though changing the tiling dramatically, this dynamics does not violate its global 12-fold symmetry. An analysis by projection method [10-11] associates the flip with a fluctuation of the acceptance region, defined in the phason space; hence it is a phason fluctuation.

Fig. 2 depicts the geomerty of a rhombus-shield flip. In projection, the atomic motions producing the flip are seen as doubling of one of the vertices. This corresponds to a collective motion of four atoms, which move both along the axis an apart. It is important to note, that this tranformation involves vacancies, acting as catalyzing agents. The vacancies restrict axial extent of flips, and, in this way, their presence is indispensable for initiating the localized phason fluctuations observed. The prohibitingly high energy cost of the vacancy creation implies that the phason dynamics must preserve their number. Note that the two structural blocks involved in the flip contain an octahedron, which is topologically moved from its location in the center of the rhombus to the center of the shield [11]. Thus, the flip, preserving both vacancies and octahedra, is degenerate [12].

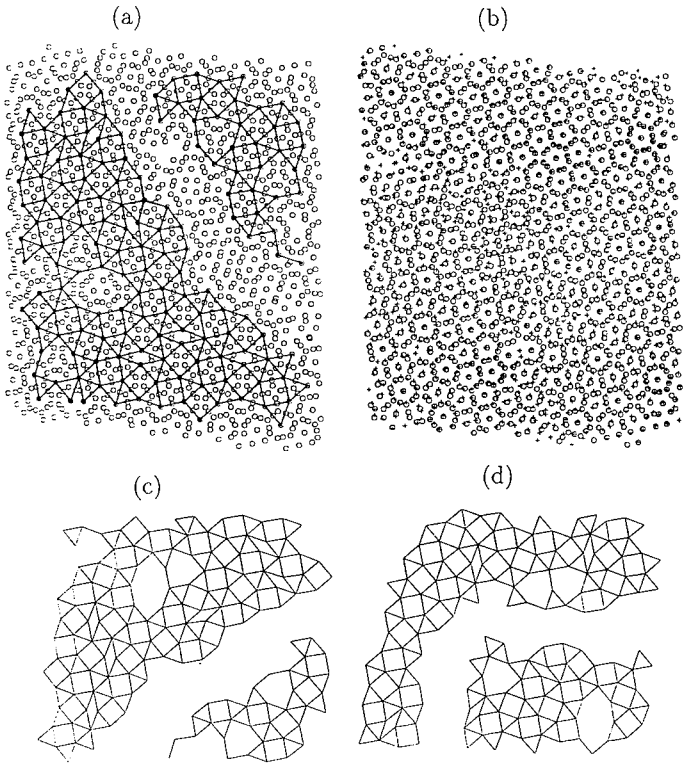


FIG. 1. (a) A configuration of a layer. Tiling is produced by connecting the adjacent centers of apparent dodecagons. (b) Superposition of two configurations of a layer separated by 10^6 timesteps. (c) and (d) show the tilings produced from these configurations.

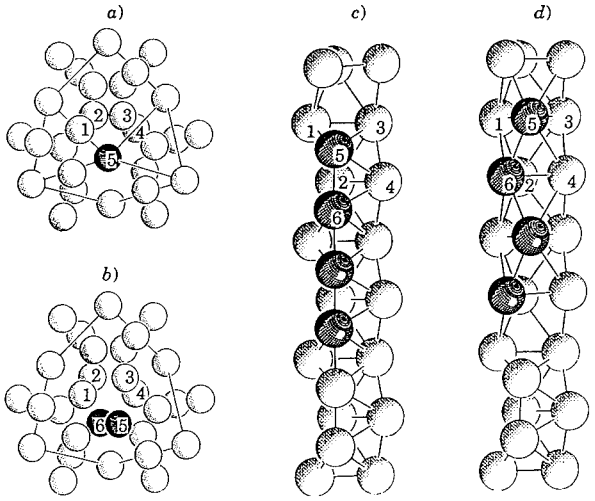


FIG. 2. (a) and (b) A rhombus-shield flip as viewed from the axial direction. (c) and (d), respectively, transformation of the axially oriented configuration in the flip. The flipping atoms are shaded dark. Enumerated atoms are those that are common for the two pairs of configurations shown.

The phason flips described involve recurrently each atom in an uncorrelated hopping, which gives rise to the unbounded diffusion. For sufficiently large times, the atomic motion is a random walk with asymptotically linear mean square displacement, Fig. 3. The temperature variation of the estimated diffusion coefficient demonstrates Arrhenius behaviour in the temperature domain that corresponds to the stable quasicrystal phase, Fig. 4, indicating stability of the diffusion mechanism involved. Since the axial component of en elementary step (Fig. 2) along the axis is about twice as large as the transversal one, the diffusion shown in Fig. 3 is axially anisotropic. But the anisotropy observed is well below the aforementioned estimation, indicating that the diffusion is contributed by the isotropic conventional vacancy-driven hopping. Presumably, this is mostly confined to the distinct defective structure region, possessing high density of vacancies, which can be observed in Fig. 1. This region, separating two coherently oriented quasicrystal domains, can be identified with 'glue phase', suggested by compartmentalization model of quasicrystal structure [13].

The tagged particle dynamics in the simulated quasicrystal was probed by calculating the incoherent intermediate scattering function $F_s(Q,t)$. Its time decay for the Q value corresponding to the position of the main peak of S(Q) is shown in Fig. 5. It shows an apparent similarity with the corresponding curves for the supercooled liquid and glassy systems [1]. The initial fast decay, describing microscopic atomic motions, is followed by a time window of the β-relaxation regime. In the diffusive -relaxation window, the function

is found to be agree perfectly with the Kohlrausch law. The fit produces the value of stretching exponent $\beta = 0.47$, which is much below of what is observed in the supercooled liquids and glasses of simple constitution [1].

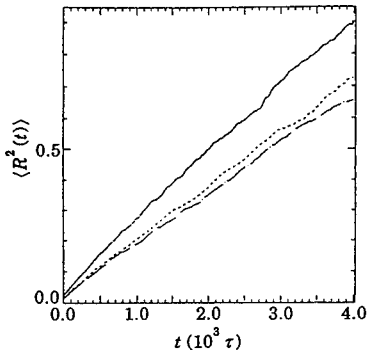


FIG. 3. Mean square displacement. Solid line, axial component; dashed and chain-dashed lines transversal components.

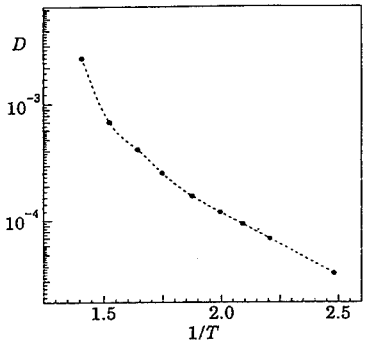


FIG. 4. Arrhenius plot of the estimated self-diffusion coefficient

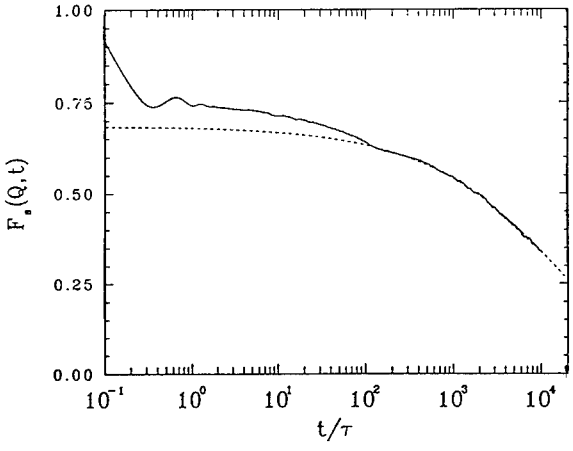


FIG. 5. Solid line, the intermediate scattering function Fs(Q,t); dashed line, Kohlrausch law fit with β=0.47.

CONCLUSIONS

An important aspect of the atomic dynamics in the quasicrystal described is that it is driven by degenerate flips of local structural units which appear to be separated by a single potential barrier. The fact that this dynamics results in a pronounced stretching of relaxation times indicates that one need not associate this phenomenon with the distribution of energy barriers; rather, it appears to be brought about by the relaxation geometry.

The anomalous distribution of waiting times that manifests itself in the non-exponential decay arises as a result of the constraints imposed on the motion of the flipping units, which suggest an analogy with the Wiener sausage model [14]. A similar geometric interpretation can be thought of for the slow dynamics in supercooled liquids and glasses, at least in those of simple atomic constitution. Atomic hopping in these systems can be regarded as arising from the local structural flips catalized by defective local units walking around.

ACKNOWLEDGEMENT

The author would like to thank J. C. Phillips, A. Sjölander, F. Gähler and C. Beeli for numerous and helpfull discussions

References

[1] W. Götze and L. Sjögren, Rep. Progr. in Phys, **55**, p241-376 (1992)

[2] M. Dzugutov, Europhys. Lett., **26**,p. 533-538 (1994)

[3] J. E. C. Socolar, T. C. Lubensky, and P. J. Steinhardt, Phys. Rev. B**34**,p. 3345-3357 (1986); T. C. Lubensky, S. Ramaswamy, and J. Toner, Phys. Rev. B**32**, p. 7444-7462 (1985)

[4] C. Henley, in Quasicrystals: the state of the art, edited by D. P. Di Vincenco and P. J. Steinhardt, World Scientific, Singapore, 1991, pp. 429-521

[5] P. Kalugin and A. Katz, Europhys. Lett. **21**, p. 921-926 (1993)

[6] G. Coddens, R. Bellissent, Y. Calvayarac, and J. R. Ambroise, Europhys. Lett. **16**, p. 271-276 (1991)

[7] M. Dzugutov, Phys. Rev. Lett **70**, p. 2924-2927 (1993)

[8] M. Dzugutov, Phys. Rev A**46**, p. R2984-R2987 (1992)

[9] H. Chen, D. X. Li, and K. H. Kuo, Phys. Rev. Lett. **60**, p. 1645-1648 (1988); T. Ishimasa, H. U. Nissen, and Y. Fukano, Phys. Rev. Lett. **55**, p. 511-514 (1985)

[10] C. Beeli, Doctoral thesis, ETH, Zurich, 1992; C. Beeli, unpublished

[11] F. Gähler, in Quasicrystalline Materials, Edited by C. Janot and J. M. Dubois, World Scientific, Singapore, 1988, pp. 34-42

[12] M. Dzugutov, Europhys. Lett **31**, p. 95-98 (1995)

[13] J. C. Phillips, and K. Rabe, Phys. Rev. Lett., **66**, p. 923-926 (1991)

[14] M. Dzugutov and J. C. Phillips, to be published; P. Grassberger, and I. Procaccia, Phys. Rev. A**26**, p. 3686-3698 (1982)

STRUCTURE OF SILANE FILMS AND THEIR ADHESION PROPERTIES

Y. CAROLINA ARAUJO AND PEDRO G. TOLEDO
Intevep, S. A., Research and Technological Support Center of Petróleos de Venezuela, S. A., P.O. Box 76343, Caracas, 1070–A, Venezuela

ABSTRACT

Silane films, their structure and stability, are of great interest in processes such as flow in porous media, mineral flotation, chromatography and corrosion. Here, the structure of octadecyl thriclorosilane (OTS) films on glass surfaces is studied by scanning electron microscopy (SEM) and atomic force microscopy (AFM), their adhesion properties by contact angle measurements and adhesion tests. Complete glass surface coverage by the silane is attained after an immersion time t_c characteristic of the OTS compound. The time evolution of the OTS films regarding surface coverage is monitored by SEM with a BSE detector, by measuring the OTS film thicknesses from XPS data, by AFM and by contact angle measurement. At t_c the structure of the films changes from micromolecular to macromolecular. Below t_c the glass coverage has a fractal geometry and various degrees of hydrophobicity are possible. At $t \geq t_c$ the surface coverage is complete and the contact angle achieved a well defined constant value.

INTRODUCTION

Silane coupling agents are widely used for preparation of hydrophobic films on hydrophilic surfaces [1–5]. However, the structure, wettability and stability of these films are still an important topic of study. The subject is of great industrial interest in assessing the impact of wettability in processes such as flow in porous media, mineral flotation, chromatography, corrosion, etc. Here we describe the structure and adhesive properties of octadecyl thrichlorosilane (OTS) films on glass slides.

Complete glass surface coverage by the silane is attained after a characteristic immersion time t_c in OTS. X-ray photoelectron spectroscopy (XPS) is used to determine surface compositions. The thickness of the OTS films on the glass surfaces is estimated from the XPS data. Contact angles and adhesion behavior are used for the wettability assessment of the silane-treated glass slides. The structure of the OTS films as a function of the immersion time in OTS is monitored by scanning electron microscopy (SEM) with a backscattering secondary electron (BSE) detector. Surface coverage is evaluated by image analysis of the SEM–BSE micrographs after digitization. In addition, the samples are studied by atomic force microscopy (AFM). At t_c the structure of the OTS films changes from micromolecular to macromolecular. Below t_c the glass coverage has a fractal geometry and various degrees of hydrophobicity are possible. The silane clusters are compact but still ramified. At $t \geq t_c$ the surface coverage is complete, the contact angle achieved a well defined constant value, and the adhesion of oil to the silane film is permanent.

SAMPLE PREPARATION

Microscope glass slides $10 \times 10 \times 1$ mm were used as solid substrates. The glass slides and glassware were rigorously cleaned according to standard procedures [6,7]. The degree of cleanliness of the glass slides and glassware was determined by the "steam test" described by

Mat. Res. Soc. Symp. Proc. Vol. 407 © 1996 Materials Research Society

Vig *et al.* [8], and by measuring water-receding contact angles. IR spectroscopy was used occasionally to verify the cleanliness of the glass slides. Teflon tweezers were used in the handling of the slides. When necessary, the cleaning procedure was repeated until satisfactory results were obtained.

Octadecyl thrichloro silane (OTS) [$CH_3(CH_2)_{17}SiCl_3$] (synthesized with a Grignard type reaction) was used for glass surface modification. Test liquids for contact angle measurement and adhesion test were mineral oil and brine.

Silane films were prepared on glass slides by immersing the clean substrates in the OTS solution for varying periods of time; 1 to 15 minutes, followed by a quick withdrawal. After reaction, the surfaces were rinsed many times with cyclohexane, dried at 100 °C overnight, and cooled in a vacuum desiccator. The slides were used immediately.

EXPERIMENTAL METHODS

The OTS films were characterized by X-ray photoelectron spectroscopy (XPS). The XPS data were obtained with a Leybold-Hereaus equipment with a LH-11 analyzer using a source of Al (13 kV, 30 mA) Kα X-rays for sample excitation. The base pressure was below 1×10^{-8} mbar. Data collection was accomplished with a microprocessor interfaced to a PC computer. The SPECS GmbH software "Spectra 5" was used for processing the XPS data.

An average thickness for the adsorbed films was determined from the XPS data. The OTS film thickness was estimated by the relation [9]

$$h = -\lambda_C \ln\left(1 - \frac{I_C}{I_C^*}\right) \tag{1}$$

where $\lambda_C = 0.08\sqrt{E}$ is the mean free path for the C1s photoelectron [10], E is the kinetic energy of the C1s photoelectron, I_C is the measured carbon concentration of an OTS-treated glass and I_C^* is the carbon concentration of an infinitely thick film of OTS. The mean free path for the C1s photoelectron is 2.7 nm.

Contact angle and adhesion behavior were used for the wettability assessment of treated and untreated glass slides. A drop of mineral oil on water-covered silane-treated glass slides was used. Contact angles were measured within $\pm 1°$. After contact angle measurement, the oil drop was slowly retracted from the substrate. Two behaviors are possible, the drop detached from the surface, indicating that non-adhesion occurred, or the drop adhered permanently to the surface.

Scanning electron microscopy (SEM) micrographs were obtained with a ISI SEM microscope with a backscattered secondary electron (BSE) detector at 10kV. SEM micrographs allow visualization of structural changes of the OTS films as a function of the immersion time of the glass in the silane solution.

In addition, we used atomic force microscopy for topographic characterization of the OTS-treated glass slides. The atomic force microscope used in this study was a Nanoscope II (Digital Instrument). High resolution (from 1 to 1000 nm) and medium resolution (from 100 to 14000 nm) OTS/glass images were obtained. We used the conventional contact mode AFM; the tip of the probe is simply dragged across the surface and the resulting image is a topographical map of the surface of the sample. AFM images were obtained at ambient conditions.

RESULTS AND DISCUSSION

XPS data. Table I gives the atomic surface composition of the OTS-treated and the untreated glass slides as determined by XPS as a function of the immersion time of the glass in the silane solution.

OTS film thickness from XPS data. Table II gives the OTS film thicknesses computed from eq. 1 and the XPS data reported in Table I. According to Table II, the OTS produces layers whose thicknesses increase from 0.19 nm to 5.15 nm as the immersion time increases from 1 to 15 min. Below $t = 10$ min the silane partially covers the glass and thus the thicknesses reported in Table II for samples M-1, M-2 and M-3 are averages only.

Contact angle and adhesion tests. The contact angle has been offered as the best wettability indicator when pure fluids and smooth surfaces are used. Table II summarizes the results on equilibrium contact angles, contact angle hystereses, adhesion behaviors and wettability states.

Table I. XPS atomic composition (At%) of OTS-treated and untreated glass slides as a function of the immersion time in OTS.

			Samples				
	OTS	M	M-1	M-3	M-6	M-10	M-15
Immersion time (min)		0	1	3	6	10	15
C – O	-	0.97	1.97	2.61	-	-	
C – H	81.8	4.79	4.79	58.28	72.83	85.01	85.05
O	-	65.92	59.84	18.47	14.98	7.99	8.06
Si – O	-	25.99	30.72	-	-	-	-
Si – CH	4.6	-	-	18.46	10.52	6.18	6.08
Ca	-	0.42	1.32	1.47	0.95	-	-
Na	-	0.47	0.73	-	-	-	-
S	-	1.4	0.63	-	-	-	-
Cl	13.6	-	-	-	-	-	-
Others	-	-	-	0.71	0.72	0.82	0.81

Sample M-15 with a surface carbon content of 85 At% exhibits an equilibrium contact angle of 106° indicative of an oil wet surface. Conversely, sample M (clean glass) with a low surface carbon content, less than 5 At%, exhibits an equilibrium contact angle of only 15° indicative of a water wet surface. Sample M-1 also with a low surface carbon content exhibits a contact angle of 30° characteristic of an intermediate wet surface. Sample M-3 with a surface carbon content of 58 At% and an equilibrium contact angle of 60° is characteristic of a weakly oil wet surface. Contact angle and surface carbon content achieve a well defined value after a characteristic immersion time of 10 minutes. These results suggest the existence of strong correlation between the surface carbon content, the equilibrium contact angle and the immersion time.

The adhesion behavior of an oil drop on a water-covered surface also reveals information on the wettability state of the surface and the stability of the silane film [6,7]. Upon withdrawal

of the oil drop from the M-3, M-6, M-10 and M-15 samples, the water advancing contact angle increased. A thin bridge of capillary-held oil developed between the oil dispenser and the glass surface. Eventually, the oil bridge becomes unstable and collapses, leaving a small drop of oil anchored to the solid surface. After several weeks of aging, the drop remained adhered to the solid surface revealing strong attractive molecular-level forces which first act to thin the water film and then to break it, allowing the oil to contact the surface. This adhesion behavior is typical of strongly-oil wet surfaces.

Table II. Equilibrium contact angles, adhesion behaviors and wettability state as a function of the immersion time in OTS. P: permanent adhesion and N: non adhesion, WW: water wet, WO: weakly-oil wet, OW: oil wet and I: intermediate wet.

		Samples				
	M	M-1	M-3	M-6	M-10	M-15
Immersion time (min)	0	1	3	6	10	15
Silane film thickness (nm)	-	0.19	2.54	5.14	5.15	5.15
Contact angle	15	30	60	104	106	106
Hysteresis[a]	0.17	0.22	0.29	0.38	0.58	0.59
Adhesion behavior	N	N	P	P	P	P
Wettability state	WW	I	WO	OW	OW	OW
Fractal dimensionality	-	1.53	1.69	1.99	2	2

[a] $\cos\theta_{adv} - \cos\theta_{rec}$, adv : advancing, rec : receding

Complete withdrawal of the oil drop was observed in the case of samples M and M-1. Stable thin films of water between the oil drop and the solid surface precluded the oil from contacting the surface. The molecular-level forces are repulsive in this case, thereby they act to stabilize a relatively thick water film. This non-adhesion behavior is typical of strongly-water wet surfaces.

OTS surface coverage by SEM and AFM. The first column of Fig. 1 shows typical SEM micrographs of silane-treated glass slides. Corresponding AFM images and profiles are shown in the second and third columns of Fig. 1 respectively. The immersion time of the glass slides in the silane solution increases from top to bottom in Fig. 1. Complete glass surface coverage by the silane is attained after an immersion time t_c between 6 and 10 min, characteristic of the OTS compound. At t_c the structure of the films changes from micromolecular to macromolecular as SEM photos in Fig. 1 reveal. Below t_c the silane films obey a fractal structure and according to the contact angle measurements various degrees of hydrophobicity are possible. At $t \geq t_c$ the surface coverage is complete. A common feature to all AFM images shown in Fig. 1 are the constituent islands of the silane clusters of roughly 100 nm in diameter, independent of the immersion time. This value is also suggested by the AFM profiles shown in Fig. 1. The SEM micrographs of Fig. 1 were digitized and their corresponding global fractal dimensions were estimated by using the box counting theorem. The fractal dimensionalities obtained are for perpendicular projections of the SEM photos shown in Fig. 1. For sample M-1 we obtained a global fractal dimension $d_f = 1.53$. The silane clusters are compact but still ramified as in any chemically-controlled aggregation process. For sample M-2 we obtained a global fractal

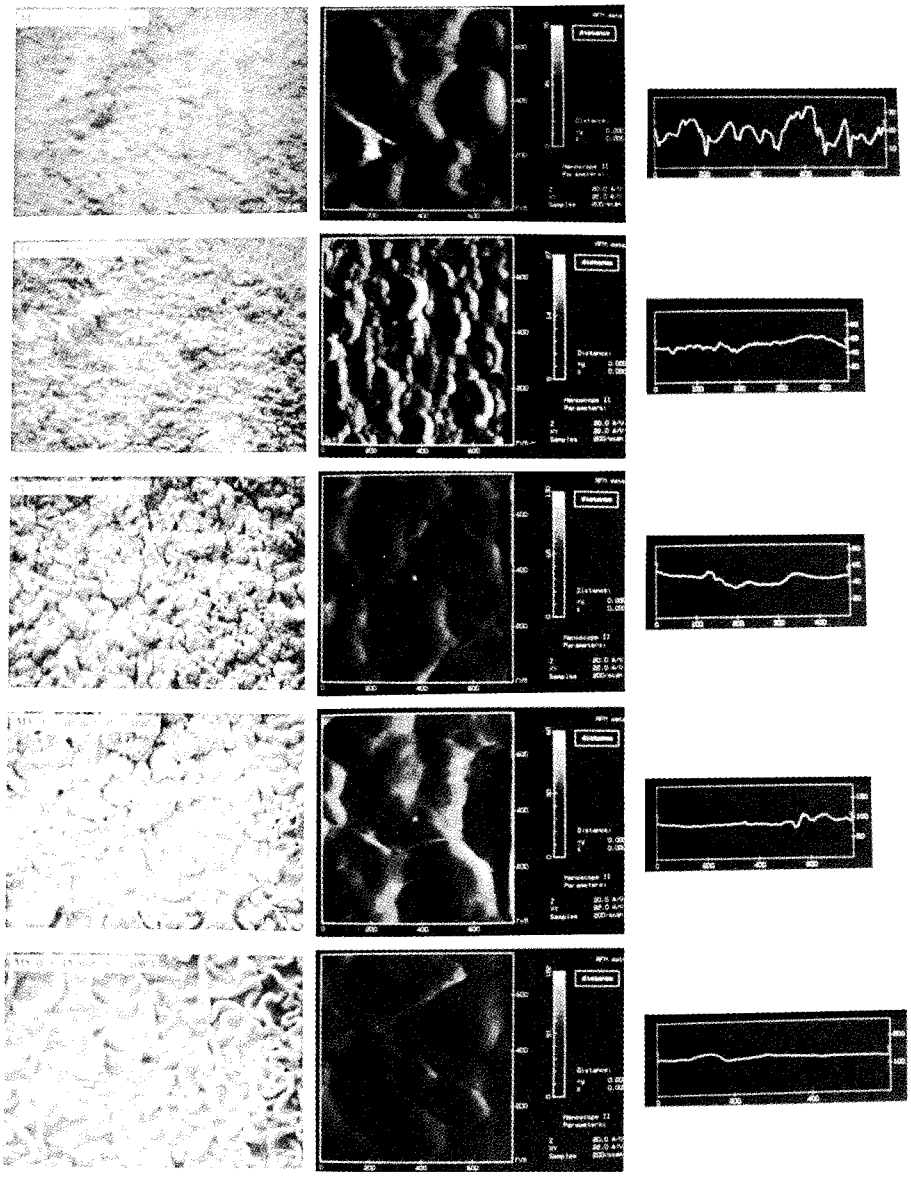


Figure 1. SEM micrographs (first column), AFM images (second column) and profiles (third column) for octadecyl thrichloro silane films on glass slides. The immersion time of the glass on the silane solution increases from top to bottom.

dimension $d_f = 1.69$. The silane clusters begin to fill the glass surface, their structures are more compact with only minor ramifications. The perpendicular projection of the SEM photo for sample M-3 has a global fractal dimension $d_f = 1.99$. A single silane cluster covers the entire surface. According to the corresponding AFM image in Fig. 1 the constituent islands, again of 100 nm, are arranged in a close packing. The AFM profiles in Fig. 1 indicate that surface roughness decreases as the immersion time of the glass substrates in the OTS solution increases. Above t_c the profile correspond to a uniform surface coverage.

The basic understanding of the structure and the adhesion properties of OTS-treated glass slides reported here is currently being applied to develop a better understanding of the influence of surface wettability in the distribution of fluid phases in porous media.

CONCLUSIONS

The structure of OTS-treated glass slides has been characterized by XPS, SEM-BSE and AFM. The adhesion behavior of the silane films has been characterized by contact angle measurement and adhesion test. The results indicate the existence of a characteristic immersion time t_c below which the structure of the silane films is self-similar and various degrees of hydrophobicity are possible. At $t \geq t_c$ the silane covers the glass surface completely and the structure is well defined by euclidean geometry, the contact angle achieves a well defined constant value, and the adhesion of oil to the silane film is permanent.

ACKNOWLEDGMENT

We thank Petróleos de Venezuela (PDVSA) and its subsidiary INTEVEP, S. A. for permission to publish this paper. We thank V. León and A. Tusa of Intevep, S. A. for assistance in the XPS and AFM work and J. Guzmán also of Intevep, S. A. for processing the SEM micrographs.

REFERENCES

1. W. Mike, R.S. Bowman, J.L. Wilson and N.R. Morrow, J. Colloid Interface Sci., **157**, 154 (1993).
2. G. Newcombe, and J. Ralston, Langmuir, **8**, 190 (1992).
3. C.R. Kessel, and S. Granick, Langmuir, **7**, 532 (1991).
4. S.R. Wasserman, Y. Tao and G.M. Whitesides, Langmuir, **5**, 1074–1087 (1989).
5. R. Maoz and J. Sagiv, J. Colloid Interface Sci., **100**(2), (1984).
6. Y.C. Araujo, P.G. Toledo, V. León and H.Y. González, J. Colloid Interface Sci., Accepted (1995).
7. P.G. Toledo, Y.C. Araujo, and V. León, Visión Tecnológica, **3**(1), 43 (1995).
8. J.R. Vig, J.W. Lebus, R.L. Filler, Proc. Annual Freq. Control Symposium, **29**, 220 (1975).
9. C.G. Pantano and T.N. Wittberg, Surface and Interface Analysis, **15**, 498 (1990).
10. M.P. Seah and W.A. Dench, Surface Interface Anal., **1**, 2 (1979).

MORPHOLOGICAL CHANGES OF BRANCHED Ge CLUSTERS CAUSED BY DIFFUSION FIELDS AND SURFACE ROUGHNESS OF Au UNDERLAYER

A. Sugawara, T. Kikukawa, Y. Haga and O. Nittono,
Department of Metallurgical Engineering, Tokyo Institute of Technology,
Oh-okayama 2-12-1, Meguro-ku, Tokyo 152, Japan.

ABSTRACT

The formation of polycrystalline Ge clusters, during annealing of amorphous Ge/ polycrystalline Au bilayers, has been studied by in-situ transmission and scanning electron microscopy. The experimentally observed generation of branching patterns, and the evolution mechanism of branches, are discussed on the basis of finite diffusion length aggregation simulations.

INTRODUCTION

Branching pattern formation during crystallization has been extensively studied for last ten years. The amorphous Ge/polycrystalline Au bilayer system is an attractive example[1-3], in which the branched growth morphology depends strongly on experimental conditions, including annealing temperature and Au underlayer thickness. The basic reason for these various morphologies is not yet understood.

We think that the pattern formation should be explained in terms of Mullins-Sekerka instability [4]: e.g. branching can take place if local mass (or heat) transport is fast enough near a perturbed growth front to overcome stabilization due to surface tension. Diffusion-limited aggregation (DLA) gives a limit of infinite diffusion length and no surface tension, in which the perturbation is given by random noise arising from stochastic processes [5]. Once these branches have been generated, their evolution creates a screening effect: diffusing particles are preferentially trapped at growth tips.

Branch generation has not been well understood experimentally. We reported previously that the growth morphology strongly depends on the Au thickness [1], and that branching takes place where the growth front is pinned by some Au grains in the underlayer [6]. This result suggests that the microstructure of the Au underlayer may affect growth morphology through generation of branches. In this study we report the growth behavior of Ge clusters on Au underlayers having three typical grain sizes. The three-dimensional morphology of the Ge clusters is also investigated.

Furthermore, the diffusion length is finite in real material systems. We reported that Ge-depleted zones surrounds the growing clusters, in which the Au underlayer becomes exposed [1]. Our results strongly suggested that the diffusion length, i.e. the widths of the Ge-depleted zones, dominates the growth morphology. We examined the spatial extent of the diffusion field by scanning electron microscopy, because it is sensitive to chemical species on the surface, as well as to surface topography. In addition we studied the effect of the diffusion length on the growth morphology from a point seed by finite diffusion length (FDL) simulation.

Finally we discuss the relation between the microscopic branch generation mechanism and the macroscopic evolution mechanism, taking into account the three-dimensional morphology of the Ge clusters.

EXPERIMENTAL AND COMPUTATIONAL METHODS

Ge/Au bilayer films were deposited onto NaCl substrates by ion beam sputtering at room temperature. Prior to deposition of Ge, Au layers were annealed at different temperatures for

Mat. Res. Soc. Symp. Proc. Vol. 407 © 1996 Materials Research Society

various times to control the microstructure of Au layers. The microstructure of the films was examined mainly by transmission electron microscopy (TEM). We also used scanning electron microscopy (SEM), because diffraction contrast in TEM images makes it difficult to observe the diffusion field clearly when the Au layer is thick. In-situ annealing experiments were done in both TEM and SEM on selected specimens.

A principle of finite diffusion length aggregation has been described by Smith et al. [7]. While particles come from infinitely far away from a cluster in the DLA model, diffusing particles start from an envelope that is a finite distance away from a cluster. We think that this is a good approximation for previous experimental results of the diffusion field. The simulations were done for 800x800 square lattices, on which a point seed was placed at an origin. We simulated four predefined diffusion lengths (l=2, 5, 10, 30 lattice constants). The density-density correlation function was calculated by a method based on fast Fourier transform (FFT). The "box-counting" method was commonly used in previous studies, though statistical accuracy was low. We can evaluate pair-correlations between growth tips by this FFT-based method. However, the raw data obtained also contains correlations between two points inside and outside of the mask. In order to avoid this edge effect, we normalized the raw data ($c_{cluster}(r)$) with the correlation obtained for the circle as large as masks used for FFT ($c_{circle}(r)$). The same method was used on the experimentally observed Ge clusters .

RESULTS AND DISCUSSION

Fig.1 shows density-density correlations. obtained from TEM images of the clusters grown on surface of Ge(10nm)/ Au(Xnm):[X=(a)2, (b)10, (c)50nm]. Original TEM images have been shown in fig.1 of Ref.1. Density of branches decreases with increasing Au underlayer thickness. The slope of the density-density correlation becomes zero above a "characteristic length", shown by arrows. Below the characteristic length, the density-density correlations shows power-law decay, and their slope was almost as large as the value obtained for DLA clusters. i. e. about -0.3. Hence, the present result indicates that the clusters are non-fractal, although we described this density change as a change of fractal dimension in the previous paper [1]. We think that the characteristic length corresponds to the average spacing between branches. As previously mentioned, we reported that the branches grow through tip-splitting due to the local pinning of the growth front. This suggests that Ge clusters grow preferentially along microgrooves formed on the Au underlayer. Morphological changes which depend on the Au underlayer thickness may therefore be explained in terms of grain size in Au underlayers, because the grain size generally increases with increasing the film thickness.

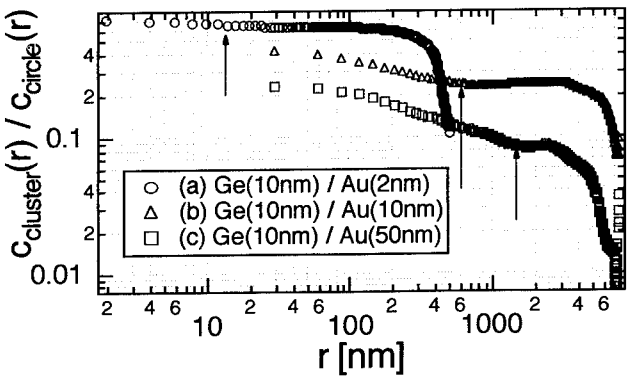


Fig.1 Density-density correlations obtained from TEM images of the clusters grown on surfaces of Ge(10nm) / Au (Xnm): [X= (a) 2nm, (b) 10nm, and (c) 50nm] [1]

Fig. 2(a-c) shows TEM images of annealed Au underlayers, showing that the grain size increased as a result of the heat treatment. Typical grain sizes in Fig. 2(a-c) are 50, 70, 150nm, respectively. After 10nm of Ge was deposited, three specimens were put into a vacuum furnace together, and were annealed at 200°C for 3hours. Fig.2 (d-f) shows corresponding crystallization patterns observed by SEM. Since nucleation density decreases, the clusters grew bigger with increasing the Au grain sizes. In fig.2(f), interesting morphological transition was observed during the growth. The cluster shape is almost circular at the beginning, and after it turned to branched growth. Fig. 3 shows the surface topography of the cluster in fig.2(f). The thickness of the central region is smaller than that of the outer branched arms. This can be understood in terms of mass conservation. Since the area covered by Ge decreases after branching takes place, the height of the cluster must increase. This also means that diffusion length is not long enough, in comparison with the cluster diameter, to screen the diffusion atoms at the initial stage. We also confirmed that the height of the clusters increased with increasing Au grain size. As a result, the Ge diffusion zone widened, as described below. The growth tip of the Ge cluster is quite flat, maybe due to good wettability between Au and Ge [fig.3(b)]. It is also seen that the growth front is pinned by coarse Au grains. However, the roughness of the Au layer is considerably smaller than the Ge grain height. Further studies should be made on this point.

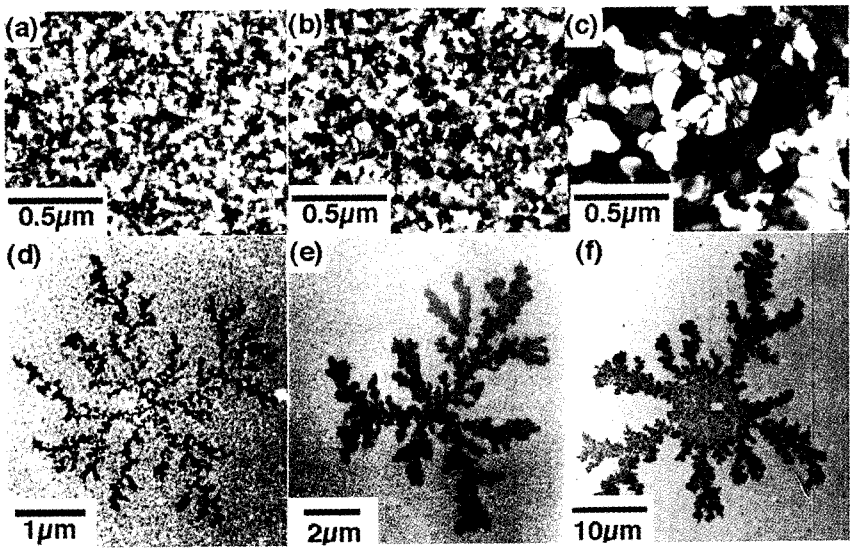


Fig. 2 TEM bright field images of Au (50nm) underlayers [(a) as-deposited, (b) annealed at 200°C for 3 hours, (c) annealed at 400°C for 3 min] and (d-f) corresponding crystallization patterns of 10nm Ge deposited onto Au layers (a-c). The crystallization was carried out at 200°C for 3 hours.

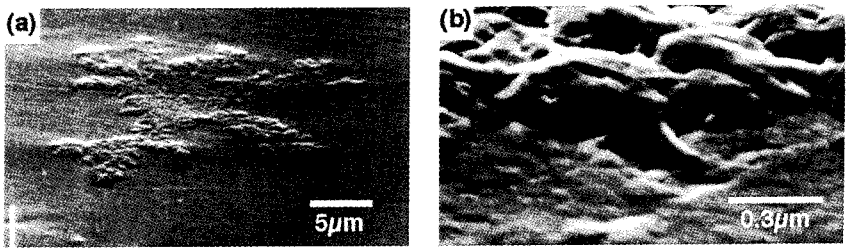


Fig. 3 Surface topography of the Ge cluster shown in fig.2(c). (a)Whole view of the cluster and (b) high magnification image of a growth tip.

Fig.4 shows SEM photographs of clusters during growth, on which calculated equi-potential lines are imposed. The Ge diffusion zone, where the Au underlayer is exposed, shows brighter contrast than Ge phases, because of high secondary electron emission from Au. The diffusion zone separates the crystalline clusters from the amorphous phase. Hence, we think that random successive nucleation mechanism, in which direct contact between amorphous and crystal is assumed, is not applicable for this growth [2, 3]. When spacing between two neighboring branch is large, the diffusion zone is wide. This means that the branch density is determined by the diffusion length. It is also important to analyze the periphery of the diffusion field on the basis of diffusion equations. The periphery should be related to an equi-potential line of Ge. We couldn't measure concentration profile of Ge in the diffusion zones. Instead, we solved Laplace equation numerically around the clusters by the successive overrelaxation method [8]. The same type of calculation has been done for DLA aggregates by Family et al. [9]. We assumed ideal chemical potential that is zero at the cluster edge, and is 1 at the edge of a 800x800 square lattice. The lattice size is three times as big as the diameters of the digitized clusters. This is large enough to avoid any unexpected edge effect. We can see that the calculated equi-potential line qualitatively fits the periphery observed in SEM photographs. The potential gradient is small between neighboring branches (screening effect), and is large near growth tips (preferential trapping). This is an evidence that the long-range diffusion field dominates the cluster morphology

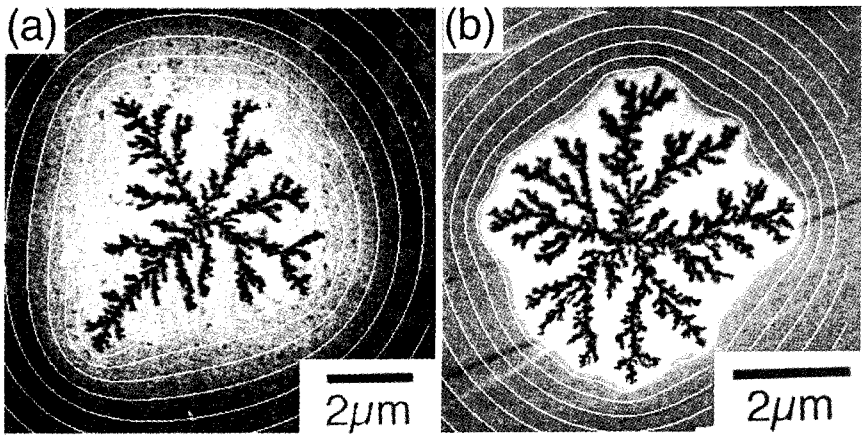


Fig.4 Scanning electron micrographs of clusters surrounded by Ge-depleted diffusion zone. Equi-potential lines calculated are imposed on the photographs. (a) Ge(10nm)/Au(10nm), (b) Ge(10nm)/ Au (10nm)

Fig.5 shows typical morphology of the clusters composed of 10000 particles generated by the simulation (only a quarter of each cluster is shown), and the corresponding density-density correlations. The gray regions surrounding the clusters are diffusion zones. The diffusion particles start from periphery of these zones. The branch density decreases with increasing diffusion length. This means that the averaged branch separations are roughly twice the diffusion length, as found previously [7]. The density-density correlations shows power-law decay in ranges shorter than the predefined diffusion length; however, the slope becomes zero above the diffusion length. The appearance of the plateaus agrees with the experimental results qualitatively. The periphery of the diffusion zones agrees qualitatively with the equi-potential lines calculated by the method described above.

However, simulation results cannot be compared with experiments directly. While the slopes of correlations change at predefined diffusion length in the simulation results, the experimental transition length shown in fig.1 are longer than the widths of the diffusion zone. This may be due to the fact that the surface tension is assumed to be zero in the simulation We probably have to take into account another characteristic length concerning surface tension or local pinning effect to reproduce the experimental results more closely. Furthermore, in-situ observation of the growth showed that the width of the diffusion zone increased with increasing cluster size during the growth , because of mass conservation of Ge. This kind of mass conservation condition should be also introduced to the FDL simulations to get better reproduction of the experimental data.

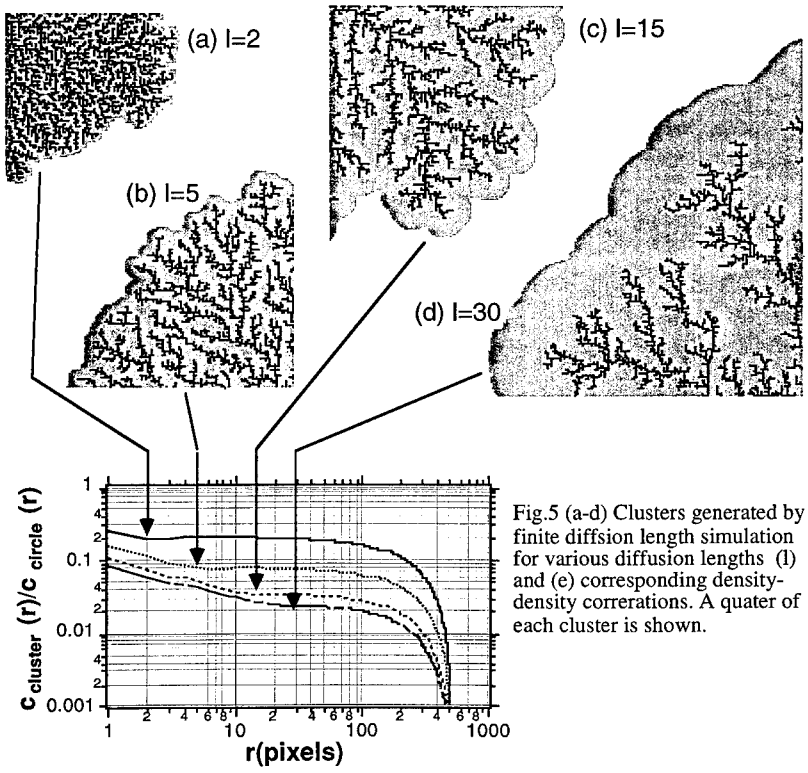


Fig.5 (a-d) Clusters generated by finite diffsion length simulation for various diffusion lengths (l) and (e) corresponding density-density correrations. A quater of each cluster is shown.

Recently Röder et al. reported that similar growth morphology is formed in metallic sub-monolayer growth systems, which can be regarded as real two-dimensional systems [10]. In contrast, the clusters observed were three-dimensional in this study. The clusters were composed of Ge crystallites larger than several tens of nanometers in diameter. This kind of three-dimensional morphology of the Ge clusters has not been taken care of in previous studies. The pattern formation is explained in terms of the long-range diffusion field from a macroscopic viewpoint. However, the spatial extension of the diffusion field itself is determined by the width, height, and spacing of the branches. Thus, we have to take into account the three-dimensional morphology to understand the mass conservation.

CONCLUSIONS

We investigated pattern formation mechanism of the branching Ge clusters during crystallization. The Ge branches grow along the microgrooves on the Au underlayer surface. Hence, curvature of the Ge growth front and widths of the branches increases with increasing the Au grain size as a result of the "local pinning effect". The extended growth tip is evolved by the screening effect in Laplace field surrounding the cluster. The branch density decreased with increasing diffusion length. This tendency was also confirmed by simulation of finite diffusion length aggregation.

ACKNOWLEDGMENT

A part of this study is supporeted by Kazama foundation.

REFERENCES

[1] A. Sugawara, T. Kikukawa and O. Nittono, Mat. Sci. Eng., **179**, 355, (1994).
[2] J. q. Hou and Z. q. Wu, Phys. Rev., **B40**, 1008 (1989).
[3] J. Z. Duan and Z. Q. Wu, Sol. Stat. Comm., **65**, 7 (1988).
[4] W. W. Mullins and R. F. Sekerka, J. Appl. Phys., **34**, 323 (1963).
[5] R. C. Ball and T. A. Witten, Phys. Rev. **A29**, 2966, (1982)
[6] A. Sugawara, T. Kikukawa and O. Nittono, Proceedings of 14th International Conference on Electron Microscopy (1994, Paris, France) p467.
[7] R. L. Smith and R. D. Collons, Phys. Rev., **A39**, 5409, (1989)
[8] *"Numerical Recipes in Pascal"*, Ed. William H. Press, Cambridge University Press, Cambridge, 1989.
[9] F. Family and T. Vicsek, *Computer Phys.* p44(1990).
[10] H. Röder, E. Hahn, H. Brune, J. P. Bucher and K. Kern, Nature, **366**, 141, (1993).

ATR-FTIR SPECTRAL INVESTIGATION OF SO_2-TREATED SODA-LIME-SILICATE FLOAT GLASS

U. SENTURK, D.H. LEE, R.A. CONDRATE Sr., and J.R. VARNER
New York State College of Ceramics at Alfred University, 2 Pine st., Alfred, NY 14802.

ABSTRACT

The near-**surface** infrared spectral changes that occurred on a commercial **soda-lime-silicate glass**, which was heat treated in SO_2/H_2O/air atmospheres, were measured, in the region 1200 to 600 cm^{-1}, using attenuated total reflectance Fourier-transform infrared **(ATR-FTIR) spectroscopy**. Sets of spectra were taken at different angles of incidence of the infrared beam corresponding to successive penetration depths on the surface, hence, giving a surface spectral profile. It was found that the Si-O-Si vibrational band, observed in the region ~1100 cm^{-1}, is the most affected; with increasing depth the band becomes weaker, depending on the treatment temperature and water content in the treatment atmosphere. The two different sides (the side in contact with the tin bath (tin side) and the opposite side (air side)) were determined to have a different character as a result of the **dealkalization** treatments.

INTRODUCTION

Exposure of glass surface to SO_2 at temperatures in the annealing range improves the chemical resistance and mechanical behavior of silicate glasses containing alkalis or alkalis and alkaline-earths [1-4]. The dealkalized glass surface corresponds to a Type II surface, as described by Hench and Clark [5], which is defined as one that possesses a silica-rich protective film due to selective alkali ion removal. The net effect in the process is the removal of alkali near the surface, which, after reacting with sulphur oxide, remains in the form of micro-crystallites of alkali-sulfate on the surface, referred to as the bloom (Na_2SO_4 forms as the main constituent of the bloom). Treatment temperatures, as well as the presence and concentration of water in the treatment atmosphere, have a big influence on the extraction of the alkalis [1,3].

Analytical surface characterization techniques have been quite useful in describing the formation of the surface silica-rich layer as a result of SO_2 treatments [6]. Internal reflection spectroscopy (IRS) has been used as a method of obtaining absorption spectra of species that are located at the surface of a sample. However, not much has been done in the field of glass research [7] to characterize the surface structural formation using the ATR-FTIR spectral technique. The method seems promising for giving knowledge about the surface structural changes that are occurring at different depths of the sample surface. Hence, a surface "structural profiling" is possible with this technique. The objective of this study is to perform an ATR-FTIR spectral analysis on a commercial soda-lime-silicate float glass surface in its as-received state and treated with SO_2. The aim is to investigate the structural changes that are taking place on the surface, as a function of the depth, for the different applied dealkalization conditions.

EXPERIMENTAL PROCEDURES

A commercial soda-lime-silicate float glass (provided by Ford Motor Co.) was used to investigate the effects of SO_2 treatments on the surface properties. The dealkalization treatments were performed in a fused silica tube furnace. Glass samples, cut to a size of 5x4cm from plates that were 0.4cm thick, were treated at 500 and 600°C (which were determined to be below and

Mat. Res. Soc. Symp. Proc. Vol. 407 © 1996 Materials Research Society

above the glass transition region, respectively, by differential scanning calorimetry) for 36 minutes. Temperature variation along the glass surface was ±2°C. Appropriate gas mixtures were obtained by mixing SO_2 with dry and wet air. Water in the atmosphere was obtained by bubbling air through distilled water that was heated to ~60°C. SO_2 gas flow was kept at around 4-6% of the flow of air during the treatment period. Both surfaces of the float glass (i.e., the side in contact with the tin bath during the float process and the opposite side) were treated under the same conditions. The bloom formed on the surface after treatment was washed away, and the surface was cleaned further by carefully wiping the surface of any organic contaminants, using methyl alcohol, prior to placing the sample in the ATR sample holder.

The ATR-FTIR spectra were obtained using a Nicolet 60SXR-FTIR spectrometer at 4 cm^{-1} resolution with a variable-angle (30° to 60° range) ATR attachment, in the 1200 cm^{-1} to 600 cm^{-1} wave number region. A KRS-5 internal reflection element (IRE), which has a refractive index of 2.4, was used with the attachment. The sample surfaces to be investigated were placed on the two sides of the IRE. A good physical contact between the sample surface and the IRE was achieved, since float glass has a flat, smooth surface. The details of the principles of internal reflection spectroscopy have been discussed elsewhere [8].

Depth of penetration (d_p) of the infrared beam into the sample surface is defined by the following relation [8]:

$$d_p = \frac{\lambda}{2\pi n_1[\sin^2\theta - (n_2/n_1)^2]^{1/2}} \qquad (1)$$

where λ is the wavelength of infrared radiation, n_1 is the refractive index of IRE (2.4 for KRS-5), n_2 is the refractive index of the sample (1.51-1.52 for soda-lime-silicate glass), and θ is the angle of incidence of the infrared beam. In general, penetration depth decreases as the angle of incidence increases. The theoretical penetration depth of the infrared beam, according to the above relation, was calculated to be in the 1.1-6.4 μm range, for the incidence angles in the range 54°-41°. However, it should be noted dealkalization would cause a variation in the refractive index due to changes in the alkali content and incorporation of protons on the surface of the glass. In addition to this, the refractive index of the surface would also change with the change in the wavelength in the infrared region [7]. Due to these reasons, deviations from the theoretically calculated depth of penetration should be expected.

RESULTS AND DISCUSSION

ATR-FTIR spectra of the tin and air sides of the as-received glasses, for the different angles of incidence of the infrared beam, are illustrated in Figures 1 (a) and (b), respectively. The spectra show bands of different intensity that appear at around 1160, 1100, 1030-1050, 870 and 760 cm^{-1}. The assignments of these bands to their characteristic vibrational features are given in Table I. Table II lists the individual band position of Si-O-Si vibrations for the different angles

Table I: Assignment of infrared bands of soda-lime-silicate glass

Wavenumber (cm^{-1})	Assignment	Type of vibration	References
1160-1140	SiO_4^{4-}	Polymerization	6, 9
1100	Si-O-Si	Antisymmetric stretching	10-13
1050-1030	Si-O	Stretching of $Si\text{-}O^-Na^+$ (NBO)	10-13
900-860	Si-OH	Stretching of Si-OH	6
770-730	Si-O-Si	Symmetric stretching	10-13

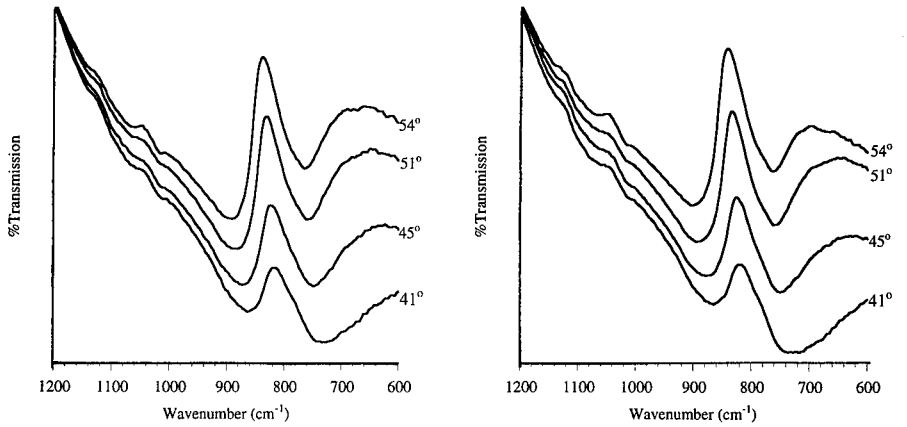


Figure 1. ATR-FTIR spectra of the as-received float-glass **(a)** tin side, **(b)** air side.

Table II. Wavenumber band locations of the Si-O-Si stretching mode for the as-received and treated conditions on both sides of the float glass.

		Air Side	Tin Side
TreatmentCondition	**IR angle of incidence**	**Si-O-Si**	**Si-O-Si**
As-Received	41	731	733
	45	750	748
	51	762	760
	54	764	766
500°C	41	729	731
Dry Air	45	752	754
	51	764	762
	54	764	766
600°C	41	746	748
Dry Air	45	758	758
	51	764	764
	54	769	766
500°C	41	741	725
Wet Air	45	756	752
	51	764	764
	54	766	766
600°C	41	746	735
Wet Air	45	754	750
	51	762	762
	54	766	768

of infrared beam incidence on the two surfaces at its as-received and treated conditions. The spectra for the two sides show no significant difference for the band intensities and positions at the same incident angles, indicating that the two surfaces of the float glass, in its as-received condition, are similar in their structural formation.

Figures 2 (a) to (d) show the ATR-FTIR spectra of the glass surfaces treated in SO_2-dry air atmosphere, and Figures 3 (a) to (d) show the same for treatments done in SO_2-wet air atmosphere for the two sides of the float glass at different angles of incidence of the infrared beam. The spectra after these treatments show deviations from those of the as-received glass. The major difference is for the 1100 cm^{-1} band, which is associated with the antisymmetric Si-O-Si stretching vibration, that shows an intensity dependency on the incidence angle; in general, this band gets stronger as the angle of incidence increases (i.e., at the very near surface) and is usually weak at the low angle of incidence. The strengthening of this band (which can also be referred to as the bridging-oxygen band) as one approaches the surface indicates that there is an increasing amount of silica formation at the surface which coincides with the removal of alkali. Accordingly, the air side is recognized to be more dealkalized, for all the temperature and atmosphere conditions applied, since this band appears stronger compared to the tin side for all the angles of incidence. The optimum condition for dealkalization, in this sense, is the treatment done at 600°C in SO_2 -wet air. This treatment condition causes the band to be stronger at all the angles of incidence, indicating that dealkalization has occurred further into the surface. The 1050-1030 cm^{-1} band, which is associated with the stretching vibration of the $Si\text{-}O^{-}Na^{+}$ bond, disappears, except for the 54° angle of incidence, for all of the treatment conditions and sides. This strengthens the argument that the SO_2 treatment has been effective in the removal of the surface alkali. The reason for the presence of this band at the 54° incidence angle is, as yet, not known.

Shifts in the band positions for each incidence angle can be recognized with the change in temperature and humidity conditions. The shift of the Si-O-Si related band to higher wavenumbers is consistent with decreases in the alkali content of the glass composition [6,12,14] as well as with proton-alkali ion exchange during aqueous corrosion of the glass surace [14]. The higher incidence angles (54° and 51°) show no significant shift. 45° angle of incidence shows an increasing shift with increasing temperature for both sides of the glass, with the shift for the dry treatment being higher. 41° angle of incidence shows a slight decrease for the dry 500°C treatment on both sides and on the tin side for the humidity-treated sample. High-temperature treatment moves the band to higher wavenumbers for both sides, the bands for the air side being shifted to higher wavenumbers.

The results indicate that the air side is more dealkalized, since this side shows higher shifts, which agrees with the results obtained from the band intensities. The fact that the infrared spectra for the 54° and 51° angles of incidence do not show any significant shift might be because the near surface is depleted of alkali for all of the treatment conditions applied. For the low incidence angles, the infrared beam encounters increasing alkali concentration. Variation in the surface alkali concentration, thus, would have an increasing effect on the Si-O-Si band shift. Hence, significant shifts at the higher penetration angles indicate the changing dealkalization depths on the surface. The small decrease in band position at the 500°C dry air treatment indicates an increase in alkali content, thus implying that the treatment has not been effective at this temperature-atmosphere condition, on both sides of the glass. Shifts in the band positions to higher wavenumbers indicate that humidity in the atmosphere and high treatment temperatures are important factors that affect surface alkali depletion. The comparison of band intensities also indicated the same trend.

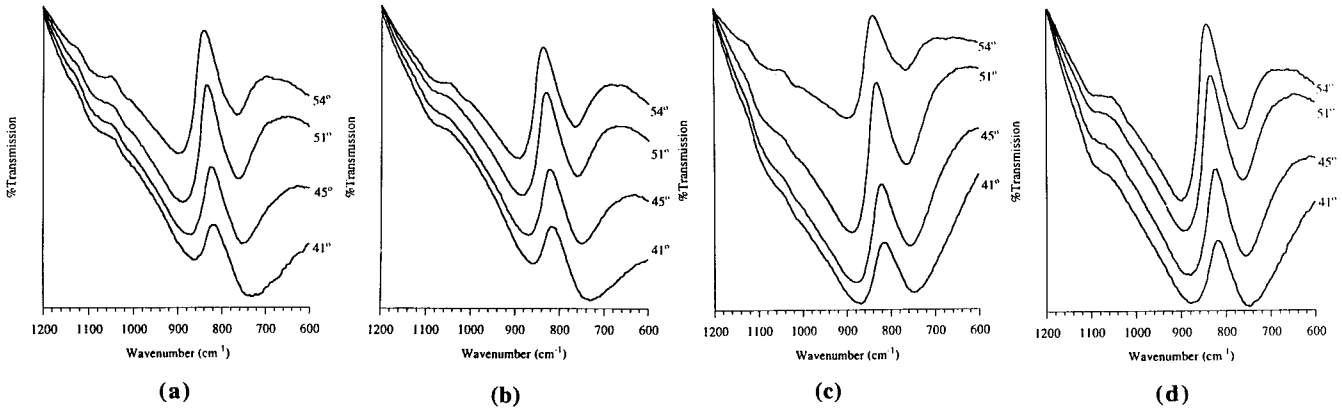


Figure 2. ATR-FTIR spectra of the SO_2-treated float glass in dry air atmosphere at **(a)** 500°C (tin side), **(b)** 500°C (air side), **(c)** 600°C (tin side), **(d)** 600°C (air side).

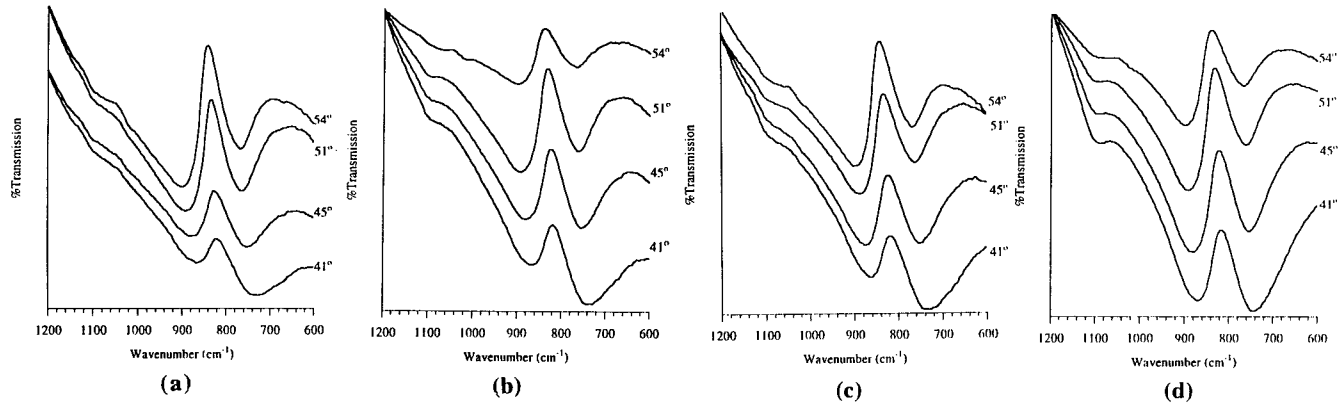


Figure 3. ATR-FTIR spectra of the SO_2-treated float glass in wet air atmosphere at **(a)** 500°C (tin side), **(b)** 500°C (air side), **(c)** 600°C (tin side), **(d)** 600°C (air side).

Another significant shift in the positions of the individual bands occurs as a function of incidence angle of infrared at the same treatment conditions and glass side. These shifts have a tendency to increase in wavenumber as the angle of incidence increases (in other words, the penetration depth of the infrared beam decreases, in accordance with equation (1)). This effect is due to the fact that there is a dispersion in refractive index in the vicinity of these absorption bands; therefore, the higher the angle of incidence, the more the spectra is affected by dispersion [8].

CONCLUSIONS

ATR-FTIR was applied for the surface "structural profiling" of soda-lime-silicate float glass that was treated in several SO_2/H_2O/air atmosphere conditions, at temperatures in the glass transition region. Changes in the intensity of the Si-O-Si vibrational band at ~1100 cm^{-1}, the shifts in the band position at 770-730 cm^{-1}, and the disappearance of the band associated with $Si\text{-}O^-Na^+$ at ~1150-1130 cm^{-1} indicated that the surface was depleted in alkali content and the Si-O-Si linkages increased as a result of the treatments. Water in the treatment atmosphere increased the possibility of proton incorporation in the surface, which also was consistent with the shift of the band at ~770-730 cm^{-1} to higher wavenumbers [14]. Similar spectral features revealed that the air side of the float glass was dealkalized to higher depths. Spectral features at different angles of infrared incidence of the treatments illustrated that temperature and humidity in the treatment atmosphere were effective in improving the removal of alkali and the formation of the bridging-oxygen links.

REFERENCES

1. J.N. Coward and W.E.S. Turner, J. Soc. Glass. Technol., **22**, 309 (1938).
2. H.S. Williams, and W.A. Weyl, Glass. Ind. **26**, 275 (1945).
3. W.A. Weyl, Glass. Ind. **26**, 369 (1945).
4. R.W. Douglas, and J.O. Isard, J. Soc. Glass. Technol., **33**, 289 (1949).
5. L.L. Hench and D.E. Clark, J. Non-Cryst. Solids, **28**, 343 (1977).
6. N.A. Sharaf, S.M. Brzytwa, R.A. Condrate, Sr., R.P. Hapanowicz, W.C. LaCourse, and P. Shen, in The Physics of Non-Crystalline Solids, edited by L.D. Pye, W.C. LaCourse, and H.V. Stevens (Taylor and Francis, London, 1992), p.236.
7. T. Uchino, T. Sakka, K. Hotta, and M. Iwasaki, J. Amer. Ceram. Soc., **72**, 2173 (1989).
8. N.J. Harrick, Internal Reflectence Spectroscopy (Wiley Interscience, New York, 1967).
9. D.E. Clark, E.C. Ethridge, M.F. Dilmore, and L.L. Hench, Glass. Tech., **18**,121 (1977).
10. R. Hanna and G-J. Su, J. Amer. Ceram. Soc., **47**, 597 (1967).
11. D.M. Sanders, W.P. Person, and L.L. Hench, Appl. Spectrosc., **28**, 247 (1974).
12. J.R. Ferraro and M.H. Mangnani, J. Appl. Phys., **43**, 4595 (1972).
13. I. Simon and H.O. McMahon, J. Amer. Ceram. Soc., **36**, 160 (1953).
14. D.E. Clark, M.F. Dilmore, E.C. Ethridge, and L.L. Hench, J. Amer. Ceram. Soc., **59**, 62 (1976).

STEREOLOGICAL ESTIMATION OF FRACTAL NUMBER OF FRACTURE PLANES IN CONCRETE

P. STROEVEN
Faculty of Civil Engineering, Delft University of Technology, 2628 CN Delft, The Netherlands, p.stroeven@ct.tudelft.nl.

ABSTRACT

Concrete is a man-made material containing a particulate filler designed on the basis of a sieve curve. In case of river aggregate, the particles are approximately spherical and smooth-textured. The particle-matrix interface is mostly the weakest chain link in the mechanical system. This implies damage evolution to start at particle-matrix interfaces. In case of direct tension, these interface cracks will be on average perpendicular to the loading direction. In case of direct compression, they will be parallel to the loading direction. A single fracture surface is formed in tension and a series of fracture surfaces in compression. They are the result of crack concentration within a process zone, in which the engineering crack closely meanders around a dividing plane. This allows to model these fracture surfaces on different resolution levels. It is shown, using stereological notions, that the very phenomenon is of a non-ideal fractal nature. Estimates for fractal dimension of fracture surfaces in concretes based on sieve curves at the border of the practical range are found to closely match experimental data reported in the literature.

INTRODUCTION

Concrete is a composite encompassing a wide range of aggregate particles . The aggregate's largest particles are 31.5 or 62 mm, depending on the application. The finer sand fractions have particles in the sub-millimeter range. The aggregate forms a skeletton glued together by a cementitious binder. The binder also fills the open spaces to guarantee durability. In normal concrete the particulate skeletton transfers the major part of the compressive loadings. Since the tensile strength is inferior, a steel reinforcement is applied for that purpose in constructions. Bond between aggregate and the cementitious matrix forms the weakest chain link in the micromechanical system, particularly when river aggregate is employed. Under increasing loadings the material's integrity will gradually break down. Structural loosening manifests itself in cracking on the various levels of the microstructure, ultimately leading to the development of engineering cracks. In a global way, total crack extension is denominated as "damage", so that crack formation leads to damage evolution. The damage evolution process is characteristic for the material structure under the particular loading conditions.

Studies of damage evolution in opaque materials like concrete are pursued by following different strategies. The deminishing material density can be detected by measuring the delay in ultrasonic wave propagation through the material. It is a low-sensitivity and global approach. Acoustic emissions accompanying crack formation are employed to characterize some damage evolution stages. Since miriads of mesoscopic and microscopic cracks have already developed in virgin specimens of normal concrete, source location is complicated. So the general approach is also a global one, though more sensitive than the wave propagation method. Visual inspection offers direct and local information, but when applied to specimens under increasing loadings, it's scope is restricted to the analysis of cracking at surfaces. High-sensitivity observations are realized with holographic interferometry. Alternatively, pre-loaded specimens can be subjected to serial sectioning, whereupon the internal crack structure can be studied. Basically, it offers local information and the sensitivity level can be selected by the researcher.

The naked eye constitutes a low-sensitivity approach, allowing the detection of crack traces on engineering level. Qualitatively similar results can be obtained by applying pho-

Mat. Res. Soc. Symp. Proc. Vol. 407 © 1996 Materials Research Society

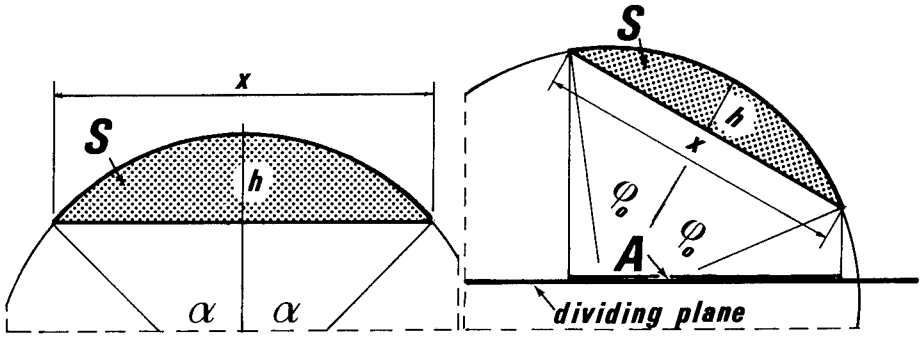


Fig. 1. Bond cracks contributing to damage (left) and to fracture surface roughness (right).

toelastic coatings. The sensitivity can be improved by artificially increasing the contrast between cracks and background. Under such conditions also the larger mesocracks will be visible, so that damage seems to be more severe. Further enhancement can be achieved by observing the phenomenon with the help of a microscope. The higher the magnification, the more traces become discernable. With SEM or TEM cracks can be detected on an even lower level of the microstructure. These should be added to the ones detected under lower magnifications. This shows total crack length per unit of area, L_A, to be clearly resolution-dependent. The same holds for the total crack surface area per unit of volume, S_V, as a global 3-dimensional measure for damage. The latter can be estimated using stereological methods for quantitative image analysis [1]. The fractal concept offers possibilities to give a quantitative basis to this phenomenon [2].

DAMAGE AND RESOLUTION

The 'elastic limit', 'discontinuity point' or 'crack initiation strength' in concrete technology is characterized by a certain stage of particle-matrix debonding: the supposedly spherical river gravel particles (diameter d) are assumed to be debonded over a similar angular extension, 2α. The surface area of a bond crack is given by (Fig. 1, at th left)

$$S = \pi(h^2 + \frac{1}{4}x^2) \tag{1}$$

h and x are the crack's height and span, respectively. Substitution of $h = d/2(1-\cos\alpha)$ and $x = d\sin\alpha$ yields $\overline{S} = \pi\overline{d^2}(1-\cos\alpha)/2$, with $\overline{d^2}$ being the second moment of the particle size distribution function (psd). The upper and lower boundaries of the sieve curves in the building codes can generally be approximated by a straight line and a second order parabola in a semi-logarithmic plot (Fig. 2). Transformation readily leads to the psd's

$$f(d)_u = 2.5\frac{d_0^{2.5}}{d^{3.5}} \quad \text{and} \quad f(d)_l = 3\frac{d_0^3}{d^4} \tag{2}$$

The first, second and third moments of these psd's are presented in Table 1.

d_c is the average size of the grains intersecting a (fracture) plane. Total amount of damage is $\overline{S}.N_V$, where the particle density, N_V, is given by $N_V = 6V_V/\pi\overline{d^3}$. As an example, substitution for the upper bound yields [3]

$$\overline{S}N_V = S_{Vc} = 3(1-\cos\alpha)\frac{\overline{d^2}}{\overline{d^3}}V_V = \frac{3(1-\cos\alpha)\sqrt{M}}{d_m}V_V \tag{3}$$

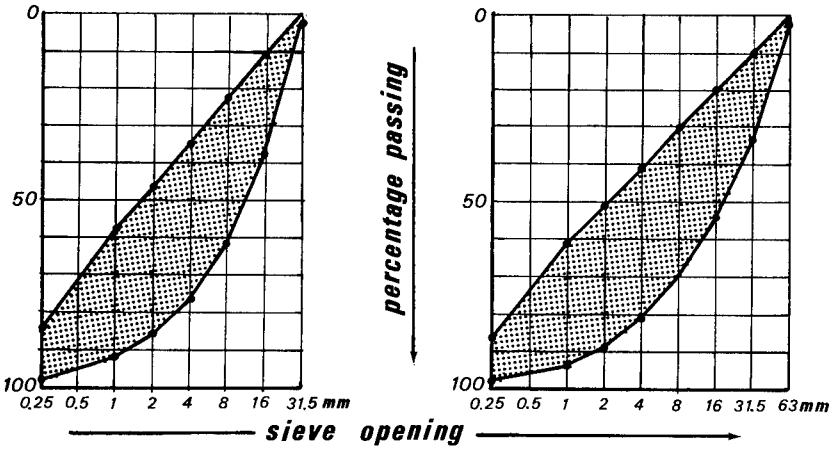


Fig. 2. Area prescribed for sieve curves (Dutch building code NEN 3861)

Table 1. Moments of the psd's corresponding to the boundaries for the sieve curves prescribed by the building code.

	$\overline{d}$	$\overline{d^2}$	$\overline{d^3}$	$\overline{d_c}$	$\overline{d_c^2}$
$f(d)_{upper} = \frac{5}{2}\frac{d_0^{2.5}}{d^{3.5}}$	$\frac{5}{3}d_0$	$5d_0^2$	$5d_0^2 d_m^{0.5}$	$3d_0$	$3d_0^{1.5}d_m^{0.5}$
$f(d)_{lower} = 3\frac{d_0^3}{d^4}$	$\frac{3}{2}d_0$	$3d_0^2$	$3d_0^3 \ln\frac{d_m}{d_0}$	$2d_0$	$2d_0^2 \ln\frac{d_m}{d_0}$

Table 2 presents estimates for 'damage' as a function of resolution, determined by eq (3) assuming $\alpha = 45^0$. The influence of magification (M) is obvious. An experimental approach with a sensitivity level of 1mm (=lower boundary for detecting crack trace length) would yield a specific crack surface area of about 0.2 mm^2/mm^3, which is quite close to experimental findings [1].

FRACTURE AND RESOLUTION

Basically, two extreme cases of crack coalescence could be modelled. In the first, the particle-matrix interface cracks will extend to the dividing suface. This implies the *angular bond crack extension to be a variable*. Since the curvature of the dividing surface will be considerably less than that of the largest particles in the mix, for modelling purposes the dividing surface can be assumed planar. In the second, the bond cracks have developed to a constant angular extension, $2\phi_0$, so that slightly out-of-plane cracks have to coalesce in order to create the macro crack. Although the width of the so called fracture process zone is governed by the largest particles in the mixture, d_m, the distances of the microcracks to the dividing plane can be expressed in terms of average particle size, $\overline{d_c}$. In practice, the bond cracks which will constitute part of the fracture surface *in statu nascendi* will not necessarily form a parallel array. Instead a system with a *partially planar* orientation distribution has to be emphasized. The model selected for this paper reflects features of both extremes, thereby taking an intermediate position. The size distribution of intersection circles of the bond cracks with the dividing surface are taken according to the first case. Size

Table 2. Damage as a function of resolution

$M = d_m/d_0$	V_V	d [mm]	d_0 [mm]	d_m [mm]	S_{Vc} [mm^{-1}]
2	0.1	16-32	16	32	0.004
4	0.2	8-32	8	32	0.011
8	0.3	4-32	4	32	0.023
16	0.4	2-32	2	32	0.044
32	0.5	1-32	1	32	0.078
64	0.6	0.5-32	0.5	32	0.132
128	0.7	0.25-32	0.25	32	0.217

distribution function of the cracks is governed by an integral equation of Abel's type [4]. The intersection circles have a partially-planar orientation distribution in accordance with experimental observations as to crack trace distributions [1] [2] (Fig. 2, at the right).

The relevant parameter for fractal interpretation of the fracture surface in the model will be the total crack surface area per unit of the dividing surface, S_A. The increase in surface area is due to particle indentations of the dividing surface. Individual contributions are given by eq. (1). Using the moments of the psd's presented in Table 1, S_A is determined for the two different sieve curves given by eq (2). Hence,

Lower boundary case: $f(d)_l = 3d_0^3/d^4$

$$\begin{aligned}
\overline{x} &= J_2\overline{d^2}/\overline{d} &&= \tfrac{\pi}{2}d_0 \\
\overline{x^2} &= J_3\overline{d^3}/\overline{d} &&= \tfrac{4}{3}d_0^2 \ln\tfrac{d_m}{d_0} \\
\overline{h} &= \overline{d_c}/4 &&= \tfrac{1}{2}d_0 \\
\overline{h^2} &= (\overline{d_c^2} - \overline{x^2})/4 &&= \tfrac{1}{6}d_0^2 \ln\tfrac{d_m}{d_0} \\
\overline{S} &= \pi(\tfrac{1}{6} + \tfrac{1}{4}\cdot\tfrac{4}{3})d_0^2 \ln\tfrac{d_m}{d_0} &&= \tfrac{\pi}{2}d_0^2 \ln\tfrac{d_m}{d_0} \\
N_A &= (6V_V\overline{d})/(\pi\overline{d^3}) &&= \tfrac{3}{\pi}\tfrac{V_V}{d_0^2} \ln\tfrac{d_m}{d_0} \\
\overline{S}N_A &= S_A &&= \tfrac{3}{2}V_V
\end{aligned}$$

Upper boundary case: $f(d)_u = \frac{5}{2}d_0^{2.5}/d^{3.5}$

$$\begin{aligned}
\overline{x} &= J_2\overline{d^2}/\overline{d} &&= \tfrac{3\pi}{4}d_0 \\
\overline{x^2} &= J_3\overline{d^3}/\overline{d} &&= 2d_0^{1.5}d_m^{0.5} \\
\overline{h} &= \overline{d_c}/4 &&= \tfrac{3}{4}d_0 \\
\overline{h^2} &= (\overline{d_c^2} - \overline{x^2})/4 &&= \tfrac{1}{4}d_0^{1.5}d_m^{0.5} \\
\overline{S} &= \pi(\tfrac{1}{4} + 2.\tfrac{1}{4})d_0^{1.5}d_m^{0.5} &&= \tfrac{3}{4}\pi d_0^{1.5}d_m^{0.5} \\
N_A &= (6V_V\overline{d})/(\pi\overline{d^3}) &&= \tfrac{2}{\pi}\tfrac{V_V}{d_0^{1.5}d_m^{0.5}} \\
\overline{S}N_A &= S_A &&= \tfrac{3}{2}V_V
\end{aligned}$$

in which $J_2 = \int_0^{\pi/2} \sin^2\theta d\theta$ and $J_3 = \int_0^{\pi/2} \sin^3\theta d\theta$ [4]. d_0 and d_m are the smallest and largest particles included in the model. Note that magnification $M = d_m/d_0$.

FRACTAL PROPERTIES OF FRACTURE SURFACES

The average value of the bond crack surface area per unit of the corresponding area of the dividing plane, S_A, is the major parameter to define the roughness of the fracture surface. The planar roughness index, R_S, being the ratio of total fracture surface area and the corresponding area of the dividing plane, is obviously given by

$$R_S = A_{Am} + S_A = 1 + S_A - V_V \tag{4}$$

Basically this holds only for a 2-D portion of cracks in a partially planar system in which the orientation plane is parallel to the the dividing plane. An additional 3-D 'random' system of bond cracks has to be considered. The demarcation line along the particle-matrix interface from which the bond crack enters the matrix forms a circle. The size distribution function of the associated circular planes is identital to the size ditribution obtained with a plane intersecting with the particles. Orientation distribution of this circular-facetted system is IUR. The average surface area of the bond cracks per unit of the circular facet area is 3/2. The average area of the circular-facetted system per unit of the dividing plane is 2. Hence, eq (4) can be modified to encompass both the 2-D and 3-D portions,

$$R_S = 1 - V_V + 3V_{V3} + \frac{3}{2}V_{V2} = 1 + 2V_V(1 - \frac{3}{4}\omega) \quad (\omega = \frac{V_{V2}}{V_V}) \tag{5}$$

where the indices 2 and 3 refer to the 2-D and 3-D portions, respectively. The linear roughness index, R_L can be approximated according to [5] by $R_L = 1 + \pi(R_S - 1)/4$. Substitution of eq (5), assuming $\omega = \frac{1}{3}$ and $\omega = 0$, respectively, gives

$$R_L = 1 + \frac{\pi}{4}.\frac{3}{2}V_V \qquad \text{and} \qquad R_L = 1 + \frac{\pi}{4}.2V_V \tag{6}$$

The sieve curves lead to near self-similarity situations as to the texture of the fracture surface at different resolution levels [2]. The resolution-dependency can be expressed by means of the fractal equation [6]

$$\log R_L = (D_l - 1)\log M + C \tag{7}$$

D_l is the fractal profile dimension and C a constant (determination of which can be avoided by considering the slope of the curves). Fig. 3 presents solutions of eq (7) using eqs (6) and (2). Fractal dimensions around 1.08 to 1.13 fall close to the sofar available experimental data [7]. In general, slightly curved lines either with positive or with negative curvature will be obtained, revealing the non-ideal fractal properties of the fracture surface. High density concretes reveal an increased brittleness. As a result, cleavage of particles will be more dominant, reducing fractal dimension. This has been experimentally confirmed [8].

CONCLUSIONS

Stereological modelling of the fracture surface is achieved for concretes containing river gravel aggregate. The development of bond cracks is a major phenomenon in the damage evolution process under tensile or compressive loadings. A fracture process zone is formed encompassing the larger coalescing bond cracks, finally forming the frcature surface. The dividing surface will be weakly curved. On the different magnification levels, particles discernable on the very level put their marks (ie spherical indentations) on the dividing surface. The commonly applied sieve curves lead to near self-similarity situations. Estimates for fractal dimension of the fracture surface are developed on this basis. They closely match experimental findings.

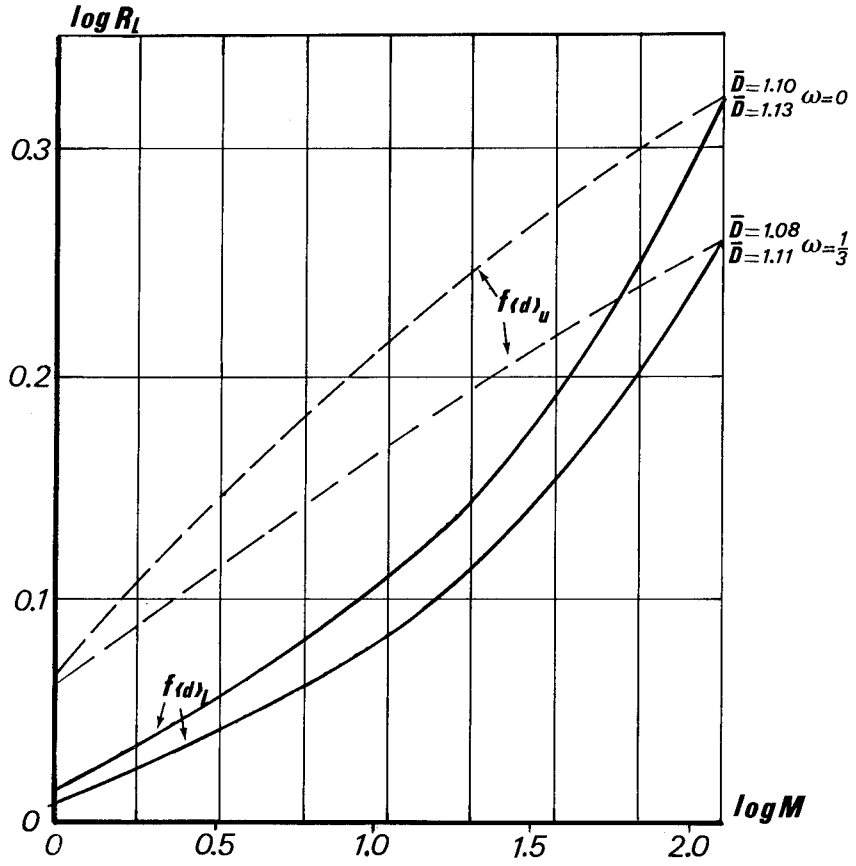


Fig. 3. log-log plot of linear roughness index, R_L, versus magnification, M.

REFERENCES

1. P. Stroeven, Engr. Frac. Mech. **35**, 775 (1990).
2. P. Stroeven, *Brittle Matrix Composites*, edited by A.M. Brandt and A.M. Marshall (Elsevier Science Publishers, London, 1991), 1.
3. P. Stroeven, *Advanced Studies on Structural Concrete*, (LNEC, Lisbon, 1994), p. 125.
4. P. Stroeven, J. Composites, **4**, 129 (1982).
5. E.E. Underwood, Acta Stereol., **6** (II), 170 (1987).
6. D. Paumgartner, G. Losa and E.R.Weibel, J Microsc. **121** (Pt1), 51-63 (1981).
7. V.E. El-Saouma, C.C. Barton and N.A. Gamaleldin, Engr. Frac. Mech. **35**, 47 (1990).
8. Z. Rawicki and L. Wojnar, Acta Stereol., **11** (2), 185 (1992).

VERIFICATION AND APPLICATION OF A NEW ADSORPTION MODEL FOR FRACTAL SURFACES

Ronald Segars and Louis Piscitelle
U.S. Army Natick RD&E Center, Natick MA.

ABSTRACT

A recently proposed isotherm model for adsorption on fractal surfaces is fitted to a wide range of isotherm data obtained from the literature. All curve fitting attempts produced good fits and the model parameters obtained are shown to be physically reasonable. Also, all significant model parametrs can be obtained from a single isotherm. As expected, when surface roughness is taken into account, the specific surface area determined from monolayer volume may be significantly higher than that obtained using the standard smooth surface isotherm models.

INTRODUCTION

Physical adsorption/desorption of gases and vapors on solid surfaces plays an important role in many fields of science. In most cases, the sorption data are obtained under equilibrium conditions and are fitted to one of several isotherm models to extract the physical parameters such as the surface area of the adsorbent, interaction potential, hysteresis behavior or some other physical property of interest in the particular study. One theory often used is that of Brunauer, Emmett and Teller (BET) which holds only for smooth surfaces. It was shown previously that this model can lead to significant errors when used with issotherm data obtained on rough surfaces. The new model, which considers surface roughness and the surface smoothing that occurs as successive layers of molecules are deposited, is now shown to fit the isotherms obtained on a wide range of materials. Parameters obtained with the new model are compared to values obtained by the standard BET model, and whenever possible, to parameters obtained by independent measures. In all cases the model provides physically reasonable values that compare favourably with other measures of these parameters. It is expected that the new model, which takes into account the roughness of the adsorbent surface, will give a better prediction of the physical parameters.

EXPERIMENTAL

The new model is centered on an isotherm equation, Eq. 1, published by Brunauer, Emmett and Teller in 1938. In this equation, B_n is the fraction of the adsorbent surface that is covered by n and only n layers of adsorbate. Since these fractions could not be determined, the authors assumed all layers to have the same surface area as that of the adsorbent and that

Mat. Res. Soc. Symp. Proc. Vol. 407 © 1996 Materials Research Society

an infinite number of layers would be adsorbed. Thus the summation in Eq.1 has a single term with $B_n=1$ and $n=\infty$. Then for low concentrations ($X=P/Po<<1$) Eq.1 simplifies to the well known BET equation.

$$\frac{V}{V_m}=\frac{CX}{1-X}\sum_{n=1}^{\infty}\beta_n\left(\frac{1-(n+1)X^n+nX^{n+1}}{1+(C-1)X-CX^{n+1}}\right) \quad (1)$$

By applying the ideas from fractal analyses of surfaces, particularly the smoothing effect of adsorbed molecules on a fractal surface, an expression for B_n was obtained, Eq.2. The values used in Eq.2 are obtained from Eq.3 which describes the smoothing of a fractal surface on adsorption of molecules of size r.

$$\beta_n=\left(\frac{r}{L}\right)^{D-D_{n-1}}-\left(\frac{r}{L}\right)^{D-D_n} \quad (2)$$

$$D_{n+1}=\left[1-\ln\left(\frac{r}{L}\right)\right]-\sqrt{\left[1-\ln\left(\frac{r}{L}\right)\right]^2+2\left[D_n\ln\left(\frac{r}{L}\right)+(D-2)\ln 2-\ln(3-D_n)\right]} \quad (3)$$

Isotherm data on activated carbon fibers, wood, activated carbons and other materials was taken from the literature. These data were usually presented in graphical form and thus had to bescaled from the graphs. The graphs were scanned with a Hewlett-Packard ScanJet IIc and the scanned images imported to a Data Translation image analysis program. The image analysis program scaled the graphs and provided digitized real values for the isotherm data points. In several cases, the isotherm data points were imported into a MatLab program written to provide the best least squares fit of the data to the new isotherm model. The program gave the values of the fractal dimension, D, the monolayer coverage, Vm, the interaction potential, C, the size of the adsorbed molecule, r, and the number of layers deposited, n. In most cases the molecule size is known and can be supplied to the program. Other parameters can also be supplied to the model if known or are obtained from other experiments.

In most cases, the data points from the image analysis program were imported into a Lotus spreadsheet which contained a macro that calculated isotherms using the new model. By trial and error the fit between the data and the model was adjusted until a good match was obtained. The model parametrs that provided the best match were used in subsequent comparisons of the model.

RESULTS AND DISCUSSION

Isotherns calculated from the model are shown in Fig.1 for different numbers of adsorbed layers, N. Calculations are for a

surface of intermediate roughness, D=2.5, with a strong interaction potential C=100. From this plot it is easily seen that multilayer adsorption is only evidenced at high concentrations; the low concentration region is nearly the same for all values of N. In Fig. 2 isotherms are plotted for different levels of surface roughness, as measured by the fractal dimension, d, for the case where only a few (N=5) layers are adsorbed. After the initial steep rise, the curves fan out and the nearly constant slopes from P/Po=0.1 to saturation increase significantly as the fractal dimension decreases. This region of the isotherm gives a good measure of the surface fractal dimension of the adsorbent. Figure 3. is similar to Fig.2 except that the number of adsorbed layers has increased (N=30). The intermediate concentration region of the isotherm is still sensitive to the fractal dimension but now the onset of capillary condensation is seen. This rapid rise in the volume adsorbed as saturation is approached allows determination of the adsorbate molecule size. In all cases, the steepness of the rise at the lowest concentrations gives a good measure of the interaction potential while the intermediate concentration region, in addition to determining the fractal dimension, gives the value of the monolayer volume, Vm. Thus from a single complete isotherm it is possible to obtain all the important model parameters including the fractal dimension, d, the interaction potential, C, the number of adsorbed layers, N, and the monolayer volume, Vm. If in addition, the isotherm exhibits the onset of capillary condensation, then some measure of the size of the adsorbate molecule is also possible. In this case, all

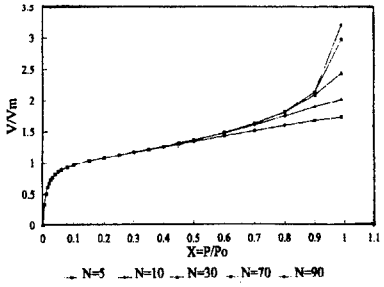


Figure 1. Isotherms calculated from the model for D=2.5, C=100, r/L=0.001

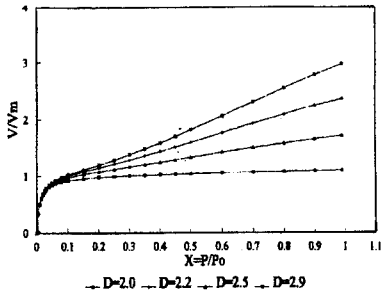


Figure 2. Isotherms calculated from the model for N=30, C=100, r/L=0.001

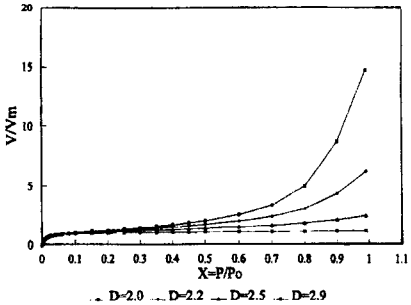


Figure 3. Isotherms calculated from the model for N=30, C=100, r/L=0.001

model parameters are determined.

Values of the model paramete matching were compared to values obtained from the standard BET model. In a few cases some of the parameters were known from independent measurements, particularly the fractal dimension, and these data were also used to verify the model. Figure 4 shows adsorption isotherms for methanol adsorbed on activated carbon particles along with a matching curve obtained from the new model. Model parameters obtained from this match are shown in the figure. Figures 5-7 show isotherms for benzene adsorbed on activated carbon fibers, untreated and with two different surface treatments , along with matching curves from the model. Model parameters from these matches are given in the figures. The model suggests that the primary effect of these surface treatments was a change in monolayer volume. The interaction potential was also slightly affected by the treatments.

Figure 8 is an isotherm for the adsorption of water vapor on pine wood along with the fitted model and model parmeters. The initial portion of the isotherm rises much more gradually than in the previous isotherms. The intermediate concentration region rises gradually until a significant rise sets in as saturation is approached, suggesting the onset of capillary condensation. This complete isotherm permits obtaining all of the model parameters with some degree of certainty as discussed earlier.

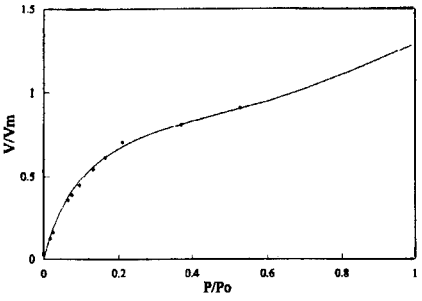


Figure 4. Model matched to data for methanol adsorbed on active carbon. Model parameters:D=2.9, C=9.5, N=10, Vm=3.95, r/L=0.08

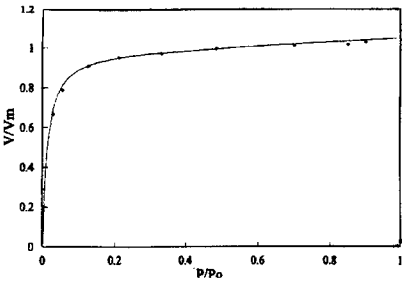


Figure 5. Model matched to data for benzene adsorbed on activated carbon fibers. Model parameters:D=2.97, C=80, N=5, Vm=470

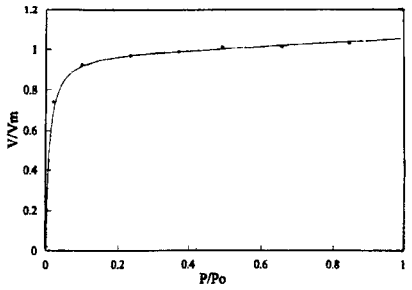


Figure 6. Model matched to data for benzene adsorbed onsurface treated carbon fibers. Model parameters:D=2.95, C=10, N=5, Vm=350, r/L=0.08

It is of interest to see how this new model, which includes the effect of surface

roughness, differs from the standard BET analysis in determining the monolayer volume. Figure 9 shows the ratio of monolayer volumes obtained from BET anaysis, (Vm)_BET, and the new model, (Vm)_MODEL, as a function of the fractal dimension. The curve and the data points ahown in the figure were obtained from the isotherms in Figs. 4-8. (Vm)_BET was obtained by standard BET analysis of the isotherm data points and (Vm)_MODEL was taken as the value obtained from the curve matching operation.

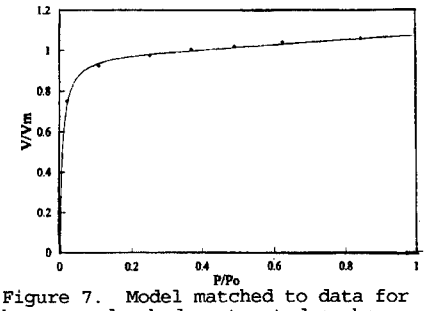


Figure 7. Model matched to data for benzene adsorbed on treated carbon fibers. Model parameters:D=2.95, C=130, N=5, Vm=350, r/L=0.08

CONCLUSIONS

The new model can generate a wide variety of isotherm shapes and thus can be made to fit a wide variety of materials. This includes materials that exhibit single layer Langmuir type adsorption to materials that follow multilayer BET adsorption behavior.

The different model parameters are sensitive to different concentration regions of the isotherm. Thus if a complete isotherm (from zero concentration to saturation) is obtained, all model parameters can be determined from this single isotherm.

In the few cases where independent measures of the fractal dimension have been available, the new model gives good agreement with these measures.

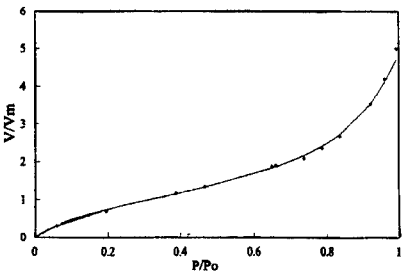


Figure 8. Model matched to data for water vapor adsorbed on pine wood. Model parameters:D=2.25, C=7, N=50, r/L=1E-5

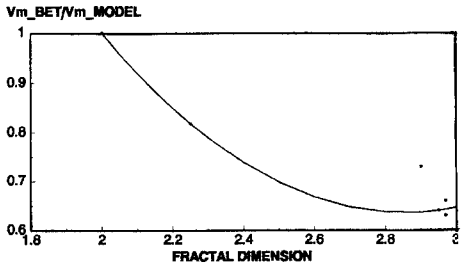


Figure 9.Comparison of monolayer volume; BET versus model

In determining monolayer volumes it appears that BET analyses of isotherm data obtained on rough surfaces underestimates the monolayervolume by about 35%. In a "worst case" situation, BET analysis could underestimate monolayer volume by more than 50%.

REFERENCES

1. R. Segars and L. Piscitelle, Mat.Res.Soc.Symp.Proc.Vol.366, p247, 1995 Materials Research Society.
2. S. Brunauer, P.H. Emmett and E. Teller, J.Am.Chem.Soc. 60, 309 (1938).
3. R. Tsunoda, J.Colloid and Interface Sci. 152,571 (1992).
4. K. Kaneko and N. Shindo, Carbon, 27, 6, 815 (1989).
5. S.G. Halzikiriakos and S. Avramidis, Wood Sci. and Tech. 28,275 (1994).

A GROWTH MODEL FOR RAMIFIED ELECTROCHEMICAL DEPOSITION

Guillermo Marshall *#, Pablo Mocskos* and Martin Olivella*,

*University of Buenos Aires, # National Research Council.

Abstract

We introduce a macroscopic model for the description of growth pattern formation in ramified electrochemical deposition. The theoretical model is formulated as a 2D time-dependent problem consisting in the Nernst-Planck equations for the concentration of the solute (cations and anions), coupled to a Poisson equation for the electrostatic potential and the Navier-Stokes equations for the solvent, with a moving boundary. A dimensional analysis is performed and a new set of dimensionless numbers governing the flow regime is derived.
A 2D discrete version of these equations in a DBM scheme with a random moving boundary constitutes the computational model. We present numerical results which show that our growth model, with a proper variation of the set of dimensionless numbers, gives a reasonable picture of the interplay of the electroconvective, migration and diffusive motion of the ions near the growing tips.

Introduction

Growth pattern formation (GPF), that is, the unstable growth of interfaces , is a common phenomenon in a wide range of problems from physics to biology. It produces complex geometries of fractal or dendritic character and chaotic patterns [1]-[7] and has been extensively studied in the context of far from equilibrium phenomena.

An example is electrochemical deposition (ECD) of ramified metallic salt clusters in thin cells, which appears to be the paradigm of GPF problems driven by nonlinear fields. The quasi two-dimensional electrolytic cell consists of two glass plates sandwiching two parallel electrodes and the electrolyte. A voltage difference (or a current) applied between electrodes produces a ramified deposit. The main variables controlling the experiment are: solution concentration, voltage difference and cell thickness. Literature shows that when these are varied, growth patterns ranging from fractal to dense-branched aggregates can be obtained. The morphology transition has not been yet fully understood.

The interaction of fields due to salt ions concentration gradients, migration and electroconvection in ECD are described, through first principles [8], by the Nernst-Planck equations for ions concentration, the Poisson equation for the electrostatic potential and the Navier-Stokes equations for the fluid, with a moving boundary. Literature shows that this system was studied through analytic methods, such as perturbation analysis or the search for exact solutions, and numerical techniques. Analytic techniques are crucial in the present understanding of the basic phenomena in ECD ([9]-[13]), however their extension to nonlinear problems is extremely difficult. Numerical techniques fall in three main categories: purely deterministic, purely stochastic and mixed deterministic-stochastic methods. Purely deterministic techniques solve the ECD system, for instance, with finite differences and relaxation techniques ([12]). Albeit their generality, their lack of noise,

Mat. Res. Soc. Symp. Proc. Vol. 407 © 1996 Materials Research Society

which is inherent in the physics of ECD, limit somehow the range of applications of these methods. Purely stochastic methods, such as the DLA or the BRW simulate a scalar version of the ECD system (interpreted as Fokker-Planck type equation) with Monte Carlo techniques ([14]-[20]). While succeeding in obtaining aggregations ranging from fractal to dense branch morphology, they still are simplifications of reality. Hybrid methods such as the DBM [21] solve the ECD system with relaxation techniques and a random moving boundary [22]. These methods possess the advantages of deterministic techniques, while at the same time introducing noise in a natural way through first principles.

There is at present a considerable amount of experimental data on ECD ([23-[36]) which can be used to check the existing linear theory and advance into the nonlinear field. In particular, [27] and [36] presented experimental results and an analysis of ECD with dense-branched morphology, and proposed a mechanism for a morphology transition in ECD, showing that electroconvection produces physical displacements that split and fan the growing tips.

Our main goal here is to design a growth model able to describe the most relevant features of ECD through its control parameters. For this, we introduce a GPF model consisting in the study of the full ECD system and its discrete version in the context of a DBM scheme. In addition, we perform a dimensional analysis that notably simplifies the otherwise large number of parameters. The plan of the paper is the following. In the second section we examine the physics of the problem, the equations describing it and its dimensional analysis. The third section presents the growth model, numerical results and some general conclusions.

The physics and mathematics of the growth model

The physical scenario envisaged is ECD of ramified copper clusters in a 2D cell, with an unsupported binary electrolyte and with constant voltage applied between electrodes [8]. The driving fields are diffusion, migration and electroconvective motion of the ions in a space-time dependent incompressible viscous fluid. Secondary chemical reactions, density gradients or heat transfer are not considered here. Initially the electrolyte is electrically neutral everywhere, with uniform concentration of cations and anions in space. Applying a voltage difference between electrodes, cations move toward the cathode where they are discharged and aggregated, producing a depletion of cations near the cathode. For electroneutrality to hold, anions must be expelled from this region at the same speed at which cations aggregate; however, anions migrate toward the anode with a drift speed proportional to the anion mobility and the electric field. Theory and experimental evidence show that cation aggregation is slower than anion migration, thus a local positive charge is generated near the cathode. At the anode, anions pile up since they cannot exit the solution; electroneutrality is maintained by cations entering the solution from the dissolving anode.

In transport phenomena in fluids, two limiting types of processes can be studied: forced convection and free or natural convection. Their salient differences are that in forced convection the flow pattern is determined primarily by some external forces, while in free convection the forces are within the flow. In the literature, experiments have been put arbitrarily into either one of these two limiting categories; in some problems, however, both effects must be taken into account. A free convection analysis of ECD was performed in [9] and [10]. In the present work, observing that the Coulomb forces have almost compact support, that is, they are approximately limited to a space region where electroneutrality does not hold, and that they could be considered to be external forces relative to the fluid, we assume a forced convection process. In this context, assuming that the ECD is a quasi-two dimensional process (this is a gross approximation of reality, only justified on the grounds of rendering the ECD problem more tractable), the ECD is described by

$$
\begin{aligned}
&\partial C/\partial t + u^{*}\partial C/\partial x + v^{*}\partial C/\partial y = 1/(RSchc)\nabla^2 C \\
&\qquad + 1/(RMarc) C\nabla^2\phi; \\
&\partial A/\partial t + u^{*}\partial A/\partial x + v^{*}\partial A/\partial y = 1/(RScha)\nabla^2 A \\
&\qquad + 1/(RMara) A\nabla^2\phi; \\
&\nabla^2\phi = -1/XcC + 1/XaA; \\
&\partial\omega/\partial t + u\partial\omega/\partial x + v\partial\omega/\partial y = 1/R\nabla^2\omega \\
&+ 1/Froc(\partial C/\partial y\partial\phi/\partial x - \partial C/\partial x\partial\phi/\partial y) \\
&+ 1/Froa(\partial A/\partial x\partial\phi/\partial y - \partial A/\partial y\partial\phi/\partial x); \\
&\nabla^2\psi = -\omega;
\end{aligned}
\qquad (1)
$$

where the following dimensionless variables have been introduced: $x=x'/x_0$, $y=y'/x_0$, $u=u'/u_0$, $v=v'/u_0$, $C=C'/C_0$, $A=A'/C_0$ and $\phi=\phi'/\phi_0$. Here, C and A are cation and anion concentrations, ϕ is the electrostatic potential, ω and ψ are the vorticity and stream functions, u and v are the fluid velocities, x, y and t are the space and time coordinates, respectively. The zero subindex indicates reference values. Schc (Scha) $=\nu/Dc$, are the Schmidt numbers, ν and Dc(Da) are the kinematic viscosity and diffusion constants; $R=u_0 x_0/\nu$ is the Reynolds number; Marc(Mara)$=\nu/\mu c\,\phi_0$ (μc and μa are the ions mobility) are a new set of dimensionless numbers relating viscous forces to electrostatic potential and migration forces; $u^{*}=u-1/(RMarc)\partial\phi/\partial x$ and $v^{*}=v-1/(RMara)\partial\phi/\partial y$ are compound velocities due to electroconvection and migration; $Xc(Xa)=\epsilon\phi_0/(x_0^2 FzcC_0)$ are dimensionless numbers relating electrostatic potential to solute concentration; and Froc(Froa)$=\rho u_0^2/(ezaC_0\phi_0)$ are the Froude numbers relating viscosity to electrostatic potential and concentration.

In real experiments the following physical parameters, corresponding to a solution of copper sulphate in distilled water (0.01M) are used: $\mu c=5.37.10^{-4}$ cm^2/Vs, $\mu a=8.29.10^{-4}$ cm^2/Vs, $Da(Dc)=10^{-5}$ cm^2/s, $\nu=10^{-2}$ cm^2/s, zc=za=1, T=293 K and $C_0=10^{18}$ cm^{-3}. For x_0=1cm, u_0=0.1 cm/s and ϕ_0=1V, the dimensionless numbers become: R=10, Schc=Scha=10^3, Mara=12.06, Marc=18.06, Xc=Xa=4.52. 10^{-11}, Froc=Froa=6.24.10^{-4}. An increase in the R number leaving all other numbers constant increases fluid convection, thus electroconvection in system (1). It also increases migration (convective motion due to the electric field). A similar effect is produced increasing the Schc(Scha) number. An increase in the Froc(Froa) number decreases electroconvection (fluid density increases). An increase of the Marc(Marc) number reduces migration. A decrease in the Xc(Xa) number increases the source term in the electrostatic Poisson equation in system (1) and therefore the curvature of the electric potential; this reduces the width of the boundary layer. Therefore, this number which is orders of magnitude higher than the rest of the dimensionless numbers, is extremely important since it governs the singular perturbation nature of the whole system and in particular, the source term in the electrostatic Poisson equation.

A 2-D growth model approximation

Studies of the ramified electrodeposit growth aims mainly to establish the relation between the driving nonlinear fields and the morphology of the deposit. Here, to simulate this relation we use the experimental results presented in [27] and [36]. In a first step, as in [12], we assume a dense parallel morphology for the ramified electrodeposit and we study the distribution of concentrations, electrostatic potential and fluid velocities. The deposit is replaced by a set of parallel spaced rectilinear filaments in the form of a comb, and only one filament of the comb is analyzed by symmetry. The problem is described by system (1) in the 2D rectangular domain with one short filament grown in the middle of the cathode. In a second step, we include the basic instability effect that yields ramified deposits. For this, we assume that in a laboratory experiment the instability is triggered at random locations near the cathode, due to an imperfection in its surface or a perturbation due to chemical impurities or local gradient concentrations or any other imaginable disturbance. Accordingly, in our growth model approximation, the interface of the deposit is moved with a stochastic rule. Our main assumption is that the flux of cations entering the deposit governs the aggregation process. Two different cases corresponding to two different scales can be considered. The first case includes the simulation of the whole cell, the second one is a zoom of a small region near the tip of the filament. The boundary conditions for both cases differ and details can be found in [12]. The boundary conditions for the stream function on every solid boundary are the usual nonslip conditions.

The computational model solves system (1), for each time step, in a fixed domain, in a lattice using finite differences and deterministic relaxation techniques. Its solution is obtained via the system of difference equations:

$$W_k^{n+1} = \Sigma_j a_j W_j^n \qquad (2)$$

where j represents the nearest-neighbour site of the site k, the summation ranges over all nearest-neighbour sites, W_k is a vector valued function, whose components are the concentrations C and A, the electrostatic potential ϕ, the vorticity function ω and the stream function ψ, and a_j is a diagonal matrix whose elements contain the nonlinear coefficients of the discretized equations. The resulting solution W_k^{n+1} is then used to modify the domain (advance the interface) with a DBM scheme [22]. Then the stocastic rule is: $p_k=\mathrm{mod}(j_c{}^c{}_k)/\ \Sigma_i \mathrm{mod}(j_c{}^c{}_i)$, where the summation is over all nearest neighbor sites of the aggregation in the lattice, p_k is the probability of selecting the neighbor site k to advance the interface, $j_c{}^c{}_k$ is the flux of cations flowing from the neighbor site k into the aggregation. In this process each new advance of the interface changes locally the boundary and hence the solution of system (2), that must be recalculated, in principle, at every time step. In this way the aggregation process, the ionic species and the hydrodynamics are coupled. The boundary conditions are discretized by finite differences in the standard way.

The results that follow aim to describe qualitatively the evolution of the interface as an interplay of the convective vortices near the tips, the concentration and the migration fields, following as close as possible the experimental conditions presented in [27] and [36]. Initially, the fluid is at rest, there is no aggregation except at the bottom layer,where the initial instability is mimicked with a deposit of 11 occupied cells; the voltage varies linearly from 1 at the top (anode) to 0 at the bottom and the deposit.

A simulation of the growth in a small region near the tip of one filament is shown next. The region is represented by a grid of 40x40 cells. Fig. 1 shows a sequence of vortex-tip interactions for

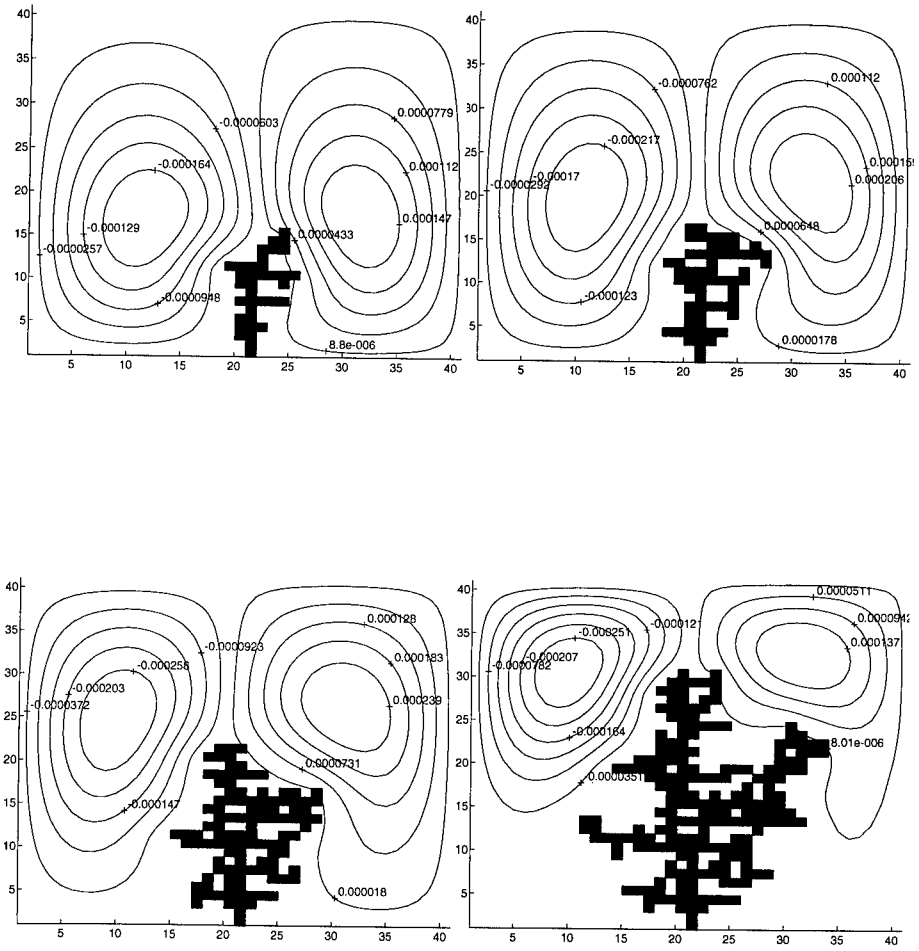


Fig. 1. Snapshots at four different times of the vortex-tip interaction: contours of the stream function and the deposit.

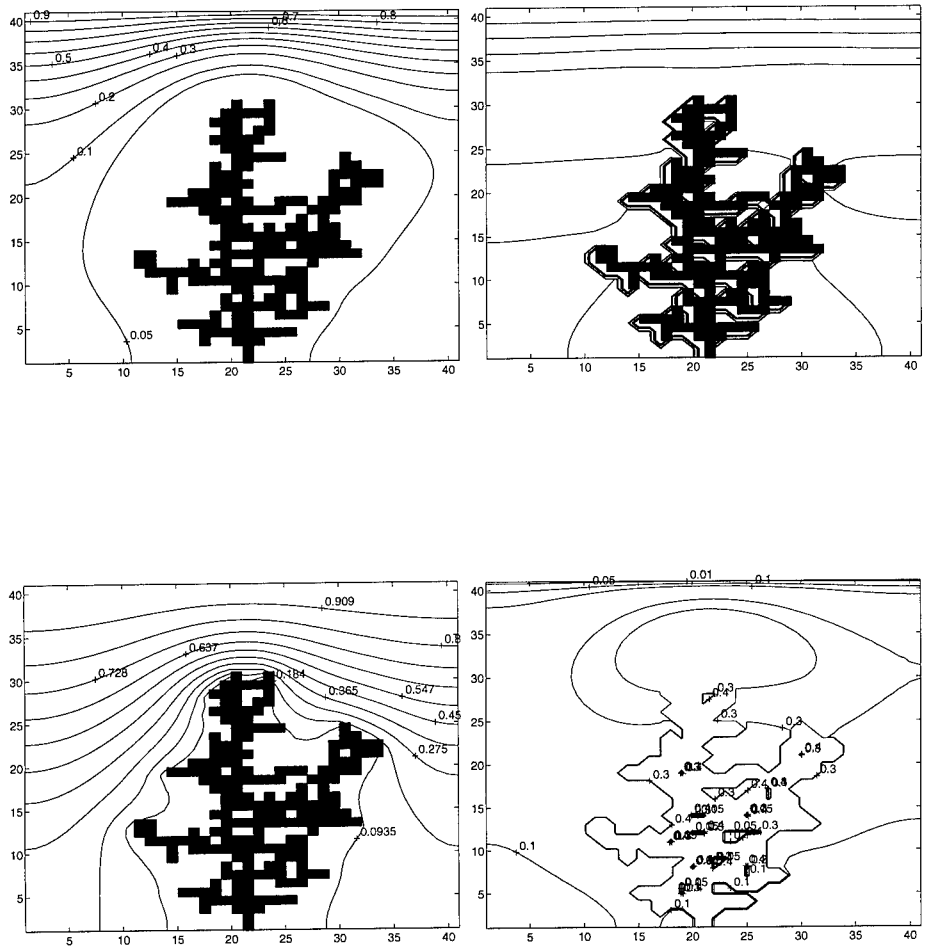


Fig. 2. Snapshot at 200 seconds of the contours of cations and anions concentration (top), electrostatic potential and forcing function f (bottom).

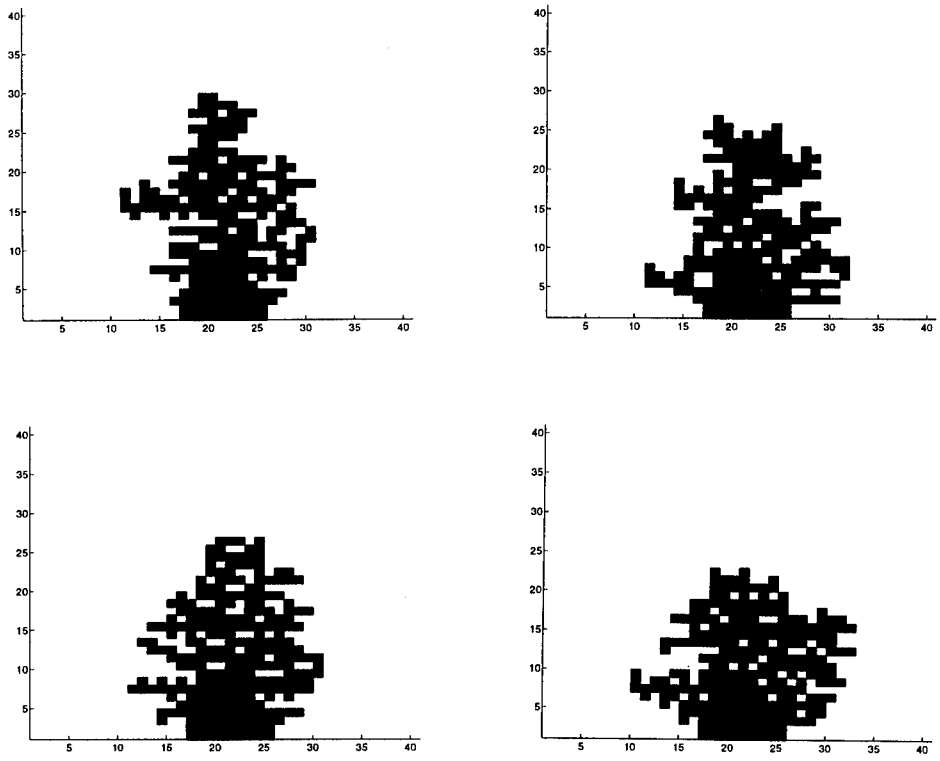


Fig. 3. Top: growth with 50 cell/sec and Fro=0.1 (left) and 100 (right); bottom: growth with 100 cell/sec and Fro=0.1 (left) and 100 (right).

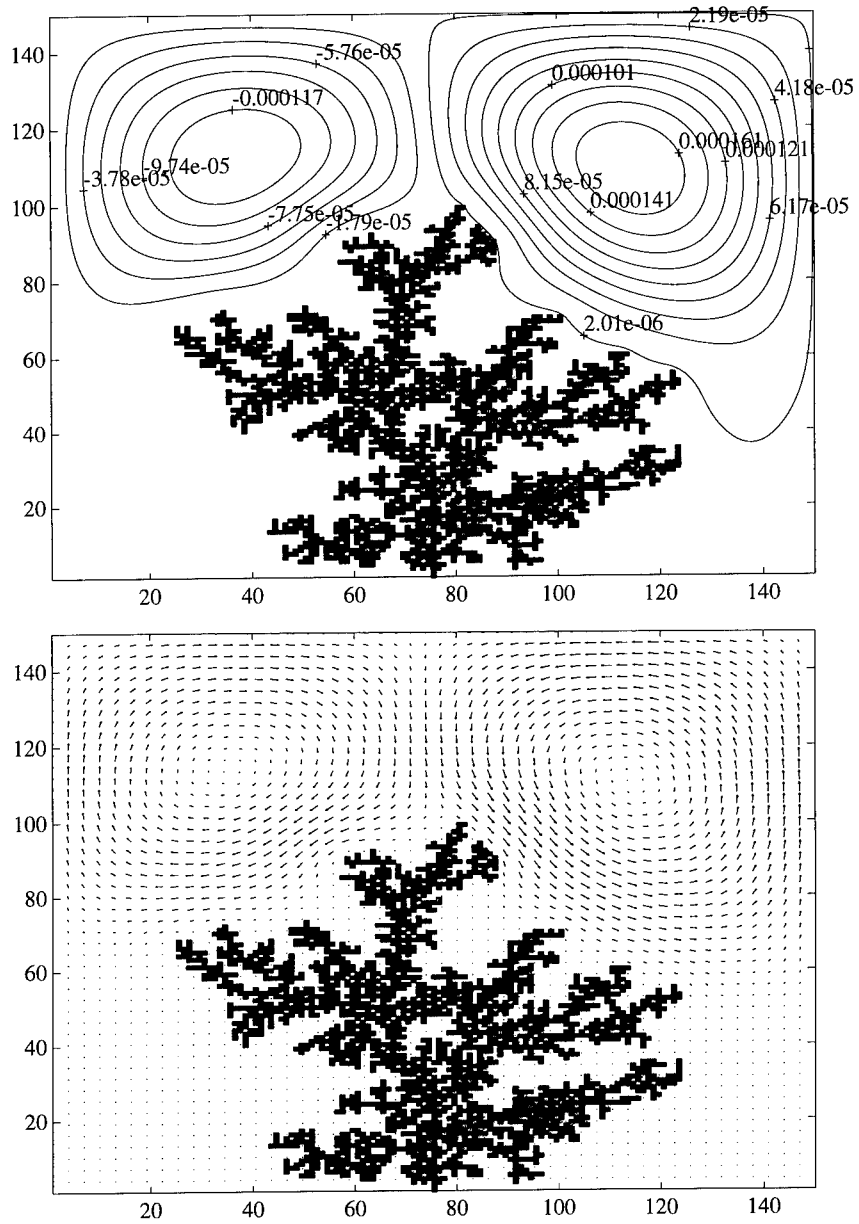


Fig. 4. Snapshots at 2000 seconds of the contours of the stream function (top) and velocities map (bottom), for Fro=6.25.

different times; the time step is 1 sec. and the aggregation speed is 1 cell/sec. The dimensionless numbers used are R=10, Schc=Scha=100, Mara=12.06, Marc=18.62, Xa=Xc=0.0443, Froc=Froa=6.25. This sequence shows clearly the mutual interaction of the tip of the deposit with its surrounding fluid: growth and bifurcation of the deposit due to neighboring vortices and vortex stretching due to the presence of the deposit.

Figure 2 shows a snapshot at 200 sec. of the contours and aggregation of the forcing function f ($f\alpha$ (C-A)), ϕ, A and C, respectively. Let us imaginary join two neighboring contrarotating filament tips (Figs. 1 and 2) with an arch containing the positive vortex of the left tip and the negative vortex of the right tip (only one half of this virtual figure can be visualized here); the inner zone of this arch is depleted of ions while the outer zone rapidly reaches the bulk concentration value.

Figure 3 at the top shows snapshots of the deposit at t=4 sec., aggregation speed of 50 cell/sec and Fro numbers 0.1 and 100 (left and right). Figure 3 at the bottom shows the same for an aggregation speed of 50 cell/sec. These results suggest that a decrease in the Fro number produces deposits with less side branching (they are higher, i.e., their front speed is larger). The reason is that vortex intensity and velocities increase, cation flux is higher at the tip and thus the sticking probability is higher. When the Fro number increases, the flux is more uniform and hence the sticking probability is more uniform too. This yields more side branching.

Finally, fig. 4 shows snapshots at t=2000 sec, of the streamlines contour (top) and velocities map (bottom) in a grid of 150x150 cells, for Fro number 6.25. The main contrarotating vortices at the leading tip are well developed, but the reproduction of smaller vortices (as observed in physical experiments) requires lower Fro and Xa(Xc) numbers, and finer grids.

It is concluded that, with a proper variation of the set of dimensionless numbers introduced, it is possible to obtain a streamline pattern showing the existence of local charges near the tips of the filaments, the associated pair of contrarotating vortices and a funnel like shape through which the copper ions are sucked into the tip. The evolution of the vortex-tip interaction shows the birth, stretching, division and death of vortexes, and the associated birth, splitting, fanning and death of tip filaments. The streamline, ion concentrations and electrostatic potential fields values agree with theoretical predictions and with experimental results.

Acknowledgements

We are indebted to J. de Bruyn, J. N. Chazalviel, V. Fleury, S. Morris, and B. Sapoval for enlightening discussions. The work of the first author was done with partial support from CONICET project PIA-369/92, UBA project EX233/95 and a Thalmann Foundation Fellowship. This paper was partially written while G. M. was visiting the Department of Physics at the University of Toronto, he gratefully acknowledges its hospitality.

References

1. B. B. Mandelbrot, *The Fractal Geometry of Nature* (Freeman, San Francisco, 1982).
2. T. Vicsek, *Fractal Growth Phenomena* 2nd. edn (World Scientific, Singapore, 1992).
3. G. Stanley and N. Ostrowsky (eds.) *On Growth and Form* ,NATO ASI Ser. vol. 100 (Kluwer, Boston, 1986).
4. L. Kadanoff, J. Stat. Phys. **39**, 267 (1985).
5. M. Matsushita, M. Sano, Y. Hayasawa, H. Honjo and Y Sawada, Phys. Rev. Lett. **53**, 286 (1984).
6. E. Ben-Jacob and P. Garik, Nature **343**, 523 (1990).
7. F. Argoul, J. Huth,P. Merzeau, A. Arneodo and H. L. Swinney, Physica D **62**, 170 (1993).

8. J. S. Newman, *Electrochemical Systems* (Prentice Hall, New Jersey, 1973).
9. I. Rubinstein, *Electro-Diffusion of Ions* (SIAM Studies in Applied Math. Philadelphia, 1990).
10. R. Bruinsma and S. Alexander, J. Chem. Phys. **92**, 3075 (1990).
11. M. Z. Bazant, Phys. Rev. E **52**, 1903 (1995).
12. J. N. Chazalviel, Phys. Rev. E **42**, 7355 (1990).
13. V. Fleury, J. Kaufman and B. Hibbert, Phys. Rev. E **48**, 3831 (1993).
14. T. A. Witten and L. M. Sander, Phys. Rev. B **27**, 5686 (1983).
15. P. Meakin, Phys. Rev. B. **28**, 5221 (1983).
16. L. Lam, R. D. Pochy and V. M. Castillo, in *Nonlinear Structures in Physical Systems*, ed. L. Lam and H. C. Morris (Springer, New York, 1990).
17. G. Marshall, Comput. Phys. Commun. **56**, 51 (1989).
18. G. Marshall, Growth Patterns Driven by a Nonlinear Field, 10th. Int. Conf. on Nonlinear Science, Los Alamos, 1990 (unpublished).
19. G. Marshall and E. Arguijo, Chaos, Solitons and Fractals **5**, 531 (1992).
20. G. Marshall, S. Tagtachian and L. Lam, Chaos, Solitons and Fractals, **6**, 325 (1995).
21. L. Pietronero and H. J. Weismann, J. Stat. Phys. **36**, 909 (1984).
22. G. Marshall, E. Perone, P. Tarela and P. Mocskos, Chaos, Solitons and Fractals **6**, 315 (1995).
23. J. R. Melrose, D. B. Hibbert and R. C. Ball, Phys. Rev. Lett. **65**, 3009 (1990).
24. V. Fleury, J. N. Chazalviel, M. Rosso, and B. Sapoval, Phys. Rev. A **44**, 6693 (1991).
25. V. Fleury,M. Rosso and J. N. Chazalviel, Phys. Rev. A **43**, 6908 (1991).
26. V. Fleury, J. N. Chazalviel and M. Rosso, Phys. Rev. Lett. **68**, 2492 (1992).
27. V. Fleury, J. N. Chazalviel and M. Rosso, Phys. Rev. E **48**, 1279 (1993).
28. P. P. Trigueros, F. Mas, J. Claret and F. Sagues, J. Electroanal. **348**, 221 (1993).
29. D. Barkey, J. Electrochem. Soc. **138**, 2912 (1991).
30. R. H. Kork, D. C. Pritchard and W. Y. Tam, Phys. Rev. A **44**, 6940 (1991).
31. M. Wang and N. Ming, Phys. Rev. A **45**, 2493 (1992).
32. A. Kuhn and F. Argoul, Fractals **3**, 451 (1993).
33. C. Livermore and Po-zen Wong, Phys. Rev. Lett. **72**, 3847 (1994).
34. K. A. Linehan and J. R. de Bruyn, Can. J. Phys. **73**, 177 (1995).
35. D. Otero, G. Marshall and S. Tagtachian, Fractals, World Scientific (in press 1996).
36. V. Fleury, J. Kaufman and B. Hibbert, Nature **367**, 435 (1994).

ELECTROCHEMICAL OSCILLATIONS,SURFACE MORPHOLOGY AND CORROSION OF SELECTED THERMAL SPRAYED ALLOYS.

ELIA V. ESCHENAZI*,YAMLAK TSEGA**,NINJA BALLARD*AND GARY GLASS+
* Department of Physics, Xavier University of Louisiana, New Orleans, LA 70125
** Graduate Program in Engineering Science, Tulane University, New Orleans, LA 70118
+ Department of Physics, University of Southwestern Louisiana, Lafayette, LA 70504

ABSTRACT

The effects of the surface morphology on the electrochemical behavior of various metal substrates and coated materials have been studied by analyzing impedance spectra, and electrochemical current oscillations in acidic solutions. The objective of this study is the search for a correlation between the surface complexity of the metallic samples and the impedance spectra, the structure of the current chaotic oscillations, the corrosion dynamics. Electrochemical current oscillations were studied for pure metals such as copper (Cu), iron (Fe) and titanium (Ti) in form of wire-electrodes. From the current time series the dynamics was reconstructed by using time delay and embedding techniques. The results showed, in agreement with other studies, the presence of a deterministic dynamics on chaotic, quasi periodic and periodic attractors in the reconstructed phase space. Furthermore, for the metal wire-electrodes the fractal dimension indicated the presence of low dimensional chaos. We then studied bigger pure metallic samples with a different electrochemical cell configuration. The results showed again deterministic behavior with the development of chaotic dynamics. The fractal dimensions in this case, however, were considerably larger than in the previous experiments with the microcell. In both cases the electrochemical oscillations changed structure as the surface undergoes a metamorphosis due to corrosion processes, formations of salt films or because on purpose we changed the roughness of the surface. Bifurcations from one time behavior of the current to another were observed. To better analyze the influence of the surface morphology on the current oscillations and in general on the electrochemical behavior of the sample we coupled our chronoamperometric studies with an analysis of the impedance spectra. We studied three pure iron samples mechanically at three grain sizes (600,400, 240). The dimension of the chaotic attractor decreased with the roughness. The constant phase angle (CPA) calculated from the impedance spectra increased with the roughness. The corrosion rate, as measured by the polarization resistance technique, increased with the roughness. Using the previous results as a "standard", with the same techniques, we then studied steel samples coated with various "flavors" of Tungsten Carbide coatings, provided by Cooper Oil Tools Co. The roughness of the samples was measured using a Scanning Tunneling Microscope (STM). Atomic Force Microscope (AFM). We measured the CPA from the impedance spectra and compared with the roughness data. The results obtained indicate no trivial correlation and the need for new characterization of surface complexity more connected to the electrochemical sensitivity of the surface morphology. This sensitivity has its fingerprints in the structure of the electrochemical oscillations and the CPA. While this study is presently in progress, the results of this investigation showed a new avenue to study the electrochemical behavior and corrosion resistance of thermal spray coated materials and their substrates.

INTRODUCTION

Thermal sprayed coatings are used to enhance wear resistance of certain industrial parts. However, these parts are often exposed to corrosive environments. In these conditions, it is important to study the general corrosion behavior of both coating and substrate. Since the electrochemical behavior and the corrosion dynamics depend crucially on the surface morphology of the coating and the substrate, a search for a correlation between surface complexity (porosity, roughness, fractal geometry) and corrosion charactheristics is essential.

Mat. Res. Soc. Symp. Proc. Vol. 407 © 1996 Materials Research Society

The most frequently used means of measuring the corrosion resistance of a coated material have been by salt-spray testing or by immersion. Corrosion is evaluated by weight change or microscopic analysis. These techniques are lengthy and provide little information on the corrosion dynamics and its inner mechanisms. The use of electrochemical techniques for thermal spray coated materials is still quite limited [1-6] . In this paper, it is shown that special electrochemical techniques can be used to gain more understanding on how corrosion and electrochemical behavior of coated-substrate systems are affected by the surface morphology.

Electrochemical oscillations have been observed in the active-passive transition for a variety of metal-electrolyte systems for many years [7-17]. While the inner mechanisms of these oscillations are still far from being understood the behavior of the film/surface and current oscillations seem to be related: i.e. a given type of film of surface morphology produces a given type of current oscillation [18-19]. Furthermore, various studies [15,18-26], have shown that these oscillations describe an underlying deterministic dynamics which generates chaotic, quasi periodic and periodic trajectories in the phase space reconstructed from the current time series. Fractal dimensions of the chaotic attractors emerging from the analysis of the time series can be calculated. The analysis of electrochemical oscillations, in the framework of non-linear dynamics and fractal geometry can give the study of corrosion a new dimension. Thus, it would be of great interest to ask if these oscillations and their metamorphosis are in anyway the fingerprints of the surface complexity as it evolves due to various electrochemical processes. Addressing this question can provide not only a better understanding of passivation and corrosion in metals but also a tool for designing better coating conditions for corrosion resistance.

On the other hand,several recent studies [27-33] adopted impedance techniques to investigate how geometry and structure of the electrode's surface affect the electrochemical behavior of the metallic sample. The quantity which seems to be related to the surface geometry of the electrode is the so called constant phase angle(CPE) which can be calculated from the impedance spectrum [34]. In the impedance technique, a small alternating electrical signal is applied to the electrochemical cell and the system response can be analyzed in the frequency domain. In general, an electrochemical cell can be represented by a pure electronic model [34]. The impedance analysis consists then in extracting the impedance of the electrochemical cell after the small electrical perturbation is applied; this is a measurement of the response of the system to the signal applied. It has been found that for complex and rough electrodes, the impedance depends on the frequency. In many cases this dispersive behavior can be described by the relation: $Z= \sigma(j\omega)^{-\alpha}$ where σ is a frequency-independent constant and $j = (-1)^{1/2}$. The element corresponding to this impedance has been called the Constant Phase Element and seems to be related to the characteristics of the surface. The quantity α is related to the angle by which, in the Nyquist plot of the impedance, the semicircular arc is depressed below the real axis. This angle has been called Constant Phase Angle (CPA). While the physical meaning of α, and the corresponding CPA, still remain unclarified, various authors have tried to relate this quantity to the fractal dimension, D, of the surface [27-33] . In an extensive study of the electrical response of fractal and porous interfaces, Sapoval et al. [32], have shown that in general there is norelation between fractal dimension and α except in case of diffusive regime. They also have shown that the response of irregular electrodes is related to fractal dimension when the electrochemical regime is local [32] . While the issue is not completely resolved, it is worthwhile to further explore the connectivity between CPA and surface morphology, incorporating the new insight obtainable from the electrochemical oscillations and expanding the horizon of the investigation to real and more complex materials.

In this paper, we present a study of the electrochemical behavior of various bare substrates and samples coated with various "flavors" of Tungsten Carbide. The approach used is a combination of the techniques described above. Electrochemical oscillations, impedance spectra, and microscope scans are analyzed, compared, and discussed.

EXPERIMENTAL

The samples used in the first phase of the experiments included pure copper (Cu), iron (Fe) and titanium (Ti) in wire form (1 mm diameter) covered by an epoxy cylinder so that only the surface of the tip was exposed to the solution. In the second phase, we used large samples which included iron samples mechanically pretreated at different grain sizes (600, 400, 240), and various samples coated with different " flavors' of Tungsten Carbide coatings provided by Cooper Oil Tools Co.

For the wire-electrodes, a microcell was used whereas for the larger samples we used the EG&G flat cell in which about 1 cm^2 of the surface was exposed to the solution. The electrodes were immersed in various solutions such as 3.56% NaCl solution or1M or 2M H_2SO_4+ 3.56% NaCl solution.

Current oscillations, impedance spectra, and corrosion rates were measured using an EG&G electrochemical analysis system. This includes an EG&G Potentiostat, lock-in amplifier, and a PC computer with impedance and corrosion software. For electrochemical oscillations, the current was recorded as a function of time under potentiostatic conditions. For impedance spectra, the impedance response of the system to a periodic signal was recorded at various frequencies. A Nyquist plot gives the imaginary part of the impedance as a function of the real part at various frequencies. For irregular electrodes, the first high frequency section of the Nyquist plot typically is an arc of a semicircle, the center of which is below the real axis. The angle by which the semicircle is depressed below the real axis is the Constant Phase Angle (CPA).

The current time series recorded in the experiment was analyzed through numerical techniques. Attractors and the phase space were reconstructed by using time delay and embedding techniques [35]. The dimension of the emerging chaotic attractors were calculated by using a modification of the Grassberger-Procaccia algorithm [36]. Data points from the Nyquist plot were fitted with a non-linear least squares routine to calculate the CPA. All numerical analyses were performed on a Silicon Graphics Indigo^2 workstation. Microscopy analyses were conducted by researchers at the University of Southwestern Louisiana, Lafayette, LA.

RESULTS AND DISCUSSION

In the first phase of our study, we examined electrochemical current oscillations for pure metal electrodes, copper (Cu), iron (Fe) and titanium (Ti). In potentiostatic conditions the current was recorded as function of time. From the time series, we reconstructed the phase space and the dynamics. Figure 1, (a)-(c) shows the chaotic attractor, the power spectrum, and the time series for a pure copper (Cu) wire electrode immersed in .5M H_2SO_4 and 0.3 M NaCl at the potential of 320 mV. Figure 2 shows the chaotic attractor of a pure iron (Fe) wire-electrode immersed in 2M H_2SO_4 at 350 mV.

We observed that oscillations undergo sequences of metamorphosis as time progresses and a plethora of different dynamical behaviors is displayed: quasi periodicity, periodicity, chaos. Bifurcations and transitions between the various oscillatory regimes seem to occur in combination with the metamorphosis on the surface of the electrode. In the case of copper electrodes, changes in the oscillatory regimes seem to be connected with the gradual covering of the surface by a film. When the surface is completely covered, the oscillation gradually disappears. These results agree with studies performed with similar configurations and metal [20-26]. Fractal dimensions calculated from the reconstructed attractors show the presence of

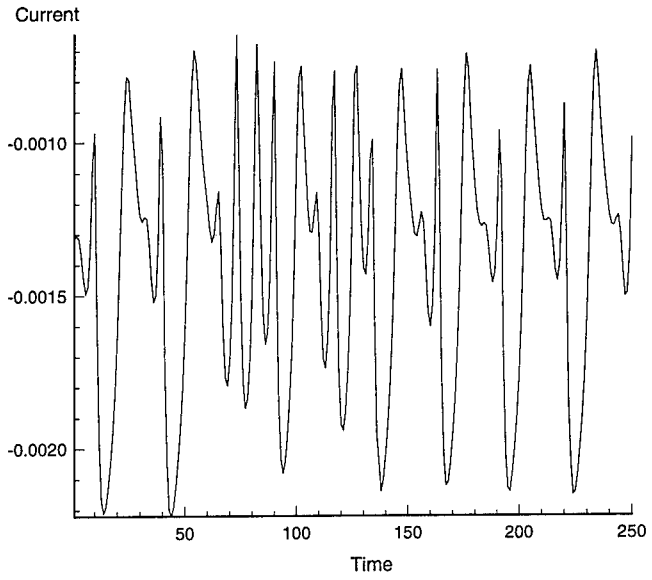


Figure 1 (a)

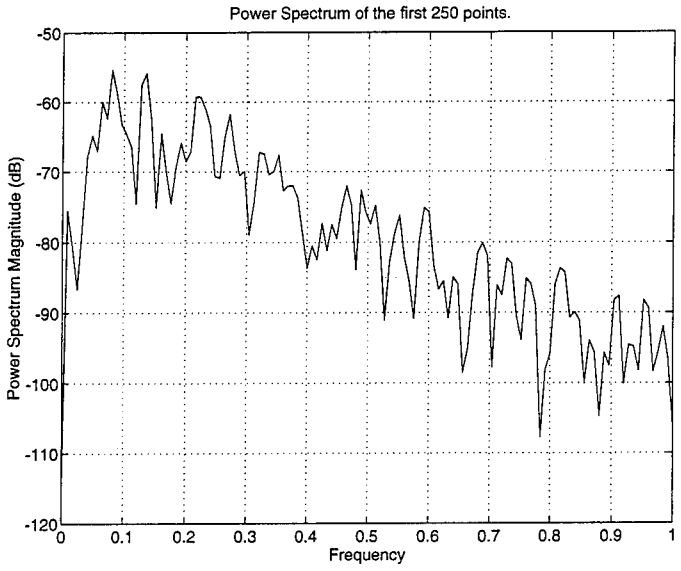


Figure 1 (b)

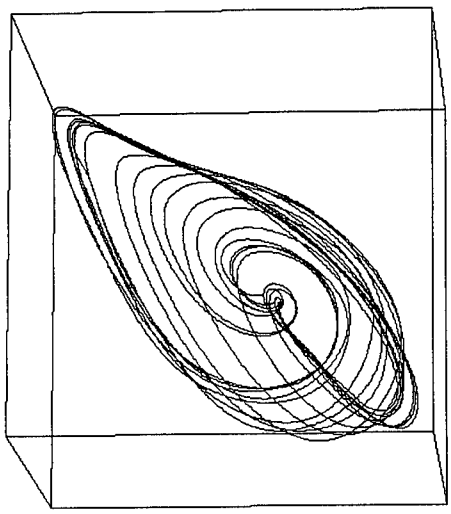


Figure 1 (c)

Figure 1. Electrochemical current oscillations for a pure copper (Cu) wire-electrodes immersed in a .5M H_2SO_4 and 0.3 M NaCl solution at the potential of 320 mV. (a) time series (b) power spectrum (c) reconstructed chaotic attractor.

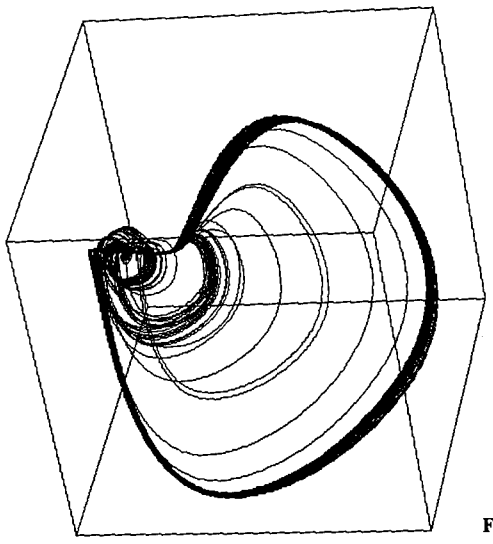


Figure 2

Figure 2. The chaotic attractor of a pure iron (Fe) wire-electrode immersed in a 2M H_2SO_4 solution at 350 mV.

low dimensional chaos. In order to test the robustness of the phenomena observed and to expand the horizons of the investigation to coated samples, we used bigger electrodes and the EG&G flat cell. Even if the shape of the attractor changed, the phenomena observed with the wire-electrodes persisted. However, dimensions of attractors increased considerably, around 6 and above , indicating the presence of an extended system. Similar phenomena of higher fractal dimensions have been encountered in other areas where time series was analyzed with similar techniques. In particular, in studies of the EEG of the human brain high dimensions have been found [37]. Whereas in cases like these we cannot speak of dimensions in the strict sense, the calculations of "dimension" have meaning mainly in a comparative sense. We can more appropriately speak about dimensional complexity. The higher dimensionality could indicate the presence of complex space-time phenomena occurring at the extended surface of the electrode. In order to better understand the phenomena observed and the influence of the surface morphology, we first studied electrochemical current oscillations for iron electrodes mechanically pretreated at different grain sizes (600,400,240). It is worth noticing that these samples are prototypes of steel substrates of the coated material we used later. Figure 3 (a) - (c) shows the chaotic attractors, the time series, and the power spectrum for the sample treated at 240 grain size (IRON240), immersed in a solution of 2M H_2SO_4 + 3.56 % NaCl . Figure 4 (a) - (c) shows the chaotic attractors, the time series, and the power spectrum for the sample treated at 600 grain size (IRON600), immersed in a solution of 2M H_2SO_4 + 3.56 % NaCl . Although oscillations look similar, the attractors are slightly different, as indicated by the different fractal dimensions (D=5.86 for IRON240 and D=6.25 for IRON600).

The next step in our investigation was to use the impedance technique to observe how the CPA angle changes with the roughness of the three iron samples (IRON600, IRON400, IRON240). We calculated the constant phase angle (CPA) by fitting the impedance spectra obtained with the EG&G electrochemical apparatus and the EG&G flat cell by using a nonlinear least squares routine. The CPA increases with the roughness going from $\theta=20.96^{o}$ for the IRON600 to $\theta=24.05^{o}$ for the IRON240. Figure 5 shows the Nyquist plot of the impedance (the dots) at various frequencies for the IRON600 sample. Frequency is decreasing toward the right of the figure. The corrosion rate calculated by the polarization resistance techniques increases with roughness. These results set for us a "standard" which helps us to analyze more complex surfaces such as the ones of steel industrially sprayed with Tungsten Carbide coatings. We studied several samples coated with various techniques and in various "flavors" of Tungsten Carbide. The samples were provided by Cooper Oil Tools Co. We recorded the impedance spectra and measured the CPA for the various samples. Furthermore, researchers of University of Southwestern Louisiana, with whom we are collaborating in this project, provided us with the measurements of roughness obtained by STM at the USL microscopy center. Table I shows the θ (CPA) and roughness measurements for the various samples. Correlations between CPA and roughness are not as clear as for the pure iron samples. For instance, higher value of the roughness does not necessarily imply higher value of the θ . Sample #3 has the highest value of roughness although the highest value of θ belongs to sample #7. However, samples with similar characteristics have close values for both roughness and θ . For example, sample # 11 and sample 12 have the same value for θ (12.2) and roughness (416). A clear path is not discernable, however. As suggested by Bates et al. [33] the shapes of the protrusions on the surface of the

electrodes are an important factor which determine the value of θ . Sharp protrusions seem to give more different contributions to the CPA and corrosion than flattened or rounded protrusions. This could be due to the different structure of dislocations at the protrusion site. The fact is, that CPA is determined by those geometrical factors of the surface which most affect the electrochemical behavior, in particular corrosion.

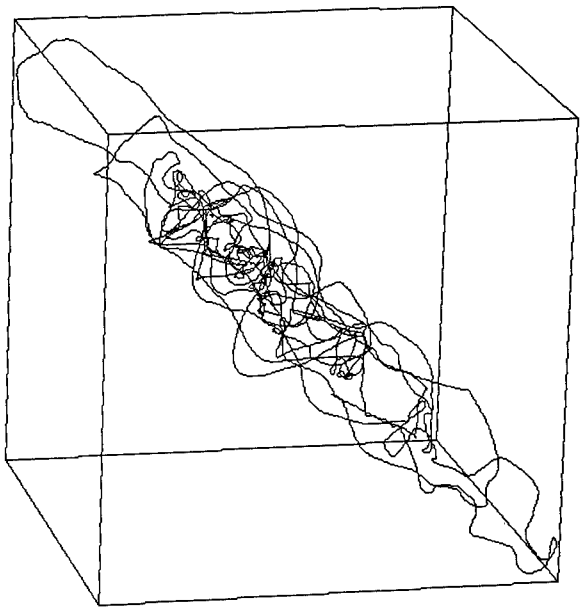


Figure 3 (a)

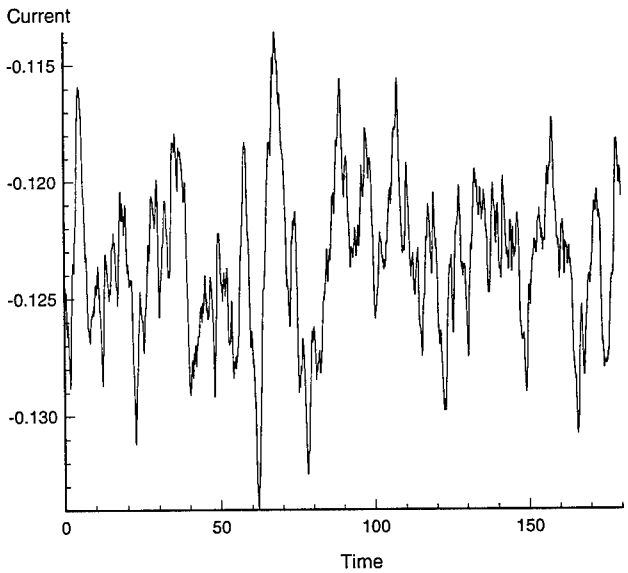


Figure 3 (b)

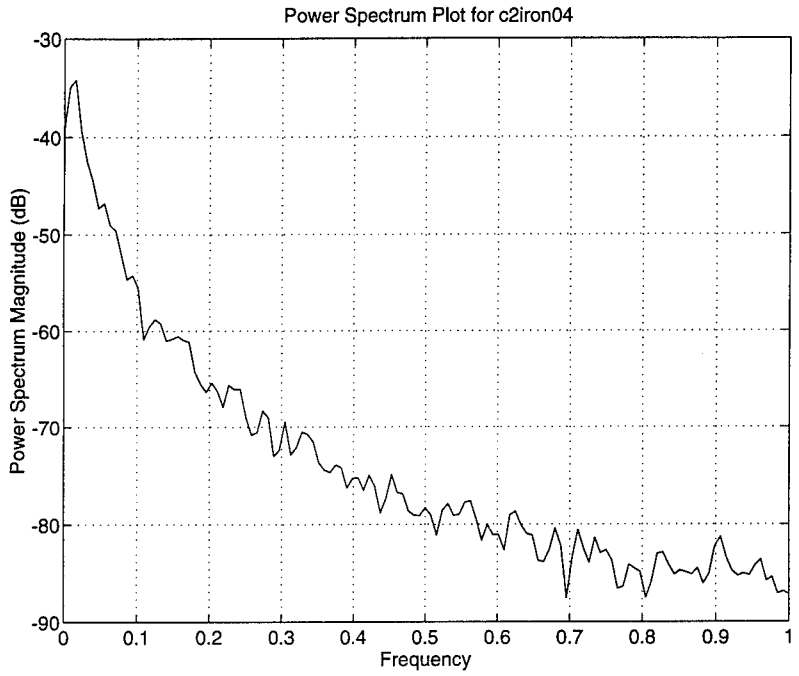


Figure 3 (c)

Figure 3. The chaotic attractor (a), time series (b) and the power spectrum (c) for the iron sample treated at 600 grain size (IRON240) , immersed in a solution of 2M H_2SO_4 + 3.56 % NaCl .

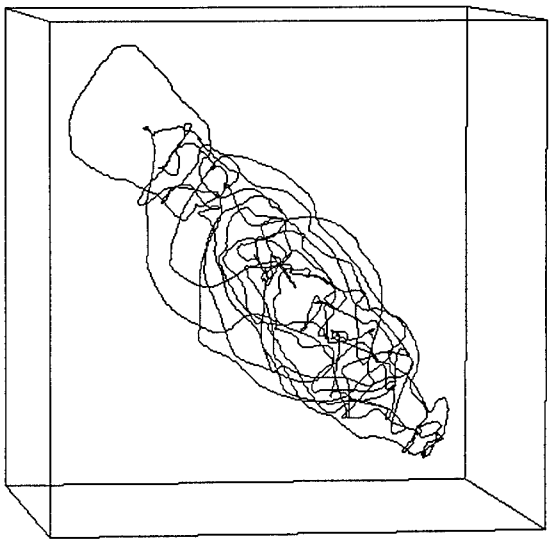


Figure 4 (a)

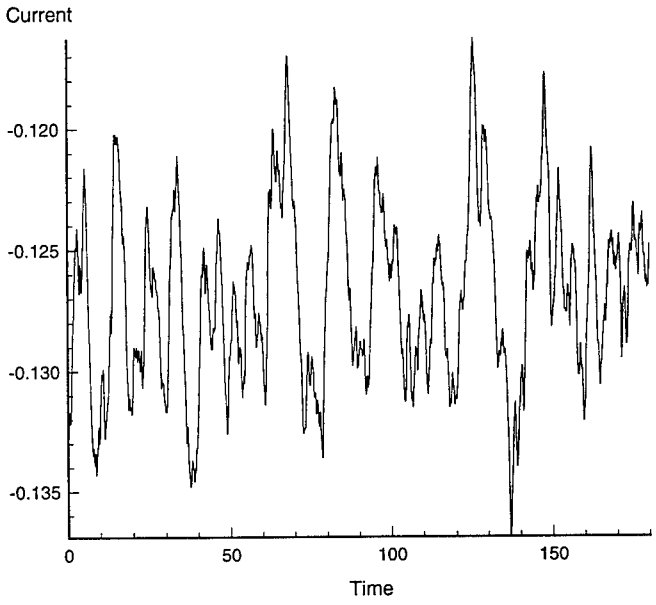


Figure 4 (b)

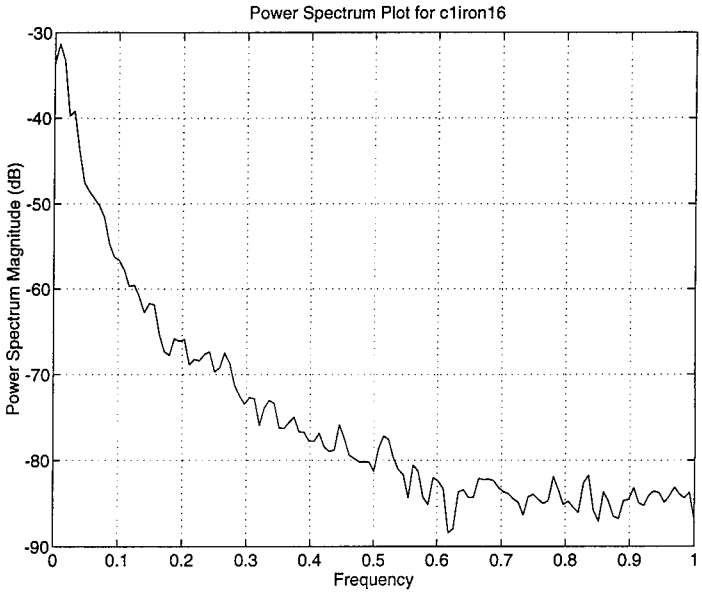


Figure 4 (c)

Figure 4. The chaotic attractor (a), the time series (b) and the power spectrum (c) for the iron sample treated at 240 grain size(IRON600), immersed in a solution of 2M H_2SO_4 + 3.56 % NaCl .

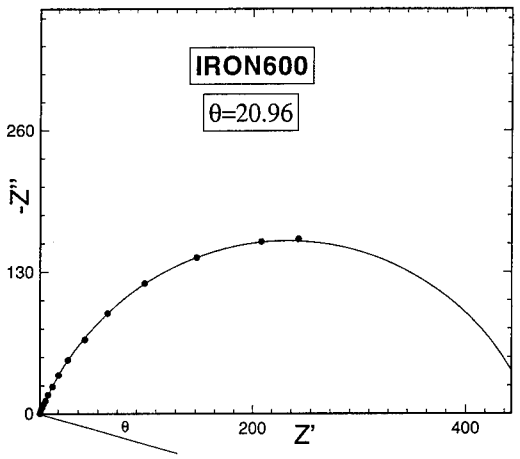


Figure 5

Figure 5. The Nyquist plot of the impedance (the dots) at various frequencies for the IRON600 sample. Z" and Z' is the imaginary and the real part of the impedance Z. The data points were fitted with a nonlinear least squares fitting routine. The solid semicircle joining the dots is the fitted semicircle. Since the fitting gives also the position of the center of the fitted semicircle, θ (CPA) can be calculated.

TABLE I
CPA AND ROUGHNESS FOR TUNGSTEN CARBIDE COATED SAMPLES

SAMPLE #	(CPA) θ	ROUGHNESS (nm)
1	12.35	365 ± 68
2	15.9	357 ± 78
3	16.4	1445 ± 301
5	19.01	907 ± 217
6	10.65	241 ± 68
7	34.36	650 ± 104
8	25.58	509 ± 88
9	8.6	295 ± 46
11	12.2	416 ± 82
12	12.2	416 ± 51
13	9.36	581 ± 74
14	8.93	642 ± 66

New measurements presently under study are needed to characterize the surface morphology from a more "electrochemical viewpoint" as well as its correlation with the dynamics of electrochemical oscillations generated by the surface methamorphosis.

CONCLUSIONS

The results presented in this paper show a new avenue to study electrochemical behavior and dynamics of corrosion in coating/substrate systems by using a combination of various techniques such as the analysis of temporal evolution of electrochemical oscillations, impedance spectra, and microscopy scans. In the search for a correlation among the results obtained emerged the need of surface characterization that is not only sensitive to general geometrical complexity of the surface but it also incorporates those geometrical and physical factors which mainly affect electrochemical behavior. In particular distributions of protrusions in function of their relative sharpness, structure of dislocations need to be incorporated in the analysis.

On the other hand, electrochemical oscillations can be used as investigative tools to study changes in the surface morphology such as the generation of micro - cracks in the coating and the production of corrosion fronts that break through the coatings. We are presently performing these studies. Furthermore, we will investigate, with the help of the AFM and an attached electrochemical cell, how the surface changes with the various oscillatory regimes. We will use the digitized image of the AFM for two dimensional space forecasting to design space-time maps which will model the electrochemical behavior at the surface.

AKNOWLEDGEMENT

This project is supported by the Louisiana Education Quality Support Fund (LEQSF) and the Department of Energy (DOE), Contract # LEQSF (1993-95)-03. The authors are grateful for the support received from these funds.

REFERENCES

1. A. A. Ashary and R.C. Tucker,Jr. , Corrosion '93, Paper No.24, 1993.
2. J.D Reardon, F.N. Longo,C.R. Clayton and K.G. Doss, Thin Solid Films **108**, 459 (1983).
3. B. Tsujino, S. Miyase, N. Twamoto and H. Mikami, Thin Solid Films **135**, 51 (1986).
4. L.V. Leaven, M.N. Alias and R. Brown, Surface and Coatings Technology **53**, 25 (1992).
5. J.L He and M. H. Hon, Surface And Coatings Technology **53**, 93 (1992).
6. Y. Arata, A. Ohmori and C.J. Li, Thin Solid Films **156**, 315 (1988).
7. J.H.Bartlett, Trans. Electrochem. Soc. **87**, 521 (1945).
8. K.F. Bonhoeffer and W. Jena, Z. Elektrochem. **55**, 151 (1951).
9. D. Gilroy and B. E. Conway, J. Phys. Chem. **69**, 1259 (1965).
10. M.L.B. Rao, J. Electrochem. Soc. **114**, 665 (1967).
11. U.F. Franck, Faraday Symp. Chem. Soc. **9**, 137 (1974).
12. P. Poncet, M Braizas, B. Pointer, J. Rousseau and N. Muhlstein, J. Chim Phys. **75**, 287 (1978).
13. R. De Levie, J. Electroanal. Chem., **25**, 257 (1970).
14. P. Russell and J. Newman, J. Electrochem. Soc. **133**, (1986).
15. A. L. Kawcznski, M. Przasayski and B. Baranowski, J. Electroanal. Chem. **179**, 285 (1984).
16. H. Glarum and J. H. Marshall, J. Electrochem. Soc. **132**, 2872 (1985).
17. H.P. Lee, K. Nobe and A.J. Pearlstein, J. Electrochem. Soc. **132**, 2159 (1985).
18. M.R.Bassett and J.L. Hudson, Physica D **35**, 289 (1989).
19. M.R.Bassett and J.L. Hudson, J. Electrochem. Soc. **137**, 1815 (1990).
20. C. B. Diem and J. L. Hudson, A.I.Ch. E. J. **33**, 218 (1987).
21. M.R.Bassett and J.L. Hudson, Chem. Eng. Commun. **60**, 145 (1987).
22. M.R.Bassett and J.L. Hudson, J. Phys. Chem. **92**, 6963 (1988).
23. F.N. Albahadily and M. Schell, J. Chem.Phys. **88**, 4312 (1988).
24. M. Schell and F.N. Albahadily, J. Chem.Phys. **90**, 822 (1989).
25. F.N. Albahadily, J. Ringland and M. Schell, J. Chem.Phys. **90**, 813 (1989).
26. A. Karantonis, M. Pagitsas and D. Sazou, Chaos **3**, 243 (1993).
27. L. Nyikos and T. Pajkossy, Electrochimica Acta **30**, 1533 (1985).
28. M. Jeddam and H. Takenouti, Electrochimica Acta **33**, 445 (1988).
29. S.H. Liu, Phys. Rev. Lett. **55**, 529 (1985).
30. R. Levie, J. Electroanal. Chem. **281**, 1 (1990).
31. U. Rammelt and G. Reinhard, Electrochimica Acta **35**, 1045 (1990).
32. B. Sapoval and J.N. Chazalviel, Phys. Rev. A **38**, 5867 (1988).
33. J.B. Bates, Y.T. Chu and W.T. Stribling, Phys. Rev. Lett. **60**, 627 (1987).
34. J.R. Macdonald, Impedance Spectroscopy , John Wiley & Sons, New York, 1987. pp. 77.
35. Eckmann J.P. and Ruelle D., Rev. Mod. Phys. **57**, 617(1985).
36. Grassberger P. and Procaccia I., Phys. Rev. Lett. **50**, 349 (1983).
37. S.P Layne, G. Mayer-Kress and J. Holzfuss, in Dimensionsand Entropies in Chaotic Systems, edited by G.Mayer-Kress, Springer Verlag, New York, (1986).

Part VI

Scaling and Nanostructures

FRACTAL AND DENDRITIC GROWTH OF SURFACE AGGREGATES

H. BRUNE, K. BROMANN, and K. KERN
Institut de Physique Expérimentale, EPFL, CH-1015 Lausanne, Switzerland

J. JACOBSEN, P. STOLTZE, K. JACOBSEN, and J. NØRSKOV
Center for Atomic-scale Materials Physics and Physics Department
Technical University of Denmark, DK-2800 Lyngby, Denmark

ABSTRACT

The similarity of patterns formed in non-equilibrium growth processes in physics, chemistry and biology is conspicuous and many attempts have been made to discover common mechanisms underlying their growth. The central question in this context is what causes some patterns to be dendritic, as e.g. snowflakes, while others grow fractal (randomly ramified). Here we report a crossover from fractal to dendritic patterns for growth in two dimensions: the diffusion limited aggregation of Ag atoms on a Pt(111) surface as observed by means of variable temperature STM. The microscopic mechanism of dendritic growth can be analyzed for the present system. It originates from the anisotropy of the diffusion of adatoms at corner sites which is linked to the trigonal symmetry of the substrate. This corner diffusion is observed to be active as soon as islands form, therefore, the classical DLA clusters with the hit and stick mechanism do not form. The ideas on the mechanism for dendritic growth have been verified by kinetic Monte-Carlo simulations which are in excellent agreement with experiment.

INTRODUCTION

In the "classical" Diffusion Limited Aggregation (DLA) computer codes, clusters are formed as randomly diffusing particles stick irreversibly to the perimeter of a growing aggregate **[1-3]**. These models always produce *randomly ramified* aggregates, no matter whether they are carried out on a lattice or not (off-lattice DLA) **[3, 4]**. Nonequilibrium aggregation processes in nature, however, quite often result in *dendritic* patterns which are characterized by preferred growth directions **[5-7]**. Despite a considerable theoretical effort, the relationship between ordered and randomly ramified patterns has not yet been solved **[8, 9]**. Both objects have a fractal dimension close to 1.7 **[10, 11]**, but their different shape is evident for the unaided eye (compare e.g. Figs. 1 and 2 below).

It is generally accepted that the key to dendritic growth is anisotropy **[12-15]**. This can either be linked to the symmetry of the aggregating particles themselves, which is then amplified to the overall pattern shape as the aggregate grows (a well known example for this is the snowflake **[16]**), or it can be due to the symmetry of the underlying substrate. Examples for this are given in Fig. 2 below, where we observe dendritic growth for two-dimensional metal aggregation on three hexagonally close packed substrates.

In order to reproduce dendritic structures basically two approaches have been followed to modify the hit and stick mechanism in DLA-models. One is the introduction of curvature dependent sticking probabilities **[17]** and the second noise reduction, where atoms are only attached if the approached site has been visited m-1 times before **[18]**. Both mechanisms are, however, irrelevant for low temperature metal epitaxy, since there the sticking probability is 1 and independent of curvature.

In the first metal deposition experiments carried out with the STM (at 300K), ramified growth and irregular island shapes were reported **[19-21]**. In particular, the Au aggregates on Ru(0001) have been considered as an example for classical DLA because of their fractal dimension **[21]**. However, it had been realized later that their branch width (100-200Å) points to a considerable amount of edge diffusion **[22-25]**. Similarly, the first results reported for lower temperature, showing ramified islands for homoepitaxy on Pt(111), were also interpreted as the physical realization of the hit and stick mechanism **[26]**.

The first time dendrites have been reported, and their distinction to randomly ramified aggregates was made clear, was for the aggregation of Ag on Pt(111) **[11, 27, 28]**. These

Mat. Res. Soc. Symp. Proc. Vol. 407 © 1996 Materials Research Society

results have inspired simulations which were very successful in reproducing island densities **[29, 30]**. However, they assume a hit and stick mechanism and neglect the specific substrate symmetry (which both holds for aggregation of much bigger clusters **[31]**) and therefore are not suited to simulate dendritic growth. The same is true for most of the models that study metal nucleation. since they were carried out on a square lattice **[23, 32-34]**. Those Kinetic Monte-Carlo (KMC) simulations which have been performed on a hexagonal lattice either focused on the shape of compact islands on Pt **[35, 36]**, or they do not distinguish between the two types of close packed steps present on a hexagonal substrate **[22, 37]**. There are close packed {111}-facets and more open {100}-facets (see vacancy islands in Fig. 3 and model in Fig. 4). They have been called B- and A-steps, respectively **[38]**.

Thus to date, a realistic description of the atomic processes leading to dendritic growth in metal aggregation on hexagonal substrates was lacking. We will present a microscopic model explaining dendrite formation and discuss the importance of the different relaxation processes at the island edge and their influence on the aggregate's shape.

EXPERIMENTAL

The experiments have been performed with a variable-temperature STM mounted in UHV, which operates in the temperature range from 25K to 800K (for experimental setup see e.g. ref. **[28]**). The Pt(111) crystal has been cleaned by repeated cycles of Ar ion bombardment (650eV) at 830K, annealing in oxygen atmosphere (880K, $1x10^{-7}$ mbar) and subsequent flash to 1300K. The Ag (purity 99.995%) aggregates were grown by vapor-phase epitaxy with an MBE-Knudsen-cell at a background pressure better than $2x10^{-10}$ mbar. The STM images have been measured in the constant current mode. All images shown here were recorded in differential mode, which means that the derivative $\partial z/\partial x$ of the lines of constant tunnel current is recorded. They therefore appear as illuminated from the left. The images are not corrected for thermal drift and have not been filtered.

RESULTS

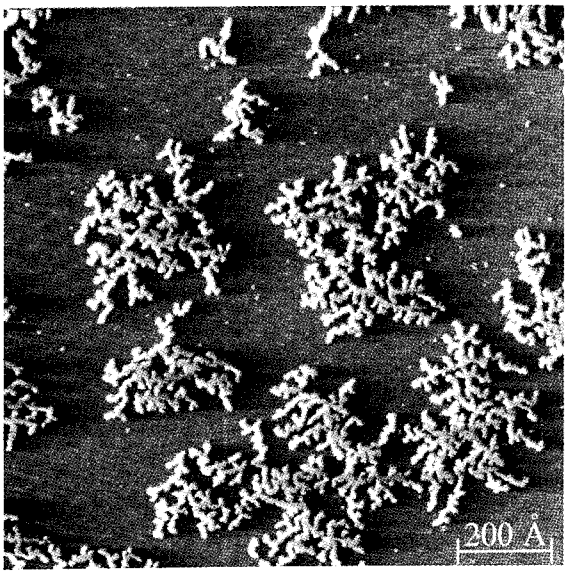


Fig. 1: Fractal Ag aggregates grown on Pt(111) at 110K and extremely low deposition flux of F = $1.6x10^{-5}$ML/s (1200Å x 1200Å, coverage Θ = 0.12ML).

The two-dimensional Ag aggregates shown in Fig. 1 have been grown at 110K. The coverage of 0.12 monolayers has been deposited at an extremely low Ag flux of 1.6×10^{-5} ML/s. Under these conditions, large clusters (~3000 Ag atoms) with an open ramified structure are formed. The branches of the clusters frequently alter their direction of growth and thus show no long range correlation with the symmetry axes of the substrate. The branch thickness is almost constant over the entire aggregate and much smaller than its radius of gyration. In fact the arms are only 2±1 atoms wide as determined from the total arm length and the cluster size. (Branches are imaged (14±1)Å wide in Fig. 1, which is consistent with their actual width if the finite curvature of the STM-tip is taken into account.) The shape of the Ag aggregates grown at 110K is very similar to that of fractal aggregates simulated with the classical DLA computer codes. However, for aggregation on hexagonal substrates, these patterns are the exception rather than the rule.

Patterns formed by the aggregation of Ag at moderate growth speeds on three hexagonally close packed metal surfaces, i.e. the (111) surfaces of Pt, Ag, and one Ag monolayer pseudomorphically adsorbed on Pt(111) **[39]**, all have in common a nice dendritic shape (see Fig. 2). The variable temperature STM images show that their branches preferentially grow into three directions, which are rotated by 120° with respect to each other. As will become evident from Fig. 3 below, they are the crystallographic $\langle 1\,\bar{1}\,2 \rangle$-directions which are perpendicular to A-steps, one of them has been labeled A.

For the first case of Ag/Pt(111) (Fig. 2A) the trigonal symmetry of the aggregate is best seen from its triangular envelope, but also the longest central branches clearly point into the preferred growth directions. Notice also that the material attached to the straight substrate step in the lower part of the image does not grow perpendicular to the edge (which would be the B-direction since this step is a {111}-facet, i.e. of B-type) but instead in two of the A-directions forming angles of ±30° with respect to the step. At 80K islands are too small to branch more than once and the growth anisotropy leads to equally oriented Y's (inset Fig. 2A). For Ag/Ag(111) (Fig. 2B) the preferred growth in three directions is clearly seen from of the central branches of the aggregates. The trigonal symmetry of the aggregates on one pseudomorphic Ag layer is even more pronounced. Their shape resembles very much that of needle crystals, which are the extreme case of anisotropic growth **[40]**. These examples strongly suggest that dendritic growth is common for low temperature metal aggregation on hexagonally close packed metal surfaces at usual growth rates. In fact also Pt islands formed at low T seem to have dendritic shapes with preferential growth in A-direction **[41]**.

In order to analyze the atomistic process responsible for the formation of dendrites on hexagonal surfaces, we will distinguish between two diffusion processes that can take place at the island edge. Depending on whether an adatom starts from a site which is laterally *two-* or *one-fold* coordinated to the island, i.e. whether the initial site is an edge or a corner, we will call its displacement *edge-* or *corner*-diffusion, respectively **[42]**. For corner diffusion the final coordination can be 1 or 2. For edge diffusion the final coordination is 2. The case where an edge atom (2-fold coordinated) goes to a corner (1-fold) becomes important at higher temperatures, and should be treated separately.

It turns out that this distinction is rather useful since these processes have quite different effects on the aggregate's shape. Edge diffusion leads to a thickening of the aggregates' branches **[22-25]**. Closer inspection of the dendrites in Fig. 2 indeed reveals that the branches become thicker in going from images (A) to (C) (notice the different scale). From the narrow branches for Ag on Pt(111) in Fig. 2A (2±1 atoms wide) we can deduce that edge diffusion is practically frozen (at 130K and the applied deposition flux) **[25]**. Edge diffusion is active for Ag/Ag(111) at 110K, since branches are 8±1.5 atoms wide **[25]** (Fig. 2B). It is even more involved in the case of Ag/1MLAg/Pt(111) leading to 18±3 atoms wide branches (Fig. 2C). From the fact that dendritic growth occurs in all examples shown in Figure 2, independent from the amount to which edge diffusion is involved, we can argue that it is very unlikely to be the origin of dendritic growth **[43]**.

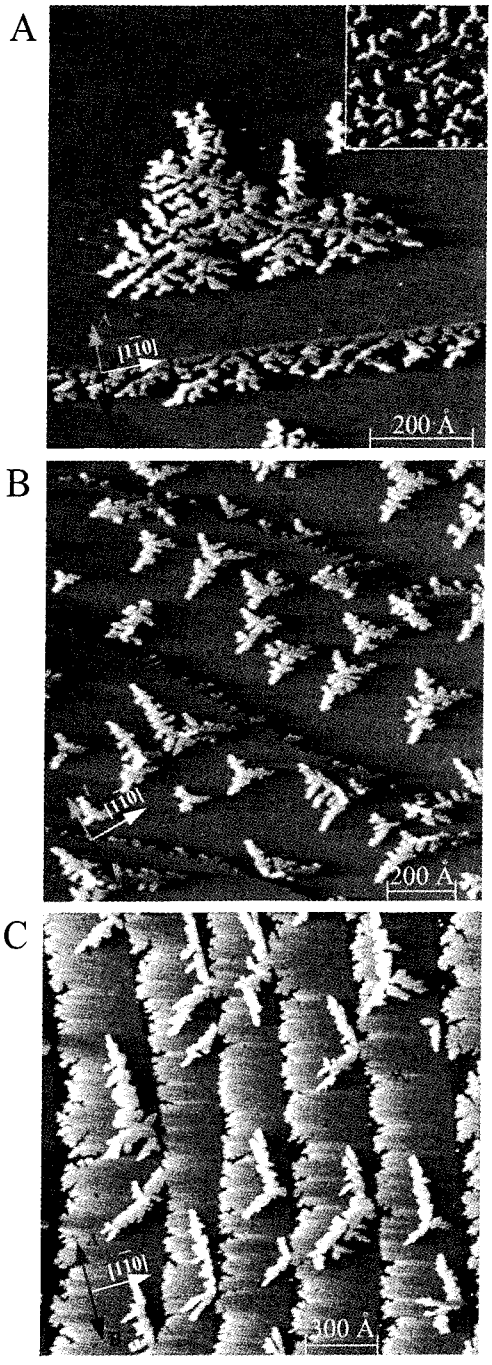


Fig. 2: Dendritic patterns form for deposition of Ag onto Pt(111) at 130K (**A**) and 80K (inset), onto Ag(111) at 110K (**B**), and on a pseudomorphic monolayer of Ag adsorbed on Pt(111) at 170K (**C**). The STM topographs have been recorded isothermally to deposition and show the surface as it appears when illuminated from the left. The Ag coverage is Θ = 0.12ML, the deposition flux F = $1.1 \times 10^{-3} MLs^{-1}$.

In order to proceed further in our analysis we identify the crystallographic directions in which branching preferentially occurs in the experiment (see Fig. 3). One way to calibrate the crystallographic directions on a hexagonal substrate is to create vacancy islands with the thermodynamic equilibrium shape **[44]**. These quasi hexagons are bound by 6 monoatomic steps running in the close packed $\langle 1\bar{1}0 \rangle$-directions. They devide up into B- and A-type steps opposing each other. Due to their lower free energy, the first ({111}-facets) are the long sides of the hexagons, while the latter ({100}-facets) form the short ones. Ag has been deposited at 100K onto a substrate where these vacancy island mark the crystallographic directions. At this temperature, the aggregates obey Y-shape for the same reason as at 80K (inset in Fig. 2A), they are too small to branch more than once. Their branches are oriented exclusively into the $\langle 1\bar{1}2 \rangle$-directions, i.e. perpendicular to A-steps, which are also the preferred growth directions for the bigger aggregates shown above (Fig. 2).

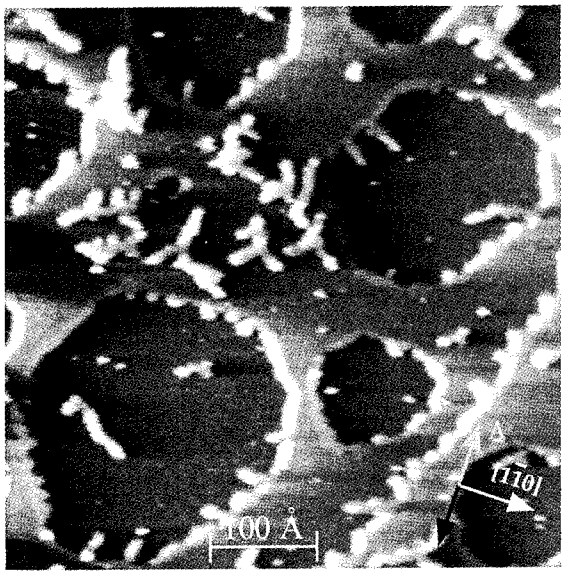


Fig. 3: The anisotropic growth leads to small Y-shaped dendrites for Ag on Pt(111) at 100K. Removal of about 0.5ML of the Pt(111) substrate by sputtering (600K) and subsequent annealing (700K) creates equilibrium vacancy islands. They serve as calibration for the two different crystallographic directions labeled A for $\langle 1\bar{1}2 \rangle$, and B for $\langle 11\bar{2} \rangle$, respectively. It is evident that the branches of these Y's exclusively grow into A-directions, i.e., perpendicular to A-steps.

In order to get insight into the relaxation processes at the aggregate's perimeter we have calculated diffusion barriers with Effective Medium Theory (EMT) **[45, 46]**. The results show that for all three cases where we found dendritic growth in the STM experiment, corner diffusion to an A-step has a much lower barrier than displacement from a corner to a B-step (Fig. 4 and Table 1). This asymmetry can be rationalized from simple geometric reasons. From inspection of the model in Fig. 4 it becomes evident that displacement from a corner to an A-step can be done via an hcp-hollow site without loosing the coordination to the heptamer, whereas for diffusion towards a B-step the hcp-site is situated too close towards the island. Thus the adatom has to walk almost over an on-top site, which is much more costly in energy.

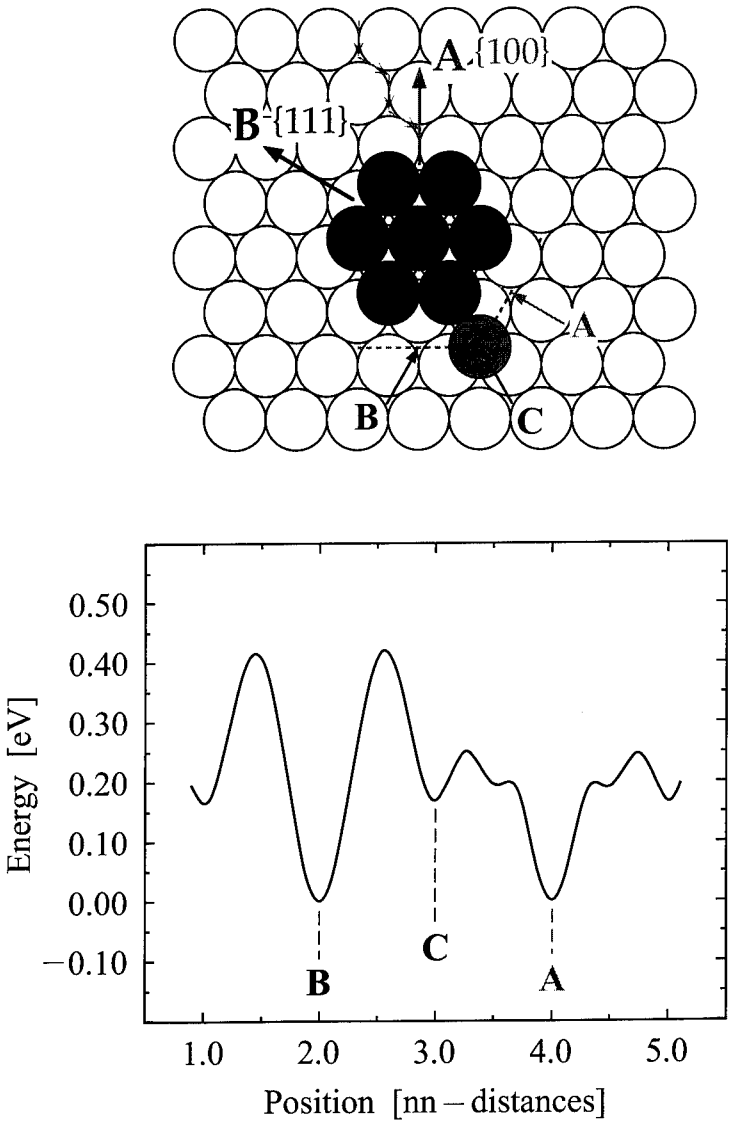


Fig. 4: Difference in total energy of a Ag adatom diffusing around a Ag heptamer on Pt(111) as calculated with EMT (A- and B-directions are indicated in the ball model). The diffusion processes with the lowest barriers evidently are that from a corner (C) and the hcp-site close to it to an A-step.

For some systems like Pt(111) **[36]** and Au(111) homoepitaxy, the corner asymmetry is less pronounced in the EMT-calculations and the direction is even inverted, i.e., displacement to B-steps is slightly preferred (Pt: E_{Ac}/E_{Bc} = 212meV/173meV, Au: E_{Ac}/E_{Bc} = 146meV/101meV).

Therefore, it is important to notice that there is a second anisotropy which generally holds for hexagonally close packed surfaces. An atom that diffuses towards an A-step close to a corner does this via the hcp-site located between the two fcc-sites at the corner and the A-step (ball model Fig. 4). Already at this point, it feels the two-fold coordination at the step and has a much lower barrier to go there than to diffuse to the corner site (see asymmetry in activation energy around the hcp-site and the flashes indicating an approaching atom in Fig. 4). On a B-step, the decision whether the atom goes to the corner or the step is made much earlier so that it is not guided to the step.

Both these asymmetries give a significant preference in populating A-steps. It is important to note that both diffusion processes, i.e., corner to A-step and that from the hcp-site to an A-step, have an activation energy comparable to, or even below, that obtained for terrace diffusion. Therefore, relaxation towards A-steps is active as soon as nucleation and aggregation set in, and the classical hit and stick DLA cluster do not form. The barriers for the more difficult corner process (corner-to-B step), and those for edge diffusion, as well as to escape from an edge to a corner, are significantly higher, which implies that these processes can be frozen at low temperatures.

Let us now see how this specific preference for A-steps decides on the shape of the growing aggregate. We assume to start from a tetramer which is bound by two A- and B-steps. Atoms impinging at corners adjacent to an A-step, as well as those approaching the A-step at the two neighboring hcp-sites, will end up at the A-step, which significantly increases the probability of attachment there. Once the atoms are at A-steps, they form a protruding tip and thus have a slightly higher capture rate than straight steps. This is known as "tip-effect" or Mullins Sekerka instability **[2, 47]**. Atoms arriving at such an atomic "tip", can diffuse force and back between the two corner sites but they cannot escape from there, since this would be diffusion to the adjacent B-steps, which is frozen. If a second atom arrives at the respective free corner, a new A-step is formed, which then again collects very effectively diffusing atoms and growth in the A-direction proceeds. If the atom arrives such that a linear chain in the close packed direction would be formed, the EMT calculations suggest that these chains can relax with a low energy barrier to a more compact form which also ends with an A-step. Therefore, growth of Y's occurs as A-steps effectively capture atoms, these atoms form tips which are traps for attaching atoms due to the frozen corner-to-B diffusion. Atoms attached there thus stay until a partner arrives to form a dimer which provides new A-steps. Direct attachment to B-steps leads to statistical deviations from this behavior. However, it also creates new A-steps which can be the origin for a new branch in the preferred A-directions.

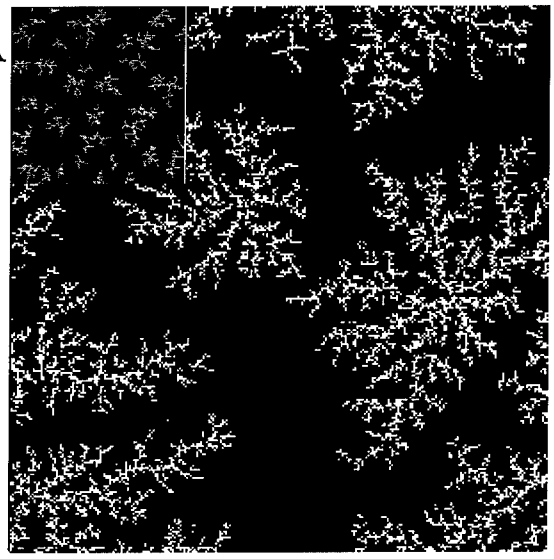
Table 1: Energy barriers for the most relevant atomic diffusion processes involved in metal aggregation on hexagonal substrates for the systems studied in Figs. 1 and 2 (E_m stands for terrace diffusion, E_{Ac} for corner-to-A-step, E_{Bc} for corner-to-B-step, E_{Ae} and E_{Be} denote A- and B-edge diffusion). The experimental values for terrace diffusion have been obtained by the analysis of the saturation island density as a function of T at a critical cluster size of 1 **[48, 49]**. (* in Fig. 4D E_{Bc} has been lowered, ** E_m has been lowered for 130K in order to account for dimer instability at this temperature, see text.)

Ag diffusion on substrates:	E_m [meV] STM	E_m [meV] EMT	E_{Ac}/E_{Bc} EMT	E_{Ae}/E_{Be} EMT	E_{Ac}/E_{Bc} KMC	E_m [meV] KMC
Pt(111)	157±10	80	80/248	187/389	160/500 160/320*	160 120**
Ag(111)	97±10	67	73/139	222/300	—	—
1MLAg/Pt(111)	60±10	50	39/165	167/354	—	—

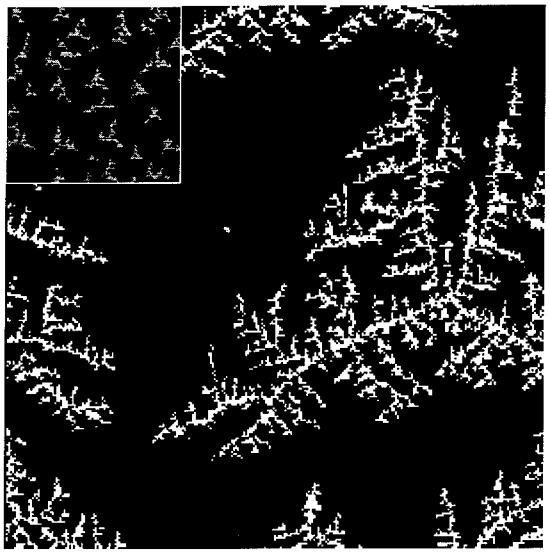
To test the ideas on the mechanism for dendritic growth we performed Kinetic Monte-Carlo (KMC) simulations (the KMC-program has been described in ref. **[36]**) for Ag/Pt(111) on a hexagonal lattice where we distinguish between A- and B-directions (see Fig. 5). Activation energies on surfaces are often underestimated by the EMT. However, the EMT generally gives a

good idea on the energetic hierarchy of different diffusion processes. Therefore, as a first input for the KMC we use the EMT activation energies scaled by a common factor of 2, since then the barrier for terrace diffusion equals the experimental value of E_m = 160meV **[48]**. All prefactors have been set to the experimental value for terrace diffusion of $1x10^{13}s^{-1}$. Using E_m = 160meV in a KMC simulation nicely reproduces the experimental island densities at temperatures up to 110K, where dimers are stable and immobile. In our simulations done at 130K, we have used E_m = 120meV as an effective barrier for terrace diffusion which then also accounts for the dimer instability or mobility. This way, we again get the experimental island density at 130K and thus the correct lateral impinging rate of atoms to each island.

A



B



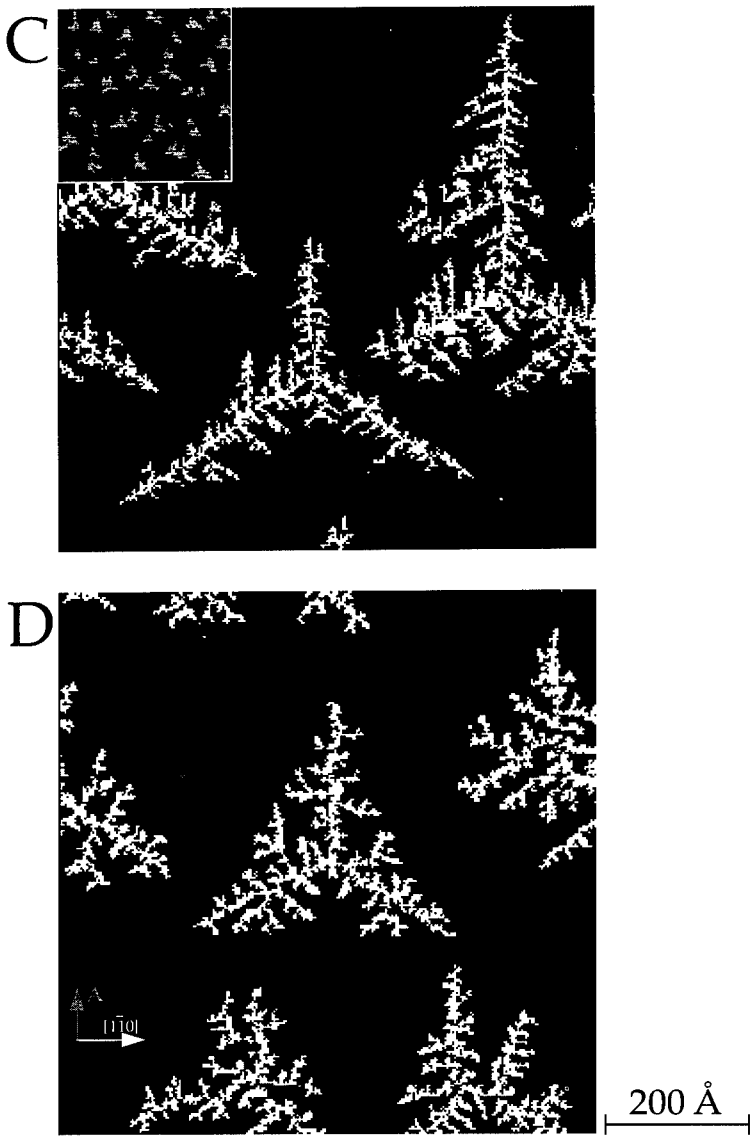


Fig. 5: KMC simulations of the STM experiments for Ag/Pt(111). As in Fig. 2A, the scale is the same for figures and insets, they correspond to growth temperatures of 130K and 80K, respectively. Coverages and deposition rates are as in the experiment. For hit and stick, classical DLA fractals result (**A**). The key process for dendritic islands is diffusion from corner to A-steps (**B**). Close packed chains that occasionally form in (B) are no more observed when a small atomic row is allowed to relax (**C**). Best agreement with experiment is obtained when corner to B-step diffusion is introduced (**D**).

The KMC simulations shown in Fig. 5 nicely illustrate the influence of the different processes on the island shape. The hit and stick case, where terrace diffusion and jump down from island tops are the only atomic displacements allowed, gives the classical randomly ramified DLA fractals where the substrate symmetry is not visible in the overall cluster shape (Fig. 5A). Turning on corner diffusion towards A-steps induces a marked change towards trigonal symmetry with branches predominantly growing into A-direction (Fig. 5B). However the aggregates form monoatomic chains along $\langle 1\bar{1}0 \rangle$ and the Y-shaped islands experimentally observed at 80K cannot be reproduced (see inset in Fig. 5B) . If we introduce further the collective relaxation of these chains, we can improve this. The scaled EMT barrier of E_{coll} = 240meV is too high for the process to happen sufficiently frequent at 80K, but choosing E_{coll} = 160meV we get a strikingly good agreement with the experimental island shapes at 130K and 80K (Fig. 5C and inset).

We want to point out that the important time scale for all relaxation processes at the island edge is the lateral impinging rate of diffusing atoms. The observed island shapes at 80K set an upper limit of 160meV for the barriers of the corner-to-A process and the collective relaxation of the $\langle 1\bar{1}0 \rangle$-chains. Speeding up these processes by reducing their energy barriers in the simulations would not significantly change the morphology of the obtained islands (Fig. 5B-D). Similarly, we find that the experimentally observed island shapes at 130K (Fig. 2A) set a lower limit of 320meV for the barrier of the corner-to-B process. The scaled EMT barrier of 500meV freezes this process completely even at 130K. In Fig. 5D, we show the result of a simulation using E_{Bc} = 320meV at 130K. This gives an even better agreement with the experimentally observed islands. There is still strongly preferred growth perpendicular to the A-steps, however, now the simulated islands bear some of the randomness characteristic of the experiment with occasional growth of the branches perpendicular to B-steps.

In general, the growth direction of the aggregate's branches is largely determined by corner diffusion. It decides whether randomly ramified or dendritic patterns will evolve, and determines the orientation of the latter. The branch width, on the other hand, is determined by edge diffusion, which has much less influence on their growth direction. Finally, compact islands can only be formed if atoms can leave the two-fold coordination at edges and diffuse around corners, a process which has a slightly higher barrier than edge diffusion.

CONCLUSIONS

In conclusion, we have presented STM experiments at low temperature showing that randomly ramified growth is the exception whereas dendritic growth is the rule for diffusion limited metal aggregation on three different hexagonal surfaces. The kinetic mechanism giving rise to the trigonal symmetry has been identified by using EMT energy calculations and kinetic Monte-Carlo simulations. The key process is the preferential diffusion of atoms from one-fold corner sites as well as from sites between a corner and a step towards A-steps. Both processes significantly increase the population of these steps and thereby promote dendritic growth. Since at least the latter is always present, dendritic growth is expected to be the rule for low temperature metal aggregation on hexagonally close packed substrates.

REFERENCES

[1] T. A. Witten and L. M. Sander, Phys. Rev. Lett. **47**, 1400 (1981).
[2] T. A. Witten and L. M. Sander, Phys. Rev. B **27**, 5686 (1983).
[3] P. Meakin, Phys. Rev. A **27**, 1495 (1983).
[4] J. P. Eckmann, P. Meakin, I. Procaccia and R. Zeitak, Phys. Rev. Lett. **65**, 52 (1990).
[5] D. Grier, E. Ben-Jacob, R. Clarke and L. M. Sander, Phys. Rev. Lett. **56**, 1264 (1986).
[6] Y. Sawada, A. Dougherty and J. P. Gollub, Phys. Rev. Lett. **56**, 1260 (1986).
[7] J. S. Langer, Rev. Mod. Phys. **52**, 1 (1980).
[8] M. B. Amer, P. Pelcé and P. Tabeling, *Growth and Form: nonlinear aspects* (Plenum Press, New York, 1991).
[9] H. Takayasu, *Fractals in the physical sciences* (Manchester University Press, Manchester, New York, 1990).
[10] P. Meakin, Phys. Rev. A **33**, 3371 (1986).
[11] H. Brune, C. Romainczyk, H. Röder and K. Kern, Nature **369**, 469 (1994).

[12] J. Nittmann and H. E. Stanley, J. Phys. Math. Gen. **20**, L981 (1997).
[13] A. Buka, J. Kertész and T. Vicsek, Nature **323**, 424 (1986).
[14] E. Ben-Jacob, R. Godbey, N. D. Goldenfeld, J. Koplik, H. Levine, T. Mueller and L. M. Sander, Phys. Rev. Lett. **55**, 1315 (1985).
[15] V. Horváth, T. Vicsek and J. Kertész, Phys. Rev. A **35**, 2353 (1987).
[16] J. Nittmann and H. E. Stanley, Nature **321**, 663 (1986).
[17] T. Vicsek, *Fractal Growth Phenomena* (World Scientific, Signapore, 1989).
[18] P. Meakin, Phys. Rev. A **36**, 332 (1987).
[19] D. D. Chambliss and R. J. Wilson, J. Vac. Sci. Technol. B **9**, 928 (1991).
[20] A. Brodde, G. Wilhelmi, D. Badt, H. Wengelnik and H. Neddermeyer, J. Vac. Sci. Technol. B **9**, 920 (1991).
[21] R. Q. Hwang, J. Schröder, C. Günther and R. J. Behm, Phys. Rev. Lett. **67**, 3279 (1991).
[22] M. C. Bartelt and J. W. Evans, Surf. Sci. **314**, L829 (1994).
[23] G. S. Bales and D. C. Chrzan, Phys. Rev. Lett. **74**, 4879 (1995).
[24] A. Pimpinelli, J. Villain and D. E. Wolf, J. Phys. (Paris) **3**, 447 (1993).
[25] H. Röder, K. Bromann, H. Brune and K. Kern, Phys. Rev. Lett. **74**, 3217 (1995).
[26] T. Michely, M. Hohage, M. Bott and G. Comsa, Phys. Rev. Lett. **70**, 3943 (1993).
[27] H. Röder, H. Brune, J. P. Bucher and K. Kern, Surf. Sci. **298**, 121 (1993).
[28] H. Brune, H. Röder, C. Romainczyk, C. Boragno and K. Kern, Appl. Phys. A **60**, 167 (1995).
[29] P. Jensen, A. L. Barabási, H. Larralde, S. Halvin and H. E. Stanley, Nature **368**, 22 (1994).
[30] P. Jensen, A. L. Barabási, H. Larralde, S. Halvin and H. E. Stanley, Phys. Rev. B **50**, 15316 (1994).
[31] L. Bardotti, P. Jensen, A. Hoareau, M. Treilleux and B. Cabaud, Phys. Rev. Lett. **74**, 4694 (1995).
[32] M. C. Bartelt and J. W. Evans, Phys. Rev. B **46**, 12675 (1992).
[33] G. S. Bales and D. C. Chrzan, Phys. Rev. B **50**, 6057 (1994).
[34] J. G. Amar and F. Family, Phys. Rev. Lett. **74**, 2066 (1995).
[35] S. Liu, Z. Zhang, G. Comsa and H. Metiu, Phys. Rev. Lett. **71**, 2967 (1993).
[36] J. Jacobsen, K. W. Jacobsen, P. Stoltze and J. K. Nørskov, Phys. Rev. Lett. **74**, 2295 (1995).
[37] Z. Zhang, X. Chen and M. G. Lagally, Phys. Rev. Lett. **73**, 1829 (1994).
[38] S. C. Wang and G. Ehrlich, Phys. Rev. Lett. **67**, 2509 (1991).
[39] H. Brune, H. Röder, C. Boragno and K. Kern, Phys. Rev. B **49**, 2997 (1994).
[40] J. Kertész and T. Vicsek, J. Phys. A: Math. Gen. **19**, L257 (1986).
[41] During preparation of this manuscript it came to our attention that also Michely et al. interpret their islands as dendritic. They suggest a similar explanation based on anisotropic corner diffusion.
[42] This important difference has first been realized by Zhang et al. in ref. 37
[43] In a former publication (ref. 11) we have suggested that anisotropy in edge diffusion might be responsible for dendritic growth.
[44] T. Michely and G. Comsa, Surface Science **256**, 217 (1991).
[45] K. W. Jacobsen, J. K. Nørskov and M. J. Puska, Phys. Rev. B **35**, 7423 (1987).
[46] P. Stoltze, J. Phys. Condens. Matter **6**, 9495 (1994).
[47] W. W. Mullins and R. F. Sekerka, J. Appl. Phys. A **34**, 323 (1963).
[48] H. Brune, H. Röder, C. Boragno and K. Kern, Phys. Rev. Lett. **73**, 1955 (1994).
[49] H. Brune, K. Bromann, H. Röder, K. Kern, J. Jacobsen, P. Stolze, K. Jacobsen and J. Nørskov, Phys. Rev. B rapid communications in press (1995).

Why are computer simulations of growth useful?

Pablo Jensen [a*], Laurent Bardotti [a], Albert-László Barabási [b], Hernán Larralde [c], Shlomo Havlin [d] and H. Eugene Stanley [e]

(a) Département de Physique des Matériaux, Université Claude Bernard Lyon-1, 69622 Villeurbanne Cedex, France; (b) University of Notre Dame, Department of Physics, Notre Dame, IN 46556, USA (c) Instituto de Física, UNAM, Apdo. Postal 139-B, C.P. 62210, Cuernavaca, Mexico (d) Physics Department, Bar Ilan University, Ramat Gan, Israel; (e) Center for Polymer Studies and Department of Physics, Boston University, Boston, MA 02215, USA

Abstract

We show how computer simulations can give unique information on the growth of nanostructures and thin films. Specifically, they can predict the morphologies and the island size distributions corresponding to different growth mechanisms. This information cannot be obtained from other approaches such as mean-field mathematical theories or scaling analysis. Special attention is given to the effects of small cluster mobility on experimental results.

Introduction

Controlled growth of both thin films and nanostructures lies at the heart of the present and future of the electronics industry. It is no suprise then that great efforts have been put into gaining a deeper understanding of the growth mechanisms [1]. The essential ingredients are well-known (Fig. 1) : *deposition* of the atoms onto a surface with a fixed flux, *diffusion* of these atoms on the surface and some *aggregation* mechanism that explains the growth of islands onto the initially empty substrate [2]. Still, predicting the way these ingredients combine to generate the growth is a formidable task for several reasons : the number of atoms deposited on the surface (typically 10^{12} per second), the *randomness* of several processes including the deposition site and time, the diffusion direction, etc.

There have been great improvements in our understanding of the first stages of thin film growth these last years [1]. We believe that they are due to the conjunction of two major breakthroughs. On the experimental side, scanning tunneling microscopy permits the investigation of atomic details of the embryonic "sub-monolayer" stages of film growth [3, 4, 5]. On the theoretical side, the increase of computer performance has allowed precise *simulations* of the growth in some simple cases to be carried out, thus enabling a better understanding of the growth [6, 7, 8, 9]. Here we show a model that incorporates three physical ingredients of thin film growth: deposition, diffusion and aggregation (DDA). We have shown in detail elsewhere [7] how the DDA model generates a wide variety of fractal structures characteristic of different models such as percolation, diffusion limited aggregation (DLA) or cluster cluster aggregation (CCA) [10, 11]. We compare the different information that can be derived from the different treatments (analytical, scaling and computer simulations), and we show that computer simulations give *unique* information on the growth.

Insufficiencies of existing theories : two examples

What is usually measured experimentally is the evolution of the saturation island density N_{max} as a function of the substrate temperature. This yields in general several activation energies E_m that have to be connected to the relevant microscopic activation energies of the deposition experiment (diffusion activation energy E_d, desorption energy E_a, binding

Mat. Res. Soc. Symp. Proc. Vol. 407 © 1996 Materials Research Society

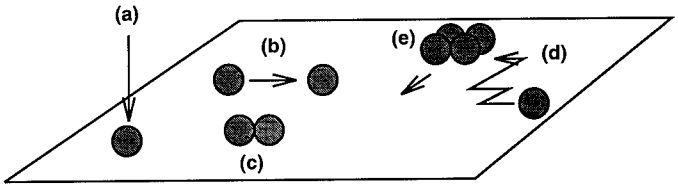


Figure 1: Schematic representation of the basic processes considered in this model: (a) deposition, (b) and (d) particle diffusion, (e) island diffusion and (c) aggregation. (b) corresponds to *nucleation* (i.e. a new island (c) is created) while (d) corresponds to *growth* of an already existing island.

energy of an atom within a cluster E_b, etc.). It is precisely the link between E_m and the different unknown energies that is important. This relation depends specifically on the detailed growth mechanisms present during the growth, namely : dimer or larger cluster diffusion, evaporation of atoms from the surface or from clusters, etc. For example, in the simplest case when only monomers can move and any kind of evaporation is neglected, one finds [12, 13, 14] $E_m = E_d/3$.

More generally, if one still asssumes that only monomers can move:

$$N_{max} \sim F^{\chi} exp[\chi(E_d + E_i/i)/(k_B T)] \tag{1}$$

where F is the incident flux, k_B Boltzmann constant, T the substrate temperature, E_d the activation energy for the diffusion of a monomer, i the size of the critical nucleus [13, 14] E_i the binding energy to the critical nucleus and $\chi = i/(i+2)$ if diffusion of single atoms is isotropic, while $\chi = i/(2i+2)$ if it is one dimensional.

If one asssumes that dimers can move too [7, 12, 16] (we take i=1):

$$N_{max} \sim F^{\chi} exp[(E_d + E_d{}^*)/(5k_B T)] \tag{2}$$

where now $E_d{}^*$ is the activation energy for the dimer and $\chi = 2/5$.

Then, it is essential to have a precise idea of the mechanisms present on the surface (do only monomers move? or do dimers too? is aggregation irreversible? do atoms evaporate from the surface? etc.). This is the condition to extract useful data (meaning activation energies for diffusion, evaporation, etc.). We illustrate this with two examples :

(1) experiments by Günther et al. [15] of gold atomic deposition on gold surfaces. By studying the flux dependence of N_{max}, they found $\chi = 0.37 \pm 0.03$. They interpreted this (and other verifications, see [15] for details) as the sign of one dimensional diffusion with i=3. Alternatively, one can account for the exponent by assuming that dimers can move too ($\chi = 2/5$) [7, 16]. How can we decide between the two interpretations?

(2) Antimony aggregate deposition on graphite [17, 18]. It was dificult to know whether dimers could move on this surface or not. Plotting the island density as a function of the flux leads to $\chi = .37 \pm 0.05$ [19] again too imprecise to discriminate between the two hypothesis.

The point is that, depending on the interpretation, the activation energies found for monomer diffusion for example are different: how can we decide? We need other caracteristics of the growth than the flux dependence of the saturation density, but these are difficult to obtain with usual theories. In contrast, computers provide an "exact" solution to the growth problem (no mean-field approximations are made). We will show here how computer simulations can predict the island morphologies and the island size distributions as a function of the growth hypothesis, thus providing more criteria to discriminate between different growth hypothesis. But let us first sketch how a computer model is built up.

How to make a computer model for nanostructure growth?

Once the essential ingredients of the simulation have been indentified, implementing a computer program is not difficult. Specifically, the DDA model [7] is defined as follows :

(1) *Deposition.* Particles are deposited at randomly-chosen positions of the surface at a flux F per lattice site per unit time.

(2) *Diffusion.* All particles and clusters (sets of connected particles) are chosen at random and attempted to move in one of the six directions of the triangular network by one lattice constant per unit time. The probability that they actually move is proportional to their mobility, which we assume to be given by $D_s = D_1 s^{-\gamma}$. Here s is the number of particles in the cluster, D_1 is the diffusion coefficient for a monomer ($s = 1$), and the parameter γ characterizes the dependence of D_s on cluster size.

(3) *Aggregation.* If two particles come to occupy neighboring sites, they (and therefore the clusters to which they belong) stick irreversibly.

We call *particles* the isolated atoms (or monomers) that are deposited on the surface, *clusters* any set of connected particles (including the monomers) and *islands* the clusters containing more than one particle. Physically, two competing mechanisms are introduced in the model, each one with its own time scale: deposition and diffusion. It is useful to introduce the normalized flux defined as the number of particles deposited per unit site per *diffusion time* τ, where τ is the mean time needed by a monomer to jump by a lattice site. The monomer diffusion coefficient is then given by $D_1 = 1/(4\tau)$, and the normalized flux by $\phi = F\tau$. Then, from experimental values of F and D_1 it is possible to calculate ϕ and the morphologies predicted by our model. The program has actually been written in the form of a repeating loop. At each loop, we calculate the probability for dropping a particle: $p_{drop} = \phi L^2/(\phi L^2 + N_{cl})$ where L is the system size and N_{cl} is the total number of clusters present in the system. A random number p is chosen and compared to p_{drop}. If $p < p_{drop}$, a particle is added at a random position on the lattice. If $p > p_{drop}$, a cluster or a particle is chosen at random and attempted to move. In both cases, the time is increased by $\tau/(\phi L^2 + N_{cl})$.

Structure Morphologies and Dynamical Evolution

Mathematical models are faced with great difficulties to predict the morphologies arising from *random* phenomena. The typical example is diffusion limited aggregation [11], for which there exists no satisfactory analytical theory of the aggregate morphology or fractal dimension. On the other hand, computer simulations can predict the shapes of such structures, as shown below. We present here snapshots of the system at different times to show the formation of the islands for two different aggregation hypothesis. These images were obtained for $\phi = 1.2\ 10^{-8}$ and $\gamma = \infty$ (i.e., only monomers are allowed to move). A more detailed presentation of the dynamical evolution of the model has been given elsewhere [7]. Actually, it is more interesting to use the surface coverage θ instead of the time as the evolution parameter. θ is defined as the ratio of the number of occupied sites to the total number of sites on the surface, and for the times studied here we have $\theta \sim Ft$.

At very short times ($\theta \leq 0.001$), mainly monomers (isolated particles) are found on the substrate, since they have not yet met another one to form a cluster. Later, small clusters are homogeneously grown on the surface, and the island density (i.e. the number of islands per lattice site) starts to grow. These small clusters can be considered as the "nucleation centers" for the growth (Fig. 2a). As time increases, large clusters grow on these nucleation centers, by addition of single particles. These clusters are very similar to some nanostructures obtained experimentally [4, 17]. We have found that their fractal dimension is 1.65, very close to the fractal dimension of the DLA clusters. This (DLA-like) growth mechanism goes on until the linear dimension of the clusters becomes comparable to

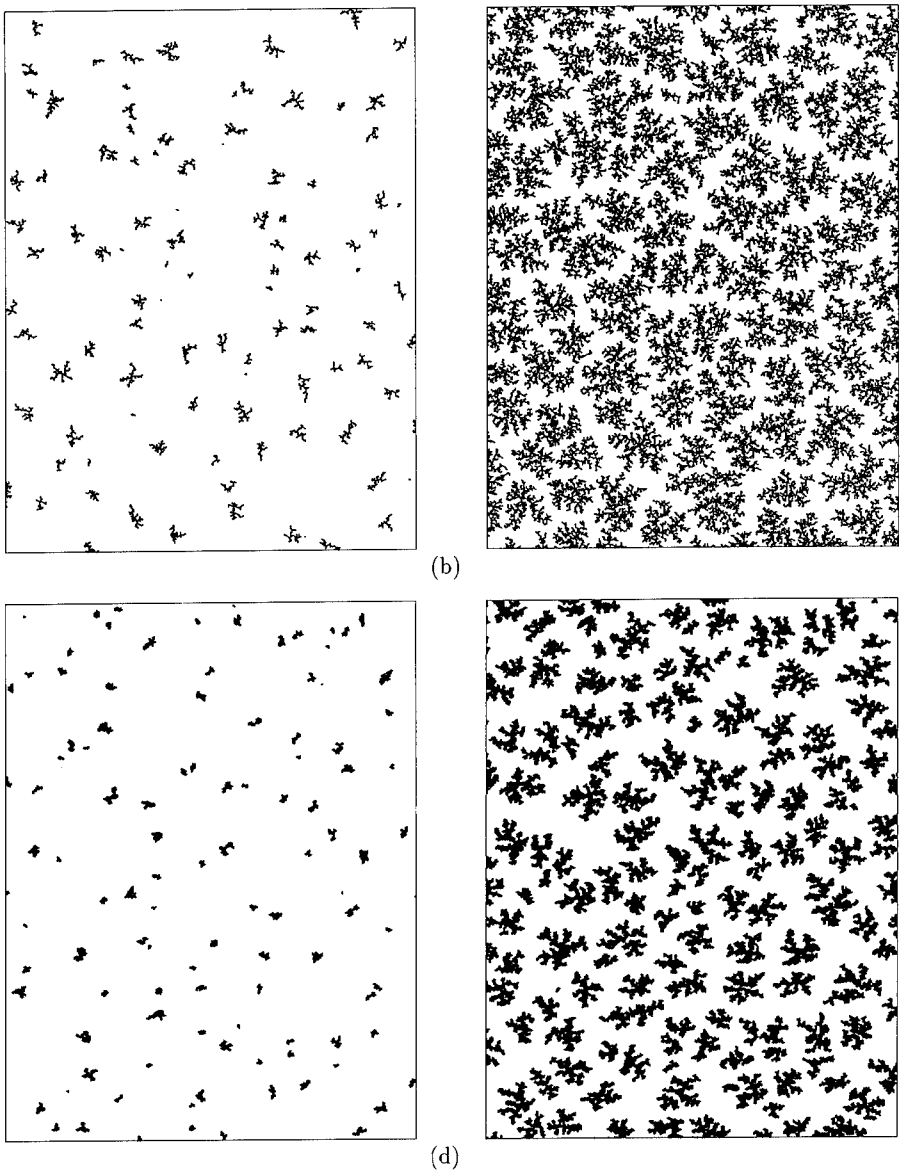


Figure 2: Morphologies obtained for a normalized flux $\phi = 1.2\ 10^{-8}$, a system size $L = 500$ and $\gamma = \infty$. The images show a portion 400 x 300 of the triangular lattice. Two different coverages (corresponding to two different times of deposition) are shown: (a) and (c) coverage 0.02 (b) and (d) coverage 0.25. (a) and (b) illustrate *irreversible* aggregation : each particle attaches to an island at the point where it touched it. (c) and (d) show the morphologies obtained when some restructuring is allowed : the particles can search for a more coordinated site (and go there) when they reach the island

the separation between them (Fig. 2b). Then, many particles start to fall *inside* the clusters and their fractal dimension rapidly increases. Eventually a cluster of a size comparable to the system size is built : the effective fractal dimension of this cluster reaches a value close to 1.9 [7]. When non-irreversible attachement is introduced, the morphologies become more compact, as shown in Figs. 2c-d (see also Refs. [9, 20]).

Island size distributions

In the last paragraph we have studied the behavior of the model when only monomers are allowed to move but the aggregation mechanisms can change. In this section, we want to address some consequences of (small) cluster diffusion. It has long been recognized that cluster diffusion can influence the growth of the films [13, 21], even if at that time experimental proofs were lacking. Recently, experiments [22] and molecular dynamics studies have shown that small clusters can move on the surfaces without breaking [23]. Generally, however, the experimental results are analyzed in the framework of the different models containing only monomer diffusion. Then, the interpretation of the experiments in the framework of these models can lead to wrong conclusions if small cluster mobilty is indeed present in the experiments [16].

We have shown previously [7] that the introduction of cluster mobility considerably changes the dynamics of the growth. Here we show a simple method to detect cluster mobility : island size distributions [9, 24]. The idea is to rescale the island size distributions into a universal distribution that depends only on the ingredients of the model (i.e. the detailed mechanisms of deposition, diffusion and aggregation) but not on the values of the flux or the coverage. Very recently, Mulheran and Blackman [25] have given some interesting insights of why such a universal function should exist, at least for the case of heterogeneous growth. Their argument can be summarized as follows. At the beginning of the growth, nucleation centers form (Fig. 2a). Then, each center grows by catching the monomers falling inside its "capture zone", roughly identified with its Voronoï polyhedron. Therefore its size is, at any time, proportional to the surface of its Voronoï polyhedron, which does not change with time (if one neglects nucleation of new islands in the case of homogeneous nucleation). The result is that at any coverage the size distribution of the islands reproduces that of the Voronoï cells, which explains the rescaling for different coverages. We show in Figure 3 new results that show that the scaling of the size distributions also occurs when clusters are allowed to move, but the universal function is different from that found when only monomers move. Three different diffusion hypothesis have been made: only monomers move, monomers and dimers diffuse, all clusters up to size 100 do move ($\gamma = 1$ has been taken in the two last cases). We see that the universal function becomes narrower and has a higher maximum when larger and larger clusters are allowed to diffuse.

A comparison between the rescaled experimental size distribution and those predicted by the DDA model (Fig 3) can help decide whether dimers or larger clusters can move on the surface. In the case of aggregate deposition [17], the size distribution clearly shows that only monomers move on the surface (Fig 3).

Conclusion

We have shown how computer simulations can provide *unique* information on the growth of thin films. The Deposition, Diffusion and Aggregation (DDA) model has been presented. This model, which incorporates deposition, particle and cluster diffusion, and aggregation closely reproduces some experimental images (compare for example Figs 2 to the figures published in Refs [4, 5, 17]). We find that the model permits one to distinguish the effects of deposition, diffusion and aggregation, raising the possibility that it may prove useful in future studies seeking the controlled design of nanostructure morphologies.

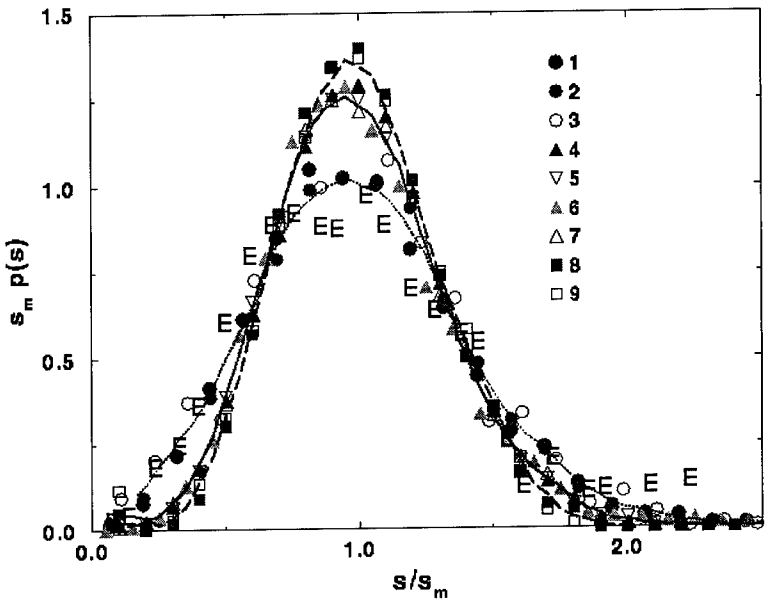


Figure 3: Rescaled island size distributions. The island distributions are transformed to p(s) which represents the probability that a randomly chosen cluster belongs to an island containing s clusters [9]. The island size s is scaled by the mean island size s_m. Sets (1) to (3) correspond to simulations where only monomers are allowed to move ($\gamma = \infty$). For sets (4) to (6), $\gamma = 1$ but only dimers can move, while for sets (7) and (8) clusters containing up to 100 monomers can move. (E) indicate the *experimental* island size distribution obtained in Ref [17]. The detailed parameters used for each set are as follows: (1) $\phi = 10^{-8}$, coverage 0.3 ;(2) $\phi = 10^{-8}$, coverage 0.15 ; (3) $\phi = 10^{-9}$, coverage 0.1 ; (4) $\phi = 10^{-9}$, coverage 0.05 ; (5) $\phi = 10^{-9}$, coverage 0.1 ; (6) $\phi = 10^{-8}$, coverage 0.3 ; (7) $\phi = 10^{-8}$, coverage 0.15 ; (8) $\phi = 10^{-8}$, coverage 0.05 ; (9) $\phi = 10^{-8}$, coverage 0.1. The lines represent averages of the distributions for each diffusion hypothesis.

PJ acknowledges CNRS for financial support. HL thanks CONACYT, Mexico, for support. A-LB and HES thank the Hungary-USA exchange program of the Hungarian Academy of Sciences. SH acknowledge the USA-Israel Binational Science Foundation for financial support. The Center for Polymer Studies is supported by NSF.

References

[*] Corresponding author. e-mail: jensen@dpm.univ-lyon1.fr

[1] A.-L. Barabasi and H. E.Stanley, *Fractal Concepts in Surface Growth* (Cambridge University Press, 1995); M. Lagally (ed), *Kinetics of Ordering and Growth at Surfaces* (Plenum, New York, 1990); M. Lagally, Physics Today , 24 (1993); S. Das Sarma, J. Vac. Sci. Technol. A **8**, 2714 (1990).

[2] These ingredients are those which are indispensable. Of course, in real experiments, other processes (long range interactions between particles, particle evaporation from the surface, surface exchange between adatoms and bulk atoms, etc.) can be present and further complicate the description.

[3] Y. W. Mo, J. Kleiner, M.B. Webb and M.G. Lagally, Phys. Rev. Lett. **66**, 1998 (1991).

[4] R. Q. Hwang, J. Schröder, C. Günther and R. J. Behm, Phys. Rev. Lett. **67**, 3279 (1991); T. Michely, M. Hohage, M. Bott, and G. Comsa, Phys. Rev. Lett. **70**, 3943 (1993)

[5] H. Röder, E. Hahn, H. Brune, J.-P. Bucher, and K. Kern, Nature **366**, 141 (1993); H. Brune, C. Romainczyk, H. Röder, and K. Kern, Nature **369**, 469 (1994); H. Brune, H. Röder, C. Boragno, and K. Kern, Phys. Rev. Lett. **73**, 1955 (1994)

[6] L.-H. Tang, J. Phys. I France **3**, 935 (1993)

[7] P. Jensen, A.-L. Barabási, H. Larralde, S. Havlin, and H. E. Stanley, Nature **368**, 22 (1994); Phys. Rev. E **50**, 618-621 (1994); Physica A **207**, 219-227 (1994); Phys. Rev. B **50**, 15316 (1994).

[8] M.C. Bartelt and J. W. Evans, Phys. Rev. B **46**, 12675 (1992);

[9] G.S. Bales and D.C. Chrzan, Phys. Rev. B **50**, 6057 (1994)

[10] A. Bunde and S. Havlin (eds.), *Fractals and Disordered Systems* (Springer-Verlag, Berlin, 1991)

[11] T. Vicsek, *Fractal Growth Phenomena, Second Edition* (World Scientific, Singapore, 1992).

[12] J. Villain, A. Pimpinelli, L.-H. Tang, and D. E. Wolf, J. Phys. I France **2**, 2107 (1992)

[13] S. Stoyanov and D. Kaschiev, *Current Topics in Mat. Science*, Ed. E. Kaldis, (North-Holland, 1981)

[14] J. A. Venables, G. D. T. Spiller, and M. Hanbücken, Rep. Prog. Phys. **47**, 399 (1984).

[15] S. Günther, E. Kopatzi, M.C. Bartelt, J. W. Evans and R. J. Behm, Phys. Rev. Lett. **73**, 553 (1994)

[16] S. Liu, L. Bönig and H. Metiu, Phys. Rev. B **52** 2907 (1995)

[17] L. Bardotti, P. Jensen, M. Treilleux, B. Cabaud and A. Hoareau, Phys. Rev. Lett. **74**, 4694 (1995) .

[18] P. Melinon et al. Int. J. of Mod. Phys. B **9**, 339-397 (1995)

[19] L. Bardotti et al. (to be published)

[20] C. Ratsch, A. Zangwill, P. Smilauer, and D.D. Vvedensky, Phys. Rev. Lett. **72**, 3194 (1994)

[21] R. Kern, A. Masson and J.J. Métois, *Current Topics in Mat. Science vol.3*, Ed. E. Kaldis, (North-Holland, 1979); Surf. Sci. **27**, 483 (1971); C. Chapon and C. R. Henry, Surf. Science **106**, 152 (1981).

[22] G.L. Kellogg, Phys. Rev. Lett. **73**, 1833 (1994) and references therein.

[23] T. J. Raeker and A. E. DePristo, Surf. Sci. **317**, 283 (1994)

[24] M.C. Bartelt, M.C. Tringides and J. W. Evans, Phys. Rev. B **47**, 13891 (1993); J. G. Amar and F. Family, Phys. Rev. Lett. **74**, 2066 (1995)

[25] P. A. Mulheran and J. A. Blackman, Phil. Mag. Lett. **72**, 55 (1995)

INVESTIGATION OF AGGREGATE STRUCTURES ON LENGTH SCALES FROM ABOUT 5 TO 10,000 Å#

PAUL W. SCHMIDT*, FRANCOISE EHRBURGER-DOLLE**, PETER PFEIFER*, THOMAS RIEKER***, YOGENDRA M. KAPOOR****, AND DANIEL J. VOSS*

* Department of Physics and Astronomy, University of Missouri, Columbia, MO 65211.
** Institut de Chimie des Surfaces et Interfaces (ICSI) CNRS, 15, rue Jean Starcky, BP n° 2478, F 68057 Mulhouse Cedex, FRANCE.
*** Sandia National Laboratories, Advanced Materials Laboratory, 1001 University Ave. SE, Albuquerque, NM 87106.
*** Dept. of Natural Sciences and Mathematics, Lincoln University, Jefferson City, MO 65102.
# Acknowledgment is made to the Donors of the Petroleum Research Fund, administered by the American Chemical Society, for support of this work.

ABSTRACT

Small-angle x-ray scattering has been used to investigate the structure of some carbon blacks, some silicas, and an alumina-silica catalyst carrier on length scales from about 5 to 10,000 Å. Equations developed for structural studies of fractal and non-fractal aggregates of primary particles have been employed to analyze the scattering data. From the intensity data, the average diameters of the primary particles could be calculated or estimated. Despite the very different origins of the samples and the fact that the average diameters of the particles varied from about 30 to over 1000 Å, the scattered intensities from the samples had many common features. The data showed that the primary particles had a uniform density and were bounded by smooth or fractal surfaces. On length scales greater than the diameters of the primary particles but not more than a few times larger than the average diameters of the aggregates, some of the aggregates were mass fractals, and others were surface fractals.

INTRODUCTION

Many disordered solids, such as dried silica gels and carbon blacks, are aggregates of primary particles. The diameters of the primary particles can be as small as 10 Å or as large as a few thousand Å. These solids have many important uses. For example, in the sol-gel process for making glass, silica xerogels (dried gels) are precursors for glasses that have applications that range from glass fibers to packaging materials for electronic components. Carbon blacks are often added to synthetic polymers to reinforce them or to make them electrically conducting.

Information about the structure of silicas and carbon blacks can suggest how to employ these materials both more effectively and also more widely.

We have recently used small-angle x-ray scattering to determine the structure of some silicas and carbon blacks. The following sections give a preliminary report of some of our results.

ANALYSIS OF THE SCATTERING DATA

Small-angle x-ray scattering[1--3] is a technique for investigating structures on length scales from about 5 through 10,000 Å. In a small-angle scattering study, a beam of x-rays strikes the sample being investigated. A small fraction of the beam that strikes the sample is scattered (*i. e.* re-emitted) in other directions. The structure of the sample determines the intensity scattered at an angle θ with respect to the incoming beam. (Often θ is called the scattering angle.) From analysis of the dependence of the scattered intensity on the scattering angle θ, information can be obtained about the structure of the sample.

The scattered intensity can be conveniently described by the quantity[4]

$$q = \frac{4\pi}{\lambda}\sin(\theta/2), \qquad (1)$$

Mat. Res. Soc. Symp. Proc. Vol. 407 © 1996 Materials Research Society

where θ is the scattering angle, and λ is the wavelength. When a structure characterized by a length A is studied by scattering, most of the information about the structure of the scatterer will be obtained for values of q for which[4,5]

$$0.1 \leq qA \leq 20. \tag{2}$$

According to Inequalities (2), the scattered intensity I(q) from a scatterer of diameter A depends on the quantity qA. (The diameter of a structure is defined to be the largest distance by which two points in the structure can be separated. For a sphere, this definition is equivalent to the ordinary diameter.) Therefore the scattered intensity from structures of large diameter is observed almost entirely at relatively small values of q, and in scattering studies of the structure of scatterers with smaller diameters, the intensity must be measured at larger q values. Inequalities (2) are a guide to what the terms "large q" and "small q" mean in a given investigation. In the rest of this report, we will refer to Inequalities (2) as the resolution criterion.

For systems of *randomly oriented, independent* scatterers, I(q) will not differ appreciably from I(0) when $qA < 0.1$. If qA is not large compared to 1, the approximation

$$I(q) = I(0)\, e^{-(1/3)(qR_g)^2} \tag{3}$$

can be used to find the radius of gyration R_g.[6] Equation (3) is often useful for order-of-magnitude estimates of the average diameter A of the structure that causes the scattering. The relationship between A and the radius of gyration R_g depends on the shape and charge distribution of the scatterer, but in most cases, $2\,R_g \leq A \leq 3.5\,R_g$. For a spherical scatterer of diameter A that has a uniform density, $A = (20/3)^{1/2} R_g \approx 2.6\,R_g$.

When $qA >> 1$, the intensity can usually be approximated by the equation[5,7]

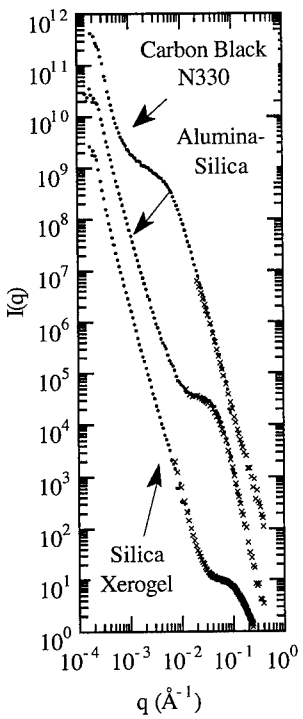
$$I(q) = I_e\, d(A,\alpha)\, q^{-\alpha} \tag{4}$$

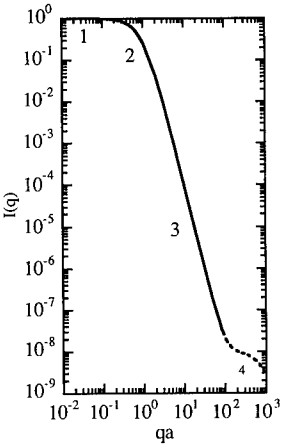
where α and $d(A, \alpha)$ are positive constants, and I_e is the scattered intensity that would be observed from one electron. Scattered intensities that can be described by Eq. (4) are often referred to as "power-law scattering", because I(q) is proportional to a negative power of q. Important information can be obtained from the magnitude of the power-law-scattering exponent α in Eq. (4). Often it is possible to determine whether scatterers have smooth or fractal surfaces.[5,7] When the scatterer has a uniform density and surfaces with a fractal dimension D, $\alpha = 6 - D$. If the boundary surfaces are smooth,[8] $D = 2$, and $\alpha = 4$. (A smooth surface is a limiting case of a fractal surface.) If the scatterer is a mass fractal with a fractal dimension D, $\alpha = D$. For mass fractal scatterers, $D < 3$, and $2 \leq D < 3$ for surface fractals. Thus, $\alpha < 3$ for a mass fractal scatterer, and for solid scatterers with a uniform-density that are bounded by fractal or smooth surfaces, $3 < \alpha \leq 4$.

We define the parts of the intensity I(q) in which I(q) can be described by Eqs. (3) and (4) as the radius-of-gyration region and the power-law region, respectively.

The intensity curves in Fig. 1, which were obtained from a carbon black, an alumina-silica, and a silica gel, are very different from what would have been expected for the scattered intensity from a system of scatterers that can be characterized by a single length, which is the average diameter of the scatterers. Instead of a radius-of-gyration region at the smallest values of q, followed by a power-law region at larger q, there is a power law region at the *smallest* q values included in Fig. 1, and at *larger* q there is a region in which I(q) could be described by Eq. (3).

To explain and analyze data like those plotted in Fig. 1, we have developed a model that we call the "bunch of grapes" model.[9] This model, which makes use of the resolution criterion expressed by Inequalities (2), considers a system of N *independently-scattering* aggregates that have an average diameter A and that are composed of an average number n of primary particles with average diameter b. We assume that $A >> b$. Then, when qA does not greatly exceed 1, the intensity I(q) can be approximated by Eq. (3), with a radius of gyration R_g that is the average value for the system of aggregates. This part of the I(q) curve is equivalent to Regions 1 and 2 of Fig. 2. When $qA >> 1$, but $qb << 1$, the scattering process "sees" only the aggregates, and the intensity can be approximated by Eq. (4). Thus Regions 1 and 2 in Fig. 2 are the radius-of-gyration region for the aggregates, and Region 3 is the power-law region, with an exponent that gives information about the aggregates. When q no longer is negligible with respect to 1, a region like Region 4 can often be observed in this part of the I(q) curve. This part of the curve, which can contain both a radius of gyration region and





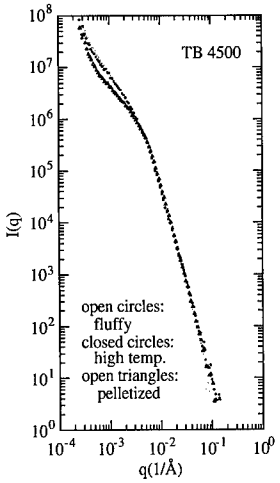


Fig. 1 (left). The scattered intensity I(q) from a carbon black (upper curve), an alumina-silica (middle curve), and a silica xerogel (lower curve). Point measured with the Bonse-Hart system are shown by circles, and x's denote intensities records on the Oak Ridge pinhole system (lower curve), or (upper two curves) with the Kratky system at the University of Missouri, or with the New Mexico pinhole system.

Fig. 2. (center) A typical intensity curve from a system of aggregates. The numbers on the curve are discussed in the text.

Fig. 3. (right) The scattered intensity from the three TB4500 carbon black samples.

a power-law region, gives information about the average diameter and boundary surfaces of the primary particles.

To use the bunch of grapes model to analyze the intensity curves in Fig. 1 and Figs. 3--6, we consider that the aggregates are so large that Regions 1 and 2 in Fig. 2 cannot be recorded with the available equipment, and so only Regions 3 and 4 in Fig. 2 appear in the intensity curves. Then the power laws at the smaller values of q in Fig. 1 and Figs. 3--6 correspond to Region 3 in Fig. 2 and the intensities at larger q make up Region 4, which gives information about the properties of the primary particles. If intensities can be measured at large enough q, Region 4 will have both a radius-of-gyration region and power law region.

To obtain quantitative information, we expressed the intensity I(q) by the equation[9]

$$I(q) = P(q)S(q). \tag{5}$$

In Eq. (5), P(q), the form factor, is equal to the average scattered intensity that would be obtained from the nN primary particles if these particles scattered independently, and S(q) describes the effects of interactions between particles. We have found that the equation[10]

$$I(q) = P(q)\left[\frac{F}{q^{\alpha}} + 1\right] = \frac{P(0)}{[1 + (ql)^2]^{\beta/2}}\left[\frac{F}{q^{\alpha}} + 1\right] \tag{6}$$

is useful for analysis of the scattering data. The constants F, P(0), l, α, and β can be evaluated from fits of Eq. (6) to the data.

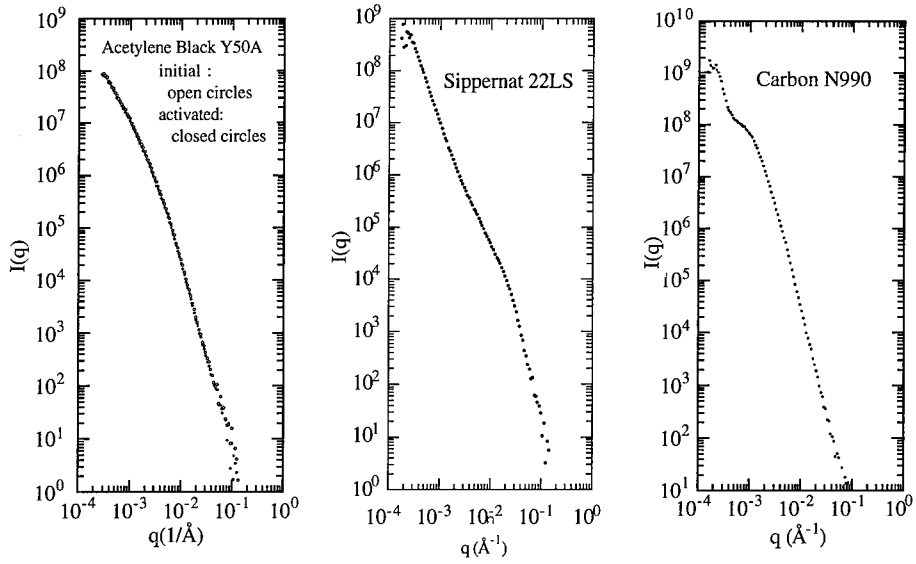


Fig. 4. (left) The scattered intensity I(q) from the initial and the activated Acetylene Black Y50A.
Fig. 5 (middle) The scattered intensity I(q) from Sipernat 22LS precipitated silica.
Fig. 6 (right) The scattered intensity I(q) from carbon black N990.

EXPERIMENTAL TECHNIQUES

The silica xerogel was hydrolyzed from tetramethoxysilane at a molar water-silane ratio of 9.4 by D. Avnir and his colleagues at the Hebrew University of Jerusalem.[11] The alumina silica is equivalent to Alumina-Silica SA 6173 catalyst carrier, which is a product of Norton Chemical Process Corp. Sipernat 22LS precipitated silica is made by Degussa. All of the carbon blacks are commercial products.

The small-angle scattering data for q smaller than about 0.2 Å^{-1} were measured on a Bonse-Hart scattering system[12] at the Sandia National Laboratories-University of New Mexico Scattering Laboratory in Albuquerque, New Mexico. Data for $q > 0.01$ Å were obtained either on a Kratky scattering system[13] at the University of Missouri or on a pinhole scattering system[14] at the Sandia National Laboratories--University of New Mexico Scattering Laboratory. The intensity curve for the silica xerogel was recorded at the Scattering Centers in Albuquerque, New Mexico and at Oak Ridge National Laboratory in Oak Ridge, Tennessee.[14]

RESULTS, DISCUSSION, AND CONCLUSIONS

Our results are presented in Fig. 1, Figs. 3--6, and Table I. To analyze our results in these figures, we have concluded that the power-law and radius-of-gyration regions in Fig. 1 and Figs. 3--6 correspond to Regions 3 and 4 in Fig. 2. According to the bunch of grapes model and the resolution criterion expressed in Inequalities (2), at the smaller values of q in these plots, the scattering process is unable to resolve the primary particles and instead "sees" the "bunch of grapes" as a single, relatively large scatterer, (*i. e.,* as an aggregate). When q has become larger, the individual grapes can be resolved. Therefore, in Fig. 1 and Figs. 3--6, the inner power-law at smaller q gives D_s or D_m for the aggregates. The region of the intensity at larger q gives information about the average radius of gyration and the boundary surfaces of the primary particles.

TABLE I
PROPERTIES OF THE AGGREGATES

Name	Grade or Type	S_{BET} (m^2/g) (a)	D_S (b)	D_S (c)	D_m or D_s (d)	b (Å) (e)	b (Å) (f)
Carbon Black N330	Reinforcing	79	2.4	2.6	2*	$6x10^2$	$4.2x10^2$
Acetylene Black Y50A	Conductive	59	2.4	2.6	2	$1x10^3$.	$5.6x10^2$
Acetylene Black Y50A1	Conductive	70	2.4	2.5	2	$1x10^3$.	$4.8x10^2$
Carbon Black TB4500f	Conductive	60	2.1	2.0	1.8.	$7x10^2$	$5.6x10^2$
Carbon Black TB4500p	Conductive	60	2.1	2.0	2.6	$7x10^2$	$5.6x10^2$
Carbon Black TB4500h	Conductive	51	2.1	2.0	1.9	$7x10^2$	$6.6x10^2$
Carbon Black N990	Thermal	9	2.0	2.0	2*	$4x10^3$	$3.7x10^3$
SA 673 (Norton)	Alumina-Silica	>100†	2.3		2.3*	$9x10^2$	$<2.7x10^2$
Sipernat 22LS	Precipitated Silica	167	2.0	2.0	.2.0	$2x10^2$	$1.7x1o^2$
Silica Xerogel		620			2.3*	$3x10^1$	$4.4x10^1$

Notes for Table I

* These values are *surface* fractal dimensions D_s, because the intensity curves show that these *aggregates* are surface fractals.

† Information supplied by the manufacturer.

(a) Some of the S_{BET} values are listed in Ref. 15. The others come from our unpublished results.

(b) Surface-fractal dimensions of the primary particles obtained with Eq. (4) from the region of the intensity curve that corresponds to the power-law region of Region 4 in Fig. 2.

(c) Surface-fractal dimensions calculated from Frenkel-Halsey-Hill plots. Some of these results are included in Ref. 15, and others are our unpublished calculations.

(d) Mass-fractal dimensions D_m or surface fractal dimensions D_s calculated from the exponents α from the region of the intensity curve that corresponds to Region 3 in Fig. 2.

(e) Average primary particle diameter b estimated from the part of the the intensity curve that corresponds to Region 4 in Fig. 2.

(f) Average primary particle diameter b estimated from the the BET specific surface S_{BET} and the mass density ρ by use of the equation $b = 6/(\rho S_{BET})$. The mass density values $\rho = 1.8$ g/cm^3 and $\rho = 2.2$ g/cm^3 were used for carbon black and silica, respectively. (With this equation, we calculated b in cgs units. These b values are converted to Å in Table I.)

As we have mentioned, the power law at the smaller q values corresponds to Region 3 in Fig. 2 and so the exponent α calculated from this part of the intensity curve is associated with the properties of the aggregates. (According to the resolution criterion expressed by Inequalities (2), q is not large enough in this region to resolve the individual primary particles.)

In all of the samples except the silica xerogel, the primary particles are large enough that both the average radius of gyration and the power-law-scattering exponent $\beta = 6 - D_s$ can be computed.

We calculated b for the silica xerogel by a least-squares fit of an equation equivalent to Eq. (6).[10] The other b values in this column of Table I were estimated by a comparison of the radius-of-gyration region of the plot of I(q) for the sample with corresponding region of the I(q) plot for the silica xerogel.

The column labeled "D_m or D_s" in Table 1 gives the either mass-fractal dimensions D_m or surface-fractal dimensions D_s that we calculated from the the power-law scattering exponents α that we obtained from fits to the I(q) curve. These fits showed that some of the aggregates were mass fractals and that other aggregates were surface fractals. In Table I, surface-fractal dimensions are denoted by asterisks. In some of the I(q) plots, the the power-law region in the I(q) curve from which we computed the exponent α was so short that in Table I, these values of D_s could legitimately be expressed to only one significant figure.

The average diameters and the surface-fractal dimensions D_s of the primary particles obtained from the scattering data and from the adsorption measurements are in reasonable agreement.

The aggregates in all of the samples are so large that from the scattering data, we could find only the lower limit of the aggregate diameter. Figures 1 and 3--6 show that there is power-law scattering even for $q_{min} = 3 \times 10^{-4}$ Å^{-1} which is the smallest q value at which we recorded *reliable* data. Therefore, the condition $qA >> 1$ was satisfied even at q_{min}. Since our experience has shown that this condition is reasonably well satisfied for $qA > \pi$, we have concluded that for all samples that we examined, $A > \pi/q_{min} = 1$ μm .

We now conclude with a few comments about some of our results. First, the α values that we obtained show that the silica xerogel, the alumina-silica, and carbon blacks N330 and N990 are surface-fractal aggregates. All of the other aggregates are mass-fractals.

Acetylene black Y50A1 was activated by oxidizing Y50A at 1000° C. The small-angle scattering intensities from the two acetylene blacks are indistinguishable. Carbon black TB4500h was prepared by heating fluffy carbon black TB4500f at 1800°C. The intensity curves from the two samples are very nearly identical. Also, the difference between estimates of the diameters of the particles of the three TB4500 samples obtained from the intensity curves and from S_{BET} do not exceed the uncertainty in our estimates of b from the I(q) curves. Carbon black TB4500p was produced by pelletizing TB4500f. The mass-fractal dimension D_m of TB4500p is appreciably higher than those of TB4500f and TB4500h, and for $q < 10^{-3}$ Å^{-1}, the I(q) curve for TB4500p is different from those for TB4500f and TB4500h . Thus, our examination of the TB4500 and the Y50A samples shows that although heat treatment or oxidation produce no detectable change in in I(q), the form of I(q) for $q < 10^{-3}$ Å^{-1} is considerably changed by pelletization.

ACKNOWLEDGEMENTS

We are very grateful to Alan J. Hurd and Douglas M. Smith for much helpful advice and for arranging for us to record the scattering data that we obtained at the Sandia National Laboratories-University of New Mexico Scattering Center. Also, we are pleased to acknowledge the assistance of J. S. Lin and Mathias Steiner for the measurements of the scattered intensity from the silica xerogel. Finally, we thank A. Raman of the Chemical Engineering Department of Kansas State University for sending us the alumina-silica sample.

REFERENCES

1. A. Guinier, G. Fournet, C. B. Walker, and K. L. Yudowitch, *Small-Angle Scattering of X-Rays,* Wiley, New York, 1955.
2. O. Glatter and O. Kratky, *Small-Angle X-Ray Scattering,* Academic Press, New York, 1982.
3. D. I. Svergun and L. A. Feigin, *Structure Analysis by Small-Angle X-Ray and Neutron Scattering,* Mir, Moscow, 1986. [English translation: (edited by G. W. Taylor) Plenum, New York, 1987.]
4. Ref. 1, Chapter 1.
5. P. W. Schmidt, J. Appl. Cryst. **24,** 414-435. (1991), Sections 1--3.
6. Ref. 1, pp. 24-28.
7. P. W. Schmidt, in *Modern Aspects of Small-Angle Scattering,* edited by H. Brumberger, Kluwer, Dordrecht, the Netherlands, 1994, Sections 2.2 and 2.3, pp. 31-54.
8. Ref. 1, p. 17.
9. Ref. 7, pp.Sect. 2.3.2, pp. 49-54.
10. P. W. Schmidt, unpublished research.
11. D. Avnir and V. R. Kaufman, J. Non-Cryst. Solids **92,** 180 (1987).
12. (a) U. Bonse and M. Hart, Appl. Phys. Lett. **6,** 155-156 (1955). (b) U. Bonse and M. Hart, in *Small-Angle Scattering of X-rays,* edited by H. Brumberger, (Gordan and Breach, New York, London, 1967), pp. 121-130.
13. O. Kratky and Z. Skala, Z. Elektrochem. **62,** 73-77 (1958).
14. G. D. Wignall, J. S. Lin, and S. Spooner, J. Appl. Cryst, **23,** 241-245 (1990).
15. F. Ehrburger-Dolle, M. Holz, and J. Lahaye, Pure & Appl. Chem. ***65,*** 2223 (1993).

DEHYDRATION OF FRACTAL PARTICLES OF IRON (III) AND ALUMINUM HYDROXIDES

A.A. VERTEGEL, S.V. KALININ, N.N. OLEYNIKOV, Yu.D. TRETYAKOV
Dept. of Chemistry, Moscow State University, 119899, Moscow, Russia,
oleg@tret.chem.msu.su

ABSTRACT

The kinetic behavior of $Fe(OH)_3$ and $Al(OH)_3$ powders during thermal dehydration is investigated. It has been shown that the dehydration rate is governed by the value of fractal dimension of the sample without any respect to the nature of metal atom in hydroxide. The quantitative model for dehydration of fractal particles with particular value of fractal dimension is suggested. Theoretical predictions are in a good agreement with experimental data.

INTRODUCTION

Synthesis of the most multicomponent oxide materials usually requires methods based on the chemical homogenization of initial reagents. Application of these methods (like sol-gel process, spray drying and freeze drying) leads to oxide precursors with high reactivity that implies that solid state reagents can effectively participate in chemical reaction. However, the notion "reactivity" is rather qualitative and it is yet not clear how to characterize it for any given solid state sample.

Recently in refs. [1] the idea that reactivity is determined by surface fractal dimension of the sample has been suggested. It is well-known that the rate of solid state reaction strongly depends upon surface structure, and the latter may be quantitatively described in terms of fractal geometry [2]. In the present work we synthesized iron (III) and aluminum hydroxides with different fractal dimensions and tried to find out how would the difference in fractal structure influence kinetics and mechanism of their dehydration.

EXPERIMENT

Synthesis of the samples

Iron (III) and aluminum hydroxides were synthesized as follows: 0.5 M water solution of corresponding nitrate was treated by portions of anion-exchange resin. The latter was preliminary transformed into OH^- - form using 4M KOH solution and then washed by distilled water to pH=7. The formation of colloidal particles of iron and aluminum hydroxonitrates accompanied the ion exchange. The solutions were treated by small portions of the resin so that their pH could be controlled. We prepared three colloidal solutions of iron hydroxide (pH=2.43, 3.37, 3.9) and five colloidal solutions of aluminum hydroxide (pH=5.04, 5.80, 5.94, 6.49, 7.01). These samples are mentioned below as samples FE-2.43, FE-3.37, FE-3.9 and AL-5.04, AL-5.80, AL-5.94, AL-6.49, AL-7.01 respectively.

Measurement of fractal dimension of colloidal particles

The fractal dimension of colloidal particles in the obtained solutions was measured by means of optical method. This method is based on the correlation between optical density of the solution and wavelength of incident radiation λ [1]. Substantial broadening of electron transition peaks in visible range was observed for all of the samples. We assume

Mat. Res. Soc. Symp. Proc. Vol. 407 © 1996 Materials Research Society

that the broadening arise due to the existence of large colloidal particles possessing many oscillation modes.

It is quiet natural to suppose that particles in the solution are fractal with particular fractal dimension, D. Let us determine the connection between the shape of electron transfer peak and the value of D. Solid state oscillation theory gives us the following functions of wave vectors density $g(k)$ upon oscillatory wave vector k [3]:

$g(k)=const$ - for one-dimensional chains;

$g(k) \propto k$ - for two-dimensional layers;

$g(k) \propto k^2$ - for three dimensional body.

One can suppose that for the fractal particle with dimension large enough D:

$$g(k) \propto k^{D-1} \qquad (1)$$

For low oscillation frequencies ω, k is proportional to ω and therefore

$$g(\omega) \propto \omega^{D-1} \qquad (2)$$

According to the Boltsman law only very low frequencies are populated in the main state. Thus, the probability of transfer to the excited state as a function of ω is given by the following formula:

$$P(\omega) \propto \omega^{D-1} \qquad (3)$$

Using the classical approach, we should take into account that absorption of light with frequency ω may lead to transitions with frequencies $\omega_i < \omega$. Therefore, intensity of absorption can be calculated as

$$I(\omega) = \int_{\omega_0}^{\omega} P(\omega) d\omega \propto \omega^D \qquad (4)$$

and

$$I(\lambda) \propto \lambda^{-D} \qquad (5)$$

In fig.1 the plot of dependence $\log I$ - $\log \lambda$ for sample AL-6.49 is given. One can see that dependence is linear with the tangent $D=1.97\pm0.03$ in the region of large λ (i.e. for low frequencies for which eqn.(2) is correct). The analogous plots for other samples are similar to that shown on fig.1, differing only by the slopes of the lines.

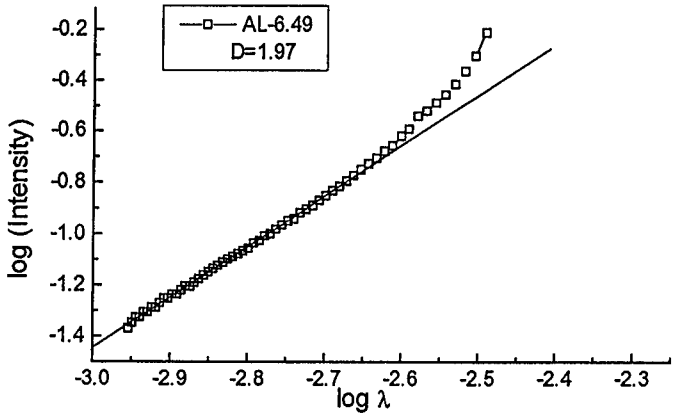


Fig.1. Dependence between absorption intensity and light wavelength for sample AL-6.49 in logarithmic coordinates.

The values of fractal dimension obtained by the technique mentioned above are in a good agreement with adsorption experiment data [1].

Freeze drying and TG analysis

After the measurement of fractal dimension the solutions were subjected to freeze drying. This technique was used to preserve the fractal properties of the obtained powders.

Dehydration of iron (III) and aluminum hydroxides was investigated in polythermal regimes (heating rates 5, 7 and 10°/min). We found that TG curves at heating rates of 5 and 7°/min coincided (see fig.2).

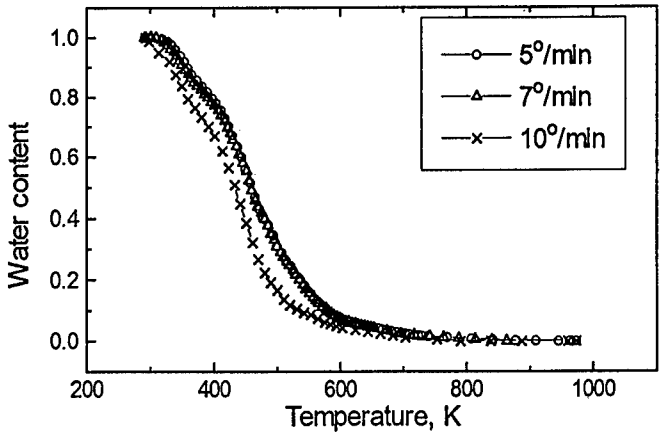


Fig.2. Dehydration of $Fe(OH)_3$ sample (D=2.17) at different heating rates.

This implies that at every temperature the water content of the samples is equilibrium. At the same time the outlook of TG curves regularly changed together with the increase of fractal dimension.

RESULTS

In the present section we tried to define the way fractal dimension governs the rate of dehydration of the samples. Let us consider a fractal particle as a porous media with power distribution of pore sizes. According to the Calvin-Thompson law the boiling temperature of water filling in the small capillaries is higher than that of water in big capillaries. Therefore, assuming the dehydration to be equilibrium, we can suggest the following quantitative model for dehydration of fractal particle with particular value of fractal dimension. The model is based on the following assumptions:

1) boiling point of water in pore $T(r)$ increases with the decrease of pore radius r;
2) dehydration is equilibrium, therefore at temperature T_i water contains only in pores with
radii $r < R_{max}(T_i)$;
3) mass of water in a pore with radius r: $m(r) \propto r^2$;
4) pore size distribution function for fractal with dimension D:

$$f(r) \propto r^{-D} \qquad (6)$$

5) surface tension σ decreases with the increase of temperature:

$$\sigma(T)=\sigma_b(1-\beta(T-T_b)) \qquad (7)$$

where σ_b is surface tension at boiling point T_b (T_b=373K), β=const;

Thus, the mass of water m containing in the sample at temperature T is defined by the following equation:

$$m(T) \propto \int_{R_0}^{R_{max}(T)} r^{2-D} dr \qquad (8)$$

where R_0 is the minimal pore radius, $R_{max}(T)$ -radius of the largest pore still containing water.

$R_{max}(T)$ can be derived from thermodynamic considerations:

$$\Delta G_b=\Delta H_b-T\Delta S_b+2\sigma(T)/R_{max}=\Delta H_b-T\Delta S_b+2\sigma_b(1-\beta(T-T_b))/R_{max}=0 \qquad (9)$$

$$R_{max}=\frac{2\sigma_b(1-\beta(T-T_b))}{(T-T_b)\Delta S_b} \qquad (10)$$

Since at the critical temperature T_{crit}

$$\sigma(T_{crit})=0 \Rightarrow T_{crit}=T_b+1/\beta \qquad (11)$$

Therefore, $R_{max}(T)$ can be found as:

$$R_{max}(T)=2\sigma_b\beta(T_{crit}-T)/(T-T_b)\Delta S_b \propto [(T_{crit}-T)/(T-T_b)] \qquad (12)$$

Integrating (7) taking in account eqn. (12) gives:

$$m(T) \propto 1-\alpha \propto [(T_{crit}-T)/(T-T_{bl})]^{3-D} \qquad (13)$$

where α is the degree of decomposition, D - fractal dimension.

We plotted the experimental TG curves in coordinates log (m) - log $[(T_{crit}-T)/(T-T_{bl})]$. In these coordinates they have the linear areas in the temperature range 350 - 600 K (fig.3).

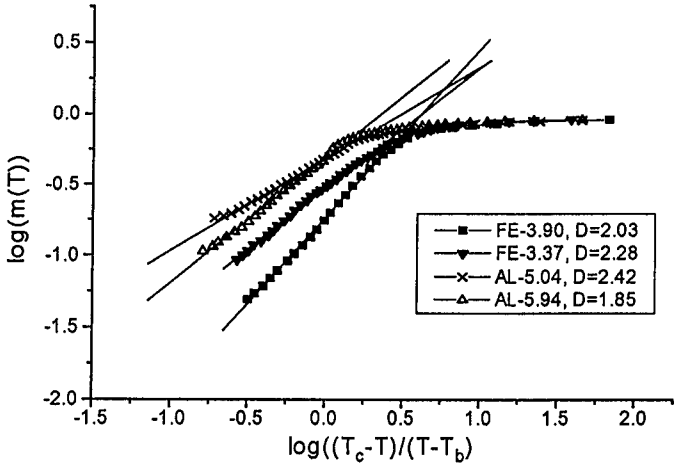


Fig.3. TG curves for the samples with different values of fractal dimension, D, plotted in logarithmic coordinates corresponding to eqn. (13).

Comparison of the slopes of the lines plotted in coordinates corresponding to eqn. (13) with fractal dimensions of the samples measured by optical method is given in table 1.

Table 1. Correlation between fractal dimension and the slopes, $tg\ \alpha$, of TG curves shown in fig.3.

Sample	D	(3-tg α)
FE-2.43	2.17±0.03	2.09±0.05
FE-3.37	2.28±0.03	2.16±0.09
FE-3.90	2.03±0.03	1.88±0.14
AL-5.04	2.42±0.01	2.34±0.03
AL-5.80	2.69±0.03	2.61±0.09
AL-5.94	1.85±0.03	2.14±0.05
Al-6.49	1.97±0.03	2.02±0.07
AL-7.01	2.52±0.03	2.48±0.06

CONCLUSIONS

In the present work we have found quantitative correlation between the value of surface fractal dimension of solid-state samples and thermodynamic parameters of their dehydration. Therefore fractal model was shown to be useful for description of dehydration of highly-dispersed powders.

REFERENCES.

1. A.A.Vertegel, S.V.Kalinin, N.N.Oleynikov, Yu.D.Tretyakov, The fractal particles of iron (III) hydroxonitrate: from solution to solid state, Journal of Non-Crystalline Solids, 181 (1995), 146-150.

2. A.Harrison, Fractals in Chemistry (Oxford University Press, Oxford, 1995) p. 66

3. R. Blakemore, Physics of Solid State, "Mir", Moscow, 1991, pp. 65-68 (in Russian).

ACKNOWLEDGMENTS

This work was partially supported by International Science Foundation (grant No. MPI300), ISSEP grants a-440x and 191_s and Russian Foundation of Fundamental Research (grant No. 93-03-5811).

FRACTAL ANALYSIS OF THE MICROSTRUCTURE OF AISI 304 STEEL.

M. Hinojosa, V. Trejo and U. Ortiz.
DIMAT, Facultad de Ingeniería Mecánica y Eléctrica, Universidad Autónoma de Nuevo León, A.P. 076 suc. F, 66450. San Nicolás de los Garza, N.L. México.

ABSTRACT

The present work reports the results of fractal analysis of the grain boundaries of AISI 304 stainless steel. Microstructure in the non deformed condition is compared against microstructure with 50% tensile strain. Observations were made by optical microscopy, magnifications used were 50, 100, 200, 400, and 1000x. Measurements were made over digitized images using image analysis. Fractal dimension of the grain boundaries were obtained using Richardson plots of perimeter against yardstick length. Our results agree well with reported values for different natural fractal curves. We found that, in general , grains exhibit two different fractal dimensions: one structure dimension that gives information about the morfology of the grain and one texture dimension which accounts for the fine details of the grain boundary.

INTRODUCTION

Fractal Geometry offers new tools for the analysis of microstructural features[1-4]. Natural objects are often too irregular to be described by traditional geometry. Fractal dimension and self-similarity are essential features of a fractal object. Fractal dimension is a measure of the complexity of a figure or the efficiency of a set to fill the metric space in which it lies. For natural curves, fractal dimension can be estimated by several experimental techniques[5]. Fractal analysis assumes that certain microstructural features can be well described as natural fractals with a characteristic fractal dimension that can be measured by simple experimental procedures. Fractal analysis had been applied by a number of workers[6-14] to explore the fractal nature of a variety of microstructural features (fracture surfaces, dislocations, dendrites, carbides, among others). In the present work we apply fractal analysis techniques to describe the microstructure of AISI 304 stainless steel. Grain boundaries are treated and described as natural fractals whose length depends on the magnification used to observe and measure them.

MATERIAL

Samples were obtained from an AISI 304 stainless steel cilindrical bar of the following chemical composition (% wt): 19.94 Cr, 8.55 Ni, 1.3 Mn, 0.06 C.

EXPERIMENTAL

Samples in the non deformed condition, as well as samples with 50% tensile strain were prepared for metallographic observation. Observations were made by optical microscopy using magnifications of 50, 100, 200, 400, and 1000 X. Microstructures were digitized to a resolution of 640 x 480 pixels. Measurements were taken with the aid of an automatic image analizer (Leica Quantimet 520) with calibration factors of 1.904, 0.952, 0.479, 0.239, and 0.095 microns per

Mat. Res. Soc. Symp. Proc. Vol. 407 © 1996 Materials Research Society

pixel. This calibration factor is the yardstick length used to made the measurements at each magnification. For each specimen, measurements of grain boundary length were made over randomly selected grains. Fractal dimensions of the microstructures were obtained using Richardson plots of normalized perimeter against normalized yardstick length. Normalization was made with respect to Feret diameter of the grains.

RESULTS

Fig.1 shows the digitized images of the microstructure of the AISI 304 steel. The effect of plastic deformation is observed as a reduction in grain size, and a higher degree of disorder in the microstructure. *Table I* gives results of the measurements made over a typical grain in particular. The increase in perimeter at progressively higher magnifications is clearly seen. Calibration factors at each magnification are included in this table, along with maximum Feret diameter of the grain. These calibration factors are the yardstick used in the measurements. In order to allow comparison with different natural profiles, measurements and yardstick were normalized with respect to Feret diameter, λ represents the normalized yardstick.

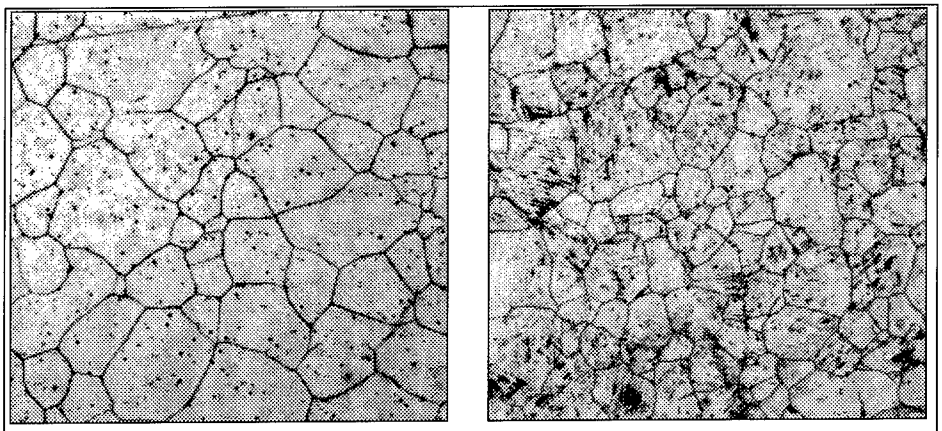


Fig. 1.-Digitized images of the microstructure of AISI 304 stainless steel. 100x.

AISI 304 STEEL , NON DEFORMED CONDITION.				
Magnification	**calibration factor = yardstick length (μm/pixel)**	**perimeter (μm)**	**perimeter (μm)**	**λ (normalized yardstick length)**
50	**1.904**	**223**	**83.4**	**0.02283**
100	**0.952**	**229.5**		**0.01141**
200	**0.479**	**232**		**0.00574**
400	**0.095**	**237**		**0.00286**

Tabla I.- Results obtained over a particular grain in the non deformed samples.

Data obtained were plotted on Richardson plots of normalized perimeter against normalized yardstick length. *Fig. 2* shows the Richardson plot for the grain whose data are presented in *table I*. The linear regression line is included, for this this line $r = 0.986$. From this line , fractal dimension, D, is calculated according to the expression $D = 1 - m$, where m is the slope of the regression line in the Richardson plot. For this grain, fractal dimension was calculated as *1.028*. Similar values were obtained for a number of grains[14], both in the non deformed and the deformed samples.

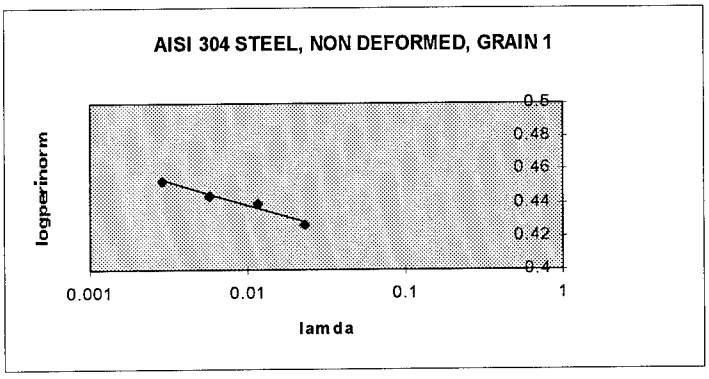


Fig. 2.- Richardson plot for a grain in the non deformed sample."lamda" represents the normalized calibration factor or the normalized yardstick length;"logperinorm" represents the normalized perimeter. For this grain D has value of 1.028.

Fig. 3 shows the Richardson plot for another grain in the non deformed sample, for this grain data were fitted by two different regression lines. Two different fractal dimensions, with values 1.208 and 1.149 were calculated for this grain. A number of grains in both kind of samples showed this behavior.

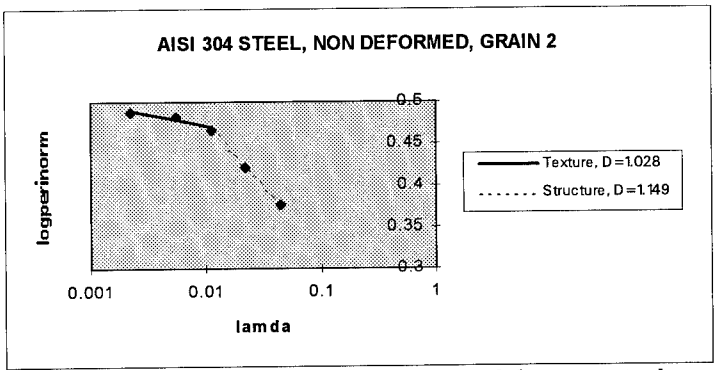


Fig. 3.- Richardson plot for a grain with two different fractal dimensions in the non deformed samples.

Fig. 4 shows the Richardson plots for 5 representative randomly selected grains in the non deformed sample. *Fig. 5* Shows results for another 5 grains, this time in the 50% deformed samples. Data for grains with one fractal dimension, as well as grains with two fractal dimension are included in both figures.

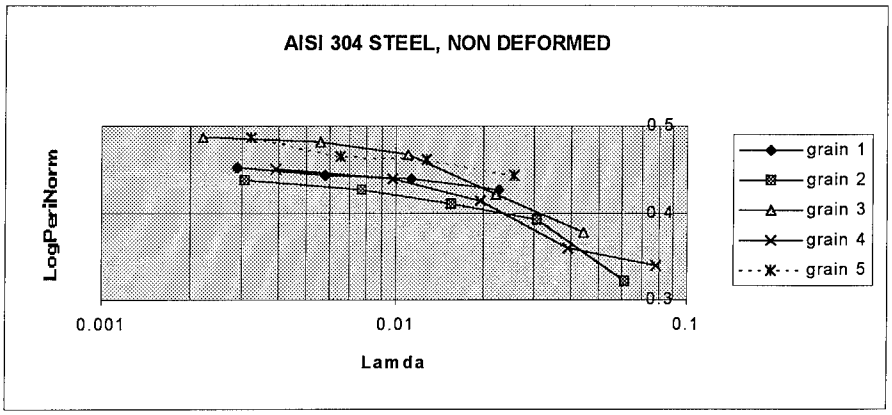


Fig. 4.- Richardson plots for five grains in the non deformed samples.

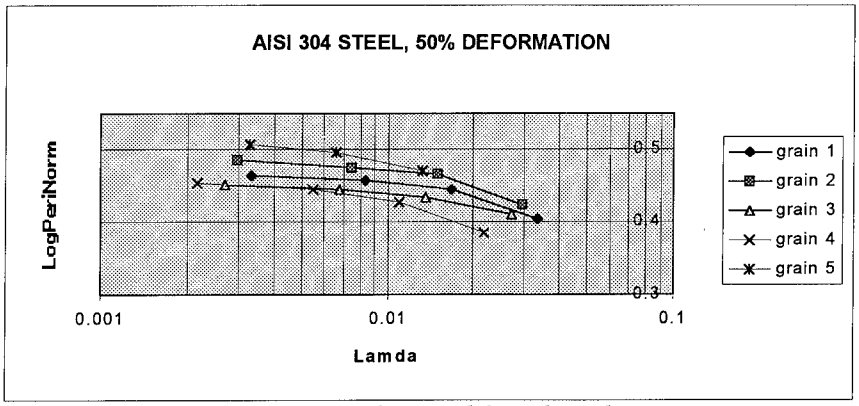


Fig. 5.- Richardson plot for five grains in the 50 % deformed sample.

DISCUSSION

Microstructures analized in this work show austenite grains with boundaries that look quite straigth. However, results of the measurements show that the measured perimeter of grains depends on magnification used, i.e. they exhibit Richardson effect[14]. This fact reveals the fractal character of these grain boundaries. From this result, we can say that grain boundaries on this material can be treated and described as natural fractals.

The use of normalized quantities in Richardson plots allows comparison of the results obtained in grains with different sizes, as well as with results published for different natural fractals. Yardstick

length, λ, was normalized with respect to Feret diameter, and, as can be seen in *figs 3* and *4*, had values in the range 0.001- 0.1. It had been established[5] that in order to obtain adecuate results in applying this fractal analysis, this parameter must take values not greater than 0.3. Our measurements are well below this upper limit. Richardson plot, *fig 2*, for grain 1 in the non deformed sample shows an excellent fit with the regression line, with a value of r = 0.986. This high value is typical and representative of the data analized.

In the case of grain 2, Richardson plot, *fig 3*, shows that these data were well fitted by two regression lines that give two different fractal dimension. The break point of these lines is λ~0.011. For values of λ lower than 0.011, measurements and fractal dimension give information about the fine details of the grain boundary. Using the nomencalture of Kaye[5], we called this dimension "texture dimension". For values of λ higher than 0.011, the corresponding fractal dimension gives information about the general structure and morfology of the grain, this dimension is called "structure dimension", and was observed to take higher values than texture dimension. The values of fractal dimension obtained in this work are of the order of previously reported values for grain boundaries in AISI 316L steel, carbide profiles in tool steels, and several other natural fractal curves. As an example, Kaye[5] reports values in the order of 1.15 for fractal dimension of irregular aggregates of particles of carbon black.

Figs. 4 and *5* show that in this material, in the non deformed condition, as well as in the 50 % deformed condition, there exist two different types of grains: those can can be described with just one fractal dimension and those that exhibit the two fractal dimensions discussed above. The effect of deformation on the fractal structure of the grains is reflected in sligth differences in Richardson plots.

CONCLUSIONS

Grain boundaries in the material analized show statistical self similarity and exhibit Richardson effect in the range of yardstick lengths used in the present work. These facts indicate that grain boundaries can be described as natural fractals with dimension that can be calculated easily with the aid of Richardson plots.

In the microstructures studied, two types of grains were identified: grains with only one fractal dimension and grains with two different fractal dimensions. In the case of grains with two fractal dimensions, texture dimension gives information about the ruggedness of the boundary, whereas structure dimension accounts for the general structure of the grains, and has a greater value than texture dimension. Richardson plots reflects slight differences between the non deformed and the 50% deformed samples.

ACKNOWLEDGMENTS

Authors wish to express their gratitude to CONACYT (National Science and Technology Council) for financial support.

REFERENCES.

1. Mandelbrot, B.B.. *The Fractal Geometry of Nature*. Freeman, New York, 1982.
2. Falconer, K.J. *Fractal Geometry*, John Wiley and sons, 1990.
3. Barnsley, *Fractals Everywhere*. Academic Press, 1988.
4. Peitgen, Jurgens and Saupe. *Chaos and Fractals*. Springer-Verlag, New York, 1992.
5. Kaye, *A Random Walk Through Fractal Dimensions*, VCH Publishers, New York 1994.
6. Hornbogen. E. Trans. ASM, 1961,**53**, 569.
7. Underwood. E. and Banerji. K., Mater. Sci. Eng. **80** (1986) 1.
8. Mitchell M. and Bonell D. . J. Mater. Res., **5**, No 10, Oct 1990. 2244.
9. Richards and Dempsey. Scripta Metallurgica **22**, 1988, p. 687.
10. Gao. H.J. et al. J. Mater. Res., **9**, No. 9, sep 1994, 2216.
11. Mandelbrot, B.B., D.E. Passoja and Paullay A. J. Nature 1984, **308**, 721.
12. Tsuda et al. J.of the Society of Materials Science, Japan/Zayro, **40,** No. 455 Aug 1991 p. 1066.
13. M. Hinojosa, R. Rodríguez and U. Ortiz, MRS Symposium Proceedings vol. **367** "Fractal Aspects of Materials". Materials Research Society.Pittsburgh, 1995. p. 125.
14. M. Hinojosa, doctoral work, Facultad de Ingeniería Mecánica y Eléctrica, Universidad Autónoma de Nuevo León, 1995.
15. Mandelbrot, B.B. , Science 1967, **156**, 636.

AUTHOR INDEX

Abkemeier, Kristin M., 271
Aizawa, Takashi, 197
Aldinger, F., 313
Aliev, Fouad M., 125
Andreozzi, L., 233
Araujo, Mariela, 63
Araujo, Y. Carolina, 325

Balázs, Lazlo, 281, 287
Ballard, Ninja, 365
Barabási, Albert-László, 259, 391
Bardotti, Laurent, 391
Bass, J.D., 209
Beaufils, S., 155
Bertault, M., 155
Blacher, S., 33, 39
Bromann, K., 379
Brouers, F., 33, 39
Brune, H., 379
Butler, B.D., 87

Coddens, G., 155
Colucci, D.M., 227
Condrate, Sr., R.A., 337
Cuerno, R., 259, 307

Dalnoki-Veress, K., 131
Darmstadt, H., 39
Delker, Thomas, 27
Délugeard, Y., 155
Deppe, Denise D., 221
Diez, B., 33
Donati, C., 233
Donley, James P., 15
Doyama, M., 185, 245
Dreyfus, C., 161
Duclos, Franck, 287
Dutcher, J.R., 131
Dzugutov, M., 319

Écolivet, C., 155
Ehrburger-Dolle, Françoise, 399
Eschenazi, Elia V., 365
Español, Pep, 81
Esquivel-Sirvent, R., 99
Etrillard, J., 155
Even, J., 155

Fleury, Vincent, 287
Forrest, J.A., 131
Fuchs, Matthias, 167
Fukumi, Kohei, 179

Gallier, J., 155
Gan, Hao, 203
Gavartin, J.L., 45
Giordano, M., 233
Glass, Gary, 365
Golubovi , Leonardo, 275
Gonzalez, Orlando, 63
Gouyet, J-F., 281
Green, D.H., 99
Grier, David G., 271

Haga, Y., 331
Hanley, H.J.M., 87
Harrington, S.T., 307
Havlin, Shlomo, 57, 391
Heilmann, Ralf K., 239
Hinojosa, M., 411
Hinze, U., 93
Hishita, Shunichi, 197
Hott, Morgan, 27

Inoue, Satoru, 197

Jacobsen, J., 379
Jacobsen, K., 379
Jain, H., 215
Jensen, Pablo, 391
Jeong, Yoon-Hee, 191

Kalinin, S.V., 405
Kaneko, K., 51
Kapoor, Yogendra M., 399
Kern, K., 379
Kieffer, J., 209
Kikukawa, T., 331
King, Peter R., 57
Kitamura, Naoyuki, 179
Kogure, Y., 185, 245
Kopelman, Raoul, 107, 119, 137
Kumar, S., 21
Kunitomi, K., 185
Kurnaz, M. Levent, 71

Larralde, Hernán, 391
Lauritsen, Kent Bækgaard, 295
Lee, D.H., 337
Leporini, D., 233
Lin, Anna L., 107, 137
Liu, Andrea J., 15

Maher, James V., 71
Makihara, Masaki, 179
Makse, Hernan A., 57, 307
Marshall, Guillermo, 355
Masnik, J.E., 209
Masuyama, H., 245
Matsuura, Shu, 301
Matthai, C.C., 45
McKenna, G.B., 227
Miyazima, Sasuke, 301
Mocskos, Pablo, 355
Moon, I.K., 191
Muller, Laura J., 145

Muzny, C.D., 87

Nadtotchi, Vladimir V., 125
Nakamura, Y., 185
Nelson, Keith A., 145
Nickolayev, O., 209
Nittono, O., 331
Nørskov, J., 379
Nukui, Akihiko, 197
Nyquist, Rebecca M., 15

Oleynikov, N.N., 405
Olivella, Martin, 355
Oritz, U., 411

Paradies, H.H., 93
Pengra, David B., 3, 27
Perez-Cardenas, Fernando C., 203
Pfeifer, Peter, 399
Piché, L., 173
Pick, R., 161
Pirard, J.P., 33
Pirard, R., 33
Piscitelle, Louis, 349

Reich, D.H., 21
Rieker, Thomas, 399
Robbins, M.O., 21
Rowat, A.C., 131
Roy, C., 39
Rufflé, B., 155
Russ, S., 253

Sahnoune, A., 173
Sahouli, B., 33, 39
Sapoval, B., 253
Schmidt, Paul W., 399
Schultheisz, C.R., 227
Segars, Ronald, 349
Senturk, U., 337
Setoyama, N., 51
Shiraishi, M., 51
Sigmund, W.M., 313
Sobry, R., 33, 39
Sommer, R., 215
Stanley, H. Eugene, 57, 307, 391
Stevens, J.R., 131
Stoltze, P., 379
Stroeven, P., 343
Suehara, Shigeru, 197
Sugawara, A., 331
Suter, Robert M., 239

Thies, M., 93
Tihon, Ph., 33
Toledo, Pedro G., 325
Tomassone, S., 307
Torkelson, John M., 221
Toudic, B., 155
Toulouse, J., 161, 215
Trejo, V., 411
Tretyakov, Yu.D., 405
Tsega, Yamlak, 365

Van den Bosshe, G., 33, 39
Varner, J.R., 337
Vertegel, A.A., 405
Voss, Daniel J., 399

Wegner, G., 313
Wong, Po-zen, 3, 27

Yamada, Y., 51
Yamamoto, Kazuo, 197
Yamashita, Hiroshi, 179
Yang, Yongwu, 145
Yen, Andrew, 119
Yoshizawa, N., 51

Zúñiga, Ignacio, 81

SUBJECT INDEX

activated carbon system, 51
adhesion, 325
adsorption, 349
aerogel, 33
aggregates, 391
alkali phosphate glass, 155
alpha-relaxation, 221
alumina surfaces, 313
aluminum thin films, 287
amorphous solids, 203
annealing, 287
anomalous relaxation, 63
atomic kinetics, 319
attenuation, 99

binary liquid mixture, 15
biopolymeric interface, 93
Boson peak, 155
Brillouin light scattering, 131, 209

capillary rise, 27
carbon blacks, 39
ceramic slurry, 313
chaotic attractor, 365
colloidal
  silica, 87
  slurry, 313
complex mechanical modulus, 209
compressional waves, 99
computer simulations, 391
concrete, 343
conductance fluctuations, 271
contact
  angle, 325
  lines, 21
coordination number, 197
copper oxides, 93
corrosion, 365
critical depinning transition, 21
crystallization, 331

damage evolution, 343
dealkalization, 337
Debye-Bueche plot, 51
dehydration, 409
dendritic
  growth, 379
  pattern, 379
dense branching morphology, 331
diffusion, 221
  length, 331
  -limited
    aggregation, 45, 379
    reaction, 107
dilute porous media, 15
disordered systems, 63
disperant, 313
dispersing properties, 313
dissipative particle dynamics, 81
dynamic(s), 167
  measurement, 125
  scaling, 239
  specific heat, 191

EAM potential, 245
Eden model, 301
electrokinetic phenomena, 3
electron spin resonance spectroscopy, 233
electroosmosis, 3
electrostatic potential, 355
embedded atom method, 185
encapsulated volume (EV), 275
enthalpy relaxation, 191

far-from-equilibrium dynamics, 275
fcc metals, 245
first-principles molecular orbital
  calculations, 197
fish oil, 313
fluid flow through rocks, 57
fluids in dilute porous media, 15
fluorescence, 221
fractal, 33, 87, 93, 107, 301, 325
  dimension, 107, 343, 365, 405
  pattern, 383
  surfaces, 349
fractality, 253
fractional Debye-Stokes-Einstein law, 233
fracture surface, 343
freely-standing films, 131
front width, 119
fungi, 301

gelation, 87
glass
  state, 185
  structure, 179
  surfaces, 325
  transition, 131, 155, 173, 191,
    203, 221
glasses, 253
global reaction, 119
growing tips, 355
growth
  in two dimensions, 379
  models, 281, 355
  of nanostructures, 391
  pattern formation (GPF), 355

Havriliak-Negami model, 173
heterogeneity exponent, 107

image analysis, 33
imbibition, 27
impedance spectra, 365
in situ measurements, 239
inaccessible pore, 51
infrared spectral changes, 337

initially-segregated reactants, 107
interaction, 313
interface growth equation, 295
ion
  bombardment, 259
  sputtering, 307
irregular boundaries, 253
isotherm model, 349

Kardar-Parisi-Zhang (KPZ) equation, 295, 307
kinetic
  behavior, 405
  rate law, 137
  roughening, 239
Kuramoto-Sivashinsky (KS) equation, 307

Laplace field, 331
Lennard-Jones, 87
light scattering measurement, 125
liposomes, 275
liquid-liquid interface, 21
local production rate, 119
localization, 253
location of reaction center, 119
long-range power-law correlations, 57

melting, 245
microhydrodynamics, 81
mixed solvents, 71
mode coupling theory (MCT), 167
molecular-beam epitaxy (MBE) equation, 295
molecular dynamics, 185
molten salts, 167
Monte Carlo simulations, 137, 379

near-critical mixtures, 15
Nernst-Planck equations, 355
neutron scattering, 155
non-classical kinetics, 107
nonlinear intergrain coupling, 271

one dimension, 137
orbital overlap population, 197
organic additives, 313

passivation, 281
pattern formation, 307
permeability, 3
permeability patterns, 57
phason disorder, 319
phonons, 253
physical aging, 227
pinning, 27
pitting corrosion, 281
polydisperse ensemble, 275
polymer, 221
polymeric liquid crystals, 233
porous
  matrices, 125
  media, 3, 27, 63
  silicon, 45

quantitative model for dehydration, 405
quasicrystal, 319
quenched Xe films, 239
quenching, 185

radial distribution function, 45
Raman scattering, 155
ramified electrochemical deposition, 355
random-field Ising model, 27
random walk, 63
reactant, 107
reaction
  front, 119
  rate, 107
relaxation
  behavior, 173
  dynamics, 319
  process, 125
  time spectrum, 203
reversible aggregation, 71
ripple structure, 259, 307
rotational correlation times, 233
rough surfaces, 307

sandstone, 57
scattering, 93
second viral coefficient, 71
self-affine fractal surfaces, 259
silane films, 325
silica, 287
silica glass, 179
simple liquids, 15
simulation technique, 81
Si-O-Si vibrational band, 337
small-angle
  neutron scattering (SANS), 87
  x-ray scattering (SAXS), 33, 39, 51, 399
small molecule, 221
solid-liquid transition, 245
sputtering, 259
steady state conditions, 137
stereological estimation, 343
stochastic noise, 203
streaming potential, 3
stretched
  exponential, 319
  exponential relaxation function, 179
structural
  relaxation dynamics, 167, 179, 203
  unit, 197
structure, 325
Sun-Guo-Grant (SGG) equation, 295
supercooled liquid, 167, 191
surface
  area, 349
  fractal, 39, 399
  morphology, 365
  plasmon resonance (SPR) spectroscopy, 313
  roughness, 349

tellurite glass, 197
thermoviscoelastic model, 227
thin films, 239
time dependence of rate coefficient, 107
topological disorder, 271
torsional dilatometer, 227
trapping reaction, 137

ultrasonic
  absorption, 99
  modulus, 175
  properties, 99
  velocity, 99

velocity, 99
very dilute colloidal particles, 71
vesicles, 275
vibrational density of states, 45
viscoelastic
  film-guided waves, 131
  model, 209
viscosities, 233
Vogel-Tammann-Fulcher equation, 173
volume recovery, 227
Voronoi, resistor network, 271

Wolf-Villain model, 27

x-ray reflectivity, 239

zero shear rate viscosity, 209
zeta-potential, 3